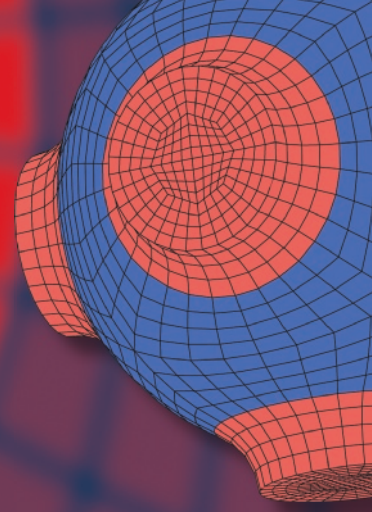


Advanced Structured Materials

Holm Altenbach
Natalia Chinchaladze
Reinhold Kienzler
Wolfgang H. Müller *Editors*



Analysis of Shells, Plates, and Beams

A State of the Art Report

 Springer


Advanced Structured Materials

Volume 134

Series Editors

Andreas Öchsner, Faculty of Mechanical Engineering, Esslingen University of Applied Sciences, Esslingen, Germany

Lucas F. M. da Silva, Department of Mechanical Engineering, Faculty of Engineering, University of Porto, Porto, Portugal

Holm Altenbach , Faculty of Mechanical Engineering, Otto von Guericke University Magdeburg, Magdeburg, Sachsen-Anhalt, Germany

Common engineering materials reach in many applications their limits and new developments are required to fulfil increasing demands on engineering materials. The performance of materials can be increased by combining different materials to achieve better properties than a single constituent or by shaping the material or constituents in a specific structure. The interaction between material and structure may arise on different length scales, such as micro-, meso- or macroscale, and offers possible applications in quite diverse fields.

This book series addresses the fundamental relationship between materials and their structure on the overall properties (e.g. mechanical, thermal, chemical or magnetic etc) and applications.

The topics of *Advanced Structured Materials* include but are not limited to

- classical fibre-reinforced composites (e.g. glass, carbon or Aramid reinforced plastics)
- metal matrix composites (MMCs)
- micro porous composites
- micro channel materials
- multilayered materials
- cellular materials (e.g., metallic or polymer foams, sponges, hollow sphere structures)
- porous materials
- truss structures
- nanocomposite materials
- biomaterials
- nanoporous metals
- concrete
- coated materials
- smart materials

Advanced Structured Materials is indexed in Google Scholar and Scopus.

More information about this series at <http://www.springer.com/series/8611>


Holm Altenbach · Natalia Chinchaladze ·
Reinhold Kienzler · Wolfgang H. Müller
Editors

Analysis of Shells, Plates, and Beams

A State of the Art Report

 Springer

Editors

Holm Altenbach 
Chair of Engineering Mechanics
Institute of Mechanics
Faculty of Mechanical Engineering
Otto von Guericke University Magdeburg
Magdeburg, Sachsen-Anhalt, Germany

Reinhold Kienzler
Universität Bremen
Bremen, Germany

Natalia Chinchaladze
Institute of Applied Mathematics
Tbilisi State University
Tbilisi, Georgia

Wolfgang H. Müller
Institut für Mechanik
TU Berlin
Berlin, Germany

ISSN 1869-8433

ISSN 1869-8441 (electronic)

Advanced Structured Materials

ISBN 978-3-030-47490-4

ISBN 978-3-030-47491-1 (eBook)

<https://doi.org/10.1007/978-3-030-47491-1>

© Springer Nature Switzerland AG 2020

Chapter 20 is licensed under the terms of the Creative Commons Attribution 4.0 International License (<http://creativecommons.org/licenses/by/4.0/>). For further details see license information in the chapter.

This work is subject to copyright. All rights are reserved by the Publisher, whether the whole or part of the material is concerned, specifically the rights of translation, reprinting, reuse of illustrations, recitation, broadcasting, reproduction on microfilms or in any other physical way, and transmission or information storage and retrieval, electronic adaptation, computer software, or by similar or dissimilar methodology now known or hereafter developed.

The use of general descriptive names, registered names, trademarks, service marks, etc. in this publication does not imply, even in the absence of a specific statement, that such names are exempt from the relevant protective laws and regulations and therefore free for general use.

The publisher, the authors and the editors are safe to assume that the advice and information in this book are believed to be true and accurate at the date of publication. Neither the publisher nor the authors or the editors give a warranty, expressed or implied, with respect to the material contained herein or for any errors or omissions that may have been made. The publisher remains neutral with regard to jurisdictional claims in published maps and institutional affiliations.

This Springer imprint is published by the registered company Springer Nature Switzerland AG
The registered company address is: Gewerbestrasse 11, 6330 Cham, Switzerland

*Dedicated to George Jaiani on the occasion
of his 75th birthday.*

Preface



Geoge Jaiani was born on June 19th, 1945 in Tbilisi, Soviet Union (now Republic of Georgia). In 1962, he was graduated from the 55th Tbilisi secondary school with a gold medal. He entered the I. Javakhishvili Tbilisi State University for Mathematics and Mechanics and obtained in January 1968 the diploma of honour in Mechanics. His Ph.D. (Candidate of Sci.) thesis "Some Problems for Prismatic Shells with Cusped Edge" (specialization "Mechanics of Deformable Bodies") he prepared under the supervision of Academician Professor Ilya Vekua at the Razmadze Institute of Mathematics of the Georgian Academy of Sciences. In 1986 he obtained the Doctor of Science

degree at the same institute. The title of the thesis was "Boundary Value Problems for Linear Elliptic Equations with Order Degeneration and Their Applications".

His professional life is mostly related to the I. Javakhishvili Tbilisi State University (TSU). He started in 1968 as post-graduate and in 1971 he became an invited assistant. From 1974 up to 1987 he was the Scientific Secretary of the I. Vekua Institute of Applied Mathematics of the TSU. From 1974 up to 1978 he was an

invited docent (lecturer) of the TSU and from 1981 up to 1988 an invited professor of TSU. In 1989 he received a main research fellow position of the Department of Partial Differential Equations (part-time position) at the I. Vekua Institute of Applied Mathematics (up to 1994). In 1987 he was appointed as the deputy director of the I. Vekua Institute of Applied Mathematics of TSU and later he was elected as the director of this institute. Since 2009 he is also a full professor at the TSU and acts as head of the Chair of Mechanics of the Faculty of Exact and Natural Sciences of the I. Javakhishvili Tbilisi State University.

He supervised 6 Ph.D. thesis (among them was the thesis of one of the editors (N.C.) of this book). He is the author/co-author or editor/co-editor of six monographs, five textbooks, six edited books, and 113 papers (see complete list of publications at <http://www.viam.science.tsu.ge/curi/jaiani/index.html>). His fields of scientific interests are

- Partial Differential Equations,
- Mathematical Modelling,
- Solid Mechanics,
- Solid-Fluid Interaction Problems,
- Shell and Plate Theory.

In particular, his focus is on boundary value problems for singular elliptic and hyperbolic equations and their application to the theory of Cusped Plates and Shells.

In 1978, George Jaiani was awarded the medal and prize of the Georgian Academy of Sciences for young researchers, in 1998 the medal and in 2013 the order of merit of the Georgian president for achievements in scientific and educational activities. During the last 25 years he received several grants, among them a grant of the International Science Foundation (George Soros Foundation) in 1993, a scholarship of the German Academic Exchange Service (DAAD) in 1994, a grant of NATO-CNR (Consiglio Nazionale delle Ricerche, Italy) for the project "Solid-fluid mathematical models describing the stress state of a dam together with its environment under non-ordinary actions" in 1995/6, a grant of the Max-Planck-Gesellschaft for the project "Application of singular integral operators to problems of mathematical physics" (1996), a grant of Ateneo (University of Rome "La Sapienza", 1996), a grant of the DFG (German Science Foundation) for the project "Investigation of cusped bars, plates, and connected with them degenerate ordinary, elliptic and hyperbolic differential equations" (1999), etc. During the last years he obtained several grants from the Ministry of Education and Sciences of Georgia and the Shota Rustaveli National Science Foundation. The project titles were close to his scientific interest, for example,

- Investigation of cusped elastic plate and beam hierarchical models,
- Construction and investigation of hierarchical mathematical models for a medium consisting of deformable solid and fluid parts,
- Some nonclassical problems for thin structures,
- Non-classical problems of fluid-elastic cusped plate (beam) interaction,
- Boundary and initial boundary value problems for hierarchical models for cusped plates,

- Investigations of the theory of elasticity and thermoelasticity for microstructures,
- Some classes of PDE and PDE systems with applications to mechanics and biology,
- Development of analytical and numerical methods for cusped prismatic shells and beams,
- Modeling and calculating of in practice widely-distributed structures with complicated geometry, and
- Construction and investigation of hierarchical models for thermoelastic piezo-electric structures.

George Jaiani is a well-known scientist in Georgia and abroad. Due to his ability of speaking Georgian (native), German, Russian, English, and Italian languages, he has a lot of international contacts. During the last years, he delivered many talks and plenary lectures on national and international conferences and seminars. At the same time, many colleagues from abroad got a deep impression of his hospitality. He was among the organizers and the host of the IUTAM Symposium *On Relation of Shell, Plate, Beam, and 3D Models* (dedicated to the Centenary of Ilia Vekua, April 23-27, 2007, Tbilisi). He was several times invited as Visiting Professor by universities in Germany, Italy, and Poland.

Finally, it should be mentioned that George Jaiani is the chairman of the Georgian National Committee of Theoretical and Applied Mechanics, a member of the International Association of Applied Mathematics and Mechanics [Gesellschaft für Angewandte Mathematik und Mechanik (GAMM)], a member of the Georgian Engineering Academy, a member of the General Assembly of the International Union of Theoretical and Applied Mechanics (IUTAM), since 1994 a member (Academician) of the Georgian Academy of Natural Sciences and since 2002 of the European Academy of Sciences (EurASc), etc.

Last but not least, George Jaiani likes to be with his family: with his lovely wife Natela, with his two children and their families including four grandchildren. Moments with them often serve as starting point for his new scientific ideas.

Magdeburg

Holm Altenbach

Tbilisi

Natalia Chinchaladze

Bremen

Reinhold Kienzler

Berlin

Wolfgang H. Müller

June 2020

List of Publications by George Jaiani (Other transcriptions: Dzhaiani, Dzaiani)

Papers

1. Some Questions Connected with Spherical Functions, Collection of Students Scientific Works, Tbilisi State University, X, 13-18, 1970 (coauthor Z. Siradze, in Russian)
2. On the Deflections of Thin Wedge-shaped Shells, Bulletin of the Academy of Sciences of the Georgian SSR, 65 (3), 543-546, 1972 (in Russian, Georgian and English summaries)
3. On One Problem of an Elastic Wedge-shaped Body, Bulletin of the Academy of Sciences of the Georgian SSR, 70 (3), 557-560, 1973 (in Russian, Georgian and English summaries)
4. On One Problem for the Fourth Order Degenerate Equation, Bulletin of the Academy of Sciences of the Georgian SSR, 75 (1), 17-20, 1974 (in Russian, Georgian and English summaries)
5. On a Wedge-shaped Body Arbitrary Loaded Along the Cusped Edge, Bulletin of the Academy of Sciences of the Georgian SSR, 75 (2), 309-312, 1974 (in Russian, Georgian and English summaries)
6. Arbitrary Loaded Elastic Half-plane Whose Young's Modulus is Power Function of Depth, Materials of the I All-union School in Theory and Numerical Methods in Shell and Plate Theory, Tbilisi University Press, 351-361, 1975 (in Russian)
7. On a Wedge-shaped Shell, Proceedings of X All-union Conference in Shell and Plate Theory, Tbilisi: Metsniereba, 94-101, 1975 (in Russian)
8. Cylindrical Bending of a Rectangular Plate with Power Law Changing Stiffness, Proceedings of Conference of Young Scientists in Mathematics, Tbilisi University Press, 49-52, 1976 (in Russian)
9. Riquier Problems with Weight for a Fourth Order Degenerate Equation, Dokl., Akad. Nauk SSSR, 231 (6), 1285-1288, 1976 (in Russian)
10. Riquier Problems with Weight for a Certain Degenerate Equation of Fourth Order, Soviet Math. Dokl., 17 (6), 1715- 1719, 1976
11. A Generalization of the Poisson Formula in Case of a Half-plane for a Degenerate Equation of Even Order, Dokl. Akad. Nauk SSSR, 235 (6), 1245-1248, 1977 (in Russian)
12. A Generalization of the Half-plane Poisson Formula for a Degenerate Equation of Even Order, Soviet Math. Dokl. 18 (4), 1132-1135, 1977 (in Russian)
13. Bending of a Plate with Power Law Changing Stiffness, Annuaire des Ecoles Supérieures Mécanique Technique, XII (2), 15-19, 1977
14. The Riquier Problem for a Degenerate Equation, Complex Analysis and its Applications, Papers Dedicated to I. Vekua's 70th Anniversary, Moscow: Nauka, 209-216, 1978 (in Russian)

15. On a Generalized Formula of Schwarz in a Case of Half-plane, Proceedings of Tbilisi State University, Cybernetics and Applied Mathematics, 207, 31-37, 1979 (in Russian)
16. On Some Boundary Value Problems for Prismatic Cusped Shells, in Theory of Shells, W.T. Koiter and G.K. Mikhailov (Eds.), North-Holland, 339-343, 1980
17. On a Physical Interpretation of Fichera's Function, Acad. Naz. dei Lincei, Rend. della Sc. Fis. Mat. e Nat., S. VIII, Vol. LXVIII (fasc. 5), 426-435, 1980
18. The Problem V for the Euler-Poisson-Darboux Equation, Reports of Seminar of I. Vekua Institute of Applied Mathematics, 15, 77-83, 1981 (in Russian)
19. Boundary Value Problems of Mathematical Theory of Prismatic Shells with Cusps, Proceedings of All-union Seminar in Theory and Numerical Methods in Shell and Plate Theory, Tbilisi University Press, 126-142, 1984 (in Russian)
20. Problems with Discontinuous Boundary Conditions for the Euler-Poisson-Darboux Equation, Reports of Seminar of I. Vekua Institute of Applied Mathematics, 18, 74-77, 1984 (in Russian)
21. Approximate Solution of Boundary Value Problems in the Case of the Euler-Poisson-Darboux Equation, Reports of Seminar of I. Vekua Institute of Applied Mathematics, 18, 78-82, 1984 (in Russian)
22. On the Behaviour of a Solution of the Vekua Problem for the Euler-Poisson-Darboux Equation in the Half-plane, Reports of Seminar of I. Vekua Institute of Applied Mathematics, 19, 23-26, 1985 (in Russian)
23. On a Non-local Boundary Value Problem for the Euler-Poisson-Darboux Equation in the Half-plane, Papers of Conference on Non-local Problems for Partial Differential Equations, Nalchick University Press, 74, 1986 (in Russian)
24. Weak Extremum Principle for the Euler-Poisson-Darboux Equation, Theses of the XI Conference of Mathematicians of Universities and Colleges of Republic of Georgia, Tbilisi University Press, 193-194, 1986 (in Russian)
25. Formulas of Schwarz Type for a Singular Differential Equation, Bulletin of the Academy of Sciences of the Georgian SSR, 122 (3), 469-472, 1986 (in Russian, Georgian and English summaries)
26. On the Influence of Coefficients of Junior Terms on Posing of Boundary Value Problems for Elliptic Equations with Order Degeneration, Reports of Enlarged Sessions of the Seminar of I. Vekua Institute of Applied Mathematics, 2 (1), 31-34, 1986 (in Russian)
27. The Weighted Dirichlet Problem with Discontinuous Boundary Data for the Euler-Poisson-Darboux Equation in a Half-Plane, Proceedings of I. Vekua Institute of Applied Mathematics, 19, 38-59, 1987 (in Russian)
28. Weighted Boundary Value Problems for a Linear Degenerate Elliptic Equation of Second Order, Uspekhi Matematichskikh Nauk, 42, 4 (256), 174, 1987 (in Russian)
29. Bending of a Prismatic Cusped Shell With Power Law Changing Stiffness, Proceedings of the XIV All-union Conference on Shell and Plate Theories, Tbilisi University Press, 474-479, 1987 (in Russian)

30. Linear Elliptic Equations with Order Degeneration and Prismatic Shells with Cusps, Proceedings of All-union Conference in Modern Problems of Mathematical Physics, Tbilisi University Press, 1, 207-213, 1987 (in Russian)
31. The First Boundary Value Problem of Cusped Prismatic Shell Theory in Zero Approximation of Vekua Theory, Proceedings of I. Vekua Institute of Applied Mathematics, 29, 5-38, 1988 (in Russian, Georgian and English summaries)
32. On the Problem of Behaviour of Solutions of Boundary Value Problems in the Neighbourhood of Discontinuity Points of Boundary Data, Reports of Enlarged Sessions of the Seminar of I. Vekua Institute of Applied Mathematics, 4 (1), 34-37, 1989
33. On a Way of Construction of Solutions of Boundary Value Problems for Higher Order Equations, Rendiconti di Matematica, Serie VII, 10, 717-731, 1990
34. Some Main Boundary Value Problems of the Mathematical Theory of Cusped Prismatic Shells, Collection of Reports of the Scientific Session on the Statics and Dynamics of Thin-Shelled Constructions, Tbilisi, 29,30, 1990 (in Georgian)
35. Problems of Mathematical Physics Connected with Mathematical Modelling of Non-ordinary Events, Abstracts, Seminar on Non-ordinary Events, Tbilisi University Press, 17-19, 1990 (in Georgian)
36. The Generalized Holmgren Problem for the Equation $y\Delta u + bu_y = 0$ in the Case of a Half-circle, Reports of Enlarged Session of the Seminar of I. Vekua Institute of Applied Mathematics of Tbilisi State University, 6 (1), 21-24, 1991
37. On Some Applications of Variational Methods in the Bending Theory of Prismatic Cusped Shells, Proceedings of I. Vekua Institute of Applied Mathematics of Tbilisi State University, 47, 36-44, 1992
38. An Example of Non-unique Solvability of Fichera Problem in the Classical Sense, Reports of Enlarged Session of the Seminar of I. Vekua Institute of Applied Mathematics of Tbilisi State University, 8 (1), 31-34, 1993
39. On a Way of Solution of BVPs for a Class of Third Order Partial Differential Equations, Reports of Enlarged Session of the Seminar of I. Vekua Institute of Applied Mathematics of Tbilisi State University, 10 (1), 32-35, 1995
40. On a Generalization of the Keldysh Theorem, Georgian Mathematical Journal, 2 (3), 291-297, 1995
41. Elastic Bodies with Non-smooth Boundaries – Cusped Plates and Shells, ZAMM-Zeitschrift für Angewandte Mathematik und Mechanik, 76, Supplement 2, 117-120, 1996
42. The Main Boundary Value Problems of Bending of a Cusped Plate in Weighted Sobolev Spaces, Applied Mathematics and Informatics, 1 (1), 78-84, 1996
43. Bending of an Orthotropic Cusped Plate, Theses of Reports, International Symposium on Problems of Continuum Mechanics, Tbilisi: Intelect Publishing House, 17-18, 1997
44. On a Modification of the Lax-Milgram Theorem, Reports of Enlarged Session of the Seminar of I. Vekua Institute of Applied Mathematics of Tbilisi State University, 12 (1), 5-8, 1997
45. On Boundary Value Problems for Conjugate Generalized Harmonic Functions, Ricerche di Matematica, 47, fasc. 2, 231-256, 1998

46. On a Model of a Bar with Variable Thickness, Bull. of TICMI, 2, 36-40, 1998 (<http://www.viam.science.tsu.ge/others/ticmi>)
47. On a Cylindrical Bending of a Prismatic Shell with Two Cusped Edges Under Action of an Ideal Fluid, Bull. of TICMI, 2, 30-34, 1998 (coauthor N. Chinchaladze, <http://www.viam.science.tsu.ge/others/ticmi>)
48. On a Mathematical Model of a Bar with Variable Rectangular Cross-section, Preprint 98/21, Universität Potsdam, Institut für Mathematik, Potsdam, 1998
49. Bending of an Orthotropic Cusped Plate, Preprint 98/23, Universität Potsdam, Institut für Mathematik, Potsdam, 1998
50. Boundary value problems in (1,0) approximation of a mathematical model of bars. Bulletin of TICMI, 3, 7-11, 1999 (<http://www.emis.de/journals/TICMI>)
51. Relation of a Mathematical Model of Bars to the Three-dimensional Theory of Elasticity, Workshop in Partial Differential Equations, University of Potsdam, July 19-23, 1999
52. Bending of an Orthotropic Cusped Plate, Appl. Math. Inform., 4 (1), 29-65, 1999
53. Initial and Boundary Value Problems for Singular Differential Equations and Applications to the Theory of Cusped Bars and Plates, Complex methods for partial differential equations (ISAAC Serials, 6), H. Begehr, O. Celebi, W. Tutschke (Eds.). Kluwer, Dordrecht, 113-149, 1999
54. Oscillation of an Orthotropic Cusped Plate, Reports of Enlarged Session of the Seminar of I.Vekua Institute of Applied Mathematics of Tbilisi State University, 14 (1), 24-31, 1999
55. On a Vibration of an Elastic Cusped Bar, Bull. of TICMI, 4, 24-28, 2000 (coauthor S. Kharibegashvili, <http://www.viam.science.tsu.ge/others/ticmi>)
56. The First Boundary Value Problem for the System of Cusped Prismatic Shells in the First Approximation, Appl. Math. Inform., 5 (2), 26-46, 2000 (with G. Devdariani, S. Kharibegashvili, D. Natroshvili)
57. On a Mathematical Model of Bars with Variable Rectangular Cross-sections, ZAMM-Zeitschrift für Angewandte Mathematik und Mechanik, 81 (3), 147-173, 2001
58. Application of Vekua's Dimension Reduction Method to Cusped Plates and Bars, Bull. TICMI, 5, 27-34, 2001 (<http://www.viam.science/tsu.ge/others/ticmi>)
59. Dynamical Problems in the (0,0) and (1,0) Approximations of a Mathematical Model of Bars. In "Functional-Analytic and complex Methods, Interactions, and Applications to PDEs". Proceedings of the International Graz Workshop, Graz, Austria, 12-16 February, 2001, World Scientific, 188-248, 2001 (with S.S. Kharibegashvili)
60. On a Cusped Elastic Solid-Fluid Interaction Problem, Appl. Math. Inform., 6 (2), 25-64, 2001 (with N. Chinchaladze)
61. Oscillation of Cusped Euler-Bernoulli Beams and Kirchhoff-Love Plates, Preprint 145, Academy of Sciences of the Czech Republic, Mathematical Institute, Prague, 2002 (with A. Kufner)
62. Hierarchical Models for Cusped Plates, Preprint 2002/13, University of Stuttgart, Mathematical Institute A, Stuttgart, 2002 (with S. Kharibegashvili, D. Natroshvili, W.L. Wendland)

63. Static and Dynamical Problems for a Cusped Beam, Proceedings of I. Vekua Institute of Applied Mathematics of Tbilisi State University, 52, 1-29, 2002
64. On the Relation of Hierarchical Models of Cusped Elastic Plates and Beams to the Three-dimensional Models, Reports of the Seminar of I. Vekua Institute of Applied Mathematics, 28, 40-51, 2002
65. Some Remarks Concerning Cusped Plates And Beams, Transactions of the Georgian Technical University, 1 (447), 44-48, Tbilisi, 2003
66. Bending of a Cusped Plate on an Elastic Foundation, Bull. of TICMI, 8, 22-31, 2004 (<http://www.viam.science.tsu.ge/others/ticmi>)
67. Some Degenerate Elliptic Systems and Applications to Cusped Plates, Preprint 2004/27, Universität Potsdam, Institut für Mathematik, Potsdam, 2004 (with B.-W. Schulze)
68. Two-dimensional Hierarchical Models for Prismatic Shells with Thickness Vanishing at the Boundary, Journal of Elasticity, 77 (2), 95-122, 2005 (with S. Kharibegashvili, D. Natroshvili, W.L. Wendland)
69. On Big Deflections of Cusped Plates, Bull. of TICMI, 9, 6-13, 2005 (with N. Chinchaladze, <http://www.viam.science.tsu.ge/others/ticmi>)
70. Oscillation of Cusped Euler-Bernoulli Beams and Kirchhoff-Love Plates, Hacettepe Journal of Mathematics and Statistics, 35 (1), 7-53, 2006 (with A. Kufner)
71. A cusped Prismatic Shell-like Body with the Angular Projection under the Action of a Concentrated Force, Rendiconti Accademia Nazionale delle Scienze detta dei XL, Memorie di Matematica e Applicazioni, 124 0 (2006), Vol. XXX, fasc. 1, 65-82
72. On Some Classes of Special Functions, Proceedings of I. Vekua Institute of Applied Mathematics, 56-57, 1-20, 2006-2007, <http://www.viam.science.tsu.ge/publish/proceed.html>
73. A Cusped Kirchhoff-Love Plate Under the Action of Concentrated Loadings, Reports of Seminar of I. Vekua Institute of Applied Mathematics, 32-33, 1-4, 2006-2007, <http://www.viam.science.tsu.ge/reports.htm>
74. Some Degenerate Elliptic Systems and Applications to Cusped Plates, Mathematische Nachrichten, 280 (4), 388-407, 2007 (with B.-Wolfgang Schulze)
75. Big Deflections of a Cusped Plate with the Flexural Rigidity as a Power Function, Transactions of the International Conference on Problems of Continuum Mechanics, Tbilisi, Georgia, 27-28 October, 2007, 11-13, Tbilisi, 2007 (with N. Chinchaladze)
76. On Boundary Value Problems in Displacements for Hierarchical Models of Cusped Prismatic Shells and Beams, Materials of the International Conference on Non-classic Problems of Mechanics, Kutaisi, Georgia, 25-27 October, 2007, 1, 191-196, Kutaisi, 2007
77. Hierarchical Mathematical Models for Solid-Fluid interaction Problems, Materials of the International Conference on Non-classic Problems of Mechanics, Kutaisi, Georgia, 25-27 October, 2007, 2, 59-64, Kutaisi, 2007 (in Georgian, with N. Chinchaladze)

78. Nonlocal Boundary Value Problem for a System of Singular Differential Equations and Applications to Cusped Prismatic Shells, PAMM–Proceedings in Applied Mathematics and Mechanics, 7 (1), 2090011 – 2090012, 2007
79. A Cusped Prismatic Shell-like Body under the Action of Concentrated Moments, ZAMP-Zeitschrift für Angewandte Mathematik und Physik, 59, 518-536, 2008
80. On a Nonlocal Boundary Value problem for a System of Singular Differential Equations, Applicable Analysis: An International Journal, 87 (1), 83 – 97, 2008
81. Cylindrical Bending of a Cusped Plate with Big Deflections, Sovremennaya Matematika i ee Prilozheniya (Contemporary Mathematics and its Applications), 51, Differential Equations and Their Applications, 2008 (in Russian, with N. Chinchaladze)
82. Existence and Uniqueness Theorems for Cusped Prismatic Shells in the N-th Hierarchical Model, Mathematical Methods in Applied Sciences, 31 (11), 1345-1367, 2008 (with N. Chinchaladze, R. Gilbert, S. Kharibegashvili, D. Natroshvili)
83. On Physical and Mathematical Moments and the Setting of Boundary Conditions for Cusped Prismatic Shells and Beams, Proceedings of the IUTAM Symposium on Relation of Shell, Plate, Beam, and 3D Models, Dedicated to Centenary of Ilia Vekua, 23-27 April, 2007, Tbilisi, Georgia. IUTAM Bookseries, 9, 133-146, G. Jaiani, P. Podio-Guidugli (Eds.). Springer, 2008
84. On a Class of Special Functions, Reports of Enlarged Sessions of the Seminar of I. Vekua Institute of Applied Mathematics, 22, 41-45, 2008, http://www.viam.science.tsu.ge/en_ses.htm
85. Equations with Order Degeneration and Axially Symmetric Solutions of Elliptic Equations. Reports of the Seminar of I. Vekua Institute of Applied Mathematics, 35, 56-59, 2009
86. Cylindrical Bending of a Cusped Plate with Big Deflections, Journal of Mathematical Sciences, 157 (1), 52-69, Springer, 2009, [Translated from Sovremennaya Matematika i ee Prilozheniya (Contemporary Mathematics and its Applications), 51, Differential Equations and Their Applications, 2008] (with N. Chinchaladze)
87. Cusped Elastic Beams under the Action of Stresses and Concentrated Forces. Applicable Analysis, 89 (5), 757–774, 2010 (with N. Chinchaladze, R.P. Gilbert, S. Kharibegashvili, D. Natroshvili)
88. Hierarchical Models for Bi-modular Prismatic Rods. Proceedings of the International Scientific-Technical Conference (June 15-17, 2010, Tbilisi) “Civil Engineering Mechanics Actual Problems” in Scientific-Technical Journal “Building”, 2 (17), 208-210, 2010
89. Cusped Prismatic Shells and Beams. Proceedings of the International Conference (October 4-8, 2010, Dilijan, Armenia) “Topical Problems of Continuum Mechanics”, 2, 286-290, 2010
90. Systems of linear partial differential equations in thin prismatic domains. Reports of Seminar of I. Vekua Institute of Applied Mathematics, vol. 36-37, pp. 1-4, 2010-2011
91. A Remark concerning peculiarities of two models of cusped prismatic shells. Reports of Seminar of I. Vekua Institute of Applied Mathematics, vol. 36-37, pp. 66-79, 2010-2011

92. On Cusped Shell-like Structures. Shell-like Structures: Non-classical Theories Applications in Advanced Structured Materials. Ed.: H. Altenbach and V. Eremeyev, 63-74, 2011
93. Concentrated contact interactions in cuspidate prismatic shell-like bodies, *Archive of Applied Mechanics*, 81 (10), 1487-1505, 2011 (with N. Chinchaladze, B. Maistrenko, and P. Podio-Guidugli)
94. On fundamental and singular solutions of the system of equations of the equilibrium of the plane thermoelasticity theory with microtemperatures, *Bull. of TICMI*, 15, 5-12, 2011, <http://www.viam.science.tsu.ge/others/ticmi/blt/bulletin.htm> (with M. Bacheleishvili, L. Bitsadze)
95. Theorems for the Third and Fourth BVPs of 2D Theory of Thermoelasticity with Microtemperatures, *Mechanics of The Continuous Environment Issues, Dedicated to the 120th Birth Anniversary of Academician Nikoloz Muskhelishvili*, Nova Science Publishers, 99-118, 2012 (with L. Bitsadze)
96. Zero Order Approximation of Hierarchical Models for Elastic Prismatic Shells with Microtemperatures, *Bulletin of TICMI*, 16 (2), 66-73, 2012
97. Explicit Solutions of BVPs of 2D Theory of Thermoelasticity with Microtemperatures for the Half-plane. *Proceedings of I. Vekua Institute of Applied Mathematics*, 61-62, 1-12, 2011-2012 (with L. Bitsadze)
98. A Kirchoff-Love Plate of Variable Flexural Rigidity under the Action of Concentrated Loads, *Information and Computer Technologies - Theory and Practice*, Ed. I. Gorgidze, Nova Science Publishers, Inc., 591-595, 2012.
99. Initial-boundary value problems for solid-fluid composite structures, *Zeitschrift für Angewandte Mathematik und Physik (ZAMP)*, 63 (4), 625-653, 2012 (with N. Chinchaladze, R. Gilbert, S. Kharibegashvili, D. Natroshvili)
100. Some Basic Boundary Value Problems of the Plane Thermoelasticity with Microtemperatures, *Mathematical Methods in the Applied Sciences*, 36 (8), 956-966, 2013 (with L. Bitsadze)
101. Hierarchical Models for Prismatic Shells with Mixed Conditions on Face Surfaces. *Bull. TICMI*, 17 (2), 24-48, 2013
102. On a Model of Layered Prismatic Shells. *Proceedings of I. Vekua Institute of Applied Mathematics*, 63, 13-24, 2013
103. A Boundary-contact Problem for two Rectangularly Linked Elastic Bars, *Bull. of TICMI*, 18 (2), 82-101, 2014
104. Differential Hierarchical Models for Elastic Prismatic Shells with Microtemperatures. *ZAMM-Zeitschrift für Angewandte Mathematik und Mechanik*, 95 (1), 77-90, 2015
105. Antiplane Strain (Shear) of Isotropic Non-Homogeneous Prismatic Shell-Like Bodies. *Bull. of TICMI*, 19 (2), 40-54, 2015
106. A Model of Layered Prismatic Shells. *Continuum Mechanics and Thermodynamics*, 28, 765-784, 2016
107. On basic problems for elastic prismatic shells with microtemperatures. *ZAMM-Zeitschrift für Angewandte Mathematik und Mechanik*, 96 (9), 1082-1088, 2016 (with L. Bitsadze)

108. Vekua type hierarchical models for prismatic shells with mixed conditions on face surfaces. *Composite Structures*, 152, 226-238, 2016
109. On micropolar elastic cusped prismatic shells. *Transactions of A. Razmadze Mathematical Institute*, 170, 376-384, 2016
110. Hierarchical models for viscoelastic Kelvin-Voigt prismatic shells with voids. *Bull. of TICMI*, 21 (2), 33-44, 2017
111. Antiplane strain (shear) of orthotropic non-homogeneous prismatic shell-like bodies. *Archives of Mechanics*, 69 (4-5), 1-12, 2017 (with N. Chinchaladze)
112. Basic problems of thermoelasticity with microtemperatures for the half-space. *Journal of Thermal Stresses*, 41 (9), 1101-1114, 2018 (with L. Bitsadze)
113. On BVPs for piezoelectric transversely isotropic cusped bars. *Bull. of TICMI*, 23 (1), 35-66, 2019

Monographs

1. Solution of some Problems for a Degenerate Elliptic Equation of Higher Order and their Applications to Prismatic Shells, Tbilisi University Press, 1982, 178 p. (in Russian, Georgian and English summaries)
2. Euler-Poisson-Darboux Equation, Tbilisi University Press, 1984, 79 p. (in Russian, Georgian and English summaries)
3. Theory of Cusped Euler-Bernoulli Beams and Kirchoff-Love Plates, Lecture Notes of TICMI, 3, 2002, 132 p. (<http://www.viam.science.tsu.ge/others/ticmi>)
4. Hierarchical Models for Elastic Cusped Plates and Beams, Lecture Notes of TICMI, 4, 2003, 121 p. (with S. Kharibegashvili, D. Natroshvili, W.L. Wendland, <http://www.viam.science.tsu.ge/others/ticmi>)
5. Cusped Shell-like Structures, SpringerBriefs in Applied Science and Technology, Springer-Heidelberg-Dordrecht-London-New York, 2011, 84 p.
6. Piezoelectric Viscoelastic Kelvin-Voigt Cusped Prismatic Shells, Lecture Notes of TICMI, 19, 2018, 83 p.

Textbooks

1. Corso Introduttivo Alle Equazioni Integrali Singolari, Universita degli Studi di Roma "La Sapienza", Dipartimento di Matematica-Istituto "G. Castelnuovo", 1996, 97 p.
2. Mathematical Models of Mechanics of Continua, Tbilisi University Press, Tbilisi, 2004, 338 p. (in Georgian)
3. Advanced Mathematics, Part I: Calculus for Chemistry, Biology, and Life Sciences. Lecture Course, Tbilisi University Press, 2009, 111 p. (in Georgian)

4. Advanced Mathematics, Part II: Differential Models for Chemistry, Biology, and Life Sciences. Lecture Course, Tbilisi University Press, 2009, 127 p. (with N. Chinchaladze, in Georgian)
5. Mathematical Models of Mechanics of Continua (Second Edition), Tbilisi University Press, Tbilisi, 2018, 526 p. (in Georgian)

Electronic Textbooks

1. Equations of Mathematical Physics. Lecture Course, 2007 (in Georgian): <http://www.viam.science.tsu.ge/others/ticmi/lecturecourses/maing.htm>
2. Calculus for Natural Sciences. Lecture Course, 2009 (in Georgian): <http://www.viam.science.tsu.ge/others/ticmi/lecturecourses/maing.htm>
3. Advanced Mathematics, Part I: Calculus (4) for Chemistry, Biology, and Ecology. Lecture Course, 2014 (in Georgian): <http://www.viam.science.tsu.ge/others/ticmi/lecturecourses/maing.htm>
4. Advanced Mathematics, Part II: Differential Models for Chemistry. Lecture Course, 2015 (with N. Chinchaladze, in Georgian): <http://www.viam.science.tsu.ge/others/ticmi/lecturecourses/maing.htm>
5. Differential Equations and Mathematical Physics, 2010 (in Georgian): <http://www.viam.science.tsu.ge/others/ticmi/lecturecourses/maing.htm>
6. Theory of Degenerate Partial Differential Equations, 2012 (in Georgian): <http://www.viam.science.tsu.ge/others/ticmi/lecturecourses/maing.htm>
7. Mathematical Models of Mechanics of Continua, 2015 (in Georgian): <http://www.viam.science.tsu.ge/others/ticmi/lecturecourses/maing.htm>

Edited Books

1. Mathematics, Informatics, and Their Applications in Natural Sciences and Engineering, Springer Proceedings in Mathematics & Statistics, vol. 276, Editors G. Jaiani, D. Natroshvili, Springer, 2019, 175 p.
2. Proceedings of the IUTAM Symposium on Relation of Shell, plate, Beam, and 3D Models, Dedicated to Centenary of Ilia Vekua, 23-27 April, 2007, Tbilisi, Georgia. IUTAM Bookseries, Vol. 9, Editors G. Jaiani, P. Podio-Guidugli. Springer, 2008, 220p.
3. English-Georgian-Russian-German-French-Italian Glossary of Mathematical Terms, Edited by G.V. Jaiani (Compiler: J. Antidze, G. Datashvili, Ts. Gabiskiria, G. Jaiani), Lecture Notes of TICMI, Vol. 6, 2005, 227p.
4. Problems and Examples in Elementary Mathematics, Edited by G.V. Jaiani (Compiler: A. Ambroladze, G. Lobshanidze, N. Mchedlishvili, K. Shvania, T. Sashe-niuk, K. Tsiskaridze, A. Kharazishvili, G. Jaiani, T. Jangveladze), Tbilisi, 1992, 270 p. (in Georgian)

5. *Sovremennye problemy matematicheskoi fiziki. Tom I (Russian) [Current Problems in Mathematical Physics. Vol. I]* Proceedings of All-Union Symposium held in Tbilisi, April 22-25, 1987. Edited by G.V. Jaiani and I.K. Kiguradze. Tbilisi Gos. Universitet, Tbilisi, 1987, 511 p.
6. *Differentsial'nye uravneniya v chastnykh proizvodnykh I ikh prilozhenia. (Russian) [Partial Differential Equations and Their Applications]* Proceedings of All-Union Symposium held in Tbilisi, April 21-23, 1982. Edited by L.G. Magnaradze and G.V. Jaiani. Tbilisi Gos. Universitet, Tbilisi, 1986, 256 p.

Edited Journals

1. Editor of

- a. *Bulletin of TICMI*, Vol. 1 (1997), 2 (1998), 3 (1999), 4 (2000), 5 (2001), 6 (2002), 7 (2003), 8 (2004), 9 (2005), 10 (2006), 11(2007), 12 (2008), 13 (2009), 14 (2010), 15 (2011), 16 No.1, No. 2 (2012), 17 No. 1, 2 (2013), 18 No. 1, 2 (2014), 19 No.1, No. 2 (2015), 20 No.1, No. 2 (2016), 21 No.1, No. 2 (2017), 22 No.1, No. 2 (2018), 22 No.1 (2019), No.2 (2019)
- b. *Lecture Notes of TICMI*, Vol. 1 (2000), 2 (2001), 3 (2002), 4 (2003), 5 (2004), 6 (2005), 7 (2006), 8 (2007), 9 (2008), 10 (2009), 11(2010), 12 (2011), 13 (2012), 14 (2013), 15 (2014), 16 (2015), 17 (2016), 18 (2017), 19 (2018), 20 (2019)

2. Associate Editor of

- a. *Applied Mathematics and Informatics* (since 2003, Vol. 8, No.1 under the title *Applied Mathematics, Informatics, and Mechanics*) Vol. 3 (1998); Vol. 4, No. 1, No. 2 (1999); Vol.5, No. 1, No. 2 (2000); Vol.6, No. 1, No. 2 (2001); Vol. 7, No. 1, No. 2 (2002); Vol. 8, No. 1, No. 2 (2003); Vol. 9, No. 1, No. 2 (2004), Vol. 10, No. 1, No. 2 (2005), Vol. 11, No.1, No. 2 (2006).

Other Publications

1. *Life and Activities of David Gordeziani (with Temur Jangveladze)*. Jaiani G., Natroshvili D. (Eds.) *Mathematics, Informatics, and Their Applications in Natural Sciences and Engineering*. AMINSE 2017. Springer Proceedings in Mathematics & Statistics, vol 276. Springer, Cham, 1-15
2. Third International Conference on "Modern Problems in Applied Mathematics", *Scientific Popular Journal - Mathematics*, No. 5, 4-6, 2018 (with N. Chinchaladze, in Georgian)

3. Second International Conference on "Modern Problems in Applied Mathematics", Scientific Popular Journal - Mathematics, No. 2, 115-118, 2014 (with N. Chinchaladze, in Georgian)
4. I. Vekua Institute of Applied Mathematics of Tbilisi State University – 45, Bull. of TICMI, 18(2), 2014, 3-9 (with N. Avazashvili)
5. Scientific Educational School in Applied Mathematics for Pupils, Scientific Popular Journal - Mathematics, No. 1, 90-92, 2013 (with N. Chinchaladze)
6. "Ilia Vekua", Proceedings of the IUTAM Symposium on Relation of Shell, plate, Beam, and 3D Models Dedicated to Centenary of Ilia Vekua, 23-27 April, 2007, Tbilisi, Georgia. IUTAM Bookseries, Vol. 9, Editors G. Jaiani, P. Podio-Guidugli. Springer, 2008
7. Ilia Vekua's Centenary. Lecture Notes of TICMI, 8, 2007, 3-4 (with R.P. Gilbert)
8. Ilia Vekua's 90th birthday anniversary. International Symposium on Differential Equations and Mathematical Physics (Tbilisi, 1997). Mem. Differential Equations and Math. Phys. 12 (1997), 1-10 (with R. Gilbert, G. Manjavidze)
9. All-Union Symposium "Partial Differential Equations and Their Applications", Differentialnye uravneniya, Vol. 19, 1, 175-176, 1983 (in Russian)

Contents

1	On some Classes of Three-dimensional Dynamic Problems of Plates and Shells and an Asymptotic Method of Solving them	1
	Lenser A. Aghalovyan	
1.1	Introduction	1
1.2	Asymptotic Solutions of Dynamic Problems for Orthotropic Plates	2
1.3	About Mathematically Precise Solutions	7
1.4	About the Boundary Layer	9
1.5	Conclusions	13
	References	13
2	New Hamiltonian Semi-analytical Approach for 3D Solution of Piezoelectric Smart Composites	15
	Orlando Andrianarison and Ayeche Benjeddou	
2.1	Introduction	16
2.2	Problem and Notations	19
2.3	New Mixed Hamiltonian Semi-analytical Solution	21
2.4	Benchmarking Examples	28
	2.4.1 Numerical Convergence Analysis	29
	2.4.2 Square Cantilever PZT Angle-ply Composite Plate	35
	2.4.3 Square SS PZT Angle-ply Composite Plate	36
2.5	Conclusions and Perspectives	38
	References	39
3	On Static Two-dimensional Models of Thermo-electro-magneto-elastic Shells	41
	Gia Avalishvili and Mariam Avalishvili	
3.1	Introduction	42
3.2	Three-dimensional Model	44
3.3	Hierarchical Two-dimensional Models	53
3.4	Conclusions	61
	References	62

4 On Buckling Behavior Of Inhomogeneous Shallow Spherical Caps with Elastically Restrained Edge 65
 Svetlana M. Bauer and Eva B. Voronkova

4.1 Introduction 65
 4.2 Problem Formulation 66
 4.3 Equations for Buckling 69
 4.4 Numerical Results 70
 4.5 Conclusion 72
 Appendix 73
 References 73

5 Some Two-dimensional Non-classical Models of Anisotropic Plates . . 75
 Alexander K. Belyaev, Nikita F. Morozov, Peter E. Tovstik, and Tatyana P. Tovstik

5.1 Introduction 76
 5.2 Kirchhoff–Love and Timoshenko–Reissner Models for a Beam . . . 77
 5.3 Kirchhoff-Love and Timoshenko-Reissner Models of a Transversely Isotropic Plate 79
 5.4 Asymptotic Expansion of Solutions of 3D Equations of Anisotropic Plates 82
 5.5 Transversely Isotropic Plate Heterogeneous in the Thickness Direction 85
 5.6 Multilayered Plates Bending 88
 5.7 General Anisotropic Plate 90
 5.8 Conclusion 92
 References 92

6 Interface Strength Assessments of Sandwich Panels with a Face Sheet/Core Debond 95
 Vyacheslav N. Burlayenko, Holm Altenbach, and Svetlana D. Dimitrova

6.1 Introduction 96
 6.2 Mechanics of Bi-material Interface Cracks 98
 6.3 Numerical Evaluation of Interface Fracture Parameters 101
 6.3.1 Interaction Integral Method (IIM) 101
 6.3.2 Crack Surface Displacements (CSD) Method 102
 6.4 Numerical Solutions 104
 6.4.1 DCB-UBM Sandwich Specimen 104
 6.4.2 DCB Sandwich Specimen 107
 6.4.3 SCB Sandwich Specimen 113
 6.5 Conclusions 117
 References 118

7 Asymptotic Approximations for Frequencies and Vibration Modes of Cylindrical Shell Stiffened by Annular Plates 123
 Sergei B. Filippov

7.1 Introduction 123

7.2	Basic Equations	125
7.3	Boundary Conditions for the Shell's Equations	127
7.4	Asymptotic Solution Corresponding Vibrations of the First Type	129
7.5	Main Continuity Conditions	130
7.6	Example 1	134
7.7	Vibration of the Second Type	135
7.8	Flexural Vibrations of the Plate	137
7.9	Example 2	138
7.10	Conclusions	138
	References	139
8	Free Vibrations of an Open Non-circular Cylindrical Shell of Variable Thickness	141
	Alexander Ya. Grigorenko, Maksym Yu. Borysenko, Olena V. Boychuk, and Larisa Ya. Vasil'eva	
8.1	Introduction	141
8.2	Basic FEM Relations for Natural Vibrations Problems	143
8.3	Solution to the Test Problem	144
8.4	Construction of the Calculation Model	145
8.5	Results of Numerical Calculations	146
8.6	Conclusion	153
	References	154
9	Use of Quadratic Strain Interpolation Functions in a Mixed Quadrilateral Shell Element	155
	Friedrich Gruttmann and Werner Wagner	
9.1	Introduction	155
9.2	Hu–Washizu Variational Formulation	157
9.3	Finite Element Equations	159
9.4	Examples	162
	9.4.1 Membrane and Bending Patch Test	162
	9.4.2 Hemispherical Shell	163
	9.4.3 Cylindrical Shell Segment	164
	9.4.4 Twisted Beam	165
9.5	Conclusions	168
	References	169
10	Development of a Method for Determining One of the Additional Elastic Moduli of Curvilinear Rods	171
	Elena A. Ivanova and Valentina A. Timoshenko	
10.1	Introduction	171
10.2	Basic Equations of the Linear Theory of Curvilinear Rods	172
10.3	Formulation and Solution of the Model Problem	175
10.4	Method for Determining the Elastic Modulus B_{32}	177
10.5	Discussion	182
	References	183

11	Beam Dynamics Using a Generalized Beam Theory Based on the Solution of a Reference Beam Problem	185
	Stephan Kugler, Peter A. Fotiu, and Justin Murín	
11.1	Introduction, Motivation and State of the Art	186
11.2	Preliminaries and Basic Idea of Present Approach	189
11.3	Generalized Beam Model Based on the Reference Beam Problem .	194
	11.3.1 Reference Beam Problem for the Cross-sectional Analysis	194
	11.3.2 Member Analysis Based on Generalized Beam Finite Elements	200
11.4	Examples	203
	11.4.1 Static Analysis of Single Cantilever with an Unsymmetrical Thin-walled Cross-section	203
	11.4.2 Homogeneous Rectangular Hollow Cross-section	205
	11.4.3 Homogeneous Unsymmetrical Thin-walled Multi-cell Cross-section	207
	11.4.4 Hollow Thin-walled Box Cross-section made of Functionally Graded Material	210
11.5	Conclusion	212
	References	213
12	Free Vibration of Flexomagnetic Nanostructured Tubes Based on Stress-driven Nonlocal Elasticity	215
	Mohammad Malikan and Victor A. Eremeyev	
12.1	Introduction	215
12.2	Applied Mathematical Model	216
12.3	Solution of the Equation	220
12.4	Results and Discussions	221
	12.4.1 Results' Validation	221
	12.4.2 Computational Model	221
12.5	Conclusions	224
	References	225
13	Coupled, Thermo-elastic, Large Amplitude Vibration of Bi-material Beams	227
	Emil Manoach, Simona Doneva, and Jerzy Warminski	
13.1	Introduction	227
13.2	Basic Equations	228
	13.2.1 Geometrical Relationships	229
	13.2.2 Constitutive Equations	229
13.3	Field Equations	230
	13.3.1 Governing Equations	230
	13.3.2 Boundary and Initial Conditions	232
	13.3.3 Dimensionless Variables	232
13.4	Numerical Approach	233
	13.4.1 Discretization of the Equation for the Heat Transfer	233
	13.4.2 Algorithm for the Solution of the Beam Vibration Problem	234

13.5	Numerical Examples	235
13.5.1	Eigenfrequencies	236
13.5.2	Beam at Elevated Temperature	236
13.5.3	Beam Subjected to Heat Impact	237
13.6	Discussion and Conclusions	239
	References	241
14	Effect of Longitudinal Variation of Material Properties in Warping	
	Torsion of FGM Beams	243
	Justín Murín, Juraj Hrabovský, Stephan Kugler, Vladimír Kutíš, and Mehdi Aminbaghai	
14.1	Introduction	244
14.2	Non-uniform Torsion FGM Beam Finite Element	245
14.3	Numerical Investigation	251
14.3.1	Case 1 - Polynomial Variation	251
14.3.2	Case 2 - Polynomial Variation	252
14.3.3	Case 3 - Parabolic Variation 1 and 2	253
14.3.4	Elastostatic Analysis of a Cantilever Beam with an I Cross-section, with Longitudinally Varying Material Properties	254
14.3.4.1	Elastostatic Analysis of a Cantilever Beam with an I Cross-section, with Longitudinally Varying Material Properties for the Case 1 and Case 2	256
14.3.4.2	Elastostatic Analysis of a Cantilever Beam with an I Cross-section, with Longitudinally Varying Material Properties for the Case 3	268
14.3.5	Elastostatic Analysis of a Cantilever Beam with a Rectangular Hollow Cross-section, with Longitudinally Varying Material Properties	273
14.3.5.1	Elastostatic Analysis of a Cantilever Beam with a Rectangular Hollow Cross-section, with Longitudinally Varying Material Properties for the Case 1 and Case 2	274
14.3.5.2	Elastostatic Analysis of a Cantilever Beam with a Rectangular Hollow Cross-section, with Longitudinally Varying Material Properties for the Case 3	284
14.4	Summary and Conclusions	288
	Appendix	290
	A.1 Variable polynomial parameters in (14.12)	290
	A.2 Detailed description of the transformation matrix \mathbf{T}	291
	A.3 Coefficients of the stiffness matrix \mathbf{K} and the load vector \mathbf{F} in (14.17)	293
	References	295

15	Laminated Plates with Non-linear Visco-elastic Interlayer: The Governing Equations	297
	Konstantin Naumenko and Holm Altenbach	
15.1	Introduction	297
15.2	Equilibrium Conditions	299
15.3	Constitutive Equations	301
	15.3.1 Skin Layers	301
	15.3.2 Core Layer	302
15.4	Compatibility Conditions and Constraints	303
15.5	Model Reduction	304
15.6	Discussion	307
	References	308
16	Open Circular Hole in a Finite Plate Under Tension Treated by Airy Stress Function Method	311
	Minh Nguyen-Hoang and Wilfried Becker	
16.1	Introduction	311
16.2	Determination of the Stress Field	313
	16.2.1 Fundamentals of the Airy Stress Function	313
	16.2.2 Overview of Used Stress Functions	314
	16.2.3 Stress Function F^{inf} Modelling the Infinite Dimension Problem	315
	16.2.4 Cancellation of Tractions in Load Direction Along Straight Edges	316
	16.2.5 Cancellation of Tractions Perpendicular to the Load Direction Along Straight Edges	318
	16.2.6 Cancellation of Tractions Along Hole Boundary	320
	16.2.7 Overall Iterative Calculation Procedure	322
16.3	Discussion of the Stress Results	325
16.4	Conclusion	328
	References	328
17	Theory of Flexible Mesh-Type Shallow Kirchhoff-Love Structures Based on the Modified Couple Stress Theory	331
	Irina V. Papkova, Jan Awrejcewicz, Anton V. Krysko, Ekatarina Yu. Krylova, and Vadim A. Krysko	
17.1	Introduction	332
17.2	Problem Statement	332
17.3	Governing Equations	334
17.4	Computational Results	341
17.5	Concluding remarks	342
	References	343

18 Buckling of the Nonuniformly Compressed Plate with Dislocations and Disclinations 345
 Isa M. Peshkhoev and Alexander M. Stolyar

18.1 Introduction 346

18.2 Governing Equations 348

18.3 Critical Loads 351

18.4 Behavior of Plate After Loss of Stability 355

18.5 Numerical Results 361

18.6 Conclusion 364

References 364

19 On Null-Lagrangian Energy and Plate Paradoxes 367
 Paolo Podio-Guidugli

19.1 Introduction 367

19.2 Null-Lagrangian Energy in Linear Elasticity 368

19.3 Null-Lagrangian Energy and Plate Paradoxes 369

19.4 Conclusions 371

References 371

20 A Shell Finite Element Model for Superelasticity of Shape Memory Alloys 373
 Luka Porenta, Boštjan Brank, Jaka Dujc, Miha Brojan, and Jaka Tušek

20.1 Introduction 373

20.2 Constitutive Model for SMA 375

20.3 Seven-parameter Shell Model 379

20.4 Numerical Examples 382

20.4.1 Square Wall Under Uniaxial Loading 382

20.4.2 Square Wall Under Biaxial Loading 383

20.4.3 Compression of a Twisted Beam 385

20.5 Conclusions 385

References 386

21 Validity of the Reduced Bending Stiffness Method for Stacked Laminates 389
 Jakob C. Schilling and Christian Mittelstedt

21.1 Introduction 389

21.2 Classical Laminated Plate Theory 392

21.3 Change of Reference Plane 395

21.4 Reduced Bending Stiffness Method 396

21.5 Analytical Solution 397

21.6 Results and Discussion 399

21.6.1 Influence of the Ratio $\frac{t_f}{h}$ 400

21.6.2 Influence of the Number of Layers 405

21.6.3 Influence of the Ratio $\frac{E_1}{E_2}$ 406

21.7 Conclusion 407

References 407

22 Asymptotic Estimate of the Potential Energy of a Plastically Deformed Thin Shell 409
 Milad Shirani and David J. Steigmann

22.1 Introduction 409

22.2 Three-dimensional Theory 411

22.3 Geometric and Kinematic Formulae 413

22.4 Expansion of the Three-dimensional Energy 415

22.5 Optimal Energy 418

References 420

23 On Transverse Shear Strains Treatment in Nine-Node Shell Element MITC9i 421
 Krzysztof Wiśniewski and Ewa Turska

23.1 Introduction 421

23.2 Shell Equations with Drilling Rotation 423

23.2.1 Two-field Functional 423

23.2.2 Reissner-Mindlin Kinematics 423

23.3 Characteristics of MITC9i2 Shell Element 424

23.3.1 Corrected Shape Functions for Nine-node Shell Element . 425

23.3.2 Alternative Version of MITCi Method for Transverse Shear Strains 426

23.3.2.1 Scheme of MITC9i 427

23.3.2.2 Sampling in MITC9i2 428

23.4 Numerical Examples 428

23.4.1 Patch Tests 429

23.4.2 Curved Cantilever 430

23.4.3 Homogeneous circular shell 432

23.4.4 Twisted Beam 435

23.4.5 Pinched Hemispherical Shell with Hole 437

23.5 Final remarks 438

References 438

24 Nonlocal Theory of Plates and Shells Based on Legendre’s Polynomial Expansion 441
 Volodymyr V. Zozulya

24.1 Introduction 442

24.2 3-D Nonlocal Elasticity in Orthogonal Coordinates 445

24.3 Simplification of the 3-D Nonlocal Elasticity in Coordinates Related to the Middle Surface of a Shell 449

24.4 2-D Formulation of the Problem 451

24.5 Higher Order Theory of Nonlocal Plates in Cartesian Coordinates . 456

24.6 Higher Order Theory of Nonlocal Plates in Polar Coordinates . . . 459

24.7 Higher Order Theory of Nonlocal Cylindrical Shell 461

24.8 Higher Order Theory of Nonlocal Spherical Shells 463

24.9 Conclusions 466

References 467

List of Contributors

Lenser A. Aghalovyan
Institute of Mechanics of NAS of Armenia, Marshal Baghramyan Ave. 24/2,
0019 Yerevan, Armenia
e-mail: lagal@sci.am

Holm Altenbach
Lehrstuhl für Technische Mechanik, Institut für Mechanik, Otto-von-Guericke-
Universität Magdeburg, Universitätsplatz 2, 39106 Magdeburg, Germany
e-mail: holm.altenbach@ovgu.de

Mehdi Aminbaghai
Vienna University of Technology, Institute for Mechanics of Materials and
Structures, Karlsplatz 13, 1040 Vienna, Austria
e-mail: mehdi.aminbaghai@tuwien.ac.at

Orlando Andrianarison
Institut Supérieur de l'Automobile et des Transports, 49 rue Mademoiselle
Bourgeois, 58000 Nevers, France
e-mail: orlando.andrianarison@u-bourgogne.fr

Gia Avalishvili
Faculty of Exact and Natural Sciences, I. Javakhishvili Tbilisi State University,
3 I. Tchavtchavadze Ave., 0179 Tbilisi, Georgia
e-mail: gavalish@yahoo.com

Mariam Avalishvili
School of Science and Technology, University of Georgia, 77a M. Kostava St., 0175
Tbilisi, Georgia
e-mail: m.avalishvili@ug.edu.ge

Jan Awrejcewicz
Department of Automation, Biomechanics and Mechatronics, Łódź University of
Technology, 1/15 Stefanowski St., 90-924 Łódź, Poland
e-mail: jan.awrejcewicz@p.lodz.pl

Svetlana M. Bauer

St. Petersburg State University, 7/9 Universitetskaya nab., St. Petersburg, 199034 & Don State Technical University, Research and Education Center (REC) "Materials", Rostov-on-Don, 1 Gagarin sq., 344000, Russian Federation
e-mail: s.bauer@spbu.ru

Wilfried Becker

Fachgebiet Strukturmechanik, TU Darmstadt, Franziska-Braun-Str. 7, 64287 Darmstadt, Germany
e-mail: becker@fsm.tu-darmstadt.de

Alexander K. Belyaev

Institute for Problems in Mechanical Engineering RAS, 61 Bolshoy pr. V. O., 199178 St. Petersburg, Russian Federation
e-mail: 13augen@mail.ru

Ayech Benjeddou

Institut Supérieur de Mécanique de Paris, 3 rue Fernand Hainaut, 93400 Saint Ouen & ROBERVAL, FRE 2012 UTC/CNRS, rue Personne de Roberval, 60200 Compiègne, France
e-mail: benjeddou@supmeca.fr, ayech.benjeddou@utc.fr

Maksym Yu. Borysenko

S.P. Timoshenko Institute of Mechanics, National Academy of Sciences of Ukraine, 3 Nesterova St., 03057 Kyiv, Ukraine
e-mail: mechanics530@gmail.com

Olena V. Boychuk

Nikolaev National Agrarian University, 9 Georgy Gongadze St., 54030 Nikolaev, Ukraine
e-mail: boychuklena@outlook.com

Boštjan Brank

University of Ljubljana, Faculty of Civil and Geodetic Engineering, Jamova c. 2, Ljubljana, Slovenia
e-mail: bbrank@fgg.uni-lj.si

Miha Brojan

University of Ljubljana, Faculty of Mechanical Engineering, Aškerčeva c. 6, Ljubljana, Slovenia
e-mail: miha.brojan@fs.uni-lj.si

Vyacheslav N. Burlayenko

Department of Applied Mathematics, National Technical University KhPI, 2 Kyrpychova str., 61002 Kharkiv, Ukraine
e-mail: burlayenko@yahoo.com

Svetlana D. Dimitrova

Department of Higher Mathematics, National Technical University KhPI, 2 Kyrpychova str., 61002 Kharkiv, Ukraine
e-mail: s.dimitrovaburlayenko@gmail.com

Simona Doneva

Institute of Mechanics, BAS, Acad. G. Bochev Str. Bl. 4, 1113 Sofia, Bulgaria & Lublin University of Technology, Nadbystrzycka 36, 20-618 Lublin, Poland
e-mail: s.doneva@imbm.bas.bg

Jaka Dujc

University of Ljubljana, Faculty of Civil and Geodetic Engineering, Jamova c. 2, Ljubljana, Slovenia
e-mail: jaka.dujc@fgg.uni-lj.si

Victor A. Eremeyev

Department of Mechanics of Materials and Structures, Faculty of Civil and Environmental Engineering, Gdansk University of Technology, 80-233, Gdansk, Poland & Don State Technical University, Gagarina sq., 1, Rostov on Don 344000, Russian Federation
e-mail: victor.eremeev@pg.edu.pl, eremeyev.victor@gmail.com

Sergei B. Filippov

St. Petersburg State University, 7/9 University Embankment, St. Petersburg, 199034, Russian Federation
e-mail: s_b_filippov@mail.ru

Peter A. Fotiu

Department of Applied and Numerical Mechanics, University of Applied Sciences in Wiener Neustadt, Johannes Gutenberg-Straße 3, 2700 Wiener Neustadt, Austria
e-mail: fotiu@fhwn.ac.at

Alexander Ya. Grigorenko

S.P. Timoshenko Institute of Mechanics, National Academy of Sciences of Ukraine, 3 Nesterova St., 03057 Kyiv, Ukraine
e-mail: ayagrigorenko1991@gmail.com

Friedrich Gruttmann

Fachgebiet Festkörpermechanik, Technische Universität Darmstadt, Franziska-Braun-Str. 7, 64287 Darmstadt, Germany
e-mail: gruttmann@mechanik.tu-darmstadt.de

Juraj Hrabovsky

Department of Applied Mechanics and Mechatronics, IAMM FEI STU, Bratislava, Ilkovicova 3, 812 19 Bratislava, Slovakia
e-mail: juraj.hrabovsky@stuba.sk

Elena A. Ivanova

Higher School of Theoretical Mechanics, Peter the Great St.Petersburg Polytechnic University, Polytechnicheskaya, 29, 195251, Saint-Petersburg & Institute for Problems in Mechanical Engineering of Russian Academy of Sciences, Bolshoy pr. V.O., 61, 199178, Saint-Petersburg, Russia
e-mail: elenaivanova239@gmail.com

Ekatarina Yu. Krylova

Department of Mathematic and Computer Modeling, Saratov State University,
83 Astrakhanskaya St., 410012 Saratov, Russian Federation
e-mail: kat.krylova@bk.ru83

Anton V. Krysko

Department of Applied Mathematics and Systems Analysis, Saratov State Technical
University, 77 Politehnicheskaya St., 410054 Saratov, Russian Federation
e-mail: anton.krysko@gmail.com

Vadim A. Krysko

Department of Mathematics and Modeling, Saratov State Technical University, 77
Politekhnicheskaya St., 410054 Saratov, Russian Federation
e-mail: tak@san.ru

Stephan Kugler

University of Applied Sciences, Johannes Gutenberg-Strasse 3, 2700 Wiener
Neustadt, Austria
e-mail: kugler@fhwn.ac.at

Vladimir Kutiš

Department of Applied Mechanics and Mechatronics, IAMM FEI, STU Bratislava,
Ilkovicova 3, 812 19 Bratislava, Slovakia
e-mail: vladimir.kutis@stuba.sk

Mohammad Malikan

Department of Mechanics of Materials and Structures, Faculty of Civil and
Environmental Engineering, Gdansk University of Technology, 80-233, Gdansk,
Poland
e-mail: mohammad.malikan@pg.edu.pl

Emil Manoach

Institute of Mechanics, BAS, Acad. G. Bochev Str. Bl. 4, 1113 Sofia, Bulgaria
e-mail: e.manoach@imbm.bas.bg

Christian Mittelstedt

Technische Universität Darmstadt, Institute for Lightweight Construction and
Design, Otto-Berndt-Straße 2, 64287 Darmstadt, Germany
e-mail: christian.mittelstedt@klub.tu-darmstadt.de

Nikita F. Morozov

St. Petersburg State University, 7/9 University Embankment, St. Petersburg, 199034,
Russian Federation
e-mail: morozov@nm1016.spb.edu

Justín Murín

Department of Applied Mechanics and Mechatronics, IAMM FEI, STU Bratislava,
Ilkovicova 3, 812 19 Bratislava, Slovakia
e-mail: justin.murin@stuba.sk

Konstantin Naumenko

Lehrstuhl für Technische Mechanik, Institut für Mechanik, Otto-von-Guericke-Universität Magdeburg, 39106 Magdeburg, Germany
e-mail: konstantin.naumenko@ovgu.de

Minh Nguyen-Hoang

Fachgebiet Strukturmechanik, TU Darmstadt, Franziska-Braun-Str. 7, 64287 Darmstadt, Germany
e-mail: nguyen-hoang@fsm.tu-darmstadt.de

Irina V. Papkova

Department of Mathematics and Modeling, Saratov State Technical University, 77 Politekhnikeskaya St., 410054 Saratov, Russian Federation
e-mail: ikravzova@mail.ru

Isa M. Peshkoev

Don State Technical University, Rostov-on-Don, Russian Federation
e-mail: peshkoev@gmail.com

Paolo Podio-Guidugli

Accademia Nazionale dei Lincei, Palazzo Corsini – Via della Lungara 10, 00165 Roma, Italy
e-mail: p.podioguidugli@gmail.com

Luka Porenta

University of Ljubljana, Faculty of Mechanical Engineering, Aškerčeva c. 6, Ljubljana, Slovenia
e-mail: luka.porenta@fs.uni-lj.si

Jakob C. Schilling

Technische Universität Darmstadt, Institute for Lightweight Construction and Design, Otto-Berndt-Straße 2, 64287 Darmstadt, Germany
e-mail: jakob.schilling@klub.tu-darmstadt.de

Milad Shirani

Department of Mechanical Engineering, University of California, Berkeley, CA 94720, USA
e-mail: milad_shirani@berkeley.edu

David J. Steigmann

Department of Mechanical Engineering, University of California, Berkeley, CA 94720, USA
e-mail: dsteigmann@berkeley.edu

Alexander M. Stolyar

Southern Federal University, Rostov-on-Don, Russian Federation
e-mail: ajoiner@mail.ru

Valentina A. Timoshenko

Higher School of Theoretical Mechanics, Peter the Great St.Petersburg Polytechnic University, Polytechnicheskaya, 29, 195251, Saint-Petersburg, Russia
e-mail: alya.tim.2012@mail.ru

Peter E. Tovstik
St. Petersburg State University, 7/9 University Embankment, St. Petersburg, 199034,
Russian Federation
e-mail: peter.tovstik@mail.ru

Tatyana P. Tovstik
Institute for Problems in Mechanical Engineering RAS, 61 Bolshoy pr. V. O.,
199178 St. Petersburg, Russian Federation
e-mail: tovstik_t@mail.ru

Ewa Turska
Polish Japanese Academy of Information Technology, Warsaw, Poland
e-mail: eturska@pjwstk.edu.pl

Jaka Tušek
University of Ljubljana, Faculty of Mechanical Engineering, Aškerčeva c. 6,
Ljubljana, Slovenia
e-mail: jaka.tusek@fs.uni-lj.si

Larisa Ya. Vasil'eva
V. O. Sukhomlinsky Nikolaev National University, 24 Nikolskaya St.,
54030 Nikolaev, Ukraine
e-mail: lara@vasiliev.mk.ua

Eva B. Voronkova
St. Petersburg State University, 7/9 Universitetskaya nab., St. Petersburg, 199034 &
Don State Technical University, Research and Education Center (REC) "Materials",
Rostov-on-Don, 1 Gagarin sq., 344000, Russian Federation
e-mail: e.voronkova@spbu.ru

Werner Wagner
Institut für Baustatik, Karlsruher Institut für Technologie, Kaiserstr. 12,
76131 Karlsruhe, Germany
e-mail: werner.wagner@kit.edu

Jerzy Warminski
Lublin University of Technology, Nadbystrzycka 36, 20-618 Lublin, Poland
e-mail: j.warminski@pollub.pl

Krzysztof Wiśniewski
Institute of Fundamental Technological Research, Polish Academy of Sciences,
Warsaw, Poland
e-mail: kwisn@ippt.pan.pl

Volodymyr Zozulya
Centro de Investigacion Cientifica de Yucatan, A.C., Calle 43, No 130, Colonia:
Chuburna de Hidalgo, C.P. 97200, Merida, Yucatan, Mexico
e-mail: zozulya@cicy.mx



Chapter 1

On some Classes of Three-dimensional Dynamic Problems of Plates and Shells and an Asymptotic Method of Solving them

Lenser A. Aghalovyan

Abstract The equations of the dynamic problem of the theory of elasticity, written in dimensionless coordinates and displacements, are singularly perturbed relatively with a geometric small parameter. For solving the corresponding system of differential equations, the asymptotic method turned effective. The asymptotic solutions of three classes of dynamical problems with classical boundary conditions were found. The amplitudes of the forced oscillations were determined. The conditions for the appearance of resonance were established and when the asymptotic solution become mathematically exact. The procedure for constructing a solution for a boundary layer in orthotropic plates and its conjugation with the solution of an external problem was described.

Key words: Orthotropic plates and shells · Spatial problems · Forced vibrations · Asymptotic solution · Resonance

1.1 Introduction

The classical theory of plates and shells of Kirchhoff-Love and the more precise theories of Reissner, Ambartsumian, and the Timoshenko type consider only one class of problems, although it is very wide when the values of the corresponding components of the stress tensor are specified on the facial surfaces of a thin body, such as beams, plates, and shells (conditions of the first boundary value problem of the theory of elasticity). If on the facial surfaces of a thin body the conditions of the second or mixed boundary value problems of elasticity theory were given, we have proved that to solve such problems the hypotheses of the classical and refined theories were not applicable.

Lenser A. Aghalovyan
Institute of Mechanics of NAS of Armenia, Marshal Baghramyan Ave. 24/2, 0019 Yerevan, Armenia
e-mail: lagal@sci.am

Apparently for this reason, for a long time, these tasks, which are very important for applications, have not been solved. We have found a fundamentally new asymptotics for the components of the stress tensor and displacement vector, allowing to solve these classes of problems, as well as new classes of problems of statics and dynamics of thin bodies, including layered, based on the asymptotic method for solving singularly perturbed differential equations.

The equations of elasticity theory for thin bodies (beams, rods, plates, shells), written in dimensionless coordinates and displacements are singularly perturbed by a small geometrical characteristic parameter. For solving such equations and systems of differential equations, the asymptotic method turned out effective. The solution consists of an external problem (I^{out}) and a boundary layer problem (I_b). The solution to an external problem is sought in the form of a specific series in a small geometric parameter $\varepsilon = h/l$, where h – half thickness, l - characteristic tangential size of the thin body:

$$I^{\text{out}} = \varepsilon^{q_I + s} I^{(s)}, \quad s = \overline{0, N} \quad (1.1)$$

where q_I – intensity (order) of the corresponding desired q quantity, N - number of approximations. The values q_I are set in this way, so that after substituting (1.1) into equations transformed to dimensionless, we obtain a consistent system for determining $I^{(s)}$. Finding non-contradictory values q_I – is the most difficult moment when using the asymptotic method. In the case of the first boundary value problem of the theory of elasticity (classical theory) for isotropic and anisotropic plates, it was established (Gol'denveizer, 1962; Aghalovyan, 2015)

$$q_{\sigma_{xx}, \sigma_{xy}, \sigma_{yy}} = -2, \quad q_{\sigma_{xz}, \sigma_{yz}} = -1, \quad q_{\sigma_{zz}} = 0, \quad q_{\sigma_{u,v}} = -2, \quad q_w = -3 \quad (1.2)$$

In the case of the second and mixed boundary value problems for beams and plates, we established (Aghalovyan, 2015, 1982)

$$q_{\sigma_{ij}} = -1, \quad q_{u,v,w} = 0 \quad (1.3)$$

Asymptotics (1.1), (1.2) and (1.1), (1.3) remains valid for layered beams and plates. The corresponding boundary value problems of statics solved in (Aghalovyan, 2015; Aghalovyan and Gevorgyan, 2005).

When solving dynamic problems of thin bodies, as usual, inertial terms simplified by the adoption of hypotheses are formally added to the equations of the classical theory. As a result of this, below, based on the solution of the corresponding spatial dynamic problem, we make sure that the nature of the oscillatory process along the transverse coordinate distorted.

1.2 Asymptotic Solutions of Dynamic Problems for Orthotropic Plates

Let us assume that the plate occupies the area

$$Z = \{(x, y, z) : 0 \leq x \leq a, 0 \leq y \leq b, -h \leq z \leq h, \min(a, b) = l, h \ll l\}.$$

Consider the steady vibrations of an orthotropic plate caused by harmonically varying in time external influences.

It is required to find a solution to the equations of the three-dimensional problem of the theory of elasticity:

- equations of motion

$$\frac{\partial \sigma_{jx}}{\partial x} + \frac{\partial \sigma_{jy}}{\partial y} + \frac{\partial \sigma_{jz}}{\partial z} = \rho \frac{\partial^2 u}{\partial t^2} \quad (j = x, y, z; u, v, w), \quad (1.4)$$

- relations of elasticity of an orthotropic body (generalized Hooke's law)

$$\begin{aligned} \frac{\partial u}{\partial x} &= a_{11}\sigma_{xx} + a_{12}\sigma_{yy} + a_{13}\sigma_{zz}, & (x, y, z, 1, 2, 3, u, v, w); \\ \frac{\partial u}{\partial y} + \frac{\partial v}{\partial x} &= a_{66}\sigma_{xy}, \quad \frac{\partial w}{\partial x} + \frac{\partial u}{\partial z} = a_{55}\sigma_{xz}, \quad \frac{\partial w}{\partial y} + \frac{\partial v}{\partial z} = a_{44}\sigma_{yz} \end{aligned} \quad (1.5)$$

under the following, of the most interest to applications, variants boundary conditions:

- plate vibrations caused by applied to its facial surfaces normal and tangential loads

$$\sigma_{jz}(x, y, \pm h) = \pm \sigma_{jz}^{\pm}(x, y) \exp(i\Omega t), \quad j = x, y, z \quad (1.6)$$

- vibrations of a plate fixed with absolutely rigid flat base

$$u(x, y, -h) = v(x, y, -h) = w(x, y, -h) = 0, \quad (1.7)$$

$$\sigma_{jz}(x, y, h) = \sigma_{jz}^{+}(x, y) \exp(i\Omega t), \quad j = x, y, z \quad (1.8)$$

or

$$u(x, y, h) = u^{+}(x, y) \exp(i\Omega t), \quad (u, v, w) \quad (1.9)$$

- plate vibrations caused by a displacement vector applied to the facial surface $z = -h$

$$u(x, y, -h) = u^{-}(x, y) \exp(i\Omega t), \quad (u, v, w), \quad (1.10)$$

$$\sigma_{jz}(x, y, h) = 0, \quad j = x, y, z \quad (1.11)$$

or

$$u(x, y, h) = 0, \quad (u, v, w) \quad (1.12)$$

where $\sigma_{jz}^{\pm h}, u^{\pm h}, v^{\pm h}, w^{\pm h}$ - given functions, Ω - frequency of external coercive influence.

Since the process is steady, solving of systems of Eqs. (1.4), (1.5) we will sought in the form

$$\begin{aligned}\sigma_{\alpha\beta}(x, y, z, t) &= \sigma_{jk}(x, y, z) \exp(i\Omega t), & \alpha, \beta &= x, y, z; j, k = 1, 2, 3, \\ u(x, y, z, t) &= \bar{u}(x, y, z) \exp(i\Omega t), & (u, v, w).\end{aligned}\quad (1.13)$$

Substituting (1.13) into Eqs. (1.4), (1.5) and passing to dimensionless coordinates and displacements

$$\xi = \frac{x}{l}, \quad \eta = \frac{y}{l}, \quad \zeta = \frac{z}{h}, \quad U = \frac{\bar{u}}{l}, \quad V = \frac{\bar{v}}{l}, \quad W = \frac{\bar{w}}{l}, \quad (1.14)$$

we obtain a system singularly perturbed by a small parameter $\varepsilon = h/l$:

$$\begin{aligned}\frac{\partial \sigma_{11}}{\partial \xi} + \frac{\partial \sigma_{12}}{\partial \eta} + \varepsilon^{-1} \frac{\partial \sigma_{13}}{\partial \zeta} + \varepsilon^{-2} \Omega_*^2 U &= 0, \\ \frac{\partial \sigma_{12}}{\partial \xi} + \frac{\partial \sigma_{22}}{\partial \eta} + \varepsilon^{-1} \frac{\partial \sigma_{23}}{\partial \zeta} + \varepsilon^{-2} \Omega_*^2 V &= 0, \\ \frac{\partial \sigma_{13}}{\partial \xi} + \frac{\partial \sigma_{23}}{\partial \eta} + \varepsilon^{-1} \frac{\partial \sigma_{33}}{\partial \zeta} + \varepsilon^{-2} \Omega_*^2 W &= 0, \\ \frac{\partial U}{\partial \xi} &= a_{11} \sigma_{11} + a_{12} \sigma_{22} + a_{13} \sigma_{33}, \\ \frac{\partial V}{\partial \eta} &= a_{12} \sigma_{11} + a_{22} \sigma_{22} + a_{23} \sigma_{33}, \\ \varepsilon^{-1} \frac{\partial W}{\partial \zeta} &= a_{13} \sigma_{11} + a_{23} \sigma_{22} + a_{33} \sigma_{33}, \\ \frac{\partial W}{\partial \xi} + \varepsilon^{-1} \frac{\partial U}{\partial \zeta} &= a_{55} \sigma_{13}, \\ \frac{\partial W}{\partial \eta} + \varepsilon^{-1} \frac{\partial V}{\partial \zeta} &= a_{44} \sigma_{23}, \\ \frac{\partial V}{\partial \xi} + \frac{\partial U}{\partial \eta} &= a_{66} \sigma_{12},\end{aligned}\quad (1.15)$$

where $\Omega_*^2 = \rho h^2 \Omega^2$, ρ – density. We obtain a non-contradictory system for determining all quantities in an external problem if expansion (1.1) will has the form

$$\begin{aligned}\sigma_{jk}^{(\text{out})} &= \varepsilon^{-1+s} \sigma_{jk}^{(s)}(\xi, \eta, \zeta), \quad j, k = 1, 2, 3, s = \overline{0, N}, \\ (U^{(\text{out})}, V^{(\text{out})}, W^{(\text{out})}) &= \varepsilon^s (U^s, V^s, W^s),\end{aligned}\quad (1.16)$$

where the designation $s = \overline{0, N}$ means that little by little (by repeating) index s is taken place summed over integer values from zero to N . Formula (1.16) shows that asymptotic (1.1), (1.3) turned out universal for solving the dynamic problems, formulated above for all classes (1.6) - (1.12), while in static problems (1.2), (1.3) asymptotics are fundamentally different.

By substituting (1.16) into system (1.15) and equating the coefficients in each equation for the same degree ε , we will obtain a system for determining $\sigma_{jk}^{(s)}, U^{(s)}, V^{(s)}$,

$W^{(s)}$. From this system, all stresses can be expressed through displacements by formulas

$$\begin{aligned}
 \sigma_{13}^{(s)} &= \frac{1}{a_{55}} \left(\frac{\partial U^{(s)}}{\partial \zeta} + \frac{\partial W^{(s-1)}}{\partial \xi} \right), & \sigma_{23}^{(s)} &= \frac{1}{a_{44}} \left(\frac{\partial V^{(s)}}{\partial \zeta} + \frac{\partial W^{(s-1)}}{\partial \eta} \right), \\
 \sigma_{12}^{(s)} &= \frac{1}{a_{66}} \left(\frac{\partial V^{(s-1)}}{\partial \xi} + \frac{\partial U^{(s-1)}}{\partial \eta} \right), & Q^{(m)} &\equiv 0 \quad \text{when } m < 0 \\
 \sigma_{11}^{(s)} &= -A_{23} \frac{\partial W^{(s)}}{\partial \zeta} + A_{22} \frac{\partial U^{(s-1)}}{\partial \xi} - A_{12} \frac{\partial V^{(s-1)}}{\partial \eta}, \\
 \sigma_{22}^{(s)} &= -A_{13} \frac{\partial W^{(s)}}{\partial \zeta} - A_{12} \frac{\partial U^{(s-1)}}{\partial \xi} + A_{33} \frac{\partial V^{(s-1)}}{\partial \eta}, \\
 \sigma_{33}^{(s)} &= A_{11} \frac{\partial W^{(s)}}{\partial \zeta} - A_{23} \frac{\partial U^{(s-1)}}{\partial \xi} - A_{13} \frac{\partial V^{(s-1)}}{\partial \eta},
 \end{aligned} \tag{1.17}$$

where

$$\begin{aligned}
 A_{11} &= \frac{a_{11}a_{22} - a_{12}^2}{\Delta}, & A_{22} &= \frac{a_{22}a_{23} - a_{23}^2}{\Delta}, & A_{33} &= \frac{a_{11}a_{33} - a_{13}^2}{\Delta}, \\
 A_{13} &= \frac{a_{11}a_{23} - a_{12}a_{13}}{\Delta}, & A_{23} &= \frac{a_{22}a_{13} - a_{12}a_{23}}{\Delta}, & A_{12} &= \frac{a_{12}a_{33} - a_{13}a_{23}}{\Delta}, \\
 \Delta &= a_{11}a_{22}a_{33} + 2a_{12}a_{13}a_{23} - a_{11}a_{23}^2 - a_{22}a_{13}^2 - a_{33}a_{12}^2
 \end{aligned} \tag{1.18}$$

and for determining $U^{(s)}, V^{(s)}, W^{(s)}$ we obtain the equations

$$\begin{aligned}
 \frac{\partial^2 U^{(s)}}{\partial \zeta^2} + a_{55} \Omega_*^2 U^{(s)} &= R_U^{(s)}, \\
 R_U^{(s)} &= -\frac{\partial^2 W^{(s-1)}}{\partial \xi \partial \zeta} - a_{55} \left(\frac{\partial \sigma_{11}^{(s-1)}}{\partial \xi} + \frac{\partial \sigma_{12}^{(s-1)}}{\partial \eta} \right),
 \end{aligned} \tag{1.19}$$

$$\begin{aligned}
 \frac{\partial^2 V^{(s)}}{\partial \zeta^2} + a_{44} \Omega_*^2 V^{(s)} &= R_V^{(s)}, \\
 R_V^{(s)} &= -\frac{\partial^2 W^{(s-1)}}{\partial \eta \partial \zeta} - a_{44} \left(\frac{\partial \sigma_{12}^{(s-1)}}{\partial \xi} + \frac{\partial \sigma_{22}^{(s-1)}}{\partial \eta} \right),
 \end{aligned} \tag{1.20}$$

$$\begin{aligned}
 A_{11} \frac{\partial^2 W^{(s)}}{\partial \zeta^2} + \Omega_*^2 W^{(s)} &= R_W^{(s)}, \\
 R_W^{(s)} &= A_{23} \frac{\partial^2 U^{(s-1)}}{\partial \xi \partial \zeta} + A_{13} \frac{\partial^2 V^{(s-1)}}{\partial \eta \partial \zeta} - \left(\frac{\partial \sigma_{13}^{(s-1)}}{\partial \xi} + \frac{\partial \sigma_{23}^{(s-1)}}{\partial \eta} \right)
 \end{aligned} \tag{1.21}$$

The solutions of Eqs. (1.19) - (1.21) are

$$U^{(s)} = U_0^{(s)}(\xi, \eta, \zeta) + U_\tau^{(s)}(\xi, \eta, \zeta), \quad (U, V, W), \tag{1.22}$$

where the first term is the solution of the homogeneous equation, the second term is the particular solution of the inhomogeneous equation. Solutions of homogeneous equations are

$$\begin{aligned} U_0^{(s)} &= C_1^{(s)}(\xi, \eta) \sin \gamma_1 \zeta + C_2^{(s)}(\xi, \eta) \cos \gamma_1 \zeta, \quad \gamma_1 = \Omega_* \sqrt{a_{55}}, \\ V_0^{(s)} &= C_3^{(s)}(\xi, \eta) \sin \gamma_2 \zeta + C_4^{(s)}(\xi, \eta) \cos \gamma_2 \zeta, \quad \gamma_2 = \Omega_* \sqrt{a_{44}}, \\ W_0^{(s)} &= C_5^{(s)}(\xi, \eta) \sin \gamma_3 \zeta + C_6^{(s)}(\xi, \eta) \cos \gamma_3 \zeta, \quad \gamma_3 = \Omega_* (\sqrt{A_{11}})^{-1}. \end{aligned} \quad (1.23)$$

Having the values (1.22), (1.23) of displacements, stresses are calculated by formulas (1.17). Then satisfying each of the groups of boundary conditions (1.6) - (1.12), uniquely determined the unknown integration functions $C_j^{(s)}(\xi, \eta)$ and the final solution of the external problem. Let us give this solution corresponding to conditions (1.6)

$$\begin{aligned} U^{(s)} &= \frac{-a_{55}}{\gamma_1 \sin 2\gamma_1} \left\{ \left[\sigma_{xz}^{+(s)} - \sigma_{13\tau}^{(s)}(\xi, \eta, 1) \right] \cos(1 + \zeta) \gamma_1 \right. \\ &\quad \left. + \left[\sigma_{xz}^{-(s)} + \sigma_{13\tau}^{(s)}(\xi, \eta, -1) \right] \cos(1 - \zeta) \gamma_1 \right\} + U_\tau^{(s)}(\xi, \eta, \zeta), \\ \sigma_{13}^{(s)} &= \frac{1}{\sin 2\gamma_1} \left\{ \left[\sigma_{xz}^{+(s)} - \sigma_{13\tau}^{(s)}(\xi, \eta, 1) \right] \sin(1 + \zeta) \gamma_1 \right. \\ &\quad \left. - \left[\sigma_{xz}^{-(s)} + \sigma_{13\tau}^{(s)}(\xi, \eta, -1) \right] \sin(1 - \zeta) \gamma_1 \right\} + \sigma_{13\tau}^{(s)}(\xi, \eta, \zeta), \\ W^{(s)} &= -\frac{1}{A_{11} \gamma_3 \sin 2\gamma_3} \left\{ \left[\sigma_{zz}^{+(s)} - \sigma_{33\tau}^{(s)}(\xi, \eta, 1) \right] \cos(1 + \zeta) \gamma_3 \right. \\ &\quad \left. + \left[\sigma_{zz}^{-(s)} + \sigma_{33\tau}^{(s)}(\xi, \eta, -1) \right] \cos(1 - \zeta) \gamma_3 \right\} + W_\tau^{(s)}(\xi, \eta, \zeta), \\ \sigma_{33}^{(s)} &= \frac{1}{\sin 2\gamma_3} \left\{ \left[\sigma_{zz}^{+(s)} - \sigma_{33\tau}^{(s)}(\xi, \eta, 1) \right] \sin(1 + \zeta) \gamma_3 \right. \\ &\quad \left. - \left[\sigma_{zz}^{-(s)} + \sigma_{33\tau}^{(s)}(\xi, \eta, -1) \right] \sin(1 - \zeta) \gamma_3 \right\} + \sigma_{33\tau}^{(s)}(\xi, \eta, \zeta), \\ \sigma_{xz}^{\pm(0)} &= \varepsilon \sigma_{xz}^\pm, \quad \sigma_{xz}^{\pm(s)} = 0, \quad s \neq 0, (x, y, z) \end{aligned} \quad (1.24)$$

The formula for $V^{(s)}, \sigma_{23}^{(1)}$ can be obtained from cyclic permutation

$$(u, v; a_{55}, a_{44}; xz, yz; 13, 23; \gamma_1, \gamma_2).$$

The final solution, corresponding to this case is determined by formulas (1.13), (1.16), (1.24). The solution will be finite if $\sin 2\gamma_1 \neq 0; \sin 2\gamma_2 \neq 0; \sin 2\gamma_3 \neq 0$. If any of these conditions be broken resonance will occur. The resonant frequencies coincide with the frequencies of the natural oscillations of the plate.

We also give a solution to problem (1.10), (1.11), simulating the effect of a seismic wave on the foundation of a structure:

$$\begin{aligned}
U^{(s)} &= \frac{1}{\cos 2\gamma_1} \left[u^{-(s)} - U_\tau^{(s)}(\xi, \eta, -1) \right] \cos \gamma_1 (1 - \zeta) \\
&\quad - \frac{a_{55}}{\gamma_1} \sigma_{13\tau}^{(s)}(\xi, \eta, 1) \sin(1 + \zeta) \gamma_1 + U_\tau^{(s)}(\xi, \eta, \zeta), \quad (u, v; a_{55}, a_{44}; 1, 2), \\
W^{(s)} &= \frac{1}{\cos 2\gamma_3} \left[w^{-(s)} - W_\tau^{(s)}(\xi, \eta, -1) \right] \cos \gamma_3 (1 - \zeta) \\
&\quad - \frac{1}{\gamma_3 A_{11}} \sigma_{33\tau}^{(s)}(\xi, \eta, 1) \sin(1 + \zeta) \gamma_3 + W_\tau^{(s)}(\xi, \eta, \zeta), \\
u^{-(0)} &= \frac{u^-}{l}, \quad u^{-(s)} = 0, \quad s \neq 0, \quad (u, v, w), \\
\sigma_{13\tau}^{(s)} &= \frac{1}{a_{55}} \left(\frac{\partial U_\tau^{(s)}}{\partial \zeta} + \frac{\partial W^{(s-1)}}{\partial \xi} \right), \quad (1, 2; u, v; a_{55}, a_{44}; \xi, \eta)
\end{aligned} \tag{1.25}$$

Stresses are calculated by formulas (1.13), (1.16), (1.17), (1.25). It is not difficult to write out solutions corresponding to other conditions (1.7) - (1.12). Thus, conditions (1.6) - (1.12) on the facial surfaces are sufficient to determine the solution of external problem.

1.3 About Mathematically Precise Solutions

If the functions $\sigma_{jz}^\pm, u^\pm, v^\pm, w^\pm$ entering into the boundary conditions (1.6), (1.8) - (1.10) are algebraic polynomials with respect to the tangential coordinates, the iterative process of determining unknowns break off after a finite number of steps, depending on the degree of the polynomial. As a result is a mathematically precise solution to an external problem (solution for the spatial layer). Lets give these solutions for some variants of the boundary conditions.

If denote by Q any of the stresses and displacements, based on formulas (1.6), (1.13), (1.16), the solution can be written in the form

$$Q(x, y, z, t) = \tilde{Q}(x, y, z) \exp(i\Omega t) \tag{1.26}$$

Of particular interest is obtaining a mathematically exact solution corresponding to the boundary conditions (1.6), if only because finding the corresponding solution in a static problem is associated with overcoming significant mathematical difficulties. When $\sigma_{jz}^\pm = \text{const}$ iteration breaks at the initial approximation and using formulas (1.13), (1.16), (1.17), (1.24) we obtain the exact solution to the external problem

$$\begin{aligned}
\tilde{u} &= -\frac{a_{55}h}{\gamma_1 \sin 2\gamma_1} \left[\sigma_{xz}^+ \cos \gamma_1 (1 + \zeta) + \sigma_{xz}^- \cos \gamma_1 (1 - \zeta) \right], \\
\tilde{\sigma}_{xz} &= \frac{1}{\sin 2\gamma_1} \left[\sigma_{xz}^+ \sin \gamma_1 (1 + \zeta) - \sigma_{xz}^- \sin \gamma_1 (1 - \zeta) \right], \quad (u, v; x, y; a_{55}, a_{44}; \gamma_1, \gamma_2)
\end{aligned}$$

$$\begin{aligned}
\tilde{w} &= -\frac{h}{A_{11}\gamma_3 \sin 2\gamma_3} [\sigma_{zz}^+ \cos \gamma_3(1+\zeta) + \sigma_{zz}^- \cos \gamma_3(1-\zeta)], \\
\tilde{\sigma}_{zz} &= \frac{1}{\sin 2\gamma_3} [\sigma_{zz}^+ \sin \gamma_3(1+\zeta) - \sigma_{zz}^- \sin \gamma_3(1-\zeta)], \\
\tilde{\sigma}_{xx} &= -\frac{A_{23}}{h} \frac{\partial \tilde{w}}{\partial \zeta}, \quad \tilde{\sigma}_{yy} = -\frac{A_{13}}{h} \frac{\partial \tilde{w}}{\partial \zeta}, \quad \tilde{\sigma}_{xy} = 0
\end{aligned} \tag{1.27}$$

The boundary conditions (1.7), (1.8), when $\sigma_{jz}^+ = \text{const}$, correspond to mathematically exact solution

$$\begin{aligned}
\tilde{u} &= \frac{ha_{55}\sigma_{xz}^+}{\gamma_1 \cos 2\gamma_1} \sin \gamma_1(1+\zeta), \quad \tilde{\sigma}_{xz} = \frac{\sigma_{xz}^+}{\cos 2\gamma_1} \cos \gamma_1(1+\zeta), \\
&\quad (u, v; x, y; a_{55}, a_{44}; \gamma_1, \gamma_2), \\
\tilde{w} &= \frac{h\sigma_{zz}^+}{A_{11}\gamma_3 \cos 2\gamma_3} \sin \gamma_3(1+\zeta), \quad \tilde{\sigma}_{zz} = \frac{\sigma_{zz}^+}{\cos 2\gamma_3} \cos \gamma_3(1+\zeta), \\
\tilde{\sigma}_{xx} &= -\frac{A_{23}}{h} \frac{\partial \tilde{w}}{\partial \zeta}, \quad \tilde{\sigma}_{yy} = -\frac{A_{13}}{h} \frac{\partial \tilde{w}}{\partial \zeta}, \quad \tilde{\sigma}_{xy} = 0
\end{aligned} \tag{1.28}$$

When the boundary conditions (1.10), (1.12) are valid, and if $u^-, v^-, w^- = \text{const}$ we have mathematically exact solution

$$\begin{aligned}
\tilde{u} &= \frac{u^-}{\sin 2\gamma_1} \sin \gamma_1(1-\zeta), \quad \tilde{\sigma}_{xz} = -\frac{u^- \gamma_1}{a_{55}h \sin 2\gamma_1} \cos \gamma_1(1-\zeta), \\
&\quad (u, v; x, y; a_{55}, a_{44}; \gamma_1, \gamma_2), \\
\tilde{w} &= \frac{w^-}{\sin 2\gamma_3} \sin \gamma_3(1-\zeta), \quad \tilde{\sigma}_{zz} = -A_{11} \frac{w^- \gamma_3}{h \sin 2\gamma_3} \cos \gamma_3(1-\zeta), \\
\tilde{\sigma}_{xx} &= \frac{A_{23}w^- \gamma_3}{h \sin 2\gamma_3} \cos \gamma_3(1-\zeta), \quad \tilde{\sigma}_{yy} = \frac{A_{13}w^- \gamma_3}{h \sin 2\gamma_3} \cos \gamma_3(1-\zeta), \quad \tilde{\sigma}_{xy} = 0
\end{aligned} \tag{1.29}$$

Using the solutions (1.13), (1.16), (1.17), (1.24), (1.25) it is not difficult to write out exact solutions corresponding to external polynomial loads of various degrees.

From formulas deduced above, it follows that in the plate arise two types of shear vibration and one longitudinal, which are independent in the initial approximation. In subsequent approximations, they are dependent and one type of oscillation generates another type of oscillation, but with a smaller amplitude compared to the main.

As is known, in the classical theory of plates and shells based on the Kirchhoff-Love hypotheses, displacement w does not depend on the transverse coordinate, but solutions (1.24) - (1.29) indicate that all quantities substantially depend on this coordinate. The asymptotics (1.2) of the classical theory is also fundamentally different from the asymptotics (1.16) in dynamic problems of plates and shells. This means that the dynamic process can sharply change the character of the stress-strain state. The formal addition to the classical equations of the statics inertial terms cannot provide a description of the true dynamic state of the plate or shell.

Asymptotics (1.3) is applicable for solving similar and new classes of problems for isotropic and anisotropic shells (Aghalovyan and Ghulghazaryan, 2009, 2012, 2018).

The above derived formulas are right for determining solutions of all considered variants of the boundary conditions. They were derived under the condition that in (1.15) $\Omega_*^2 = \rho h^2 \Omega^2$ of the order of one. If $\Omega_*^2 = 0(\varepsilon)$, the process is quasi-static in the first boundary-value static problem is true the asymptotic (1.2). If $\Omega_*^2 = 0(\varepsilon^{-1})$ we can again use system (1.15), but considering that $\Omega_*^2 = \rho l h \Omega^2$, and at $\Omega_*^2 = 0(\varepsilon^{-2})$ considering that $\Omega_*^2 = \rho l^2 \Omega^2$. At $\Omega_*^2 \geq 0(\varepsilon^{-3})$ it is necessary to search for other asymptotic.

1.4 About the Boundary Layer

The solution of the external problem satisfies all the equations and relations of 3D the elasticity theory problem and the boundary conditions on the facial surfaces of the plate. As a rule, it does not satisfy the boundary conditions on the side surface of the plate. Arisen hitch is resolved by the boundary layer solution. Let describe the procedure for constructing this solution near the side surface $x = 0$.

In Eqs. (1.15) entered a new change of variable $\gamma = \xi/\varepsilon$ and all the sought quantities are assigned the index “b” (from the word boundary). The solution of the newly obtained system should decrease rapidly with distance from the side surface $x = 0(\gamma = 0)$ into the inside of the plate. This solution is sought in the form

$$\begin{aligned} \sigma_{jkb} &= \varepsilon^{-1+s} \sigma_{jkb}^{(s)}(\eta, \zeta) \exp(-\lambda\gamma), \quad j, k = 1, 2, 3; \quad s = \overline{0, N}, \\ (U_b, V_b, W_b) &= \varepsilon^s (U_b^{(s)}(\eta, \zeta), V_b^{(s)}(\eta, \zeta), W_b^{(s)}(\eta, \zeta)) \exp(-\lambda\gamma), \end{aligned} \tag{1.30}$$

where λ – so far unknown number that characterizes the velocities of decrease of values of stress and states of the boundary layer ($\exp(-\gamma \operatorname{Re} \lambda)$), $\operatorname{Re} \lambda > 0$. Substituting (1.30) into the aforementioned transformed system, from the newly obtained system, the stresses can be expressed through the components of the displacement vector by the formulas

$$\begin{aligned} \sigma_{12b}^{(s)} &= \frac{1}{a_{66}} \left(-\lambda V_b^{(s)} + \frac{\partial U_b^{(s-1)}}{\partial \eta} \right), \quad \sigma_{13b}^{(s)} = \frac{1}{a_{55}} \left(-\lambda W_b^{(s)} + \frac{\partial U_b^{(s)}}{\partial \zeta} \right), \\ \sigma_{23b}^{(s)} &= \frac{1}{a_{44}} \left(\frac{\partial V_b^{(s)}}{\partial \zeta} + \frac{\partial W_b^{(s-1)}}{\partial \eta} \right), \quad Q^{(m)} \equiv 0 \quad \text{when } m < 0, \end{aligned}$$

$$\sigma_{11b}^{(s)} = -\lambda A_{22} U_b^{(s)} - A_{23} \frac{\partial W_b^{(s)}}{\partial \zeta} - A_{12} \frac{\partial V_b^{(s-1)}}{\partial \eta}, \quad (1.31)$$

$$\sigma_{22b}^{(s)} = \lambda A_{12} U_b^{(s)} - A_{13} \frac{\partial W_b^{(s)}}{\partial \zeta} + A_{33} \frac{\partial V_b^{(s-1)}}{\partial \eta},$$

$$\sigma_{33b}^{(s)} = \lambda A_{23} U_b^{(s)} + A_{11} \frac{\partial W_b^{(s)}}{\partial \zeta} - A_{13} \frac{\partial V_b^{(s-1)}}{\partial \eta}$$

To determine $V_b^{(s)}$ from the same system follows the equation

$$\begin{aligned} \frac{\partial^2 V_b^{(s)}}{\partial \zeta^2} + \left(\frac{a_{44}}{a_{66}} \lambda^2 + a_{44} \Omega_*^2 \right) V_b^{(s)} &= f_{vb}^{(s)}, \\ f_{vb}^{(s)} &= \frac{a_{44}}{a_{66}} \lambda \frac{\partial U_b^{(s-1)}}{\partial \eta} - a_{44} \frac{\partial \sigma_{22b}^{(s-1)}}{\partial \eta} - \frac{\partial^2 W_b^{(s-1)}}{\partial \zeta \partial \eta} \end{aligned} \quad (1.32)$$

Displacements $U_b^{(s)}, W_b^{(s)}$ are determined from the system

$$\begin{aligned} \frac{\partial^2 U_b^{(s)}}{\partial \zeta^2} + a_{55} (\lambda^2 A_{22} + \Omega_*^2) U_b^{(s)} + \lambda (A_{23} a_{55} - 1) \frac{\partial W_b^{(s)}}{\partial \zeta} &= f_{ub}^{(s)}, \\ A_{11} a_{55} \frac{\partial^2 W_b^{(s)}}{\partial \zeta^2} + (\lambda^2 + a_{55} \Omega_*^2) W_b^{(s)} + \lambda (A_{23} a_{55} - 1) \frac{\partial U_b^{(s)}}{\partial \zeta} &= f_{wb}^{(s)} \end{aligned} \quad (1.33)$$

System (1.33) can be reduced to one equation

$$\frac{\partial^4 U_b^{(s)}}{\partial \zeta^4} + B_{11} \frac{\partial^2 U_b^{(s)}}{\partial \zeta^2} + B_{22} U_b^{(s)} = \psi_u^{(s)}, \quad (1.34)$$

where

$$B_{11} = \frac{\lambda^2}{A_{11}} [a_{55} (A_{11} A_{22} - A_{23}^2) + 2A_{23}] + \frac{\Omega_*^2}{A_{11}} (1 + A_{11} a_{55}),$$

$$B_{22} = \frac{1}{A_{11}} (\lambda^2 A_{22} + \Omega_*^2) (\lambda^2 + a_{55} \Omega_*^2),$$

$$\psi_u^{(s)} = \frac{1}{A_{11} a_{55}} (\lambda^2 + a_{55} \Omega_*^2) f_{ub}^{(s)} - \frac{1}{A_{11} a_{55}} \frac{\partial f_{uwb}^{(s)}}{\partial \zeta},$$

$$\begin{aligned}
 f_{ub}^{(s)} &= -a_{55} \left(\lambda A_{12} \frac{\partial V_b^{(s-1)}}{\partial \eta} + \frac{\partial \sigma_{12b}^{(s-1)}}{\partial \eta} \right), \\
 f_{wb}^{(s)} &= a_{55} \left(A_{13} \frac{\partial^2 V_b^{(s-1)}}{\partial \eta \partial \zeta} - \frac{\partial \sigma_{22b}^{(s-1)}}{\partial \eta} \right), \\
 f_{uwb}^{(s)} &= -A_{11} a_{55} \frac{\partial f_{ub}^{(s)}}{\partial \zeta} + \lambda (A_{23} a_{55} - 1) f_{wb}^{(s)}, \\
 f_{ub}^{(0)} &= f_{wb}^{(0)} = f_{vb}^{(0)} = f_{uwb}^{(0)} = \psi_u^{(0)} = 0
 \end{aligned}$$

The solution to the Eq. (1.34) is

$$U_b^{(s)} = A_1^{(s)} \psi_1 + A_2^{(s)} \psi_2 + A_3^{(s)} \psi_3 + A_4^{(s)} \psi_4 + U_{\tau b}^{(s)}, \tag{1.35}$$

where $U_{\tau b}^{(s)}$ is the particular solution, and

$$\begin{aligned}
 \psi_1 &= \cosh k_1 \zeta, \quad \psi_2 = \sinh k_1 \zeta, \quad \psi_3 = \cosh k_2 \zeta, \quad \psi_4 = \sinh k_2 \zeta, \\
 k_{1,2} &= \sqrt{\frac{1}{2}(-B_{11} \pm \sqrt{B_{11}^2 - 4B_{22}})}
 \end{aligned} \tag{1.36}$$

From system (1.33) $W_b^{(s)}$ it is expressed through $U_b^{(s)}$ by formulas

$$\begin{aligned}
 W_b^{(s)} &= C_1 \left(A_{11} a_{55} \frac{\partial^3 U_b^{(s)}}{\partial \zeta^3} + C_2 \frac{\partial U_b^{(s)}}{\partial \zeta} + f_{uwb}^{(s)} \right), \\
 C_1 &= \frac{1}{\lambda(\lambda^2 + a_{55} \Omega_*^2)(A_{23} a_{55} - 1)}, \quad C_2 = A_{11} a_{55}^2 (\lambda^2 A_{22} + \Omega_*^2) - \lambda^2 (A_{23} a_{55} - 1)^2
 \end{aligned} \tag{1.37}$$

The solution to the Eq. (1.32) is

$$V_b^{(s)} = B_1^{(s)} \sin m \zeta + B_2^{(s)} \cos m \zeta + V_{\tau b}^{(s)}(\eta, \zeta), \tag{1.38}$$

with

$$m = \sqrt{\frac{a_{44}}{a_{66}} \lambda^2 + a_{44} \Omega_*^2}$$

Having the values of displacements $U_b^{(s)}, V_b^{(s)}, W_b^{(s)}$, stresses are determined by formulas (1.31).

Since the solution of the external problem satisfies the inhomogeneous boundary conditions (1.6) - (1.10), the solution for the boundary layer must satisfy the corresponding homogeneous (zero) boundary conditions:

$$\text{a) } \sigma_{j3b}(0, \eta, \pm 1) = 0, \quad j = 1, 2, 3 \quad (1.39)$$

$$\begin{aligned} \text{b) } U_b(0, \eta, -1) &= 0, (U, V, W) \\ \sigma_{j3b}(0, \eta, 1) &= 0 \quad \text{or} \quad U_b(0, \eta, -1) = 0, (U, V, W) \end{aligned} \quad (1.40)$$

$$\begin{aligned} \text{c) } U_b(0, \eta, \pm 1) &= 0, (U, V, W) \\ \text{or } U_b(0, \eta, -1) &= 0, (U, V, W), \quad \sigma_{j3b}(0, \eta, 1) = 0, \quad j = 1, 2, 3 \end{aligned} \quad (1.41)$$

The general solution for the boundary layer determined by formulas (1.30), (1.31), (1.35) - (1.38) allows to satisfy each of the groups of conditions (1.39) - (1.41). Satisfaction of the each group of conditions (1.39) - (1.41) leads to the solution of two systems of homogeneous algebraic equations. One of the systems relatively to unknown functions in the solution for $V_b^{(s)}$. Another algebraic system relatively to the unknowns in the solution for $U_b^{(s)}, W_b^{(s)}$. For these algebraic systems to have nontrivial solutions, it is necessary that their determinants become equal to zero. From the corresponding transcendental equations, the values of λ are determined. As a result, we have two groups of values for λ , to which correspond to antiplane (λ_n^a) and plane (λ_n^p) boundary layers. For an antiplane boundary layer λ_n^a have real values, and for a plane boundary layer λ_n^p - complex conjugate.

For example, for boundary conditions (1.40) relatively V_b and σ_{23b} according to (1.38), (1.31) correspond the equation $\cos 2m = 0$, from which follows

$$\lambda_n^a = \sqrt{\frac{a_{66}}{a_{44}} \left[(2n+1)^2 \frac{\pi^2}{16} - \Omega_*^2 a_{44} \right]}, \quad n \in N \quad \forall n > \frac{2}{\pi} \Omega_* \sqrt{a_{44}} - \frac{1}{2} \quad (1.42)$$

The flat boundary layer breaks up into symmetric (tension-compression) and skew-symmetric (bend) boundary layers. When $s = 0$ antiplane and plane boundary layers are independent. When $s > 0$ they are dependent, and the antiplane boundary layer generates a plane boundary layer and vice versa (accompanying boundary layers). However, the accompanying boundary layers have amplitudes on an order of magnitude smaller than the main ones. Having determined λ_n^a, λ_n^p - the final solution for the boundary layer is written out and it is conjugated with the already known solution of the external problem. The procedure for conjugation these solutions is described in Aghalovyan (2015). The asymptotic method can be used to solve new classes of dynamic problems of the theory of elasticity, in particular, when studying the interaction of thin bodies with various physical fields, in problems of seismology, earthquake prediction, etc.

In conclusion, we note that a number of important questions on the problems of plates and shells were considered by Altenbach et al (2015, 2018); Kaplunov et al (1988, 2017); Boutin et al (2017); Mikhasev and Tovstik (2009); Chapman (2013); Belyaev et al (2019).

1.5 Conclusions

The efficiency of the asymptotic method for solving spatial dynamic problems of thin bodies (beams, plates, shells) is shown. The dependence of the components of the stress tensor and displacement vector on the transverse (thickness) coordinate is shown. The necessity for a more careful use of the classical theory of plates and shells in dynamic problems is mentioned.

The 3D boundary layer in the plates was studied. It has been shown that in thin bodies antiplane and plane boundary layers appear.

References

- Aghalovyan LA (1982) On the structure of solution of one class of plane problems of elasticity theory of asymptotic body. In: *Interuniversity Transactions: Mechanics*, Yerevan State University Publishing House, vol 2, pp 7–12
- Aghalovyan LA (2015) *Asymptotic Theory of Anisotropic Plates and Shells*. World Scientific Publishing, Singapore-London
- Aghalovyan LA, Gevorgyan RS (2005) *Nonclassical Boundary-value Problems of Anisotropic Layered Beams, Plates and Shells (in Russ.)*. Publishing House of NAS RA, Yerevan
- Aghalovyan LA, Ghulghazaryan LG (2009) Non-classical boundary-value problems of the forced vibrations of orthotropic shells. *International Sciences Journal of Applied Mechanics* 45(8):888–903
- Aghalovyan LA, Ghulghazaryan LG (2012) About defending solutions of a class of dynamic space problems of mathematical theory of elasticity for orthotropic shells "(in russ.)". *Scientific News ASPV after Kh Abovyan* 17(2):29–42
- Aghalovyan LA, Ghulghazaryan LG (2018) Forced vibrations of two-layered shells on the case of viscous resistance. *Journal of Physics: Conf Ser* 991:012,002
- Altenbach H, Eremeyev VA, Naumenko K (2015) On the use of the first order shear deformation plate theory for the analysis of three-layer plates with thin soft core layer. *ZAMM - Zeitschrift für Angewandte Mathematik und Mechanik* 95(10):1004–1011
- Altenbach H, Altenbach J, Kissing W (2018) *Mechanics of Composite Structural Elements*, 2nd edn. Springer
- Belyaev A, Morozov NF, Tovstik PE, Tovstik TP, Zelinskaya AV (2019) Two-dimensional model of plate made of material with general anisotropy. In: Altenbach H, Chróścielewski J, Eremeyev V, Wiśniewski K (eds) *Recent Developments in the Theory of Shells, Advanced Structured Materials*, vol 110, Springer, Singapore, pp 91–108
- Boutin C, dell’Isola F, Giorgio I, Placidi L (2017) Linear pantographic sheets: Asymptotic micro-macro models identification. *Mathematics and Mechanics of Complex Systems* 5(2):127–162

- Chapman CJ (2013) An asymptotic decoupling method for waves in layered media. *Proceedings of the Royal Society A: Mathematical, Physical and Engineering Sciences* 469(2153):20120,659
- Gol'denveizer AL (1962) Derivation of an approximate theory of bending of a plate by the method of asymptotic integration of the equations of the theory of elasticity. *Journal of Applied Mathematics and Mechanics* 26(4):1000–1025
- Kaplunov J, Prikazchikov DA, Prikazchikova LA (2017) Dispersion of elastic waves in a strongly inhomogeneous three-layered plate. *International Journal of Solids and Structures* 113-114:169–179
- Kaplunov JD, Kossovich LY, Nolde EV (1988) *Dynamics of Thin Walled Elastic Bodies*. Academic Press
- Mikhasev GI, Tovstik PE (2009) *Localized Vibrations and Waves in Thin Shells. Asymptotic Methods (in Russ.)*. Fizmatlit



Chapter 2

New Hamiltonian Semi-analytical Approach for 3D Solution of Piezoelectric Smart Composites

Orlando Andrianarison and Ayeche Benjeddou

Abstract This chapter addresses the development of a new semi-analytical Lagrangian-Hamiltonian method for the three-dimensional solution of piezoelectric smart composite plates. It is based on the analytic *state space symplectic Hamiltonian approach* to fulfil the electromechanical multilayer interface continuity constraints and two-dimensional *in-plane finite element* (FE) numerical discretization to deal with arbitrary boundary conditions (BC) on the composite lateral edges. The originality of the proposed semi-analytical solution is that the latter feature (arbitrary BC handling) is reached through a mechanical displacements-electric potential primary variables-based Lagrangian formalism, while the solution accuracy feature is reached through a primary and dual (transverse stresses and electric displacement) variables-based partial mixed Hamiltonian formalism. The transformation of the Lagrangian FE discretized formulation to a state space Hamiltonian one is made through the Legendre transformation. The proposed methodology is applied to the static actuation and sensing of *piezoelectric* hybrid laminated composite plates subjected to various BC. The obtained results comparison to reference ones of various benchmarks solutions, for non classical BC (cantilever), multilayer composite layups (angle-ply) and electromechanical loadings (uniform), from the open literature shows good computational convergence (coarse mesh), low cost (few FE degrees of freedom) and high accuracy (exact through-the-thickness) of the present new Hamiltonian semi-analytical solutions. Thus, the provided tabulated numerical results can be used safely for benchmarking other closed-form, numerical or semi-analytical solutions.

Orlando Andrianarison

Institut Supérieur de l'Automobile et des Transports, 49 rue Mademoiselle Bourgeois, 58000 Nevers, France

e-mail: orlando.andrianarison@u-bourgogne.fr

Ayeche Benjeddou

Institut Supérieur de Mécanique de Paris, 3 rue Fernand Hainaut, 93400 Saint Ouen, France & ROBERVAL, FRE 2012 UTC/CNRS, rue Personne de Roberval, 60200 Compiègne

e-mail: benjeddou@supmeca.fr, ayeche.benjeddou@utc.fr

Key words: Lagrangian finite element · Partial-mixed state space · Symplectic Hamiltonian · Three-dimensional semi-analytic solution · Piezoelectric actuation and sensing · Multilayer composites

2.1 Introduction

Structural elements made of *composite* materials are already being used for a long time in various fields of engineering. The range of their applications covers several branches of industries such as aircraft and automotive constructions, medical equipment or marine and civil engineering. Nowadays, the research activities on composites mostly evolve to the integration (surface-bonding or embedding) of the so-called *smart* materials. Among the latter, the *piezoelectric* sensors and actuators are being widely used thanks to their undeniable advantages, like excellent electromechanical coupling properties, low cost fabrication, design flexibility and, most importantly, applicability in vibration control, health monitoring and damage prognosis of load-carrying structures.

Over the past few decades, considerable efforts have been devoted to the development of theories and numerical modelling of smart piezoelectric laminated composites and structures (Benjeddou, 2000; Kapuria et al, 2010; Li, 2020). It appears that the main issues are the computational cost and accuracy. Indeed, it is a fact that they are anisotropic and three-dimensional (3D) in nature. Thus, their accurate electromechanical modelling requires appropriate descriptions of their mechanical and electrical variables, particularly through the thickness direction. The compatibility and equilibrium conditions at the interfaces state that an efficient modelling of such structures must deal with the so-called *interface continuity* (IC) constraints; namely, the continuity of the transverse (out-of-plane) mechanical stresses and electric displacement through the interfaces of the laminate. Among the numerous models and tools available in the literature, only few can cope with these specific features; nevertheless, natural theoretical frameworks to deal with these requirements are the full/hybrid (Sze and Pan, 1999) and partial (Carrera et al, 2010) mixed ones.

Analytically, the mixed *state space method* (SSM) that uses the mechanical displacements and electric potential variables, augmented with the transverse stresses and electric displacement as independent variables (Benjeddou and Deü, 2001), is a good example of *partial-mixed* frameworks. However, it is limited by the a priori fulfilment of the boundary conditions (BC) and cross-ply laminate schemes so that it is not usable for realistic BC other than the full simply-supported (SS) ones. The practical cantilever (clamped-free) BC have been considered (Leung et al, 2008) analytically through the exact symplectic approach, which review (Lim and Xu, 2010) shows other solutions for various BC combinations with the classical SS ones. Alternative approaches to the purely analytical ones are the so-called semi-analytical solutions (Wu and Liu, 2016) which combine in-plane numerical discretization, such as the finite element (FE) method, and through-the-thickness analytical methods, such as the SSM. Only the authors' earlier work (Andrianarison and Benjeddou,

2012) was cited, in the previous review (Wu and Liu, 2016), in the category of state space-FE semi-analytical solutions for the quasi-3D analysis of smart composites and functionally graded materials. Another type of semi-analytical methods was also suggested in Benedetti et al (2010) for the 3D analysis of damaged structures, modelled by the numerical dual boundary element method, with bonded piezoelectric sensors, modelled by the analytical SSM.

Numerically, 3D full/hybrid (Sze and Pan, 1999) and mixed FE are suitable but expensive, due to the thinness of the multilayer plies that often requires fine meshes. Partial-mixed *variational formulations* (VF) that use the mechanical displacements and electric potential, augmented with the transverse stresses and transverse electric displacement through Lagrange multipliers, are a good alternative for reducing the number of independent variables (Benjeddou and Andrianarison, 2005). By retaining the primary variables along with their dual ones, the aforementioned mixed formulations share a common mathematical issue: they must be able to satisfy the so-called *Brezzi-Babuška* (BB) inf-sup conditions (Boffi et al, 2013). This saddle-point property of the mixed VF in general is of crucial importance in the effectiveness of such formulations. To tackle this issue, a *Layer-Wise* (LW) mixed least-square framework was presented in Moleiro et al (2015) for example. Another option that permits to deal with the special requirements of the smart laminated composites modelling is to use the *semi-analytical* approach that combines an analytical mixed SSM through-the-thickness and a numerical discretization of the reference plane. Its major advantages are the significant reduction of the computational cost and the increase of the solution accuracy. The starting point of the retained semi-analytical method consists in decomposing the 3D volume into a reference two-dimensional (2D) in-plane domain and a one-dimensional transverse direction, in combination with the application of the method of separation of variables. The high-order 3D partial differential equilibrium equations are then solved exactly along the transverse direction thanks to the SSM, whereas a weak solution is searched in the reference plane. Therefore, the main issue of semi-analytical methods concerns the chosen numerical method to discretize the 2D in-plane problem. For example, the method developed in Shan et al (2018) aims at applying the scaled boundary FE method to the static bending of a piezoelectric beam. In Zhou et al (2020), the traditional FE method is used to compute the deformation of general curved beams under various BC. A similar approach is presented in Zhou et al (2015) where a state space-FE semi-analytic approach is used to study the cylindrical bending of a straight cantilever beam. Under plane strain conditions of elasticity (cylindrical bending), the 3D governing equations transform into a two-point boundary value problem (BVP) so that a numerical method can be bypassed for the benefit of an analytic method such as the eigenfunction expansion. This is done in Zhang and Wang (2018) where the axisymmetric static deformation of a piezoelectric cylinder under arbitrary BC is investigated in the framework of a Hamiltonian symplectic superposition approach. Through the literature review in the ongoing section, the partial mixed VF, assorted with the semi-analytical approach, therefore constitutes a suitable framework for modeling piezoelectric smart composites. Indeed, this allows a straightforward fulfilment of the laminate transverse stresses and electric displace-

ment IC without cumbersome manipulations (Khandelwal et al, 2013) as for the equivalent single-layer or LW classical 2D models.

Alternatively to the classical Lagrange-type formulations, the partial mixed VF presented in Andrianarison and Benjeddou (2012) has been derived in the framework of the *Hamiltonian* formalism after a Legendre transformation. The latter allowed the natural introduction of the transverse stresses and electric displacement as primary variables, and made the final partial differential equations (PDE) lower in order, compared to the Lagrange-type formulations. Besides, the Hamiltonian formalism allowed transforming, in a systematic way, the equations of 3D piezoelectricity (4th order PDE) into first-order linear ordinary differential equations (ODE) for which the coordinate in the thickness direction is the only independent geometric parameter. This feature appears to be interesting in the perspective of developing efficient numerical tools for multilayer smart composites since the propagator matrix approach, used for the analytical mixed SSM, can then be exploited. Thus, the resulting model simplifies considerably the computational treatment of the IC, leading potentially to accurate predictions of the detailed response characteristics, such as the through-the-thickness distributions of the state variables. However, recasting the classical VF into a mixed one has also some inevitable drawbacks. As a matter of fact, by incorporating the transverse stresses and electric displacement as dual variables into the VF, the question of the proper treatment of the BC arises for realistic ones other than SS. Indeed, the use of the SSM to compute the through-the-thickness distributions of the state variables implicitly requires that the final matrix is square so that its exponential function can be used. This requirement determines the well-posedness of this approach and explains why the VF in Andrianarison and Benjeddou (2012) is only efficient for the theoretical SS BC; indeed, it can be shown that the problem is well-posed if and only if the number of primal and dual variables to be constrained on a given edge is equal, as is the case for the well-known Navier-type analytical solutions.

In summary, according to the above discussion, it appears that the use of the partial mixed VF is relevant since it makes possible the fulfilment of the IC conditions when needed. However, the corresponding numerical models are non-standard and must be used with care due to the BB stability conditions. Moreover, the use of the Hamiltonian framework in combination with the partial Legendre transformation offers a good compromise between high needs of computer resources of LW approaches and complexities of the 3D full mixed VF. Therefore, the purpose of this chapter is to present a new partial-mixed VF where the above mentioned drawbacks are circumvented by choosing a new set of dual stress-like variables that coincide with the out-of-plane *nodal* transverse stresses-like *resultants*. This can be seen as one of the main original contributions of the present work. Moreover, a semi-analytic procedure is retained to solve the problem in the thickness direction. This is done through a 2D FE discretization of the mechanical displacements and electric potential on the plate reference plane only and the mixed SSM is used to compute the through-the-thickness distributions of the dependent variables. The proposed approach is then used to compute the 3D static solutions of piezoelectric multi-layered composite plates with symmetric and anti-symmetric lamination

schemes as well as non-standard edges BC of cantilever type. Both sensor and actuator configurations are analysed and some tabulated results are given for future reference in view of validating other numerical solutions. It is worthy to mention that the validation benchmarks choice is guided by the need to show that the proposed new semi-analytic FE-state space symplectic Hamiltonian methodology can solve problems of realistic BC, multilayer composites layups and electromechanical loads other than the classical SS, cross-ply and trigonometric ones, which are the limitations of earlier semi-analytic and analytic proposed 3D solutions in the open literature. This can be seen as another original contribution of the present work.

The chapter is structured in four subsequent sections. First, Sect. 2.2 describes the in-hand problem and related notations. Then, Sect. 2.3 is devoted to the derivation of the new mixed Hamiltonian semi-analytical solution. Next, Sect. 2.4 provides few benchmarking examples to illustrate the effectiveness of the presented approach. Finally, conclusions and perspectives close the chapter.

2.2 Problem and Notations

Consider a 3D linear piezoelectric body that occupies a simply connected domain Ω to which a Cartesian global coordinate system (O, x, y, z) is attached. It is bounded by a sufficiently regular surface $\Gamma = \partial\Omega$, with outward unit vector $\underline{\mathbf{n}}$, and is subjected to a known surface traction vector $\underline{\mathbf{F}}$ on Γ_F and a scalar electric surface charge Q on Γ_Q , where Γ_F and Γ_Q are parts of its boundary Γ . The latter can also support an imposed scalar electric potential $\tilde{\varphi}$ on Γ_φ , so that $\Gamma_\varphi \cup \Gamma_Q = \Gamma$ and $\Gamma_\varphi \cap \Gamma_Q = \emptyset$, and a mechanical displacements vector $\underline{\mathbf{u}}$ on Γ_u , so that $\Gamma_u \cup \Gamma_F = \Gamma$ and $\Gamma_u \cap \Gamma_F = \emptyset$. For simplicity, the body loads are not considered. Besides, in the following, an underlined variable represents a vector while a doubled underlined one is used for a matrix. Also a tilted quantity is an applied (imposed) one and a bold parameter represents a tensor.

The electromechanical equations, describing the above stated static problem, are (Benjeddou, 2000) the:

- Cauchy's and Gauss' equilibrium equations

$$\begin{cases} \text{Div}\underline{\boldsymbol{\sigma}} = \underline{\mathbf{0}} \\ \text{Div}\underline{\mathbf{D}} = 0 \end{cases} \quad \text{in } \Omega \quad (2.1)$$

where $\underline{\boldsymbol{\sigma}}$ and $\underline{\mathbf{D}}$ are the Cauchy linear stress tensor and electric displacement (induction) vector. 'Div' represents the divergence operator.

- Mechanical strains-displacements and electric fields-potential relations

$$\begin{cases} \underline{\boldsymbol{\varepsilon}} = \frac{1}{2} \left(\text{Grad}\underline{\mathbf{u}} + \text{Grad}^T \underline{\mathbf{u}} \right) \\ \underline{\mathbf{E}} = -\text{Grad}\varphi \end{cases} \quad \text{in } \Omega \quad (2.2)$$

with $\underline{\underline{\boldsymbol{\varepsilon}}}$ and $\underline{\underline{\mathbf{E}}}$ being the engineering Lagrange linear strain tensor and electric field vector. $\underline{\underline{\mathbf{u}}}$ and φ are the mechanical displacements vector and electric potential. ‘Grad’ denotes the gradient operator.

- Converse and direct e-form piezoelectric constitutive equations

$$\begin{cases} \underline{\underline{\boldsymbol{\sigma}}} = \underline{\underline{\mathbf{C}}}^E \underline{\underline{\boldsymbol{\varepsilon}}} - \underline{\underline{\mathbf{e}}}^T \underline{\underline{\mathbf{E}}} \\ \underline{\underline{\mathbf{D}}} = \underline{\underline{\mathbf{e}}}\underline{\underline{\boldsymbol{\varepsilon}}} + \underline{\underline{\boldsymbol{\varepsilon}}}^E \underline{\underline{\mathbf{E}}} \end{cases} \quad \text{in } \Omega \quad (2.3)$$

where $\underline{\underline{\mathbf{C}}}^E$, $\underline{\underline{\mathbf{e}}}$ and $\underline{\underline{\boldsymbol{\varepsilon}}}^E$ are the elastic stiffness (at constant electric field), stress piezoelectric and dielectric (at constant strains) matrices; here, $\underline{\underline{\boldsymbol{\sigma}}}$ and $\underline{\underline{\boldsymbol{\varepsilon}}}$ are the engineering (in the Voigt notations) stress and strain vectors.

- Dirichlet (essential) BC

$$\begin{cases} \underline{\underline{\mathbf{u}}} = \underline{\underline{\tilde{\mathbf{u}}}} & \text{on } \Gamma_u \\ \varphi = \tilde{\varphi} & \text{on } \Gamma_\varphi \end{cases} \quad (2.4)$$

- Neumann (natural) BC

$$\begin{cases} \underline{\underline{\boldsymbol{\sigma}}}\underline{\underline{\mathbf{n}}} = \underline{\underline{\mathbf{F}}} & \text{on } \Gamma_F \\ \underline{\underline{\mathbf{D}}}^T \underline{\underline{\mathbf{n}}} = -Q & \text{on } \Gamma_Q \end{cases} \quad (2.5)$$

where $\underline{\underline{\boldsymbol{\sigma}}}$ is the matrix representing the stress tensor.

In order to formulate the reference problem in a generalized way, the following generalized displacement $\underline{\underline{\mathbf{U}}}$, strain $\underline{\underline{\mathbf{S}}}$, stress $\underline{\underline{\mathbf{T}}}$ and load $\underline{\underline{\mathbf{G}}}$ vectors are introduced (Benjeddou and Andrianarison, 2005)

$$\underline{\underline{\mathbf{U}}} = \begin{Bmatrix} \underline{\underline{\mathbf{u}}} \\ \varphi \end{Bmatrix}; \quad \underline{\underline{\mathbf{S}}} = \begin{Bmatrix} \underline{\underline{\boldsymbol{\varepsilon}}} \\ -\underline{\underline{\mathbf{E}}} \end{Bmatrix}; \quad \underline{\underline{\mathbf{T}}} = \begin{Bmatrix} \underline{\underline{\boldsymbol{\sigma}}} \\ \underline{\underline{\mathbf{D}}} \end{Bmatrix}; \quad \underline{\underline{\mathbf{G}}} = \begin{Bmatrix} \underline{\underline{\mathbf{F}}} \\ -Q \end{Bmatrix} \quad (2.6)$$

As a consequence, the piezoelectric constitutive equations (2.3) rewrite as this generalized Hooke’s elastic law-like form

$$\underline{\underline{\mathbf{T}}} = \underline{\underline{\mathbf{C}}}\underline{\underline{\mathbf{S}}} \quad (2.7)$$

with $\underline{\underline{\mathbf{C}}}$ being the constitutive behaviour generalized matrix (Andrianarison and Benjeddou, 2012).

It should be noticed that the negative sign before the electric field in the generalized strain vector in (2.6) is introduced in order to get a symmetric piezoelectric constitutive behaviour matrix in (2.7), as the initial equations in (2.3) are not symmetric. The equilibria equations (2.1) and gradient relations (2.2) are reformulated as:

$$\begin{cases} \underline{\underline{\mathbf{L}}}^T \underline{\underline{\mathbf{T}}} = \underline{\underline{\mathbf{0}}} \\ \underline{\underline{\mathbf{L}}}\underline{\underline{\mathbf{U}}} = \underline{\underline{\mathbf{S}}} \end{cases} \quad \text{in } \Omega \quad (2.8)$$

where $\underline{\underline{\mathbf{L}}}$ is the linear 3D derivation matrix defined as

$$\underline{\underline{\mathbf{L}}}^T = \begin{bmatrix} \partial_x & 0 & 0 & 0 & \partial_z & \partial_y & 0 & 0 & 0 \\ 0 & \partial_y & 0 & \partial_z & 0 & \partial_x & 0 & 0 & 0 \\ 0 & 0 & \partial_z & \partial_y & \partial_x & 0 & 0 & 0 & 0 \\ 0 & 0 & 0 & 0 & 0 & 0 & \partial_x & \partial_y & \partial_z \end{bmatrix}$$

with $\partial_i, i = x, y, z$ standing for partial derivation with respect to i . Moreover, the Dirichlet and Neumann BC are re-stated as:

$$\begin{cases} \underline{\underline{\mathbf{U}}} = \underline{\underline{\tilde{\mathbf{U}}}} & \text{on } \Gamma_U = \Gamma_u \cup \Gamma_\varphi \\ \underline{\underline{\mathbf{T}\mathbf{n}}} = \underline{\underline{\mathbf{G}}} & \text{on } \Gamma_G = \Gamma_F \cup \Gamma_Q \end{cases} \quad (2.9)$$

Here, the generalized stress tensor 4th order matrix $\underline{\underline{\mathbf{T}}}$ is so that $\underline{\underline{\mathbf{T}}}^T = \begin{bmatrix} \underline{\underline{\boldsymbol{\sigma}}} & \underline{\underline{\mathbf{D}}} \end{bmatrix}$.

In summary, the strong form linear static BVP in hand was reduced to find $\underline{\underline{\mathbf{U}}}$ that satisfies Eqs. (2.7)-(2.9). Worth noticeable is that for practical problems having complex geometries, loadings and BC, closed-form solutions to this BVP are unreachable. Hence, numerical solution techniques, built in the framework of VF, are necessary.

2.3 New Mixed Hamiltonian Semi-analytical Solution

In the context of multilayer composite structures modelling, the issue of enforcement of the IC conditions is a difficult task. Straightforward fulfilment of the transverse stresses and electric displacement IC constraints at the laminate interfaces is usually done in the framework of a mixed VF. Therefore, thanks to a partial Legendre transformation, a four-field *partial-mixed* VF has been established (Andrianarison and Benjeddou, 2012) so that it inherits the algebraic properties of Hamiltonian matrices, making easy its numerical implementation. However, the detailed inspection of this partial-mixed VF shows that it suffers from inconsistencies when dealing with arbitrary BC. Namely, one can show that for BC other than SS, there is not any more a one to one correspondence between the primary and conjugate nodal variables to be constrained at the discretized level. Hence, in order to overcome this drawback, the here developed approach follows two steps: in the first one, the classical generalized displacement-type VF is stated at the continuum level; then, the FE discretization and enforcement of the prescribed *essential* BC are made for the mechanical *displacements* and *electric potential*. In the second step, the Hamiltonian formalism and Legendre transformation are used to recast the Lagrange formulation into a mixed one so that the mixed SSM can be used to deal with the IC constraints enforcement at the layered composite interfaces.

The starting point in the derivation of the new VF is to state that the linear generalized constitutive equation (2.7) is resulting from this generalized quadratic strain energy density $\mathcal{E}(\underline{\underline{\mathbf{S}}})$

$$\mathcal{E}(\underline{\underline{\mathbf{S}}}) = \frac{1}{2} \underline{\underline{\mathbf{S}}}^T \underline{\underline{\mathbf{C}}} \underline{\underline{\mathbf{S}}} \quad (2.10)$$

through this derivation with respect to the generalized strains vector

$$\underline{\mathbf{T}} = \frac{d\mathcal{E}}{d\underline{\mathbf{S}}} \quad (2.11)$$

Then, the Lagrange functional associated to Eqs. (2.8)-(2.9) is defined as

$$\mathbb{L}(\underline{\mathbf{U}}) = \int_{\Omega} \mathcal{E}(\underline{\mathbf{S}}) d\Omega - \int_{\Gamma_G} \underline{\mathbf{U}}^T \underline{\mathbf{G}} d\Gamma \quad (2.12)$$

and has to be stationary for the admissible solutions

$$\int_{\Omega} \delta \mathcal{E}(\underline{\mathbf{U}}) d\Omega - \int_{\Gamma_G} \delta \underline{\mathbf{U}}^T \underline{\mathbf{G}} d\Gamma = 0 \quad (2.13)$$

Usual techniques of variational calculus can be used to show that Eq. (2.13) enforces Eqs. (2.7)-(2.8) as Euler-Lagrange equations as well as Neumann BC (2.9)_b as natural ones provided that the enlarged displacement vector $\underline{\mathbf{U}}$ is searched as kinematically admissible on Γ_U i.e. $\underline{\mathbf{U}} = \underline{\tilde{\mathbf{U}}}$ on Γ_U (essential BC).

In the case of a layered body with adjoining laminae perfectly bonded together and without internal electrodes, the generalized displacement vector,

$$\underline{\mathbf{U}} = \{u_x, u_y, u_z, \varphi\}^T,$$

and transverse surface traction vector,

$$\underline{\mathbf{T}}_z = \{\sigma_{xz}, \sigma_{yz}, \sigma_{zz}, D_z\}^T,$$

should be continuous through the laminate interfaces so that these IC conditions hold

$$[\underline{\mathbf{U}}] = \underline{\mathbf{0}}; [\underline{\mathbf{T}}_z] = \underline{\mathbf{0}} \quad (2.14)$$

with $[*]$ denoting the jump in the value of the enclosed quantity * across an interface.

Now, following the procedure described in Andrianarison and Benjeddou (2012), the generalized strains vector (2.8) is split into thickness (z),

$$\underline{\mathbf{S}}_z = \{\gamma_{xz}, \gamma_{yz}, \varepsilon_{zz}, -E_z\}^T$$

and in-plane (p),

$$\underline{\mathbf{S}}_p = \{\varepsilon_{xx}, \varepsilon_{yy}, \gamma_{xy}, -E_x, -E_y\}^T,$$

contributions as

$$\underline{\mathbf{S}}_z = \underline{\dot{\mathbf{U}}} + \underline{\mathbf{D}}_1 \underline{\mathbf{U}}; \underline{\mathbf{S}}_p = \underline{\mathbf{D}}_2 \underline{\mathbf{U}} \quad (2.15)$$

where

$$\underline{\dot{\mathbf{U}}} = \frac{\partial \underline{\mathbf{U}}}{\partial z}; \quad \underline{\mathbf{D}}_{\underline{1}} = \begin{bmatrix} 0 & 0 & \partial_x & 0 \\ 0 & 0 & \partial_y & 0 \\ 0 & 0 & 0 & 0 \\ 0 & 0 & 0 & 0 \end{bmatrix}; \quad \underline{\mathbf{D}}_{\underline{2}} = \begin{bmatrix} \partial_x & 0 & 0 & 0 \\ 0 & \partial_y & 0 & 0 \\ \partial_y & \partial_x & 0 & 0 \\ 0 & 0 & 0 & \partial_x \\ 0 & 0 & 0 & \partial_y \end{bmatrix}$$

Next, the above partition leads to this similar decomposition of the generalized piezoelectric constitutive equation (2.7)

$$\begin{Bmatrix} \underline{\mathbf{T}}_p \\ \underline{\mathbf{T}}_z \end{Bmatrix} = \begin{bmatrix} \underline{\mathbf{C}}_{pp} & \underline{\mathbf{C}}_{pz} \\ \underline{\mathbf{C}}_{pz}^T & \underline{\mathbf{C}}_{zz} \end{bmatrix} \begin{Bmatrix} \underline{\mathbf{S}}_p \\ \underline{\mathbf{S}}_z \end{Bmatrix} \quad (2.16)$$

with

$$\underline{\mathbf{T}}_p = \{\sigma_{xx}, \sigma_{yy}, \sigma_{xy}, D_x, D_y\}^T$$

standing for the in-plane generalized stress vector. It should be noticed here that the original generalized Hooke's matrix coefficients of Eq. (2.7) need to be reorganized in compliance with components re-ordering for defining the in-plane and thickness generalized strain and stress vectors used in Eqs. (2.15)-(2.16).

Now, substituting Eq. (2.16) into (2.10), and having in mind generalized strains-displacements relation (2.8), provides this decomposed generalized strain energy density into thickness, in-plane and their coupling contributions

$$\mathcal{E}(\underline{\mathbf{U}}, \underline{\dot{\mathbf{U}}}) = \frac{1}{2} \left[\underline{\mathbf{S}}_p^T \underline{\mathbf{C}}_{pp} \underline{\mathbf{S}}_p + 2 \underline{\mathbf{S}}_p^T \underline{\mathbf{C}}_{pz} \underline{\mathbf{S}}_z + \underline{\mathbf{S}}_z^T \underline{\mathbf{C}}_{zz} \underline{\mathbf{S}}_z \right] \quad (2.17)$$

After that, when considering the thickness and in-plane partitions of the generalized strains, as in Eq. (2.15), this explicit expression of (2.17) is obtained

$$\begin{aligned} \mathcal{E}(\underline{\mathbf{U}}, \underline{\dot{\mathbf{U}}}) &= \frac{1}{2} \underline{\mathbf{U}}^T \underline{\mathbf{D}}_{\underline{2}}^T \underline{\mathbf{C}}_{pp} \underline{\mathbf{D}}_{\underline{2}} \underline{\mathbf{U}} + \underline{\mathbf{U}}^T \underline{\mathbf{D}}_{\underline{2}}^T \underline{\mathbf{C}}_{pz} \underline{\mathbf{D}}_{\underline{1}} \underline{\mathbf{U}} + \frac{1}{2} \underline{\mathbf{U}}^T \underline{\mathbf{D}}_{\underline{1}}^T \underline{\mathbf{C}}_{zz} \underline{\mathbf{D}}_{\underline{1}} \underline{\mathbf{U}} \\ &+ \underline{\mathbf{U}}^T \underline{\mathbf{D}}_{\underline{2}}^T \underline{\mathbf{C}}_{pz} \underline{\dot{\mathbf{U}}} + \underline{\mathbf{U}}^T \underline{\mathbf{D}}_{\underline{1}}^T \underline{\mathbf{C}}_{zz} \underline{\dot{\mathbf{U}}} + \frac{1}{2} \underline{\dot{\mathbf{U}}}^T \underline{\mathbf{C}}_{zz} \underline{\dot{\mathbf{U}}} \end{aligned} \quad (2.18)$$

And the variational equation (2.13) becomes

$$\int_{\Omega} \delta \mathcal{E}(\underline{\mathbf{U}}, \underline{\dot{\mathbf{U}}}) d\Omega - \int_{\Gamma_G} \delta \underline{\mathbf{U}}^T \underline{\mathbf{G}} d\Gamma = 0 \quad (2.19)$$

The generalized displacements are now postulated in this separated in-plane (x, y) and thickness (z) coordinates dependence

$$\underline{\mathbf{U}}(x, y, z) = \underline{\mathbf{N}}(x, y) \underline{\mathbf{U}}^*(z) \quad (2.20)$$

where, the 2D shape functions of the in-plane interpolation matrix, $\underline{\underline{N}}(x, y)$, are constructed in practice using the well-known isoparametric Lagrange interpolation and the nodal amplitudes, $\underline{\underline{U}}^*(z)$, are to be determined.

Similarly, the body domain and its boundary can be separated, respectively, as $\Omega(x, y, z) = \Sigma_p(x, y) \times \Sigma_z$ and $\Gamma_G = \Sigma_p^G \times \partial \Sigma_z$ with $\Sigma_z = [z_b, z_t]$ referring to the whole thickness having z_b and z_t as bottom and top coordinates. This allows to rewrite the VF (2.19) as

$$\delta \int_{\Sigma_z} \left[\frac{1}{2} \underline{\underline{U}}^{*T} \left(\underline{\underline{K}}_{\underline{\underline{1}}} + \underline{\underline{K}}_{\underline{\underline{4}}} + 2\underline{\underline{K}}_{\underline{\underline{6}}} \right) \underline{\underline{U}}^* + \underline{\underline{U}}^{*T} \left(\underline{\underline{K}}_{\underline{\underline{3}}} + \underline{\underline{K}}_{\underline{\underline{5}}} \right) \underline{\underline{\dot{U}}}^* + \frac{1}{2} \underline{\underline{\dot{U}}}^{*T} \underline{\underline{K}}_{\underline{\underline{2}}} \underline{\underline{\dot{U}}}^* + \right] dz - \left[\delta \underline{\underline{U}}^{*T} \underline{\underline{\hat{L}}} \right]_{z_b}^{z_t} = 0 \quad (2.21)$$

where

$$\underline{\underline{\dot{U}}}^* = \frac{d\underline{\underline{U}}^*}{dz}$$

and the pre-integrated in-plane matrices and vector are

$$\begin{aligned} \underline{\underline{K}}_{\underline{\underline{1}}} &= \int_{\Sigma_p} \underline{\underline{N}}^T \underline{\underline{D}}^T \underline{\underline{C}} \underline{\underline{D}} \underline{\underline{N}} d\Sigma & \underline{\underline{K}}_{\underline{\underline{2}}} &= \int_{\Sigma_p} \underline{\underline{N}}^T \underline{\underline{C}} \underline{\underline{N}} d\Sigma \\ \underline{\underline{K}}_{\underline{\underline{3}}} &= \int_{\Sigma_p} \underline{\underline{N}}^T \underline{\underline{D}}^T \underline{\underline{C}} \underline{\underline{N}}_{zz} d\Sigma & \underline{\underline{K}}_{\underline{\underline{4}}} &= \int_{\Sigma_p} \underline{\underline{N}}^T \underline{\underline{D}}^T \underline{\underline{C}} \underline{\underline{D}} \underline{\underline{N}}_{zz} d\Sigma \\ \underline{\underline{K}}_{\underline{\underline{5}}} &= \int_{\Sigma_p} \underline{\underline{N}}^T \underline{\underline{D}}^T \underline{\underline{C}} \underline{\underline{N}}_{pz} d\Sigma & \underline{\underline{K}}_{\underline{\underline{6}}} &= \int_{\Sigma_p} \underline{\underline{N}}^T \underline{\underline{D}}^T \underline{\underline{C}} \underline{\underline{D}} \underline{\underline{N}}_{pz} d\Sigma \\ \underline{\underline{\hat{L}}} &= \int_{\Sigma_p^G} \underline{\underline{N}}^T \underline{\underline{G}} d\Sigma \end{aligned} \quad (2.22)$$

Now, performing an integration by parts with respect to the nodal variables $\delta \underline{\underline{\dot{U}}}^*(z)$ and allowing the resulting variational equation to be satisfied for arbitrary virtual nodal variables $\delta \underline{\underline{U}}^*$, this second-order ODE system is obtained

$$\begin{cases} -\underline{\underline{K}}_{\underline{\underline{2}}} \underline{\underline{\dot{U}}}^* + \left(\underline{\underline{K}}_{\underline{\underline{3}}} + \underline{\underline{K}}_{\underline{\underline{5}}} - \underline{\underline{K}}_{\underline{\underline{3}}}^T - \underline{\underline{K}}_{\underline{\underline{5}}}^T \right) \underline{\underline{\dot{U}}}^* + \left(\underline{\underline{K}}_{\underline{\underline{1}}} + \underline{\underline{K}}_{\underline{\underline{4}}} + \underline{\underline{K}}_{\underline{\underline{6}}} + \underline{\underline{K}}_{\underline{\underline{6}}}^T \right) \underline{\underline{U}}^* = \underline{\underline{0}} \\ \underline{\underline{K}}_{\underline{\underline{2}}} \underline{\underline{\dot{U}}}^* + \left(\underline{\underline{K}}_{\underline{\underline{3}}}^T + \underline{\underline{K}}_{\underline{\underline{5}}}^T \right) \underline{\underline{U}}^* = \underline{\underline{\hat{L}}} \quad \text{for } z = \{z_b, z_t\} \end{cases} \quad (2.23)$$

As can be seen from Eq. (2.23), the quantity

$$\underline{\underline{\hat{L}}}^* = \underline{\underline{K}}_{\underline{\underline{2}}} \underline{\underline{\dot{U}}}^* + \left(\underline{\underline{K}}_{\underline{\underline{3}}}^T + \underline{\underline{K}}_{\underline{\underline{5}}}^T \right) \underline{\underline{U}}^*$$

can be formally assimilated to a *nodal generalized stress vector resultant* thanks to the definition of the load vector $\underline{\underline{\hat{L}}}$. It is also to be noticed that the essential BC have

been enforced at this stage and $\underline{\mathbf{U}}^*(z)$ now refers to the unconstrained degrees of freedom (DOF). The system of coupled ODE (2.23) can usually be solved in the framework of quadratic eigenvalue problem of gyroscopic type through a standard linearisation procedure which leads to a first-order ODE. However, to obtain the latter, a more systematic and elegant approach based on Legendre-Fenchel transformation of Hamiltonian systems is here adopted. For this purpose, the construction of the extended mixed Hamiltonian formulation first requires the determination of the dual or conjugate variable associated to $\underline{\dot{\mathbf{U}}}^*$. This is achieved by deriving this discretized generalized energy density, already used in the VF (2.21),

$$\mathcal{E}^*(\underline{\mathbf{U}}^*, \underline{\dot{\mathbf{U}}}^*) = \frac{1}{2} \underline{\mathbf{U}}^{*T} \left(\underline{\mathbf{K}}_{\underline{\underline{1}}} + \underline{\mathbf{K}}_{\underline{\underline{4}}} + 2\underline{\mathbf{K}}_{\underline{\underline{6}}} \right) \underline{\mathbf{U}}^* + \underline{\mathbf{U}}^{*T} \left(\underline{\mathbf{K}}_{\underline{\underline{3}}} + \underline{\mathbf{K}}_{\underline{\underline{5}}} \right) \underline{\dot{\mathbf{U}}}^* + \frac{1}{2} \underline{\dot{\mathbf{U}}}^{*T} \underline{\mathbf{K}}_{\underline{\underline{2}}} \underline{\dot{\mathbf{U}}}^* \quad (2.24)$$

with respect to $\underline{\dot{\mathbf{U}}}^*$ so that the conjugate variable $\underline{\mathbf{P}}_z^*$ has this expression

$$\underline{\mathbf{P}}_z^* = \frac{\partial \mathcal{E}^*}{\partial \underline{\dot{\mathbf{U}}}^*} = \underline{\mathbf{K}}_{\underline{\underline{2}}} \underline{\dot{\mathbf{U}}}^* + \left(\underline{\mathbf{K}}_{\underline{\underline{3}}}^T + \underline{\mathbf{K}}_{\underline{\underline{5}}}^T \right) \underline{\mathbf{U}}^* \quad (2.25)$$

By replacing the matrices in (2.25) by their expressions obtained after (2.22), it is easy to show that the conjugate nodal variables vector $\underline{\mathbf{P}}_z^*$ actually coincides with the *out-of-plane nodal transverse stresses resultant*, namely

$$\begin{aligned} \underline{\mathbf{P}}_z^* &= \int_{\Sigma_p} \left[\underline{\mathbf{N}}^T \left(\underline{\mathbf{C}}_{\underline{\underline{z}z}} \underline{\mathbf{N}} \underline{\dot{\mathbf{U}}}^* + \underline{\mathbf{C}}_{\underline{\underline{z}z}} \underline{\mathbf{N}} \underline{\mathbf{D}} \underline{\mathbf{U}}^* + \underline{\mathbf{C}}_{\underline{\underline{p}z}}^T \underline{\mathbf{N}} \underline{\mathbf{D}} \underline{\mathbf{U}}^* \right) \right] d\Sigma \\ &= \int_{\Sigma_p} \underline{\mathbf{N}}^T \left(\underline{\mathbf{C}}_{\underline{\underline{p}z}}^T \underline{\mathbf{S}}_p + \underline{\mathbf{C}}_{\underline{\underline{z}z}} \underline{\mathbf{S}}_z \right) d\Sigma \\ &\equiv \int_{\Sigma_p} \underline{\mathbf{N}}(x, y)^T \underline{\mathbf{T}}_z d\Sigma \end{aligned} \quad (2.26)$$

Next, Eq. (2.25) is solved for $\underline{\dot{\mathbf{U}}}^*$ so that:

$$\underline{\dot{\mathbf{U}}}^* = \underline{\mathbf{K}}_{\underline{\underline{2}}}^{-1} \underline{\mathbf{P}}_z^* - \underline{\mathbf{K}}_{\underline{\underline{2}}}^{-1} \left(\underline{\mathbf{K}}_{\underline{\underline{3}}}^T + \underline{\mathbf{K}}_{\underline{\underline{5}}}^T \right) \underline{\mathbf{U}}^* \quad (2.27)$$

Now, the elimination of $\underline{\dot{\mathbf{U}}}^*$ from the generalized strain energy density functional (2.24), combined with a Legendre transformation defined as,

$$\mathcal{H}^*(\underline{\mathbf{U}}^*, \underline{\mathbf{P}}_z^*) = \underline{\mathbf{P}}_z^{*T} \underline{\dot{\mathbf{U}}}^* - \mathcal{E}^*(\underline{\mathbf{U}}^*, \underline{\dot{\mathbf{U}}}^*) \quad (2.28)$$

leads to this explicit expression of the earlier Hamiltonian energy density functional

$$\begin{aligned} \mathcal{H}^*(\underline{\mathbf{U}}^*, \underline{\mathbf{P}}_z^*) &= \frac{1}{2} \underline{\mathbf{P}}_z^{*T} \underline{\mathbf{K}}_2^{-1} \underline{\mathbf{P}}_z^* - \underline{\mathbf{P}}_z^{*T} \underline{\mathbf{K}}_2^{-1} (\underline{\mathbf{K}}_3^T + \underline{\mathbf{K}}_5^T) \underline{\mathbf{U}}^* \\ &\quad - \frac{1}{2} \underline{\mathbf{U}}^{*T} \left[\underline{\mathbf{K}}_1 + \underline{\mathbf{K}}_4 + \underline{\mathbf{K}}_6 + \underline{\mathbf{K}}_6^T - (\underline{\mathbf{K}}_3 + \underline{\mathbf{K}}_5) \underline{\mathbf{K}}_2^{-1} (\underline{\mathbf{K}}_3^T + \underline{\mathbf{K}}_5^T) \underline{\mathbf{U}}^* \right] \end{aligned} \quad (2.29)$$

Thus, using (2.28), the Lagrangian VF (2.21) transforms into this Hamiltonian one

$$\delta \int_{\Sigma_z} \left[\underline{\mathbf{P}}_z^{*T} \dot{\underline{\mathbf{U}}}^* - \mathcal{H}^*(\underline{\mathbf{U}}^*, \underline{\mathbf{P}}_z^*) \right] dz - \left[\delta \underline{\mathbf{U}}^{*T} \widehat{\underline{\mathbf{L}}} \right]_{z_b}^{z_t} = 0 \quad (2.30)$$

Now, expliciting the variation in (2.30), combined with an integration by parts with regards to $\delta \underline{\mathbf{U}}^*$, gives

$$\int_{\Sigma_z} \left[\delta \underline{\mathbf{P}}_z^{*T} \dot{\underline{\mathbf{U}}}^* - \delta \underline{\mathbf{U}}^{*T} \dot{\underline{\mathbf{P}}}_z^* - \delta \underline{\mathbf{U}}^{*T} \left(\frac{\partial \mathcal{H}^*}{\partial \underline{\mathbf{U}}^*} \right) - \delta \underline{\mathbf{P}}_z^{*T} \left(\frac{\partial \mathcal{H}^*}{\partial \underline{\mathbf{P}}_z^*} \right) \right] dz + \left[\delta \underline{\mathbf{U}}^{*T} (\underline{\mathbf{P}}_z^* - \widehat{\underline{\mathbf{L}}}) \right]_{z_b}^{z_t} = 0 \quad (2.31)$$

After grouping together the terms relative to the same virtual nodal variables, the previous equation turns into the following one

$$\begin{aligned} \int_{\Sigma_z} \delta \underline{\mathbf{U}}^{*T} \left(-\dot{\underline{\mathbf{P}}}_z^* - \frac{\partial \mathcal{H}^*}{\partial \underline{\mathbf{U}}^*} \right) d\Sigma_z + \int_{\Sigma_z} \delta \underline{\mathbf{P}}_z^{*T} \left(\dot{\underline{\mathbf{U}}}^* - \frac{\partial \mathcal{H}^*}{\partial \underline{\mathbf{P}}_z^*} \right) dz &= 0 \quad (2.32) \\ \forall \left(\delta \underline{\mathbf{U}}^*, \delta \underline{\mathbf{P}}_z^* \right) / \underline{\mathbf{P}}_z^* = \widehat{\underline{\mathbf{L}}} \quad \text{on } z = \{z_b, z_t\} \end{aligned}$$

Now, the expression (2.29) of \mathcal{H}^* is substituted in Equation (2.32), leading to

$$\begin{aligned} \sum_{k=1}^{k=\text{NL}} \int_{z_k}^{z_{k+1}} \left[\delta \underline{\mathbf{P}}_z^{*T} \dot{\underline{\mathbf{U}}}^* - \delta \underline{\mathbf{U}}^{*T} \dot{\underline{\mathbf{P}}}_z^* + \delta \underline{\mathbf{U}}^{*T} \left(\underline{\mathbf{B}}_k \underline{\mathbf{U}}^* + \underline{\mathbf{A}}_k^T \underline{\mathbf{P}}_z^* \right) \right. \\ \left. + \delta \underline{\mathbf{P}}_z^{*T} \left(-\underline{\mathbf{D}}_k \underline{\mathbf{P}}_z^* + \underline{\mathbf{A}}_k \underline{\mathbf{U}}^* \right) \right] dz = 0 \end{aligned} \quad (2.33)$$

where, NL is the number of layers and the layer-dependent matrices are given by

$$\begin{aligned} \underline{\mathbf{D}}_k &= \underline{\mathbf{K}}_2^{-1} \quad ; \quad \underline{\mathbf{A}}_k = \underline{\mathbf{K}}_2^{-1} (\underline{\mathbf{K}}_3^T + \underline{\mathbf{K}}_5^T) \\ \underline{\mathbf{B}}_k &= \underline{\mathbf{K}}_1 + \underline{\mathbf{K}}_4 + \underline{\mathbf{K}}_6 + \underline{\mathbf{K}}_6^T - (\underline{\mathbf{K}}_3 + \underline{\mathbf{K}}_5) \underline{\mathbf{K}}_2^{-1} (\underline{\mathbf{K}}_3^T + \underline{\mathbf{K}}_5^T) \end{aligned}$$

Hence, thanks to the arbitrariness of $\delta \underline{\mathbf{U}}^*$ and $\delta \underline{\mathbf{P}}_z^*$, Eq. (2.33) leads to this first-order ODE system for the k-th layer

$$\begin{pmatrix} \dot{\underline{\mathbf{U}}}^* \\ \dot{\underline{\mathbf{P}}}_z^* \end{pmatrix} = \begin{bmatrix} -\underline{\mathbf{A}}_k & \underline{\mathbf{D}}_k \\ \underline{\mathbf{B}}_k & \underline{\mathbf{A}}_k^T \end{bmatrix} \begin{pmatrix} \underline{\mathbf{U}}^* \\ \underline{\mathbf{P}}_z^* \end{pmatrix} \quad (2.34)$$

It is worth mentioning from Eq. (2.34) that the number of *dual* nodal generalized stress resultants $\underline{\mathbf{P}}_z^*$ variables is now equal to the number of unconstrained N *primary* nodal generalized displacements $\underline{\mathbf{U}}^*$ ones so that Equation (2.34) is actually a $2N$ linear system with $2N$ unknowns. Besides, it can be readily shown that the system matrix of (2.34) is of Hamiltonian type since it satisfies the following identity for a given layer k

$$\underline{\underline{\mathbf{JH}}} = \left(\underline{\underline{\mathbf{JH}}} \right)^T \quad (2.35)$$

with

$$\underline{\underline{\mathbf{H}}} = \begin{bmatrix} -\underline{\underline{\mathbf{A}}} & \underline{\underline{\mathbf{D}}} \\ \underline{\underline{\mathbf{B}}} & \underline{\underline{\mathbf{A}}}^T \end{bmatrix}; \underline{\underline{\mathbf{J}}} = \begin{bmatrix} \underline{\underline{\mathbf{0}}} & \underline{\underline{\mathbf{I}}} \\ -\underline{\underline{\mathbf{I}}} & \underline{\underline{\mathbf{0}}} \end{bmatrix} \quad (2.36)$$

Furthermore, the diagonalization of the Hamiltonian matrix $\underline{\underline{\mathbf{H}}}$ is reached using the eigen solutions, $\left\{ \underline{\underline{\boldsymbol{\mu}}}_k; \underline{\underline{\boldsymbol{\Psi}}}_k \right\}$ of the following Hamiltonian eigenvalue problem

$$\underline{\underline{\mathbf{H}}} \underline{\underline{\boldsymbol{\Psi}}}_k = \underline{\underline{\boldsymbol{\Psi}}}_k \text{Diag} \left(\underline{\underline{\boldsymbol{\mu}}}_k \right) \quad (2.37)$$

As it can be noticed, $\text{tr} \left(\underline{\underline{\mathbf{H}}} \right) = 0$ (tr is the trace operator) so that the spectrum of the eigenvalue problem can be partitioned as

$$\text{Diag} \left(\underline{\underline{\boldsymbol{\mu}}}_k \right) = \begin{bmatrix} \text{Diag} \left(\underline{\underline{\boldsymbol{\mu}}}_k^+ \right) & \underline{\underline{\mathbf{0}}} \\ \underline{\underline{\mathbf{0}}} & -\text{Diag} \left(\underline{\underline{\boldsymbol{\mu}}}_k^+ \right) \end{bmatrix}; \underline{\underline{\boldsymbol{\mu}}}_k^+ \in \mathbb{C}/\text{Re} \left(\underline{\underline{\boldsymbol{\mu}}}_k^+ \right) > 0 \quad (2.38)$$

Similarly, the eigen matrix splits into two parts as

$$\underline{\underline{\boldsymbol{\Psi}}}_k = \begin{bmatrix} \underline{\underline{\boldsymbol{\Psi}}}_k^+ & \underline{\underline{\boldsymbol{\Psi}}}_k^- \end{bmatrix} \quad (2.39)$$

Where, each of its bloc matrices satisfies the following symplectic-orthogonality relation

$$\underline{\underline{\boldsymbol{\Psi}}}_k^{iT} \underline{\underline{\mathbf{J}}} \underline{\underline{\boldsymbol{\Psi}}}_k^j = - \left(\underline{\underline{\boldsymbol{\Psi}}}_k^j \underline{\underline{\mathbf{J}}} \underline{\underline{\boldsymbol{\Psi}}}_k^i \right)^T = \delta_{ij} \underline{\underline{\mathbf{I}}} \quad (2.40)$$

Further on, considering this generalized state vector $\underline{\underline{\mathbf{Z}}}_k^* = \left\{ \underline{\underline{\mathbf{U}}}^* \quad \underline{\underline{\mathbf{P}}}_z^* \right\}_k^T$, and making use of its modal projection as $\underline{\underline{\boldsymbol{\Pi}}}_k^* = \underline{\underline{\boldsymbol{\Psi}}}_k \underline{\underline{\mathbf{Z}}}_k^*$, the Hamiltonian eigenvalue problem (2.37) and the symplectic-orthogonality relation (2.40) allow to recast Eq. (2.37) into a diagonal form so that its general solution writes, for a given layer k , as

$$\underline{\underline{\mathbf{Z}}}_k^* = \underline{\underline{\boldsymbol{\Psi}}}_k \text{Diag} \left(e^{\underline{\underline{\boldsymbol{\mu}}}_k z} \right) \underline{\underline{\boldsymbol{\Lambda}}}_k \quad (2.41)$$

Where, the unknown layer-dependent coefficients vectors $\underline{\underline{\boldsymbol{\Lambda}}}_k$ are determined with the help of the IC constraints together with the BC on top and bottom surfaces of the composite, thereby completing the resolution of Eq. (2.35). Clearly this solution is of analytic type and hence the capacity to account for the exact satisfaction of the

IC as well as the BC on the top and bottom of the composite is expected. Finally, the formulation of the problem in terms of the state vector $\underline{\mathbf{Z}}_k^*$ allows to use the well-known mixed SSM to compute the solution throughout the whole thickness. The case of a layered composite is then treated through a propagator matrix which maps the state vector on the bottom to any height while satisfying the IC and BC (see Andrianarison and Benjeddou, 2012, for more details).

2.4 Benchmarking Examples

In this section, several numerical examples are investigated to test the stability and accuracy of the proposed method. The focus is made here on open literature benchmarks that provide tabulated results for non-classical BC (cantilever), multilayer composite layups (angle-ply) and electromechanical loads (uniform). The aim is to avoid, as much as possible, graphical (curves)-induced comparison errors and exact, closed-form and earlier solutions limitations to SS BC, cross-ply composite layups and trigonometric electromechanical loads. Such classical benchmarks are abundant in the open literature and have been already analysed in an earlier work (Andrianarison and Benjeddou, 2012). It is worthy to mention that tabulated results for the above mentioned non-classical configurations are rather seldom in the open literature and related benchmarks choice is very limited. Therefore, a numerical convergence analysis is first performed through the test-case of a cantilever PVDF bimorph, that is clamped on the edge $x = 0$ and free elsewhere. The actuator configuration is furthermore considered and the results are compared with reference 3D FE solutions. Next, the assessment of the accuracy of the method is obtained by analysing the bending of a PZT angle-ply composite plate under sensor configuration for which the cantilever and SS BC are successively analysed.

Before we proceed to the presentation of the benchmarking examples, it is worthwhile to show how the BC are actually taken into account in the numerical procedure. Let us consider the case of *a sensor* configuration where a mechanical force is applied on the top surface and a zero potential is applied on both lower and upper surfaces (Fig. 2.1a). We recall that, at the final stage of the aforementioned Hamiltonian VF, a $2N$ algebraic system is obtained after the *mechanical* displacement variables are constrained in agreement with the actual lateral BC, that is

$$\left\{ \begin{array}{c} \underline{\mathbf{u}} \\ \underline{\varphi} \\ \underline{\mathbf{P}}^m \\ \underline{\mathbf{P}}^e \end{array} \right\}_t = \left[\begin{array}{cccc} \underline{\underline{\mathbf{H}}}_{uu} & \underline{\underline{\mathbf{H}}}_{u\varphi} & \underline{\underline{\mathbf{H}}}_{u p_m} & \underline{\underline{\mathbf{H}}}_{u p_e} \\ \underline{\underline{\mathbf{H}}}_{\varphi u} & \underline{\underline{\mathbf{H}}}_{\varphi\varphi} & \underline{\underline{\mathbf{H}}}_{\varphi p_m} & \underline{\underline{\mathbf{H}}}_{\varphi p_e} \\ \underline{\underline{\mathbf{H}}}_{p_m u} & \underline{\underline{\mathbf{H}}}_{p_m \varphi} & \underline{\underline{\mathbf{H}}}_{p_m p_m} & \underline{\underline{\mathbf{H}}}_{p_m p_e} \\ \underline{\underline{\mathbf{H}}}_{p_e u} & \underline{\underline{\mathbf{H}}}_{p_e \varphi} & \underline{\underline{\mathbf{H}}}_{p_e p_m} & \underline{\underline{\mathbf{H}}}_{p_e p_e} \end{array} \right] \left\{ \begin{array}{c} \underline{\mathbf{u}} \\ \underline{\varphi} \\ \underline{\mathbf{P}}^m \\ \underline{\mathbf{P}}^e \end{array} \right\}_b \quad (2.42)$$

where index m (resp. e) refers to *mechanical* (resp. *electric*) type variables.

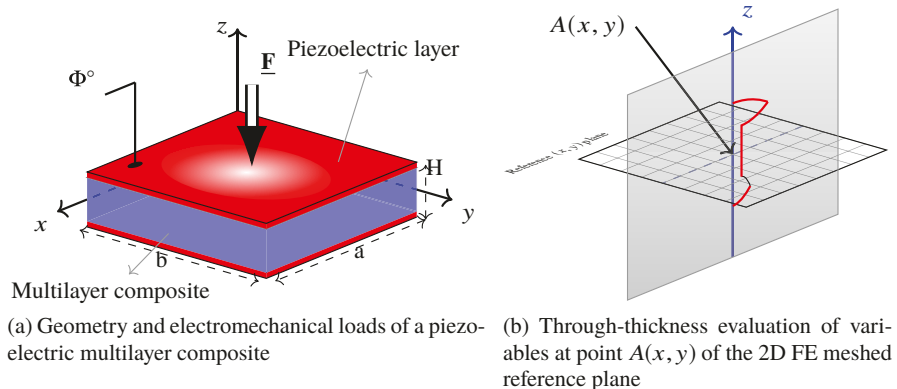


Fig. 2.1. Geometry and FE-SSM semi-analytical point 3D solution for a piezoelectric multilayer plate

As soon as the electric potential is fixed on the bottom and top surfaces, the second equation of (2.42) can be solved for the electric displacement nodal unknowns in terms of the mechanical nodal unknowns $\underline{\mathbf{u}}^b$ so that

$$\underline{\mathbf{P}}_e^b = \underline{\underline{\mathbf{H}}}_{\varphi p_e}^{-1} \left(\underline{\varphi}^t - \underline{\underline{\mathbf{H}}}_{\varphi u} \underline{\mathbf{u}}^b + \underline{\underline{\mathbf{H}}}_{\varphi \varphi} \underline{\varphi}^b + \underline{\underline{\mathbf{H}}}_{\varphi p_m} \underline{\mathbf{P}}_m^b \right) \quad (2.43)$$

Next, combining equation (2.43) with the third equation of (2.42) allows us to solve $\underline{\mathbf{u}}^b$ as the solution of

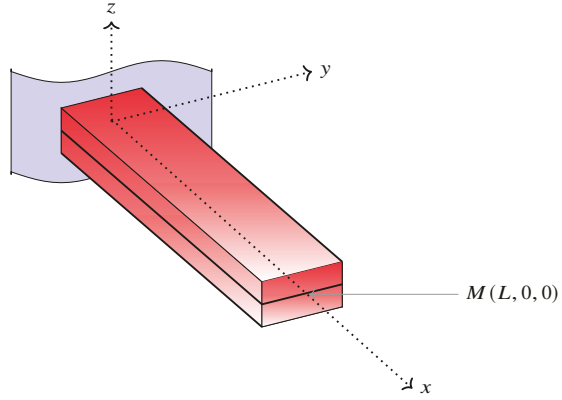
$$\begin{aligned} & \left(\underline{\underline{\mathbf{H}}}_{p_m u} \quad -\underline{\underline{\mathbf{H}}}_{p_m p_e} \quad \underline{\underline{\mathbf{H}}}_{\varphi p_e}^{-1} \quad \underline{\underline{\mathbf{H}}}_{\varphi u} \right) \underline{\mathbf{u}}^b = \underline{\mathbf{P}}_m^t - \left(\underline{\underline{\mathbf{H}}}_{p_m p_e} \quad -\underline{\underline{\mathbf{H}}}_{p_m p_m} \quad \underline{\underline{\mathbf{H}}}_{\varphi p_e}^{-1} \quad \underline{\underline{\mathbf{H}}}_{\varphi p_m} \right) \underline{\mathbf{P}}_m^b \\ & - \left(\underline{\underline{\mathbf{H}}}_{p_m \varphi} \quad -\underline{\underline{\mathbf{H}}}_{p_m p_e} \quad \underline{\underline{\mathbf{H}}}_{\varphi p_e}^{-1} \quad \underline{\underline{\mathbf{H}}}_{\varphi \varphi} \right) \underline{\varphi}^b - \underline{\underline{\mathbf{H}}}_{p_m p_e} \quad \underline{\underline{\mathbf{H}}}_{\varphi p_e}^{-1} \quad \underline{\varphi}^t \end{aligned} \quad (2.44)$$

Once $\underline{\mathbf{u}}^b$ are determined, all other nodal variables on the lower surface are easily recovered recursively and the solution through-the-thickness of the plate is computed with the help of the propagator matrix.

2.4.1 Numerical Convergence Analysis

In this first example, a piezoelectric cantilever bimorph (Fig. 2.2) under *uniform* electric load is investigated using the proposed method. It is made of two-ply PVDF identical layers with outward opposite polarities to obtain a bending actuator. The bimorph total thickness is $h = 1$ mm whereas the length is $a = 100$ mm and the width is $b = 5$ mm. The actuator configuration is considered here so that a uniform electric potential $\underline{\Phi} = 1$ V is applied on the top surface. The edge BC of the bimorph are assumed clamped on the edge $x = 0$; that is $u_x|_{x=0} = u_y|_{x=0} = u_z|_{x=0} = 0$ and free

Fig. 2.2 Bimorph actuator configuration



elsewhere. The material properties of the PVDF layers used in this numerical example are (Tzou, 1993): $E_1 = E_2 = E_3 = 2 \text{ GPa}$, $\nu_{12} = \nu_{13} = \nu_{23} = 0.29$, $G_{12} = G_{13} = G_{23} = 1 \text{ GPa}$, $e_{31} = e_{32} = 0.046 \text{ C/m}^2$, $e_{33} = e_{24} = e_{15} = 0.0$, $\epsilon_{11}^S = \epsilon_{22}^S = \epsilon_{33}^S = 106.2 \text{ pF/m}$.

Some selected references are given here for comparison. The results in Tahani and Naserian-Nik (2013); Phung-Van et al (2015); Li et al (2014); Vidal et al (2011) were obtained through 3D FE, 2D plate isogeometric FE, plate B-Spline finite point and refined shell FE methods, respectively. These reference solutions are used here to analyse the behaviour of the present semi-analytical solution in terms of accuracy, stability and convergence. The variables are thus evaluated in specific in-plane locations along the bimorph where their values are compared with those obtained by the references. Therefore, the static deflection of the bimorph at those specific points are given in Table 2.1 for the here implemented Q4 FE different mesh discretizations. It can be seen that the results obtained with the present approach agree very well with the 3D FEM solution as given in Tahani and Naserian-Nik (2013) and are more accurate than those of the other 2D methods (isogeometric FE of Phung-Van et al (2015), B-spline finite point of Li et al (2014) and refined shell FE of Vidal et al (2011)). Besides, it is clear that the convergence of the present semi-analytical approach is very rapid as the reference values are reached for the five evaluation points with a maximum relative deviation of less than 1.5% using a coarse mesh of 16 (8x2) in-plane FE (Fig. 2.3). Moreover, the through-the-normalized ($Z = z/h$) thickness distributions of the non-dimensional transverse stresses

$$(\tilde{\sigma}_{xz}, \tilde{\sigma}_{zz}) = (\sigma_{xz}, \sigma_{zz}) \times \frac{a}{\Phi e_{31}}$$

and the non-dimensional transverse electric displacement

$$\tilde{D}_z = \frac{D_z}{e_{31}} \times 10^6$$

displayed in Figs. 2.4 and 2.5 confirm that the IC constraints are satisfied.

Table 2.1
 Transverse displacement ($u_z \times 10^{-7}$ m) at point (x mm, 0, 0) for a PVDF bimorph actuator

Solution method	Mesh	Point location x (mm)				
		20	40	60	80	100
Present (2D Q4 FE-SSM)	4 × 2	0.125	0.505	0.99	1.75	2.815
	6 × 2	0.131	0.532	1.140	2.054	3.210
	8 × 2	0.134	0.543	1.223	2.183	3.434
	10 × 2	0.134	0.543	1.225	2.183	3.435
	12 × 2	0.134	0.543	1.224	2.183	3.435
Error _{3D} (%) ^b		-1.47	-0.55	-0.65	-0.55	0.73
3D H8 FE (Tahani and Naserian-Nik, 2013) ^a	5 × 1 × 2	0.136	0.546	1.232	2.193	3.410
2D plate quadratic isogeometric FE (Phung-Van et al, 2015)	101 × 6	0.138	0.550	1.236	2.201	3.443
Error _{3D} (%) ^b		1.47	0.97	0.73	0.36	0.32
2D plate B-Spline finite point (Li et al, 2014)	5 × 4	0.137	0.551	1.241	2.207	3.449
Error _{3D} (%) ^b		0.74	0.92	0.73	0.64	1.14
2D refined shell Q8 FE Vidal et al (2011)	5 × 1	0.137	0.551	1.241	2.207	3.449
Error _{3D} (%) ^b		0.73	0.91	0.73	0.64	1.14

^a The numerical values are obtained from non-dimensional quantities in Tahani and Naserian-Nik (2013)

^b The errors are computed with respect to 3D FE results

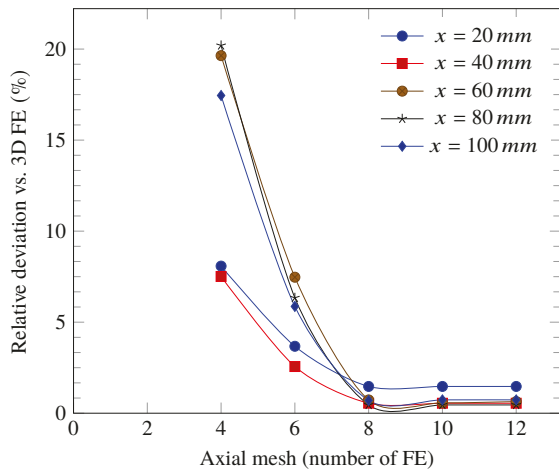
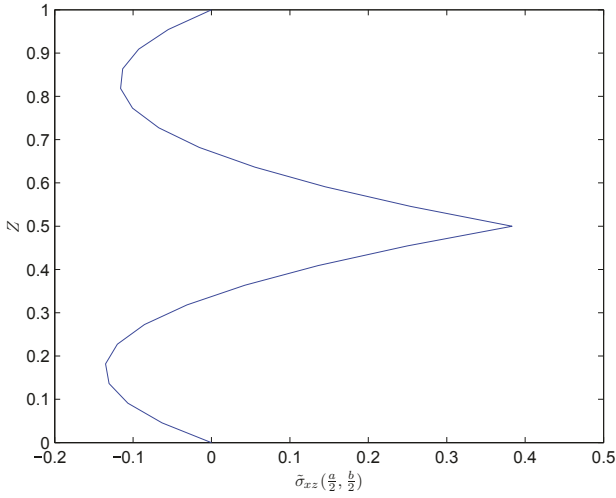
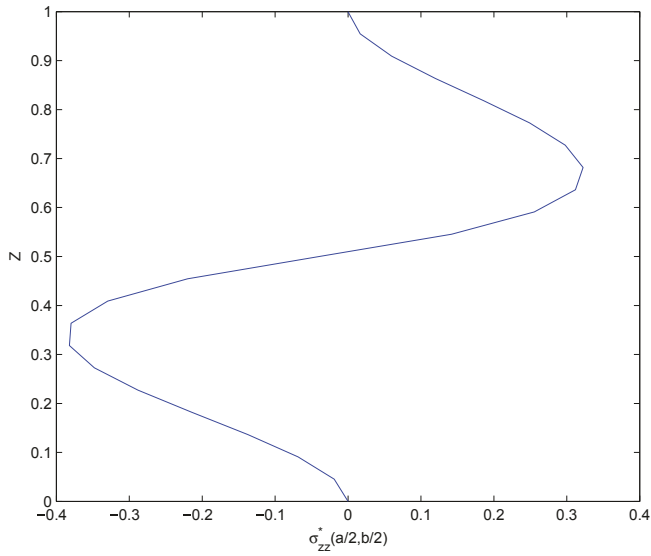


Fig. 2.3 Deflection convergence plots at different axial positions for the PVDF bimorph actuator



(a) Through-the-thickness distribution of $\tilde{\sigma}_{xz}$



(b) Through-the-thickness distribution of $\tilde{\sigma}_{zz}$

Fig. 2.4. Through-the-thickness distributions of non-dimensional transverse stresses in the PVDF bimorph actuator

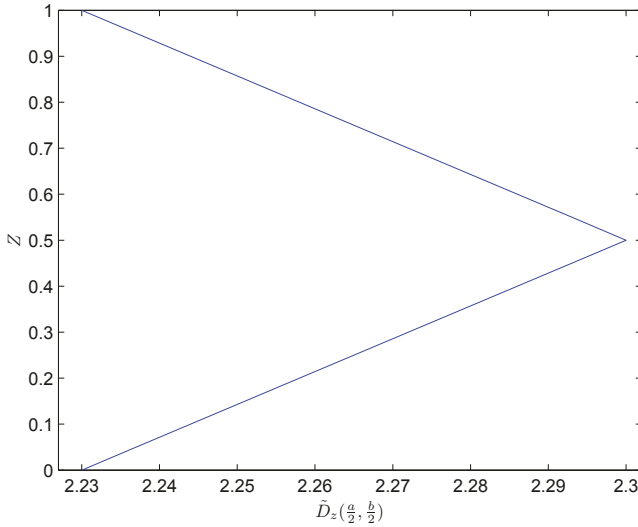


Fig. 2.5. Through-thickness distribution of \tilde{D}_z in the PVDF bimorph actuator

Table 2.2 shows the results relative to the bimorph tip deflection when different voltages are applied. They are compared with those of 2D B-spline finite point approach (Li et al, 2014) and with the theoretical and experimental data provided by Tzou (1989). First, the observed relatively high deviations of the numerical results with respect to the experimental ones can be explained by the stiffer clamping BC numerical representation compared to the softer actual ones, and by the non-realistic (electromechanical isotropic behaviour, nil elastic Poisson’s ratio and piezoelectric

Table 2.2
Tip deflection ($u_z \times 10^{-7}$ m) of the PVDF bimorph for different applied voltages

Method	Voltage (V)					
	10	40	80	130	160	200
Present (10×2)	3.460	13.771	27.407	45.433	54.703	68.228
Error* _{exp} (%)	5.33	10.48	12.37	13.06	9.22	7.91
Experiment (Tzou, 1989)	3.285	12.465	24.390	40.185	50.085	63.225
Classical beam theory (Tzou, 1989)	3.450	13.800	27.600	44.850	55.200	69.000
Error* _{exp} (%)	5.02	10.71	13.16	11.61	10.21	9.13
2D B-spline finite point (Li et al, 2014)	3.449	13.797	27.794	44.841	55.188	68.986
Error* _{exp} (%)	4.99	10.6	13.96	11.59	10.19	9.11

* The errors are computed with respect to the experimental results

coupling coefficients, etc.) PVDF available material data. Then, it can be seen that the results obtained with the present method match well the theoretical ones obtained in Tzou (1989) and are the closest to the experimental values, in particular for the last two highest actuation voltages (see Fig. 2.6). To assess the computational cost, a comparison of different models in terms of the number of DOF is presented in Table 2.3 when the convergence is reached. It can be observed that the present 2D Q4 FE-SSM semi-analytical 3D solution is the cheapest (lowest total DOF) and, as expected, its characteristics are closer to the 3D FE solution in terms of cost (total non-nil DOF) and accuracy (relative deviation, see Table 2.1).

Table 2.3

Computational cost (out of clamped nodes and DOF) comparison of the present 3D semi-analytic solution with others for the PVDF bimorph actuator

Method	FE	Free nodes	Mechanical (free DOF)	Electrical (non nil DOF)	Total (non nil DOF)
Present 3D semi-analytical (Q4 FE-SSM)	16	24	72	24	96
3D H8 FE (Tzou, 1993)	10	30	90	24	114
2D refined shell Q8 FE (Vidal et al, 2011)	5	25	175	10	185
2D plate B-Spline finite point (Li et al, 2014)	20	25	125	50	175

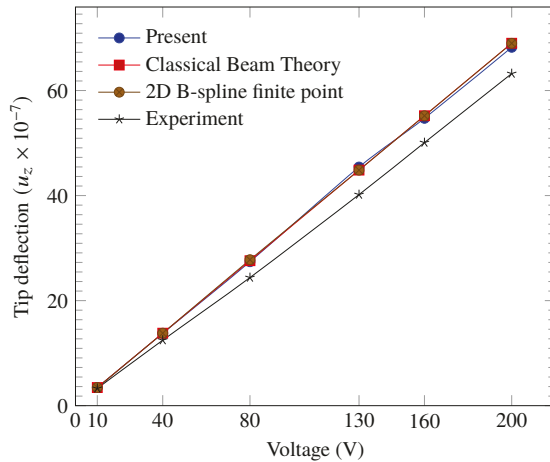


Fig. 2.6 Bimorph tip deflection under different actuation voltages

2.4.2 Square Cantilever PZT Angle-ply Composite Plate

A (20 cm × 20 cm) six-layer cantilever plate, made of T300/976 Graphite-Epoxy (GE) and piezoceramic (PZT-G1195N) materials, is considered (Pablo et al, 2009). The BC are thus $u_x|_{x=0} = u_y|_{x=0} = u_z|_{x=0} = 0$. The GE composite is bonded by PZT layers on its bottom and top surfaces and each of its laminae is of equal thickness (see Fig. 2.1a). The composite plate total thickness is fixed as $h = 1$ mm whereas that of each PZT layer is 0.1 mm. The anti-symmetric (as) laminate angle-ply sequence is considered; that is $[PZT/-\theta/\theta]_{as}$ where θ (here 45°) is the fiber orientation angle of the ply. The material properties are summarized in Table 2.4. It should be noticed that the PZT-G1195N material properties given in Pablo et al (2009) are unrealistically considered as elastically isotropic whereas those in Benjeddou et al (2002) are realistically anisotropic (transverse-isotropic). The simulation is conducted for both datasets in order to show the influence of the unrealistic assumption of PZT isotropic elastic behaviour. Besides, only the sensor configuration is considered in this test-case; that is, a uniform mechanical pressure of amplitude $p^\circ = 100\text{N/m}^2$ is applied on the upper surface whereas a zero equipotential voltage is imposed on the plate bottom and top surfaces. Table 2.5 shows that the present semi-analytical approach is able to recover, with -0.18% of relative deviation for the same mesh, the 2D FE solution (Pablo et al, 2009) based on the classical plate theory and without electric DOF. Besides, it is clear that the unrealistic behaviour assumption for the PZT-G1195N greatly overestimates its realistic anisotropic (transverse-isotropic) one. Indeed, the converged tip deflection computed using the former over estimates by

Table 2.4
Material properties of the PZT composite plate ($\epsilon^\circ = 8.85 \times 10^{-12}\text{C/Nm}^2$)

Property	Pablo et al (2009)		Benjeddou et al (2002)		Benjeddou et al (2002)	
	T300/976 GE	PZT-G1195N	Property	T300/976 GE	Property	PZT-G1195N
E_1 , GPa	150	63.0	E_1 , GPa	150	C_{11} , GPa	148
E_2 , GPa	9.0	63.0	E_2 , GPa	9.0	C_{22} , GPa	148
E_3 , GPa	9.0	63.0	E_3 , GPa	9.0	C_{33} , GPa	131
G_{12} , GPa	7.1	24.2	G_{12} , GPa	7.1	C_{12} , GPa	76.2
G_{13} , GPa	7.1	24.2	G_{13} , GPa	7.1	C_{13} , GPa	74.2
G_{23} , GPa	2.5	24.2	G_{23} , GPa	2.5	C_{23} , GPa	74.2
ν_{12}	0.3	0.3	ν_{12}	0.30	C_{66} , GPa	35.9
ν_{23}	0.3	0.3	ν_{23}	0.30	C_{44} , GPa	25.4
ν_{13}	0.3	0.3	ν_{13}	0.30	C_{55} , GPa	25.4
d_{31} , pmV $^{-1}$	0.0	-254	e_{31} , C/m 2	0.0	e_{31} , C/m 2	-2.1
d_{32} , pmV $^{-1}$	0.0	-254	e_{32} , C/m 2	0.0	e_{32} , C/m 2	-2.1
d_{33} , pmV $^{-1}$	0.0	374	e_{33} , C/m 2	0.0	e_{33} , C/m 2	9.5
d_{15} , pmV $^{-1}$	0.0	584	e_{15} , C/m 2	0.0	e_{15} , C/m 2	9.2
d_{24} , pmV $^{-1}$	0.0	584	e_{24} , C/m 2	0.0	e_{24} , C/m 2	9.2
ϵ_{11}^T , nFm $^{-1}$	0.0	15.3	$\epsilon_{11}^S/\epsilon^\circ$	3.5	$\epsilon_{11}^S/\epsilon^\circ$	460
ϵ_{22}^T , nFm $^{-1}$	0.0	15.3	$\epsilon_{22}^S/\epsilon^\circ$	3.0	$\epsilon_{22}^S/\epsilon^\circ$	460
ϵ_{33}^T , nFm $^{-1}$	0.0	15.0	$\epsilon_{33}^S/\epsilon^\circ$	3.0	$\epsilon_{33}^S/\epsilon^\circ$	235

Table 2.5

Tip deflection u_z (mm) at point (0.2m, 0, 0) of cantilever PZT composite plate under uniform pressure

Method	Mesh	Isotropic PZT (Pablo et al, 2009)	Transverse-Isotropic PZT (Benjeddou et al, 2002)
2D plate FE (Pablo et al, 2009)	6×6	2.750 ^a	–
Present (2D Q4 FE-SSM) (deviation)	6×6	2.745 (–0.18%)	1.408
	8×8	2.748 (–0.07%)	1.410
	10×10	2.748 (–0.07%)	1.410

^a This numerical value is estimated from Fig. 4 of Pablo et al (2009) and may be subjected to inaccuracies

94.89% that obtained using the latter (see the last line and column values of Table 2.5).

2.4.3 Square SS PZT Angle-ply Composite Plate

The same PZT composite plate investigated in Subsect. 2.4.2 is considered here. However, the plate is here supposed to be under SS-2 BC defined as $u_y = u_z = 0$ at $x = \{0, a\}$ and $u_x = u_z = 0$ at $y = \{0, b\}$. The PZT-G1195N electro-mechanical properties given in Table 2.4 (Pablo et al, 2009) are retained. Both symmetric (s) and anti-symmetric stacking sequences are considered; that is $[PZT/-\theta/\theta]_{as}$ and $[PZT/-\theta/\theta]_s$ with $\theta = 45^\circ$.

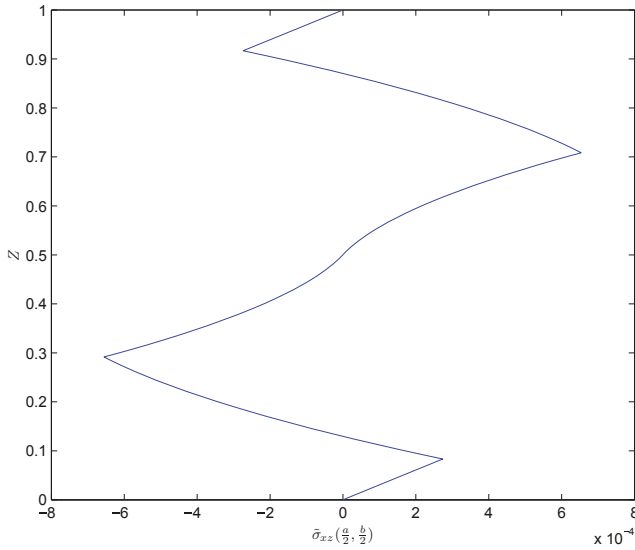
Table 2.6 shows that the present semi-analytical approach is able to predict accurate results with relative deviations of –0.03% for the symmetric and 0.06% for the anti-symmetric 45° stacking with regards to the meshless Radial Point Interpolation Method (RPIM) presented in Liu et al (2004). It can be also observed that the central deflection is higher for all anti-symmetric layups and increases with decreasing the ply angle. Moreover, the through-the-normalized ($Z = z/H, H = h + 2h_p$) thickness distributions of the non-dimensional transverse shear stress $\tilde{\sigma}_{xz} = \sigma_{xz} \times (H/ap^\circ)$ and

Table 2.6

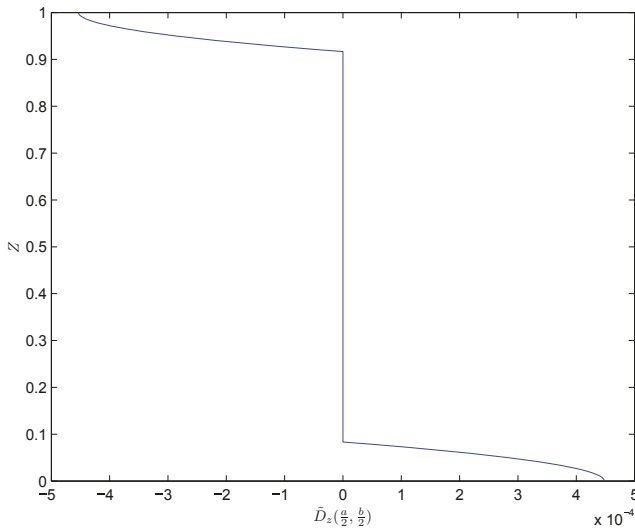
Central point deflection ($\times 10^{-5}m$) of a SS PZT composite plate under uniform pressure

Stacking sequence	θ (°)	2D Plate meshless RPIM	Present	
		(Liu et al, 2004) (15×15)	(2D FE Q4-SSM) (8×8)	(10×10)
$[PZT/-\theta/\theta]_{as}$	15	7.222	7.235 (0.18%)	7.235 (0.18%)
$[PZT/-\theta/\theta]_{as}$	30	6.542	6.537 (–0.08%)	6.537 (–0.08%)
$[PZT/-\theta/\theta]_{as}$	45	6.217	6.221 (0.06%)	6.221 (0.06%)
$[PZT/-\theta/\theta]_s$	45	6.038	6.036 (–0.03%)	6.036 (–0.03%)

the non-dimensional transverse electric displacement $\tilde{D}_z = D_z/e_{31}$ displayed in Figs. 2.7 and 2.8 confirm that the IC constraints are satisfied.



(a) Through-the-normalized ($Z = z/H$) thickness distribution of non-dimensional transverse shear stress $\bar{\sigma}_{xz}$



(b) Through-the-normalized ($Z = z/H$) thickness distribution of the non-dimensional transverse electric displacement \tilde{D}_z

Fig. 2.7. [PZT/ $-45^\circ/45^\circ$] $_{as}$ SS composite plate under uniform pressure

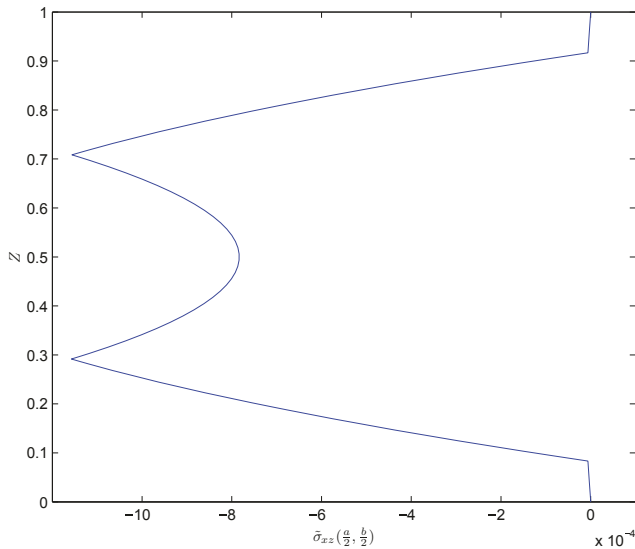


Fig. 2.8. Through-the-normalized thickness distribution of $\bar{\sigma}_{xz}$ in the $[PZT/-45^\circ/45^\circ]_S$ SS composite plate under uniform pressure

2.5 Conclusions and Perspectives

This chapter presented a new mixed Hamiltonian semi-analytical 3D static analysis solution. It is based on Lagrangian 2D in-plane FE discretization, allowing arbitrary edges BC, and mixed Hamiltonian VF, single-layer symplectic solution and propagator matrix through the thickness of the multilayer smart composite, allowing automatic satisfaction of the IC constraints. This combination of in-plane Lagrangian and through-the-thickness Hamiltonian formalisms, through the Legendre transformation, and the use of the nodal transverse stresses and electric displacement resultants as dual independent variables are the main originalities of the presented research work. It is applied to the analysis of multilayered piezoelectric structures static actuation and sensing and the comparison of the results with various reference solutions shows its rapid convergence and high accuracy. Moreover, the results also show that the present method is able to take into account realistic BC such as clamped and free edges, as well as non-classical multilayer composites stacking sequences such as symmetric and anti-symmetric angle-ply layouts.

This work focused on presenting the detailed derivation of the new mixed Hamiltonian semi-analytic 3D solution with application to the static actuation and sensing of multilayered piezoelectric smart composites. It is worthwhile to investigate its extension to vibration and dynamic analyses.

References

- Andrianarison O, Benjeddou A (2012) Hamiltonian partial mixed finite element-state space symplectic semi-analytical approach for the piezoelectric smart composites and FGM analysis. *Acta Mechanica* 223(8):1597–1610
- Benedetti I, Aliabadi MH, Milazzo A (2010) A fast BEM for the analysis of damaged structures with bonded piezoelectric sensors. *Computer Methods in Applied Mechanics and Engineering* 199(9):490–501
- Benjeddou A (2000) Advances in piezoelectric finite element modeling of adaptive structural elements: a survey. *Computers & Structures* 76(1–3):347–363
- Benjeddou A, Andrianarison O (2005) A piezoelectric mixed variational theorem for smart multilayered composites. *Mechanics of Advanced Materials and Structures* 12(1):1–11
- Benjeddou A, Deü JF (2001) Piezoelectric transverse shear actuation and sensing of plates, part 1: A three-dimensional mixed state space formulation. *Journal of Intelligent Material Systems and Structures* 12(7):435–449
- Benjeddou A, Deü JF, Letombe S (2002) Free vibrations of simply-supported piezoelectric adaptive plates: an exact sandwich formulation. *Thin-Walled Structures* 40(7):573 – 593
- Boffi D, Brezzi F, Fortin M (2013) *Mixed Finite Element Approach and Applications*. Springer, Berlin, Heidelberg
- Carrera E, Büttner A, Nali P (2010) Mixed elements for the analysis of anisotropic multilayered piezoelectric plates. *Journal of Intelligent Material Systems and Structures* 21(7):701–717
- Kapurja S, Kumari P, Nath JK (2010) Efficient modeling of smart piezoelectric composite laminates: a review. *Acta Mechanica* 214(1–2):31–48
- Khandelwal RP, Chakrabarti A, Bhargava P (2013) An efficient hybrid plate model for accurate analysis of smart composite laminates. *Journal of Intelligent Material Systems and Structures* 24(16):1927–1950
- Leung AYT, Zheng JJ, Lim CW, Zhang X, Xu XS, Gu Q (2008) A new symplectic approach for piezoelectric cantilever composite plates. *Computers & Structures* 86(19):1865–1874
- Li D (2020) Layerwise theories of laminated composite structures and their applications: A review. *Archives of Computational Methods in Engineering* online first:1–24, DOI 10.1007/s11831-019-09392-2
- Li S, Huang L, Jiang L, Qin R (2014) A bidirectional B-spline finite point method for the analysis of piezoelectric laminated composite plates and its application in material parameter identification. *Composite Structures* 107:346–362
- Lim CW, Xu XS (2010) *Symplectic Elasticity: Theory and Applications*. *Applied Mechanics Reviews* 63(5):1–10
- Liu GR, Dai KY, Lim KM (2004) Static and vibration control of composite laminates integrated with piezoelectric sensors and actuators using the radial point interpolation method. *Smart Materials and Structures* 13(6):1438–1447

- Moleiro F, Mota Soares CM, Mota Soares CA, Reddy J (2015) Layerwise mixed models for analysis of multilayered piezoelectric composite plates using least-squares formulation. *Composite Structures* 119:134 – 149
- Pablo F, Bruant I, Polit O (2009) Use of classical plate finite elements for the analysis of electroactive composite plates. Numerical validations. *Journal of Intelligent Material Systems and Structures* 20(15):1861–1873
- Phung-Van P, Lorenzis LD, Thai CH, Abdel-Wahab M, Nguyen-Xuan H (2015) Analysis of laminated composite plates integrated with piezoelectric sensors and actuators using higher-order shear deformation theory and isogeometric finite elements. *Computational Materials Science* 96(PartB):495 – 505
- Shan L, Jun L, Gao L, Zhang Z, Zhang P (2018) The static solution for the layered piezoelectric bounded domain with side face load by the modified SBFEM. *Advances in Applied Mathematics and Mechanics* 10:209–241
- Sze KY, Pan YS (1999) Hybrid finite element models for piezoelectric materials. *Journal of Sound and Vibration* 226(3):519 – 547
- Tahani M, Naserian-Nik AM (2013) Bending analysis of piezolaminated rectangular plates under electromechanical loadings using multi-term extended Kantorovich method. *Mechanics of Advanced Materials and Structures* 20(6):415–433
- Tzou HS (1989) Development of a light-weight robot end-effector using polymeric piezoelectric bimorph. In: *Proceedings, 1989 International Conference on Robotics and Automation, IEEE, Scottsdale, AZ, vol 3, pp 1704–1709*
- Tzou HS (1993) *Piezoelectric Shells: Distributed Sensing and Control of Continua*. Kluwer Academic Publishers
- Vidal P, D’Ottavio M, Thaïer MB, Polit O (2011) An efficient finite shell element for the static response of piezoelectric laminates. *Journal of Intelligent Material Systems and Structures* 22(7):671–690
- Wu CP, Liu YC (2016) A review of semi-analytical numerical methods for laminated composite and multilayered functionally graded elastic/piezoelectric plates and shells. *Composite Structures* 147:1–15
- Zhang WX, Wang H (2018) Axisymmetric boundary condition problems for transversely isotropic piezoelectric materials. *Mechanics Research Communications* 87:7 – 12
- Zhou Y, Li S, Zhou H (2015) State space finite element analysis for piezoelectric precision positioning considering secondary converse piezoelectric effect. *Finite Elements in Analysis and Design* 102-103:85 – 94
- Zhou Y, Nyberg T, Xiong G, Li S (2020) State space finite element analysis for piezoelectric laminated curved beam with variable curvature. *Mechanics of Advanced Materials and Structures* 27(4):265–273



Chapter 3

On Static Two-dimensional Models of Thermo-electro-magneto-elastic Shells

Gia Avalishvili and Mariam Avalishvili

Abstract This paper is devoted to the construction and investigation of two-dimensional models for anisotropic inhomogeneous thermo-electro-magneto-elastic shells with variable thickness, which may vanish on a part of the lateral boundary. The variational formulation in curvilinear coordinates of the boundary value problem corresponding to the three-dimensional model of the shell, when density of surface force and components of electric displacement, magnetic induction and heat flux along the outward normal vector are given along the upper and lower face surfaces of the shell, is obtained and the well-posedness result in suitable factor space of Sobolev space is given. The subspaces with special structures of the spaces corresponding to the original three-dimensional problem are considered and applying variational formulation a hierarchy of static two-dimensional models is constructed. The boundary value problems corresponding to the obtained two-dimensional models are investigated in factor spaces of suitable weighted Sobolev spaces, and the relationship between the constructed hierarchical two-dimensional models and the original three-dimensional one is studied.

Key words: Thermo-electro-magneto-elasticity · Shells · Two-dimensional models · Boundary value problems · Existence and uniqueness of solution · Modeling error estimate

Gia Avalishvili
Faculty of Exact and Natural Sciences, I. Javakhishvili Tbilisi State University, 3 I. Tchavtchavadze Ave., 0179 Tbilisi, Georgia
e-mail: gavalish@yahoo.com

Mariam Avalishvili
School of Science and Technology, University of Georgia, 77a M. Kostava St., 0175 Tbilisi, Georgia
e-mail: m.avalishvili@ug.edu.ge

3.1 Introduction

Many parts of smart structures made of piezoelectric materials come in the forms of plates or shells, which undergo high mechanical and thermal loads. Since inhomogeneous, in particular, functionally graded (Udupa et al, 2014), materials are used to increase the durability and efficiency of devices, and two-dimensional models of elastic structures are always preferable to three-dimensional ones, it is important to construct and investigate mathematical models of inhomogeneous anisotropic thermo-electro-magneto-elastic plates and shells.

Mathematical models of a three-dimensional piezoelectric and pyroelectric continuum and hypotheses of linear constitutive relations first were developed by Voigt (1890). Later on, Tiersten (1964) studied problems of vibration of piezoelectric plates. The three-dimensional equations of the linear thermopiezoelectricity were considered by Mindlin (1974) and two-dimensional equations for plates were derived on the basis of variational principle and approximation by polynomials with respect to the variable of plate thickness. Nowacki (1978) developed some general theorems for thermoelastic piezoelectric materials. Dhaliwal and Wang (1994) proved a uniqueness theorem for linear three-dimensional thermopiezoelectricity without making any restrictions on the coupling constant between temperature and electric field, and with only symmetry assumptions imposed on the elasticity tensor, which further was generalized by Aouadi (2007) for thermo-electro-magneto-elasticity and, in addition, the result was proved without positive definiteness assumptions on the thermal conductivity tensor. The analogue of the Reissner's mixed variational theorem for thermopiezoelectric multilayered composites was obtained by Benjeddou and Andrianarison (2005). Mathematical modeling of electro-magneto-elastic thin plates by using asymptotic method was discussed by Weller and Licht (2007). Applying the potential method and theory of pseudodifferential equations, Natroshvili (2011) studied static and pseudo-oscillation problems with basic, mixed and crack-type boundary conditions for homogeneous anisotropic thermo-electro-magneto-elastic bodies. Static and dynamic problems for inhomogeneous anisotropic thermo-electro-magneto-elastic solids with general mixed boundary conditions were investigated applying variational approach by Avalishvili et al (2017a,b).

In the present paper, we consider the static three-dimensional model of thermo-electro-magneto-elastic shell and construct a hierarchy of two-dimensional models, which approximates the original three-dimensional boundary value problem, by applying generalization of dimensional reduction algorithm suggested by Vekua (1955) for homogeneous isotropic plates with variable thickness in the classical linear theory of elasticity. In Vekua (1955) components of the displacement vector-function were expanded into orthogonal Fourier-Legendre series with respect to the variable of plate thickness and then leaving only the first finite number of terms in the expansions and corresponding equations a hierarchy of differential two-dimensional models was constructed. Note that the classical Kirchhoff-Love and Reissner-Mindlin models can be incorporated into the hierarchy obtained by Vekua so that it can be considered as an extension of the frequently used engineering plate models. Further, various mathematical models of plates and shells constructed by Vekua were

collected in his monograph (Vekua, 1985). Static two-dimensional models constructed by Vekua (1985) for shallow shells first were investigated by Gordeziani (1974b), and the estimates of the order of approximation of the exact solution of the static three-dimensional problem for elastic plate by vector-functions of three variables restored from the solutions of the reduced two-dimensional problems, constructed in Vekua (1955), in the spaces of classical smooth functions were obtained in Gordeziani (1974a). The hierarchy of static two-dimensional models constructed in Vekua (1955) for plates was investigated in Sobolev spaces, convergence result and estimate of the rate of convergence was obtained by Avalishvili (1999). Static and dynamic hierarchical two-dimensional models were constructed and modeling error was estimated for plates with variable thickness by Avalishvili and Gordeziani (2003) and for shells by Avalishvili and Avalishvili (2004); Gordeziani et al (2006). Applying variational approach and generalization of Vekua's dimensional reduction method static and dynamic one-dimensional hierarchical models and corresponding convergence results for elastic bars were obtained by Avalishvili (2002, 2006). Mathematical models constructed by applying dimensional reduction methods of Vekua (1955, 1985) and their modifications, and related mathematical problems were studied by many researchers (see Vogelius and Babuška, 1981; Miara, 1989; Jaiani, 2001; Dauge et al, 2017; Gordeziani and Avalishvili, 2005; Avalishvili and Avalishvili, 2007; Avalishvili et al, 2010; Avalishvili and Avalishvili, 2014, and the references given therein).

It should be pointed out that two-dimensional hierarchical models for anisotropic inhomogeneous thermo-electro-magneto-elastic shells with general geometrical shape have not been constructed and investigated yet. The static and dynamic hierarchical two-dimensional models for thermo-electro-magneto-elastic plates with variable thickness were constructed and investigated by Avalishvili and Avalishvili (2018a,b). In the present paper, we consider thermo-electro-magneto-elastic shells made of anisotropic inhomogeneous material and construct a hierarchy of static two-dimensional models approximating three-dimensional one where, on certain parts of the lateral boundary, mechanical displacement, electric and magnetic potentials, and temperature vanish and, on the corresponding remaining part of the boundary, components of the mechanical stress vector, electric displacement and magnetic induction, and heat flux along the outward normal vector of the boundary are given. We investigate the constructed two-dimensional models and obtain new well-posedness results for corresponding boundary value problems and modeling error estimates in suitable factor spaces of Sobolev spaces.

In Sect. 3.2, we consider the differential formulation of the boundary value problem in Cartesian coordinates corresponding to the linear static three-dimensional model of inhomogeneous anisotropic thermo-electro-magneto-elastic shell with mixed boundary conditions. We obtain integral equations that are equivalent to the original problem in the space of twice continuously differentiable functions and applying them we present variational formulation in curvilinear coordinates of the three-dimensional boundary value problem in corresponding Sobolev spaces. Furthermore, we formulate theorem regarding the existence, uniqueness and con-

tinuous dependence of a solution on the given data in suitable factor space of the corresponding Sobolev space.

In Sect. 3.3, we introduce subspaces with special structures of the spaces corresponding to the original three-dimensional problem and on these subspaces we obtain a hierarchy of two-dimensional models for inhomogeneous anisotropic thermo-electro-magneto-elastic shells. We investigate the existence and uniqueness of solutions of the two-dimensional problems, and continuous dependence on the given data in factor space of suitable weighted Sobolev space. Moreover, we present the result regarding convergence of the sequence of vector-functions of three variables restored from the solutions of the two-dimensional problems to the solution of the three-dimensional boundary value problem and an estimate of the rate of convergence.

3.2 Three-dimensional Model

Throughout this work, for each real $0 \leq s \leq 1$, we denote by $H^s(D)$ and $H^s(\check{\Gamma})$ the Sobolev spaces of real-valued functions based on $H^0(D) = L^2(D)$ and $H^0(\check{\Gamma}) = L^2(\check{\Gamma})$, respectively, where $D \subset \mathbb{R}^n$, $n \in \mathbb{N}$, is a bounded Lipschitz domain and $\check{\Gamma}$ is an element of a Lipschitz dissection of the boundary ∂D (McLean, 2000). We denote the corresponding spaces of vector-valued functions by $\mathbf{H}^s(D) = [H^s(D)]^3$, $\mathbf{H}^s(\Gamma) = [H^s(\Gamma)]^3$, $0 \leq s \leq 1$, $\mathbf{L}^{s_1}(\check{\Gamma}) = [L^{s_1}(\check{\Gamma})]^3$, $s_1 \geq 1$ and by $\text{tr}_{\check{\Gamma}} : H^1(D) \rightarrow H^{1/2}(\check{\Gamma})$, $\text{tr}_{\check{\Gamma}} : \mathbf{H}^1(D) \rightarrow \mathbf{H}^{1/2}(\check{\Gamma})$ the trace operators. For any measurable set $D \subset \mathbb{R}^n$, $n \in \mathbb{N}$, $(\cdot, \cdot)_{\mathbf{L}^2(D)}$ and $(\cdot, \cdot)_{L^2(D)}$ are the classical scalar products in $\mathbf{L}^2(D)$ and $L^2(D)$, respectively.

Let us consider a thermo-electro-magneto-elastic shell with initial configuration $\overline{\Omega^*} = \xi(\overline{\Omega})$, where Ω is of the following form

$$\Omega = \{(x_1, x_2, x_3) \in \mathbb{R}^3; h^-(x_1, x_2) < x_3 < h^+(x_1, x_2), (x_1, x_2) \in \omega \subset \mathbb{R}^2\},$$

where ξ is a C^2 diffeomorphism of $\overline{\Omega}$ onto $\overline{\Omega^*}$, so that the vectors $\mathbf{G}_i(x) = \partial_i \xi(x)$ are linearly independent at all points of $\overline{\Omega}$, ∂_i denotes the partial derivative with respect to x_i ($i = 1, 2, 3$). Since ξ is an injective mapping, each point $x^* \in \overline{\Omega^*}$ in Cartesian coordinates $x^* = (x_1^*, x_2^*, x_3^*)$ can be unambiguously written as $x^* = \xi(x)$, $x \in \overline{\Omega}$, and the coordinates x_i of x are the curvilinear coordinates of x^* . The triplets $\{\mathbf{G}_i(x)\}$ and $\{\mathbf{G}^i(x)\}$ form the covariant and contravariant bases at the point $x^* = \xi(x)$, respectively, where $\mathbf{G}_i(x) \cdot \mathbf{G}^j(x) = \delta_{ij}$, δ_{ij} is the Kronecker delta, $\mathbf{G}_i(x) \cdot \mathbf{G}^j(x)$ is the Euclidean inner product in \mathbb{R}^3 of the vectors $\mathbf{G}_i(x)$ and $\mathbf{G}^j(x)$. The mapping ξ defines the metric tensor of $\overline{\Omega^*}$ with covariant components $G_{ij} = \mathbf{G}_i \cdot \mathbf{G}_j$ and Christoffel symbols $\Gamma_{ij}^p = \mathbf{G}^p \cdot \partial_i \mathbf{G}_j$, $i, j, p = 1, 2, 3$. $\Omega \subset \mathbb{R}^3$ and $\omega \subset \mathbb{R}^2$ are bounded Lipschitz domains with boundaries $\Gamma = \partial\Omega$ and $\gamma = \partial\omega$, respectively, the functions $h^\pm \in C^0(\overline{\omega}) \cap C_{loc}^{0,1}(\omega)$ are continuous on $\overline{\omega}$ and Lipschitz-continuous in ω , i.e., $h^\pm \in C^{0,1}(\omega^*)$, for all subdomains ω^* , $\overline{\omega^*} \subset \omega$, $h^+(x_1, x_2) > h^-(x_1, x_2)$, for $(x_1, x_2) \in \omega \cup \tilde{\gamma}$, $\tilde{\gamma} \subset \partial\omega$

is a Lipschitz curve, $h^+(x_1, x_2) = h^-(x_1, x_2)$, for $(x_1, x_2) \in \partial\omega \setminus \tilde{\gamma}$. The upper and lower face surfaces of Ω , defined by the equations $x_3 = h^+(x_1, x_2)$ and $x_3 = h^-(x_1, x_2)$, $(x_1, x_2) \in \omega$, are denoted by Γ^+ and Γ^- , respectively, and the lateral surface of Ω , where the thickness of Ω is positive, is denoted by

$$\tilde{\Gamma} = \{(x_1, x_2, x_3) \in \mathbb{R}^3; h^-(x_1, x_2) < x_3 < h^+(x_1, x_2), (x_1, x_2) \in \tilde{\gamma}\}.$$

The static linear three-dimensional model of the stress-strain state of thermo-electro-magneto-elastic shell $\overline{\Omega^*}$ in differential form is given by the following system of partial differential equations (Natroshvili, 2011; Avalishvili et al, 2017a):

$$-\sum_{j=1}^3 \frac{\partial \sigma_{ij}^*}{\partial x_j^*} = f_i^* \quad \text{in } \Omega^*, \quad i = 1, 2, 3, \quad (3.1)$$

$$\sum_{i=1}^3 \frac{\partial D_i^*}{\partial x_i^*} = f^{\varphi^*} \quad \text{in } \Omega^*, \quad (3.2)$$

$$\sum_{i=1}^3 \frac{\partial B_i^*}{\partial x_i^*} = 0 \quad \text{in } \Omega^*, \quad (3.3)$$

$$-\sum_{i,j=1}^3 \frac{\partial}{\partial x_i^*} \left(\eta_{ij}^* \frac{\partial \theta^*}{\partial x_j^*} \right) = f^{\theta^*} \quad \text{in } \Omega^*, \quad (3.4)$$

where $(\sigma_{ij}^*)_{i,j=1}^3$ is the mechanical stress tensor, which is given by the following linear constitutive equation for a thermo-electro-magneto-elastic solid:

$$\sigma_{ij}^* = \sum_{p,q=1}^3 c_{ijpq}^* e_{pq}^*(\mathbf{u}^*) + \sum_{p=1}^3 \varepsilon_{pij}^* \frac{\partial \varphi^*}{\partial x_p^*} + \sum_{p=1}^3 b_{pij}^* \frac{\partial \psi^*}{\partial x_p^*} - \lambda_{ij}^* \theta^*, \quad i, j = 1, 2, 3 \quad (3.5)$$

where $\mathbf{u}^* = (u_i^*)_{i=1}^3 : \overline{\Omega^*} \rightarrow \mathbb{R}^3$ is the mechanical displacement vector-function, $\varphi^* : \overline{\Omega^*} \rightarrow \mathbb{R}$ and $\psi^* : \overline{\Omega^*} \rightarrow \mathbb{R}$ stand for the electric and magnetic potentials such that electric and magnetic fields are

$$\mathbf{E}^* = -(\partial \varphi^* / \partial x_i^*)_{i=1}^3 \quad \text{and} \quad \mathbf{H}^* = -(\partial \psi^* / \partial x_i^*)_{i=1}^3$$

$\theta^* : \overline{\Omega^*} \rightarrow \mathbb{R}$ is the temperature distribution,

$$e_{ij}^*(v^*) = 1/2(\partial v_i^* / \partial x_j^* + \partial v_j^* / \partial x_i^*), \quad i, j = 1, 2, 3, \quad v^* = (v_i^*)_{i=1}^3,$$

is the strain tensor,

$$(c_{ijpq}^*(x^*))_{i,j,p,q=1}^3$$

is the elasticity tensor,

$$(\varepsilon_{pij}^*(x^*))_{i,j,p=1}^3 \quad \text{and} \quad (b_{pij}^*(x^*))_{i,j,p=1}^3$$

are piezoelectric and piezomagnetic coefficients,

$$(\lambda_{ij}^*(x^*))_{i,j=1}^3$$

is the stress-temperature tensor,

$$\mathbf{f}^* = (f_i^*)_{i=1}^3 : \Omega^* \rightarrow \mathbb{R}^3$$

is the density of the applied body force. $\mathbf{D}^* = (D_j^*)_{j=1}^3$ is the electric displacement vector and $\mathbf{B}^* = (B_j^*)_{j=1}^3$ is the magnetic induction vector; the latter are given, respectively, by the following linear constitutive equations:

$$D_i^* = \sum_{p,q=1}^3 \varepsilon_{ipq}^* e_{pq}^*(\mathbf{u}^*) - \sum_{j=1}^3 d_{ij}^* \frac{\partial \varphi^*}{\partial x_j^*} - \sum_{j=1}^3 a_{ij}^* \frac{\partial \psi^*}{\partial x_j^*} + \mu_i^* \theta^*, \quad i = 1, 2, 3, \quad (3.6)$$

$$B_i^* = \sum_{p,q=1}^3 b_{ipq}^* e_{pq}^*(\mathbf{u}^*) - \sum_{j=1}^3 a_{ij}^* \frac{\partial \varphi^*}{\partial x_j^*} - \sum_{j=1}^3 \zeta_{ij}^* \frac{\partial \psi^*}{\partial x_j^*} + m_i^* \theta^*, \quad i = 1, 2, 3, \quad (3.7)$$

where $(d_{ij}^*(x^*))_{i,j=1}^3$ and $(\zeta_{ij}^*(x^*))_{i,j=1}^3$ are the permittivity and permeability tensors, $(a_{ij}^*(x^*))_{i,j=1}^3$ are the coupling coefficients connecting electric and magnetic fields, $(\mu_i^*(x^*))_{i=1}^3$ and $(m_i^*(x^*))_{i=1}^3$ are pyroelectric and pyromagnetic coefficients, respectively; $f^{\varphi^*} : \Omega^* \rightarrow \mathbb{R}^3$ is the density of electric charges. $(\eta_{ij}^*(x^*))_{i,j=1}^3$ is the thermal conductivity tensor and $f^{\theta^*} : \Omega^* \rightarrow \mathbb{R}^3$ is the density of heat sources.

We assume that the thermo-electro-magneto-elastic shell $\overline{\Omega^*}$ is clamped along a part $\widetilde{\Gamma}_0^* = \xi(\widetilde{\Gamma}_0)$, $\widetilde{\Gamma}_0^* = \{(x_1, x_2, x_3) \in \widetilde{\Gamma}; (x_1, x_2) \in \widetilde{\gamma}_0\}$, $\widetilde{\gamma}_0 \subset \widetilde{\gamma}$ is a Lipschitz curve, of the lateral surface $\widetilde{\Gamma}^* = \xi(\widetilde{\Gamma})$ of the shell, and on the remaining part $\Gamma_1^* = \xi(\Gamma_1)$, $\Gamma_1 = \Gamma \setminus \widetilde{\Gamma}_0$ of the boundary surface force with density $\mathbf{g}^* = (g_i^*)_{i=1}^3 : \Gamma_1^* \rightarrow \mathbb{R}^3$ is given:

$$\mathbf{u}^* = \mathbf{0} \quad \text{on } \widetilde{\Gamma}_0^*, \quad \sum_{j=1}^3 \sigma_{ij}^* n_j^* = g_i^* \quad \text{on } \Gamma_1^*, \quad i = 1, 2, 3, \quad (3.8)$$

where $\mathbf{n}^* = (n_i^*)_{i=1}^3$ is the unit outward normal vector to Γ_1^* . The electric potential φ^* vanishes along a part $\widetilde{\Gamma}_0^{\varphi^*} = \xi(\widetilde{\Gamma}_0^{\varphi^*})$, $\widetilde{\Gamma}_0^{\varphi^*} = \{(x_1, x_2, x_3) \in \widetilde{\Gamma}; (x_1, x_2) \in \widetilde{\gamma}_0^{\varphi^*}\}$, $\widetilde{\gamma}_0^{\varphi^*} \subset \widetilde{\gamma}$ is a Lipschitz curve, of the lateral surface $\widetilde{\Gamma}^*$ of the shell and on the remaining part $\Gamma_1^{\varphi^*} = \xi(\Gamma_1^{\varphi^*})$, $\Gamma_1^{\varphi^*} = \Gamma \setminus \widetilde{\Gamma}_0^{\varphi^*}$ of the boundary the normal component of the electric displacement with density $g^{\varphi^*} : \Gamma_1^{\varphi^*} \rightarrow \mathbb{R}$ is given:

$$\varphi^* = 0 \quad \text{on } \widetilde{\Gamma}_0^{\varphi^*}, \quad \sum_{i=1}^3 D_i^* n_i^* = g^{\varphi^*} \quad \text{on } \Gamma_1^{\varphi^*}, \quad (3.9)$$

where $\mathbf{n}^* = (n_i^*)_{i=1}^3$ is the unit outward normal vector to $\Gamma_1^{\varphi^*}$. The magnetic potential ψ^* vanishes along $\widetilde{\Gamma}_0^{\psi^*} = \xi(\widetilde{\Gamma}_0^{\psi^*})$, $\widetilde{\Gamma}_0^{\psi^*} = \{(x_1, x_2, x_3) \in \widetilde{\Gamma}; (x_1, x_2) \in \widetilde{\gamma}_0^{\psi^*}\}$, $\widetilde{\gamma}_0^{\psi^*} \subset \widetilde{\gamma}$ is a

Lipschitz curve, of the lateral surface $\widetilde{\Gamma}^*$ of the shell and on the remaining part $\Gamma_1^{\psi^*} = \xi(\Gamma_1^{\psi})$, $\Gamma_1^{\psi} = \Gamma \setminus \widetilde{\Gamma}_0^{\psi}$ of the boundary the normal component of the magnetic induction with density $g^{\psi^*} : \Gamma_1^{\psi^*} \rightarrow \mathbb{R}$ is given:

$$\psi^* = 0 \quad \text{on } \widetilde{\Gamma}_0^{\psi^*}, \quad \sum_{i=1}^3 B_i^* n_i^* = g^{\psi^*} \quad \text{on } \Gamma_1^{\psi^*}, \quad (3.10)$$

where $\mathbf{n}^* = (n_i^*)_{i=1}^3$ is the unit outward normal vector to $\Gamma_1^{\psi^*}$. The temperature θ^* vanishes along a part $\widetilde{\Gamma}_0^{\theta^*} = \xi(\widetilde{\Gamma}_0^{\theta})$, $\widetilde{\Gamma}_0^{\theta} = \{(x_1, x_2, x_3) \in \widetilde{\Gamma}; (x_1, x_2) \in \widetilde{\gamma}_0^{\theta}\}$, $\widetilde{\gamma}_0^{\theta} \subset \widetilde{\gamma}$ is a Lipschitz curve, of the lateral surface $\widetilde{\Gamma}^*$ of the shell and on the remaining part $\Gamma_1^{\theta^*} = \xi(\Gamma_1^{\theta})$, $\Gamma_1^{\theta} = \Gamma \setminus \widetilde{\Gamma}_0^{\theta}$ of the boundary the normal component of the heat flux with density $g^{\theta^*} : \Gamma_1^{\theta^*} \rightarrow \mathbb{R}$ is given:

$$\theta^* = 0 \quad \text{on } \widetilde{\Gamma}_0^{\theta^*}, \quad - \sum_{i,j=1}^3 \eta_{ij}^* \frac{\partial \theta^*}{\partial x_j} n_i^* = g^{\theta^*} \quad \text{on } \Gamma_1^{\theta^*}, \quad (3.11)$$

where $\mathbf{n}^* = (n_i^*)_{i=1}^3$ is the unit outward normal vector to $\Gamma_1^{\theta^*}$.

We assume that the elasticity tensor $(c_{ijpq}^*)_{i,j,p,q=1}^3$, the stress-temperature tensor $(\lambda_{ij}^*)_{i,j=1}^3$, and piezoelectric $(\varepsilon_{pij}^*)_{i,j,p=1}^3$ and piezomagnetic $(b_{pij}^*)_{i,j,p=1}^3$ tensors satisfy the following symmetry conditions:

$$c_{ijpq}^* = c_{ijqp}^* = c_{jipq}^*, \quad \lambda_{ij}^* = \lambda_{ji}^*, \quad \varepsilon_{pij}^* = \varepsilon_{pji}^*, \quad b_{pij}^* = b_{pji}^*, \quad i, j, p, q = 1, 2, 3. \quad (3.12)$$

If $\mathbf{u}^* = (u_i^*)_{i=1}^3 : \overline{\Omega}^* \rightarrow \mathbb{R}^3$, $\varphi^* : \overline{\Omega}^* \rightarrow \mathbb{R}$, $\psi^* : \overline{\Omega}^* \rightarrow \mathbb{R}$, and $\theta^* : \overline{\Omega}^* \rightarrow \mathbb{R}$, are twice continuously differentiable, then by multiplying Eqs. (3.1) by arbitrary continuously differentiable functions $v_i^* : \overline{\Omega}^* \rightarrow \mathbb{R}$ ($i = 1, 2, 3$), which vanish on $\widetilde{\Gamma}_0^*$, Eq. (3.2) by a continuously differentiable function $\overline{\varphi}^* : \overline{\Omega}^* \rightarrow \mathbb{R}$, such that $\overline{\varphi}^* = 0$ on $\widetilde{\Gamma}_0^{\varphi^*}$, Eq. (3.3) by a continuously differentiable function $\overline{\psi}^* : \overline{\Omega}^* \rightarrow \mathbb{R}$, which vanishes on $\widetilde{\Gamma}_0^{\psi^*}$, and Eq. (3.4) by a continuously differentiable function $\overline{\theta}^* : \overline{\Omega}^* \rightarrow \mathbb{R}$, such that $\overline{\theta}^* = 0$ on $\widetilde{\Gamma}_0^{\theta^*}$, by integrating on Ω^* and by using Green's formula, and taking into account constitutive Eqs. (3.5)-(3.7), symmetry conditions (3.12) and boundary conditions (3.8)-(3.11), we obtain:

$$\begin{aligned} & \int_{\Omega^*} \sum_{i,j,p,q=1}^3 c_{ijpq}^* e_{pq}^*(\mathbf{u}^*) e_{ij}^*(\mathbf{v}^*) dx^* + \int_{\Omega^*} \sum_{i,j,p=1}^3 \varepsilon_{pij}^* \frac{\partial \varphi^*}{\partial x_p} e_{ij}^*(\mathbf{v}^*) dx^* \\ & + \int_{\Omega^*} \sum_{i,j,p=1}^3 b_{pij}^* \frac{\partial \psi^*}{\partial x_p} e_{ij}^*(\mathbf{v}^*) dx^* - \int_{\Omega^*} \sum_{i,j=1}^3 \lambda_{ij}^* \theta^* e_{ij}^*(\mathbf{v}^*) dx^* = \int_{\Omega^*} \sum_{i=1}^3 f_i^* v_i^* dx^* + \int_{\Gamma_1^*} \sum_{i=1}^3 g_i^* v_i^* d\Gamma^*, \end{aligned} \quad (3.13)$$

$$\begin{aligned}
& - \int_{\Omega^*} \sum_{i,j,p=1}^3 \varepsilon_{ipq}^* e_{pq}^*(\mathbf{u}^*) \frac{\partial \bar{\varphi}^*}{\partial x_i^*} dx^* + \int_{\Omega^*} \sum_{i,j=1}^3 \left(d_{ij}^* \frac{\partial \varphi^*}{\partial x_j^*} \frac{\partial \bar{\varphi}^*}{\partial x_i^*} + a_{ij}^* \frac{\partial \psi^*}{\partial x_j^*} \frac{\partial \bar{\varphi}^*}{\partial x_i^*} \right) dx^* \\
& - \int_{\Omega^*} \sum_{i=1}^3 \mu_i^* \theta^* \frac{\partial \bar{\varphi}^*}{\partial x_i^*} dx^* = \int_{\Omega^*} f^{\varphi^*} \bar{\varphi}^* dx^* - \int_{\Gamma_1^{\varphi^*}} g^{\varphi^*} \bar{\varphi}^* d\Gamma^*, \tag{3.14}
\end{aligned}$$

$$\begin{aligned}
& - \int_{\Omega^*} \sum_{i,j,p=1}^3 b_{ipq}^* e_{pq}^*(\mathbf{u}^*) \frac{\partial \bar{\psi}^*}{\partial x_i^*} dx^* + \int_{\Omega^*} \sum_{i,j=1}^3 a_{ij}^* \frac{\partial \varphi^*}{\partial x_j^*} \frac{\partial \bar{\psi}^*}{\partial x_i^*} dx^* \\
& + \int_{\Omega^*} \sum_{i,j=1}^3 \zeta_{ij}^* \frac{\partial \psi^*}{\partial x_j^*} \frac{\partial \bar{\psi}^*}{\partial x_i^*} dx^* - \int_{\Omega^*} \sum_{i=1}^3 m_i^* \theta^* \frac{\partial \bar{\psi}^*}{\partial x_i^*} dx^* = - \int_{\Gamma_1^{\psi^*}} g^{\psi^*} \bar{\psi}^* d\Gamma^*, \tag{3.15}
\end{aligned}$$

$$\int_{\Omega^*} \sum_{i,j=1}^3 \eta_{ij}^* \frac{\partial \theta^*}{\partial x_j^*} \frac{\partial \bar{\theta}^*}{\partial x_i^*} dx^* = \int_{\Omega^*} f^{\theta^*} \bar{\theta}^* dx^* - \int_{\Gamma_1^{\theta^*}} g^{\theta^*} \bar{\theta}^* d\Gamma^*. \tag{3.16}$$

Therefore, if $\mathbf{u}^* = (u_i^*)_{i=1}^3 : \bar{\Omega}^* \rightarrow \mathbb{R}^3$, $\varphi^* : \bar{\Omega}^* \rightarrow \mathbb{R}$, $\psi^* : \bar{\Omega}^* \rightarrow \mathbb{R}$, and $\theta^* : \bar{\Omega}^* \rightarrow \mathbb{R}$, are solutions of Eqs. (3.1)-(3.4) and satisfy boundary conditions (3.8)-(3.11), then \mathbf{u}^* , φ^* , ψ^* and θ^* are solutions of Eqs. (3.13)-(3.16). Conversely, if \mathbf{u}^* , φ^* , ψ^* and θ^* are twice continuously differentiable solutions of integral Eqs. (3.13)-(3.16), then by using Green's formula we obtain:

$$\begin{aligned}
& \int_{\Gamma_1^*} \sum_{i,j=1}^3 \sigma_{ij}^* n_j^* v_i^* d\Gamma - \int_{\Omega^*} \sum_{j=1}^3 \frac{\partial}{\partial x_j^*} \left(\sum_{p,q=1}^3 c_{ijpq}^* e_{pq}^*(\mathbf{u}^*) + \sum_{p=1}^3 \varepsilon_{pij}^* \frac{\partial \varphi^*}{\partial x_p^*} \right. \\
& \left. + \sum_{p=1}^3 b_{pij}^* \frac{\partial \psi^*}{\partial x_p^*} - \lambda_{ij}^* \theta^* \right) v_i^* dx^* = \int_{\Omega^*} \sum_{i=1}^3 f_i^* v_i^* dx^* + \int_{\Gamma_1^*} \sum_{i=1}^3 g_i^* v_i^* d\Gamma^*, \tag{3.17}
\end{aligned}$$

$$\begin{aligned}
& - \int_{\Gamma_1^{\varphi^*}} \sum_{i=1}^3 D_i^* n_i^* \bar{\varphi}^* d\Gamma^* + \int_{\Omega^*} \sum_{i=1}^3 \frac{\partial}{\partial x_i^*} \left(\sum_{p,q=1}^3 \varepsilon_{ipq}^* e_{pq}^*(\mathbf{u}^*) - \sum_{j=1}^3 d_{ij}^* \frac{\partial \varphi^*}{\partial x_j^*} \right. \\
& \left. - \sum_{j=1}^3 a_{ij}^* \frac{\partial \psi^*}{\partial x_j^*} + \mu_i^* \theta^* \right) \bar{\varphi}^* dx^* = \int_{\Omega^*} f^{\varphi^*} \bar{\varphi}^* dx^* - \int_{\Gamma_1^{\varphi^*}} g^{\varphi^*} \bar{\varphi}^* d\Gamma^*, \tag{3.18}
\end{aligned}$$

$$\begin{aligned}
& - \int_{\Gamma_1^{\psi^*}} \sum_{i=1}^3 B_i^* n_i^* \bar{\psi}^* d\Gamma^* + \int_{\Omega^*} \sum_{i=1}^3 \frac{\partial}{\partial x_i^*} \left(\sum_{p,q=1}^3 b_{ipq}^* e_{pq}^*(\mathbf{u}^*) - \sum_{j=1}^3 a_{ij}^* \frac{\partial \varphi^*}{\partial x_j^*} \right. \\
& \left. - \sum_{j=1}^3 \zeta_{ij}^* \frac{\partial \psi^*}{\partial x_j^*} + m_i^* \theta^* \right) \bar{\psi}^* dx^* = - \int_{\Gamma_1^{\psi^*}} g^{\psi^*} \bar{\psi}^* d\Gamma^*, \tag{3.19}
\end{aligned}$$

$$\int_{\Gamma_1^{\theta^*}} \sum_{i,j=1}^3 \eta_{ij}^* \frac{\partial \theta^*}{\partial x_j^*} n_i^* \bar{\theta}^* d\Gamma^* - \int_{\Omega^*} \sum_{i,j=1}^3 \frac{\partial}{\partial x_i^*} \left(\eta_{ij}^* \frac{\partial \theta^*}{\partial x_j^*} \right) \bar{\theta}^* dx^* = \int_{\Omega^*} f^{\theta^*} \bar{\theta}^* dx^* - \int_{\Gamma_1^{\theta^*}} g^{\theta^*} \bar{\theta}^* d\Gamma^*, \quad (3.20)$$

where $\mathbf{v}^* = (v_i^*)_{i=1}^3$, $\bar{\varphi}^*$, $\bar{\psi}^*$, $\bar{\theta}^*$ are continuously differentiable functions on $\bar{\Omega}^*$, such that $v_i^* = 0$ on Γ_0^* , $\bar{\varphi}^* = 0$ on $\Gamma_0^{\varphi^*}$, $\bar{\psi}^* = 0$ on $\Gamma_0^{\psi^*}$, $\bar{\theta}^* = 0$ on $\Gamma_0^{\theta^*}$. By letting $\mathbf{v}^* \in (C_0^1(\bar{\Omega}^*))^3$, $C_0^1(\bar{\Omega}^*) = \{v \in C^1(\bar{\Omega}^*) \mid v = 0 \text{ on } \Gamma^*\}$, $\bar{\varphi}^* \in C_0^1(\bar{\Omega}^*)$, $\bar{\psi}^* \in C_0^1(\bar{\Omega}^*)$, $\bar{\theta}^* \in C_0^1(\bar{\Omega}^*)$ and by taking account of density of $C_0^1(\bar{\Omega}^*)$ in $L^2(\Omega)$, we obtain, from (3.13)-(3.16), that \mathbf{u}^* , φ^* , ψ^* and θ^* satisfy Eqs. (3.1)-(3.4). Now, if functions \mathbf{v}^* , $\bar{\varphi}^*$, $\bar{\psi}^*$ and $\bar{\theta}^*$ are arbitrary continuous functions on the surfaces Γ_1^* , $\Gamma_1^{\varphi^*}$, $\Gamma_1^{\psi^*}$ and $\Gamma_1^{\theta^*}$ and vanish on the remaining parts of the boundary Γ^* , then by applying Eqs. (3.1)-(3.4) and density of the sets of continuous functions vanishing on the boundaries of Γ_1^* , $\Gamma_1^{\varphi^*}$, $\Gamma_1^{\psi^*}$ and $\Gamma_1^{\theta^*}$ in spaces $L^2(\Gamma_1^*)$, $L^2(\Gamma_1^{\varphi^*})$, $L^2(\Gamma_1^{\psi^*})$ and $L^2(\Gamma_1^{\theta^*})$, we infer, from (3.13)-(3.16), that \mathbf{u}^* , φ^* , ψ^* and θ^* satisfy the boundary conditions (3.8)-(3.11).

Hence the boundary value problem (3.1)-(3.4), (3.8)-(3.11) corresponding to the static three-dimensional model in Cartesian coordinates of anisotropic inhomogeneous thermo-electro-magneto-elastic shell is equivalent to integral Eqs. (3.13)-(3.16) in the space of twice continuously differentiable functions. Therefore, from Eqs. (3.13)-(3.16) by expressing all integrals in terms of curvilinear coordinates x_1, x_2, x_3 we obtain the following variational formulation in curvilinear coordinates of the boundary value problem (3.1)-(3.4), (3.8)-(3.11): Find $\mathbf{u} \in \mathbf{V}(\Omega) = \{\mathbf{v} \in \mathbf{H}^1(\Omega); \mathbf{tr}_\Gamma(\mathbf{v}) = \mathbf{0} \text{ on } \tilde{\Gamma}_0\}$, $\varphi \in V^\varphi(\Omega) = \{\bar{\varphi} \in H^1(\Omega); \mathbf{tr}_\Gamma(\bar{\varphi}) = 0 \text{ on } \tilde{\Gamma}_0^\varphi\}$, $\psi \in V^\psi(\Omega) = \{\bar{\psi} \in H^1(\Omega); \mathbf{tr}_\Gamma(\bar{\psi}) = 0 \text{ on } \tilde{\Gamma}_0^\psi\}$, $\theta \in V^\theta(\Omega) = \{\bar{\theta} \in H^1(\Omega); \mathbf{tr}_\Gamma(\bar{\theta}) = 0 \text{ on } \tilde{\Gamma}_0^\theta\}$ such that

$$c(\mathbf{u}, \mathbf{v}) + \varepsilon(\varphi, \mathbf{v}) + b(\psi, \mathbf{v}) - \lambda(\theta, \mathbf{v}) = L^u(\mathbf{v}), \quad \forall \mathbf{v} \in \mathbf{V}(\Omega), \quad (3.21)$$

$$-\varepsilon(\bar{\varphi}, \mathbf{u}) + d(\varphi, \bar{\varphi}) + a(\psi, \bar{\varphi}) - \mu(\theta, \bar{\varphi}) = L^\varphi(\bar{\varphi}), \quad \forall \bar{\varphi} \in V^\varphi(\Omega), \quad (3.22)$$

$$-b(\bar{\psi}, \mathbf{u}) + a(\varphi, \bar{\psi}) + \zeta(\psi, \bar{\psi}) - m(\theta, \bar{\psi}) = L^\psi(\bar{\psi}), \quad \forall \bar{\psi} \in V^\psi(\Omega), \quad (3.23)$$

$$\eta(\theta, \bar{\theta}) = L^\theta(\bar{\theta}), \quad \forall \bar{\theta} \in V^\theta(\Omega), \quad (3.24)$$

where

$$c(\mathbf{u}, \mathbf{v}) = \int_{\Omega} \sum_{i,j,p,q=1}^3 c_{ijpq}^G e_{p||q}(\mathbf{u}) e_{i||j}(\mathbf{v}) dx, \quad \lambda(\theta, \mathbf{v}) = \int_{\Omega} \sum_{i,j=1}^3 \lambda_{ij}^G \theta e_{i||j}(\mathbf{v}) dx,$$

$$\varepsilon(\varphi, \mathbf{v}) = \int_{\Omega} \sum_{i,j,p=1}^3 \varepsilon_{pij}^G \frac{\partial \varphi}{\partial x_p} e_{i||j}(\mathbf{v}) dx, \quad b(\psi, \mathbf{v}) = \int_{\Omega} \sum_{i,j,p=1}^3 b_{pij}^G \frac{\partial \psi}{\partial x_p} e_{i||j}(\mathbf{v}) dx,$$

$$d(\varphi, \bar{\varphi}) = \int_{\Omega} \sum_{i,j=1}^3 d_{ij}^G \frac{\partial \varphi}{\partial x_j} \frac{\partial \bar{\varphi}}{\partial x_i} dx, \quad a(\psi, \bar{\varphi}) = \int_{\Omega} \sum_{i,j=1}^3 a_{ij}^G \frac{\partial \psi}{\partial x_j} \frac{\partial \bar{\varphi}}{\partial x_i} dx,$$

$$\begin{aligned}
\zeta(\psi, \bar{\psi}) &= \int_{\Omega} \sum_{i,j=1}^3 \zeta_{ij}^G \frac{\partial \psi}{\partial x_j} \frac{\partial \bar{\psi}}{\partial x_i} dx, & \mu(\theta, \bar{\varphi}) &= \int_{\Omega} \sum_{i=1}^3 \mu_i^G \theta \frac{\partial \bar{\varphi}}{\partial x_i} dx, \\
m(\theta, \bar{\psi}) &= \int_{\Omega} \sum_{i=1}^3 m_i^G \theta \frac{\partial \bar{\psi}}{\partial x_i} dx, & \eta(\theta, \bar{\theta}) &= \int_{\Omega} \sum_{i,j=1}^3 \eta_{ij}^G \frac{\partial \theta}{\partial x_j} \frac{\partial \bar{\theta}}{\partial x_i} dx, \\
L^u(\mathbf{v}) &= \int_{\Omega} \sum_{i=1}^3 f^i v_i \sqrt{G} dx + \int_{\Gamma_1} \sum_{i=1}^3 g^i \text{tr}_{\Gamma_1}(v_i) \sqrt{G} d\Gamma, \\
L^\varphi(\bar{\varphi}) &= \int_{\Omega} f^\varphi \bar{\varphi} \sqrt{G} dx - \int_{\Gamma_1^\varphi} g^\varphi \text{tr}_{\Gamma_1^\varphi}(\bar{\varphi}) \sqrt{G} d\Gamma, \\
L^\psi(\bar{\psi}) &= - \int_{\Gamma_1^\psi} g^\psi \text{tr}_{\Gamma_1^\psi}(\bar{\psi}) \sqrt{G} d\Gamma, \\
L^\theta(\bar{\theta}) &= \int_{\Omega} f^\theta \bar{\theta} \sqrt{G} dx - \int_{\Gamma_1^\theta} g^\theta \text{tr}_{\Gamma_1^\theta}(\bar{\theta}) \sqrt{G} d\Gamma,
\end{aligned}$$

$\mathbf{u} = (u_i)_{i=1}^3$, u_i ($i = 1, 2, 3$) are the covariant components of the mechanical displacement, $\theta(x) = \theta^*(x^*)$, $x^* = \boldsymbol{\xi}(x)$, $x \in \bar{\Omega}$, f^i and g^i ($i = 1, 2, 3$) are the contravariant components of the applied body force \mathbf{f}^* and surface force \mathbf{g}^* densities, $e_{p||q}(\mathbf{v}) = 1/2(\partial_p v_q + \partial_q v_p) - \sum_{i=1}^3 \Gamma_{pq}^i v_i$ ($p, q = 1, 2, 3$), $\mathbf{v} = (v_i)_{i=1}^3$, are the covariant components of the strain tensor (Ciarlet, 2000), $G = \det(G_{ij})$,

$$\begin{aligned}
c_{ijpq}^G(x) &= \sum_{k,l,r,s=1}^3 c_{klrs}(x) (\mathbf{G}^i)_k (\mathbf{G}^j)_l (\mathbf{G}^p)_r (\mathbf{G}^q)_s \sqrt{G}, \\
\varepsilon_{pij}^G(x) &= \sum_{r,s,k=1}^3 \varepsilon_{rsk}(x) (\mathbf{G}^p)_r (\mathbf{G}^i)_s (\mathbf{G}^j)_k \sqrt{G}, \\
b_{pij}^G(x) &= \sum_{r,s,k=1}^3 b_{rsk}(x) (\mathbf{G}^p)_r (\mathbf{G}^i)_s (\mathbf{G}^j)_k \sqrt{G}, \\
\lambda_{ij}^G(x) &= \sum_{r,s=1}^3 \lambda_{rs}(x) (\mathbf{G}^i)_r (\mathbf{G}^j)_s \sqrt{G}, & d_{ij}^G(x) &= \sum_{r,s=1}^3 d_{rs}(x) (\mathbf{G}^i)_r (\mathbf{G}^j)_s \sqrt{G}, \\
a_{ij}^G(x) &= \sum_{r,s=1}^3 a_{rs}(x) (\mathbf{G}^i)_r (\mathbf{G}^j)_s \sqrt{G}, & \zeta_{ij}^G(x) &= \sum_{r,s=1}^3 \zeta_{rs}(x) (\mathbf{G}^i)_r (\mathbf{G}^j)_s \sqrt{G}, \\
\mu_i^G(x) &= \sum_{r=1}^3 \mu_r(x) (\mathbf{G}^i)_r \sqrt{G}, & m_i^G(x) &= \sum_{r=1}^3 m_r(x) (\mathbf{G}^i)_r \sqrt{G}, \\
\eta_{ij}^G(x) &= \sum_{r,s=1}^3 \eta_{rs}(x) (\mathbf{G}^i)_r (\mathbf{G}^j)_s \sqrt{G},
\end{aligned}$$

$$\begin{aligned} c_{klrs}(x) &= c_{klrs}^*(x^*), \quad \varepsilon_{rsk}(x) = \varepsilon_{rsk}^*(x^*), \quad b_{rsk}(x) = b_{rsk}^*(x^*), \\ \lambda_{rs}(x) &= \lambda_{rs}^*(x^*), \quad d_{rs}(x) = d_{rs}^*(x^*), \quad a_{rs}(x) = a_{rs}^*(x^*), \\ \zeta_{rs}(x) &= \zeta_{rs}^*(x^*), \quad \mu_r(x) = \mu_r^*(x^*), \quad m_r(x) = m_r^*(x^*), \quad \eta_{rs}(x) = \eta_{rs}^*(x^*), \end{aligned}$$

$i, j, p, q, k, l, r, s = 1, 2, 3,$

$$f^\varphi(x) = f^{\varphi^*}(x^*), \quad f^\theta(x) = f^{\theta^*}(x^*), \quad x^* = \boldsymbol{\xi}(x), x \in \Omega,$$

$$g^\varphi(x) = g^{\varphi^*}(x^*), \quad x^* = \boldsymbol{\xi}(x), \quad x \in \Gamma_1^\varphi, \quad g^\psi(x) = g^{\psi^*}(x^*), \quad x^* = \boldsymbol{\xi}(x), x \in \Gamma_1^\psi,$$

$$g^\theta(x) = g^{\theta^*}(x^*), \quad x^* = \boldsymbol{\xi}(x), x \in \Gamma_1^\theta.$$

Hereafter, we assume that $c_{ijpq}, \varepsilon_{pij}, b_{pij}, d_{ij}, a_{ij}, \zeta_{ij}, \lambda_{ij}, \mu_i, m_i, \eta_{ij} \in L^\infty(\Omega)$, $i, j, p, q = 1, 2, 3$, satisfy the following positive definiteness conditions

$$\sum_{i,j,p,q=1}^3 c_{ijpq}(x) \xi_{ij} \xi_{pq} \geq \alpha_c \sum_{i,j=1}^3 (\xi_{ij})^2, \quad \sum_{i,j=1}^3 \eta_{ij}(x) \xi_j \xi_j \geq \alpha_\eta \sum_{i=1}^3 (\xi_i)^2, \quad (3.25)$$

$$\begin{aligned} & \sum_{i,j=1}^3 d_{ij}(x) \xi_j \xi_i + \sum_{i,j=1}^3 a_{ij}(x) \bar{\xi}_j \xi_i + \sum_{i,j=1}^3 a_{ij}(x) \xi_j \bar{\xi}_i \\ & + \sum_{i,j=1}^3 \zeta_{ij}(x) \bar{\xi}_j \bar{\xi}_i \geq \alpha \sum_{i=1}^3 ((\xi_i)^2 + (\bar{\xi}_i)^2), \end{aligned} \quad (3.26)$$

for all $\xi_{ij} \in \mathbb{R}$, $\xi_{ij} = \xi_{ji}$, $\xi_i, \bar{\xi}_i \in \mathbb{R}$, $i, j = 1, 2, 3$, and for almost all $x \in \Omega$, where $\alpha_c, \alpha_\eta, \alpha$ are positive constants.

Note that if the parts $\tilde{\Gamma}_0^*$, $\tilde{\Gamma}_0^{\varphi^*}$, $\tilde{\Gamma}_0^{\psi^*}$ and $\tilde{\Gamma}_0^{\theta^*}$ of the boundary of the shell $\overline{\Omega^*}$, where mechanical displacement, electric and magnetic potentials, and temperature vanish, are empty sets, then the parts $\tilde{\Gamma}_0$, $\tilde{\Gamma}_0^\varphi$, $\tilde{\Gamma}_0^\psi$ and $\tilde{\Gamma}_0^\theta$ of the boundary Γ are empty sets and the homogeneous problem (3.21)-(3.24), i.e., with $\mathbf{f} = (f^i)_{i=1}^3 \equiv \mathbf{0}$, $\mathbf{g} = (g^i)_{i=1}^3 \equiv \mathbf{0}$, $f^\varphi \equiv 0$, $g^\varphi \equiv 0$, $g^\psi \equiv 0$, $f^\theta \equiv 0$, $g^\theta \equiv 0$, has non-trivial solutions. Hence, the solution of problem (3.21)-(3.24) is not unique in the first-order Sobolev spaces mentioned in the variational formulation and it is necessary to introduce suitable factor spaces, where the solution of problem (3.21)-(3.24) is unique. We denote by \mathfrak{R} the set of solutions of the homogeneous problem (3.21)-(3.24), where $L^u(\mathbf{v}) \equiv 0$, $L^\varphi(\bar{\varphi}) = 0$, $L^\psi(\bar{\psi}) = 0$, $L^\theta(\bar{\theta}) = 0$, for all $\mathbf{v} \in \mathbf{V}(\Omega)$, $\bar{\varphi} \in V^\varphi(\Omega)$, $\bar{\psi} \in V^\psi(\Omega)$ and $\bar{\theta} \in V^\theta(\Omega)$.

By applying generalized Poincaré's inequality (Ciarlet, 1988), Korn's inequality in curvilinear coordinates (Ciarlet, 2000), corollary from Korn's inequality in factor spaces (Duvaut and Lions, 1972), and Lax-Milgram theorem (McLean, 2000), we determine the structure of the set \mathfrak{R} , which is of the following form:

$$\mathfrak{R} = \left\{ (\mathbf{v}^{r\theta^r}, \bar{\varphi}^{r\theta^r}, \bar{\psi}^{r\theta^r}, \theta^r); \mathbf{v}^{r\theta^r} = \mathbf{v}^r + \mathbf{u}^{r\theta^r}, \bar{\varphi}^{r\theta^r} = \bar{\varphi}^r + \varphi^{r\theta^r}, \right. \\ \left. \bar{\psi}^{r\theta^r} = \bar{\psi}^r + \psi^{r\theta^r}, (\mathbf{v}^r, \bar{\varphi}^r, \bar{\psi}^r) \in \mathfrak{R}^{\mathbf{u}\varphi\psi}, \theta^r \in \mathfrak{R}^\theta \right\},$$

where

$$\mathfrak{R}^{\mathbf{u}\varphi\psi} = \{(\mathbf{v}^r, \bar{\varphi}^r, \bar{\psi}^r) \in \mathbf{V}(\Omega) \times V^\varphi(\Omega) \times V^\psi(\Omega);$$

$$\mathbf{v}^r = \alpha + \beta \times \mathbf{o}\mathbf{x}, \alpha, \beta \in \mathbb{R}^3, \bar{\varphi}^r = \alpha_\varphi, \alpha_\varphi \in \mathbb{R}, \bar{\psi}^r = \alpha_\psi, \alpha_\psi \in \mathbb{R}\},$$

$\beta \times \mathbf{o}\mathbf{x}$ is the exterior product of vectors $\beta \in \mathbb{R}^3$ and $\mathbf{o}\mathbf{x} = (x_i)_{i=1}^3 \in \mathbb{R}^3$,

$$\mathfrak{R}^\theta = \{\theta^r \in V^\theta(\Omega); \theta^r = \alpha_\theta, \alpha_\theta \in \mathbb{R}\}$$

and $(\mathbf{u}^{r\theta^r}, \varphi^{r\theta^r}, \psi^{r\theta^r}) \in \mathbf{V}(\Omega) \times V^\varphi(\Omega) \times V^\psi(\Omega)$ is a solution of the homogeneous Eqs. (3.21)-(3.23) with $\theta = \theta^r$ and $\mathbf{f} \equiv \mathbf{0}$, $\mathbf{g} \equiv \mathbf{0}$, $f^\varphi \equiv 0$, $g^\varphi \equiv 0$, $g^\psi \equiv 0$.

The set \mathfrak{R} defines the factor space

$$\mathbf{V}_{\mathfrak{R}}^{\mathbf{u}\varphi\psi\theta}(\Omega) = (\mathbf{V}(\Omega) \times V^\varphi(\Omega) \times V^\psi(\Omega) \times V^\theta(\Omega)) / \mathfrak{R},$$

which consists of the following equivalence classes

$$(\mathbf{v}, \bar{\varphi}, \bar{\psi}, \bar{\theta})^{\mathfrak{R}} = \left\{ (\mathbf{v}, \bar{\varphi}, \bar{\psi}, \bar{\theta}) + (\mathbf{v}^{r\theta^r}, \bar{\varphi}^{r\theta^r}, \bar{\psi}^{r\theta^r}, \theta^r); (\mathbf{v}^{r\theta^r}, \bar{\varphi}^{r\theta^r}, \bar{\psi}^{r\theta^r}, \theta^r) \in \mathfrak{R} \right\},$$

for each $(\mathbf{v}, \bar{\varphi}, \bar{\psi}, \bar{\theta}) \in \mathbf{V}(\Omega) \times V^\varphi(\Omega) \times V^\psi(\Omega) \times V^\theta(\Omega)$. The factor space $\mathbf{V}_{\mathfrak{R}}^{\mathbf{u}\varphi\psi\theta}(\Omega)$ is a Hilbert space equipped with the following norm:

$$\left\| (\mathbf{v}, \bar{\varphi}, \bar{\psi}, \bar{\theta})^{\mathfrak{R}} \right\|_{\mathbf{V}_{\mathfrak{R}}^{\mathbf{u}\varphi\psi\theta}(\Omega)} = \inf \left\{ \left\| (\mathbf{v}, \bar{\varphi}, \bar{\psi}, \bar{\theta}) + (\mathbf{v}^{r\theta^r}, \bar{\varphi}^{r\theta^r}, \bar{\psi}^{r\theta^r}, \theta^r) \right\|_{(H^1(\Omega))^6}; \right. \\ \left. (\mathbf{v}^{r\theta^r}, \bar{\varphi}^{r\theta^r}, \bar{\psi}^{r\theta^r}, \theta^r) \in \mathfrak{R} \right\}.$$

Note that, for all $(\mathbf{v}^r, \bar{\varphi}^r, \bar{\psi}^r) \in \mathfrak{R}^{\mathbf{u}\varphi\psi}$ and $\theta^r \in \mathfrak{R}^\theta$ we have

$$c(\mathbf{v}^r, \mathbf{v}) + \varepsilon(\bar{\varphi}^r, \mathbf{v}) + b(\bar{\psi}^r, \mathbf{v}) - \lambda(\theta^r, \mathbf{v}) = 0, \quad \forall \mathbf{v} \in \mathbf{V}(\Omega), \\ -\varepsilon(\bar{\varphi}, \mathbf{v}^r) + d(\bar{\varphi}^r, \bar{\varphi}) + a(\bar{\psi}^r, \bar{\varphi}) - \mu(\theta^r, \bar{\varphi}) = 0, \quad \forall \bar{\varphi} \in V^\varphi(\Omega), \\ -b(\bar{\psi}, \mathbf{v}^r) + a(\bar{\varphi}^r, \bar{\psi}) + \zeta(\bar{\psi}^r, \bar{\psi}) - m(\theta^r, \bar{\psi}) = 0, \quad \forall \bar{\psi} \in V^\psi(\Omega), \\ \eta(\theta^r, \bar{\theta}) = 0, \quad \forall \bar{\theta} \in V^\theta(\Omega),$$

and, consequently, for solvability of problem (3.21)-(3.24) it is necessary that $L^{\mathbf{u}}(\mathbf{v}^r) = 0$, $L^\varphi(\bar{\varphi}^r) = 0$, $L^\psi(\bar{\psi}^r) = 0$ and $L^\theta(\theta^r) = 0$. Therefore, for each solution $(\mathbf{u}, \varphi, \psi, \theta)$ of problem (3.21)-(3.24), any vector-function

$$(\mathbf{u}, \varphi, \psi, \theta) + (\mathbf{v}^{r\theta^r}, \bar{\varphi}^{r\theta^r}, \bar{\psi}^{r\theta^r}, \theta^r),$$

where $(\mathbf{v}^{r\theta^r}, \bar{\varphi}^{r\theta^r}, \bar{\psi}^{r\theta^r}, \theta^r) \in \mathfrak{R}$ is also a solution of (3.21)-(3.24), and problem (3.21)-(3.24) in the factor space $\mathbf{V}_{\mathfrak{R}}^{\mathbf{u}\varphi\psi\theta}(\Omega)$ can be formulated as follows: Find

$(\mathbf{u}, \varphi, \psi, \theta)^{\mathfrak{R}} \in \mathbf{V}_{\mathfrak{R}}^{\mathbf{u}\varphi\psi\theta}(\Omega)$ such that any vector-function from the equivalence class $(\mathbf{u}, \varphi, \psi, \theta)^{\mathfrak{R}}$ is a solution of problem (3.21)-(3.24).

For problem (3.21)-(3.24), which is equivalent to the boundary value problem (3.1)-(3.4), (3.8)-(3.11) in the spaces of classical twice continuously differentiable functions, the following existence, uniqueness and continuous dependence theorem is valid.

Theorem 3.1. *Suppose that $\Omega \subset \mathbb{R}^3$ is a bounded Lipschitz domain, the parameters $c_{ijpq}, \varepsilon_{pij}, b_{pij}, \lambda_{ij}, d_{ij}, a_{ij}, \zeta_{ij}, \mu_i, m_i, \eta_{ij} \in L^\infty(\Omega)$, $i, j, p, q = 1, 2, 3$, satisfy the symmetry and positive definiteness conditions (3.12) and (3.25), (3.26). If $\mathbf{f} \in \mathbf{L}^{6/5}(\Omega)$, $\mathbf{g} \in \mathbf{L}^{4/3}(\Gamma_1)$, $f^\varphi \in L^{6/5}(\Omega)$, $g^\varphi \in L^{4/3}(\Gamma_1^\varphi)$, $g^\psi \in L^{4/3}(\Gamma_1^\psi)$, $f^\theta \in L^{6/5}(\Omega)$, $g^\theta \in L^{4/3}(\Gamma_1^\theta)$, and*

$$L^{\mathbf{u}}(\mathbf{v}^r) = 0, \quad L^\varphi(\overline{\varphi}^r) = 0, \quad L^\psi(\overline{\psi}^r) = 0, \quad L^\theta(\theta^r) = 0, \quad (3.27)$$

for all $(\mathbf{v}^r, \overline{\varphi}^r, \overline{\psi}^r) \in \mathfrak{R}^{\mathbf{u}\varphi\psi}, \theta^r \in \mathfrak{R}^\theta$, then problem (3.21)-(3.24) possesses a unique solution $(\mathbf{u}, \varphi, \psi, \theta)^{\mathfrak{R}} \in \mathbf{V}_{\mathfrak{R}}^{\mathbf{u}\varphi\psi\theta}(\Omega)$, which continuously depends on the given data, i.e., the mapping $(\mathbf{f}, \mathbf{g}, f^\varphi, g^\varphi, g^\psi, f^\theta, g^\theta) \rightarrow (\mathbf{u}, \varphi, \psi, \theta)^{\mathfrak{R}}$ is linear and continuous from the space $\mathbf{L}^{6/5}(\Omega) \times \mathbf{L}^{4/3}(\Gamma_1) \times L^{6/5}(\Omega) \times L^{4/3}(\Gamma_1^\varphi) \times L^{4/3}(\Gamma_1^\psi) \times L^{6/5}(\Omega) \times L^{4/3}(\Gamma_1^\theta)$ to the space $\mathbf{V}_{\mathfrak{R}}^{\mathbf{u}\varphi\psi\theta}(\Omega)$.

Remark 3.1. If the areas of the surfaces $\Gamma_0, \Gamma_0^\varphi, \Gamma_0^\psi, \Gamma_0^\theta$ are positive, then the homogeneous problem (3.21)-(3.24) has only a trivial solution. Hence, $\mathfrak{R}^{\mathbf{u}\varphi\psi} = \{(\mathbf{0}, 0, 0)\}, \mathfrak{R}^\theta = \{0\}, \mathfrak{R} = \{(\mathbf{0}, 0, 0, 0)\}$, the factor space $\mathbf{V}_{\mathfrak{R}}^{\mathbf{u}\varphi\psi\theta}(\Omega)$ coincides with $\mathbf{V}(\Omega) \times V^\varphi(\Omega) \times V^\psi(\Omega) \times V^\theta(\Omega)$ and Theorem 3.1 is valid in the subspaces of first-order Sobolev spaces mentioned in the variational formulation (3.21)-(3.24).

3.3 Hierarchical Two-dimensional Models

In order to construct a hierarchy of two-dimensional models let us consider the subspaces $\mathbf{V}_{\mathbf{N}}(\Omega)$ of $\mathbf{V}(\Omega)$, $\mathbf{N} = (N_1, N_2, N_3) \in (\mathbb{N} \cup \{0\})^3$, consisting of vector-functions $\mathbf{v}_{\mathbf{N}}$ with components $v_{\mathbf{N}i}$ ($i = 1, 2, 3$), which are polynomials with respect to the variable x_3 ,

$$v_{\mathbf{N}i} = \sum_{r_i=0}^{N_i} \frac{1}{h} \left(r_i + \frac{1}{2} \right) v_{\mathbf{N}i}^{r_i} P_{r_i}(z) \quad \text{in } \Omega, \quad h^{-1/2} v_{\mathbf{N}i}^{r_i} \in L^2(\omega), \quad 0 \leq r_i \leq N_i, \quad i = 1, 2, 3,$$

where $z = \frac{x_3 - \bar{h}}{h}$, $h = \frac{h^+ - h^-}{2}$, $\bar{h} = \frac{h^+ + h^-}{2}$, and P_r denotes the Legendre polynomial of order $r \in \mathbb{N} \cup \{0\}$. We also consider the subspaces $V_{N_\varphi}^\varphi(\Omega)$, $N_\varphi \in \mathbb{N} \cup \{0\}$, $V_{N_\psi}^\psi(\Omega)$, $N_\psi \in \mathbb{N} \cup \{0\}$ and $V_{N_\theta}^\theta(\Omega)$, $N_\theta \in \mathbb{N} \cup \{0\}$, of $V^\varphi(\Omega)$, $V^\psi(\Omega)$ and $V^\theta(\Omega)$, respectively, which consist of the following functions

$$\begin{aligned}\bar{\varphi}_{N_\varphi} &= \sum_{r_\varphi=0}^{N_\varphi} \frac{1}{h} \left(r_\varphi + \frac{1}{2} \right) \bar{\varphi}_{N_\varphi}^{r_\varphi} P_{r_\varphi}(z) \text{ in } \Omega, \quad h^{-1/2} \bar{\varphi}_{N_\varphi}^{r_\varphi} \in L^2(\omega), \quad 0 \leq r_\varphi \leq N_\varphi, \\ \bar{\psi}_{N_\psi} &= \sum_{r_\psi=0}^{N_\psi} \frac{1}{h} \left(r_\psi + \frac{1}{2} \right) \bar{\psi}_{N_\psi}^{r_\psi} P_{r_\psi}(z) \text{ in } \Omega, \quad h^{-1/2} \bar{\psi}_{N_\psi}^{r_\psi} \in L^2(\omega), \quad 0 \leq r_\psi \leq N_\psi, \\ \bar{\theta}_{N_\theta} &= \sum_{r_\theta=0}^{N_\theta} \frac{1}{h} \left(r_\theta + \frac{1}{2} \right) \bar{\theta}_{N_\theta}^{r_\theta} P_{r_\theta}(z) \text{ in } \Omega, \quad h^{-1/2} \bar{\theta}_{N_\theta}^{r_\theta} \in L^2(\omega), \quad 0 \leq r_\theta \leq N_\theta.\end{aligned}$$

Since the functions h^+ and h^- are Lipschitz-continuous in ω from Rademacher's theorem (Whitney, 1957) we have that h^+ and h^- are differentiable almost everywhere in ω and $\partial_\alpha h^\pm \in L^\infty(\omega^*)$ for all subdomains ω^* , $\bar{\omega}^* \subset \omega$, $\alpha = 1, 2$. Therefore, the positiveness of h in ω implies that for any vector-function $\mathbf{v}_\mathbf{N} = (v_{\mathbf{N}i})_{i=1}^3 \in \mathbf{V}_\mathbf{N}(\Omega)$ the corresponding functions $v_{\mathbf{N}i}^{r_i} \in H^1(\omega^*)$, for all ω^* , $\bar{\omega}^* \subset \omega$, i.e. $v_{\mathbf{N}i}^{r_i} \in H_{loc}^1(\omega)$, $r_i = 0, \dots, N_i$, $i = 1, 2, 3$. Similarly, for all functions $\bar{\varphi}_{N_\varphi} \in V_{N_\varphi}^\varphi(\Omega)$, $\bar{\psi}_{N_\psi} \in V_{N_\psi}^\psi(\Omega)$, $\bar{\theta}_{N_\theta} \in V_{N_\theta}^\theta(\Omega)$, the functions $\bar{\varphi}_{N_\varphi}^{r_\varphi}$, $\bar{\psi}_{N_\psi}^{r_\psi}$, $\bar{\theta}_{N_\theta}^{r_\theta}$ of two variables in the expressions of $\bar{\varphi}_{N_\varphi}$, $\bar{\psi}_{N_\psi}$, $\bar{\theta}_{N_\theta}$ belong to $H^1(\omega^*)$, i.e. $\bar{\varphi}_{N_\varphi}^{r_\varphi}$, $\bar{\psi}_{N_\psi}^{r_\psi}$, $\bar{\theta}_{N_\theta}^{r_\theta} \in H_{loc}^1(\omega)$, $r_\varphi = 0, \dots, N_\varphi$, $r_\psi = 0, \dots, N_\psi$, $r_\theta = 0, \dots, N_\theta$. Moreover, the norms $\|\cdot\|_{\mathbf{H}^1(\Omega)}$ and $\|\cdot\|_{H^1(\Omega)}$ in the spaces $\mathbf{H}^1(\Omega)$ and $H^1(\Omega)$ define weighted norms $\|\cdot\|_*$ and $\|\cdot\|_{\varphi^*}$, $\|\cdot\|_{\psi^*}$, $\|\cdot\|_{\theta^*}$ of vector-functions $\vec{\mathbf{v}}_\mathbf{N} = (v_{\mathbf{N}i}^{r_i}) \in [H_{loc}^1(\omega)]^{N_{1,2,3}}$, $N_{1,2,3} = N_1 + N_2 + N_3 + 3$, and $\vec{\bar{\varphi}}_{N_\varphi} = (\bar{\varphi}_{N_\varphi}^{r_\varphi}) \in [H_{loc}^1(\omega)]^{N_\varphi+1}$, $\vec{\bar{\psi}}_{N_\psi} = (\bar{\psi}_{N_\psi}^{r_\psi}) \in [H_{loc}^1(\omega)]^{N_\psi+1}$, $\vec{\bar{\theta}}_{N_\theta} = (\bar{\theta}_{N_\theta}^{r_\theta}) \in [H_{loc}^1(\omega)]^{N_\theta+1}$, such that $\|\vec{\mathbf{v}}_\mathbf{N}\|_* = \|\mathbf{v}_\mathbf{N}\|_{\mathbf{H}^1(\Omega)}$ and $\|\vec{\bar{\varphi}}_{N_\varphi}\|_{\varphi^*} = \|\bar{\varphi}_{N_\varphi}\|_{H^1(\Omega)}$, $\|\vec{\bar{\psi}}_{N_\psi}\|_{\psi^*} = \|\bar{\psi}_{N_\psi}\|_{H^1(\Omega)}$, $\|\vec{\bar{\theta}}_{N_\theta}\|_{\theta^*} = \|\bar{\theta}_{N_\theta}\|_{H^1(\Omega)}$. Using the properties of the Legendre polynomials we can obtain explicit expressions for the norms $\|\cdot\|_*$ and $\|\cdot\|_{\varphi^*}$, $\|\cdot\|_{\psi^*}$, $\|\cdot\|_{\theta^*}$. In particular, $\|\cdot\|_*$ is given by the following expression:

$$\begin{aligned}\|\vec{\mathbf{v}}_\mathbf{N}\|_* &= \left(\sum_{i=1}^3 \sum_{r_i=0}^{N_i} \left(r_i + \frac{1}{2} \right) \left\| \sum_{s_i=r_i}^{N_i} \left(s_i + \frac{1}{2} \right) (1 - (-1)^{r_i+s_i}) h^{-3/2} v_{\mathbf{N}i}^{s_i} \right\|_{L^2(\omega)}^2 \right. \\ &\quad + \left\| h^{-1/2} v_{\mathbf{N}i}^{r_i} \right\|_{L^2(\omega)}^2 + \sum_{\alpha=1}^2 \left\| \sum_{s_i=r_i+1}^{N_i} \left(s_i + \frac{1}{2} \right) (\partial_\alpha h^+ - (-1)^{r_i+s_i} \partial_\alpha h^-) h^{-3/2} v_{\mathbf{N}i}^{s_i} \right. \\ &\quad \left. \left. - h^{-1/2} \partial_\alpha v_{\mathbf{N}i}^{r_i} + (r_i + 1) h^{-3/2} \partial_\alpha h v_{\mathbf{N}i}^{r_i} \right\|_{L^2(\omega)}^2 \right)^{1/2}.\end{aligned}$$

For components $v_{\mathbf{N}i}^{r_i}$ and $\bar{\varphi}_{N_\varphi}^{r_\varphi}$, $\bar{\psi}_{N_\psi}^{r_\psi}$, $\bar{\theta}_{N_\theta}^{r_\theta}$ of vector-functions $\vec{\mathbf{v}}_\mathbf{N}$ and $\vec{\bar{\varphi}}_{N_\varphi}$, $\vec{\bar{\psi}}_{N_\psi}$, $\vec{\bar{\theta}}_{N_\theta}$, which possess the properties $\|\vec{\mathbf{v}}_\mathbf{N}\|_* < \infty$ and $\|\vec{\bar{\varphi}}_{N_\varphi}\|_{\varphi^*} < \infty$, $\|\vec{\bar{\psi}}_{N_\psi}\|_{\psi^*} < \infty$,

$\|\vec{\theta}_{N_\theta}\|_{\theta*} < \infty$ we can define the traces on $\tilde{\gamma}$. Indeed, the corresponding vector-function of three variables $\mathbf{v}_N = (v_{Ni})_{i=1}^3$ and functions $\bar{\varphi}_{N_\varphi}, \bar{\psi}_{N_\psi}, \bar{\theta}_{N_\theta}$ belong to the spaces $\mathbf{V}_N(\Omega) \subset \mathbf{H}^1(\Omega)$ and $V_{N_\varphi}^\varphi(\Omega), V_{N_\psi}^\psi(\Omega), V_{N_\theta}^\theta(\Omega) \subset H^1(\Omega)$, respectively, and using the trace operator $tr_{\tilde{\gamma}}$ we define the traces of $v_{Ni}^{r_i}$ and $\bar{\varphi}_{N_\varphi}^{r_\varphi}, \bar{\psi}_{N_\psi}^{r_\psi}, \bar{\theta}_{N_\theta}^{r_\theta}$ on $\tilde{\gamma}$, in particular,

$$tr_{\tilde{\gamma}}(v_{Ni}^{r_i}) = \int_{h^-}^{h^+} tr_{\tilde{\Gamma}}(v_{Ni}) Pr_i(z) dx_3, \quad r_i = 0, \dots, N_i, \quad i = 1, 2, 3.$$

Since vector-function \mathbf{v}_N , from the subspaces $\mathbf{V}_N(\Omega)$, and functions $\bar{\varphi}_{N_\varphi} \in V_{N_\varphi}^\varphi(\Omega)$, $\bar{\psi}_{N_\psi} \in V_{N_\psi}^\psi(\Omega)$ and $\bar{\theta}_{N_\theta} \in V_{N_\theta}^\theta(\Omega)$ are uniquely defined by the functions $v_{Ni}^{r_i}, \bar{\varphi}_{N_\varphi}^{r_\varphi}, \bar{\psi}_{N_\psi}^{r_\psi}, \bar{\theta}_{N_\theta}^{r_\theta}$ of two variables, and considering the original three-dimensional problem (3.21)-(3.24) on these subspaces, we obtain the following hierarchy of two-dimensional boundary value problems: Find $\vec{u}_N \in \vec{V}_N(\omega), \vec{\varphi}_{N_\varphi} \in \vec{V}_{N_\varphi}^\varphi(\omega), \vec{\psi}_{N_\psi} \in \vec{V}_{N_\psi}^\psi(\omega), \vec{\theta}_{N_\theta} \in \vec{V}_{N_\theta}^\theta(\omega)$, which satisfy the following equations

$$c_N(\vec{u}_N, \vec{v}_N) + \varepsilon_{N_\varphi} \mathbf{N}(\vec{\varphi}_{N_\varphi}, \vec{v}_N) + b_{N_\psi} \mathbf{N}(\vec{\psi}_{N_\psi}, \vec{v}_N) - \lambda_{N_\theta} \mathbf{N}(\vec{\theta}_{N_\theta}, \vec{v}_N) = L_N^u(\vec{v}_N), \quad \forall \vec{v}_N \in \vec{V}_N(\omega), \quad (3.28)$$

$$- \varepsilon_{N_\varphi} \mathbf{N}(\vec{\varphi}_{N_\varphi}, \vec{u}_N) + d_{N_\varphi}(\vec{\varphi}_{N_\varphi}, \vec{\varphi}_{N_\varphi}) + a_{N_\psi} \mathbf{N}(\vec{\psi}_{N_\psi}, \vec{\varphi}_{N_\varphi}) - \mu_{N_\theta} \mathbf{N}(\vec{\theta}_{N_\theta}, \vec{\varphi}_{N_\varphi}) = L_{N_\varphi}^\varphi(\vec{\varphi}_{N_\varphi}), \quad \forall \vec{\varphi}_{N_\varphi} \in \vec{V}_{N_\varphi}^\varphi(\omega), \quad (3.29)$$

$$- b_{N_\psi} \mathbf{N}(\vec{\psi}_{N_\psi}, \vec{u}_N) + a_{N_\psi} \mathbf{N}(\vec{\varphi}_{N_\varphi}, \vec{\psi}_{N_\psi}) + \zeta_{N_\psi}(\vec{\psi}_{N_\psi}, \vec{\psi}_{N_\psi}) - m_{N_\theta} \mathbf{N}(\vec{\theta}_{N_\theta}, \vec{\psi}_{N_\psi}) = L_{N_\psi}^\psi(\vec{\psi}_{N_\psi}), \quad \forall \vec{\psi}_{N_\psi} \in \vec{V}_{N_\psi}^\psi(\omega), \quad (3.30)$$

$$\eta_{N_\theta}(\vec{\theta}_{N_\theta}, \vec{\theta}_{N_\theta}) = L_{N_\theta}^\theta(\vec{\theta}_{N_\theta}), \quad \forall \vec{\theta}_{N_\theta} \in \vec{V}_{N_\theta}^\theta(\omega), \quad (3.31)$$

where

$$\vec{V}_N(\omega) = \{\vec{v}_N = (v_{Ni}^{r_i}) \in [H_{loc}^1(\omega)]^{N_{1,2,3}}; \|\vec{v}_N\|_* < \infty, \quad tr_{\tilde{\gamma}}(v_{Ni}^{r_i}) = 0 \text{ on } \tilde{\gamma}_0, \quad r_i = 0, \dots, N_i, i = 1, 2, 3\},$$

$$\vec{V}_{N_\varphi}^\varphi(\omega) = \{\vec{\varphi}_{N_\varphi} = (\bar{\varphi}_{N_\varphi}^{r_\varphi}) \in [H_{loc}^1(\omega)]^{N_\varphi+1}; \|\vec{\varphi}_{N_\varphi}\|_{\varphi*} < \infty, tr_{\tilde{\gamma}}(\bar{\varphi}_{N_\varphi}^{r_\varphi}) = 0 \text{ on } \tilde{\gamma}_0^\varphi, \quad r_\varphi = 0, \dots, N_\varphi\},$$

$$\vec{V}_{N_\psi}^\psi(\omega) = \{\vec{\psi}_{N_\psi} = (\bar{\psi}_{N_\psi}^{r_\psi}) \in [H_{loc}^1(\omega)]^{N_\psi+1}; \|\vec{\psi}_{N_\psi}\|_{\psi*} < \infty, tr_{\tilde{\gamma}}(\bar{\psi}_{N_\psi}^{r_\psi}) = 0 \text{ on } \tilde{\gamma}_0^\psi, \quad r_\psi = 0, \dots, N_\psi\},$$

$$\vec{V}_{N_\theta}^\theta(\omega) = \{\vec{\theta}_{N_\theta} = (\bar{\theta}_{N_\theta}^{r_\theta}) \in [H_{loc}^1(\omega)]^{N_\theta+1}; \|\vec{\theta}_{N_\theta}\|_{\theta*} < \infty, tr_{\tilde{\gamma}}(\bar{\theta}_{N_\theta}^{r_\theta}) = 0 \text{ on } \tilde{\gamma}_0^\theta, \quad r_\theta = 0, \dots, N_\theta\},$$

the bilinear forms $c_{\mathbf{N}}$, $\varepsilon_{N_\varphi \mathbf{N}}$, $b_{N_\psi \mathbf{N}}$, $\lambda_{N_\theta \mathbf{N}}$, d_{N_φ} , $a_{N_\varphi N_\psi}$, $a_{N_\psi N_\varphi}$, ζ_{N_ψ} , $\mu_{N_\theta N_\varphi}$, $m_{N_\theta N_\psi}$, η_{N_θ} are defined by the corresponding bilinear forms of Eqs. (3.21)-(3.24), i.e., $c_{\mathbf{N}}(\vec{v}_{\mathbf{N}}, \vec{v}_{\mathbf{N}}) = c(\vec{v}_{\mathbf{N}}, v_{\mathbf{N}})$,

$$\begin{aligned} \varepsilon_{N_\varphi \mathbf{N}}(\vec{\varphi}_{N_\varphi}, \vec{v}_{\mathbf{N}}) &= \varepsilon(\bar{\varphi}_{N_\varphi}, v_{\mathbf{N}}), \quad b_{N_\psi \mathbf{N}}(\vec{\psi}_{N_\psi}, \vec{v}_{\mathbf{N}}) = b(\bar{\psi}_{N_\psi}, v_{\mathbf{N}}), \\ \lambda_{N_\theta \mathbf{N}}(\vec{\theta}_{N_\theta}, \vec{v}_{\mathbf{N}}) &= \lambda(\bar{\theta}_{N_\theta}, v_{\mathbf{N}}), \quad d_{N_\varphi}(\vec{\varphi}_{N_\varphi}, \vec{\varphi}_{N_\varphi}) = d(\bar{\varphi}_{N_\varphi}, \bar{\varphi}_{N_\varphi}), \\ a_{N_\varphi N_\psi}(\vec{\varphi}_{N_\varphi}, \vec{\psi}_{N_\psi}) &= a(\bar{\varphi}_{N_\varphi}, \bar{\psi}_{N_\psi}), \quad a_{N_\psi N_\varphi}(\vec{\psi}_{N_\psi}, \vec{\varphi}_{N_\varphi}) = a(\bar{\psi}_{N_\psi}, \bar{\varphi}_{N_\varphi}), \\ \zeta_{N_\psi}(\vec{\psi}_{N_\psi}, \vec{\psi}_{N_\psi}) &= \zeta(\bar{\psi}_{N_\psi}, \bar{\psi}_{N_\psi}), \quad \mu_{N_\theta N_\varphi}(\vec{\theta}_{N_\theta}, \vec{\varphi}_{N_\varphi}) = \mu(\bar{\theta}_{N_\theta}, \bar{\varphi}_{N_\varphi}), \\ m_{N_\theta N_\psi}(\vec{\theta}_{N_\theta}, \vec{\psi}_{N_\psi}) &= m(\bar{\theta}_{N_\theta}, \bar{\psi}_{N_\psi}), \quad \eta_{N_\theta}(\vec{\theta}_{N_\theta}, \vec{\theta}_{N_\theta}) = \eta(\bar{\theta}_{N_\theta}, \bar{\theta}_{N_\theta}), \end{aligned}$$

for all vector-functions $\vec{v}_{\mathbf{N}}, \vec{v}_{\mathbf{N}} \in \vec{V}_{\mathbf{N}}(\omega)$; $\vec{\varphi}_{N_\varphi}, \vec{\varphi}_{N_\varphi} \in \vec{V}_{N_\varphi}^\varphi(\omega)$; $\vec{\psi}_{N_\psi}, \vec{\psi}_{N_\psi} \in \vec{V}_{N_\psi}^\psi(\omega)$; $\vec{\theta}_{N_\theta}, \vec{\theta}_{N_\theta} \in \vec{V}_{N_\theta}^\theta(\omega)$, corresponding to $\tilde{v}_{\mathbf{N}}, v_{\mathbf{N}} \in \mathbf{V}_{\mathbf{N}}(\Omega)$; $\bar{\varphi}_{N_\varphi}, \bar{\varphi}_{N_\varphi} \in V_{N_\varphi}^\varphi(\Omega)$; $\bar{\psi}_{N_\psi}, \bar{\psi}_{N_\psi} \in V_{N_\psi}^\psi(\Omega)$; $\bar{\theta}_{N_\theta}, \bar{\theta}_{N_\theta} \in V_{N_\theta}^\theta(\Omega)$, respectively. The linear forms $L_{\mathbf{N}}^\varphi$, $L_{N_\varphi}^\varphi$, $L_{N_\psi}^\psi$ and $L_{N_\theta}^\theta$ are given by the following expressions:

$$\begin{aligned} L_{\mathbf{N}}^\varphi(\vec{v}_{\mathbf{N}}) &= \sum_{i=1}^3 \sum_{r_i=0}^{N_i} \left(r_i + \frac{1}{2} \right) \left(\int_{\omega} \frac{1}{h} v_{\mathbf{N}i}^{r_i} \left(f_i^{r_i, G} + g_i^{r_i, G, +} \lambda_+ + g_i^{r_i, G, -} \lambda_- (-1)^{r_i} \right) d\omega \right. \\ &\quad \left. + \int_{\gamma_1} \frac{1}{h} t r_{\vec{\gamma}}^{r_i}(v_{\mathbf{N}i}) g_i^{r_i, G} d\gamma_1 \right), \\ L_{N_\varphi}^\varphi(\vec{\varphi}_{N_\varphi}) &= \sum_{r_\varphi=0}^{N_\varphi} \left(r_\varphi + \frac{1}{2} \right) \left(\int_{\omega} \frac{1}{h} \varphi_{N_\varphi}^{r_\varphi} \left(f^{\varphi, G} - g^{\varphi, G, +} \lambda_+ - g^{\varphi, G, -} \lambda_- (-1)^{r_\varphi} \right) d\omega \right. \\ &\quad \left. - \int_{\gamma_1^\varphi} \frac{1}{h} t r_{\vec{\gamma}}^{r_\varphi}(\varphi_{N_\varphi}) g^{\varphi, G} d\gamma_1 \right), \\ L_{N_\psi}^\psi(\vec{\psi}_{N_\psi}) &= - \sum_{r_\psi=0}^{N_\psi} \left(r_\psi + \frac{1}{2} \right) \left(\int_{\omega} \frac{1}{h} \psi_{N_\psi}^{r_\psi} \left(g^{\psi, G, +} \lambda_+ + g^{\psi, G, -} \lambda_- (-1)^{r_\psi} \right) d\omega \right. \\ &\quad \left. + \int_{\gamma_1^\psi} \frac{1}{h} t r_{\vec{\gamma}}^{r_\psi}(\psi_{N_\psi}) g^{\psi, G} d\gamma_1 \right), \\ L_{N_\theta}^\theta(\vec{\theta}_{N_\theta}) &= \sum_{r_\theta=0}^{N_\theta} \left(r_\theta + \frac{1}{2} \right) \left(\int_{\omega} \frac{1}{h} \theta_{N_\theta}^{r_\theta} \left(f^{\theta, G} - g^{\theta, G, +} \lambda_+ - g^{\theta, G, -} \lambda_- (-1)^{r_\theta} \right) d\omega \right. \\ &\quad \left. - \int_{\gamma_1^\theta} \frac{1}{h} t r_{\vec{\gamma}}^{r_\theta}(\theta_{N_\theta}) g^{\theta, G} d\gamma_1 \right), \end{aligned}$$

where $f_i^G = f^i \sqrt{G}$, $f^{\varphi,G} = f^\varphi \sqrt{G}$, $f^{\theta,G} = f^\theta \sqrt{G}$, $g_i^G = g^i \sqrt{G}$, $g^{\varphi,G} = g^\varphi \sqrt{G}$, $g^{\psi,G} = g^\psi \sqrt{G}$, $g_i^{G,\pm}(x_1, x_2) = g^i(x_1, x_2, x_3) \sqrt{G}$, $g^{\varphi,G,\pm}(x_1, x_2) = g^\varphi(x_1, x_2, x_3) \sqrt{G}$, $g^{\psi,G,\pm}(x_1, x_2) = g^\psi(x_1, x_2, x_3) \sqrt{G}$, $g^{\theta,G,\pm}(x_1, x_2) = g^\theta(x_1, x_2, x_3) \sqrt{G}$, for $(x_1, x_2, x_3) \in \Gamma^\pm$, and $\gamma_1 = \bar{\gamma} \setminus \tilde{\gamma}_0$, $\gamma_1^\varphi = \bar{\gamma} \setminus \tilde{\gamma}_0^\varphi$, $\gamma_1^\psi = \bar{\gamma} \setminus \tilde{\gamma}_0^\psi$, $\gamma_1^\theta = \bar{\gamma} \setminus \tilde{\gamma}_0^\theta$, $\lambda_\pm = \sqrt{1 + (\partial_1 h^\pm)^2 + (\partial_2 h^\pm)^2}$,
 $\overset{r}{v} = \int \overset{h^+}{v} P_r(z) dx_3$, for all functions $v \in L^2(\Omega)$ and $v \in L^2(\bar{\Gamma})$, $r \in \mathbb{N} \cup \{0\}$.

Since the homogeneous problem (3.28)-(3.31), where $L_{\vec{N}}^u(\vec{v}_N) = 0$, $L_{N_\varphi}^\varphi(\vec{\varphi}_{N_\varphi}) = 0$, $L_{N_\psi}^\psi(\vec{\psi}_{N_\psi}) = 0$, $L_{N_\theta}^\theta(\vec{\theta}_{N_\theta}) = 0$, for all $\vec{v}_N \in \vec{V}_N(\omega)$, $\vec{\varphi}_{N_\varphi} \in \vec{V}_{N_\varphi}^\varphi(\omega)$, $\vec{\psi}_{N_\psi} \in \vec{V}_{N_\psi}^\psi(\omega)$ and $\vec{\theta}_{N_\theta} \in \vec{V}_{N_\theta}^\theta(\omega)$, has non-trivial solutions, if the parts $\tilde{\gamma}_0$, $\tilde{\gamma}_0^\varphi$, $\tilde{\gamma}_0^\psi$ and $\tilde{\gamma}_0^\theta$ of the boundary of the two-dimensional domain ω are empty sets, therefore the solution of problem (3.28)-(3.31) is not unique in the mentioned spaces and it is necessary to introduce suitable factor spaces, where the solution of problem (3.28)-(3.31) is unique.

The set $\vec{\mathfrak{R}}_{\mathfrak{N}}$ of solutions of the homogeneous problem (3.28)-(3.31) is of the following form:

$$\vec{\mathfrak{R}}_{\mathfrak{N}} = \left\{ \left(\overset{r}{\vec{v}}_{N_1}, \overset{r}{\vec{\varphi}}_{N_\varphi}, \overset{r}{\vec{\psi}}_{N_\psi}, \overset{r}{\vec{\theta}}_{N_\theta} \right); \overset{r}{\vec{v}}_{N_1} = \overset{r}{\vec{v}}_{N_1} + \overset{r}{\vec{u}}_{N_1}, \right. \\ \left. \begin{aligned} \overset{r}{\vec{\varphi}}_{N_\varphi} &= \overset{r}{\vec{\varphi}}_{N_\varphi} + \overset{r}{\vec{\varphi}}_{N_\varphi}, \quad \overset{r}{\vec{\psi}}_{N_\psi} = \overset{r}{\vec{\psi}}_{N_\psi} + \overset{r}{\vec{\psi}}_{N_\psi}, \\ \left(\overset{r}{\vec{v}}_{N_1}, \overset{r}{\vec{\varphi}}_{N_\varphi}, \overset{r}{\vec{\psi}}_{N_\psi} \right) &\in \vec{\mathfrak{R}}_{N_1 N_\varphi N_\psi}, \quad \overset{r}{\vec{\theta}}_{N_\theta} \in \vec{\mathfrak{R}}_{N_\theta}^\theta \end{aligned} \right\},$$

where

$$\vec{\mathfrak{R}}_{N_1 N_\varphi N_\psi}^\psi = \left\{ \left(\overset{r}{\vec{v}}_{N_1}, \overset{r}{\vec{\varphi}}_{N_\varphi}, \overset{r}{\vec{\psi}}_{N_\psi} \right) \in \vec{V}_{N_1}(\omega) \times \vec{V}_{N_\varphi}^\varphi(\omega) \times \vec{V}_{N_\psi}^\psi(\omega); \right. \\ \begin{aligned} \overset{r}{\vec{v}}_{N_1} &= (v_{N_1}^r), \quad v_{N_1}^0 = 2h(\alpha_1 - \beta_3 x_2 + \beta_2 \bar{h}), \quad v_{N_2}^0 = 2h(\alpha_2 + \beta_3 x_1 - \beta_1 \bar{h}), \\ v_{N_3}^0 &= 2h(\alpha_3 - \beta_2 x_1 + \beta_1 x_2), \quad v_{N_1}^1 = 2\beta_2 h^2/3, \text{ if } r_1 \geq 1, \\ v_{N_2}^1 &= -2\beta_1 h^2/3, \text{ if } r_2 \geq 1, \quad v_{N_3}^1 = 0, \text{ if } r_3 \geq 1, \\ v_{N_i}^r &= 0, \text{ for } r_i \geq 2, \quad \alpha = (\alpha_i)_{i=1}^3, \quad \beta = (\beta_i)_{i=1}^3 \in \mathbb{R}^3, \\ \overset{r}{\vec{\varphi}}_{N_\varphi} &= (\overset{r}{\varphi}_{N_\varphi}^r), \quad \overset{0}{\vec{\varphi}}_{N_\varphi} = 2h\alpha_\varphi, \quad \overset{r_\varphi}{\vec{\varphi}}_{N_\varphi} = 0, \text{ for } r_\varphi \geq 1, \quad \alpha_\varphi \in \mathbb{R}, \\ \overset{r}{\vec{\psi}}_{N_\psi} &= (\overset{r}{\psi}_{N_\psi}^r), \quad \overset{0}{\vec{\psi}}_{N_\psi} = 2h\alpha_\psi, \quad \overset{r_\psi}{\vec{\psi}}_{N_\psi} = 0, \text{ for } r_\psi \geq 1, \quad \alpha_\psi \in \mathbb{R} \end{aligned} \right\},$$

$$\vec{\mathfrak{R}}_{N_\theta}^\theta = \left\{ \overset{r}{\vec{\theta}}_{N_\theta} \in \vec{V}_{N_\theta}^\theta(\omega); \overset{r}{\vec{\theta}}_{N_\theta} = (\overset{r_\theta}{\theta}_{N_\theta}^r), \overset{0}{\vec{\theta}}_{N_\theta} = 2h\alpha_\theta, \overset{r_\theta}{\vec{\theta}}_{N_\theta} = 0, \text{ for } r_\theta \geq 1, \alpha_\theta \in \mathbb{R} \right\}$$

and $(\vec{u}_{\mathbf{N}}^{r\vec{\theta}_{\mathbf{N}\theta}^r}, \vec{\varphi}_{N_\varphi}^{r\vec{\theta}_{\mathbf{N}\theta}^r}, \vec{\psi}_{N_\psi}^{r\vec{\theta}_{\mathbf{N}\theta}^r}) \in \vec{V}_{\mathbf{N}}(\omega) \times \vec{V}_{N_\varphi}^\varphi(\omega) \times \vec{V}_{N_\psi}^\psi(\omega)$ is a solution of the homogeneous Eqs. (3.28)-(3.31) with $\vec{\theta}_{N_\theta} = \vec{\theta}_{N_\theta}^r$.

By applying the set $\vec{\mathfrak{R}}_{\mathfrak{R}}$ we define the factor space

$$\vec{V}_{\vec{\mathfrak{R}}_{\mathfrak{R}}}^{\mathbf{u}\varphi\psi\theta}(\omega) = (\vec{V}_{\mathbf{N}}(\omega) \times \vec{V}_{N_\varphi}^\varphi(\omega) \times \vec{V}_{N_\psi}^\psi(\omega) \times \vec{V}_{N_\theta}^\theta(\omega)) / \vec{\mathfrak{R}}_{\mathfrak{R}},$$

which consists of the following equivalence classes

$$\begin{aligned} (\vec{v}_{\mathbf{N}}, \vec{\varphi}_{N_\varphi}, \vec{\psi}_{N_\psi}, \vec{\theta}_{N_\theta})^{\vec{\mathfrak{R}}_{\mathfrak{R}}} = \{ & (\vec{v}_{\mathbf{N}}, \vec{\varphi}_{N_\varphi}, \vec{\psi}_{N_\psi}, \vec{\theta}_{N_\theta}) + (\vec{v}_{\mathbf{N}}^{r\vec{\theta}_{\mathbf{N}\theta}^r}, \vec{\varphi}_{N_\varphi}^{r\vec{\theta}_{\mathbf{N}\theta}^r}, \vec{\psi}_{N_\psi}^{r\vec{\theta}_{\mathbf{N}\theta}^r}, \vec{\theta}_{N_\theta}^{r\vec{\theta}_{\mathbf{N}\theta}^r}); \\ & (\vec{v}_{\mathbf{N}}^{r\vec{\theta}_{\mathbf{N}\theta}^r}, \vec{\varphi}_{N_\varphi}^{r\vec{\theta}_{\mathbf{N}\theta}^r}, \vec{\psi}_{N_\psi}^{r\vec{\theta}_{\mathbf{N}\theta}^r}, \vec{\theta}_{N_\theta}^{r\vec{\theta}_{\mathbf{N}\theta}^r}) \in \vec{\mathfrak{R}}_{\mathfrak{R}} \}, \end{aligned}$$

for each $(\vec{v}_{\mathbf{N}}, \vec{\varphi}_{N_\varphi}, \vec{\psi}_{N_\psi}, \vec{\theta}_{N_\theta}) \in \vec{V}_{\mathbf{N}}(\omega) \times \vec{V}_{N_\varphi}^\varphi(\omega) \times \vec{V}_{N_\psi}^\psi(\omega) \times \vec{V}_{N_\theta}^\theta(\omega)$. The factor space is a Hilbert space equipped with the following norm:

$$\begin{aligned} \left\| (\vec{v}_{\mathbf{N}}, \vec{\varphi}_{N_\varphi}, \vec{\psi}_{N_\psi}, \vec{\theta}_{N_\theta})^{\vec{\mathfrak{R}}_{\mathfrak{R}}} \right\|_{\vec{V}_{\vec{\mathfrak{R}}_{\mathfrak{R}}}^{\mathbf{u}\varphi\psi\theta}(\omega)} &= \inf \{ \| (\vec{v}_{\mathbf{N}}, \vec{\varphi}_{N_\varphi}, \vec{\psi}_{N_\psi}, \vec{\theta}_{N_\theta}) \\ &+ (\vec{v}_{\mathbf{N}}^{r\vec{\theta}_{\mathbf{N}\theta}^r}, \vec{\varphi}_{N_\varphi}^{r\vec{\theta}_{\mathbf{N}\theta}^r}, \vec{\psi}_{N_\psi}^{r\vec{\theta}_{\mathbf{N}\theta}^r}, \vec{\theta}_{N_\theta}^{r\vec{\theta}_{\mathbf{N}\theta}^r}) \|_{\vec{V}_{\mathbf{N}}(\omega) \times \vec{V}_{N_\varphi}^\varphi(\omega) \times \vec{V}_{N_\psi}^\psi(\omega) \times \vec{V}_{N_\theta}^\theta(\omega)} \}; \\ (\vec{v}_{\mathbf{N}}^{r\vec{\theta}_{\mathbf{N}\theta}^r}, \vec{\varphi}_{N_\varphi}^{r\vec{\theta}_{\mathbf{N}\theta}^r}, \vec{\psi}_{N_\psi}^{r\vec{\theta}_{\mathbf{N}\theta}^r}, \vec{\theta}_{N_\theta}^{r\vec{\theta}_{\mathbf{N}\theta}^r}) &\in \vec{\mathfrak{R}}_{\mathfrak{R}} \}. \end{aligned}$$

It follows from the definition of the sets $\vec{\mathfrak{R}}_{N_\varphi N_\psi}^{\mathbf{u}\varphi\psi}$ and $\vec{\mathfrak{R}}_{N_\theta}^\theta$ that any vector-functions $(\vec{v}_{\mathbf{N}}, \vec{\varphi}_{N_\varphi}^r, \vec{\psi}_{N_\psi}^r) \in \vec{\mathfrak{R}}_{N_\varphi N_\psi}^{\mathbf{u}\varphi\psi}$ and $\vec{\theta}_{N_\theta}^r \in \vec{\mathfrak{R}}_{N_\theta}^\theta$ satisfy the homogeneous Eqs. (3.28)-(3.31):

$$\begin{aligned} c_{\mathbf{N}}(\vec{v}_{\mathbf{N}}^r, \vec{v}_{\mathbf{N}}) + \varepsilon_{N_\varphi \mathbf{N}}(\vec{\varphi}_{N_\varphi}^r, \vec{v}_{\mathbf{N}}) + b_{N_\psi \mathbf{N}}(\vec{\psi}_{N_\psi}^r, \vec{v}_{\mathbf{N}}) - \lambda_{N_\theta \mathbf{N}}(\vec{\theta}_{N_\theta}^r, \vec{v}_{\mathbf{N}}) &= 0, \quad \forall \vec{v}_{\mathbf{N}} \in \vec{V}_{\mathbf{N}}(\omega), \\ -\varepsilon_{N_\varphi \mathbf{N}}(\vec{\varphi}_{N_\varphi}^r, \vec{v}_{\mathbf{N}}^r) + d_{N_\varphi}(\vec{\varphi}_{N_\varphi}^r, \vec{\varphi}_{N_\varphi}^r) + a_{N_\psi N_\varphi}(\vec{\psi}_{N_\psi}^r, \vec{\varphi}_{N_\varphi}^r) - \mu_{N_\theta N_\varphi}(\vec{\theta}_{N_\theta}^r, \vec{\varphi}_{N_\varphi}^r) &= 0, \\ \vec{\varphi}_{N_\varphi}^r &\in \vec{V}_{N_\varphi}^\varphi(\omega), \\ -b_{N_\psi \mathbf{N}}(\vec{\psi}_{N_\psi}^r, \vec{v}_{\mathbf{N}}^r) + a_{N_\varphi N_\psi}(\vec{\varphi}_{N_\varphi}^r, \vec{\psi}_{N_\psi}^r) + \zeta_{N_\psi}(\vec{\psi}_{N_\psi}^r, \vec{\psi}_{N_\psi}^r) - m_{N_\theta N_\psi}(\vec{\theta}_{N_\theta}^r, \vec{\psi}_{N_\psi}^r) &= 0, \\ \vec{\psi}_{N_\psi}^r &\in \vec{V}_{N_\psi}^\psi(\omega), \\ \eta_{N_\theta}(\vec{\theta}_{N_\theta}^r, \vec{\theta}_{N_\theta}^r) &= 0, \quad \forall \vec{\theta}_{N_\theta}^r \in \vec{V}_{N_\theta}^\theta(\omega), \end{aligned}$$

and, hence, we have that $L_{\mathbf{N}}^{\mathbf{u}}(\vec{v}_{\mathbf{N}}^r) = 0$, $L_{N_\varphi}^\varphi(\vec{\varphi}_{N_\varphi}^r) = 0$, $L_{N_\psi}^\psi(\vec{\psi}_{N_\psi}^r) = 0$, $L_{N_\theta}^\theta(\vec{\theta}_{N_\theta}^r) = 0$. Consequently, problem (3.28)-(3.31) can be formulated in the factor space $\vec{V}_{\vec{\mathfrak{R}}_{\mathfrak{R}}}^{\mathbf{u}\varphi\psi\theta}(\omega)$

as follows: Find $(\vec{u}_N, \vec{\varphi}_{N_\varphi}, \vec{\psi}_{N_\psi}, \vec{\theta}_{N_\theta})^{\vec{r}_{\mathfrak{R}_1}} \in \vec{V}_{\vec{r}_{\mathfrak{R}_1}}^{\mathbf{u}\varphi\psi\theta}(\omega)$ such that any function from the equivalence class $(\vec{u}_N, \vec{\varphi}_{N_\varphi}, \vec{\psi}_{N_\psi}, \vec{\theta}_{N_\theta})^{\vec{r}_{\mathfrak{R}_1}}$ is a solution of problem (3.28)-(3.31).

For the constructed hierarchical two-dimensional models (3.28)-(3.31) for thermo-electro-magneto-elastic shells the following existence and uniqueness theorem is proved, where we use the following weighted function spaces

$$\begin{aligned} L_h^{6/5}(\omega) &= \{h^{1/6}v; v \in L^{6/5}(\omega)\}, \quad L_h^{4/3}(\hat{\gamma}) = \{h^{1/4}v; v \in L^{4/3}(\omega)\}, \quad \hat{\gamma} \subset \tilde{\gamma}, \\ L_{\lambda_+}^{4/3}(\omega) &= \{\lambda_+^{-3/4}v; v \in L^{4/3}(\omega)\}, \quad L_{\lambda_-}^{4/3}(\omega) = \{\lambda_-^{-3/4}v; v \in L^{4/3}(\omega)\}. \end{aligned}$$

Theorem 3.2. *Suppose that $\Omega \subset \mathbb{R}^3$ is a bounded Lipschitz domain, the parameters $c_{ijpq}, \varepsilon_{pij}, b_{pij}, \lambda_{ij}, d_{ij}, a_{ij}, \zeta_{ij}, \mu_i, m_i, \eta_{ij} \in L^\infty(\Omega)$, $i, j, p, q = 1, 2, 3$, satisfy symmetry and positive definiteness conditions (3.12) and (3.25), (3.26). If the functions defining the linear forms $L_N^{\mathbf{u}}, L_{N_\varphi}^\varphi, L_{N_\psi}^\psi$ and $L_{N_\theta}^\theta$ are such that*

$$L_N^{\mathbf{u}}(\vec{v}_N^r) = 0, \quad L_{N_\varphi}^\varphi(\vec{\varphi}_{N_\varphi}^r) = 0, \quad L_{N_\psi}^\psi(\vec{\psi}_{N_\psi}^r) = 0, \quad L_{N_\theta}^\theta(\vec{\theta}_{N_\theta}^r) = 0,$$

for all $(\vec{v}_N^r, \vec{\varphi}_{N_\varphi}^r, \vec{\psi}_{N_\psi}^r) \in \vec{\mathfrak{R}}_{NN_\varphi N_\psi}^{\mathbf{u}\varphi\psi}$ and $\vec{\theta}_{N_\theta}^r \in \vec{\mathfrak{R}}_{N_\theta}^\theta$, and

$$\begin{aligned} f_i^{r_i, G} &\in L_h^{6/5}(\omega), \quad g_i^{G,+} \in L_{\lambda_+}^{4/3}(\omega), \quad g_i^{G,-} \in L_{\lambda_-}^{4/3}(\omega), \quad g_i^G \in L_h^{4/3}(\gamma_1), \\ f_{r_\varphi}^{r_\varphi, G} &\in L_h^{6/5}(\omega), \quad g^{\varphi, G,+} \in L_{\lambda_+}^{4/3}(\omega), \quad g^{\varphi, G,-} \in L_{\lambda_-}^{4/3}(\omega), \quad g^{\varphi, G} \in L_h^{4/3}(\gamma_1^\varphi), \\ g^{\psi, G,+} &\in L_{\lambda_+}^{4/3}(\omega), \quad g^{\psi, G,-} \in L_{\lambda_-}^{4/3}(\omega), \quad g^{\psi, G} \in L_h^{4/3}(\gamma_1^\psi), \\ f_{r_\theta}^{r_\theta, G} &\in L_h^{6/5}(\omega), \quad g^{\theta, G,+} \in L_{\lambda_+}^{4/3}(\omega), \quad g^{\theta, G,-} \in L_{\lambda_-}^{4/3}(\omega), \quad g^{\theta, G} \in L_h^{4/3}(\gamma_1^\theta), \end{aligned}$$

where $r_i = 0, \dots, N_i$, $i = 1, 2, 3$, $r_\varphi = 0, \dots, N_\varphi$, $r_\psi = 0, \dots, N_\psi$, $r_\theta = 0, \dots, N_\theta$, then the boundary value problem (3.28)-(3.31) possesses a unique solution $(\vec{u}_N, \vec{\varphi}_{N_\varphi}, \vec{\psi}_{N_\psi}, \vec{\theta}_{N_\theta})^{\vec{r}_{\mathfrak{R}_1}} \in \vec{V}_{\vec{r}_{\mathfrak{R}_1}}^{\mathbf{u}\varphi\psi\theta}(\omega)$, which continuously depends on the given data, i.e., the mapping

$$\begin{aligned} (\vec{f}_N^G, \mathbf{g}^{G,+}, \mathbf{g}^{G,-}, \vec{g}_N^G, \vec{f}_{N_\varphi}^{\varphi, G}, g^{\varphi, G,+}, g^{\varphi, G,-}, \vec{g}_{N_\varphi}^{\varphi, G}, g^{\psi, G,+}, g^{\psi, G,-}, \vec{g}_{N_\psi}^{\psi, G}, \\ \vec{f}_{N_\theta}^{\theta, G}, g^{\theta, G,+}, g^{\theta, G,-}, \vec{g}_{N_\theta}^{\theta, G}) \rightarrow (\vec{u}_N, \vec{\varphi}_{N_\varphi}, \vec{\psi}_{N_\psi}, \vec{\theta}_{N_\theta})^{\vec{r}_{\mathfrak{R}_1}} \end{aligned}$$

is linear and continuous from the space

$$\begin{aligned} (L_h^{6/5}(\omega))^{N_{1,2,3}} \times (L_{\lambda_+}^{4/3}(\omega))^3 \times (L_{\lambda_-}^{4/3}(\omega))^3 \times (L_h^{4/3}(\gamma_1))^{N_{1,2,3}} \times (L_h^{6/5}(\omega))^{N_\varphi+1} \\ \times (L_{\lambda_+}^{4/3}(\omega))^3 \times (L_{\lambda_-}^{4/3}(\omega))^3 \times (L_h^{4/3}(\gamma_1^\varphi))^{N_\varphi+1} \times (L_{\lambda_+}^{4/3}(\omega))^3 \times (L_{\lambda_-}^{4/3}(\omega))^3 \\ \times (L_h^{4/3}(\gamma_1^\psi))^{N_\psi+1} \times (L_h^{6/5}(\omega))^{N_\theta+1} \times (L_{\lambda_+}^{4/3}(\omega))^3 \times (L_{\lambda_-}^{4/3}(\omega))^3 \times (L_h^{4/3}(\gamma_1^\theta))^{N_\theta+1} \end{aligned}$$

to the space $\vec{V}_{\vec{r}_{\mathfrak{R}_1}}^{\mathbf{u}\varphi\psi\theta}(\omega)$, where

$$\begin{aligned} \vec{f}_N^G &= (f_i^G), \quad \mathbf{g}^{G,+} = (g_i^{G,+}), \quad \mathbf{g}^{G,-} = (g_i^{G,-}), \quad \vec{g}_N^G = (g_i^G), \\ \vec{f}_{N_\varphi}^{\varphi,G} &= (f^{\varphi,G}), \quad \vec{g}_{N_\varphi}^{\varphi,G} = (g^{\varphi,G}), \quad \vec{g}_{N_\psi}^{\psi,G} = (g^{\psi,G}), \quad \vec{f}_{N_\theta}^{\theta,G} = (f^{\theta,G}), \quad \vec{g}_{N_\theta}^{\theta,G} = (g^{\theta,G}). \end{aligned}$$

Remark 3.2. If the lengths of the curves $\vec{\gamma}_0$, $\vec{\gamma}_0^\varphi$, $\vec{\gamma}_0^\psi$ and $\vec{\gamma}_0^\theta$ are positive, then the homogeneous problem (3.28)-(3.31) possesses only a trivial solution. Consequently, $\vec{\mathfrak{R}}_{\mathbf{N}N_\varphi N_\psi}^{\mathbf{u}\varphi\psi}$, $\vec{\mathfrak{R}}_{N_\theta}^\theta$ and $\vec{\mathfrak{R}}_{\mathfrak{R}_\mathfrak{I}}$ consist of vector-functions with zero components. The factor space $\vec{V}_{\vec{\mathfrak{R}}_{\mathfrak{I}}}^{\mathbf{u}\varphi\psi\theta}(\omega)$ coincides with $\vec{V}_N(\omega) \times \vec{V}_{N_\varphi}^\varphi(\omega) \times \vec{V}_{N_\psi}^\psi(\omega) \times \vec{V}_{N_\theta}^\theta(\omega)$ and Theorem 3.2 is valid in the spaces mentioned in the formulation of the two-dimensional problem (3.28)-(3.31).

So, we have constructed a hierarchy of two-dimensional models for thermo-electro-magneto-elastic shells and have investigated the well-posedness of the obtained boundary value problems (3.28)-(3.31), which can be considered as approximations to the original three-dimensional problem if we estimate the difference between the exact solution of the three-dimensional problem and the functions of three variables restored from the solutions of the two-dimensional problems. We denote by $(\mathbf{u}_N, \varphi_{N_\varphi}, \psi_{N_\psi}, \theta_{N_\theta})^{\mathfrak{R}_\mathfrak{I}}$ the equivalence class consisting of vector-functions restored from the solution $(\vec{u}_N, \vec{\varphi}_{N_\varphi}, \vec{\psi}_{N_\psi}, \vec{\theta}_{N_\theta})^{\vec{\mathfrak{R}}_{\mathfrak{I}}}$ of problem (3.28)-(3.31), where

$$\begin{aligned} (\mathbf{u}_N, \varphi_{N_\varphi}, \psi_{N_\psi}, \theta_{N_\theta})^{\mathfrak{R}_\mathfrak{I}} &= \{(\mathbf{u}_N, \varphi_{N_\varphi}, \psi_{N_\psi}, \theta_{N_\theta}) + (\mathbf{v}_N^{r\theta_{N_\theta}^r}, \overline{\varphi}_{N_\varphi}^{r\theta_{N_\theta}^r}, \overline{\psi}_{N_\psi}^{r\theta_{N_\theta}^r}, \theta_{N_\theta}^r); \\ &(\mathbf{v}_N^{r\theta_{N_\theta}^r}, \overline{\varphi}_{N_\varphi}^{r\theta_{N_\theta}^r}, \overline{\psi}_{N_\psi}^{r\theta_{N_\theta}^r}, \theta_{N_\theta}^r) \in \mathfrak{R}_\mathfrak{I}\}, \end{aligned}$$

$\mathbf{u}_N \in \mathbf{V}_N(\Omega)$, $\varphi_{N_\varphi} \in V_{N_\varphi}^\varphi(\Omega)$, $\psi_{N_\psi} \in V_{N_\psi}^\psi(\Omega)$, $\theta_{N_\theta} \in V_{N_\theta}^\theta(\Omega)$ correspond to solutions $\vec{u}_N \in \vec{V}_N(\omega)$, $\vec{\varphi}_{N_\varphi} \in \vec{V}_{N_\varphi}^\varphi(\omega)$, $\vec{\psi}_{N_\psi} \in \vec{V}_{N_\psi}^\psi(\omega)$, $\vec{\theta}_{N_\theta} \in \vec{V}_{N_\theta}^\theta(\omega)$ of problem (3.28)-(3.31), and $\mathfrak{R}_\mathfrak{I}$ consists of vector-functions of three variables

$$(\mathbf{v}_N^{r\theta_{N_\theta}^r}, \overline{\varphi}_{N_\varphi}^{r\theta_{N_\theta}^r}, \overline{\psi}_{N_\psi}^{r\theta_{N_\theta}^r}, \theta_{N_\theta}^r) \in \mathbf{V}_N(\Omega) \times V_{N_\varphi}^\varphi(\Omega) \times V_{N_\psi}^\psi(\Omega) \times V_{N_\theta}^\theta(\Omega)$$

that correspond to $(\vec{v}_N^{r\theta_{N_\theta}^r}, \overline{\varphi}_{N_\varphi}^{r\theta_{N_\theta}^r}, \overline{\psi}_{N_\psi}^{r\theta_{N_\theta}^r}, \theta_{N_\theta}^r) \in \vec{\mathfrak{R}}_{\mathfrak{I}}$.

In the following theorem we present the results regarding the relationship between the constructed two-dimensional and original three-dimensional models, where we use the following anisotropic weighted Sobolev space

$$\begin{aligned} H_{h^\pm}^{1,1,s}(\Omega) &= \{v; h^{k-1} \partial_3^{k-1} \partial_i^r v \in L^2(\Omega), h^{k-1} \partial_\alpha h^\pm \partial_3^k v \in L^2(\Omega), 1 \leq k \leq s, \\ &r = 0, 1, i = 1, 2, 3, \alpha = 1, 2\}, \quad s \in \mathbb{N}, \end{aligned}$$

which is a Hilbert space equipped with the norm

$$\|v\|_{H_{h^\pm}^{1,1,s}(\Omega)} = \left(\sum_{k=1}^s \left(\sum_{r=0}^1 \sum_{i=1}^3 \|h^{k-1} \partial_3^{k-1} \partial_i^r v\|_{L^2(\Omega)}^2 + \sum_{\alpha=1}^2 \left(\|h^{k-1} \partial_\alpha h^+ \partial_3^k v\|_{L^2(\Omega)}^2 + \|h^{k-1} \partial_\alpha h^- \partial_3^k v\|_{L^2(\Omega)}^2 \right) \right) \right)^{1/2}.$$

Theorem 3.3. *If $\Omega \subset \mathbb{R}^3$ is a bounded Lipschitz domain, the parameters c_{ijpq} , ε_{pij} , b_{pij} , λ_{ij} , d_{ij} , a_{ij} , ζ_{ij} , μ_i , m_i , $\eta_{ij} \in L^\infty(\Omega)$, $i, j, p, q = 1, 2, 3$, satisfy the symmetry and positive definiteness conditions (3.12) and (3.25), (3.26), $\mathbf{f} \in \mathbf{L}^{6/5}(\Omega)$, $\mathbf{g} \in \mathbf{L}^{4/3}(\Gamma_1)$, $f^\varphi \in L^{6/5}(\Omega)$, $g^\varphi \in L^{4/3}(\Gamma_1^\varphi)$, $g^\psi \in L^{4/3}(\Gamma_1^\psi)$, $f^\theta \in L^{6/5}(\Omega)$, $g^\theta \in L^{4/3}(\Gamma_1^\theta)$, and condition (3.27) is fulfilled, then the two-dimensional problem (3.28)-(3.31) possesses a unique solution $(\vec{u}_{\mathbf{N}}, \vec{\varphi}_{N_\varphi}, \vec{\psi}_{N_\psi}, \vec{\theta}_{N_\theta})^{\mathbb{R}^3} \in \vec{V}_{\mathbb{R}^3}^{u\varphi\psi\theta}(\omega)$ and the sequence of vector-functions of three variables $(\mathbf{u}_{\mathbf{N}}, \varphi_{N_\varphi}, \psi_{N_\psi}, \theta_{N_\theta})^{\mathbb{R}^3}$ restored from the solutions $(\vec{u}_{\mathbf{N}}, \vec{\varphi}_{N_\varphi}, \vec{\psi}_{N_\psi}, \vec{\theta}_{N_\theta})^{\mathbb{R}^3}$ of problem (3.28)-(3.31) converges to the solution $(\mathbf{u}, \varphi, \psi, \theta)^{\mathbb{R}^3} \in \mathbf{V}_{\mathbb{R}^3}^{u\varphi\psi\theta}(\Omega)$ of problem (3.21)-(3.24) as $N_{\min} = \min_{1 \leq i \leq 3} \{N_i, N_\varphi, N_\psi, N_\theta\} \rightarrow \infty$. In addition, if one of the vector-functions $(\mathbf{u}, \varphi, \psi, \theta)$ from the equivalence class corresponding to the solution $(\mathbf{u}, \varphi, \psi, \theta)^{\mathbb{R}^3}$ is such that $\mathbf{u} \in (H_{h^\pm}^{1,1,s_u}(\Omega))^3$, $\varphi \in H_{h^\pm}^{1,1,s_\varphi}(\Omega)$, $\psi \in H_{h^\pm}^{1,1,s_\psi}(\Omega)$, $\theta \in H_{h^\pm}^{1,1,s_\theta}(\Omega)$, $s_u, s_\varphi, s_\psi, s_\theta \in \mathbb{N}$, $s_u, s_\varphi, s_\psi, s_\theta \geq 2$, then*

$$\|(\mathbf{u}, \varphi, \psi, \theta)^{\mathbb{R}^3} - (\mathbf{u}_{\mathbf{N}}, \varphi_{N_\varphi}, \psi_{N_\psi}, \theta_{N_\theta})^{\mathbb{R}^3}\|_{\mathbf{V}_{\mathbb{R}^3}^{u\varphi\psi\theta}(\Omega)} \leq \frac{1}{N_{\min}^{s-1}} o(\Omega, \xi, \mathbf{N}, N_\varphi, N_\psi, N_\theta),$$

where $s = \min\{s_u, s_\varphi, s_\psi, s_\theta\}$ and $o(\Omega, \xi, \mathbf{N}, N_\varphi, N_\psi, N_\theta) \rightarrow 0$ as $N_{\min} \rightarrow \infty$.

3.4 Conclusions

We studied the boundary value problem in curvilinear coordinates with mixed boundary conditions for the mechanical displacement, electric and magnetic potentials, and temperature corresponding to the linear three-dimensional model of inhomogeneous anisotropic thermo-electro-magneto-elastic shells. We obtained a variational formulation of the three-dimensional boundary value problem, in curvilinear coordinates in corresponding factor space of Sobolev space, and formulated theorem regarding the existence and uniqueness of its solution. We then constructed a hierarchy of static two-dimensional models for thermo-electro-magneto-elastic shells and studied the existence and uniqueness of solutions of the corresponding boundary value problems in factor space of suitable weighted Sobolev space. Furthermore, we investigated the relationship between the obtained two-dimensional and original three-dimensional models. Note that the lower order models of the constructed two-dimensional models can be used as engineering models of thermo-electro-magneto-elastic shells.

Acknowledgements This work was supported by Shota Rustaveli National Science Foundation (SRNSF) [Grant number 217596, Construction and investigation of hierarchical models for thermoelastic piezoelectric structures].

References

- Aouadi M (2007) On the coupled theory of thermo-magneto-electroelasticity. *The Quarterly Journal of Mechanics and Applied Mathematics* 60(4):443–456
- Avalishvili G, Avalishvili M (2004) Investigation of static hierarchic model for elastic shells. *Bulletin of the Georgian Academy of Sciences* 169(3):451–453
- Avalishvili G, Avalishvili M (2007) On dynamical hierarchical models of multistructures. *Bulletin of the Georgian Academy of Sciences* 175(2):31–34
- Avalishvili G, Avalishvili M (2014) On approximation of lord-shulman model for thermoelastic plates with variable thickness by two-dimensional problems. *Bulletin of the Georgian National Academy of Sciences* 8(2):4–14
- Avalishvili G, Avalishvili M (2018a) On approximation of three-dimensional model of thermoelastic piezoelectric plates by two-dimensional problems. *Bulletin of the Georgian National Academy of Sciences* 12(4):23–32
- Avalishvili G, Avalishvili M (2018b) On static hierarchical two-dimensional models of thermoelastic piezoelectric plates with variable thickness. *WSEAS Transactions on Applied and Theoretical Mechanics* 13:76–84
- Avalishvili G, Avalishvili M, Gordeziani D, Miara B (2010) Hierarchical modeling of thermoelastic plates with variable thickness. *Analysis and Applications* 8(2):125–159
- Avalishvili G, Avalishvili M, Müller WH (2017a) Investigation of the three-dimensional boundary value problem for thermoelastic piezoelectric solids. *Bulletin of Tbilisi International Centre of Mathematics and Informatics* 21(2):65–79
- Avalishvili G, Avalishvili M, Müller WH (2017b) On investigation of dynamical three-dimensional model of thermoelastic piezoelectric solids. *Bulletin of the Georgian Academy of Sciences* 11(4):13–21
- Avalishvili M (1999) On a dimensional reduction method in the theory of elasticity. *Rep of Enlarged Sess of the Sem of I Vekua Inst of Appl Math* 14(3):16–19
- Avalishvili M (2002) Investigation of a mathematical model of elastic bar with variable cross-section. *Bulletin of the Georgian Academy of Sciences* 166(1):37–40
- Avalishvili M (2006) On the construction and investigation of hierarchic models for elastic rods. *Hiroshima Mathematical Journal* 36:365–386
- Avalishvili M, Gordeziani D (2003) Investigation of two-dimensional models of elastic prismatic shell. *Georgian Math J* 10(1):17–36
- Benjeddou A, Andrianarison O (2005) A thermopiezoelectric mixed variational theorem for smart multilayered composites. *Computers & Structures* 83(15):1266–1276

- Ciarlet PG (1988) *Mathematical Elasticity, vol I: Three-Dimensional Elasticity*. Elsevier, Amsterdam
- Ciarlet PG (2000) *Mathematical Elasticity, vol III: Theory of Shells*. Elsevier, Amsterdam
- Dauge M, Faou E, Yosibash Z (2017) Plates and shells: Asymptotic expansions and hierarchical models. In: Stein E, deBorst R, Hughes TJR (eds) *Encyclopedia of Computational Mechanics*, Wiley, vol 1, pp 1–39
- Dhaliwal RS, Wang J (1994) A uniqueness theorem for linear theory of thermopiezoelectricity. *ZAMM - Journal of Applied Mathematics and Mechanics / Zeitschrift für Angewandte Mathematik und Mechanik* 74(11):558–560
- Duvaut G, Lions JL (1972) *Les Inéquations en Mécanique et en Physique*. Dunod, Paris
- Gordeziani D, Avalishvili G (2005) On a dynamical hierarchical model for prismatic shells in the theory of elastic mixtures. *Mathematical Methods in the Applied Sciences* 28(6):737–756
- Gordeziani D, Avalishvili G, Avalishvili M (2006) Hierarchical models of elastic shells in curvilinear coordinates. *Computers & Mathematics with Applications* 51(12):1789–1808
- Gordeziani DG (1974a) Accuracy of a variant in the theory of thin shells (in Russ.). *Dokl Akad Nauk SSSR* 216(4):751–754
- Gordeziani DG (1974b) On the solvability of some boundary value problems for a variant of the theory of thin shells (in Russ.). *Dokl Akad Nauk SSSR* 215(6):1289–1292
- Jaiani GV (2001) On a mathematical model of bars with variable rectangular cross-sections. *ZAMM - Journal of Applied Mathematics and Mechanics / Zeitschrift für Angewandte Mathematik und Mechanik* 81(3):147–173
- McLean W (2000) *Strongly Elliptic Systems and Boundary Integral Equations*. Cambridge University Press, Cambridge
- Miara B (1989) Optimal spectral approximation in linearized plate theory. *Applicable Analysis* 31(4):291–307
- Mindlin RD (1974) Equations of high frequency vibrations of thermopiezoelectric crystal plates. *International Journal of Solids and Structures* 10(6):625–637
- Natroshevili D (2011) *Mathematical problems of thermo-electro-magneto-elasticity, Lecture Notes of TICMI, vol 12*. Tbilisi University Press, Tbilisi
- Nowacki W (1978) Some general theorems of thermopiezoelectricity. *Journal of Thermal Stresses* 1(2):171–182
- Tiersten HF (1964) *Linear Piezoelectric Plate Vibrations*. Plenum, New York
- Udupa G, Rao SS, Gangadharan KV (2014) Functionally graded composite materials: An overview. *Procedia Materials Science* 5:1291–1299
- Vekua IN (1955) On a way of calculating prismatic shells (in Russ.). *Proc A Razmadze Inst Math Georgian Acad Sci* 21:191–259
- Vekua IN (1985) *Shell Theory: General Methods of Construction*. Pitman Advanced Publishing Program, Boston
- Vogelius M, Babuška I (1981) On a dimensional reduction method I. The optimal selection of basis functions. *Mathematics of Computation* 37(155):31–46

- Voigt W (1890) Allgemeine Theorie der piézo- und pyroelectrischen Erscheinungen an Krystallen. *Abhandlungen der Königlichen Gesellschaft der Wissenschaft zu Göttingen* 36:1–99
- Weller T, Licht C (2007) Modeling of linearly electromagneto-elastic thin plates. *Comptes Rendus Mécanique* 335(4):201–206
- Whitney H (1957) *Geometric Integration Theory*. Princeton University Press, Princeton



Chapter 4

On Buckling Behavior Of Inhomogeneous Shallow Spherical Caps with Elastically Restrained Edge

Svetlana M. Bauer and Eva B. Voronkova

Abstract Asymmetrical buckling of pressurized nonuniform shallow shells with elastically restrained edge under normal pressure is studied. The load is applied internally to the shell. The unsymmetric part of the solution is sought in terms of multiples of the harmonics of the angular coordinate. A numerical method is employed to obtain the lowest load value at which waves in the circumferential direction can appear. The effect of material heterogeneity and boundary on the buckling load is examined. If the outer edge can move freely in the radial direction, decreasing of the elasticity modulus to the shell (plate) edge leads to sufficient lowering of the buckling pressure. For a shell with elastically restrained edge, the buckling pressure and mode number increase with a rise of spring stiffness.

Key words: Shallow shells · Asymmetrical buckling · Elastic edge support

4.1 Introduction

Circumferential instability of pressurised spherical shells and circular plates appears in a number of pure engineering (metal or polymer sheets) and biomechanical (human tissue, living cells) applications and has been discussed by many authors (e.g., Adachi and Benicek, 1964; Bushnell, 1981; Huang, 1963; Panov and Feodosiev, 1948). Authors underlined that a precise approximation of a shell (plate) prebuckling state is crucial in predicting of buckling load and buckling mode shape (Bushnell, 1981; Feodos'ev, 1963).

Svetlana M. Bauer · Eva B. Voronkova

St. Petersburg State University, 7/9 Universitetskaya nab., St. Petersburg, 199034 & Don State Technical University, Research and Education Center (REC) "Materials", Rostov-on-Don, 1 Gagarin sq., 344000, Russia

e-mail: s.bauer@spbu.ru, e.voronkova@spbu.ru

The unsymmetrical buckling problem for a thin circular plate subjected to normal pressure was formulated by Panov and Feodosiev (1948). They approximated non-axisymmetric displacement in the form $w = (1 - r^2)^2(A + Br^4 \cos n\theta)$ and studied the bending problem using Galerkin procedure. Later, Feodos'ev showed that the elastic surface of plates or shells under large deformations could not be described by one or two unknown parameters in approximating functions (Feodos'ev, 1963).

Morozov proved the existence of unsymmetric equilibrium states for a simply supported circular plate (Morozov, 1961), the uniqueness of the asymmetric equilibrium state was proved by Piechocki (1969).

Asymmetric equilibrium states of a clamped circular plate subjected to surface load were analyzed numerically in Cheo and Reiss (1973). The authors confirmed that a ring of large circumferential compressive stress near the edge of the plate plays the crucial role in possibility of plate's wrinkling near the boundary. They also emphasized that the approximation of the prebuckling state used by Panov and Feodosiev (1948) was "too inaccurate to adequately describe the wrinkling of the plate".

Experiments on uniform heating of thin circular plates with fixed edges and formation of waves near plate's edge were discussed in Goldstein et al (2016).

Coman and Bassom (2016a) investigated the asymmetric bifurcation for a shallow spherical cap subjected to either external or internal pressure. He discussed the role of the boundary conditions in the appearance of asymmetric equilibrium states and compared numerical calculations with two-term asymptotic predictions for the buckling pressure and one-term approximations of the corresponding wave number. Comparisons of the asymptotic approximations of the wrinkling load with numerical solutions for a uniformly stretched circular plate under transverse pressure was reported in Coman and Bassom (2016b, 2018).

This paper deals with buckling of elastically restrained spherical caps and circular plates with nonuniform mechanical characteristics. Such a plate or a cap can be used as the simplest model of Lamina Cribrosa (LC) in the human eye (Bauer and Voronkova, 2014). Buckling of the LC in a nonaxisymmetric state in the neighborhood of the edge can cause edemas and folds at the periphery of the LC and loss of sight.

4.2 Problem Formulation

We consider a thin shallow spherical elastic cap of uniform thickness h , base radius a and rise H subjected to transverse uniform load p , applied to its internal surface. The middle surface of the shell can be represented by the paraboloid $z = H(1 - r^2/a^2)$ (see Fig. 4.1).

The curvature radius of the shell is $R = a^2/(2H)$. The cap is thin if the ratio of its thickness to the radius of curvature is much less than unity ($h/R \ll 1$). For a shallow spherical cap, the apex rise is assumed to be much smaller than the curvature radius ($H \ll R$). We consider a shell with the outer edge elastically restrained against

in-plane displacement. The shell material is considered as linearly isotropic with spatially varying elastic properties.

The Donnell-Mushtari-Vlasov equations for a spherical cap with meridional inhomogeneity can be written in the form (Bauer and Voronkova, 2019)

$$\begin{aligned} D\Delta\Delta w + \frac{\partial D}{\partial r}L_1^+(w) + \frac{\partial^2 D}{\partial r^2}L_2^+(w) &= P + L(w, F) - \frac{1}{R}\Delta F, \\ \frac{\Delta\Delta F}{E} + \frac{\partial}{\partial r}\left(\frac{1}{E}\right)L_1^-(F) + \frac{\partial^2}{\partial r^2}\left(\frac{1}{E}\right)L_2^-(F) &= -\frac{h}{2}L(w, w) + \frac{1}{R}\Delta w, \end{aligned} \quad (4.1)$$

where r, θ are the polar coordinates, $w(r, \theta)$ is the transverse displacement of the shell, $F(r, \theta)$ is the Airy stress function, ν is Poisson's coefficient, and

$$D(r) = \frac{E(r)h^3}{12(1-\nu^2)}$$

is the bending stiffness. Δ is the usual Laplacian in polar coordinates

$$\Delta = \frac{\partial^2}{\partial r^2} + \frac{1}{r}\frac{\partial}{\partial r} + \frac{1}{r^2}\frac{\partial^2}{\partial \theta^2},$$

and definitions of the differential operators L, L_i^\pm ($i = 1, 2$) are listed in Appendix.

The deformation of an externally pressurised spherical shell can be described by the same system of equations (4.1) with the opposite signs before the last terms on the right-hand side of both equations. Dropping these last terms one obtains the governing equations for a inhomogeneous circular plate under normal pressure.

The outer edge of the shell is clamped in transverse direction; therefore, at the edge $r = a$, we have $w = \partial w / \partial r = 0$. The standard variants of the boundary conditions require that one of the two quantities in each of the following pairs is set to zero: either $u = 0$ or $T_{rr} = 0$, and either $v = 0$ or $T_{r\theta} = 0$, where u, v are the projections of the displacement vector on the r and θ axes; $T_{rr}, T_{r\theta}$ are stress-resultants. The conditions of completely clamped edge correspond to $w = \partial w / \partial r = u = v = 0$, and if the boundary can move freely in the radial direction, the constrains are $w = \partial w / \partial r = T_{rr} = T_{r\theta} = 0$.

We suppose that the edge $r = a$ has a translational restraint: i.e. the boundary conditions are

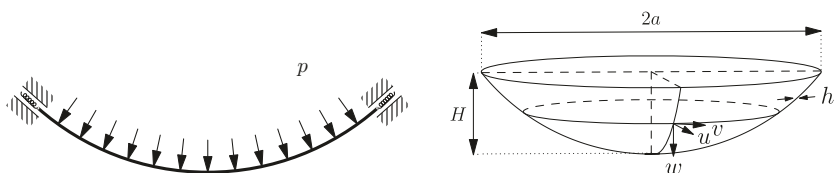


Fig. 4.1. Geometry of the spherical cap.

$$w = \partial w / \partial r = k_u u + T_{rr} = T_{r\theta} = 0 \quad \text{at } r = a, \quad (4.2)$$

where k_u is the translational flexibility coefficient. All sought-for functions must fulfil the regularity condition at the apex of the shell

$$\partial w / \partial r = \partial w / \partial \theta = \partial F / \partial r = \partial F / \partial \theta = 0 \quad \text{at } r = 0. \quad (4.3)$$

To express the constrains (4.2) in terms of the displacement component $w(r, \theta)$ and stress function $F(r, \theta)$, we use the strain-displacement and stress-strain relations. This results in the following relation on the boundary $r = a$ with consideration of the first two conditions (4.2)

$$\frac{u}{r^2} + \frac{1}{r^2} \frac{\partial^2 u}{\partial \theta^2} = \frac{T_{rr} - \nu T_{\theta\theta}}{E(r)hr} - \frac{\partial}{\partial r} \left(\frac{T_{\theta\theta} - \nu T_{rr}}{E(r)h} \right) + \frac{2(1 + \nu)}{E(r)h} \frac{\partial T_{r\theta}}{r \partial r}. \quad (4.4)$$

The function $F(r, \theta)$ is related to the stress-resultants $T_{rr}, T_{\theta\theta}, T_{r\theta}$ according to

$$T_{rr} = \frac{\partial F}{r \partial r} + \frac{\partial^2 F}{r^2 \partial \theta^2}, \quad T_{r\theta} = \frac{\partial^2 F}{\partial r^2}, \quad T_{\theta\theta} = -\frac{\partial}{\partial r} \left(\frac{\partial F}{r \partial \theta} \right).$$

We introduce the following dimensionless quantities

$$\begin{aligned} r^* &= \frac{r}{a}, \quad w^* = \beta \frac{w}{h}, \quad u^* = \beta^2 \frac{R}{h^2} u, \quad P^* = \beta^3 \frac{Pa^4}{E_{av} h^4}, \\ F^* &= \beta^2 \frac{F}{E_{av} h^3}, \quad A = \beta \frac{a^2}{Rh}, \quad k_u^* = \frac{R}{hE_{av}} k_u, \quad \beta^2 = 12(1 - \nu^2). \end{aligned} \quad (4.5)$$

Here E_{av} is an average value of Young's modulus in the radial direction

$$E_{av} = \frac{1}{S} \iint_S E(r) r \, dr d\theta, \quad E(r) = E_0 f(r), \quad (4.6)$$

where $f(r)$ is a smooth position function and S denotes the area of the shell mid-surface.

For simplicity we shall further use the notations $(\cdot)' = \partial(\cdot) / \partial r$, $(\cdot)\dot{=} = \partial(\cdot) / \partial \theta$ and drop the asterisks on the dimensionless variables. The dimensionless form of the system (4.1) is

$$\begin{aligned} g_1(r) \Delta \Delta w + g_1'(r) L_1^+(w) + g_1''(r) L_2^+(w) &= P + L(w, F) - A \Delta F, \\ g_2(r) \Delta \Delta F + g_2'(r) L_1^-(F) + g_2''(r) L_2^-(F) &= -L(w, w) / 2 + A \Delta w, \\ g_1(r) &= E_0 f(r) / E_{av}, \quad g_2(r) = 1 / g_1(r). \end{aligned} \quad (4.7)$$

For the nonlinear symmetrical problem the system (4.7) is reduced to

$$\begin{aligned}
g_1 \left(\Theta_0'' + \frac{\Theta_0'}{r} - \frac{\Theta_0}{r^2} \right) + g_1' \left(\Theta_0' + \nu \frac{\Theta_0}{r} \right) &= \frac{Pr}{2} + \frac{\Theta_0 \Phi_0}{r} - A \Phi_0, \\
g_2 \left(\Phi_0'' + \frac{\Phi_0'}{r} - \frac{\Phi_0}{r^2} \right) + g_2' \left(\Phi_0' - \nu \frac{\Phi_0}{r} \right) &= -\frac{\Theta_0^2}{2r} + A \Theta_0,
\end{aligned} \tag{4.8}$$

where $\Theta_0 = \Theta_0(r) = w'(r)$ and $\Phi_0 = \Phi_0(r) = F'(r)$. In axisymmetric case the boundary conditions (4.2)-(4.3) together with (4.4) can be rewritten as

$$\Theta_0 = k_u g_2 (\Phi_0' - \nu \Phi_0) + \Phi_0 = 0 \quad \text{at } r = 1, \quad \Theta_0 = \Phi_0 = 0 \quad \text{at } r = 0. \tag{4.9}$$

4.3 Equations for Buckling

We seek a solution of Eqs. (4.7) in the form

$$w(r, \theta) = w_0(r) + \varepsilon w_n \cos(n\theta), \quad F(r, \theta) = F_0(r) + \varepsilon F_n \cos(n\theta), \tag{4.10}$$

where $w_0(r), F_0(r)$ describe prebuckling axisymmetric state, ε is an infinitesimal parameter, n is the mode number, and $w_n(r), F_n(r)$ are non-symmetrical components.

After substitution of (4.10) in (4.7), using Eqs. (4.8), and linearization with respect to ε we obtain

$$\begin{aligned}
g_1 \Delta_n \Delta_n w_n + \mathcal{L}_1(g_1, w_n) &= -A \Delta_n F_n + \frac{w_n''}{r} \Phi_0 + \frac{F_n''}{r} \Theta_0 \\
&\quad + \Theta_0' \left(\frac{F_n'}{r} - \frac{n^2}{r^2} F_n \right) - \Phi_0' \left(\frac{w_n'}{r} - \frac{n^2}{r^2} w_n \right), \\
g_2 \Delta_n \Delta_n F_n + \mathcal{L}_2(g_2, F_n) &= A \Delta_n w_n - \frac{w_n''}{r} \Theta_0 - \Theta_0' \left(\frac{w_n'}{r} - \frac{n^2}{r^2} w_n \right).
\end{aligned} \tag{4.11}$$

The definitions of the operators $\mathcal{L}_1, \mathcal{L}_2$ are listed in Appendix and

$$\Delta_n = \frac{d^2}{dr^2} + \frac{1}{r} \frac{d}{dr} - \frac{n^2}{r^2}.$$

Boundary conditions (4.2)-(4.3) are reduced to

$$\begin{aligned}
w_n'(0) = F_n'(0) = w_n(1) = w_n'(1) = 0, \\
k_u u_n(1) + F_n'(1) - n^2 F_n(1) = F_n'(1) - F_n(1) = 0,
\end{aligned} \tag{4.12}$$

where asymmetrical part of the displacement component $u_n(r)$ on the boundary $r = 1$ can be found with the help of (4.4)

$$u_n = \frac{1}{n^2 - 1} \left(g_2 (F_n'''' - ((2 + \nu)n^2 + 1 - \nu)F_n' + 3n^2 F_n) + g_2' (F_n'' - \nu(F_n' - n^2 F_n)) \right).$$

Buckling system (4.11) with boundary conditions (4.12) constitute an eigenvalue problem, in which the parameter P is implicit and appears in the equations through the functions Θ_0 and Φ_0 . We use MATLAB functions to solve nonlinear axisymmetric problem (4.8) together with (4.9). The critical values of P , for which (4.11) with (4.12) have nontrivial solution, were calculated using the finite difference method (Cheo and Reiss, 1973; Huang, 1963). We refer to the smallest of these eigenvalues as the buckling load.

4.4 Numerical Results

The mechanism that initiates the buckling of a spherical cap or circular plate about the axisymmetric state into an unsymmetric equilibrium state is described, for example, in Cheo and Reiss (1973); Morozov (1961). A ring of large circumferential compressive stress develops near the edge of the plate and indicates possibility of wrinkling near the edge. In Fig. 4.2 we plotted the dimensionless axisymmetrical circumferential stress that developed in a non-uniform spherical cap ($A = 10$) for different values of edge restraint coefficient k_u . The value $k_u = 0$ corresponds to a freely movable in radial direction edge, in this case $T_{rr} = 0$ at the edge. For the completely clamped edge we have $u = 0$ or $k_u = \infty$. The compressive stress intensity and the width of the compressive ring decrease as the translational flexibility coefficient k_u increases. For the completely immovable outer boundary ($k_u = \infty$) the stress $T_{\theta\theta}$ takes only positive values, i.e. $T_{\theta\theta}$ is tensile stress, and the buckle of the cap about axisymmetrical state into nonsymmetrical is not possible (Cheo and Reiss, 1973; Coman and Bassom, 2016a) (Fig. 4.2).

Dependence of the normalized critical load P_{cr} and the critical mode number n on the edge-restraint coefficient for a homogeneous shallow spherical shell is illustrated in Fig. 4.3. The value P_b^{pl} corresponds to the buckling load of axisymmetric

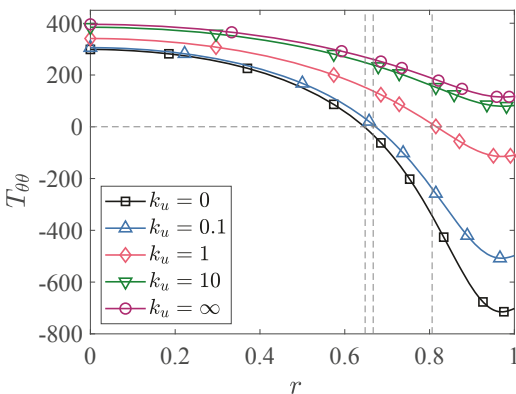
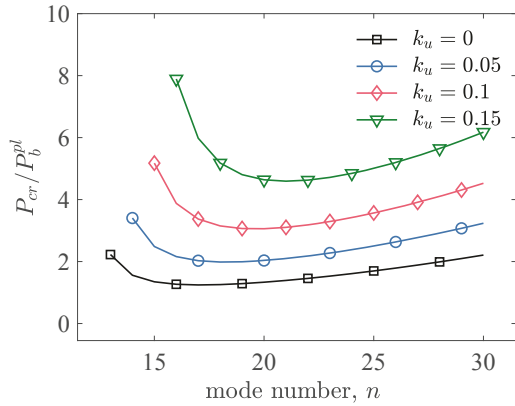


Fig. 4.2 Dimensionless circumferential stress resultant $T_{\theta\theta}$ for several values of spring stiffness k_u . For the edge movable in the radial direction $k_u = 0$, for the completely clamped edge $k_u = \infty$. Here load value $P = 30000$, $A = 10$, $\nu = 0.4$.

Fig. 4.3 Dependence of the normalized critical load P_{cr} on the mode number n and the restraint coefficient k_u for a uniform shallow spherical shell ($A = 5$). Black line with square markers corresponds to a movable outer edge ($k_u = 0$). P_b^{pl} denotes the buckling pressure for a uniform circular plate.



equilibrium states of an isotropic homogeneous circular plate ($P_b^{pl} = 64453$, $n = 14$). The larger value of the spring stiffness, the higher critical load is.

Effect of the shallowness parameter A on load-mode number relation is demonstrated in Fig. 4.4. The critical load P_{cr} and the corresponding mode number increase as the shallowness parameter A increases. Similar results we reported in Bauer and Voronkova (2018, 2019). We assumed the exponential law for material inhomogeneity ($E = E_0 e^{-qr}$) and calculated the buckling load and corresponding number of waves for a large range of parameters E_0, q and for constant average value of the elastic modulus (4.6). The results are summarized in Table 4.1 and Fig. 4.4. The heterogeneity coefficient $q = 0$ corresponds to uniform plate with constant Young’s modulus.

For a nonuniform shell or plate the loss of the stability of axisymmetric equilibrium form occurs under lower load than for a homogeneous shell or plate if the edge-restraint is equal to zero or small (see Fig. 4.5 and Table 4.1). As the

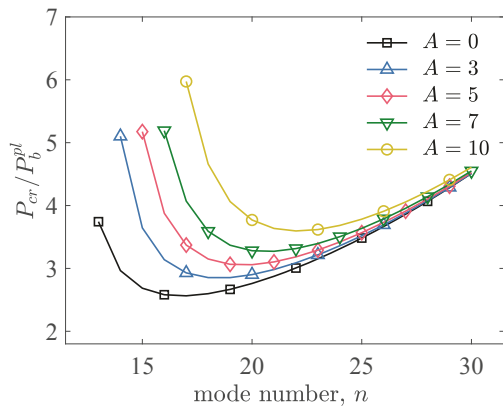


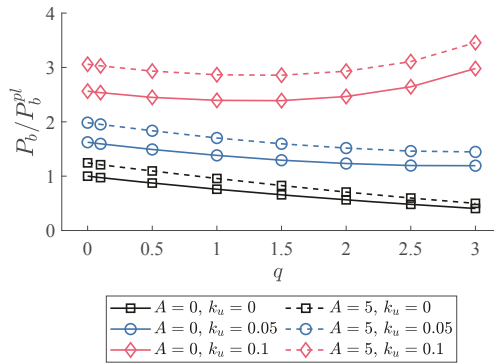
Fig. 4.4 The load-mode number curves for different values if shallowness parameter A . Black line with square marks corresponds to a circular plate ($A = 0$). Here $k_u = 0.1$, $\nu = 0.4$, P_b^{pl} denotes the buckling pressure for a uniform circular plate.

Table 4.1

Normalized buckling load (P_b/P_b^{pl}) and corresponding wave numbers for the heterogenous circular plate for different values of the restrained coefficient of the outer edge

	$q = 0$	$q = 0.5$	$q = 1$	$q = 2$
$k_u = 0$				
P^{cr}/P_{pl}^{cr}	1	0.87	0.76	0.56
Mode number, n	14	14	14	
$k_u = 0.05$				
P^{cr}/P_{pl}^{cr}	1.62	1.49	1.38	1.23
Mode number, n	14	15	16	16
$k_u = 0.15$				
P^{cr}/P_{pl}^{cr}	3.96	3.92	4.01	4.69
Mode number, n	18	19	19	21

Fig. 4.5 Effect of the heterogeneity rate and edge restraint coefficient on the buckling critical loads of a circular plate and spherical cap. Solid lines correspond to a circular plate ($A = 0$), dashed lines — to a shell with $A = 5$.



translational flexibility coefficient increases, a heterogeneous shell may buckle into asymmetrical state under a larger load than an uniform shell with the same average material properties. Thus, for the inhomogeneous plate restrained with the spring of $k_u = 0.15$ and the heterogeneity rate $q = 0.5$ the buckling load slightly decreases in comparison to a uniform plate, and then increases by 18% as the heterogeneity rate increases from $q = 0$ to $q = 2$. At the same time, the nonuniform plate (shell) losses its axisymmetrical stability with formation of larger number of waves in circumferential direction compared with the uniform plate (shell) (Table 4.1).

4.5 Conclusion

In this article we have discussed the wrinkling of the plates and shallow spherical shells with elastically restrained outer edge and subjected to internal pressure. Pre-

buckling stress-state in a narrow zone near the shell edge makes a major contribution to the unsymmetrical buckling mode and the value of the critical load. If the outer edge can move freely in the radial direction, decreasing of the elasticity modulus to the shell (plate) edge leads to sufficient lowering of the buckling pressure. For a shell with restrained against translation edge, the buckling pressure and the buckling mode number increases as the translational flexibility coefficient increases.

Acknowledgements This research was supported by the Government of Russia grant no. 14.Z50.31.0046.

Appendix

The linear differential operators that appear in (4.1) are defined by

$$L(x, y) = x'' \left(\frac{y'}{r} + \frac{\ddot{y}}{r^2} \right) + y'' \left(\frac{x'}{r} + \frac{\ddot{x}}{r^2} \right) - 2 \left(\frac{\dot{x}}{r} \right)' \left(\frac{\dot{y}}{r} \right)',$$

$$L_1^\pm(y) = 2y''' + (2 \pm \nu) \frac{y''}{r} + 2 \frac{(\ddot{y})'}{r^2} - \frac{y'}{r^2} - 3 \frac{\ddot{y}}{r^3}, \quad L_2^\pm(y) = y'' \pm \nu \left(\frac{y'}{r} + \frac{\ddot{y}}{r^2} \right).$$

Here, a prime and dot denote a derivative with respect to the radial r and circumferential θ coordinates, respectively. The differential operators introduced in (4.11) are given by

$$\mathcal{L}_1(g_1, w_n) = g_1' L_{1n}^+(w_n) + g_1'' L_{2n}^+(w_n), \quad \mathcal{L}_2(g_2, F_n) = g_2' L_{1n}^-(F_n) + g_2'' L_{2n}^-(F_n),$$

where

$$L_1^\pm(y) = 2y''' + \frac{2 \pm \nu}{r} y'' - \frac{2n^2 + 1}{r^2} \ddot{y} + \frac{3n^2}{r^3} \ddot{y}, \quad L_2^\pm(y) = y'' \pm \nu \left(\frac{y'}{r} - \frac{n^2}{r^2} \ddot{y} \right).$$

References

- Adachi J, Benicek M (1964) Buckling of torispherical shells under internal pressure. *Experimental Mechanics* 4(8):217–222, DOI 10.1007/BF02322954
- Bauer SM, Voronkova EB (2014) Models of shells and plates in the problems of ophthalmology. *Vestnik St Petersburg University: Mathematics* 47(3):123–139, DOI 10.3103/S1063454114030029
- Bauer SM, Voronkova EB (2018) On the unsymmetrical buckling of shallow spherical shells under internal pressure. *Izv Saratov Univ (NS), Ser Math Mech Inform*, 18(4):390–396

- Bauer SM, Voronkova EB (2019) Unsymmetrical wrinkling of nonuniform annular plates and spherical caps under internal pressure. In: Altenbach H, Chróścielewski J, Eremeyev VA, Wiśniewski K (eds) *Recent Developments in the Theory of Shells*, Springer International Publishing, pp 79–89, DOI 10.1007/978-3-030-17747-8_6
- Bushnell D (1981) Buckling of shells-pitfall for designers. *AIAA Journal* 19(9):1183–1226, DOI 10.2514/3.60058
- Cheo LS, Reiss EL (1973) Unsymmetric wrinkling of circular plates. *Quarterly of Applied Mathematics* 31(1):75–91, DOI 10.1090/qam/99710
- Coman CD, Bassom AP (2016a) Asymptotic limits and wrinkling patterns in a pressurised shallow spherical cap. *International Journal of Non-Linear Mechanics* 81:8–18, DOI 10.1016/j.ijnonlinmec.2015.12.004
- Coman CD, Bassom AP (2016b) On the nonlinear membrane approximation and edge-wrinkling. *International Journal of Solids and Structures* 82:85–94, DOI 10.1016/j.ijsolstr.2015.11.011
- Coman CD, Bassom AP (2018) Wrinkling structures at the rim of an initially stretched circular thin plate subjected to transverse pressure. *SIAM Journal on Applied Mathematics* 78(2):1009–1029, DOI 10.1137/17M1155193
- Feodos'ev VI (1963) On a method of solution of the nonlinear problems of stability of deformable systems. *Journal of Applied Mathematics and Mechanics* 27(2):392–404, DOI 10.1016/0021-8928(63)90008-X
- Goldstein R, Popov A, Kozintsev V, Chelyubeev D (2016) Non-axisymmetric edge buckling of circular plates when heated. *PNRPU Mechanics Bulletin* 1:45–53, DOI 10.15593/perm.mech/2016.2.04
- Huang NC (1963) Unsymmetrical buckling of shallow spherical shells. *AIAA Journal* 1(4):945, DOI 10.2514/3.1690
- Morozov NF (1961) On the existence of a non-symmetric solution in the problem of large deflections of a circular plate with a symmetric load. *Izv Vyssh Uchebn Zaved Mat* (2):126–129
- Panov DY, Feodosiev VI (1948) On the equilibrium and loss of stability of shallow shells in the case of large displacement. *Prikladnaya Matematika i Mekhanika* 12:389–406
- Piechocki W (1969) On the nonlinear theory of thin elastic spherical shells: Non-linear partial differential equations solutions in theory of thin elastic spherical shells subjected to temperature fields and external loading. *Archiwum Mechaniki Stosowanej* 21(1):81–102



Chapter 5

Some Two-dimensional Non-classical Models of Anisotropic Plates

Alexander K. Belyaev, Nikita F. Morozov, Peter E. Tovstik, and Tatyana P. Tovstik

Abstract Thin elastic plates made of an anisotropic material (with 21 elastic moduli) and heterogeneous in the thickness direction (in partial, multilayered) are considered. A short overview of various 2D models describing deformations and vibrations of a plate is given. The classical Kirchhoff–Love and the Timoshenko–Reissner models are discussed and compared in cases of isotropic and transversely isotropic materials. A correspondence of boundary conditions of these models is established. A multilayered plate with alternating soft and hard layers is considered. By using an asymptotic expansion of the solution in a series in small thickness parameter, the 2D equations of second-order accuracy are delivered. From these equations the correct choice of parameters of the single-layered Timoshenko–Reissner model is derived, which is equivalent to a given multilayered plate. In the case of general anisotropy, a model of second-order accuracy is presented as well, and the main properties of the harmonic solutions for static problems and for free vibrations of a plate are briefly described.

Key words: Anisotropic multilayered plates · 2D model of second-order accuracy · Timoshenko–Reissner model · Transversal shear influence

Alexander K. Belyaev · Tatyana P. Tovstik
Institute for Problems in Mechanical Engineering RAS, 61 Bolshoy pr. V. O., 199178 St. Petersburg,
Russian Federation
e-mail: 13augen@mail.ru, tovstik_t@mail.ru

Nikita F. Morozov · Peter E. Tovstik
St. Petersburg State University, 7/9 University Embankment, St. Petersburg, 199034, Russian Fed-
eration
e-mail: morozov@nm1016.spb.edu, peter.tovstik@mail.ru

5.1 Introduction

The main origin of the 2D models of plates and shells comes from the 3D equations of theory of elasticity. The equations of bending and vibrations of a plate can be obtained on the basis of the Kirchhoff–Love (KL) hypotheses (Kirchhoff, 1876; Love, 1927). The more complex equations, taking into account a transversal shear, follow from the Timoshenko–Reissner (TR) hypotheses (Timoshenko, 1921; Reissner, 1945). The shell theory was further developed in (Donnell, 1976; Novozhilov, 1970; Goldenweizer, 1961).

In addition to hypotheses mentioned above, we discuss various expansions of unknown functions in the thickness direction. Expansions in the series of the thickness co-ordinate is discussed in Reddy (2004). Expansions in the Legendre polynomials in the thickness direction are used in Vekua (1955); Chernykh et al (1996). Numerous investigations (Goldenweizer, 1961; Tovstik and Tovstik, 2014b; Tovstik, 2007; Kienzler and Schneider, 2014; Vetyukov et al, 2011) are devoted to the derivation of 2D equations by using asymptotic expansions in power series in the small thickness parameter $\mu = h/L$ (h and L are the thickness and the typical length of waves in the tangential directions). The other possibility (Eremeev and Zubov, 2008; Altenbach and Mikhasev, 2015) is the direct derivation of 2D equations of plates and shells without referring to a 3D media.

We discuss the plate models and their relative exactness under various assumptions about a plate material and structure. The accuracy is estimated by a comparison with test 3D problems, which have exact solutions. The KL model is known to be asymptotically correct for an isotropic homogeneous plate (Tovstik, 2007). This gives results of zero-order accuracy with respect to the parameter $\mu = h/L$. For such a plate, the TR model is not more exact than the KL model, because it describes only a part of the second order summands. For a transversely isotropic or for an orthotropic plate with a very small transversal shear modulus G the KL model becomes unacceptable. To describe a transversal shear, the shear parameter $g = \mu^2 E/G$ (E is the Young modulus) is introduced. For $g \sim 1$, the KL model is unacceptable, while the TR model gives sufficiently accurate results.

The same effect of a small transversal shear stiffness influence arises in multilayered plates with alternating hard and soft layers. Various aspects of multilayered plates are presented in Reddy (2004); Chernykh et al (1996); Ambartsumjan (1970); Agolovyan (1997); Altenbach (1998); Tovstik and Tovstik (2007, 2014a); Tovstik (2009); Berdichevsky (2010). For a simplification of analysis it is desirable to change a multilayered plate by an equivalent homogeneous single-layered plate (an ESL plate). The most important and also the most difficult task here is that of the correct choice of an equivalent transversal shear modulus, G^{equ} . Our suggestion is based on the asymptotic solution of the second-order accuracy model (the SOA model), and it is described in Tovstik and Tovstik (2014b, 2017b,a). The alternative choice of G^{equ} is discussed in Grigolyuk and Kulikov (1988b,a); Mikhasev and Altenbach (2019); Hill (1965).

The problem of general anisotropy with 21 elastic moduli is essentially more complex. The asymptotic SOA model for heterogeneous (in partial, for multilay-

ered) plates is built in Tovstik (2019); Belyaev et al (2019b). A multilayered plate consisting of orthotropic layers with arbitrary directions of orthotropy is investigated in Morozov et al (2018); Belyaev et al (2019a).

In the present paper, the classical Kirchhoff–Love and the Timoshenko–Reissner models are discussed and compared in cases of isotropic and transversely isotropic materials. A correspondence of boundary conditions of these models is established. A multilayered plate with alternating soft and hard layers is considered. By using an asymptotic expansion of solution in a series in the small thickness parameter, the 2D equations of second-order accuracy are delivered. Using these equations, we find the correct choice of parameters of an ESL Timoshenko–Reissner model, which is equivalent to those of a given multilayered plate. In the case of general anisotropy, a model of second-order accuracy is presented as well, and the main properties of the harmonic solutions for static problems and for free vibrations of a plate are shortly described.

5.2 Kirchhoff–Love and Timoshenko–Reissner Models for a Beam

First, we consider an elastic strip-beam of rectangular cross-section made of a transversely isotropic homogeneous material. According to the classical KL model, the bending of a beam is described by the well known relations

$$\begin{aligned} \frac{\partial Q}{\partial x} + F &= 0, & \frac{\partial M}{\partial x} - Q &= 0, \\ M &= D\kappa, & \kappa &= \frac{\partial \theta}{\partial x}, & \theta &= -\frac{\partial w}{\partial x}, \end{aligned} \quad (5.1)$$

with

$$F(x,t) = F_3(x,t) - \rho h \frac{d^2 w}{dt^2}, \quad D = \frac{Eh^3}{12(1-\nu^2)}.$$

Here $w(x,t)$ is the deflection, Q and M are the shear stress-resultant and the stress couple, θ is the angle of normal fiber rotation, F is the external force (with the inertia force), and D, E, ν, ρ, h, t are the bending stiffness, the Young modulus, the Poisson ratio, the mass density, the beam thickness, and the time, respectively. Relations (5.1) lead to the Bernoulli equation of a beam

$$D \frac{\partial^4 w}{\partial x^4} = F. \quad (5.2)$$

Equation (5.2) is based on the hypothesis of straight normal, and it does not take into account the transversal shear. The more complex TR model (which includes the transversal shear) is described by the same relations as in Eq. (5.1)

$$\begin{aligned} \frac{\partial Q}{\partial x} + F = 0, \quad \frac{\partial M}{\partial x} - Q - J \frac{\partial^2 \theta}{\partial t^2} + m = 0, \\ M = D\kappa, \quad \kappa = \frac{\partial \theta}{\partial x}, \quad J = \frac{\rho h^3}{12} \end{aligned} \quad (5.3)$$

with the following difference

$$\theta = \gamma - \frac{\partial w}{\partial x}, \quad Q = \Gamma \gamma, \quad \Gamma = kG_{13}h, \quad k = \frac{5}{6}. \quad (5.4)$$

Here the transversal shear angle, γ , is included. The stress-resultant, Q , is expressed by the shear angle γ , where G_{13} is the transversal shear modulus and k is the correcting factor related to the distribution of shear stresses in the normal direction. For an isotropic material, $G_{13} = E/(2(1 + \nu))$, and in the general case G_{13} is an independent parameter. The second equation in (5.3) contains two small summands: the rotation inertia moment, $-J \partial^2 \theta / \partial t^2$, and the external moment, m . In what follows for simplicity these summands will be omitted.

Equations (5.3) and (5.4) yield

$$D \frac{\partial^4 w}{\partial x^4} = F - \frac{D}{\Gamma} \frac{\partial^2 F}{\partial x^2}. \quad (5.5)$$

Unlike Eq. (5.2), here the additional summand appears on the right of Eq. (5.5). According to Donnell (1976), the entire deflection, w , consists of the bending, w_b , and of the shear, w_s , parts:

$$w = w_b + w_s, \quad D \frac{\partial^4 w_b}{\partial x^4} = F, \quad \Gamma \frac{\partial^2 w_s}{\partial x^2} = -F. \quad (5.6)$$

We consider a static problem with $F(x) = F_0 \sin rx$. In this case, the particular solution of Eq. (5.5) reads as

$$w(x) = w_0 \sin rx \quad (5.7)$$

with

$$w_0 = w^{KL}(1 + g), \quad w^{KL} = \frac{F_0}{Dr^4}, \quad g = \frac{Dr^2}{\Gamma} = \frac{\pi^2}{3(1 - \nu^2)k} \frac{E}{G_{13}} \left(\frac{h}{L} \right)^2.$$

Here the deflection w^{KL} corresponds to the KL model, the dimensionless shear parameter g describes the transversal shear influence, and $L = 2\pi/r$ is the wave length. Let the wave length, L , be much larger than the beam thickness, h ($h/L \ll 1$). Then if the elastic moduli E and G_{13} are of identical orders (in particular, for an isotropic beam), then $g \ll 1$ and the influence of a transversal shear may be neglected. In the opposite case, $G_{13} \ll E$, the shear parameter, g , is larger, and the transversal shear influence should to be taken into account.

The same conclusions are valid for free vibrations as well. Let the vibration mode be

$$w(x,t) = w_0 \sin r x \sin \omega t.$$

Then the dimensionless frequency parameter λ reads as

$$\lambda = \frac{\rho h^2 \omega^2 (1 - \nu^2)}{E} = \frac{\lambda^{KL}}{1 + g}, \quad \lambda^{KL} = \frac{\mu^4}{12}, \quad \mu = r h = \frac{2\pi h}{L} \quad (5.8)$$

where λ^{KL} is the value corresponding to the KL model, and g is the same shear parameter, as in Eq. (5.7). Here μ is the small thickness parameter.

5.3 Kirchhoff-Love and Timoshenko-Reissner Models of a Transversely Isotropic Plate

We consider the TR model of bending of a transversely isotropic homogeneous plate. The elasticity relations read as

$$M_{11} = D(\kappa_1 + \nu\kappa_2), \quad M_{22} = D(\kappa_2 + \nu\kappa_1), \quad M_{12} = (1 - \nu)D\tau, \quad Q_i = \Gamma\gamma_i, \quad i = 1, 2 \quad (5.9)$$

with

$$\gamma_i = \theta_i + \frac{\partial w}{\partial x_i}, \quad k_i = \frac{\partial \theta_i}{\partial x_i}, \quad 2\tau = \frac{\partial \theta_1}{\partial x_2} + \frac{\partial \theta_2}{\partial x_1}, \quad i = 1, 2,$$

where M_{11}, M_{22} are the bending moments, M_{12} is the torsion moment, Q_1, Q_2 are the transversal stress-resultants, γ_1, γ_2 are the transversal shear angles, and θ_1, θ_2 are the average angles of a normal fiber inclination. The elastic coefficients D and Γ are the same as for a beam (see Eqs. (5.1), (5.4)). The 2D equilibrium equations are as follows:

$$\begin{aligned} \frac{\partial M_{11}}{\partial x_1} + \frac{\partial M_{12}}{\partial x_2} - Q_1 - J \frac{\partial^2 \theta_1}{\partial t^2} + m_1 &= 0, \\ \frac{\partial M_{12}}{\partial x_1} + \frac{\partial M_{22}}{\partial x_2} - Q_2 - J \frac{\partial^2 \theta_2}{\partial t^2} + m_2 &= 0, \\ \frac{\partial Q_1}{\partial x_1} + \frac{\partial Q_2}{\partial x_2} - \rho_* h \frac{\partial^2 w}{\partial t^2} + F_3 &= 0, \end{aligned} \quad (5.10)$$

where m_1, m_2 are the external moments. As for a beam, we omit in Eqs. (5.10) the small rotation inertia moments, $J \partial^2 w / \partial t^2$, and the external moments.

For the KL model, the equilibrium equations coincide with Eqs. (5.10), and in the elasticity relations (5.9) it is necessary to put $\gamma_1 = \gamma_2 = 0$. As a result, the stress-resultants can be found from Eqs. (5.10), and now Eqs. (5.9), (5.10) yield

$$D\Delta\Delta w = F(x_1, x_2, t), \quad F(x_1, x_2, t) = F_3(x_1, x_2, t) - \rho h \frac{\partial^2 w}{\partial t^2}, \quad \Delta = \frac{\partial^2}{\partial x_1^2} + \frac{\partial^2}{\partial x_2^2}. \quad (5.11)$$

Let us return to the TR model. The basic unknowns in system (5.9), (5.10) are w, γ_1, γ_2 or w, θ_1, θ_2 . This system is of the 6th differential order, and among its solutions there are boundary-layer type solutions. To exclude the boundary layer we transform Eqs. (5.10) as follows. Instead of θ_1, θ_2 we introduce the new unknown functions Ψ and Θ by

$$\theta_1 = -\frac{\partial \Psi}{\partial x_1} + \frac{\partial \Theta}{\partial x_2}, \quad \theta_2 = -\frac{\partial \Psi}{\partial x_2} - \frac{\partial \Theta}{\partial x_1}. \quad (5.12)$$

Now Eqs. (5.10) split into the equation

$$\frac{1-\nu}{2} D \Delta \Theta - \Gamma \Theta = 0 \quad (5.13)$$

and the system

$$\Gamma(\Delta w - \Delta \Psi) - \rho h \frac{\partial^2 w}{\partial t^2} + F_3 = 0, \quad -D \Delta^2 \Psi - \rho h \frac{\partial^2 w}{\partial t^2} + F_3 = 0. \quad (5.14)$$

Equation (5.13) describes the boundary layer, and Eqs. (5.6) lead to the fourth-order equation for the internal part of deflection $w(x_1, x_2)$

$$D \Delta^2 w + \rho h \left(\frac{\partial^2 w}{\partial t^2} - \frac{D}{\Gamma} \frac{\partial^2 \Delta w}{\partial t^2} \right) - F_3 + \frac{D}{\Gamma} \Delta F_3 = 0. \quad (5.15)$$

In Tovstik and Tovstik (2017b), a more complex equation involving the rotation inertia moments was considered.

For the double periodic solution with $w = w_0 \sin r_1 x_1 \sin r_2 x_2, F_3 = F_0 \sin r_1 x_1 \sin r_2$ Eq. (5.15) assumes the form

$$D r^4 w_0 + \rho h (1+g) \frac{\partial^2 w_0}{\partial t^2} - (1+g) F_0 = 0, \quad g = \frac{D r^2}{\Gamma}, \quad r^2 = r_1^2 + r_2^2. \quad (5.16)$$

Here g is the transversal shear parameter, and, as for a beam, the similar conclusions follow. If a plate is made of an isotropic or close to it material, then $g \ll 1$, and the influence of the transversal shear is small, and the KL model (5.11) should be used. In the opposite case with $G_{13} \ll E$, Eq. (5.16) for an amplitude w_0 in the static case, and for a frequency parameter λ gives relations, similar for a beam (see Eqs. (5.7) and (5.8))

$$w_0 = w^{KL} (1+g), \quad w^{KL} = \frac{F_0}{D r^4}; \quad \lambda = \frac{\lambda^{KL}}{1+g}, \quad \lambda^{KL} = \frac{\mu^4}{12}, \quad \mu = r h, \quad (5.17)$$

where the same designations as in Eqs. (5.7) and (5.8) are used.

We consider an influence of the boundary layer on the main boundary conditions for the function w in Eq. (5.15). For definiteness we consider the edge $x_1 = 0$. The simplest possible variants of boundary conditions read as

$$\begin{aligned}
 w = 0, & \quad \text{or} \quad Q_1 = -D \left(\frac{\partial}{\partial x_1} \Delta \Psi - \frac{1-\nu}{2} \frac{\partial}{\partial x_2} \Delta \Theta \right) = 0, \\
 \theta_1 = -\frac{\partial \Psi}{\partial x_1} + \frac{\partial \Theta}{\partial x_2} = 0, & \quad \text{or} \quad M_1 = D \left(\frac{\partial^2 \Psi}{\partial x_1^2} + \nu \frac{\partial^2 \Psi}{\partial x_2^2} - (1-\nu) \frac{\partial^2 \Theta}{\partial x_1 \partial x_2} \right) = 0, \\
 \theta_2 = -\frac{\partial \Psi}{\partial x_2} - \frac{\partial \Theta}{\partial x_1} = 0, & \quad \text{or} \quad H = D \frac{1-\nu}{2} \left(2 \frac{\partial^2 \Psi}{\partial x_1 \partial x_2} + \frac{\partial^2 \Theta}{\partial x_1^2} - \frac{\partial^2 \Theta}{\partial x_2^2} \right) = 0.
 \end{aligned} \tag{5.18}$$

From the each line of Eqs. (5.18) we choose one condition, thereby getting 8 variants of boundary conditions.

We consider a static problem for a rectangular plate with $F_3(x_1, x_2) = F_3(x_1) \sin r_2 x_2$ and assume that the edges $x_2 = 0$ and $x_2 = L_2$ are simply supported, $w = M_2 = \varphi_1 = 0$. Then it is possible to separate the variables and now the solution of Eqs. (5.13)–(5.15) has the form

$$\begin{aligned}
 \{w, \Psi\}(x_1, x_2) &= \{w(x_1), \Psi(x_1)\} \sin(r_2 x_2), & r_2 &= \frac{n\pi}{L_2}. \\
 \Theta(x_1, x_2) &= \Theta(x_1) \cos(r_2 x_2), & &
 \end{aligned} \tag{5.19}$$

To obtain the dimensionless parameter we put $\hat{x}_1 = r_2 x_1$, $\hat{x}_2 = r_2 x_2$ and then drop all “hats”. Now the solution of Eq. (5.13) read as

$$\Theta(x_1) = C_1 e^{-\alpha x_1} + C_2 e^{\alpha(x_1 - L_1)}, \quad \alpha^2 = \frac{2\Gamma}{D r_2^2} + 1 = \frac{24(1-\nu)kG_{13}}{E(r_2 h)^2} + 1, \tag{5.20}$$

where C_1, C_2 are arbitrary constants. We take $\Theta(x_1) = C_1 e^{-\alpha x_1}$ and perform the asymptotic analysis under the assumption $\alpha \gg 1$. Our aim is to formulate two boundary conditions for the function w for each variant of three boundary conditions (5.18). The results are given in Table 5.1.

To obtain these results we write down the functions entering Eqs. (5.18) as follows (the constant factors are omitted):

Table 5.1
Main boundary conditions

No.	Full conditions	Main conditions
1	$w = \varphi_1 = H = 0$	
2	$w = \varphi_1 = \varphi_2 = 0$	$w = 0, w' = 0$
3	$Q_1 = \varphi_1 = \varphi_2 = 0$	
4	$w = M_1 = H = 0$	
5	$w = M_1 = \varphi_2 = 0$	$w = 0, w'' = 0$
6	$Q_1 = M_1 = \varphi_2 = 0$	
7	$Q_1 = \varphi_1 = H = 0$	$w' = 0, w''' = 0$
8	$Q_1 = M_1 = H = 0$	$w'' - \nu q^2 w = 0, w''' - (2-\nu)q^2 w = 0$

$$\begin{aligned}
Q_1 &= \frac{\partial^3 \Psi}{\partial x_1^3} - \frac{\partial \Psi}{\partial x_1} + C_1 \frac{1-\nu}{2} (\alpha^2 - 1) = 0, \\
\theta_1 &= \frac{\partial \Psi}{\partial x_1} + C_1 = 0, \quad \theta_2 = -\Psi + \alpha C_1 = 0, \\
M_1 &= \frac{\partial^2 \Psi}{\partial x_1^2} - \nu \Psi - (1-\nu) C_1 \alpha = 0, \quad H = 2 \frac{\partial \Psi}{\partial x_1} + C_1 (\alpha^2 + 1) = 0.
\end{aligned} \tag{5.21}$$

After excluding the constant C_1 from three of equations in (5.21) and taking into account that

$$\Psi = w + O(\alpha^{-2})F_0, \tag{5.22}$$

we obtain two main boundary conditions, as given in Table 5.1. For all 8 studied variants of boundary conditions, the order of error of this approximation is at most α^{-2} , namely, $C_1 = O(\alpha^{-2})w_0$.

We consider, for example, the clamped boundary conditions, $w = \theta_1 = \theta_2 = 0$. From $\theta_2 = 0$ it follows that $C_1 = O(\alpha^{-1})\Psi$, and from Eq. (5.22) with $w = 0$ it follows that $\Psi = O(\alpha^{-2})F_0$, therefore $C_1 = O(\alpha^{-3})F_0$. Three variants (1–3) of boundary conditions (5.18) of the TR model correspond to the clamped boundary conditions of the KL model, and three variants (4–6) of conditions (5.18) of the TR model correspond to the simply supported conditions of the KL model. It is interesting to note that the well known boundary conditions

$$M_1 = 0, \quad Q_1 + \frac{\partial H}{\partial x_2} = 0, \tag{5.23}$$

of the KL model for the free edge coincide with the conditions obtained from the TR model (see line 8 in Table 5.1). If the parameter α in Eq. (5.20) is not large, then the excretion of the main boundary conditions for Eq. (5.16) is impossible.

In the next sections we consider anisotropic plates and build 2D models by an asymptotic solution of 3D equations of the theory of elasticity.

5.4 Asymptotic Expansion of Solutions of 3D Equations of Anisotropic Plates

The 3D equilibrium equations of a thin elastic plate with thickness h read as

$$\sum_{j=1}^3 \frac{\partial \sigma_{ij}}{\partial x_j} + f_i = 0, \quad i = 1, 2, 3, \quad 0 \leq x_3 = z \leq h, \tag{5.24}$$

where σ_{ij} are the stresses, and f_i are the intensities of the external forces. In the case of general anisotropy of material, the stresses σ_{ij} are expressed through the strains ε_{ij} as follows (Tovstik, 2019):

$$\boldsymbol{\sigma} = \mathbf{E} \cdot \boldsymbol{\varepsilon}, \quad \mathbf{E} = (E_{ij})_{i,j=1,\dots,6},$$

$$\boldsymbol{\sigma} = (\sigma_{11}, \sigma_{22}, \sigma_{33}, \sigma_{23}, \sigma_{13}, \sigma_{12})^T, \quad \boldsymbol{\varepsilon} = (\varepsilon_{11}, \varepsilon_{22}, \varepsilon_{33}, \varepsilon_{23}, \varepsilon_{13}, \varepsilon_{12})^T, \quad (5.25)$$

$$\varepsilon_{ii} = \frac{\partial u_i}{\partial x_i}, \quad \varepsilon_{ij} = \frac{\partial u_i}{\partial x_j} + \frac{\partial u_j}{\partial x_i}, \quad i \neq j, \quad i, j = 1, 2, 3.$$

The tensor designations are not used, and strains and stresses are presented as 6D vectors. Here and in what follows, transposition is denoted by T , bold letters are used for vectors, matrices and operators, a dot denotes the product of vectors and matrices. The matrix \mathbf{E} is symmetric and positively definite. It is assumed that the elastic moduli E_{ij} do not depend on the tangential co-ordinates x_1, x_2 , but they may depend on the transversal co-ordinate $x_3 = z$. A dependence on z has place for functionally graded plates, and for multilayered plates moduli $E_{i,j}$ are piecewise functions of z .

As in Tovstik (2009); Tovstik and Tovstik (2017b,a) for an asymptotic analysis we split the stresses σ_{ij} and the strains ε_{ij} in the groups of tangential σ_t, ε_t and transversal σ_n, ε_n stresses and strains and put

$$\boldsymbol{\sigma}_t = (\sigma_{11}, \sigma_{22}, \sigma_{12})^T, \quad \boldsymbol{\sigma}_n = (\sigma_{13}, \sigma_{23}, \sigma_{33})^T,$$

$$\boldsymbol{\varepsilon}_t = (\varepsilon_{11}, \varepsilon_{22}, \varepsilon_{12})^T, \quad \boldsymbol{\varepsilon}_n = (\varepsilon_{13}, \varepsilon_{23}, \varepsilon_{33})^T, \quad (5.26)$$

where

$$\mathbf{A} = \{A_{ij}\} = \begin{pmatrix} E_{11} & E_{12} & E_{16} \\ E_{12} & E_{22} & E_{26} \\ E_{16} & E_{26} & E_{66} \end{pmatrix},$$

$$\mathbf{B} = \{B_{ij}\} = \begin{pmatrix} E_{15} & E_{25} & E_{56} \\ E_{14} & E_{24} & E_{46} \\ E_{13} & E_{23} & E_{36} \end{pmatrix}, \quad (5.27)$$

$$\mathbf{C} = \{C_{ij}\} = \begin{pmatrix} E_{55} & E_{45} & E_{35} \\ E_{45} & E_{44} & E_{34} \\ E_{35} & E_{34} & E_{33} \end{pmatrix}.$$

Now the elasticity relations (5.25) have the form

$$\boldsymbol{\sigma}_t = \mathbf{A} \cdot \boldsymbol{\varepsilon}_t + \mathbf{B} \cdot \boldsymbol{\varepsilon}_n, \quad \boldsymbol{\sigma}_n = \mathbf{B}^T \cdot \boldsymbol{\varepsilon}_t + \mathbf{C} \cdot \boldsymbol{\varepsilon}_n, \quad (5.28)$$

Excluding the transversal strains $\boldsymbol{\varepsilon}_n$ we obtain

$$\boldsymbol{\sigma}_t = \mathbf{A}^* \cdot \boldsymbol{\varepsilon}_t + \mathbf{B} \cdot \mathbf{C}^{-1} \cdot \boldsymbol{\sigma}_n, \quad \boldsymbol{\varepsilon}_n = \mathbf{C}^{-1} \cdot \boldsymbol{\sigma}_n - \mathbf{C}^{-1} \cdot \mathbf{B}^T \cdot \boldsymbol{\varepsilon}_t \quad (5.29)$$

where

$$\mathbf{A}^* = \mathbf{A} - \mathbf{B} \cdot \mathbf{C}^{-1} \cdot \mathbf{B}^T. \quad (5.30)$$

The assumption that the planes $z = -h/2$ and $z = h/2$ are free gives the boundary conditions

$$\sigma_{13} = \sigma_{23} = \sigma_{33} = 0, \quad z = 0, \quad z = h. \quad (5.31)$$

We introduce the dimensionless variables (denoted by “hats”) by relations

$$\begin{aligned} \{x_1, x_2\} &= l\{\hat{x}_1, \hat{x}_2\}, \quad \{u_1, u_2, u_3, z\} = h\{\hat{u}_1, \hat{u}_2, w, \hat{z}\}, \quad \mu = h/l, \\ \{E_{ij}, A_{ij}, B_{ij}, C_{ij}, \sigma_{ij}\} &= E_*\{\hat{E}_{ij}, \hat{A}_{ij}, \hat{B}_{ij}, \hat{C}_{ij}, \hat{\sigma}_{ij}\}, \quad f_i = (E_*/h)\hat{f}_i, \quad i, j = 1, 2, 3, \end{aligned} \quad (5.32)$$

where l is the typical length of waves in tangential directions, E_* is the typical value of elastic moduli, μ is the small thickness parameter.

For the dynamic problems we take

$$\begin{aligned} f_i &= f_{i0} + \rho\omega^2 u_i = (E_*/h)\hat{f}_i + (\Lambda\hat{\rho}/h)\hat{u}_i, \quad i = 1, 2, 3, \\ \lambda &= \frac{\rho_* h^2 \omega^2}{E_*}, \quad \rho = \rho_* \hat{\rho}, \quad \rho_* = \frac{1}{h} \int_0^h \rho(z) dz, \end{aligned} \quad (5.33)$$

where $\rho, \rho_*, \omega, \Lambda$ are the mass density, the average density, the frequency, and the frequency parameter, respectively. In what follows, we shall drop the “hat” signs. As a result, we get a system of 6th order with the small thickness parameter μ ,

$$\begin{aligned} \frac{\partial w}{\partial z} &= \mu \varepsilon_{33}, \\ \frac{\partial u_i}{\partial z} &= -\mu(p_i w - \varepsilon_{i3}), \quad p_i = \frac{\partial(\cdot)}{\partial x_i}, \quad i = 1, 2, \\ \frac{\partial \sigma_{i3}}{\partial z} &= -\mu(p_1 \sigma_{1i} + p_2 \sigma_{2i}) - \lambda \rho u_i - f_i \equiv g_i, \quad i = 1, 2, \\ \frac{\partial \sigma_{33}}{\partial z} &= -\mu(p_1 \sigma_{13} + p_2 \sigma_{23}) - \lambda \rho w - f_3 \equiv g_3. \end{aligned} \quad (5.34)$$

In this system the main unknowns are $w, u_i, \sigma_{i3}, \sigma_{33}$, $i = 1, 2$, the functions $\varepsilon_{i3}, \sigma_{ij}$, $i, j = 1, 2$ in Eqs. (5.34) are expressed in terms of the main unknowns via Eqs. (5.28), (5.29). For $j = 1, \dots, 6$ we denote $\mathbf{Y} = \{y_j\} = \{w, u_1, u_2, \sigma_{13}, \sigma_{23}, \sigma_{33}\}$, and seek the solution of Eqs. (5.34) in the form of the formal asymptotic expansions

$$y_j(x_1, x_2, z) = \mu^{\alpha_j} \left(y_j^{(0)}(x_1, x_2, z) + \mu y_j^{(1)}(x_1, x_2, z) + \mu^2 y_j^{(2)}(x_1, x_2, z) + \dots \right), \quad (5.35)$$

where the powers α_j of the unknowns depend on the studied problem. For example, for a bending problem with $f_3 \sim 1$ we get $\alpha_1 = -4$, $\alpha_2 = \alpha_3 = -3$, $\alpha_4 = \alpha_5 = -1$, $\alpha_6 = 0$. Further in Eqs. (5.35) we will be concerned only with the terms of the zero-, the first-, and the second-order accuracy.

Integrating with respect to z the first three equations of (5.34), we introduce arbitrary functions $w_0(x_1, x_2)$, $u_{10}(x_1, x_2)$, and $u_{20}(x_1, x_2)$, which are later found from the compatibility conditions of the rest three equations of (5.34)

$$\langle g_j(z) \rangle = 0, \quad j = 1, 2, 3, \quad \langle Z(z) \rangle \equiv \int_0^1 Z(z) dz, \quad (5.36)$$

which follow from the boundary conditions (5.31). Here and what follows, the average value of a function Z is denoted by $\langle Z \rangle$. As a result, the 2D particular differential equations for the functions w_0, u_{10}, u_{20} are found.

By this algorithm, the 2D model of second-order accuracy for a heterogeneous plate in the case of general anisotropy (with 21 elastic moduli) is constructed in Tovstik and Tovstik (2017b), and a multi-layered plate, made of a monoclinic material, is investigated in Morozov et al (2018); Timoshenko (1921). These models, which are quite cumbersome, have not been sufficiently studied. Here we consider the more simple problem for a plate made of a heterogeneous transversely isotropic material.

5.5 Transversely Isotropic Plate Heterogeneous in the Thickness Direction

A transversely isotropic material is described by 5 elastic moduli (instead of 21 moduli in the general case), and Eqs. (5.34)) and their asymptotic solutions become essentially simpler. The main simplification consists in the possibility of separation of the system (5.34) into two parts: one part describes the main stress state, and the other one describes the boundary layer (for the TR model the similar separation of variables is performed in Sect. 5.3).

To simplify Eqs. (5.34) we introduce the new unknown functions u, v, σ, τ

$$\begin{aligned} u &= \frac{\partial u_1}{\partial x_1} + \frac{\partial u_2}{\partial x_2}, & v &= \frac{\partial u_1}{\partial x_2} - \frac{\partial u_2}{\partial x_1}, \\ \sigma &= \frac{\partial \sigma_{13}}{\partial x_1} + \frac{\partial \sigma_{23}}{\partial x_2}, & \tau &= \frac{\partial \sigma_{13}}{\partial x_2} - \frac{\partial \sigma_{23}}{\partial x_1}. \end{aligned} \quad (5.37)$$

For a transversally isotropic material, system (5.34) is split into two sub-systems (Tovstik and Tovstik, 2017b):

$$\frac{\partial v}{\partial z} = -\mu \frac{\tau}{G_{13}}, \quad \frac{\partial \tau}{\partial z} = -\mu G_{12} \Delta v - \Lambda \rho v - m_1, \quad (5.38)$$

$$\begin{aligned} \frac{\partial w}{\partial z} &= -\mu c_\nu u + c_3 \sigma_{33}, & \frac{\partial \sigma}{\partial z} &= -\mu^2 c_0 \Delta u - \mu c_\nu \Delta \sigma_{33} - \lambda \rho u - m, \\ \frac{\partial u}{\partial z} &= -\mu \Delta w + c_g \sigma, & \frac{\partial \sigma_{33}}{\partial z} &= -\mu \sigma - \lambda \rho w - f_3, \end{aligned} \quad (5.39)$$

with $m_1 = p_2 f_1 - p_1 f_2$, $m_2 = p_1 f_1 + p_2 f_2$. Equations (5.38), which are of second differential order in z and describe the boundary layer, will not be studied here. The fourth-order equations (5.39) describe the plate bending with the designations

$$\begin{aligned}
E_0 &= E_{11} - \frac{E_{13}^2}{E_{33}} = \frac{E}{1 - \nu^2}, & E_* &= \int_0^1 E_0(z) dz, \\
c_0 &= \frac{E_0}{E_*}, & c_\nu &= \frac{E_{13}}{E_{33}}, & c_g &= \frac{E_*}{G_{13}}, & c_3 &= \frac{E_*}{E_{33}}.
\end{aligned} \tag{5.40}$$

The right-hand sides in Eqs. (5.39) are small, and the method of iterations (Tovstik, 2009; Tovstik and Tovstik, 2017b,a) is used. To construct the solution of second-order accuracy we take

$$\begin{aligned}
w &= \mu^{-4} w^{(0)} + \mu^{-2} w^{(2)}, & u &= \mu^{-3} u^{(0)} + \mu^{-1} u^{(2)}, \\
\sigma &= \mu^{-1} \sigma^{(0)} + \mu \sigma^{(2)}, & \sigma_{33} &= \sigma_{33}^{(0)} + \mu^2 \sigma_{33}^{(2)}.
\end{aligned} \tag{5.41}$$

For a transversely isotropic material, in contrary to the general case (5.35), the terms of the first-order accuracy are absent.

In the zero approximation we get

$$\begin{aligned}
w^{(0)} &= w_0(x_1, x_2), & u^{(0)} &= (a - z) \Delta^2 w_0, & a &= \langle z c_0(z) \rangle, \\
\sigma^{(0)} &= \varphi_1(z) \Delta^2 w_0, & \varphi_1(z) &= \int_0^z c_0(z)(z - a) dz, \\
D \Delta^2 w_0 &= F_3, & D &= \langle (z - a)^2 c_0(z) \rangle, & F_3 &= \langle f_3(z) \rangle, \\
\sigma_{33}^{(0)} &= -\frac{F_3}{D} \varphi_2 - \varphi_3, & \varphi_2(z) &= \int_0^z \varphi_1(z) dz, & \varphi_3(x_1, x_2, z) &= \int_0^z f_3(x_1, x_2, z) dz.
\end{aligned} \tag{5.42}$$

Here $z = a$ is the position of a plate neutral plane, D is the bending stiffness of a plate with variable elastic moduli, F_3 is the full transversal force. The equation $D \Delta^2 w_0 = F_3$ corresponds to the classical KL model. The function w_0 does not depend on z , but the small stress $\sigma_{33}^{(0)}$ depends on the distribution of the function $f_3(z)$ in the thickness direction (in the KL model, $\sigma_{33} = 0$).

In the second approximation the solution is more unwieldy. Here, we give only the function $w^{(2)}$, which depends on z . At $z = -1/2$ it satisfies the equation

$$D \Delta^2 w^{(2)}(0) = A \Delta F_3 + L(\Delta f_3) - M, \tag{5.43}$$

where

$$\begin{aligned}
A &= -A_g - A_v, \quad L(\Delta f_3) = \int_0^1 c_v(z)(a-z) \left(\int_0^z \Delta f_3 dz_1 \right) dz, \quad M = \int_0^1 (a-z)m(z)dz, \\
A_g &= -\frac{1}{D} \int_0^1 c_0(z)(z-a) \int_0^z c_g(z_1) \int_0^{z_1} c_0(z_2)(z_2-a) dz_2 dz_1 dz = \frac{1}{D} \int_0^1 c_g(z) f_1^2(z) dz, \\
A_v &= \frac{1}{D} \int_0^1 (z-a) \left(c_v(z) \int_0^z \int_0^{z_1} c_0(z_2)(z_2-a) dz_2 dz_1 + c_0(z) \int_0^z \int_0^{z_1} c_v(z_2)(z_2-a) dz_2 dz_1 \right) dz.
\end{aligned} \tag{5.44}$$

The full deflection of the plane $z = 0$ satisfies the equation

$$D\mu^4 \Delta^2 w(0) = F_3 + \mu^2 (A\Delta F_3 + L(\Delta f_3) - M) + O(\mu^4), \tag{5.45}$$

and the deflection $w(z)$ of the arbitrary plane z is expressed in terms of $w(0)$ as

$$w(z) = w(0) + \mu^2 \Delta w(0) \int_0^z c_v(z)(z-a) dz. \tag{5.46}$$

In Eqs. (5.43)–(5.46) the coefficients D, A, c_0, c_g, c_v depend of the elastic moduli distribution in the thickness direction, the summands $L(\Delta f_3)$ and M depend on the distribution of f_3 and of f_1, f_2 , respectively.

Consider a plate bending under an external harmonic loading

$$f_1 = f_2 = 0, \quad f_3(x_1, x_2, z) = f_3(z) \sin r_1 x_1 \sin r_2 x_2. \tag{46}$$

In this case, the deflection of the plane $z = 0$ is also harmonic, $w(0) = W \sin r_1 x_1 \sin r_2 x_2$, and Eqs. (5.43), (5.45) gives the following expression for an amplitude, $W(0)$,

$$\begin{aligned}
W(0) &= \frac{1}{D\mu^4} \left(F_3 + \mu^2 (A_g + A_v) F_3 - \mu^2 L_v \right) + O(\mu^4), \quad \mu = rh, \quad r^2 = r_1^2 + r_2^2, \\
L_v &= \int_0^1 c_v(z)(a-z) \int_0^z f_3(z_1) dz_1 dz.
\end{aligned} \tag{5.47}$$

Here the small thickness parameter μ is introduced according to Eq. (5.8), and in the dimensionless designations the Laplace operator Δ in the case of double periodic functions is replaced by -1 : $\Delta = -1$.

The deflection of the arbitrary plane z is equal to

$$W(z) = W(0) \left(1 - \mu^2 \int_0^z c_v(z)(z-a) dz + O(\mu^4) \right). \tag{5.48}$$

The summands in Eq. (5.47) of second order in A_g , A_v , and L_v describe, respectively, the influence of the transversal shear, of the extension of normal fibers, and of the distribution of the external loading, $f_3(z)$.

Consider free vibrations of a plate with double periodic mode,

$$w(x_1, x_2, z, t) = w(z) \sin r_1 x_1 \sin r_2 x_2. \quad (5.49)$$

Replacing the external forces in Eq. (5.45) by the inertia forces we get the asymptotic expression for the frequency parameter, λ (see Eq. (5.32)) (Tovstik and Tovstik, 2017b,a)

$$\lambda = D\mu^4 \left(1 + \mu^2 (A_g + A_v + J + A_\rho) + O(h_*^4) \right)^{-1}, \quad (5.50)$$

where the coefficients A_g and A_v are the same as in Eqs. (5.45)), and the summands with J and A_ρ take into account the rotation inertia and the inertia of the normal fibers extension

$$\begin{aligned} J &= \int_0^1 (z-a)^2 \rho_0(z) dz, \\ A_\rho &= \int_0^1 \left(c_v(z)(z-a) \int_0^z \rho_0(z_1) dz_1 - \rho_0(z) \int_0^z c_v(z_1)(z_1-a) dz_1 \right) dz. \end{aligned} \quad (5.51)$$

In the next section, Eqs. (5.47) and (5.50) will be discussed for a multilayered plate.

5.6 Multilayered Plates Bending

Consider a plate consisting of n homogeneous isotropic layers of thicknesses h_k ($h = \sum_{k=1}^n h_k$), Young's moduli E_k , Poisson ratios ν_k , and densities ρ_k , $k = 1, \dots, n$. All the relations of Section 5 can be used to analyze the bending of this plate if the corresponding piecewise coefficients in Eqs. (5.39) are taken into account. The approximate equations (5.47) and (5.50) of second-order accuracy are compared in Tovstik and Tovstik (2017b,a) for various multilayered plates with exact solutions of Eqs. (5.39). These equations after the replacement $\Delta = -1$ become one-dimensional and hence can be solved numerically.

The plates with $\mu = 0.1$ and with the various ratio η between the maximum and minimum Young moduli of layers are considered. The results of this comparison are as follows. If the ratio η is close to 1 then the relative error ε of both Eqs. (5.47) and (5.50) is very small ($\varepsilon < 0.001\%$), which justifies the correctness of Eqs. (5.47) and (5.50). With the growth of η the error also increases, and for $\eta = 1000$ the error $\varepsilon \sim 1\%$. For $\eta = 10000$ the error $\varepsilon \sim 10\text{--}30\%$, and Eqs. (5.47) and (5.50) are unacceptable.

Now we discuss an equivalent single layer (ESL) of a homogeneous transversely isotropic plate, which may describe approximately the multilayered plate bending in frames of the KL or the TR models. We set

$$z_0 = 0, \quad z_k = \sum_{i=1}^k h_i, \quad c_k = \frac{E_k}{1 - \nu_k^2}, \quad g_k = \frac{E_k}{2(1 + \nu_k)}. \quad (5.52)$$

The horizontal stiffness E_* , the coordinate $z = a$ of the neutral layer, the bending stiffness D according to Eqs. (5.42), and the average density ρ_* are as follows:

$$\begin{aligned} E_* &= \sum_{k=1}^n h_k c_k, \quad a = \frac{1}{2E_*} \sum_{k=1}^n c_k (z_k^2 - z_{k-1}^2), \\ D &= \frac{1}{3} \sum_{k=1}^n c_k (\hat{z}_k^3 - \hat{z}_{k-1}^3), \quad \hat{z}_k = z_k - a, \quad \rho_* = \frac{1}{h} \sum_{k=1}^n h_k \rho_k. \end{aligned} \quad (5.53)$$

The parameters D, ρ_* for an ESL model are the same as for the KL and the TR models. Equations (5.17) for the TR model read as

$$w_0 = w^{KL}(1 + g), \quad \lambda = \frac{\lambda^{KL}}{1 + g}, \quad g = \frac{Dr^2}{\Gamma}. \quad (5.54)$$

If we hold in Eqs. (5.47), (5.50) the summand with A_g , take into account the transversal shear, and neglect the other terms of second order, then after comparing with Eqs. (5.53) we conclude that $g = \mu^2 A_g$ and in the initial designations

$$\Gamma = khG_{13}, \quad k = \frac{5}{6}, \quad G_{13} = \frac{E_*}{10hA_g}, \quad A_g = \frac{1}{D} \int_0^h \left(\int_0^z c(z_1) dz_1 \right)^2 \frac{dz}{G(z)}. \quad (5.55)$$

Here $c(z)$ and $G(z)$ are the piecewise constant functions with the values c_k and g_k according to Eqs. (5.52). In (5.54), G_{13} is the transversal shear modulus of the ESL plate. Equations (5.52), (5.55) may be used to construct an ESL plate made of a transversely isotropic functionally graded material.

Consider the numerical values of the equivalent parameters of second order A_g , A_ν , J , A_ρ from Eq. (5.6). We take three-layered plates with soft intermediate layers with dimensionless parameters:

$$E_1 = E_3 = 1, \quad E_2 = \eta^{-1}; \quad \nu_1 = \nu_3 = 0.3, \quad \nu_2 = 0.35; \quad \rho_1 = \rho_3 = 1, \quad \rho_2 = 0.3, \quad (5.56)$$

and consider the four values $\eta = 1, 10, 1000$ of the ratio, $\eta = E_1/E_2$. The results, as found from Eqs. (5.42), (5.44), (5.51), are presented in Tables 5.2 and 5.3, respectively, for a plate symmetric in the thickness direction and for an asymmetric plate. From Tables 5.2 and 5.3 it follows that the transversal shear parameter A_g has the largest magnitude among the second-order other parameters, especially for $\eta \gg 1$. Therefore, the ELS TR model is sufficiently accurate. Its accuracy for $\eta \gg 1$

Table 5.2Second-order parameters for an symmetric plate with $h_1 = h_3 = 0.2$, $h_2 = 0.6$

η	A_g	A_v	J	A_ρ	a	D
1	0.299	-0.0913	0.1220	0.0306	0.5	0.0822
10	1.871	-0.0874	0.1220	0.0306	0.5	0.1454
100	17.567	-0.0868	0.1229	0.0306	0.5	0.1613
1000	174.517	-0.0868	0.1219	0.0306	0.5	0.1631

Table 5.3Second-order parameters for an asymmetric plate with $h_1 = 0.3$, $h_2 = 0.6$, $h_3 = 0.1$

η	A_g	A_v	J	A_ρ	a	D
1	0.299	-0.0928	0.1150	0.0308	0.502	0.0824
10	1.461	-0.0875	0.1114	0.0081	0.384	0.1202
100	12.921	-0.0844	0.1149	0.0026	0.354	0.1253
1000	127.515	-0.0840	0.1154	0.0019	0.350	0.1259

is the same as that of the SOA model, but it is simpler, because it is not necessary to calculate the parameters, A_v , J , A_ρ .

5.7 General Anisotropic Plate

The 2D model of second-order accuracy for a plate in the case of general anisotropy is built in Tovstik (2019); Belyaev et al (2019b). The PDE system for the unknown displacements $u_1(x_1, x_2), u_2(x_1, x_2), w(x_1, x_2)$ of a reference plane may be written as

$$\begin{aligned}
 L_{11}u_1 + L_{12}u_2 + \mu N_1 w + F_1 &= 0, & L_{ij} &= L_{ij}^{(2)} + \mu L_{ij}^{(3)} + \mu^2 L_{ij}^{(4)}, \quad i, j = 1, 2, \\
 L_{21}u_1 + L_{22}u_2 + \mu N_2 w + F_2 &= 0, & N_i &= N_i^{(3)} + \mu N_i^{(4)} + \mu^2 N_i^{(5)}, \quad i = 1, 2, \\
 \mu \hat{N}_1 u_1 + \mu \hat{N}_2 u_2 + \mu^2 Q w + F_3 &= 0, & Q &= Q^{(4)} + \mu Q^{(5)} + \mu^2 Q^{(6)}.
 \end{aligned} \tag{5.57}$$

Here $L_{ij}^{(k)}, N_i^{(k)}, Q^{(k)}$ are the homogeneous differential operators of order k in x_1, x_2 with the constant coefficients, which are the repeated integrals of elastic moduli $E_{ij}(z)$. The operators \hat{N}_i have the same expansions as N_i . The summands F_j , $j = 1, 2, 3$, include the external and the inertia forces. System (5.57) (of 14th differential order) is cumbersome and was not sufficiently studied. Consider some particular cases.

If the forces F_j are harmonic

$$F_j(x_1, x_2) = F_j^0 e^{i(r_1 x_1 + r_2 x_2)}, \quad i = 1, 2, 3,$$

then for the harmonic solution

$$u_j(x_1, x_2) = u_j^0 e^{i(r_1 x_1 + r_2 x_2)}, j = 1, 2, 3, u_3 = w,$$

system (5.57) becomes an algebraic system, and the amplitudes u_j may be easily found. The harmonic solution appears for an infinite plate and sometimes for a rectangular plate with a special boundary conditions.

For a monoclinic material (in particular, for transversely isotropic and for isotropic materials) Eqs. (5.57) becomes simpler. The summands involving the factor μ in the expansions (5.57) of the operators L_{ij}, N_i, Q disappear. As a result, the term with the factor μ disappears in the expansions (5.35) of solutions, and one has to build the zero and the second approximations.

For a transversely isotropic material in all cases by an appropriate choice of a reference plane, Eqs. (5.57) may be split into an equation describing the plate bending and a system describing the tangential deflections. In the remaining cases, the separate analysis of bending and tangential deformations is possible only for plates symmetric about the middle plane ($z = h/2$). In this case $N_i = \hat{N}_i = 0$, $i = 1, 2$, and Eqs. (5.57) is split into two systems. For an asymmetric plate, a joint consideration of bending and tangential deformations is necessary.

Consider a bending deformation of an infinite multilayered plate consisting of orthotropic plates with various orientations of orthotropy under the action of external forces, $F_1 = F_2 = 0$, $F_3 = F_3^0 \sin r_1 x_1 \sin r_2 x_2$. For a symmetric in the thickness direction plate, the amplitude w^0 of deflection reads as $w^0 = F_3^0 / (\mu^2 Q^{(4)} + \mu^2 Q^{(6)})$. For an asymmetric plate, the neutral plane does not exist, and it is necessary to perform a common consideration of bending and tangential deformations, and for amplitude w^0 we get the following expression (Tovstik, 2019; Belyaev et al, 2019b):

$$w^0 = F_3^0 \begin{vmatrix} L_{11}^{(2)} & L_{12}^{(2)} \\ L_{21}^{(2)} & L_{22}^{(2)} \end{vmatrix} \cdot \left(\mu^2 \begin{vmatrix} L_{11}^{(2)} & L_{12}^{(2)} & N_1^{(3)} \\ L_{21}^{(2)} & L_{22}^{(2)} & N_2^{(3)} \\ \hat{N}_1^{(3)} & \hat{N}_2^{(3)} & -Q^{(4)} \end{vmatrix} + O(\mu^4) \right)^{-1}, \quad u_j^0 = O(\mu w^0), j = 1, 2. \quad (5.58)$$

From this expression it follows that for an asymmetric plate the main term of the amplitude, w^0 , expansion, in powers in μ is changed compared with an symmetric plate.

In the case of free harmonic vibrations we put $F_j = \lambda u_j$, $j = 1, 2, 3$, with the frequency parameter, λ , as given in Eq. (5.32), and seek a solution in the same form $u_j = u_j^0 e^{i(r_1 x_1 + r_2 x_2)}$. For a symmetric plate with $N_i = \hat{N}_i = 0$ the bending and the tangential vibrations may be studied separately. The eigenvalue λ_1^s of bending vibrations is small, $\lambda_1^s \sim \mu^2$, and two eigenvalues of tangential vibrations, are of the order of 1, $\lambda_2^s, \lambda_3^s \sim 1$. For an asymmetric plate the bending parameter, λ_1^a , is of the same order as λ_1^s , but essentially differs from it,

$$\lambda = \mu^2 (Q - \hat{\mathbf{N}}^T \cdot \mathbf{L}^{-1} \cdot \mathbf{N}), \quad \mathbf{N} = (N_1^{(3)}, N_2^{(3)}), \quad \hat{\mathbf{N}} = (\hat{N}_1^{(3)}, \hat{N}_2^{(3)}), \quad \mathbf{L} = \begin{pmatrix} L_{11}^{(2)} & L_{12}^{(2)} \\ L_{21}^{(2)} & L_{22}^{(2)} \end{pmatrix}. \quad (5.59)$$

In contrast, the eigenvalues of tangential vibrations differ very small due to the asymmetry of the plate, $\lambda_j^a = \lambda_j^s + O(\mu^2)$, $j = 2, 3$.

5.8 Conclusion

A 2D model of second-order accuracy (SOA) for an anisotropic heterogeneous in the thickness direction plate is discussed. The model is cumbersome, and the particular cases should be studied more detailed. It is desirable to put forward more simple models that give the sufficiently exact results for particular static, dynamical and buckling problem. In particular, it is interesting to study the waves propagation in an anisotropic plate.

The asymptotic SOA solution describes only a main (internal) stress state. The problem of construction of a boundary layer is not solved in the general case. Only for the transversely isotropic plates a boundary layer satisfies a separate equation. It is desirable to formulate the boundary conditions with the same accuracy as that of the SOA model.

Acknowledgements This research was carried out with the financial support of the Russian Foundation for Basic Research (grant nos. 18-01-00884a, 19-01-00208, 20-51-52001MHTa).

References

- Agolovyan LA (1997) Asymptotic Theory of Anisotropic Plates and Shells (in Russ.). Nauka, Moscow
- Altenbach H (1998) Theories of laminated and sandwich plates. an overview. *Mech Compos Mater* 34(3):333–349
- Altenbach H, Mikhasev GI (eds) (2015) Shell and Membrane Theories in Mechanics and Biology, *Advanced Structured Materials*, vol 45. Springer
- Ambartsumjan SA (1970) Theory of Anisotropic Shells. *Progress in Materials Science*. Ser. II, Technomic, Stanford, Conn.
- Belyaev AK, Morozov NF, Tovstik PE, Tovstik TP (2019a) Two-dimensional linear model of multilayered anisotropic plate. *Acta Mechanica* 230:2891–2904
- Belyaev AK, Morozov NF, Tovstik PE, Tovstik TP, Zelinskaya AV (2019b) Two-dimensional model of plate made of material with general anisotropy. In: Altenbach H, Chróścielewski J, Eremeyev VA, Wiśniewski K (eds) *Recent Developments in the Theory of Shells*, *Advanced Structured Materials*, vol 110, pp 91–108
- Berdichevsky VL (2010) An asymptotic theory of sandwich plates. *International Journal of Engineering Science* 48(3):383–404
- Chernykh KF, Rodionova VA, Titaev BF (1996) *Applied Theory of Anisotropic Plates and Shells* (in Russ.). St. Petersburg Univ. Press

- Donnell LH (1976) *Beams, Plates and Shells*. McGraw-Hill, New York, NY
- Eremeev VA, Zubov LM (2008) *Mechanics of Elastic Shells* (in Russ.). Nauka, Moscow
- Goldenweizer AL (1961) *Theory of Elastic Thin Shells*. Pergamon Press, Oxford
- Grigolyuk EI, Kulikov GM (1988a) Generalized model of the mechanics of thin-walled structures made of composite materials. *Mechanics of Composite Materials* 24(4):537–543
- Grigolyuk EI, Kulikov GM (1988b) *Multilayer Reinforced Shells: Calculation of Pneumatic Tires* (in Russ.). Mashinostroenie, Moscow
- Hill R (1965) A self-consistent mechanics of composite materials. *Journal of the Mechanics and Physics of Solids* 13(4):213–222
- Kienzler R, Schneider P (2014) Comparison of various linear plate theories in the light of a consistent second order approximation. In: Pietraszkiewicz W, Górski J (eds) *Proc. 10th SSTA 2013 Conf. - Shell Structures: Theory and Applications*, CRC Press, Boca Raton, vol 3, pp 109–112
- Kirchhoff G (1876) *Vorlesungen über Mathematische Physik. Mechanik*. B.G. Teubner, Leipzig
- Love AEH (1927) *A Treatise on the Mathematical Theory of Elasticity*. Cambridge Univ. Press
- Mikhasev GI, Altenbach H (2019) *Thin-walled Laminated Structures. Buckling, Vibrations, and Their Suppression*, *Advanced Structured Materials* (eds. Öchsner, A., da Silva, Lucas F. M., Altenbach, H., vol 106. Springer
- Morozov NF, Belyaev AK, Tovstik PE, Tovstik TP (2018) Two-dimensional equations of second order accuracy for a multilayered plate with orthotropic layers. *Doklady Physics* 63(11):471–275
- Novozhilov VV (1970) *Theory of Thin Shells*. Wolters-Noordhoff, Groningen
- Reddy JN (2004) *Mechanics of Laminated Composite Plates and Shells*, 2nd edn. CRC Press, Boca Roca
- Reissner E (1945) The effect of transverse shear deformation on the bending of elastic plates. *Trans ASME J Appl Mech* 12:A69–A77
- Timoshenko SP (1921) Lxvi. on the correction for shear of the differential equation for transverse vibrations of prismatic bars. *The London, Edinburgh, and Dublin Philosophical Magazine and Journal of Science* 41(245):744–746
- Tovstik P (2009) Two-dimensional models of plates made of an anisotropic material. *Doklady Physics* 54(4):205–209
- Tovstik P, Tovstik T (2007) On the 2D models of plates and shells including the transversal shear. *ZAMM - Journal of Applied Mathematics and Mechanics / Zeitschrift für Angewandte Mathematik und Mechanik* 87(2):160–171
- Tovstik P, Tovstik T (2014a) Two-dimensional linear model of elastic shell accounting for general anisotropy of material. *Acta Mechanica* 225(3):647–661
- Tovstik PE (2007) On the asymptotic character of approximate models of beams, plates and shells. *Vestnik St Petersburg Univ Mathematics* (3):49–54
- Tovstik PE (2019) Two-dimensional model of second-order accuracy for an anisotropic plate. *Vestnik St Petersburg University, Mathematics* 52(1):112–121

- Tovstik PE, Tovstik TP (2014b) A thin-plate bending equation of second-order accuracy. *Doklady Physics* 59(8):389–392
- Tovstik PE, Tovstik TP (2017a) An elastic plate bending equation of second-order accuracy. *Acta Mechanica* 228(10):3403–3419
- Tovstik PE, Tovstik TP (2017b) Generalized Timoshenko-Reissner models for beams and plates, strongly heterogeneous in the thickness direction. *ZAMM - Journal of Applied Mathematics and Mechanics / Zeitschrift für Angewandte Mathematik und Mechanik* 97(3):296–308
- Vekua IN (1955) On one method of calculating prismatic shells (in Russ.). *Trudy Tbilis Mat Inst* 21:191–259
- Vetyukov Y, Kuzin A, Krommer M (2011) Asymptotic splitting in the three-dimensional problem of elasticity for non-homogeneous piezoelectric plates. *International Journal of Solids and Structures* 48(1):12—23



Chapter 6

Interface Strength Assessments of Sandwich Panels with a Face Sheet/Core Debond

Vyacheslav N. Burlayenko, Holm Altenbach, and Svetlana D. Dimitrova

Abstract Virtual fracture tests combining analytical considerations and a finite element analysis are performed to provide assessment of face sheet-to-core interface strength in sandwich panels. Three fracture test methods, different in laboratory testing procedures and virtual modeling solutions, such as sandwich double cantilever beam subjected to uneven bending moments (DCB-UBM), sandwich double cantilever beam (DCB) and sandwich single cantilever beam (SCB) specimens are examined with the aim to predict the fracture parameters - energy-release rate (ERR) and stress-intensity factors (SIFs) - required for the assessment of the interface strength within the framework of linear elastic fracture mechanics (LEFM). The existence of mode mixity at the bi-material interface of a sandwich panel is considered and appropriate methods applied for mode decomposition are described. The numerical analyses are carried out using the capabilities of the ABAQUS code. In general, good agreement between the results of numerically calculated fracture parameters and those obtained using analytical solutions and/or from experimental data available in the literature is observed. Finally, computational aspects of the numerical models have been revisited and put into perspective of the accurate and efficient interface strength assessments of sandwich panels.

Vyacheslav N. Burlayenko

Department of Applied Mathematics, National Technical University KhPI, 2 Kyrpychova str., 61002 Kharkiv, Ukraine

e-mail: burlayenko@yahoo.com

Holm Altenbach

Institut für Mechanik, Otto-von-Guericke-Universität Magdeburg, Universitätsplatz 2, 39106 Magdeburg, Germany

e-mail: holm.altenbach@ovgu.de

Svetlana D. Dimitrova

Department of Higher Mathematics, National Technical University KhPI, 2 Kyrpychova str., 61002 Kharkiv, Ukraine

e-mail: s.dimitrovaburlayenko@gmail.com

Key words: Sandwich panels · Face sheet/core interface strength · Fracture test methods · Finite element analysis

6.1 Introduction

A sandwich panel consists of three material layers such as a low-density core and two thin stiff face sheets bonded to each side of the core (Altenbach et al, 2018). Due to this design, sandwich panels have been widely used in various engineering applications, for which an efficient combination of high structural rigidity and low weight is required and/or whose structural properties should meet particular design features (Harne et al, 2012; Xie et al, 2016; Mouritz, 2017; Chatterjee et al, 2019). The layered structure of sandwich panels makes a premise to their inevitable susceptibility to interfacial damage between the constitutive material layers, the so-called face sheet-to-core debonding. Theoretical and experimental studies have already shown that this defect decreases the overall load-bearing capacity of sandwich panels and gives rise to quantitative and qualitative changes of their dynamic responses (Burlayenko and Sadowski, 2011a; Idriss and Mahi, 2017; Pölöskei and Szekrényes, 2017; Qu and Meng, 2017; Burlayenko and Sadowski, 2018). The latter features are exploited for identifying and quantifying such type of damage within sandwich panes as discussed, e.g., in Burlayenko and Sadowski (2011b); Mustapha and Ye (2013); Farhana et al (2016); Lu et al (2017); Seguel and Meruane (2018). The relevance of such structural monitoring techniques is justified by the evidence that the debonding propagation can lead to eventual failure of sandwich structures (Triantafyllou and Gibson, 1987; Burlayenko and Sadowski, 2014). Therefore, sandwich panels should be validated in terms of damage tolerance and possible failure.

The structural integrity of the sandwich structure is defined by the strength of its face sheet/core interface. Traditionally, the debonding between the face sheet and the core is treated as an interfacial bi-material crack, and the interface strength is quantified using the concept of interface fracture toughness within the framework of linear elastic fracture mechanics (LEFM) (Willis, 1971). Fracture specimens are used to supply necessary information regarding the interface strength. Hence, by analysing the specimens' behaviour with experimental, analytical or numerical methods, the fracture parameters such as stress-intensity factors (SIFs) or energy-release rates (ERRs) controlling the fracture process at the crack tip are obtained.

A variety of test configurations towards the face sheet/core-strength assessment of sandwich panels have been proposed during the last two decades. Some of the most popular specimens' geometries being studied in an attempt to define interfacial fracture toughness in pure or mixed fracture modes are listed in Shivakumar and Smith (2004). The strength of the face sheet/core bond corresponding to the lowest critical ERR has traditionally been measured using a double cantilever sandwich beam (DCB) (Prasad and Carlsson, 1994; Avilés and Carlsson, 2008). An alternative test method for generation of mode I dominated fracture is a single cantilever sandwich beam (SCB) as proposed in Cantwell and Davies (1996) and further improved

in Ratcliffe and Reeder (2011); Rinker et al (2011); Adams et al (2012). In order to characterize the interfacial shear strength of sandwich panels, a cracked sandwich beam (CSB) specimen developed in Carlsson et al (1991) or its modifications, e.g. Cantwell et al (1999), accommodating the sliding deformation between the face sheet and the core through three-point bending are often used. However, while the studies on the pure (strictly speaking - dominated) modes I and II are important, they are not sufficient for evaluating interface fracture toughness of sandwich panels. Dillard et al (2009) presented the findings for adhesive joints, which are similar to sandwich panels, where the most critical ERR occurs at a certain I/II mode mixity. Moreover, recently it has been recognized that the mode-III deformation and its different combinations (i.e. mixed mode I/III, II/III and even I/II/III) are also essential for the complete fracture characterization of advanced composite materials (Hernández-Pérez et al, 2013). Although some test methods have been proposed for the determination of interfacial fracture toughness involving the tearing mode, all of them have yet unresolved issues which restrain their standardization. The main issues in these test methods relate to difficulties to produce a pure mode III fracture state at the debonding front, difficulties to track the crack propagation, uncertainty in the data reduction methods and/or complexity of the test rig (Rodríguez-González et al, 2014). Thereby, the mode I and II mixity as the simplest case of mixed mode fracture is commonly analyzed in sandwich materials so far. For studying mixed mode I/II fracture, the mixed mode bending (MMB) test devised earlier for laminated composites has been adapted to sandwich structures as done in Quispitupa et al (2009). Other methods for mixed mode I/II testing has been derived from the DCB and SCB test configurations such as a double cantilever sandwich beam subjected to uneven bending moments (DCB-UBM) (Sorensen et al, 2006) and a titled sandwich debonded (TSD) specimen (Li and Carlsson, 1999), respectively.

The majority of analytical solutions relevant to the extraction of ERR or SIFs from the tests mentioned above have been found by reducing the dimension of the problem. Efficient structural models presenting the specimens as an assemblage of beams or plates can be found in Valvo et al (2015); Saseendran et al (2018); Massabò and Campi (2014); Odessa et al (2018); Kiss and Szekrényes (2019), just to name few recent publications. In doing so, either classical or first- or higher order shear-deformation structural theories as well as assumptions on either rigid or flexible flexible deformability ahead of the crack tip within the intact part are used for analysing the specimen's behaviour. Some aspects of interface fracture analysis in layered structures can be found in Thouless (2018). Moreover, since the face sheet/core interface has a bimaterial nature, the fracture analysis must recognize the mixed mode loading and be able to define the relative amount of mode I and mode II at the debonding tip. A great effort has been made to obtain such mode partition. For this either semi-analytic (numerical) solutions for particular loading cases within the interface LEFM concepts (Suo and Hill, 1990; Li et al, 2004; Kardomateas et al, 2013) or the structural models (Williams, 1988; Bruno and Greco, 2001; Wang and Qiao, 2004; Andrews and Massabò, 2007) for the fracture specimens have been exploited. Herewith, two approaches are used. The first one referred to as local approach considers debonding conditions as local stresses at the crack tip (Suo and

Hutchinson, 1990; Li et al, 2004). Alternatively, the second one is a global approach that evaluates the ERR as the first variation of the total potential energy with respect to the advancing crack area (Williams, 1988).

In an attempt to improve the accuracy of data evaluation in the tests, two- and three-dimensional analytical elasticity solutions have also been applied to the fracture analysis. In Fichter (1983); Georgiadis and Papadopoulos (1990), the exact 2-D elasticity solutions of the DCB have been obtained by using the Wiener-Hopf technique. On the other hand, the 2-D elasticity solutions are limited by the assumption of either plane stress or plane strain conditions. As a result, they are not able to capture an actual curved crack front (thumb nail shaped) associated with Poisson-strain effect under specimen bending (Samborski, 2018). Therefore, 3-D elasticity models are obviously the most accurate, but their solutions can only be obtained by using numerical methods, in particular the finite element method (FEM) (Williams and Addressio, 1997; Davis et al, 2014). Two-dimensional debonding problems have also broadly been reported in the literature by using the FEM. It has been reported if the effect of front curvature is not a main concern, the less sophisticated 2-D models would be sufficiently accurate for performing the fracture analysis (Crews et al, 1991). The FEM provides efficient techniques for the mode partitioning in bimaterial interfacial cracks. These techniques include the displacement or stress interpretation methods (Kuna, 2013), the crack surface displacement method (Smelser, 1979), the interaction integral approach based on the path independent integral technique (Shih and Asaro, 1988), the virtual crack extension (VCE) (Matos et al, 1989) and virtual crack closure techniques (VCCT) (Beuth, 1996). In addition, a large number of studies involving the strength prediction of layered structures including sandwich composites use the crack tip element approach (Davidson et al, 1995).

This paper extends some preliminary considerations by Burlayenko et al (2018, 2019c,b,a) in the light of new findings in the recent literature on interfacial strength assessments of sandwich materials. The study is aimed at understanding and reproducing the features of interfacial cracking, which are observed in the DCB-UBM, DCB and SCB sandwich specimens broadly used for fracture testing. In addition to these experimental aspects, both analytical and numerical calculations are presented to explain how the ERR and SIFs are derived from the fracture test data for those specimens. Comparisons between analytical and numerical solutions and experimental data available in the literature are also given. Finally, the accuracy of the theoretical predictions is discussed.

6.2 Mechanics of Bi-material Interface Cracks

A complexity in analysing bi-material interface cracks is that such cracks generally exhibit tension-shear coupling effects even under pure opening or shearing loading. Also, the oscillations of stress and displacement fields, increasing when approaching the crack tip, from the standpoint of LEFM (Hutchinson and Suo, 1991). Thus, to characterise the singular stress and displacement fields, a complex stress-intensity factor

(SIF), K , together with the oscillation index, ϵ , relating to the elastic properties of the materials are utilized (Rice, 1988). Following Suo and Hill (1990); Kuang-Chong (1991) the structure of the asymptotic near-tip fields for an interface crack results from the solution of the eigenvalue problem induced by the traction free boundary conditions on the crack flanks as

$$\bar{\mathbf{H}}\mathbf{w} = e^{2\pi\epsilon}\mathbf{H}\mathbf{w}, \quad (6.1)$$

where \mathbf{H} is a 3×3 positive defined compliance-like Hermitian matrix involving the bi-material elastic constants and $\bar{\mathbf{H}}$ is its complex conjugate matrix. Three eigenpairs such as (ϵ, \mathbf{w}) , $(-\epsilon, \bar{\mathbf{w}})$ and $(0, w_3)$, where \mathbf{w} , $\bar{\mathbf{w}}$ and w_3 are complex, complex conjugate and real eigenvectors, respectively, are the solutions of (6.1).

In the 2-D case of the interface crack between two dissimilar orthotropic materials, where the material symmetry axes are aligned along the interface (Fig. 6.1b), the matrix \mathbf{H} takes the form (Wang et al, 1992):

$$\begin{aligned} H_{11} &= [2n\lambda^{1/4}\sqrt{s_{11}s_{22}}]_{\#1} + [2n\lambda^{1/4}\sqrt{s_{11}s_{22}}]_{\#2}, \\ H_{22} &= [2n\lambda^{-1/4}\sqrt{s_{11}s_{22}}]_{\#1} + [2n\lambda^{-1/4}\sqrt{s_{11}s_{22}}]_{\#2}, \\ H_{12} &= \bar{H}_{21} = [\sqrt{s_{11}s_{22}} + s_{12}]_{\#2} - [\sqrt{s_{11}s_{22}} + s_{12}]_{\#1}, \end{aligned} \quad (6.2)$$

where s_{ij} , $s_{16} = s_{26} = 0$, $i, j = 1, 2, 6$ are components of the compliance matrix of the orthotropic material (#1 or #2) in plane stress; in plane strain the compliances are

$$\tilde{s}_{ij} = s_{ij} - \frac{s_{i3}s_{j3}}{s_{33}}$$

Note that

$$\lambda = \frac{s_{11}}{s_{22}} = \frac{E_2}{E_1}$$

and

$$\varrho = \frac{2s_{12} + s_{66}}{2\sqrt{s_{11}s_{22}}} = \frac{\sqrt{E_1E_2}}{2G_{12}} - \sqrt{\nu_{12}\nu_{21}}$$

are parameters of anisotropy and

$$n = \sqrt{\frac{(1 + \varrho)}{2}}.$$

The solution of the eigenvalue problem (6.1) results in the eigenvectors:

$$\mathbf{w} = \left\{ -\frac{i}{2}, \frac{1}{2}\sqrt{\frac{H_{11}}{H_{22}}}, 0 \right\}$$

and $w_3 = \{0, 0, 1\}$. The oscillation index is expressed as follows:

$$\epsilon = \frac{1}{2\pi} \ln \left(\frac{1-\beta}{1+\beta} \right), \quad (6.3)$$

where the first and second Dundurs' parameters are defined by

$$\alpha = \frac{\Sigma - 1}{\Sigma + 1} \quad \text{and} \quad \beta = \frac{H_{12}}{\sqrt{H_{11}H_{22}}}, \quad (6.4)$$

respectively, and

$$\Sigma = \frac{[\sqrt{S_{11}S_{22}}]_{\#2}}{[\sqrt{S_{11}S_{22}}]_{\#1}}.$$

The stresses σ_{22} and σ_{12} at a distance r in front of the crack tip at $\theta = 0$ (Fig. 6.1b) can be expressed as follows (Suo and Hill, 1990; Wang et al, 1992):

$$\sqrt{\frac{H_{22}}{H_{11}}} \sigma_{22} + i\sigma_{12} = \frac{Kr^{i\epsilon}}{\sqrt{2\pi r}} \quad (6.5)$$

and an associated pair of the relative crack surface displacements (jumps) Δ_1 and Δ_2 at a distance r behind the crack tip at $\theta = \pm\pi$, can be presented in the form:

$$\sqrt{\frac{H_{11}}{H_{22}}} \Delta_2 + i\Delta_1 = \frac{2H_{11}Kr^{\frac{1}{2}+i\epsilon}}{\sqrt{2\pi}(1+2i\epsilon)\cosh\pi\epsilon} \quad (6.6)$$

Here, $i = \sqrt{-1}$, $K = K_1 + iK_2 = |K|e^{i\psi}$ with K_1 and K_2 used instead of K_I and K_{II} adopted for homogeneous materials and the mode mixity phase angle ψ is specified as

$$\psi = \tan^{-1} \sqrt{\frac{H_{11}}{H_{22}}} \left(\frac{\sigma_{12}}{\sigma_{22}} \right) \quad (6.7)$$

To avoid oscillations in the mode mixity parameter, a characteristic length scale, \hat{l} chosen in consistence with discussions in Hutchinson and Suo (1991) is usually introduced. Then, the non-oscillatory phase angle $\hat{\psi}$ is established as

$$\hat{\psi} = \tan^{-1} \sqrt{\frac{H_{11}}{H_{22}}} \left(\frac{\sigma_{12}}{\sigma_{22}} \right) \Big|_{r=\hat{l}} = \tan^{-1} \left(\frac{\Im m\{K\hat{l}^{i\epsilon}\}}{\Re e\{K\hat{l}^{i\epsilon}\}} \right), \quad (6.8)$$

where $K\hat{l}^{i\epsilon} = \hat{K}$ is a normalized complex SIF with ordinary units as those in homogeneous materials. The amplitudes of \hat{K} and K are the same, but their phase angles are distinguished as $\hat{\psi} = \psi + \epsilon \ln \hat{l}$.

The ERR, \mathcal{G} is related to the components of complex SIF as follows (Suo and Hill, 1990; Kuang-Chong, 1991):

$$\mathcal{G} = \frac{H_{11}}{4\cosh^2\pi\epsilon} \left(K_1^2 + K_2^2 \right) \quad (6.9)$$

6.3 Numerical Evaluation of Interface Fracture Parameters

In this section, the numerical methods, which are appropriate for numerical solutions based on the FEM for obtaining the fracture parameters of an interfacial bimaterial system, are discussed.

6.3.1 Interaction Integral Method (IIM)

The interaction integral method is one of the most popular techniques to calculate complex SIFs by the FEM. This method is based on the Rice’s J -integral which is identical to the ERR in LEFM. A common way to calculate the J -integral within the framework of the FEM is the use of the domain integral approach (Shih and Asaro, 1988). The 2-D domain form of the J -integral over the closed counter $C + C_+ + \Gamma + C_-$ around the crack tip (Fig. 6.1a) can be expressed as follows:

$$J = \int_A \left(W\mathbf{I} - \boldsymbol{\sigma} \cdot \frac{\partial \mathbf{u}}{\partial \mathbf{x}} \right) : \frac{\partial \mathbf{q}}{\partial \mathbf{x}} dA - \int_{C_+ + C_-} \mathbf{t} \cdot \frac{\partial \mathbf{u}}{\partial \mathbf{x}} \cdot \mathbf{q} d\Gamma, \tag{6.10}$$

where W is the strain energy; \mathbf{u} and $\boldsymbol{\sigma}$ are the displacement and stress fields; A is the domain enclosed by the contour $C + C_+ + \Gamma + C_-$; \mathbf{q} is a smooth weighting parameter that takes $\mathbf{q} = \mathbf{q}_1$ on Γ and is zero on C ; \mathbf{m} is the outward vector normal to the closed contour such that $\mathbf{m} = -\mathbf{n}$ on Γ and $\mathbf{t} = \mathbf{m} \cdot \boldsymbol{\sigma}$ on $C_+ + C_-$ if the surface traction on the crack flanks are accounted for. A geometrical interpretation of \mathbf{q} is a virtual advancing of the crack tip in the local direction \mathbf{q}_1 .

Following the finite element spatial discretization, the domain integral (6.10) is computed over a group of finite elements enclosed into the domain A (a ring around the crack tip in Fig. 6.1a). The integration is achieved by using the Gaussian quadratures for each element and consecutive summation, i.e.

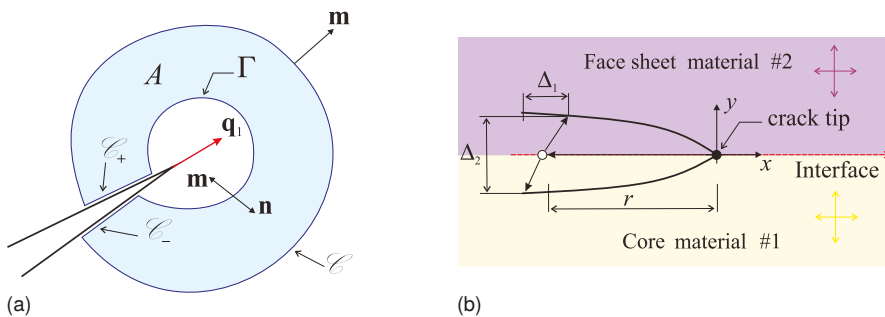


Fig. 6.1. Sketches of: (a) a closed contour $C + C_+ + \Gamma + C_-$ around the crack tip; (b) displacements of crack flanks at bi-material crack bounded by orthotropic materials.

$$J = \sum_{n=1}^{El} \left(\sum_{p=1}^G [f]^{(p)} |\mathbf{j}|^{(p)} \tilde{w}_p \right)_n, \quad (6.11)$$

where n and p indicate that all the entities are associated with the n -th finite element of the area A and are determined at the p -th Gauss integration point; $[f]$ is the integrand in (6.10), $|\mathbf{j}|$ is the determinant of Jacobian matrix and \tilde{w} is the weight of the Gauss numerical quadrature. The domain integral is calculated by post-processing the results of finite element analysis.

The basic idea of the interaction integral method for calculating separated fracture modes involves superposing actual and auxiliary (*aux*) displacement and stress fields, where the auxiliary ones are assumed to be known a priori. The asymptotic Williams type' solutions of the corresponding material system regardless of the actual geometry can be used as the auxiliary field. Then, using the relation between the ERR and the SIF components (6.9), the interaction integral takes the form:

$$J_{int}^M = \frac{2}{H} (K_1 K_1^{aux} + K_2 K_2^{aux}), \quad \text{with} \quad H = \frac{4 \cosh^2 \pi \epsilon}{H_{11}} \quad (6.12)$$

This formula is valid for each fracture mode $M = I, II$. On the other hand, the interaction integral for a straight crack can be expressed analogously to the J -integral definition in (6.10), i.e.

$$J_{int}^M = \int_A \mathbf{Q}^M : \frac{\partial \mathbf{q}}{\partial \mathbf{x}} dA \quad (6.13)$$

with the integrand \mathbf{Q}^M given by

$$\mathbf{Q}^M = \boldsymbol{\sigma} : (\boldsymbol{\varepsilon}^{aux})^M \mathbf{I} - \boldsymbol{\sigma} \cdot \left(\frac{\partial \mathbf{u}^{aux}}{\partial \mathbf{x}} \right)^M - (\boldsymbol{\sigma}^{aux})^M \cdot \frac{\partial \mathbf{u}}{\partial \mathbf{x}} \quad (6.14)$$

Since the interaction integral is formulated similar to the J -integral in (6.10), the domain integration approach identical to that in (6.11) can be applied to the numerical computation of the integral in (6.13).

Finally, making a judicious choice of the auxiliary stress intensity factors and computing auxiliary displacement and stress fields associated with them, the separated stress intensity factors can be evaluated as follows:

$$K_M = \frac{H}{2K_M^{aux}} J_{int}^M \quad (6.15)$$

6.3.2 Crack Surface Displacements (CSD) Method

The CSD method is based on the approach proposed by Smelser (1979). In accordance with this method, the complex SIF components are determined by the amplitude and phase angle of K which are calculated using the displacements at the crack faces close to the crack tip (Fig. 6.1b).

The method has an advantage for computing the SIF components in the context of the FEM since the displacement field is a direct outcome of the finite element analysis. Thus, in contrary to the IIM, the CSD method does not require the retrieval of strains and stresses. Using (6.6) in conjunction with the expressions for the mode-mixity parameter (6.8) and the ERR (6.9), it yields the formulae to compute the fracture characteristics as follows (Kardomateas et al, 2013):

$$\hat{\psi} = \tan^{-1} \left(\sqrt{\frac{H_{11}}{H_{22}}} \frac{\Delta_1}{\Delta_2} \right) - \epsilon \ln \left(\frac{r}{\hat{l}} \right) + \tan^{-1} 2\epsilon \quad (6.16)$$

and

$$\mathcal{G} = \frac{H_{11} |K|^2}{4 \cosh^2 \pi \epsilon} = \frac{\pi(1 + 4\epsilon^2)}{8H_{11}} \left(\frac{H_{11}}{H_{22}} \Delta_2^2 + \Delta_1^2 \right), \quad (6.17)$$

where

$$\Delta_j = u_j(r, \pi) - u_j(r, -\pi), \quad j = 1, 2$$

represents the relative crack flank displacements (shearing and opening modes) at distance r behind the crack tip, H_{11} and H_{22} are components of the matrix \mathbf{H} .

Thus, in accordance with the CSD method, the nodal displacements of finite elements, whose faces are adjacent to the opposite crack flanks, are extracted from the finite element results to compute the ERR and phase angle at different distances r close to the crack tip. However, approaching the crack tip, the values of ERR and phase angle tend to be incorrect due to the singular nature of the relative displacements Δ_1 and Δ_2 at $r \rightarrow 0$. Instead, the ERR and phase angle are estimated by linear extrapolation of their values in a chosen interval of r to the crack tip (Ryoji and Sang-Bong, 1989). The nodal displacements in the neighborhood of the region $-r/\hat{l}$ about $10^{-2} - 10^{-3}$ typically provides a good estimate of \mathcal{G} and $\hat{\psi}$ (Smelser, 1979). Finally, the results can be expressed in terms of stress intensity factors:

$$\begin{aligned} K_1 &= \Re\{K\hat{l}^{i\epsilon}\} = |K| \cos \psi \\ K_2 &= \Im\{K\hat{l}^{i\epsilon}\} = |K| \sin \psi, \end{aligned} \quad (6.18)$$

where $\psi = \hat{\psi} - \epsilon \ln \hat{l}$ for a given reference length, \hat{l} . A free choice of \hat{l} in the determination of ψ is proven by fulfilling a simple transformation rule from one value to another (Suo and Hutchinson, 1990): $\psi_2 = \psi_1 + \epsilon \ln(\hat{l}_2/\hat{l}_1)$ with ψ_1 and ψ_2 associated with l_1 and l_2 , respectively.

It is worth mentioning that since the analytical expressions (6.16) and (6.17) allow extracting the fracture parameters from numerical displacement data, the accuracy of this process is dependent upon the amount of data available along the crack flanks in the vicinity of the tip. Hence, a fine enough mesh in the region around the crack tip is required in the FEM calculations. Also, some accuracy difficulties may be encountered in determining the ERR and phase angle from the FEM displacements for models with high overall stiffness or when the angles are small (Smelser, 1979). The first issue can be overcome by using the J-integral and correlating the results of the both methods, whereas the second one is not critical as long as the interface bond is weak relative to the two adjoining materials. When this is the case, the crack will

most likely propagate along the interface with dominating failure mode I i.e. the angle of the stress intensity factor is not so important.

6.4 Numerical Solutions

In this section, we present the results of numerical evaluations of the fracture parameters of DCB-UBM, DCB and SCB sandwich specimens used for the interfacial bond strength assessment of sandwich panels. The calculations are carried out using the finite element code ABAQUS (2016). The interaction integral method is a built-in option of the package, but it is applied to bi-material interfaces consisting of two isotropic dissimilar materials only. The CSD method is programmed as an add-on subroutine in Matlab environment and can be utilized for orthotropic bi-material configurations. The subroutine extracts the displacements at given nodal sets from the ABAQUS’ result database file and, then, computes the required values (Burlayenko, et al, 2018, 2019a). The numerical results are compared with known analytical solutions or experimental data, when these are available in the literature.

6.4.1 DCB-UBM Sandwich Specimen

A DCB-UBM sandwich beam shown in Fig. 6.2a is selected as a first example. The DCB-UBM test method was first used in Sorensen et al (2006) for evaluating the interface strength of laminated composites and, was later extended to sandwich materials (Saseendran et al, 2018). In this test, the DCB specimen’s cracked edges are subjected to uneven bending moments, M_1 and M_2 (both being defined per unit specimen width, b), while the intact end of the specimen is fixed and generates the reactive moment $M_0 = M_1 + M_2$, as illustrated in Fig. 6.2a. The DCB-UBM test allows a variety of mixed mode I/II states by changing the ratio of the moments applied to the specimen, $MR = M_1/M_2$. Considering this, the crack is open at a negative ratio $MR < 0$, while a positive ratio $MR > 0$ generates sliding between the crack flanks. Also, it is known that the test enables to produce the crack length-inde-

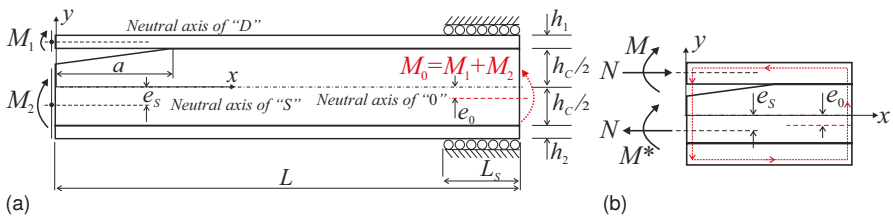


Fig. 6.2. DCB-UBM sandwich specimen: (a) geometry and loading; (b) local force and moment resultants.

pendent ERR and a constant mode mixity, when the moment ratio MR does not change during the crack growth.

The ERR can analytically be determined using the specimen geometry, elastic properties and applied external bending moments. The Euler-Bernoulli theory is utilized to model both the intact end of the specimen and each of the cracked edges. In the case of orthotropic face sheets and/or core, the principal material axes are aligned with the reference coordinate axes of the specimen and Young's moduli corresponding to the specimen axial rigidity are used in the formulation. The J -integral calculated along the outer boundaries of the specimen (Fig. 6.2b) leads to the following expression (Burlayenko et al, 2019c):

$$\mathcal{G}^{DCB-UBM} = \frac{1}{2b} \left\{ \frac{N^2}{(EA)_D} + \frac{N^2}{(EA)_S} + \frac{M^2}{(EI)_D} + \frac{M^{*2}}{(EI)_S} \right\}, \quad (6.19)$$

where $N = \gamma_2 M_0$, $M = M_1 - \gamma_3 M_0$ and

$$M^* = N \left(e_s + \frac{h_c}{2} + \frac{h_1}{2} \right) - M$$

are the equivalent axial load and bending moments, respectively, with

$$\gamma_2 = \frac{(EA)_D}{(EI)_0} \left(e_0 + \frac{h_c}{2} + \frac{h_1}{2} \right) \quad \text{and} \quad \gamma_3 = \frac{(EI)_D}{(EI)_0};$$

the parameters e_0 and e_s locate neutral axes of the intact part of specimen and the substrate, Fig. 6.2; $(EA)_i$ and $(EI)_i$ are generalized axial and flexural rigidities of the debonded portion "D", substrate "S" and intact part "0" of the specimen, i.e. $i = D, S, 0$. It should be noted that the expression of ERR (6.19) is applicable to DCB sandwich samples subjected to bending moments only, and it does not account for shear and root rotations (Thouless, 2018).

The fracture analysis was carried out for the DCB-UBM specimen with glass/epoxy composite face sheets of thicknesses $h_1 = h_2 = 2.4$ mm and a PVC H 100 core of thickness $h_c = 50$ mm. The resin rich layer between the face sheets and the core is considered to be a zero thickness, i.e. we neglect its influence on the interfacial fracture behaviour at all. The material properties of the sandwich specimen constituents are summarized in Table 6.1. The specimen of total length $L = 270$ mm with pre-crack of length $a = 90$ mm and a fixed end of length $L_s = 27$ mm was considered. It is assumed that the principal axes of the orthotropic materials of face sheet and core of the specimen are aligned with the co-ordinate axes, Fig. 6.2a. Also, the Young's moduli along the x -axis of the given orthotropic materials are adopted as the effective moduli for determining the generalized stiffness in (6.19).

A 2-D finite element model of the DCB-UBM specimen is developed using eight-node reduced integration plane strain finite elements (CPE8R) available in ABAQUS, Fig. 6.3. The finite element mesh contains a refinement in the vicinity of the crack-tip as shown in Fig. 6.3. In the calculations, the bending moments are applied to the DCB-UBM specimen edges at the points of the neutral axes of each subregion of the cracked part, Fig. 6.2a. Coupling kinematic constraints (ABAQUS, 2016) between

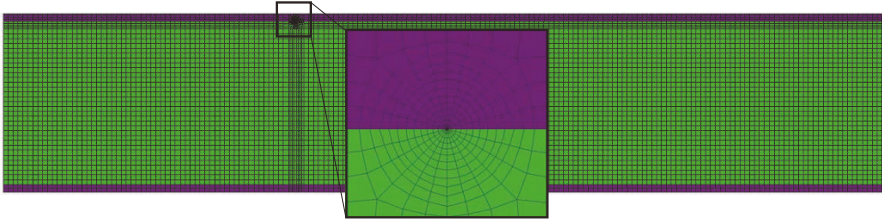


Fig. 6.3. A 2-D finite element model of the DCB-UBM sandwich specimen.

the set of nodes on the edge and the point of neutral axis are used to enforce equal rotation of the entire edge. The debonding in the specimen is modelled by a real gap of $\frac{h_1}{100}$ between the separated face sheet and core. The contact and friction conditions analogous to those in Burlayenko and Sadowski (2018) are introduced between the faces of the appropriate finite elements located along the pre-cracked bi-material interface.

To demonstrate the performance of the developed finite element model, different moment ratios, MR are considered in the calculations. Both the J -integral option of ABAQUS (2016) and the CSD method that post-processes the finite element results using the add-on Matlab-subroutine are utilized for computing the fracture characteristics. In all the calculations, the bending moments induced nearly the same ERR for each loading case. The values of ERR, \mathcal{G} computed numerically were compared with those found using the analytical formula (6.19) and the semi-analytical expression deduced in Kardomateas et al (2013). Good agreement between all the solutions has been achieved as seen in Table 6.2, where the phase angle ψ and the complex SIF components found with the CSD method are presented as well.

The contour plots of the stress tensor components associated with different moment ratios, MR listed in Table 6.2 are illustrated in Fig. 6.4, where the first row

Table 6.1

Material properties of the sandwich specimens.

Constituents	Material constants
Glass/Epoxy face sheet	$E_x = E_z = 16.5$ GPa; $E_y = 3.8$ GPa; $G_{xy} = G_{xz} = 1.3$ GPa; $G_{yz} = 6.6$ GPa; $\nu_{xy} = 0.05$; $\nu_{xz} = \nu_{yz} = 0.25$; $\rho = 1650$ kgm ⁻³
E-Glass/Epoxy face sheet	$E_x = 27.6$ GPa; $E_y = 25.2$ GPa; $E_z = 3$ GPa; $G_{xy} = 2.2$ GPa; $G_{yz} = G_{xz} = 1.2$ GPa; $\nu_{xy} = 0.24$; $\nu_{xz} = 0.12$; $\nu_{yz} = 0.06$; $\rho = 1800$ kgm ⁻³
Aluminium face sheet	$E_x = E_y = E_z = 69.5$ GPa; $\nu_{xy} = \nu_{xz} = \nu_{yz} = 0.3$; $\rho = 2700$ kgm ⁻³
PVC H 80 foam core	$E_x = E_y = E_z = 80$ MPa; $G_{xy} = G_{xz} = G_{yz} = 27.3$ MPa; $\nu_{xy} = \nu_{xz} = \nu_{yz} = 0.25$; $\rho = 80$ kgm ⁻³
PVC H 100 foam core	$E_x = E_y = E_z = 105$ MPa; $G_{xy} = G_{xz} = G_{yz} = 39.8$ MPa; $\nu_{xy} = \nu_{xz} = \nu_{yz} = 0.325$; $\rho = 100$ kgm ⁻³

of the images corresponds to σ_{11} , the second and third ones show σ_{22} , and σ_{12} , respectively. A complicated nature of the near-tip stress field is clearly observed here. One can see that the shear stress exists in the vicinity of the crack regardless of the loading cases as shown in the third row of Fig. 6.4. This is an apparent evidence of the mode mixity conditions being expected in sandwich structures. By comparing the values of the total ERR in Table 6.2, which are calculated by the FEM accounting for shear stress and by the analytical formula (6.19) neglecting it, one can conclude that the shear stress does not influence much on the total value of the ERR in this case. However, the sign of the shear stress ahead of the crack defines a favourable direction of interface crack propagation in the bi-material interface as mentioned in Adams et al (2012) and shown in Burlayenko et al (2019b).

6.4.2 DCB Sandwich Specimen

The second example considers symmetric ($h_1 = h_2 = h_f$) sandwich beam-like specimens exploited in the DCB test method. A scheme of the DCB test is illustrated in Fig. 6.5a. In this test, two piano hinges are usually used to transfer the loading to the edges of the specimen’s cracked region. The DCB sandwich specimen is subjected to an opening displacement by applying to the grip plates either two opposite transverse loads or an upward load and appropriate boundary constraints. The asymmetry of the specimen caused by the fact that the lower part (below the crack plane) being more rigid in flexure than the upper one (above the crack plane) may result in a slight rotation of the specimen at large opening displacements as shown in Fig. 6.5b, but usually such a rotation tends to be small in actual tests (Avilés and Carlsson, 2008).

The total ERR, generated by the interface crack during DCB testing can analytically be evaluated. Avilés and Carlsson (2008) used a model that considers the upper face sheet as a beam partially supported by an elastic foundation representing

Table 6.2
Calculations of the ERR and the phase angle with respect to the moment ratio MR .

	M_1 Nmm	75.6	103.42	123.4	104.13	73.8
	M_2 Nmm	-1512.2	-1034.2	-123.4	1041.3	1476
	MR	-0.05	-0.1	-1.0	0.1	0.05
ERR,	\mathcal{G}^{FEM} N/mm	0.399	0.399	0.403	0.399	0.377
	$\mathcal{G}^{(6.19)}$ N/mm	0.398	0.398	0.402	0.400	0.375
	$\mathcal{G}^{Kardomateas \text{ et al (2013)}}$ N/mm	0.351	0.363	0.376	0.365	0.332
Phase angle,	ψ^{FEM} deg.	30.26	11.31	-17.16	-51.87	-70.71
SIFs,	$\Re e \{ K \hat{h}_1^{i\epsilon} \}$ N/mm $^{\frac{3}{2}}$	9.652	10.96	10.74	6.914	3.585
	$\Im m \{ K \hat{h}_1^{i\epsilon} \}$ N/mm $^{\frac{3}{2}}$	5.631	2.192	3.313	8.809	10.24

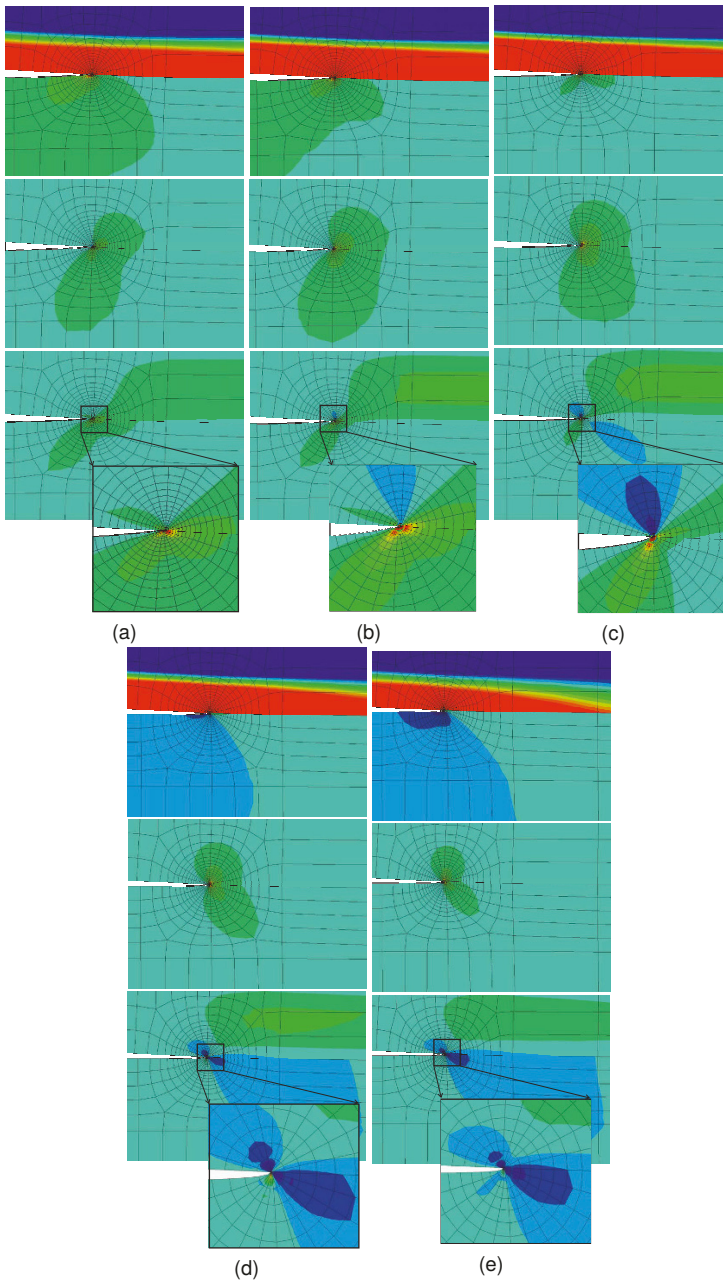


Fig. 6.4. Contour plots of the stress components at the crack tip of the DCB-UBM specimen w.r.t. the moment ratio MR equal to: (a) -0.05; (b) -0.1; (c) -1; (d) 0.1; and (e) 0.05.

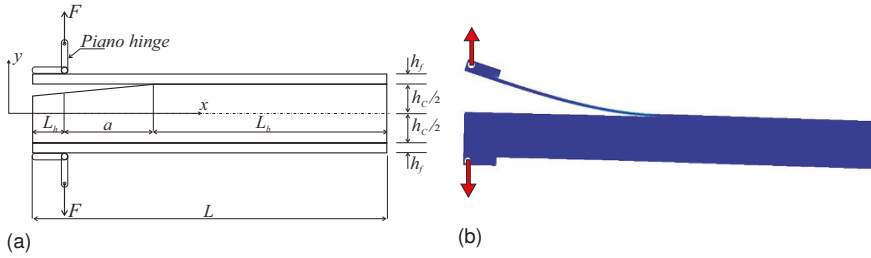


Fig. 6.5. Double Cantilever Beam sandwich specimen: (a) a schematic test; and (b) a deformed configuration.

a core. The model formulation was based on the assumptions of the Euler-Bernoulli beam theory and the Winkler elastic foundation theory for describing the deformation of the upper face sheet and the core of the DCB specimen, shown in Fig. 6.5b, respectively. The final expression of the ERR has a form:

$$\mathcal{G}^{DCB} = \frac{F^2}{2b^2} \left\{ \frac{1}{G_{xz}h_c} + \frac{a_0^2}{(D - B^2/A)} + \frac{12}{E_f h_f^3} \left(a_0^2 + 2a_0\eta^{1/4} + \eta^{1/2} \right) \right\}, \quad (6.20)$$

where the initial crack length $a = a_0$, the parameter $\eta = bh_f^3 E_f / (3K)$ and the elastic foundation coefficient $K = 2bE_c/h_c$. The 1-D extensional, coupling and bending stiffness coefficients A , B and D are computed as

$$A = E_f h_f + E_c h_c, \quad B = \frac{h_f h_c}{2} (E_c - E_f) \text{ and} \\ D = \frac{1}{12} \left\{ E_f (h_f^3 + 3h_f h_c^2) + E_c (h_c^3 + 3h_f h_c^2) \right\}$$

The finite element model similar to that used in the fracture analysis of the DCB-UBM specimen (Fig. 6.3) was adopted for the numerical calculations of the fracture parameters in the DCB specimens. To accurately reproduce the specific loading conditions in the finite element model, the hinges, modelled as rigid bodies, were linked to the face sheets of the sandwich beam using the TIE constraints (ABAQUS, 2016). Moreover, the external concentrated forces were applied to points in the centres of the hinge holes. Each the point was connected to the hole contour using Multi-point Constraints (MPCs). This type of constraint allows a hinge rotation relatively to the point of force application, i.e. it simulates the real conditions of the laboratory testing, Fig. 6.5b.

In the finite element predictions, DCB sandwich specimens of length $L = 250$ mm and width $b = 25$ mm with a PVC H 80 foam core of thickness $h_c = 25$ mm and either e-glass/epoxy composite or aluminium face sheets of thickness, h_f ranging from 0.1 mm to 10 mm at different pre-crack lengths $a=30,50,70,90$ and 110 mm are analysed. The properties of the sandwich specimen constituents are shown in Table 6.1. The comparisons of the ERR computed by resolving a 2-D elasticity problem

with the FEM in conjunction with the J -integral method and obtained using the analytic expression (6.20) based on the classical beam theory are presented in Fig. 6.6. The plot illustrates a scattering of relative errors between both the results

$$\Delta\mathcal{G} = \frac{|\mathcal{G} - \mathcal{G}^{DCB}|}{\mathcal{G}} \times 100\%$$

with respect to appropriate linear trend lines depending on the face sheet thickness and the pre-crack length. It is found that the analytical predictions mainly overestimate the numerical ones, but the differences between them do not exceed 50% and the error tends to decrease with thickening the face sheet. Also, the findings observed in Fig. 6.6 show that the differences between the two solutions are smaller for the specimens with composite face sheets (Fig. 6.6a) than with stiffer aluminium ones, i.e. for a lower material ratio, E_f/E_c . Herewith, the differences become smaller with increasing the pre-crack length in both types of the specimens. Thereby, the numerical results clearly demonstrate the limitations of the analytic formula (6.20) and justify the importance of accounting for shear deformation in the vicinity of the crack tip for accurate calculations of the ERR.

The other validation of the finite element model is done by comparing numerically computed ERRs and those obtained experimentally in Avilés and Carlsson (2008). Two types of DCB sandwich specimens denoted as 'thick DCB' and 'thin DCB' are considered. All details related to these two tests can be found in the mentioned source and the references cited there. The results of the comparison are displayed in Fig. 6.7 for a normalized value of the ERR,

$$G^* = \frac{G}{F^2}.$$

It is seen that the finite element predictions are satisfactory close to the measured data for all the crack lengths studied in both the specimens. Also, it is obvious that the trends of changing the ERRs with increasing the crack length observed

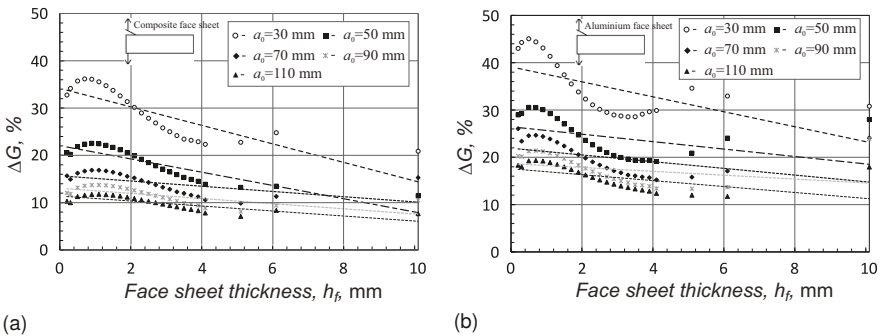


Fig. 6.6. The variation of relative errors $\Delta\mathcal{G} = \frac{|\mathcal{G} - \mathcal{G}^{DCB}|}{\mathcal{G}} \times 100\%$ vs. the face sheet thickness h_f for different pre-crack lengths in the DCB test with: (a) composite face sheets; and (b) aluminium face sheets.

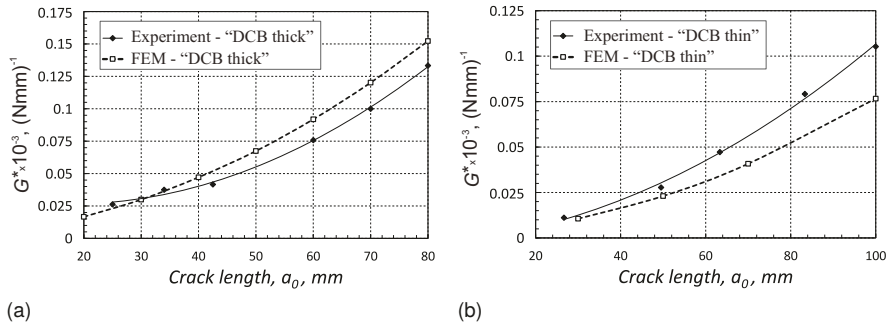


Fig. 6.7. Comparison between numerical and experimental ERRs vs. crack length for DCB sandwich specimens: (a) thick sample; and (b) thin sample.

in the experiments and predicted by the finite element analysis show quite similar behaviours. Hence, one can conclude that the computational models can accurately represent the actual DCB tests.

The ERR and the phase angle, computed by both the IIM and the CSD method for a 150 mm length and 27 mm width DCB sandwich specimen with pre-crack of $a_0 = 50$ mm, which is made up of the PVC H-100 core of thickness $h_c = 38$ mm and the e-glass/epoxy composite face sheets of thickness $h_f = 2.4$ mm, subjected to a unit load are presented in Table 6.3. It is seen that although the IIM uses effective elastic properties reduced to isotropic materials instead of actual orthotropic ones, both the numerical techniques give quite close results. Also, the calculated fracture characteristics clearly exhibit the dominated mode I deformation of the DCB specimen at the given material and geometrical parameters. The distribution of near-tip stress fields in the DCB specimen is demonstrated in Fig. 6.8. The plots show that the maximum longitudinal normal stress is primarily developed in the upper (debonded) face sheet due to its high in-plane and bending resistance, Fig. 6.8a, whereas the transverse normal stress is the biggest in the region around the crack tip, Fig. 6.8b. In addition, the shear stress exists at the crack tip, Fig. 6.8c. However, this stress component is smaller about one order of magnitude than the transverse normal stresses in the same region. Despite its relatively small magnitude, the sign of shear stress in the vicinity of the crack tip defines the orientation of presumed crack growth direction (Adams et al, 2012). As seen in Fig. 6.8c, the shear stress

Table 6.3

Calculations of the ERR, SIFs and phase angle for DCB and SCB specimens.

Specimen type	Method	\mathcal{G} N/mm	$\Re\{K\hat{h}_1^{i\epsilon}\}$ N/mm ^{3/2}	$\Im\{K\hat{h}_1^{i\epsilon}\}$ N/mm ^{3/2}	ψ deg.
DCB	IIM	67.76e-6	0.1299	-0.0321	-13.93
	CSD	67.21e-6	0.1356	-0.0448	-18.29
SCB	IIM	12.39e-6	0.0689	-0.011	-9.08
	CSD	12.01e-6	0.0586	-0.015	-13.03

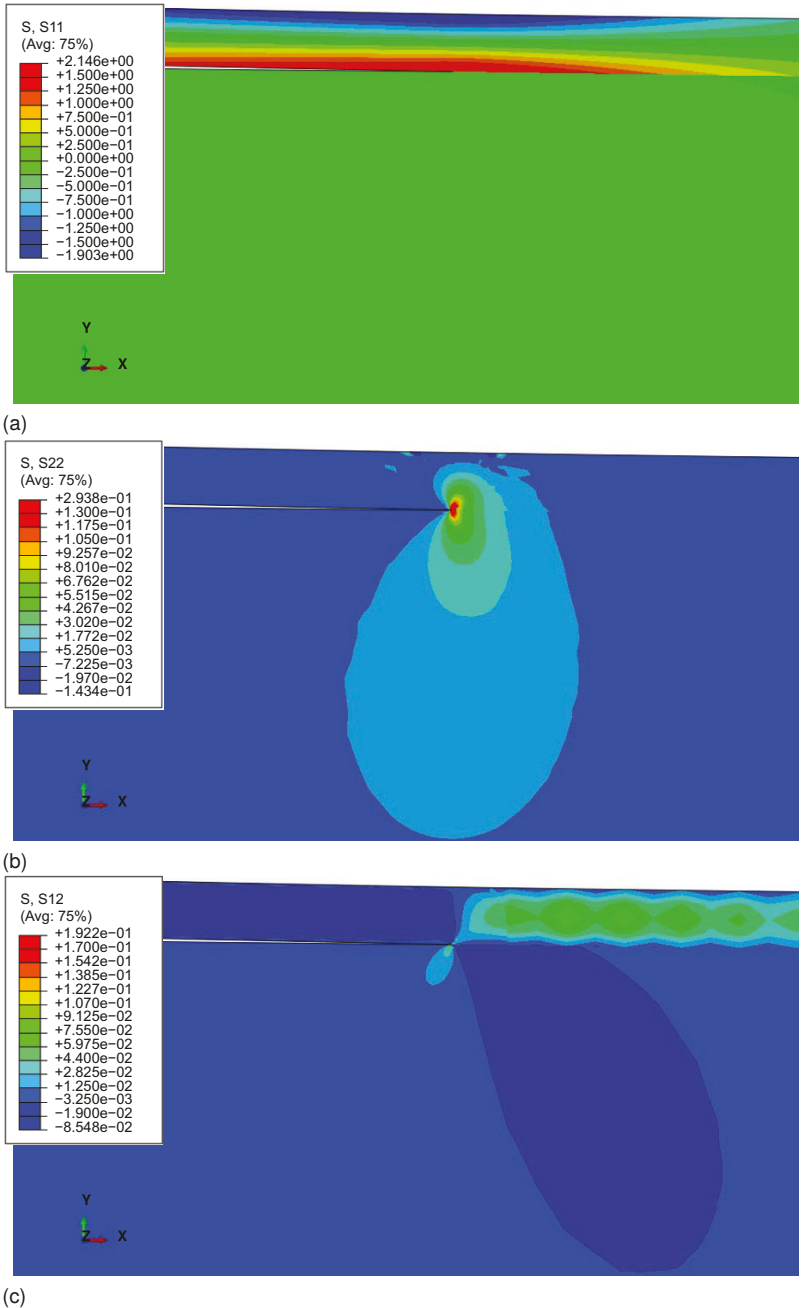


Fig. 6.8. Stress distribution in front of the debonding in DCB specimen: (a) longitudinal normal stress σ_{11} ; (b) transverse normal stress σ_{22} ; and (c) in-plane shear stress σ_{12} .

arisen in the area around the crack tip is strongly negative that confirms the finding for a negative phase angle, ψ observed in Table 6.3. This value predicts the crack propagation direction either into the face sheet material or along the face sheet/core interface during this test method. The latter crack growth path is more likely due to a weaker crack resistance of the face sheet/core interface compared with the face sheet strength.

6.4.3 SCB Sandwich Specimen

The last example is a SCB sandwich specimen, which presents the second class of test methods generating dominated mode I fracture by peeling the face sheet from the core. A SCB test method with given boundary conditions and schematic loading is illustrated in Fig 6.9a. As seen, only one upward force, F is applied to the specimen through a steel hinge mounted on the upper debonded face sheet, while the lower one is affixed to a rigid base. Moreover, to provide an accurate interface toughness measurement and to ensure that bending is the primary form of loading, the dimensions of the SCB specimen and the load rod length, h_F have to satisfy sizing requirements defined in Ratcliffe and Reeder (2011).

An analytical estimation of the total ERR \mathcal{G}^{SCB} can be deduced from a kinematic analysis of the SCB sandwich sample (Fig. 6.9b) within the elastic foundation approach. Then, the final expression can be written as follows (Rinker et al, 2011):

$$\mathcal{G}^{SCB} = \frac{4\lambda F^2}{2bK} \left\{ \lambda^3 a_0^2 + 2\lambda^2 a_0 + \lambda + \frac{K}{4b\lambda k G_{xz}^f h_f} \right\}, \tag{6.21}$$

where the parameter

$$\lambda = \left(\frac{K}{4D_f} \right)^{1/4}$$

with

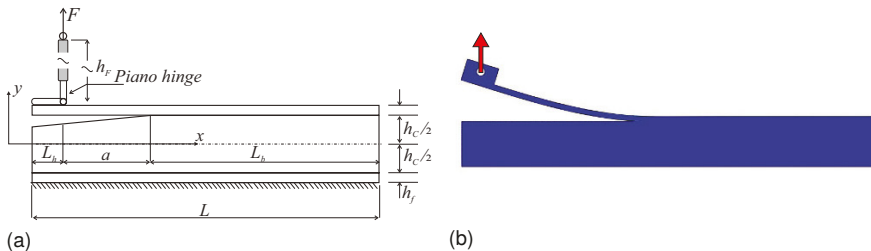


Fig. 6.9. Single Cantilever Beam sandwich specimen: (a) a schematic test; and (b) a deformed configuration.

$$D_f = \frac{bh_f^3}{12}$$

and the foundation coefficient

$$K = \frac{bE_c}{h_c}$$

is identical to that in (6.20).

In the context of comparative studies, both the analytic expression (6.21) and the general formula of LEFM (6.6) are used to calculate the ERR for a variety of SCB specimens distinguished by the pre-crack length and the face sheet thickness. The SCB specimens of a 250 mm length made up of a 50 mm thick PVC H-80 foam core and either glass/epoxy composite or aluminium face sheets of the thickness varying from 0.1 to 10 mm are analysed. The comparisons, presented by relative errors between the results computed with FEM and those found analytically

$$\Delta G = \frac{|\mathcal{G} - \mathcal{G}^{SCB}|}{\mathcal{G}} \times 100\%$$

the same as in Sect. 6.4.2, are shown in Fig. 6.10. Analogously to the predictions for the DCB specimens, it was found out that the approximate analytic formula (6.21) for the SCB specimens also mainly overestimates the ERR, especially it is apparent for short pre-cracks, but the maximal deviation does not exceed 50% in our study again. Herewith, the aluminium-PVC material configuration corresponding to a higher E_f/E_c ratio leads to bit larger differences than those in the composite-PVC system with a lower E_f/E_c ratio. This is similar to the results observed for DCB specimens considered in the previous example. Also, the errors are less for longer pre-cracks and thicker face sheets.

The comparison of the ERR values over a range of crack lengths, which are predicted with the finite element model and those known from experimental studies available in Li and Carlsson (1999), is illustrated in Fig. 6.11. The SCB specimens, tested in Li and Carlsson (1999) as tilted sandwich debond (TSD) samples at the

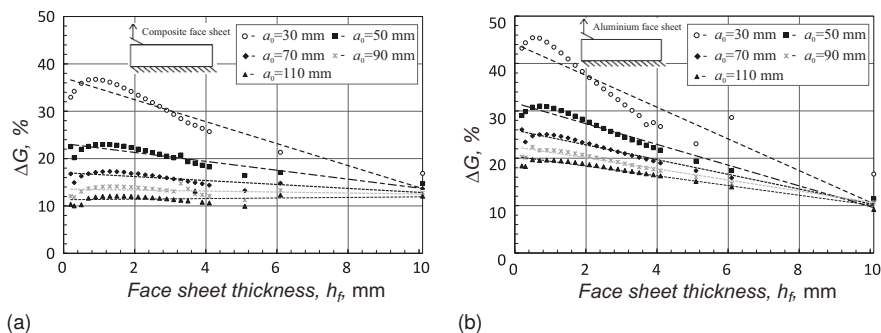


Fig. 6.10. The variation of relative errors ΔG vs. the face sheet thickness h_f for different pre-crack lengths in the SCB test with: (a) composite face sheets; and (b) aluminium face sheets.

zero tilt angle, are considered for this comparative study. Mechanical properties and dimensions of the specimens as well as the details of laboratory testing can be found in the original reference. From Fig. 6.11 one can see that the dimensionless ERRs,

$$\mathcal{G}^* = \mathcal{G} \frac{E_f h_f^3}{(Fb)^2}$$

obtained numerically and the experimental values correlate quite well between each other. This confirms high-fidelity modelling results which are provided by the finite element models developed for the SCB sandwich specimens.

In Table 6.3, the finite element calculations performed for obtaining the ERR, SIFs and phase angle of a 210 mm length and 38 mm width SCB sandwich specimen consisting of 3.6 mm thick glass/vinylester face sheets bonded to a 50 mm thick PVC H-100 foam core are summarized for the case of unit transverse force and pre-crack length of $a_0 = 50$ mm. One can see that the results provided by the IIM approach and the SCD method are in good agreement similar to the case of the DCB specimen. The distribution of near-tip stress components, associated with the deformed state of this SCB specimen is plotted in Fig. 6.12. The analysis shows that the normal longitudinal and transversal stresses have profiles close to those observed in the DCB specimen (Fig. 6.8a and b), while the magnitude of the shear stress is visibly smaller than that in the DCB specimen (Fig. 6.8c). The reason of such similarity is that the face sheets of both the specimens behave in the same manner under the applied upward force, but the difference in the shear stresses is due to additional contribution of bending moment and shear force induced by a downward force acting on the lower part (below the crack plane) of the DCB sample. Hence, it is reasonable to expect that such the deformation state with extra shear and normal stresses at the crack tip can give rise to a more complicated cracking behaviour in the DCB specimen. Thus, the SCB specimen is able to produce dominated mode I deformation conditions with less limits than the DCB sample. This conclusion correlates with a smaller negative phase angle in the SCB test sample compared with the DCB specimen for the given face sheets and core materials and specimens' geometries as displayed in Table 6.3.

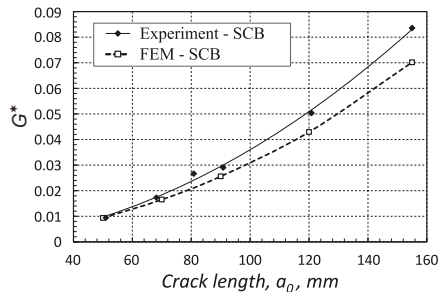
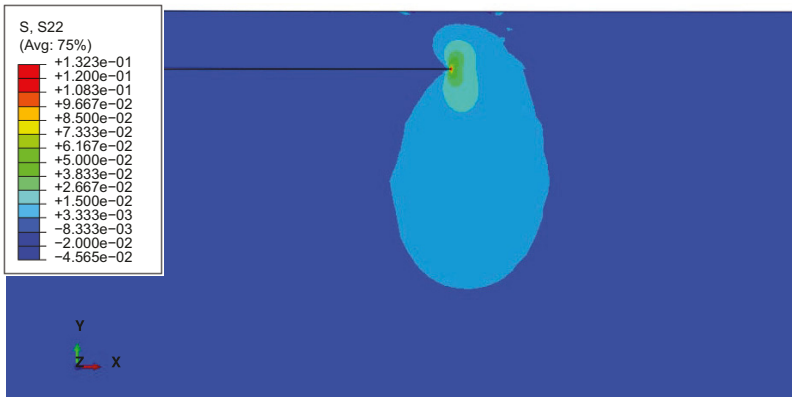


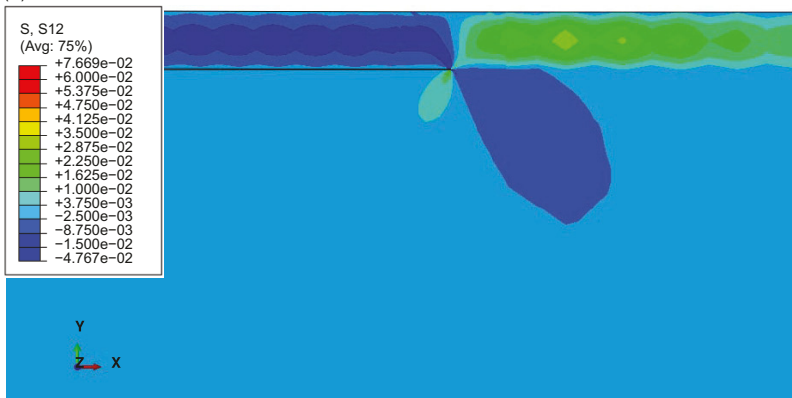
Fig. 6.11 Comparison between numerical and experimental ERRs vs. crack length for the SCB sandwich specimen.



(a)



(b)



(c)

Fig. 6.12. Stress distribution in front of the debonding in SCB specimen: (a) longitudinal normal stress σ_{11} ; (b) transverse normal stress σ_{22} ; and (c) in-plane shear stress σ_{12} .

6.5 Conclusions

In this research, efforts have been focused on evaluating the fracture parameters in virtual tests related to the assessment of face sheet-to-core interface strength in sandwich panels. Both analytical methods based on beam-like models and two-dimensional finite element analyses with ABAQUS have been applied to the computation of ERR, SIFs and phase angle in popular DCB-UBM, DCB and SCB sandwich fracture specimens. The numerically obtained results have been extracted from the finite element solutions using two techniques such as the IIM and the CSD method, which are suitable for analysing a bi-material configuration of the sandwich panel interfaces in perspective of the evaluation of mode mixity. Also, the use of these methods in finite element predictions is very efficient since they have a straightforward finite element formulation that allows one exploiting a whole power of general purpose finite element packages like the ABAQUS code.

The parametric studies in the 2-D fracture analysis of the sandwich specimens made up of either aluminium or various composite laminated face sheets and PVC foam core of different thicknesses have been carried out. Results received from the finite element simulations of all the specimens were compared with those obtained by the analytical approximate formulae and the experimental data available in the literature for DCB and SCB fracture tests. Generally, good correlation between the results has been observed. Evaluating the fracture parameters of the hypothetical sandwich specimens, it was found that the shear stress exists in the vicinity of the crack tip regardless of the specimen type and the material and geometrical configurations of those specimens. Hence, it has been recognised that the mode mixity is an inherent characteristic of sandwich panels' deformed state. This characteristic should be known a priori to accurately estimate the strength of the face sheet-to-core interface and to simulate the debonding fracture along an appropriate crack growth path in sandwich panels. In turn, the crack path can be predicted based on a mode mixity fracture criterion, which could be known after performing a comprehensive actual and virtual test campaign.

Finally, it needs to mention that although the present results are demonstrated only for the selected three sandwich samples, the 2-D finite element techniques used in this research can be applied to virtual tests of sandwich specimens of any other geometry and boundary conditions. Thus, the results presented in the paper may provide a benchmark for studying the considered DCB-UBM, DCB and SCB sandwich fracture specimens and, on the other hand, they may guide further research associated with the assessment of interfacial strength of sandwich panels.

Acknowledgements The first author would like to mention that this research has been conducted during his stay at the Institute of Mechanics of Otto-von-Guericke-Universität Magdeburg, which was supported by the German Academic Exchange Service (DAAD) Funding Programme ID No. 57440915.

References

- ABAQUS (2016) User's manual, ver. 2016. Dassault Systèmes Simulia Corp., Providence, RI, USA
- Adams DO, Nelson J, Bluth Z (2012) Development and evaluation of fracture mechanics test methods for sandwich composites. In: Proceedings of the 2012 Aircraft Airworthiness and Sustainment Conference, 2-5 April 2012, Baltimore, MD, US
- Altenbach H, Altenbach J, Kissing W (2018) Mechanics of Composite Structural Elements, 2nd edn. Springer
- Andrews MG, Massabò R (2007) The effects of shear and near tip deformations on energy release rate and mode mixity of edge-cracked orthotropic layers. *Engineering Fracture Mechanics* 74(17):2700 – 2720
- Avilés F, Carlsson LA (2008) Analysis of the sandwich DCB specimen for debond characterization. *Engineering Fracture Mechanics* 75(2):153 – 168
- Beuth JL (1996) Separation of crack extension modes in orthotropic delamination models. *International Journal of Fracture* 77:305 – 321
- Bruno D, Greco F (2001) Mixed mode delamination in plates: a refined approach. *International Journal of Solids and Structures* 38(50):9149 – 9177
- Burlayenko VN, Sadowski T (2011a) Dynamic analysis of debonded sandwich plates with flexible core - numerical aspects and simulation. In: Altenbach H, Eremeyev VA (eds) *Shell-like Structures*, Springer, Heidelberg, *Advanced Structured Materials*, vol 15, pp 415 – 440
- Burlayenko VN, Sadowski T (2011b) Numerical modeling of sandwich plates with partially dedonded skin-to-core interface for damage detection. In: DeRoeck G, Degrande G, Lombaert G, Müller G (eds) *Proceedings of the 8th International Conference on Structural Dynamics (EURODYN)*, Leuven, Belgium, pp 2242–2249
- Burlayenko VN, Sadowski T (2014) Simulations of post-impact skin/core debond growth in sandwich plates under impulsive loading. *Journal of Applied Nonlinear Dynamics* 3(4):369 – 379
- Burlayenko VN, Sadowski T (2018) Linear and nonlinear dynamic analyses of sandwich panels with face sheet-to-core debonding. *Shock and Vibration* 2018(ID 5715863)
- Burlayenko VN, Sadowski T, Pietras D (2018) A numerical analysis of near tip fields in a bending moment-loaded double cantilever sandwich beam fracture specimen. *Bulletin of NTU "KhPI"* 3(1279):9 – 14
- Burlayenko VN, Altenbach H, Sadowski T (2019a) Dynamic fracture analysis of sandwich composites with face sheet/core debond by the finite element method. In: Altenbach H, Belyaev A, Eremeyev V, Krivtsov A, Porubov A (eds) *Dynamical Processes in Generalized Continua and Structures*, *Advanced Structured Materials*, vol 103, Springer, Singapore, pp 163–194
- Burlayenko VN, Pietras D, Sadowski T (2019b) Influence of geometry, elasticity properties and boundary conditions on the Mode I purity in sandwich composites. *Composite Structures* 223, 110942

- Burlayenko VN, Sadowski T, Pietras D (2019c) Influence of dynamic loading on fracture behaviour of DCB sandwich specimen. ITM Web Conf 29, 02003 DOI 10.1051/itmconf/20192902003
- Cantwell W, Davies P (1996) A study of skin-core adhesion in glass fibre reinforced sandwich materials. *Applied Composite Materials* 3(6):407 – 420
- Cantwell WJ, Scudamore R, Ratcliffe J, Davies P (1999) Interfacial fracture in sandwich laminates. *Composites Science and Technology* 59(14):2079 – 2085
- Carlsson LA, Sendlein LS, Merry SL (1991) Characterization of face sheet/core shear fracture of composite sandwich beams. *Journal of Composite Materials* 25(1):101 – 116
- Chatterjee VA, Verma SK, Bhattacharjee D, Biswas I, Neogi S (2019) Enhancement of energy absorption by incorporation of shear thickening fluids in 3d-mat sandwich composite panels upon ballistic impact. *Composite Structures* 225:111,148
- Crews JH, Shivakumar KN, Raju IS (1991) Strain energy release rate distributions for double cantilever beam specimens. *AIAA Journal* 29(10):1686 – 1691
- Davidson BD, Hu H, Schapery RA (1995) An analytical crack-tip element for layered elastic structures. *Trans ASME Journal of Applied Mechanics* 62(2):295 – 305
- Davis BR, Wawrzynek PA, Ingraffea AR (2014) 3-D simulation of arbitrary crack growth using an energy-based formulation – Part I: Planar growth. *Engineering Fracture Mechanics* 115:204 – 220
- Dillard DA, Singh HK, Pohlit DJ, Starbuck JM (2009) Observations of decreased fracture toughness for mixed mode fracture testing of adhesively bonded joints. *Journal of Adhesion Science and Technology* 23(10 - 11):1515 – 1530
- Farhana N, Majid MA, Paulraj M, Ahmadhildi E, Fakhzan M, Gibson A (2016) A novel vibration based non-destructive testing for predicting glass fibre/matrix volume fraction in composites using a neural network model. *Composite Structures* 144:96 – 107
- Fichter WB (1983) The stress intensity factor for the double cantilever beam. *International Journal of Fracture* 22:133 – 143
- Georgiadis HG, Papadopoulos GA (1990) Elastostatics of the orthotropic double-cantilever-beam fracture specimen. *Zeitschrift für angewandte Mathematik und Physik ZAMP* 41(6):889 – 899
- Harne RL, Blanc C, Remillieux MC, Burdisso RA (2012) Structural-acoustic aspects in the modeling of sandwich structures and computation of equivalent elasticity parameters. *Thin-Walled Structures* 56:1 – 8
- Hernández-Pérez A, Avilés F, Carlsson L (2013) Evaluation of the plate twist test to characterize mode iii fracture of sandwich panels with a face/core interface crack. *Engineering Fracture Mechanics* 104:41 – 55
- Hutchinson JW, Suo Z (1991) Mixed mode cracking in layered materials. In: Hutchinson JW, Wu TY (eds) *Advances in Applied Mechanics*, vol 29, Elsevier, pp 63 – 191
- Idriss M, Mahi AE (2017) Effects of debonding length on the fatigue and vibration behaviour of sandwich composite. *Journal of Composite Materials* 51(13):1839 – 1847

- Kardomateas GA, Berggreen C, Carlsson LA (2013) Energy-release rate and mode mixity of face/core debonds in sandwich beams. *AIAA Journal* 51(4):885–892
- Kiss B, Szekrényes A (2019) Fracture and mode mixity analysis of shear deformable composite beams. *Archive of Applied Mechanics* 89(12):2485 – 2506
- Kuang-Chong W (1991) Explicit crack-tip fields of an extending interface crack in an anisotropic bimaterial. *International Journal of Solids and Structures* 27(4):455 – 466
- Kuna M (2013) *Finite Elements in Fracture Mechanics: Theory - Numerics - Applications*. Springer, Dordrecht
- Li S, Wang J, Thouless MD (2004) The effects of shear on delamination in layered materials. *Journal of the Mechanics and Physics of Solids* 52(1):193 – 214
- Li X, Carlsson LA (1999) The tilted sandwich debond (tsd) specimen for face/core interface fracture characterization. *Journal of Sandwich Structures & Materials* 1(1):60–75
- Lu L, Song H, Yuan W, Huang C (2017) Baseline-free damage identification of metallic sandwich panels with truss core based on vibration characteristics. *Structural Health Monitoring* 16(1):24 – 38
- Massabò R, Campi F (2014) Assessment and correction of theories for multilayered plates with imperfect interfaces. *Meccanica* 50:1045–1071
- Matos PPL, McMeeking RM, Charalambides PG, Drory MD (1989) A method for calculating stress intensities in bimaterial fracture. *International Journal of Fracture* 40:235 – 254
- Mouritz AP (2017) Progress toward explosive blast-resistant naval composites. In: Mouritz AP, Rajapakse YD (eds) *Explosion Blast Response of Composites*, Woodhead Publishing, pp 375 – 408
- Mustapha S, Ye L (2013) 10 - non-destructive evaluation (nde) of composites: assessing debonding in sandwich panels using guided waves. In: Karbhari VM (ed) *Non-Destructive Evaluation (NDE) of Polymer Matrix Composites*, Woodhead Publishing Series in Composites Science and Engineering, Woodhead Publishing, pp 238 – 278
- Odessa I, Frostig Y, Rabinovitch O (2018) Modeling of interfacial debonding propagation in sandwich panels. *International Journal of Solids and Structures* 148-149:67 – 78
- Pölöskei T, Szekrényes A (2017) Quasi-periodic excitation in a delaminated composite beam. *Composite Structures* 159:677 – 688
- Prasad S, Carlsson LA (1994) Debonding and crack kinking in foam core sandwich beams — I. Analysis of fracture specimens. *Engineering Fracture Mechanics* 47(6):813 – 824
- Qu Y, Meng G (2017) Nonlinear vibro-acoustic analysis of composite sandwich plates with skin–core debondings. *AIAA Journal* 55(5):1723 – 1733
- Quispitupa A, Berggreen C, Carlsson LA (2009) On the analysis of a mixed mode bending sandwich specimen for debond fracture characterization. *Engineering Fracture Mechanics* 76(4):594 – 613

- Ratcliffe JG, Reeder JR (2011) Sizing a single cantilever beam specimen for characterizing facesheet–core debonding in sandwich structure. *Journal of Composite Materials* 45(25):2669 – 2684
- Rice JR (1988) Elastic fracture mechanics concepts for interfacial cracks. *Trans ASME Journal of Applied Mechanics* 55(1):98 – 103
- Rinker M, John M, Zahlen PC, Schäuble R (2011) Face sheet debonding in CFRP/PMI sandwich structures under quasi-static and fatigue loading considering residual thermal stress. *Engineering Fracture Mechanics* 78(17):2835 – 2847
- Rodríguez-González J, May-Pat A, Avilés F (2014) A beam specimen to measure the face/core fracture toughness of sandwich materials under a tearing loading mode. *International Journal of Mechanical Sciences* 79:84 – 94
- Ryoji Y, Sang-Bong C (1989) Efficient boundary element analysis of stress intensity factors for interface cracks in dissimilar materials. *Engineering Fracture Mechanics* 34(1):179 – 188
- Samborski S (2018) Prediction of delamination front's advancement direction in the CFRP laminates with mechanical couplings subjected to different fracture toughness tests. *Composite Structures* 202:643 – 650
- Saseendran V, Carlsson LA, Berggreen C (2018) Shear and foundation effects on crack root rotation and mode-mixity in moment- and force-loaded single cantilever beam sandwich specimen. *Journal of Composite Materials* 52(18):2537 – 2547
- Seguel F, Meruane V (2018) Damage assessment in a sandwich panel based on full-field vibration measurements. *Journal of Sound and Vibration* 417:1 – 18
- Shih CF, Asaro RJ (1988) Elastic-plastic analysis of cracks on bimaterial interfaces: Part I — Small scale yielding. *Trans ASME Journal of Applied Mechanics* 55(2):299 – 316
- Shivakumar KN, Smith SA (2004) In situ fracture toughness testing of core materials in sandwich panels. *Journal of Composite Materials* 38(8):655 – 668
- Smelser RE (1979) Evaluation of stress intensity factors for bi-materials bodies using numerical crack flank displacement data. *International Journal of Fracture* 15:135 – 315
- Sorensen B, Jorgensen K, Jacobsen T, Ostergaard R (2006) DCB-specimen with uneven bending moments. *International Journal of Fracture* 141:163–176
- Suo Z, Hill R (1990) Singularities, interfaces and cracks in dissimilar anisotropic media. *Proceedings of the Royal Society of London A Mathematical and Physical Sciences* 427(1873):331 – 358
- Suo Z, Hutchinson JW (1990) Interface crack between two elastic layers. *International Journal of Fracture* 43:1 – 18
- Thouless MD (2018) Shear forces, root rotations, phase angles and delamination of layered materials. *Engineering Fracture Mechanics* 191:153 – 167
- Triantafillou TC, Gibson LJ (1987) Failure mode maps for foam core sandwich beams. *Materials Science and Engineering* 95:37 – 53
- Valvo PS, Sorensen BF, Toftegaard HL (2015) Modelling the double cantilever beam test with bending moments by using bilinear discontinuous cohesive laws. In: *Proceedings of the 20th International Conference on Composite Materials Copenhagen, 19-24 July 2015*

- Wang J, Qiao P (2004) On the energy release rate and mode mix of delaminated shear deformable composite plates. *International Journal of Solids and Structures* 41(9):2757 – 2779
- Wang TC, Shih CF, Zhigang S (1992) Crack extension and kinking in laminates and bicrystals. *International Journal of Solids and Structures* 29(3):327 – 344
- Williams JG (1988) On the calculation of energy release rate for cracked laminates. *International Journal of Fracture* 36:101 – 119
- Williams TO, Addessio FL (1997) A general theory for laminated plates with delaminations. *International Journal of Solids and Structures* 34(16):2003 – 2024
- Willis JR (1971) Fracture mechanics of interfacial cracks. *Journal of the Mechanics and Physics of Solids* 19(6):353 – 368
- Xie S, Liang X, Zhou H (2016) Design and analysis of a composite energy-absorbing structure for use on railway vehicles. *Proceedings of the Institution of Mechanical Engineers, Part F: Journal of Rail and Rapid Transit* 230(3):825 – 839



Chapter 7

Asymptotic Approximations for Frequencies and Vibration Modes of Cylindrical Shell Stiffened by Annular Plates

Sergei B. Filippov

Abstract Low frequencies and vibration modes of a closed circular cylindrical shell joined with annular plates are obtained by means of asymptotic methods. Two types of vibrations, corresponding to narrow and wide plates, are analyzed. It is shown that narrow plates can be considered as circular beams. For wide plates joined with a cylindrical shell the couple vibration problem in the first approximation is reduced to the eigenvalue problem describing the plate vibrations. An approximate solution of the last problem is obtained with the help of the perturbation approach.

Key words: Ring-stiffened shell · Annular plate · Vibration frequency · Asymptotic methods

7.1 Introduction

Ring-stiffened shells are extensively applied in submarine, vehicles, pipelines and aerospace engineering. It is therefore necessary to create accurate models of physical processes in such constructions. However, almost in all studies of ring-stiffened shells, including Filippov (2006b); Hodges et al (1985); El Raheb and Babcock (1981); Ross et al (1996), the rings have been treated as circular beams.

There are, at least, two reasons to consider the wide ring as the annular plate. First, the flexural stiffness of the beam in its plane c_b increases rapidly with ring width b . However, for the wide ring its stress-strain state localizes near the inner boundary of the ring, which is attached to cylindrical shell (Filippov, 2006a). Therefore change in b almost have no influence upon the stiffness c of the sufficiently wide ring. To catch this effect one should consider the wide ring as an annular plate. It is especially

Sergei B. Filippov
St. Petersburg State University, 7/9 University Embankment, St. Petersburg, 199034, Russia
e-mail: s_b_filippov@mail.ru

important because the stiffness c has an determinative influence on the vibration frequencies.

Secondly, vibrations of the shell, stiffened by a narrow ring, differs very much from vibrations of the shell stiffened by a wide ring. If the width of the ring b is sufficiently small, then the vibration mode of the stiffened shell is similar to the mode of the shell without rings, and the shell's surface is covered by a series of pits stretched along the generatrix of a cylinder. In this case it is possible consider the ring as a circular beam. Such vibrations we call the vibrations of the first type.

At increase in b the frequencies grows until the vibrations of the first type replace with the vibrations of the second type. The vibration mode of the second type is localized on the surface of the ring and the cylindrical shell itself does not actually deform. After the vibration mode changed, the further increase in b leads to reduction of frequencies. For studying the vibrations of the second type the beam's model can not be used, and one must consider the ring as an annular plate.

Various methods for the analysis of ring-stiffened shells vibrations have been developed. In Yang and Zhout (1995) and Loy and Lam (1997) natural frequencies of stiffened shells are obtained by Fourier expansions and Rayleigh-Ritz procedure. In Samanta and Mukhopadhyay (2004) for vibration analysis of ring-stiffened shell finite element method was used.

The equations describing a thin shells contain the dimensionless shell thickness h as a small parameter. Hence, for the solution of these equations it is possible to use asymptotic methods (Bauer et al, 2015; Tovstik and Smirnov, 2001). To get the approximate solutions of the shell's equations in this paper the Vishik-Lyusternik algorithm (Bauer et al, 2015; Vishik and Lyusternik, 1957) is applied. We seek solutions of shell equations as a sum of slowly varying functions and edge effect integrals. Thus the initial singularly perturbed system of differential equations is reduced to an approximate system of the smaller order (Tovstik and Smirnov, 2001).

The major problem in the asymptotic analyses of the ring-stiffened shell is a separation of the continuity conditions on main and additional conditions. The main conditions are used as boundary conditions for the approximate system. From additional conditions one can find arbitrary constants in the edge effect functions. As a rule, to get the main and additional conditions, it is necessary to make linear combinations of the continuity conditions.

In the case of the second type vibrations the eigenvalue problem for a cylindrical shell joined with annular plates in the first asymptotic approximation can be split into the five separated problems. Most important of them is the eigenvalue problem, describing vibrations of the annular plate. In assumption that the ratio of the plate width to the radius of its inner edge is small, approximate formulas for the frequencies was obtained.

The asymptotic analyses of low-frequency vibrations of the cylindrical shell stiffened at an edge by the annular plate was fulfilled in Filippov (2004); Filippov and Haseganu (2003). In the present contribution frequencies and vibration modes of cylindrical shell, stiffened by annular plates located on inner parallels of the shell, are evaluated.

7.2 Basic Equations

We consider small free low-frequency vibrations of the thin cylindrical shell stiffened by n identical annular plates. The plates are located on the parallels $s = s_i, i = 1, 2, \dots, n$ of the shell, where s is the dimensionless axial coordinate on the shell's middle surface. The radius of the cylindrical shell R is taken as the characteristic size. One of the plates is shown in Fig. 7.1.

After the separation of variables the non-dimensional differential equations describing free vibrations of a cylindrical shell (Filippov, 2004) may be represented in the form

$$\begin{aligned}
 T_1' + mS + \lambda u &= 0, & S' - mT_2 + Q_2 + 2H' + \lambda v &= 0, \\
 Q_1' + mQ_2 - T_2 + \lambda w &= 0, & Q_1 &= M_1' + 2mH, & Q_2 &= -mM_2, \\
 M_1 &= \mu^4(\vartheta_1' + \nu m\vartheta_2), & M_2 &= \mu^4(m\vartheta_2 + \nu\vartheta_1'), & H &= \mu^4(1 - \nu)\vartheta_2', \\
 T_1 &= u' + \nu(w + mv), & T_2 &= w + mv + \nu u', & 2S &= (1 - \nu)(v' - mu), \\
 \vartheta_1 &= -w', & \vartheta_2 &= mw + \nu,
 \end{aligned}
 \tag{7.1}$$

where (\prime) denotes the derivative with respect to the coordinate $s \in [0, l]$, l is the dimensionless shell length, m is the circumferential wave number, $\lambda = 4\pi^2\sigma\rho f^2 R^2 E^{-1}$ is the frequency parameter, $\sigma = 1 - \nu^2$, ν is Poisson's ratio, E is Young's modulus, ρ is the mass density, f is the vibration frequency, u, v and w are the components of the displacement, $T_1, T_2, S, Q_1, Q_2, M_1, M_2, H$ are the dimensionless stress-resultants and stress-couples, ϑ_1 and ϑ_2 are the angles of rotation of the normal, $\mu^4 = h^2/12$ is a small parameter, h is the dimensionless shell thickness.

The equations of plate's bending (Filippov, 2004) can be written as

$$\begin{aligned}
 (xQ_{1p})' + mQ_{2p} + \lambda xw_p &= 0, \\
 xQ_{1p} &= (xM_{1p})' - M_{2p} + 2mH_p, & xQ_{2p} &= -mM_{2p} + 2H_p, \\
 xM_{1p} &= \mu_p^4[x\vartheta_{1p}' + \nu(m\vartheta_{2p} + \vartheta_{1p})], & xM_{2p} &= \mu_p^4(m\vartheta_{2p} + \vartheta_{1p} + \nu x\vartheta_{1p}'), \\
 H_p &= \mu_p^4 x(1 - \nu)\vartheta_{2p}', & \vartheta_{1p} &= -w_p', & x\vartheta_{2p} &= mw_p.
 \end{aligned}
 \tag{7.2}$$

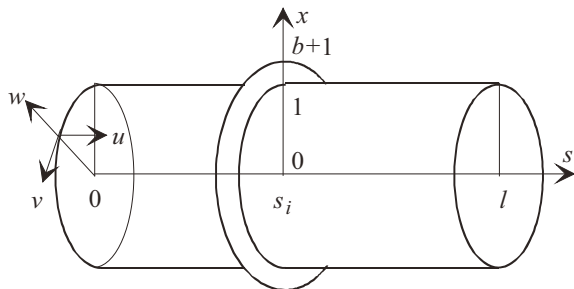


Fig. 7.1 Shell and plate

Here (') denotes the derivative with respect to the radial coordinate, $x \in [1, 1 + b]$, b is the dimensionless plate width, w_p is the transverse deflection, Q_{1p} , Q_{2p} , M_{1p} , M_{2p} , H_p are the dimensionless stress-resultants and stress-couples, ϑ_{1p} and ϑ_{2p} are the angles of rotation of the normal, $\mu_p^4 = a^2/12$ is a small parameter, a is the dimensionless plate thickness.

For the evaluation of the tangential (in plane) deformation of the plate we have the following equations (Filippov, 2004):

$$\begin{aligned} (xT_{1p})' - T_{2p} + mS_p + \lambda xu_p &= 0, & xS_p' + 2S_p - mT_{2p} + \lambda v_p &= 0, \\ xT_{1p} &= xu_p' + \nu(mv_p + u_p), & xT_{2p} &= u_p + mv_p + \nu xu_p', \\ 2xS_p &= (1 - \nu)(xv_p' - mu_p - v_p), \end{aligned} \quad (7.3)$$

where u_p and v_p are the tangential components of the displacement, T_{1p} , T_{2p} , S_p are the dimensionless stress-resultants.

We denote as $u^{(k)}$, $v^{(k)}$, $w^{(k)}$, ... the solutions of Eqs. (7.1) in the intervals

$$s \in [s_{k-1}, s_k], \quad k = 1, 2, \dots, n+1, \quad s_0 = 0, \quad s_{n+1} = l.$$

If the shell and the plates are made of the same material, then the following 12 continuity conditions have to be satisfied

$$\begin{aligned} u^{(i)} &= u^{(i+1)} = -w_p(1), & \vartheta_1^{(i)} &= \vartheta_1^{(i+1)} = \vartheta_{1p}(1), \\ w^{(i)} &= w^{(i+1)} = u_p(1), & v^{(i)} &= v^{(i+1)} = v_p(1), \\ h(T_1^{(i)} - T_1^{(i+1)}) &= -aQ_{1p}(1), & h(Q_1^{(i)} - Q_1^{(i+1)}) &= aT_{1p}(1), \\ h(M_1^{(i)} - M_1^{(i+1)}) &= aM_{1p}(1), & h(S^{(i)} - S^{(i+1)}) &= aS_p(1), \\ s &= s_i, \quad i = 1, 2, \dots, n. \end{aligned} \quad (7.4)$$

The outer edges of the plates are free, therefore

$$T_{1p} = S_p = M_{1p} = Q_{1p} = 0, \quad x = 1 + b. \quad (7.5)$$

At the edges of the shell $s = 0$ and $s = l$ any homogeneous boundary conditions can be introduced. As an example we consider the shell with simply supported edges, i.e.

$$v = w = T_1 = M_1 = 0, \quad s = 0, \quad s = l. \quad (7.6)$$

If for $\lambda = \lambda_k$ equations (7.1)-(7.3) have a nontrivial solution satisfying boundary conditions (7.4)-(7.6) then λ_k is an eigenvalue of eigenvalue problem (7.1)-(7.6). The minimal positive eigenvalue λ_1 corresponds to the fundamental frequency f_1 .

7.3 Boundary Conditions for the Shell's Equations

Let us seek the vibratons modes of the first type which are similar to the vibrations modes of the non-stiffened shell. The transverse flexural stiffness of the plate is more less than its tangential stiffness in plane. Setting to zero the flexural plate's stiffness, we obtain from (7.4)

$$v^{(i)} = v^{(i+1)}, \quad u^{(i)} = u^{(i+1)}, \quad T_1^{(i)} = T_1^{(i+1)}, \quad (7.7)$$

$$w^{(i)} = w^{(i+1)}, \quad \vartheta_1^{(i)} = \vartheta_1^{(i+1)}, \quad M_1^{(i)} = M_1^{(i+1)}, \quad (7.8)$$

$$w^{(i)} = u_p(1), \quad v^{(i)} = v_p(1), \quad (7.9)$$

$$h(Q_1^{(i)} - Q_1^{(i+1)}) = aT_{1p}(1), \quad h(S^{(i)} - S^{(i+1)}) = aS_p(1), \quad s = s_i. \quad (7.10)$$

Conditions (7.7) and (7.8) are the continuity conditions for solutions of the shell equations (7.1). To get two more conditions from relations (7.9) and (7.10) we must find the solution of Eqs. (7.3).

For the low-frequency vibrations the parameter λ is small, and we neglect of the inertial terms $\lambda x u_p$ and λv_p in Eqs. (7.3):

$$\begin{aligned} (xT_{1p})' - T_{2p} + mS_p &= 0, & xS_p' + 2S_p - mT_{2p} &= 0, \\ xT_{1p} &= xu_p' + \nu(mv_p + u_p), \\ xT_{2p} &= u_p + mv_p + \nu xu_p', & 2xS_p &= (1 - \nu)(xv_p' - mu_p - v_p). \end{aligned} \quad (7.11)$$

Then the change of variable $x = e^t$ reduces Eqs. (7.11) to equations with constant coefficients:

$$\begin{aligned} \frac{d^2 u_p}{dt^2} - u_p - \gamma m^2 u_p + \delta m \frac{dv_p}{dt} - (1 + \gamma) m v_p &= 0, \\ \gamma \frac{d^2 v_p}{dt^2} - \gamma v_p - m^2 v_p - \delta m \frac{du}{dt} - (1 + \gamma) m u_p &= 0, \end{aligned} \quad (7.12)$$

where $\gamma = (1 - \nu)/2$, $\delta = (1 + \nu)/2$. The general solution of Eqs. (7.12) have the form

$$\begin{aligned} u_p &= C_1 x^{m-1} + a_1 C_2 x^{m+1} + C_3 x^{-m-1} + a_2 C_4 x^{-m+1}, \\ v_p &= -C_1 x^{m-1} + b_1 C_2 x^{m+1} + C_3 x^{-m-1} + b_2 C_4 x^{-m+1}. \end{aligned} \quad (7.13)$$

Here C_j , $j = 1, 2, 3, 4$ are arbitrate constants,

$$a_1 = 2\gamma/(\delta m) - 1, \quad a_2 = 2\gamma/(\delta m) + 1, \quad b_1 = 2/(\delta m) + 1, \quad b_2 = 1 - 2/(\delta m).$$

From Eqs. (7.11) and (7.13) we obtain the following formulas

$$\begin{aligned}
T_{1p} &= 2C_1\gamma(m-1)x^{m-2} - 2C_2\gamma(m+1)(m-2)m^{-1}x^m \\
&\quad - 2\gamma(m+1)C_3x^{-m-2} - 2C_4\gamma(m-1)(m+2)m^{-1}x^{-m}, \\
S_p &= -2C_1\gamma(m-1)x^{m-2} + 2C_2\gamma(m+1)x^m - 2\gamma(m+1)C_3x^{-m-2} \\
&\quad - 2C_4\gamma(m-1)x^{-m}.
\end{aligned} \tag{7.14}$$

On the free edge of the plate $x = 1 + b$

$$T_{1p} = S_p = 0. \tag{7.15}$$

Substitution solutions (7.13) and (7.14) into conditions (7.9) and into boundary conditions (7.15) leads to equations

$$\begin{aligned}
C_1 + a_1C_2 + C_3 + a_2C_4 &= w^{(i)}(s_i), \quad -C_1 + b_1C_2 + C_3 + b_2C_4 = v^{(i)}(s_i), \\
(m-1)[m\beta^m C_1 - (m+2)\beta C_4] - (m+1)[(m-2)\beta^{m+1}C_2 + mC_3] &= 0, \\
(m-1)(\beta^m C_1 + \beta C_4) - (m+1)(\beta^{m+1}C_2 - C_3) &= 0,
\end{aligned} \tag{7.16}$$

where $\beta = (1 + b)^2$.

Determine the expressions for the arbitrary constants C_k from Eqs. (7.16) and substitute them into formulas (7.14). Then we obtain

$$\begin{aligned}
S_p(1) &= -2\gamma\delta[(B_1 + mB_2)w^{(i)}(s_i) + (D_1 + mD_2)v^{(i)}(s_i)]/D, \\
T_{1p}(1) &= -2\gamma\delta[(mB_1 + B_2)w^{(i)}(s_i) + (mD_1 + D_2)v^{(i)}(s_i)]/D
\end{aligned} \tag{7.17}$$

with

$$\begin{aligned}
B_1 &= \beta(\beta^{2m} - 1) - 2mb(b+2)\beta^m, \\
B_2 &= \beta(\beta^m + 1)^2 - 4\beta^m - \delta\beta(\beta^m - 1)^2 + \delta m^2 b^2 (b+2)^2 \beta^m, \\
D_1 &= \gamma\beta(\beta^m - 1)^2 + \delta m^2 b^2 (b+2)^2 \beta^m, \\
D_2 &= \beta(\beta^{2m} - 1) + 2mb(b+2)\beta^m, \\
D &= \gamma[4\beta^m + \delta\beta(\beta^m - 1)^2] + \delta[\beta(\beta^m + 1)^2 + \delta m^2 b^2 (b+2)^2 \beta^m].
\end{aligned} \tag{7.18}$$

From formulas (7.10) and (7.17) we get two following continuity conditions for solutions of shell's equations

$$\begin{aligned}
S^{(i)} - S^{(i+1)} &= -2a\gamma\delta[(B_1 + mB_2)w^{(i)} + (D_1 + mD_2)v^{(i)}]/(hD), \\
Q_1^{(i)} - Q_1^{(i+1)} &= -2a\gamma\delta[(mB_1 + B_2)w^{(i)} + (mD_1 + D_2)v^{(i)}]/(hD), \quad s = s_i.
\end{aligned} \tag{7.19}$$

7.4 Asymptotic Solution Corresponding Vibrations of the First Type

For the low-frequency vibrations the first type vibration mode of cylindrical shell stiffened by annular plates is similar to the vibration mode of the non-stiffened shell. In both cases the circumferential wave number m is large. We seek approximate solution of eigenvalue problem (7.1), (7.6)-(7.8) and (7.19) as a sum of the semi-membrane solution and the edge effect functions (Filippov, 2004):

$$y^{(k)} = m^{I_0(y)} y_0^{(k)} + m^{I_1(y)} (y_1^{(k)} + y_2^{(k)}), \quad k = 1, 2, \dots, n + 1. \tag{7.20}$$

Here y denotes any unknown function, $I(y)$ and $I_1(y)$ are the intensity indices. Table 7.1 lists values of the intensity indices for the problem under consideration

The function $v_0^{(k)}$ satisfy the semi-membrane equation

$$\frac{d^4 v_0^{(k)}}{ds^4} - \alpha^4 v_0^{(k)} = 0, \tag{7.21}$$

where

$$\alpha^4 = \frac{\lambda m^4 - \mu^4 m^8}{\sigma}, \tag{7.22}$$

and

$$w_0^{(k)} = -v_0^{(k)}, \quad u_0^{(k)} = \frac{dv_0^{(k)}}{ds}, \quad T_{10}^{(k)} = \frac{d^2 v_0^{(k)}}{ds^2}, \quad S_0^{(k)} = -\sigma \frac{d^3 v_0^{(k)}}{ds^3}. \tag{7.23}$$

The edge effect functions have the form

$$y_1^{(k)} = \sum_{j=1}^2 \hat{D}_j^{(k)} \hat{y}_j \exp(r_j(s - s_{k-1})/\mu), \quad y_2^{(k)} = \sum_{j=3}^4 \hat{D}_j^{(k)} \hat{y}_j \exp[r_j(s - s_k)/\mu]. \tag{7.24}$$

Here $\hat{D}_j \sim 1$ are arbitrary constants,

$$r_{1,2} = g(-1 \pm i), \quad r_{3,4} = g(1 \pm i), \quad g = \sigma^{1/4}/\sqrt{2}, \quad i^2 = -1.$$

Table 7.1
Intensity indices for the vibration mode of the first type

Indices	Functions							
	$u^{(k)}$	$v^{(k)}$	$w^{(k)}$	$\vartheta^{(k)}$	$T_1^{(k)}$	$S^{(k)}$	$M_1^{(k)}$	$Q_1^{(k)}$
I_0	-2	-1	0	0	-2	-3	-6	-6
I_1	-4	-5	-2	0	-4	-3	-6	-4

In particular, $\hat{w}_j = 1$, $j = 1, 2, 3, 4$. The functions $y_1^{(k)}$ and $y_2^{(k)}$ decrease rapidly at increase in s from s_{k-1} up to s_k and at reduction from s_k up to s_{k-1} , correspondingly. Assume that $s_k - s_{k-1} \gg \mu$, for $k = 1, 2, \dots, n+1$. Then

$$y_1^{(k)}(s_k) \ll 1, \quad y_2^{(k+1)}(s_k) \ll 1$$

and in the first approximation

$$y^{(k)} = m^{I_0(y)} y_0^{(k)} + m^{I_1(y)} y_2^{(k)}, \quad y^{(k+1)} = m^{I_0(y)} y_0^{(k+1)} + m^{I_1(y)} y_1^{(k+1)}, \quad s = s_k. \quad (7.25)$$

Boundary conditions for Eqs. (7.21) can be determine after a separation of the boundary conditions on main and additional conditions (Tovstik and Smirnov, 2001). From the main conditions by neglecting of small terms we obtain boundary conditions for Eqs. (7.21).

Let Δ be the difference between maximal intensity indices of semi-membrane solutions and the edge effect functions. Then

1. For the main boundary conditions the value Δ must be strict more, than for the additional boundary conditions.
2. The semi-membrane solutions included in the main boundary conditions and the edge effect solutions included in the additional boundary conditions must be independent.

In order to satisfy condition 1 and 2, as a rule, it is necessary to use linear combinations of boundary conditions.

At the edge $s = 0$

$$\begin{aligned} v &= m^{-1}v_0 + m^{-5}v_2 = 0, & w &= w_0 + m^{-2}w_2 = 0, \\ T_1 &= m^{-2}T_{10} + m^{-4}T_{12} = 0, & M_1 &= m^{-6}(M_{10} + M_{12}) = 0, \\ \Delta_1 &= 4, & \Delta_2 &= 2, & \Delta_3 &= 2, & \Delta_4 &= 0, \end{aligned} \quad (7.26)$$

where Δ_k corresponds to k -th equation (7.26). It is impossible to separate boundary conditions (7.26) on main and additional conditions so that the condition 1 has been fulfilled. However, for linear combinations of first and second conditions $mv + w = 0$, taking into account that $v_0 + w_0 = 0$, we have $\Delta = 0$. Therefore main and additional conditions are $v = T_1 = 0$ and $w + mv = M_1 = 0$. The boundary conditions for Eq. (7.26) at the edges $s = 0$ and $s = l$ have the form $v_0 = T_{10} = 0$ or

$$v_0^{(1)}(0) = \frac{d^2 v_0^{(1)}}{ds^2}(0) = 0, \quad v_0^{(n+1)}(l) = \frac{d^2 v_0^{(n+1)}}{ds^2}(l) = 0. \quad (7.27)$$

7.5 Main Continuity Conditions

For $s = s_k$ main and additional conditions are conditions (7.7) and (7.8). It follows from (7.7) three continuity conditions for Eqs. (7.21):

$$v_0^{(k)} = v_0^{(k+1)}, \quad v_0^{(k)'} = v_0^{(k+1)'}, \quad v_0^{(k)''} = v_0^{(k+1)''}, \quad s = s_k, \quad k = 1, 2, \dots, n. \quad (7.28)$$

To obtain the fourth main condition we exclude the edge effect functions

$$\begin{aligned} w_2^{(k)} &= \hat{D}_3^{(k)} + \hat{D}_4^{(k)}, \quad w_1^{(k+1)} = \hat{D}_1^{(k+1)} + \hat{D}_2^{(k+1)}, \\ \vartheta_2^{(k)} &= -gK^{-1}(r_3\hat{D}_3^{(k)} + r_4\hat{D}_4^{(k)}), \quad \vartheta_1^{(k+1)} = -gK^{-1}(r_1\hat{D}_1^{(k+1)} + r_2\hat{D}_2^{(k+1)}) \\ M_{12}^{(k)} &= -g^2K^2(r_3^2\hat{D}_3^{(k)} + r_4^2\hat{D}_4^{(k)}), \quad M_{11}^{(k+1)} = -g^2K^2(r_1^2\hat{D}_1^{(k+1)} + r_2^2\hat{D}_2^{(k+1)}), \\ S_2^{(k)} &= Q_{12}^{(k)} = -g^3K(r_3^3\hat{D}_3^{(k)} + r_4^3\hat{D}_4^{(k)}), \quad S_1^{(k+1)} = Q_{11}^{(k+1)} = -g^3K(r_1^3\hat{D}_1^{(k+1)} + r_2^3\hat{D}_2^{(k+1)}) \end{aligned}$$

from relations (7.19). Here $K = \mu m^2$.

Taking into account that

$$w_0^{(k)} = w_0^{(k+1)}, \quad \vartheta_0^{(k)'} = \vartheta_0^{(k+1)'}, \quad M_{10}^{(k)} = M_{10}^{(k+1)}, \quad s = s_k, \quad k = 1, 2, \dots, n. \quad (7.29)$$

after substituting solutions (7.20) into first and third conditions (7.8) we obtain

$$\hat{D}_1 + \hat{D}_2 = \hat{D}_3 + \hat{D}_4, \quad r_1^2\hat{D}_1^{(k+1)} + r_2^2\hat{D}_2^{(k+1)} = r_3^2\hat{D}_3 + r_4^2\hat{D}_4, \quad (7.30)$$

where

$$\hat{D}_1 = \hat{D}_1^{(k+1)}, \quad \hat{D}_2 = \hat{D}_2^{(k+1)}, \quad \hat{D}_3 = \hat{D}_3^{(k)}, \quad \hat{D}_4 = \hat{D}_4^{(k)}.$$

It follows from relation (7.30) and equalities

$$r_1^2 = r_3^2 = -r_2^2 = -r_4^2$$

that

$$\hat{D}_1 = \hat{D}_3, \quad \hat{D}_2 = \hat{D}_4. \quad (7.31)$$

Substituting solutions (7.20) into second conditions (7.8) leads to the relation

$$r_1\hat{D}_1 + r_2\hat{D}_2 = r_3\hat{D}_3 + r_4\hat{D}_4$$

which may be written as

$$\hat{C}_1 + \hat{C}_2 = 0,$$

where

$$\hat{C}_1 = \hat{D}_1 + \hat{D}_2, \quad \hat{C}_2 = \hat{D}_1 - i\hat{D}_2.$$

Finally, we substitute solutions (7.20) into conditions (7.19) using formulas

$$S_2^{(k)} - S_1^{(k+1)} = Q_{12}^{(k)} - Q_{11}^{(k+1)} = 2g^3K(r_1^3\hat{D}_1 + r_2^3\hat{D}_2) = 4g^3K(\hat{C}_1 - \hat{C}_2) = 8g^3K\hat{C}_1,$$

and after neglecting of small terms obtain the approximate continuity conditions:

$$\begin{aligned} A \left(8g^3K\hat{C}_1 + S_0^{(k)} - S_0^{(k+1)} \right) &= m(mB_2 - D_2)v_0^{(k)} - B_2\hat{C}_1, \\ A \left(S_0^{(k)} - S_0^{(k+1)} \right) &= m^2(D_1 - mB_1)v_0^{(k)} + mB_1\hat{C}_1, \quad A = \frac{hD}{2am^2\gamma\delta}. \end{aligned} \quad (7.32)$$

The linear combination of boundary conditions (7.32), which do not contains the arbitrary constant \hat{C}_1 is the fourth continuity conditions for Eqs. (7.21):

$$S_0^{(k)} - S_0^{(k+1)} + cv_0^{(k)} = 0, \quad s = s_k, \quad (7.33)$$

where

$$c = \frac{8m^2 g^3 AK(mB_1 - D_1) + m^2(B_1 D_2 - B_2 D_1)}{A(8g^3 AK + mB_1 + B_2)}. \quad (7.34)$$

The parameter c defines the tangential stiffness of the plate in plane.

It follows from formula (7.22) that the frequency parameter corresponding to the first type of vibrations is

$$\lambda^{(1)}(m, n) = \frac{\sigma \alpha_n^4(m)}{m^4} + \mu^4 m^4. \quad (7.35)$$

Here $\alpha_n^4(m)$, $n = 1, 2, \dots$ are the eigenvalues for which the eigenvalue problem for Eqs. (7.21) with boundary conditions (7.27), (7.28) and (7.33) has non-trivial solutions. This eigenvalue problem also describe the flexural vibrations of the simply supported beam, stiffened by n identical springs of stiffness c at the points $s = s_k$.

The solutions of Eqs. (7.21) can be represented in the form Timoshenko (1955)

$$v_0^{(k)} = A_k S(z_k) + B_k V(z_k) + C_k U(z_k) + D_k T(z_k), \quad z_k = \alpha(s - s_{k-1}), \\ s_{k-1} < s < s_k, \quad k = 1, 2, \dots, n+1, \quad s_0 = 0, \quad s_{n+1} = l, \quad (7.36)$$

where

$$S(z) = \cosh z + \cos z, \quad T(z) = \sinh z + \sin z, \\ U(x) = \cosh x - \cos x, \quad V(x) = \sinh x - \sin x, \quad (7.37)$$

A_k , B_k , C_k and D_k are arbitrary constants. Substituting (7.36) into boundary conditions (7.27), (7.28) and (7.33), we obtain $4(n+1)$ linear homogeneous algebraic equations in $4n+1$ unknowns A_k , B_k , C_k , and D_k . These equations have nontrivial solutions if its characteristic determinant $G(\alpha)$ is equal to zero:

$$G(\alpha) = 0. \quad (7.38)$$

The roots of Eq. (7.38) are eigenvalues of the problem (7.21), (7.27), (7.28) and (7.33).

Consider the narrow plate for which

$$bm^2 \ll 1.$$

Substituting the approximate relation

$$\beta^m = (1+b)^{2m} \simeq 1 + 2mb + \frac{2m(2m-1)b^2}{2} + \frac{2m(2m-1)(2m-2)b^3}{6}$$

into formulas (7.18) and neglecting of small terms, we obtain

$$\begin{aligned} B_1 &\simeq 4mb^2 + 8m^3b^3/3, & D_1 &\simeq 4m^2b^2, \\ B_2 &\simeq 8b + 4m^2b^2, & D_2 &\simeq 8mb, & D &\simeq 4. \end{aligned} \quad (7.39)$$

If we substitute formulas (7.39) into relation (7.34) then we obtain

$$c \simeq c_b = \frac{\sigma m^8}{h} \left(J + \frac{e^2 F}{1+d} \right), \quad d = \frac{\sigma m^2 F}{8hg^3 K}, \quad (7.40)$$

where

$$J = \frac{ab^3}{12}$$

is the dimensionless moment of inertia of the plate's cross-section with respect to the generatrix of the cylinder,

$$e = \frac{b}{2}$$

is the distance the centre of mass of the plate's cross-section from the shell's neutral surface,

$$F = ab$$

is cross-section area of the plate. The condition

$$S_0^{(k)} - S_0^{(k+1)} + c_b v_0^{(k)} = 0, \quad s = s_k, \quad (7.41)$$

is the main continuity condition for a cylindrical shell stiffened by a beam of the rectangular cross-section (Filippov, 1999). It means, that for the narrow annular plate one can use beam's model.

For the wide plate, when

$$bm \gg 1,$$

using the approximate relations

$$A = A_0 \beta^{2m+1}, \quad A_0 = \frac{h(1+\gamma)}{2am^2\gamma}, \quad B_1 = D_2 = \beta^{2m+1}, \quad B_2 = D_1 = \gamma \beta^{2m+1},$$

we obtain

$$c \simeq c_p = \frac{m^2(8g^3 m K A_0 + 1 - \gamma^2)}{A_0(8g^3 K A_0 + m)}.$$

The stiffness c_p do not depends on the width of the ring b , since the stress-strain state of the plate is localized near its inner boundary, which is attached to cylindrical shell Filippov (2006a).

7.6 Example 1

Consider the freely supported cylindrical shell of the length l stiffened by the annular plate at the parallel $s_1 = l/2$. Then Eq. (7.38) has the same roots as the following two equations

$$\tanh z - \tan z = 32z^3/c, \quad \sin z = 0, \quad z = \alpha l/2. \quad (7.42)$$

The roots of second Eq. (7.42) do not depend on the stiffness c . If we denote by z_1 and z_2 the minimal positive roots of the first and second equations, then

$$\pi/2 \leq z_1 < 3.927, \quad z_2 = \pi.$$

Assume that $l = 4$, the thicknesses of the shell and the plate $h = a = 0.01$, the Poisson's ratio of the materials is $\nu = 0.3$ and find the lowest frequency parameters

$$\lambda_1^{(1)} = \min_{m,n} \lambda^{(1)}(m,n)$$

for the various plate's width b .

First we calculate $c(m)$ by means of formula (7.34), then the root $z_1(m)$ of Eq. (7.42). Consider $b \leq 0.2$. Then $z_1 < z_2$ and

$$\lambda_1^{(1)} = \min_m \left(\frac{8\sigma z_1^4(m)}{l^4} + \mu^4 m^4 \right). \quad (7.43)$$

The function in relation (7.43) attains its minimum at $m = 4$. The results are shown in Fig. 7.2 (curve 1), where

$$\Lambda_1^{(1)} = \lambda_1^{(1)} 10^3.$$

Curve 2 plots the values $\Lambda_{1b}^{(1)}$ which are found using beam's model when $c = c_b$ (see (7.40)).

While the plate is sufficiently narrow, the using of the beam's model gives good results, which differ a little from the results obtained on the basis of plate's model. However, for sufficiently large b the frequency parameter Λ_{1b} is larger than Λ_1

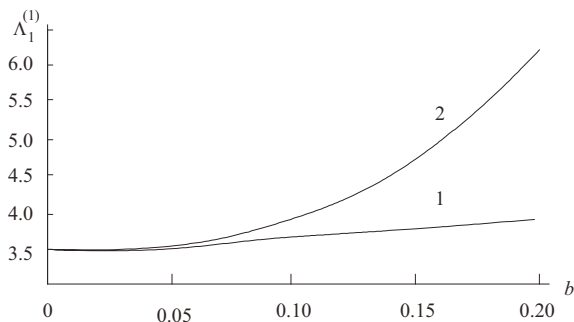


Fig. 7.2 Frequency parameter $\Lambda_1^{(1)}$ vs. the plate's width b

because the beam’s stiffness c_b is larger than the plate’s stiffness c . The values c_b and c for $m = 4$ and various b are shown in Fig. 7.3

7.7 Vibration of the Second Type

The vibration modes of the second type correspond to low frequencies and is localized on the surface of the plate. The cylindrical shell itself does not actually deform. Let us seek the approximate solution of system (7.1) as a sum of the membrane solutions and the edge effect functions:

$$\begin{aligned}
 y^{(k)} &= \mu^{I_0(y)} y_0^{(k)} + \mu^{I_1(y)} (y_1^{(k)} + y_2^{(k)}), \quad k = 2, 3, \dots, n, \\
 y^{(1)} &= \mu^{I_0(y)} y_0^{(1)} + \mu^{I_1(y)+1} y_1^{(1)} + \mu^{I_1(y)} y_2^{(1)}, \\
 y^{(n+1)} &= \mu^{I_0(y)} y_0^{(n+1)} + \mu^{I_1(y)} y_1^{(n+1)} + \mu^{I_1(y)+1} y_2^{(n+1)}
 \end{aligned}
 \tag{7.44}$$

The functions u_0, v_0, T_{10} and S_0 satisfy the membrane equations:

$$T'_{10} + mS_0 = 0, \quad S'_0 = 0, \quad 2S_0 = (1 - \nu)(v'_0 - mu_0), \quad T_{10} = \sigma u'_0.
 \tag{7.45}$$

The membrane equations (7.45) are derived from Eqs. (7.1) assuming $\mu = 0$ and neglecting the small terms $\lambda u, \lambda v$ and λw . The edge effect functions y_1 and y_2 have the form (7.24). The intensity indices are given in Table 7.2.

We suppose that

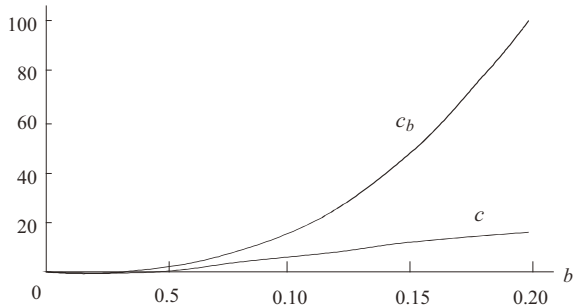


Fig. 7.3 Plate’s stiffness c and beam’s stiffness c_b vs. the plate’s width b

Table 7.2
Intensity indices for the vibration mode of the second type

Indices	Functions							
	$u^{(k)}$	$v^{(k)}$	$w^{(k)}$	$\vartheta^{(k)}$	$T_1^{(k)}$	$S^{(k)}$	$M_1^{(k)}$	$Q_1^{(k)}$
I_0	3	3	3	3	3	3	7	7
I_1	3	4	2	1	4	3	4	3

$$w_p \sim \vartheta_{1p} \sim 1, \quad M_{1p} \sim Q_{1p} \sim \mu^4, \quad u_p \sim v_p \sim T_{1p} \sim S_p \sim \mu^3. \quad (7.46)$$

After the substitution the solutions (7.44) and (7.46) into Eqs. (7.1)-(7.3), continuity conditions (7.4) and boundary conditions (7.5)-(7.6) the eigenvalue problem (7.1)-(7.6) in the first approximation can be split into the following five separated problems:

1. The eigenvalue problem for Eqs. (7.2), describing the transverse flexural deformation of the plate with the boundary conditions

$$w_p = \vartheta_{1p} = 0, \quad x = 1, \quad M_{1p} = Q_{1p} = 0, \quad x = 1 + b. \quad (7.47)$$

2. The linear algebraic equations

$$w_2^{(k)}(s_k) = w_1^{(k+1)}(s_k), \quad h[M_{12}^{(k)}(s_k) - M_{11}^{(k+1)}(s_k)] = aM_{1p}(1), \quad k = 1, 2, \dots, n. \quad (7.48)$$

for the unknown constants $\hat{D}_3^{(k)}$, $\hat{D}_4^{(k)}$, $\hat{D}_1^{(k+1)}$ and $\hat{D}_2^{(k+1)}$. The solution of these equations allows us to obtain the edge effect functions near the parallel $s = s_k$.

3. Non-homogeneous boundary value problem for membrane shell equations (7.45) with the boundary conditions

$$u_0(0) = v_0(0) = u_0(l) = v_0(l) = 0, \quad T_{10}^{(k)}(s_k) = T_{10}^{(k+1)}(s_k), \\ h[S_0^{(k)}(s_k) + S_2^{(k)}(s_k) - S_0^{(k+1)}(s_k) + S_1^{(k+1)}(s_k)] = aS_p(1), \quad k = 1, 2, \dots, n. \quad (7.49)$$

4. The linear algebraic equations

$$w_1^{(1)}(0) = w_0^{(1)}(0), \quad \vartheta_{11}^{(1)}(0) = 0, \quad w_2^{(n+1)}(l) = w_0^{(n+1)}(l), \quad \vartheta_{12}^{(n+1)}(l) = 0. \quad (7.50)$$

for the unknown constants $\hat{D}_1^{(1)}$, $\hat{D}_2^{(1)}$ and $\hat{D}_3^{(n+1)}$, $\hat{D}_4^{(n+1)}$.

5. Non-homogeneous boundary value problem for plate equations (7.3) with the boundary conditions at $x = 1$ and $x = 1 + b$

$$v_p(1) = v_0^{(k)}(s_k) - v_0^{(k+1)}(s_k), \quad aT_{1p}(1) = h[Q_{12}^{(k)}(s_k) - Q_{11}^{(k)}(s_k)], \quad T_{1p} = S_p = 0.$$

Thus, the approximate solution of the the eigenvalue problem (7.1)-(7.6) is reduced to the solution of five more simple problems. First we have to solve the eigenvalue problem 1 for the flexural plate's deformation. Then, solution of Eqs. (7.48) allows us to obtain the edge effect functions near the parallel $s = s_k$. Further we get the solution of the membrane problem 3, using boundary conditions (7.49) and find by means of equations (7.50) the edge effect integrals near the parallels $s = 0$ and $s = l$. Finally it is possible to solve the boundary value problem 5, describing tangential displacements of the plate.

We consider only the problem 1, since after its solution we find frequency parameter λ and main part of the vibration mode. The displacements of the cylindrical shell and the tangential displacement of the plate are very small in comparison with the transverse plate deflections (see relation (7.46) and Table 7.2).

7.8 Flexural Vibrations of the Plate

Equations (7.2) describing free flexural vibrations of an annular plate can be reduced to the following equation

$$\Delta^2 w - \beta^4 w = 0, \quad \beta^4 = \frac{\lambda}{\mu_p^4}, \quad (7.51)$$

where

$$\Delta = \frac{1}{x} \frac{d}{dx} \left(x \frac{d}{dx} \right) - \frac{m^2}{x^2}.$$

The exact solution of Eq. (7.51) has the form (Filippov and Kolyada, 2013)

$$w = C_1 J_m(\beta x) + C_2 Y_m(\beta x) + C_3 I_m(\beta x) + C_4 K_m(\beta x), \quad (7.52)$$

where C_j ($j = 1, 2, 3, 4$) are the arbitrary constants, J_m, Y_m are the Bessel functions and I_m, K_m are the modified Bessel functions. Solution (7.52) must satisfy the boundary conditions (7.47).

We can obtain a simple approximate solution of the problem 1 in the case $b \ll 1$. Let us suppose that the circumferential wave number $m \sim 1$. In this case replacing variable $x = 1 + b\xi$ in Eq. (7.51), boundary conditions (7.47) and neglecting small terms leads to the boundary-value problem

$$\frac{d^4 w}{d\xi^4} - \gamma^4 w = 0, \quad (7.53)$$

$$w(0) = w'(0) = w''(1) = w'''(1) = 0, \quad (7.54)$$

where

$$\gamma = b\beta, \quad w' = \frac{dw}{d\xi}.$$

The solution of Eq. (7.53) has the form

$$w = C_1 S(\gamma xi) + C_2 T(\gamma xi) + C_3 U(\gamma xi) + C_4 V(\gamma xi), \quad (7.55)$$

where C_j are arbitrary constants and the function T, S, U, V are determined by relations (7.37). Substituting solution (7.55) into boundary conditions (7.54), we get system of linear homogeneous algebraic equations in unknowns C_j . By setting to zero the characteristic determinant of this system we obtain the equation

$$\cosh \gamma \cos \gamma = 1. \quad (7.56)$$

The positive roots γ_k of Eq. (7.56) are eigenvalues of the problem (7.53), (7.54). The minimal eigenvalue is $\gamma_1 = 1.875$. It follows from the second formula (7.51) that the approximate value of a frequency parameter is

$$\lambda_k^{(2)} = \frac{a^2 \gamma_k^4}{12b^4}, \quad k = 1, 2, \dots \quad (7.57)$$

Formula (7.57) shows that the frequency parameters $\lambda_k^{(2)}$ for the second type of vibrations goes up as the width of plate b increases.

7.9 Example 2

Consider the vibrations of the cylindrical shell stiffened by the annular plate, assuming that parameter of this structure are the same as in (7.6). The dependencies of

$$\Lambda_1^{(k)} = 10^3 \lambda_1^{(k)}$$

for $k = 1, 2$ on the plate width b , is shown in Fig. 7.4.

To the fundamental frequency f_1 correspond the frequency parameter

$$\lambda_1 = \min(\lambda_1^{(1)}, \lambda_1^{(2)}).$$

At increase of the plate's width λ_1 and f_1 first increases and then decreases.

7.10 Conclusions

The application of asymptotic methods to the analysis of low-frequency vibrations of a cylindrical shell joined with annular plates permits to obtain simple approximate formulas for evaluation of frequencies and vibration modes. The different approaches were used for narrow and wide plates. If the plates are narrow then circumferential wave number m is large and frequencies increase with the width of plates b . For the wide plates frequencies in the first approximation do not depend on m and they decrease when b increases. In the both cases the solutions of shell equations were represented as a sum of slowly varying functions and edge effect integrals.

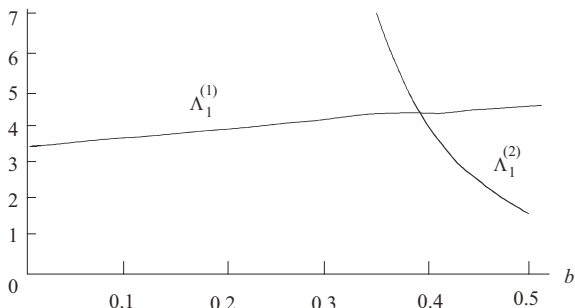


Fig. 7.4 Frequency parameter Λ_1 vs. plate's width b

As an example the vibrations of the shell stiffened by one plate are considered. For sufficiently large number of plates to the approximate calculation of frequencies the homogenization procedure may be used.

Acknowledgements This work was supported by RFBR (grant 19-01-00208) which is gratefully acknowledged.

References

- Bauer SM, Filippov SB, Smirnov AL, Tovstik PE, Vaillancourt R (2015) *Asymptotic Methods in Mechanics of Solids*, International Series of Numerical Mathematics, vol 167. Birkhäuser, Basel
- El Raheb M, Babcock CD (1981) Effect of elastic end rings on the eigenfrequencies of thin cylinders. *Journal of Sound and Vibration* 74(1):31–46
- Filippov S, Kolyada M (2013) Numerical and asymptotic modeling of annular plate vibrations. In: Dimov I, Farago I, Vulkov L (eds) *Proceedings of the NAA Conference*, Lozenetz, Bulgaria, 2012, Springer, Heidelberg, pp 295–302
- Filippov SB (1999) *Theory of Connected and Stiffened Shells* (in Russ.). St. Petersburg State University Press, St. Petersburg
- Filippov SB (2004) Optimal design of stiffened cylindrical shells based on an asymptotic approach. *Technische Mechanik* 24(3-4):221–230
- Filippov SB (2006a) Buckling of cylindrical shell joint with annular plate. In: Pietraszkiewicz W, Szymczak C (eds) *Shell Structures: Theory and Applications*. Proceedings of the 8th SSTA Conference, Jurata, Taylor & Francis, London, pp 211–214
- Filippov SB (2006b) Buckling, vibrations and optimal design of ring-stiffened thin cylindrical shells, World Scientific Publishing Co Ltd., pp 17–47. Series on Stability, Vibration and Control of Systems, Series B
- Filippov SB, Haseganu EM (2003) Low-frequency vibrations of a thin cylindrical shell joined with an annular thin plate. *Transactions of the Canadian Society for Mechanical Engineering* 27(3):183–192
- Hodges CH, Power J, Woodhouse J (1985) The low frequency vibration of a ribbed cylinder. *Journal of Sound and Vibration* 101(2):219 – 256
- Loy CT, Lam KY (1997) Vibration of cylindrical shells with ring support. *International Journal of Mechanical Sciences* 39(4):455–471
- Ross CTF, Haynes P, Richards WD (1996) Vibration of ring-stiffened circular cylinders under external water pressure. *Computers & Structures* 60(6):1013–1019
- Samanta A, Mukhopadhyay M (2004) Free vibration analysis of stiffened shells by the finite element technique. *European Journal of Mechanics - A/Solids* 23(1):159–179
- Timoshenko S (1955) *Vibration Problems in Engineering*. Van Nostrand, New York

- Tovstik PE, Smirnov AL (2001) *Asymptotic Methods in the Buckling Theory of Elastic Shells*. World Scientific Publishing Co Ltd., Singapore, New Jersey, London, Hong Kong
- Vishik MI, Lyusternik LA (1957) Regular degeneration and boundary layer for linear differential equations with small parameter. *Uspekhi Mat Nauk* 12(5(77)):3–122
- Yang B, Zhout J (1995) Analysis of ring-stiffened cylindrical shells. *Journal of Applied Mechanics* 62(4):1005–1014



Chapter 8

Free Vibrations of an Open Non-circular Cylindrical Shell of Variable Thickness

Alexander Ya. Grigorenko, Maksym Yu. Borysenko, Olena V. Boychuk, and Larisa Ya. Vasil'eva

Abstract The natural frequencies and the corresponding vibration modes of open cylindrical shells with an elliptical cross-section and variable thickness are analyzed. Variations in the cutting of the shell along both the minor and major axes are allowed and various boundary conditions are considered. The numerical solutions are obtained using the finite element package FEMAP with the NASTRAN solver. A number of low-frequency vibrations are investigated in terms of their dependence on the cutting angle along major and minor axes of the shell.

Key words: Free vibrations · Open non-circular cylindrical shell · elliptical cross-section · variable thickness · FEM

8.1 Introduction

In different industries cylindrical shells of non-circular cross-section of constant and variable thicknesses are widely used. These can have both a closed and an open contour with different variations in the boundary conditions. In this regard it is necessary to have information about their dynamic characteristics, in particular, about the frequencies and forms of natural vibrations, since under real operating

Alexander Ya. Grigorenko · Maksym Yu. Borysenko
S.P. Timoshenko Institute of Mechanics, National Academy of Sciences of Ukraine, 3 Nesterova St., 03057 Kyiv, Ukraine
e-mail: ayagrigorenko1991@gmail.com, mechanics530@gmail.com

Olena V. Boychuk
Nikolaev National Agrarian University, 9 Georgy Gongadze St., 54030 Nikolaev, Ukraine
e-mail: boychuklena@outlook.com

Larisa Ya. Vasil'eva
V. O. Sukhomlinsky Nikolaev National University, 24 Nikolskaya St., 54030 Nikolaev, Ukraine
e-mail: lara@vasiliev.mk.ua

conditions, it is necessary to avoid resonance patterns that cause structural damage. A theoretical study of this class of problems is associated with significant difficulties due to the complexity of the system of initial partial differential equations with variable coefficients and the need to satisfy boundary conditions. The solution to the problem of determining the natural frequencies in the framework of the theory of thin shells is possible for objects of simple geometric shape (Arnold and Warburton, 1953; Baron and Bleich, 1954; Greenspon, 1959; Grigorenko et al, 2017; Grigorenko and Rozhok, 2004; Leissa, 1973; Markus, 1988; Stricklin et al, 1971).

Experimental methods are also used to solve the problem of determining the frequencies and forms of natural vibrations, for example, the non-contact method of strobe-holographic interferometry (Budak et al, 2014; Grigorenko et al, 2013), which not only gives a real picture of the behavior of mechanical structures under the influence of variable loads, but also allows us to estimate the applicability limits of those or other theoretical models (Budak et al, 2014). A feature of this method is the need to manufacture a real object of study, to qualitatively implement the boundary conditions and the experiment itself, which in turn leads to significant costs in time and financial resources. Note that this experimental method can be applied not only to two-dimensional, but also to three-dimensional dynamics problems (Grigorenko et al, 2018).

In cases of a complex geometric shape – a closed shell of an elliptical cross section with variations in shell thickness, for example – it is advisable to use the finite element method (FEM) (Budak et al, 2017, 2016; Grigorenko et al, 2018), which gives good convergence with the experimental results (Grigorenko et al, 2018), thus confirming the accuracy of its application. Moreover, this numerical method does not require large expenditures of time and money.

In the literature, study of the dynamics of open shells is not given as much attention as the study of closed shells. Consider a few of these publications.

In Suzuki and Leissa (1986) an exact solution procedure is developed for determining the free vibration frequencies and mode shapes of open non-circular cylindrical shells with varying thickness along the cross-section and opposite curved two edges. The method is demonstrated for shells having elliptical cylindrical curvature and a thickness which varies quadratically in the circumferential direction, and straight edges which are fixed. For this symmetric configuration, vibration modes separate into symmetric and antisymmetric classes, and the exact frequencies are the roots of fourth order determinants. Numerical results are given showing the variations of frequencies and mode shapes of both symmetry classes with the shell length.

In Xiong-liang et al (2016) is concerned with the free vibration analysis of open circular cylindrical shells with either the two straight edges or the two curved edges simply supported and the remaining two edges supported by arbitrary classical boundary conditions. Based on the Donnell – Mushtari – Vlasov thin shell theory, an analytical solution of the traveling wave form along the simply supported edges and the modal wave form along the remaining two edges is obtained. The exact solutions for natural frequencies of the open circular cylindrical shell are obtained with the employment of a golden section search algorithm. The calculation results are compared with those obtained by the finite element method and the methods in

the available literature. The influence of length, thickness, radius, included angle, and the boundary conditions of the open circular cylindrical shell on the natural frequencies is investigated.

In Lekomtsev (2012), in the framework of two finite element realizations, the authors studied the natural vibrations of thin-walled open shells of circular cross section with different boundary conditions and with different cutting angles. In the considered range of variation of the cutting angle, an increase in all vibration frequencies is observed. This dependence is nonmonotonic. Typically, it is a significant increase in frequencies with an cutting angle $\varphi \in (60^0; 90^0)$. One of the problems solved in In Lekomtsev (2012) was taken as a test case in this paper.

This article concerns the numerical determination of the dynamic characteristics of an open cylindrical shell of an elliptical cross section of variable thickness with variations of the shell cutting - along both the minor and major axes, as well as with two variations for rigid fixes at the ends.

8.2 Basic FEM Relations for Natural Vibrations Problems

Dynamic equations for FEM can be obtained from the system of Lagrange equations of the second kind with n degrees of freedom:

$$\frac{d}{dt} \left(\frac{\partial T}{\partial \dot{\lambda}_i} \right) - \left(\frac{\partial T}{\partial \lambda_i} \right) = Q_i, \quad i = 1, 2, \dots, n. \quad (8.1)$$

Using the discrete form of the kinetic energy functional

$$T = \frac{1}{2} \{\dot{\lambda}\}_i^T M \{\dot{\lambda}\}_i, \quad (8.2)$$

The Lagrange equations (8.1) for the shell with its finite element approximation, taking into account the absence of external forces ($Q = 0$) and damping, can be rewritten in the form:

$$[M] \{\ddot{\lambda}\} + [K] \{\lambda\} = \{0\}, \quad (8.3)$$

where $[M]$ is the mass matrix of the structure; $[K]$ is stiffness matrix; and $\{\lambda\}$ is the vector of nodal displacements.

Equation (8.3) has a solution in the form

$$\{\lambda\} = \{A\} \cos(\omega t + \beta), \quad (8.4)$$

where $\{A\}$ is the vector of amplitude values of nodal displacements, which determine the form of natural vibrations; ω is cyclic frequency; and β is the initial phase of the oscillations $\cos(\omega t + \beta)$. Substituting (8.4) into (8.1) and cancelling, we obtain this system of algebraic equations:

$$\left(-\omega^2[M] + [K]\right)\{A\} = \{0\}. \quad (8.5)$$

In this system, nonzero component values $\{A\}$ are possible only under the condition

$$\det\left([K] - \omega^2[M]\right) = \{0\}. \quad (8.6)$$

If the square matrices $[M]$ and $[K]$ are positively defined, then the characteristic equations (8.6) have N positive solutions – natural frequencies ω_k , and pair values are possible (N is the number of unknowns in the system of algebraic equations (8.5)). N values of natural frequencies ω_k allows the solution of system (8.5) to be represented as a linear combination of N expressions (8.4):

$$\{\lambda\} = \sum_{k=1}^N \{A_k\} \cos(\omega_k t + \beta_k), \quad (8.7)$$

Each value ω_k corresponds to a certain ratio between the amplitudes A_{k_i} , that is, all the amplitudes of the vector can be expressed through one of them. The relations between the amplitudes A_{k_i} determine the k th natural mode of vibration. All degrees of freedom in the process of oscillations with their own frequency ω_k make synchronous movement. Thus, the configuration of the structure does not change its basic form, but only the amplitudes change. Since the values of the components of the natural vectors $\{A_k\}$ can be determined only up to a constant factor, they should be normalized as follows:

$$\{A_k\}^T [M] \{A_k\} = 1 \quad (8.8)$$

8.3 Solution to the Test Problem

To verify the reliability of the chosen methodology for studying the dynamic characteristics of an open cylindrical shell, a test problem was solved and the results were compared with the results of [13].

Using FEMAP, we constructed the geometry of two cylindrical open shells of circular cross section with the radius of the midsurface $R = 77.25$ mm, the ratio of height to radius $L/R = 2.99$, thickness $d = 1.5$ mm, cutting angle $\varphi = 30^\circ$, $\varphi = 45^\circ$, and $\varphi = 60^\circ$, physico-mechanical characteristics: Young's modulus $E = 205$ GPa, Poisson's ratio $\nu = 0.30$, and density $\rho = 7800$ kg/m³. The shells were fixed at two ends with different fixing variations: F is a free edge $u \neq v \neq w \neq \varphi_x \neq \varphi_y \neq \varphi_z \neq 0$; C is a rigid fastening $u = v = w = \varphi_x = \varphi_y = \varphi_z = 0$.

The results of the test problem, namely the first ten frequencies of natural vibrations for two options for cutting the shell with two types of fastening, are obtained using FEMAP solid elements, as well as results by another author, are presented in Tables 8.1 and 8.2, where ε is the deviation between the calculations. Analyzing the obtained results of the test problem, one can observe a small deviation between the

Table 8.1

Free vibration frequencies of an open circular cylindrical shell with an cutting angle φ , and boundary conditions C-F (own calculations compared with Lekomtsev, 2012)

No.	$f, \text{ Hz}$								
	$\varphi = 30^0$			$\varphi = 45^0$			$\varphi = 60^0$		
	Lekomtsev	FEMAP	$\varepsilon, \%$	Lekomtsev	FEMAP	$\varepsilon, \%$	Lekomtsev	FEMAP	$\varepsilon, \%$
1	256.77	259.61	1.1	259.34	257.99	0.5	252.23	244.26	3.2
2	261.90	264.78	1.1	260.53	259.18	0.5	267.34	260.01	2.7
3	591.20	599.14	1.3	608.43	611.64	0.5	588.18	569.26	3.2
4	665.87	676.80	1.6	640.49	643.25	0.4	683.98	675.06	1.3
5	724.48	727.44	0.4	726.19	718.40	1.1	726.83	698.18	3.9
6	732.29	737.78	0.7	729.67	720.58	1.2	740.19	725.32	2.0
7	749.48	755.18	0.8	818.26	821.25	0.4	856.84	811.42	5.3
8	907.77	931.72	2.6	994.47	997.72	0.3	1012.87	1028.89	1.6
9	1142.72	1146.48	0.3	1117.36	1121.51	0.4	1318.40	1259.12	4.5
10	1199.38	1223.27	2.0	1320.68	1300.85	1.5	1319.38	1260.01	4.5

Table 8.2

Free vibration frequencies of an open circular cylindrical shell with an cutting angle φ , and boundary conditions C-C (own calculations compared with Lekomtsev, 2012)

No.	$f, \text{ Hz}$								
	$\varphi = 30^0$			$\varphi = 45^0$			$\varphi = 60^0$		
	Lekomtsev	FEMAP	$\varepsilon, \%$	Lekomtsev	FEMAP	$\varepsilon, \%$	Lekomtsev	FEMAP	$\varepsilon, \%$
1	651.02	652.35	0.2	652.81	651.17	0.3	651.39	626.31	3.9
2	651.42	652.78	0.2	654.52	651.68	0.4	652.90	627.19	3.9
3	1217.19	1215.50	0.1	1220.82	1210.36	0.9	1218.61	1163.12	4.6
4	1217.26	1215.54	0.1	1223.91	1210.45	1.1	1219.46	1163.54	4.6
5	1525.10	1536.75	0.8	1537.59	1556.65	1.2	1515.20	1477.19	2.5
6	1570.98	1587.00	1.0	1557.57	1568.48	0.7	1639.62	1577.09	3.8
7	1693.53	1699.11	0.3	1744.70	1765.44	1.2	1706.47	1716.06	0.6
8	1784.50	1837.10	2.9	1846.03	1848.11	0.1	1889.38	1792.45	5.1
9	1890.76	1882.44	0.4	1898.31	1874.96	1.2	1895.76	1797.72	5.2
10	1891.08	1885.34	0.3	1909.95	1889.94	1.0	2061.30	2045.99	0.7

two finite element implementations proposed by us and Lekomtsev (2012), which does not exceed 5.5%. The reliability of the results obtained is ensured by using a sound mathematical model, the correctness of the problem statement, and the practical convergence of the results obtained using the finite element method.

8.4 Construction of the Calculation Model

Using FEMAP, the geometry of the cylindrical shell of an elliptical cross section of variable thickness was constructed with the following dimensions: height $h = 120$ mm, half-axes of the middle surface are $a = 50.810$ mm and $b = 36.295$ mm,

thickness of the shell along the major axis $d_a = 3$ mm, and along the minor axis $d_b = 1.3$ mm. Then the shell was cut at a given angle (Fig. 8.1). The material was set to steel with the characteristics: Young's modulus $E = 212$ GPa, Poisson's ratio $\nu = 0.30$, and density $\rho = 7800$ kg/m³. The shell was studied with one and two ends rigidly fixed. The simulation parameters are selected in accordance with the characteristics and dimensions of a closed non-circular cylindrical shell of constant thickness, which was studied for the frequency and shape of free vibrations of the FEM (Budak et al, 2016).

Since the shell in the cross section has the shape of an ellipse of variable thickness, it is necessary to consider different ways of its cutting about the major (Fig. 8.1, a) and minor semi-axes (Fig. 8.1, b), since its strength properties will change depending on this, and, accordingly, the frequency of free vibrations. In this study, we determine the dependence of the frequency of free vibrations on the magnitude of the cutting of the shell, which is determined by the angle of the cutting φ in the range from 0^0 to 90^0 in increments of 10^0 . Since the shells are of variable thickness, it is better to use a mesh of solid elements (Fig. 8.2).

8.5 Results of Numerical Calculations

The first ten frequencies of free vibrations calculated for a non-circular cylindrical shell of variable thickness with the cutting about the major semi-axis with one rigidly fixed end, depending on the cutting angle, are shown in Table 8.3. For comparison, frequencies for a closed non-circular cylindrical shell of variable thickness are also given for the corresponding boundary conditions. Table 8.4 shows the first ten frequencies of free vibrations of a non-circular cylindrical shell of variable thickness of the cutting about the major semi-axis, fixed at two ends, depending on the angle of the cutting. The first natural frequency of a closed non-circular cylindrical shell of variable thickness rigidly fixed at one end is 2.2 times greater than the corresponding

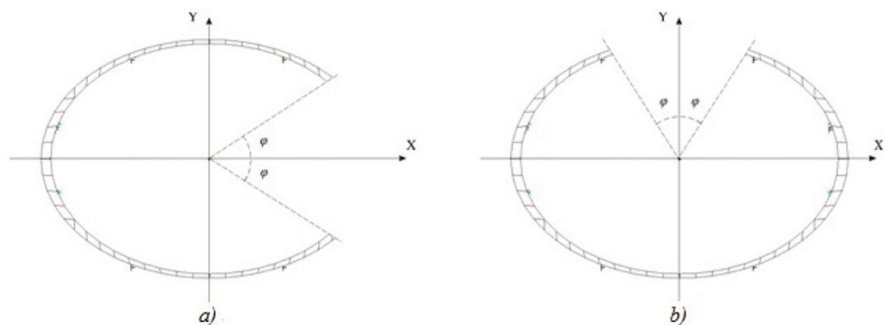


Fig. 8.1. The cross sections of open shells: a) angle of the cutting about the major semi-axis, b) angle of the cutting about the minor semi-axis

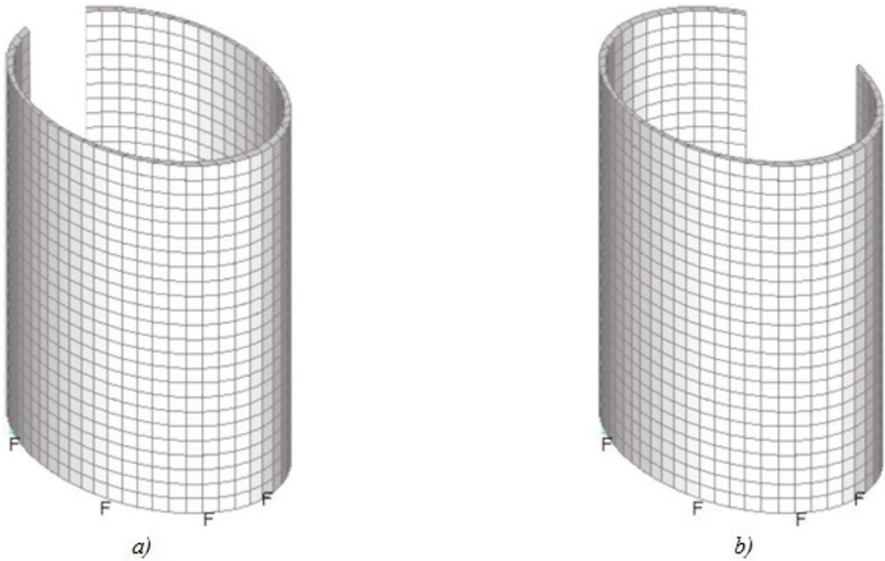


Fig. 8.2. Finite element models: a) angle of the cutting about the major semiaxis, b) angle of the cutting about the minor semiaxis

Table 8.3

Frequencies of free vibrations (f_{num} , Hz) of a shell of variable thickness rigidly fixed at one end, opened about the major semi-axis

No.	Closed	Angle of the cutting about the major semi-axis φ , degrees									
		0	10	20	30	40	50	60	70	80	90
1	1725	768	674	604	564	558	590	615	660	734	820
2	1800	781	679	614	587	579	591	655	734	802	844
3	2128	1520	1495	1531	1472	1465	1523	1564	1534	1561	1715
4	2225	1712	1629	1533	1615	1623	1587	1586	1653	1759	1888
5	3238	2003	2047	2035	1835	1700	1677	1666	1671	1762	1924
6	3718	2386	2325	2054	1869	1818	1742	1803	2070	2464	2536
7	3796	2636	2395	2271	2118	2055	2265	2647	2987	2802	3063
8	3948	2763	2467	2277	2541	2887	3095	3007	2992	3093	3274
9	4398	2799	2706	3014	3459	3288	3097	3012	3032	3099	3294
10	4446	3298	3622	3892	3628	3291	3363	3247	3179	3877	4551

frequency of an identical shell with a cut ($\varphi = 0^0$) lengthwise along the major axis and is 1.6 times greater in the case of rigid fastening of two ends.

Comparisons of the dependencies of the first four frequencies of free vibrations of a non-circular cylindrical shell of variable thickness with one base fixed on the cutting angle along a major semi-axis are shown in Fig. 8.3, and for the case of fixed two bases in Fig. 8.4. The first two natural frequencies correspond to the symmetric and antisymmetric form of vibrations of free edges along the cut. The maximum value of the first resonant frequency is observed at an cutting angle of 90^0 along

Table 8.4

Frequencies of free vibrations (f_{num} , Hz) of a shell of variable thickness rigidly fixed at two ends, opened about the major semi-axis

No. Closed	Angle of the cutting about the major semi-axis φ , degrees										
	0	10	20	30	40	50	60	70	80	90	
1	3955	2401	2062	1778	1584	1458	1408	1411	1449	1536	1677
2	3980	2403	2063	1781	1585	1461	1413	1414	1467	1564	1683
3	4360	3863	3772	3618	3392	3045	2854	2761	2745	2831	2993
4	4389	3995	3785	3715	3392	3046	2854	2763	2748	2833	3007
5	5538	4250	4386	3880	3562	3492	3496	3627	3775	3903	4190
6	5615	4523	4411	3880	3602	3568	3653	3721	3895	4285	4556
7	6539	5218	4529	4291	4436	4674	4691	4498	4402	4463	4663
8	6542	5220	4529	4659	4770	4757	4713	4500	4403	4476	4684
9	6573	5229	5391	5365	5466	5093	4730	4985	5498	5426	5784
10	6574	5854	5633	5848	5723	5099	5302	5639	5559	6428	6658

Fig. 8.3 The first four frequencies of free vibrations of a non-circular cylindrical shell of variable thickness with one base fixed on the cutting angle along a major semi-axis

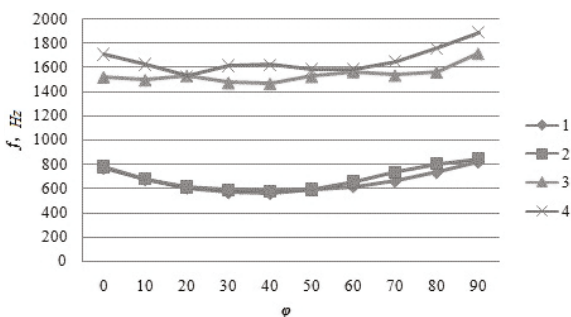
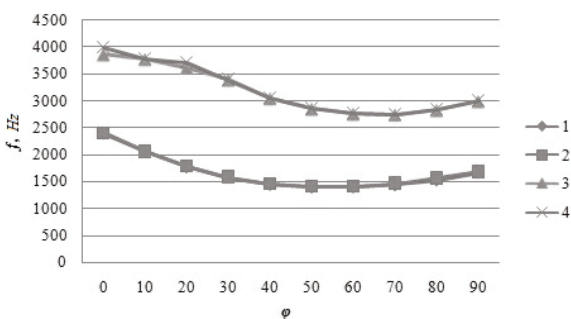


Fig. 8.4 The first four frequencies of free vibrations of a non-circular cylindrical shell of variable thickness with two bases fixed on the cutting angle along a major semi-axis



the major semi-axis for the case of rigidly fixed at one end and at 0^0 for the case of rigidly fixed at two ends. For a shell fixed at two ends, with an cutting angle of 30^0 and higher relative to the major semi-axis, the third and fourth natural frequencies correspond to vibrations of free edges, and for cutting angles of up to 30^0 , vibrations along the contour of the shell predominate. For a shell fixed at one end, there are discrepancies in the values of the third and fourth natural frequencies up to 13%.

The first ten natural frequencies of the non-circular cylindrical shell of variable thickness of the cutting along the minor semi-axis with one end rigidly fixed, de-

pending on the angle of the cutting, are shown in Table 8.5. For comparison, the frequencies for a closed non-circular cylindrical shell of variable thickness are given under the corresponding boundary conditions. Table 8.6 shows the first ten natural frequencies of a non-circular cylindrical shell of variable thickness of the cutting along the minor semi-axis, fixed at two ends, depending on the angle of the cutting. The first natural frequency of a closed non-circular cylindrical shell of variable thickness rigidly fixed at one end is 2 times greater than the corresponding frequency of an identical shell with a cut ($\varphi = 0^0$) along the minor axis and is 2.4 times greater in the case of rigid fastening of two ends.

Comparisons of the dependencies of the first four frequencies of free vibrations of a non-circular cylindrical shell of variable thickness on the angle of cutting along the minor semi-axis with one end fixed are shown in Fig. 8.5, and for the case of fixed two ends in Fig. 8.6. The first two natural frequencies correspond to the symmetric and anti-symmetric form of vibrations of free edges along the cut. The maximum

Table 8.5

Frequencies of free vibrations (f_{num} , Hz) of a shell of variable thickness rigidly fixed along one end, opened along the minor semi-axis

No. Closed	Angle of the cutting about the major semi-axis φ , degrees										
	0	10	20	30	40	50	60	70	80	90	
1	1725	841	912	959	983	990	991	992	927	804	710
2	1800	849	915	990	1055	1098	1098	1037	994	961	826
3	2128	1637	1701	1825	1815	1766	1763	1838	1679	1511	1528
4	2225	1841	1942	1882	2008	2239	2157	1917	2002	2189	2011
5	3238	1896	2025	2241	2516	2389	2535	2872	2720	2526	2703
6	3718	1963	2054	2277	2532	2813	3070	2966	3186	3025	2753
7	3796	2042	2139	2393	2597	2842	3126	3231	3282	3189	2927
8	3948	2600	2857	2766	2725	3143	3192	3317	3403	3899	4338
9	4398	3085	2938	3214	3582	3410	3685	4298	4622	4376	4480
10	4446	3269	3495	3738	3659	4236	4540	4492	4710	4875	4757

Table 8.6

Frequencies of free vibrations (f_{num} , Hz) of a shell of variable thickness rigidly fixed at two ends, opened along the minor semi-axis

No. Closed	Angle of the cutting about the major semi-axis φ , degrees										
	0	10	20	30	40	50	60	70	80	90	
1	3955	1679	1826	2028	2264	2513	2714	2821	2833	2628	2365
2	3980	1680	1826	2030	2267	2517	2746	2877	2835	2736	2436
3	4360	2997	3201	3517	3929	4143	4125	4100	4227	3959	3904
4	4389	2997	3201	3518	3929	4181	4282	4405	4252	4533	4343
5	5538	4023	4087	4076	4082	4450	5038	5493	5773	5356	5167
6	5615	4130	4097	4155	4196	4451	5046	5557	5811	5640	5275
7	6539	4338	4650	4893	5045	5335	5588	5571	5853	5733	5391
8	6542	4561	4749	5080	5591	5781	5839	6567	6080	6540	6569
9	6573	4658	4931	5367	5961	6352	6634	6653	6661	6635	6788
10	6574	4671	4935	5370	5963	6647	6684	6727	6834	6934	6931

Fig. 8.5 The first four frequencies of free vibrations of a non-circular cylindrical shell of variable thickness on the angle of cutting along the minor semi-axis with one end fixed

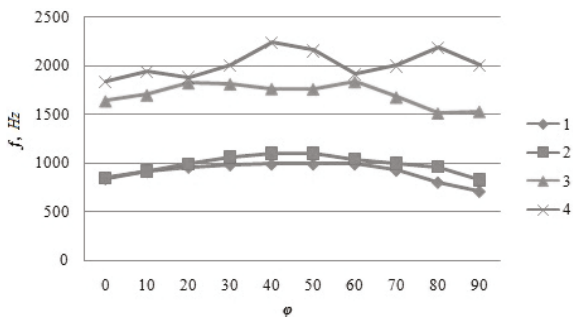
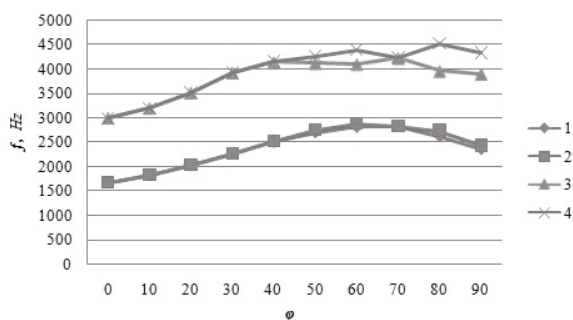


Fig. 8.6 The first four frequencies of free vibrations of a non-circular cylindrical shell of variable thickness on the angle of cutting along the minor semi-axis with two ends fixed



value of the first resonant frequency is observed at an cutting angle of 60° relative to the minor semi-axis for the case of rigidly fixed at one end and at 70° for the case of rigidly fixed at two ends.

For a shell fixed at two ends, with an angle of cutting of up to 40° along the minor semi-axis, the third and fourth frequencies correspond to vibrations of free edges, and for cutting angles of 40° and higher, vibrations along the shell contour predominate. A comparison of the nature of the dependencies of the first resonant frequency on the angle of cutting is shown in Fig. 8.7. The influence of the cutting

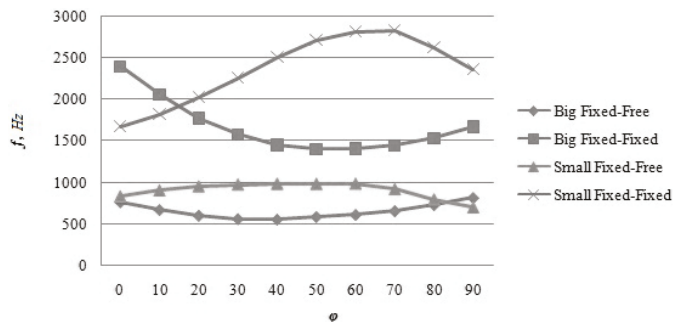


Fig. 8.7. Comparison of the nature of the dependencies of the first resonant frequency on the angle of cutting

angle is greater in the case of fixing two ends. The nature of the dependencies of the resonant frequency on the angle of cutting along the major semi-axis is opposite that along the minor semi-axis.

The first four forms of free vibrations of an open cylindrical shell of variable thickness with different values of the cutting angle along the major or minor axis for one or two rigidly fixed ends are shown in Figs. 8.8-8.15.

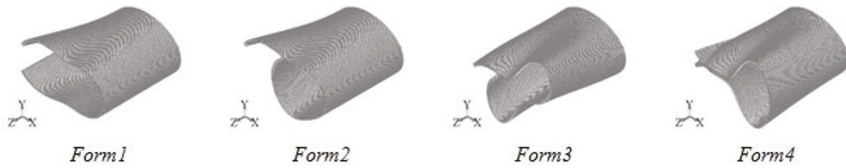


Fig. 8.8. The first four forms of free vibrations of an open cylindrical shell of variable thickness with a value of the cutting angle $\varphi = 0^0$ along the major axis for one fixed ends

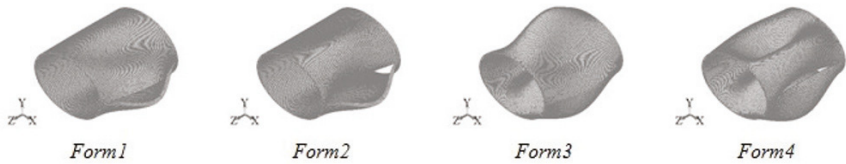


Fig. 8.9. The first four forms of free vibrations of an open cylindrical shell of variable thickness with a value of the cutting angle $\varphi = 0^0$ along the major axis for two rigidly fixed ends

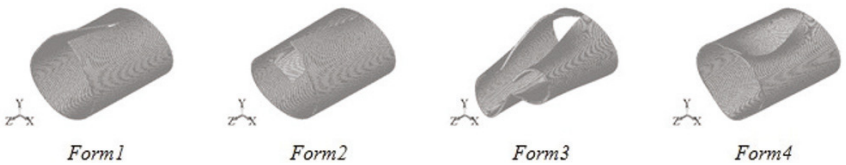


Fig. 8.10. The first four forms of free vibrations of an open cylindrical shell of variable thickness with a value of the cutting angle $\varphi = 0^0$ along the minor axis for one rigidly fixed ends

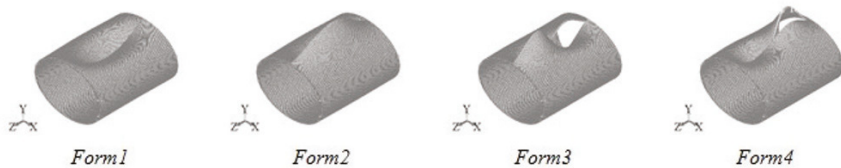


Fig. 8.11. The first four forms of free vibrations of an open cylindrical shell of variable thickness with a value of the cutting angle $\varphi = 0^0$ along the minor axis for two rigidly fixed ends

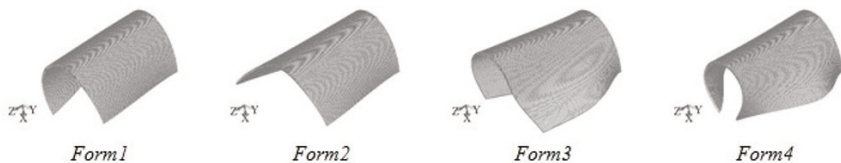


Fig. 8.12. The first four forms of free vibrations of an open cylindrical shell of variable thickness with a value of the cutting angle $\varphi = 90^0$ along the major axis for one rigidly fixed ends

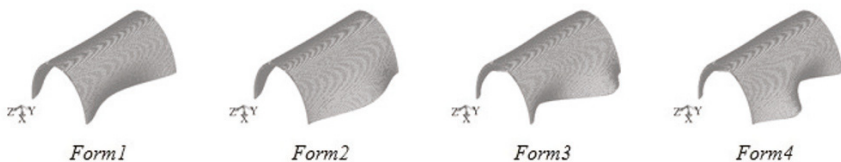


Fig. 8.13. The first four forms of free vibrations of an open cylindrical shell of variable thickness with a value of the cutting angle $\varphi = 90^0$ along the major axis for two rigidly fixed ends

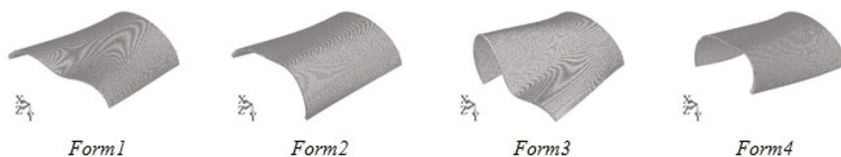


Fig. 8.14. The first four forms of free vibrations of an open cylindrical shell of variable thickness with a value of the cutting angle $\varphi = 90^0$ along the minor axis for one rigidly fixed ends

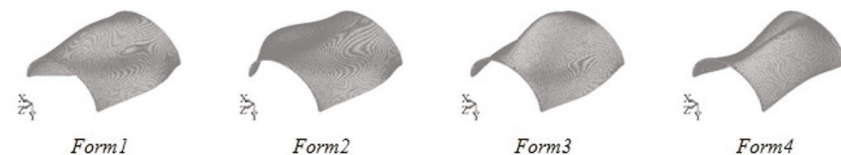


Fig. 8.15. The first four forms of free vibrations of an open cylindrical shell of variable thickness with a value of the cutting angle $\varphi = 90^0$ along the minor axis for two rigidly fixed ends

8.6 Conclusion

The resonance frequencies of free vibrations of an open cylindrical shell of an elliptical cross section of variable thickness were calculated for different cutting angles along the minor and major semi-axes with one and two rigidly fixed end by the finite element method implemented using the FEMAP software package.

Numerically obtained frequencies and forms of free vibrations of the considered shell make it possible to draw a number of conclusions:

- the first two natural frequencies of a closed non-circular cylindrical shell of variable thickness rigidly fixed along one end are 2.2-2.3 times greater than the corresponding frequencies of an identical shell with a cut along the major axis and 2.1 times with an cutting along the minor axis;
- if two ends are fixed the first two natural frequencies of the closed non-circular cylindrical shell are 1.7 times greater than the corresponding frequencies of the non-circular cylindrical shell with a cut along the major semi-axis and 2.4 times with an cutting along the minor semi-axis;
- the first two frequencies correspond to the symmetric and antisymmetric form of vibrations of free edges along the cutting;
- the maximum value of the first resonant frequency is observed at an cutting angle of 0^0 relative to the large semi-axis for rigid fixe at two ends and at 90^0 for rigid fixed at one end;
- the maximum value of the first resonant frequency is observed for a shell with one rigidly fixed end at an cutting angle of 60^0 relative to the minor axis, for fixed at two ends at an cutting angle of 70^0 relative to the minor axis;
- for a shell fixed at two ends with an cutting at an angle of 30^0 and above relative to the major semi-axis, the third and fourth natural frequencies correspond to vibrations of free edges, and for cutting at angles of up to 30^0 vibrations along the contour of the shell predominate;
- for a shell fixed at two ends with an cutting at an angle of up to 40^0 relative to the minor semi-axis, the third and fourth frequencies correspond to vibrations of free edges, and for an cutting at angles of 40^0 and above, vibrations along the shell contour predominate;
- for a shell with one rigidly fixed end, there are discrepancies in the values of the third and fourth frequencies up to 45% when the cutting is relative to the minor axis and up to 13% when the cutting is relative to the major axis;
- in the case of two fixed ends, the cutting angle more evenly affects the frequency distribution;
- the nature of the dependencies of the resonant frequency on the cutting with an angle relative to the major semi-axis are opposite those with an angle relative to the minor semi-axis.

References

- Arnold RN, Warburton GB (1953) The flexural vibrations of thin cylinders. *Proceedings of the Institution of Mechanical Engineers* 167(1):62–80
- Baron ML, Bleich HH (1954) Tables for frequencies and modes of free vibration of infinitely long thin cylindrical shells. *J Appl Mech* 21(2):178–188
- Budak VD, Grigorenko AY, Khorishko VV, Boichuk EV (2014) Holographic interferometry study of the free vibrations of cylindrical shells of constant and variable thickness. *Int Appl Mech* 50(1):68–74
- Budak VD, Grigorenko AY, Borisenko MY, Boichuk EV (2016) Natural frequencies and modes of noncircular cylindrical shells with variable thickness. *J of Mathematical Sci* 212(2):182–192
- Budak VD, Grigorenko AY, Borisenko MY, Boichuk EV (2017) Natural frequencies and modes of noncircular cylindrical shells with variable thickness. *Int Appl Mech* 53(2):167–172
- Greenspon JF (1959) Vibration of thick cylindrical shells. *J Acoust Soc Amer* 31(12):1682–1683
- Grigorenko A, Zolotoi Y, Prigoda A, Zhuk I, Khorishko V, Ovcharenko A (2013) Experimental investigation of natural vibrations of a thick-walled cylindrical shell by the method of holographic interferometry. *J of Mathematical Sci* 194(3):239–244
- Grigorenko AY, Borisenko MY, Boichuk EV, Prigoda AP (2018) Numerical determination of natural frequencies and modes of the vibrations of a thick-walled cylindrical shell. *Int Appl Mech* 54(1):75–84
- Grigorenko OY, Rozhok LS (2004) Solving the stress problem for hollow cylinders with corrugated elliptical cross section. *Int Appl Mech* 40(2):169–175
- Grigorenko OY, Parkhomenko OY, Vasil'eva LY, Borisenko MY (2017) Solution of the problem of free vibrations of a nonthin orthotropic shallow shell of variable thickness in the refined statement. *J of Mathematical Sci* 229(3):253–268
- Leissa AW (1973) *Vibration of shells*. SP 288, NASA, Washington DC
- Lekomtsev SV (2012) Finite-element algorithms for calculation of natural vibrations of three-dimensional shells. *Computational Continuum Mechanics* 5(2):233–243
- Markus S (1988) *The Mechanics of Vibrations of Cylindrical Shells*. Elsevier, Amsterdam
- Stricklin JA, Martinez JE, Tillerson JR, Hong JH, Haisler WE (1971) Nonlinear dynamic analysis of shells of revolution by matrix displacement method. *AIAA Journal* 9(4):629–636
- Suzuki K, Leissa AW (1986) Exact solutions for the free vibrations of open cylindrical shells with circumferentially varying curvature and thickness. *Journal of Sound and Vibration* 107(1):1 – 15
- Xiong-liang Y, Dong T, Fu-zhen P, Shuo L (2016) Exact free vibration analysis of open circular cylindrical shells by the method of reverberation-ray matrix. *Journal of Zhejiang University - SCIENCE A* 17(4):295 – 316



Chapter 9

Use of Quadratic Strain Interpolation Functions in a Mixed Quadrilateral Shell Element

Friedrich Gruttmann and Werner Wagner

Abstract In this paper a robust and effective shell element for the structural analysis of thin structures is presented. A Hu–Washizu functional with independent displacements, stress resultants and shell strains is the variational basis of the theory. Based on a previous paper an additional interpolation part with quadratic shape functions is introduced for the independent shell strains. This leads to a significant improved convergence behavior especially for unstructured meshes. The expanded element formulation proves to be insensitive to mesh distortion. Another essential feature of the quadrilateral element is the robustness in nonlinear applications with large deformations.

Key words: Reissner–Mindlin shell theory · Hu–Washizu variational principle · Quadratic strain interpolation functions · High accuracy for coarse meshes · Insensitivity towards mesh distortion

9.1 Introduction

Nonlinear structural analysis of thin structures requires effective and robust element formulations. Desired properties are high accuracy when using reasonable unstructured meshes and the possibility of large solution steps.

To bypass the difficulties caused by C^1 -requirements of the Kirchhoff–Love theory many of the shell models consider transverse shear deformations within a

Friedrich Gruttmann
Fachgebiet Festkörpermechanik, Technische Universität Darmstadt, Franziska-Braun-Str. 7,
64287 Darmstadt, Germany
e-mail: gruttmann@mechanik.tu-darmstadt.de

Werner Wagner
Institut für Baustatik, Karlsruher Institut für Technologie, Kaiserstr. 12, 76131 Karlsruhe, Germany
e-mail: werner.wagner@kit.edu

Reissner–Mindlin theory. Low order elements like quadrilaterals using a standard displacement interpolation are characterized by locking phenomena and lead to unacceptable stiff results when reasonable finite element meshes are employed. In shells two types of locking occur: transverse shear locking in which bending modes are excluded and nearly all energy is stored in transverse shear terms, and membrane locking in which bending energy is restrained and energy is stored in membrane terms.

An effective method to avoid transverse shear locking is based on assumed shear strain fields first proposed in MacNeal (1978), and subsequently extended among others in Hughes and Tezduyar (1981); Dvorkin and Bathe (1984). The assumed strain method has also been applied to approximate the membrane strains, e.g. Choi and Paik (1996); Koschnick et al (2005); Kulikov and Plotnikova (2010); Ko et al (2017a,b); Lavrenčič and Brank (2019, 2020). The papers show that membrane locking is relieved.

The basis for assumed strain methods are multi-field variational principles. Especially for linear elasticity the Hellinger–Reissner functional is adequate as variational foundation for mixed interpolated elements, e.g. Sze and Chow (1991); Gruttmann and Wagner (2005); Wiśniewski and Turska (2008). In case of a nonlinear material law a local iteration for the determination of the physical strains is necessary. Hence, a Hu–Washizu functional with independent displacements, stresses and strains seems to be more appropriate, e.g. Kulikov and Plotnikova (2002); Wagner and Gruttmann (2005); Gruttmann and Wagner (2006); Wiśniewski and Turska (2009); Wiśniewski et al (2010); Lavrenčič and Brank (2019, 2020). Within the so-called enhanced strain formulation the independent stresses are eliminated from the set of equations using orthogonality conditions and a two field formulation remains (Simo and Rifai, 1990). This approach has been successfully applied for shell problems in a multiplicity of publications.

An important issue within the context of developing a finite shell model is the number and type of rotation parameters on the element. Mostly general shell theories exclude explicit dependence of a rotational field about the normal to the shell surface which leads to a five parameter model (three displacements and two local rotations). Use of 5 degree-of-freedom frame requires construction of special coordinate systems for the rotational parameters. Considering the so-called drilling degree-of-freedom leads to a finite element discretization with six nodal parameters. This has some advantages since both displacement and rotation parameters are associated with a global coordinate frame (e.g. Gruttmann et al, 1992).

The essential features and new aspects of the present formulation are as follows:

- The nonlinear variational formulation is based on a Hu–Washizu functional with independent displacements, stress resultants and shell strains. The associated Euler–Lagrange equations are the static and geometric field equations, the constitutive equations and the static boundary conditions. The kinematic relations account for transverse shear deformations and are valid for finite rotations. The strain energy is chosen as a quadratic function of the independent shell strains. Based on our previous publication (Gruttmann and Wagner, 2006) the following amendments are included.

- In this paper the strain approximation is modified. The first part with 14 parameters corresponds to the stress interpolation. The second part with a variable number or parameters is expanded using quadratic shape functions. The functions of the second part are chosen orthogonal to the constant part of the strains.
- The resulting mixed hybrid quadrilateral element fulfills the membrane and bending patch test and possesses the correct rank. The element is tested by means of several nonlinear shell problems. It is shown that the expanded interpolation of the shell strains with quadratic shape functions relieves membrane locking in an effective way. It is emphasized that for pure membrane problems below presented interpolation matrices lead to results which are too soft and thus are not applicable.

9.2 Hu–Washizu Variational Formulation

Let \mathcal{B} be the three-dimensional Euclidean space occupied by the shell of thickness h in the reference configuration. With ξ^i we denote a convected coordinate system of the body. The coordinate in thickness direction ξ^3 is bounded by $h^- \leq \xi^3 \leq h^+$, where h^- and h^+ are the coordinates of the outer surfaces. In the following the summation convention is used for repeated indices, where Latin indices range from 1 to 3 and Greek indices range from 1 to 2. Commas denote partial differentiation with respect to the coordinates ξ^α . The coordinate on the boundary $\Gamma = \Gamma_u \cup \Gamma_\sigma$ of the initial reference surface Ω is denoted by s .

The position vectors of the initial and current shell reference surface are denoted as $\mathbf{X}(\xi^1, \xi^2)$ and $\mathbf{x}(\xi^1, \xi^2)$, respectively. Hence, the displacement vector of the reference surface is defined with $\mathbf{u} = \mathbf{x} - \mathbf{X}$. A vector field $\mathbf{D}(\xi^1, \xi^2)$ with $|\mathbf{D}(\xi^1, \xi^2)| = 1$, associated with the initial configuration, is introduced. The unit director \mathbf{d} of the current configuration is obtained by an orthogonal transformation of the initial vector \mathbf{D} . With $\mathbf{x}_{,\alpha} \cdot \mathbf{d} \neq 0$ shear deformations are accounted for within the Reissner–Mindlin theory.

The shell is loaded statically by surface loads $\bar{\mathbf{p}}$ on Ω as well as by boundary loads $\bar{\mathbf{t}}$ and couple loads $\bar{\mathbf{m}}$ on the boundary Γ_σ . The variational formulation is based on the Hu–Washizu functional

$$\Pi(\mathbf{v}, \boldsymbol{\sigma}, \boldsymbol{\varepsilon}) = \int_{\Omega} [W(\boldsymbol{\varepsilon}) + \boldsymbol{\sigma}^T (\boldsymbol{\varepsilon}_g(\mathbf{v}) - \boldsymbol{\varepsilon}) - \mathbf{u}^T \bar{\mathbf{p}}] dA - \int_{\Gamma_\sigma} (\mathbf{u}^T \bar{\mathbf{t}} + \boldsymbol{\varphi}^T \bar{\mathbf{m}}) ds \rightarrow \text{stat.} \quad (9.1)$$

with $dA = j d\xi^1 d\xi^2$ and $j = |\mathbf{X}_{,1} \times \mathbf{X}_{,2}|$. Here, $\mathbf{v} = [\mathbf{u}, \boldsymbol{\varphi}]^T$ contains the displacements \mathbf{u} and rotational parameters $\boldsymbol{\varphi}$, as well as $\boldsymbol{\varepsilon}$ and $\boldsymbol{\sigma}$ denote the independent shell strains and stress resultants, respectively. We assume a strain energy density $W(\boldsymbol{\varepsilon})$, which can be written as a quadratic form $W(\boldsymbol{\varepsilon}) = \frac{1}{2} \boldsymbol{\varepsilon}^T \mathbf{C} \boldsymbol{\varepsilon}$ using the constant elasticity matrix \mathbf{C} . The geometric shell strains are organized in the vector

$$\boldsymbol{\varepsilon}_g(\mathbf{v}) = [\varepsilon_{11}, \varepsilon_{22}, 2\varepsilon_{12}, \kappa_{11}, \kappa_{22}, 2\kappa_{12}, \gamma_1, \gamma_2]^T, \quad (9.2)$$

where the membrane strains $\varepsilon_{\alpha\beta}$, curvatures $\kappa_{\alpha\beta}$ and transverse shear strains γ_α are derived from the Green-Lagrangean strain tensor

$$\begin{aligned}\varepsilon_{\alpha\beta} &= \frac{1}{2}(\mathbf{x}_{,\alpha} \cdot \mathbf{x}_{,\beta} - \mathbf{X}_{,\alpha} \cdot \mathbf{X}_{,\beta}) \\ \kappa_{\alpha\beta} &= \frac{1}{2}(\mathbf{x}_{,\alpha} \cdot \mathbf{d}_{,\beta} + \mathbf{x}_{,\beta} \cdot \mathbf{d}_{,\alpha} - \mathbf{X}_{,\alpha} \cdot \mathbf{D}_{,\beta} - \mathbf{X}_{,\beta} \cdot \mathbf{D}_{,\alpha}) \\ \gamma_\alpha &= \mathbf{x}_{,\alpha} \cdot \mathbf{d} - \mathbf{X}_{,\alpha} \cdot \mathbf{D}.\end{aligned}\quad (9.3)$$

The work conjugate stress resultants are integrals of the Second Piola–Kirchhoff stress tensor

$$\boldsymbol{\sigma} = [n^{11}, n^{22}, n^{12}, m^{11}, m^{22}, m^{12}, q^1, q^2]^T \quad (9.4)$$

with membrane forces $n^{\alpha\beta} = n^{\beta\alpha}$, bending moments $m^{\alpha\beta} = m^{\beta\alpha}$ and shear forces q^α .

Introducing $\boldsymbol{\theta} := [\mathbf{v}, \boldsymbol{\sigma}, \boldsymbol{\varepsilon}]^T$ and admissible variations $\delta\boldsymbol{\theta} := [\delta\mathbf{v}, \delta\boldsymbol{\sigma}, \delta\boldsymbol{\varepsilon}]^T$ the stationary condition associated with functional (9.1) reads with displacement independent loads $\bar{\mathbf{p}}$, $\bar{\mathbf{t}}$ and $\bar{\mathbf{m}}$

$$\begin{aligned}\delta\Pi := g(\boldsymbol{\theta}, \delta\boldsymbol{\theta}) &= \int_{\Omega} [\delta\boldsymbol{\varepsilon}^T (\partial_{\boldsymbol{\varepsilon}} W - \boldsymbol{\sigma}) + \delta\boldsymbol{\sigma}^T (\boldsymbol{\varepsilon}_g - \boldsymbol{\varepsilon}) + \delta\boldsymbol{\varepsilon}_g^T \boldsymbol{\sigma}] dA + g_{\text{ext}} = 0 \\ g_{\text{ext}} &= - \int_{\Omega} \delta\mathbf{u}^T \bar{\mathbf{p}} dA - \int_{\Gamma_\sigma} (\delta\mathbf{u}^T \bar{\mathbf{t}} + \delta\varphi^T \bar{\mathbf{m}}) ds.\end{aligned}\quad (9.5)$$

With integration by parts and application of standard arguments of variational calculus one obtains the associated Euler–Lagrange equations. These are the static field equations, the geometric field equations and the constitutive equations in Ω , as well as the static boundary conditions on Γ_σ , see Wagner and Gruttmann (2005).

The associated finite element equations are iteratively solved applying Newton's method. For this purpose the linearization of the stationary condition (9.5) is derived with $\mathbf{C} = \partial_{\boldsymbol{\varepsilon}}^2 W$ as

$$\begin{aligned}\mathbf{L}[g(\boldsymbol{\theta}, \delta\boldsymbol{\theta}), \Delta\boldsymbol{\theta}] &:= g(\boldsymbol{\theta}, \delta\boldsymbol{\theta}) + \mathbf{D}g \cdot \Delta\boldsymbol{\theta} \\ &= g_{\text{ext}} + \int_{\Omega} \Delta\delta\boldsymbol{\varepsilon}_g^T \boldsymbol{\sigma} dA \\ &\quad + \int_{\Omega} \begin{bmatrix} \delta\boldsymbol{\varepsilon}_g \\ \delta\boldsymbol{\sigma} \\ \delta\boldsymbol{\varepsilon} \end{bmatrix}^T \left\{ \begin{bmatrix} \boldsymbol{\sigma} \\ \boldsymbol{\varepsilon}_g - \boldsymbol{\varepsilon} \\ \partial_{\boldsymbol{\varepsilon}} W - \boldsymbol{\sigma} \end{bmatrix} + \begin{bmatrix} \mathbf{0} & \mathbf{1} & \mathbf{0} \\ \mathbf{1} & \mathbf{0} & -\mathbf{1} \\ \mathbf{0} & -\mathbf{1} & \mathbf{C} \end{bmatrix} \begin{bmatrix} \Delta\boldsymbol{\varepsilon}_g \\ \Delta\boldsymbol{\sigma} \\ \Delta\boldsymbol{\varepsilon} \end{bmatrix} \right\} dA.\end{aligned}\quad (9.6)$$

Finally, the geometric boundary conditions $\mathbf{v} = \bar{\mathbf{v}}$ on Γ_u have to be fulfilled as constraints.

9.3 Finite Element Equations

The approximation of initial and current geometry of the shell reference surface applying the isoparametric concept for 4-node elements is specified in detail in Wagner and Gruttmann (2005); Gruttmann and Wagner (2006). Bilinear functions $N_I(\xi, \eta)$ are used, where for the coordinates of the unit square $-1 \leq \{\xi, \eta\} \leq 1$ holds. The constant orthonormal element coordinate system is denoted by $[\mathbf{t}_1, \mathbf{t}_2, \mathbf{t}_3]$, where \mathbf{t}_3 is normal vector of the approximated shell surface at the element center. Hence the Jacobian matrix \mathbf{J} follows from

$$\mathbf{J} = \begin{bmatrix} J_{11} & J_{12} \\ J_{21} & J_{22} \end{bmatrix} = \begin{bmatrix} \mathbf{X}^h_{,\xi} \cdot \mathbf{t}_1 & \mathbf{X}^h_{,\xi} \cdot \mathbf{t}_2 \\ \mathbf{X}^h_{,\eta} \cdot \mathbf{t}_1 & \mathbf{X}^h_{,\eta} \cdot \mathbf{t}_2 \end{bmatrix} \tag{9.7}$$

The superscript h refers to the finite element approximation of the particular quantity. Furthermore, commas denote the partial derivative with respect to ξ or η . The matrices

$$\mathbf{T}^0 = \begin{bmatrix} J_{11}^0 & J_{11}^0 & J_{21}^0 & J_{21}^0 & a J_{11}^0 & J_{21}^0 \\ J_{12}^0 & J_{12}^0 & J_{22}^0 & J_{22}^0 & a J_{12}^0 & J_{22}^0 \\ b J_{11}^0 & J_{12}^0 & b J_{21}^0 & J_{22}^0 & J_{11}^0 & J_{22}^0 + J_{12}^0 & J_{21}^0 \end{bmatrix} \quad \tilde{\mathbf{T}}^0 = \begin{bmatrix} J_{11}^0 & J_{21}^0 \\ J_{12}^0 & J_{22}^0 \end{bmatrix} \tag{9.8}$$

cause a transformation of contravariant tensor components to the constant element base system \mathbf{t}_i . The entries $J_{\alpha\beta}^0$ are the components of \mathbf{J} evaluated at the element center. The factors a and b are specified below. Detailed investigations on the use of ansatz functions for contravariant stress *and* strain components in the framework of a Hu–Washizu functional are contained in Wiśniewski et al (2010).

The finite element approximation of the vector $\delta\boldsymbol{\theta}^h := [\delta\boldsymbol{\varepsilon}_g^h, \delta\boldsymbol{\sigma}^h, \delta\boldsymbol{\varepsilon}^h]^T$ reads

$$\begin{bmatrix} \delta\boldsymbol{\varepsilon}_g^h \\ \delta\boldsymbol{\sigma}^h \\ \delta\boldsymbol{\varepsilon}^h \end{bmatrix} = \begin{bmatrix} \mathbf{B} & \mathbf{0} & \mathbf{0} \\ \mathbf{0} & \mathbf{N}_\sigma & \mathbf{0} \\ \mathbf{0} & \mathbf{0} & \mathbf{N}_\varepsilon \end{bmatrix} \begin{bmatrix} \delta\hat{\mathbf{v}} \\ \delta\hat{\boldsymbol{\sigma}} \\ \delta\hat{\boldsymbol{\varepsilon}} \end{bmatrix} \tag{9.9}$$

$$\delta\boldsymbol{\theta}^h = \mathbf{N}_\theta \delta\hat{\boldsymbol{\theta}}.$$

To avoid transverse shear locking, ansatz functions of the assumed strain method (Dvorkin and Bathe, 1984) are incorporated in \mathbf{B} . For details we refer to Gruttmann and Wagner (2006).

The matrix \mathbf{N}_σ for the interpolation of $\boldsymbol{\sigma}^h$ and $\delta\boldsymbol{\sigma}^h$ is chosen as follows

$$\mathbf{N}_\sigma = \begin{bmatrix} \mathbf{1}_3 & \mathbf{0} & \mathbf{0} & \mathbf{N}_\sigma^m & \mathbf{0} & \mathbf{0} \\ \mathbf{0} & \mathbf{1}_3 & \mathbf{0} & \mathbf{0} & \mathbf{N}_\sigma^b & \mathbf{0} \\ \mathbf{0} & \mathbf{0} & \mathbf{1}_2 & \mathbf{0} & \mathbf{0} & \mathbf{N}_\sigma^s \end{bmatrix}$$

$$\mathbf{N}_{\sigma}^m = \mathbf{N}_{\sigma}^b = \mathbf{T}_{\sigma}^0 \begin{bmatrix} \eta - \bar{\eta} & 0 \\ 0 & \xi - \bar{\xi} \\ 0 & 0 \end{bmatrix} \quad \mathbf{N}_{\sigma}^s = \tilde{\mathbf{T}}_{\sigma}^0 \begin{bmatrix} \eta - \bar{\eta} & 0 \\ 0 & \xi - \bar{\xi} \end{bmatrix}, \quad (9.10)$$

where $\mathbf{1}_n$ denotes a unit matrix of order n . The coefficient matrices read $\mathbf{T}_{\sigma}^0 = \mathbf{T}^0$ with $a = 2$ and $b = 1$ as well as $\tilde{\mathbf{T}}_{\sigma}^0 = \tilde{\mathbf{T}}^0$. The constants $\bar{\xi}$ and $\bar{\eta}$ are the coordinates of the center of gravity of the particular element. For rectangular elements holds $\bar{\xi} = \bar{\eta} = 0$. The parameter vector $\delta\hat{\boldsymbol{\sigma}}$ contains 8 parameters for the constant part and 6 parameters for the varying part of the stress field. The interpolation of the membrane forces and bending moments corresponds to the membrane part in Simo et al (1990). The original approach for plane stress problems was published in Pian and Sumihara (1984). Regarding requirements on the interpolation functions to fulfill the patch test and to ensure stability of the discrete system of equations we refer to the discussion in Wagner and Gruttmann (2005).

The matrix \mathbf{N}_{ε} for the interpolation of the independent strains $\boldsymbol{\varepsilon}^h = \mathbf{N}_{\varepsilon} \hat{\boldsymbol{\varepsilon}}$ as well as $\delta\boldsymbol{\varepsilon}^h = \mathbf{N}_{\varepsilon} \delta\hat{\boldsymbol{\varepsilon}}$ is subdivided in two parts

$$\mathbf{N}_{\varepsilon} = [\mathbf{N}_{\varepsilon}^1, \mathbf{N}_{\varepsilon}^2], \quad (9.11)$$

where $\hat{\boldsymbol{\varepsilon}} = [\hat{\boldsymbol{\varepsilon}}_1, \hat{\boldsymbol{\varepsilon}}_2]^T$, $\hat{\boldsymbol{\varepsilon}}_1 \in \mathbb{R}^{14}$, $\hat{\boldsymbol{\varepsilon}}_2 \in \mathbb{R}^n$. The number of parameters n of the second part is specified below. The submatrices $\mathbf{N}_{\varepsilon}^1$ and $\mathbf{N}_{\varepsilon}^2$ read

$$\mathbf{N}_{\varepsilon}^1 = \begin{bmatrix} \mathbf{1}_3 & \mathbf{0} & \mathbf{0} & \mathbf{N}_{\varepsilon}^{m1} & \mathbf{0} & \mathbf{0} \\ \mathbf{0} & \mathbf{1}_3 & \mathbf{0} & \mathbf{0} & \mathbf{N}_{\varepsilon}^{b1} & \mathbf{0} \\ \mathbf{0} & \mathbf{0} & \mathbf{1}_2 & \mathbf{0} & \mathbf{0} & \mathbf{N}_{\varepsilon}^{s1} \end{bmatrix}_{8 \times 14} \quad \mathbf{N}_{\varepsilon}^2 = \begin{bmatrix} \frac{j_0}{j} \mathbf{T}_{\varepsilon}^0 \mathbf{M}_n \\ \mathbf{0} \\ \mathbf{0} \end{bmatrix}_{8 \times n} \quad (9.12)$$

with

$$\mathbf{N}_{\varepsilon}^{m1} = \mathbf{N}_{\varepsilon}^{b1} = \mathbf{T}_{\varepsilon}^0 \begin{bmatrix} \eta - \bar{\eta} & 0 \\ 0 & \xi - \bar{\xi} \\ 0 & 0 \end{bmatrix} \quad \mathbf{N}_{\varepsilon}^{s1} = \tilde{\mathbf{T}}_{\varepsilon}^0 \begin{bmatrix} \eta - \bar{\eta} & 0 \\ 0 & \xi - \bar{\xi} \end{bmatrix} \quad (9.13)$$

as well as $\mathbf{T}_{\varepsilon}^0 = \mathbf{T}^0$ with $a = 1$, $b = 2$ and $\tilde{\mathbf{T}}_{\varepsilon}^0 = \tilde{\mathbf{T}}^0$. Furthermore, $j_0 = j(\xi = 0, \eta = 0)$ and

$$\mathbf{M}_n = \begin{bmatrix} \xi & 0 & 0 & 0 & \xi\eta & 0 & 0 & (\xi^2 - c)\eta & 0 & \eta^2\xi & 0 \\ 0 & \eta & 0 & 0 & 0 & \xi\eta & 0 & 0 & (\eta^2 - c)\xi & 0 & \xi^2\eta \\ 0 & 0 & \xi & \eta & 0 & 0 & \xi\eta & 0 & 0 & 0 & 0 \end{bmatrix}. \quad (9.14)$$

The index $n \in \{0, 2, 4, 6, 7, 9, 11\}$ has the meaning that optionally the first n columns of \mathbf{M}_n are taken. With $n = 0$ only the first part of \mathbf{N}_{ε} is used. The shape factor

$$c = \frac{\max(G_{11}, G_{22})}{\min(G_{11}, G_{22})} + \frac{|G_{12}| + |G_{21}|}{\min(G_{11}, G_{22})} \quad (9.15)$$

considers the deviation of the element form from a square in the first part and the deviation from a rectangle in the second part. Here,

$$G_{11} = \mathbf{X}_{,\xi}^0 \cdot \mathbf{X}_{,\xi}^0, \quad G_{22} = \mathbf{X}_{,\eta}^0 \cdot \mathbf{X}_{,\eta}^0, \quad G_{12} = G_{21} = \mathbf{X}_{,\xi}^0 \cdot \mathbf{X}_{,\eta}^0 \quad (9.16)$$

denote the metric coefficients of the initial reference surface evaluated at the element center. For a square element holds $c = 1$. Due to the factor j_0/j and the constant coefficient matrix \mathbf{T}_ε^0 in (9.12) the integral of all functions in \mathbf{N}_ε^2 over the element domain Ω_e vanishes, thus the functions are orthogonal to the constant part of the membrane strains. In contrast to Gruttmann and Wagner (2006) also transformations of contravariant tensor components are considered in the interpolation matrix \mathbf{N}_ε^2 .

The finite element approximation of the external virtual work of $\bar{\mathbf{p}}, \bar{\mathbf{t}}$ and $\bar{\mathbf{m}}$ leads to

$$g_{\text{ext}}^h = - \sum_{e=1}^{\text{numel}} \delta \hat{\mathbf{v}}^T \mathbf{f}^e.$$

Here, *numel* denotes the total number of finite shell elements to discretize the problem and \mathbf{f}^e corresponds to the element load vector of a standard displacement method. Furthermore, it holds

$$\int_{\Omega} \Delta \delta \boldsymbol{\varepsilon}_g^{hT} \boldsymbol{\sigma}^h dA = \sum_{e=1}^{\text{numel}} \delta \hat{\mathbf{v}}^T \mathbf{k}_g \Delta \hat{\mathbf{v}},$$

where \mathbf{k}_g is specified in detail in Wagner and Gruttmann (2005).

We insert $\delta \boldsymbol{\theta}^h = \mathbf{N}_\theta \delta \hat{\boldsymbol{\theta}}$ according to Eq. (9.9) and the corresponding equation $\Delta \boldsymbol{\theta}^h = \mathbf{N}_\theta \Delta \hat{\boldsymbol{\theta}}$ into the linearized variational equation (9.12), which now reads

$$L[g(\boldsymbol{\theta}^h, \delta \boldsymbol{\theta}^h), \Delta \boldsymbol{\theta}^h] = \sum_{e=1}^{\text{numel}} \left[\begin{array}{c} \delta \hat{\mathbf{v}} \\ \delta \hat{\boldsymbol{\sigma}} \\ \delta \hat{\boldsymbol{\varepsilon}} \end{array} \right]_e^T \left\{ \left[\begin{array}{c} \mathbf{f}^i - \mathbf{f}^e \\ \mathbf{f}^s \\ \mathbf{f}^e \end{array} \right] + \left[\begin{array}{ccc} \mathbf{k}_g & \mathbf{G}^T & \mathbf{0} \\ \mathbf{G} & \mathbf{0} & \mathbf{F}^T \\ \mathbf{0} & \mathbf{F} & \mathbf{H} \end{array} \right] \left[\begin{array}{c} \Delta \hat{\mathbf{v}} \\ \Delta \hat{\boldsymbol{\sigma}} \\ \Delta \hat{\boldsymbol{\varepsilon}} \end{array} \right] \right\}_e \quad (9.17)$$

with

$$\begin{aligned} \mathbf{f}^i &= \int_{\Omega_e} \mathbf{B}^T \boldsymbol{\sigma}^h dA & \mathbf{F} &= - \int_{\Omega_e} \mathbf{N}_\varepsilon^T \mathbf{N}_\sigma dA \\ \mathbf{f}^s &= \int_{\Omega_e} \mathbf{N}_\sigma^T \boldsymbol{\varepsilon}_g^h dA + \mathbf{F}^T \hat{\boldsymbol{\varepsilon}} & \mathbf{G} &= \int_{\Omega_e} \mathbf{N}_\sigma^T \mathbf{B} dA \\ \mathbf{f}^e &= \int_{\Omega_e} \mathbf{N}_\varepsilon^T \partial_\varepsilon W dA + \mathbf{F} \hat{\boldsymbol{\sigma}} & \mathbf{H} &= \int_{\Omega_e} \mathbf{N}_\varepsilon^T \mathbf{C} \mathbf{N}_\varepsilon dA. \end{aligned} \quad (9.18)$$

The integrals over an element domain Ω_e of a particular element e are computed numerically using a 2×2 Gauss integration scheme. With incorporation of the quadratic functions in Eq. (9.14) a 3×3 Gauss integration is necessary.

Matrix \mathbf{F} is expressed with (9.11)

$$\mathbf{F} = - \int_{\Omega_e} \begin{bmatrix} \mathbf{N}_\varepsilon^1 \\ \mathbf{N}_\varepsilon^2 \end{bmatrix}^T \mathbf{N}_\sigma dA = \begin{bmatrix} \mathbf{F}_1 \\ \mathbf{F}_2 \end{bmatrix}. \quad (9.19)$$

The last four columns with quadratic shape functions in (9.14) are not orthogonal to column 9 and 10 of \mathbf{N}_σ according to (9.10) and thus lead to entries in \mathbf{F}_2 . They are consistently omitted when setting $\mathbf{F}_2 = \mathbf{0}$ in \mathbf{F} , \mathbf{f}^e and \mathbf{f}^s .

We continue with $L[g(\boldsymbol{\theta}^h, \delta\boldsymbol{\theta}^h), \Delta\boldsymbol{\theta}^h] = 0$, where $\delta\boldsymbol{\theta}^h \neq \mathbf{0}$ and obtain for each element

$$\begin{bmatrix} \mathbf{k}_g & \mathbf{G}^T & \mathbf{0} \\ \mathbf{G} & \mathbf{0} & \mathbf{F}^T \\ \mathbf{0} & \mathbf{F} & \mathbf{H} \end{bmatrix} \begin{bmatrix} \Delta\hat{\mathbf{v}} \\ \Delta\hat{\boldsymbol{\sigma}} \\ \Delta\hat{\boldsymbol{\varepsilon}} \end{bmatrix} + \begin{bmatrix} \mathbf{f}^i - \mathbf{f}^a \\ \mathbf{f}^s \\ \mathbf{f}^e \end{bmatrix} = \begin{bmatrix} \mathbf{r} \\ \mathbf{0} \\ \mathbf{0} \end{bmatrix} \quad (9.20)$$

where \mathbf{r} denotes the vector of element nodal forces. Since the stress resultants and shell strains are interpolated discontinuously across the element boundaries the parameters $\Delta\hat{\boldsymbol{\sigma}}$ and $\Delta\hat{\boldsymbol{\varepsilon}}$ can be eliminated from the set of equations. This is done by application of a standard Gaussian elimination procedure, see Cook et al (1989). One obtains the tangential element stiffness matrix \mathbf{k}_T^e , the element residual vector $\hat{\mathbf{f}}$ and (9.17) reduces to

$$L[g(\boldsymbol{\theta}^h, \delta\boldsymbol{\theta}^h), \Delta\boldsymbol{\theta}^h] = \sum_{e=1}^{numel} \delta\hat{\mathbf{v}}^T (\mathbf{k}_T^e \Delta\hat{\mathbf{v}} + \hat{\mathbf{f}}). \quad (9.21)$$

The shell elements possess 5 or 6 degrees of freedom (dofs) at the nodes. At nodes on intersections 6 dofs (3 global displacements and 3 global rotations) and at the remaining nodes 5 dofs (3 global displacements and 2 local rotations) are present. The linear element stiffness matrix possesses with six zero eigenvalues the correct rank. The derived element formulation has been implemented in an extended version of the general purpose finite element program FEAP (Taylor, 2020).

9.4 Examples

9.4.1 Membrane and Bending Patch Test

A rectangular plate under membrane forces and bending moments according to MacNeal and Harder (1985) is considered. Both, membrane and bending patch test are fulfilled for the meaningful parameters $n \in \{0, 2, 4, 6, 7, 9, 11\}$ by the developed element.

9.4.2 Hemispherical Shell

The first problem is the hemispherical shell with an 18° cutout subjected to alternating radial point loads P at its equator, shown in Fig. 9.1a. This geometrically non-linear example is often cited as a benchmark problem for shell elements and is a test for the ability to model rigid body modes and inextensible bending (MacNeal and Harder, 1985). Considering symmetry only one quarter of the structure corresponding to the region ABCD in Fig. 9.1a is discretized using 8×8 and 12×12 uniform meshes. Geometrical and material data are chosen with $R = 10$, $\varphi = 18^\circ$, thickness $h = 0.04$ and $E = 6.825 \cdot 10^7$, $\nu = 0.3$. We employ the boundary conditions $u_y = \beta = 0$ on \overline{AD} , $u_x = \beta = 0$ on \overline{BC} and $u_z = 0$ at a point on \overline{AB} , e.g. at A. Figure 9.2 shows the load displacement curves for the uniform meshes. The defined converged solution is obtained using a 128×128 uniform mesh. Results are only presented for $P - u_{xA}$; similar output can be obtained for $P - u_{yB}$. In addition, Fig. 9.3 depicts results for distorted meshes. The principal mesh distortion is described in Fig. 9.1b for a 4×4 mesh. Here each edge is discretized using the aspect ratios $L_1 : L_2 : L_3 : \dots : L_N = 1 : 2 : 3 : \dots : N$. The 12×12 distorted mesh is illustrated in Fig. 9.1c. As can be seen in Figs. 9.2 and 9.3, significant improvements can be achieved along with the quadratic terms in Eq. (9.14) ($n = 11$), especially for distorted meshes. For comparison we add results from Ko et al (2017b) using the MITC4+ element.

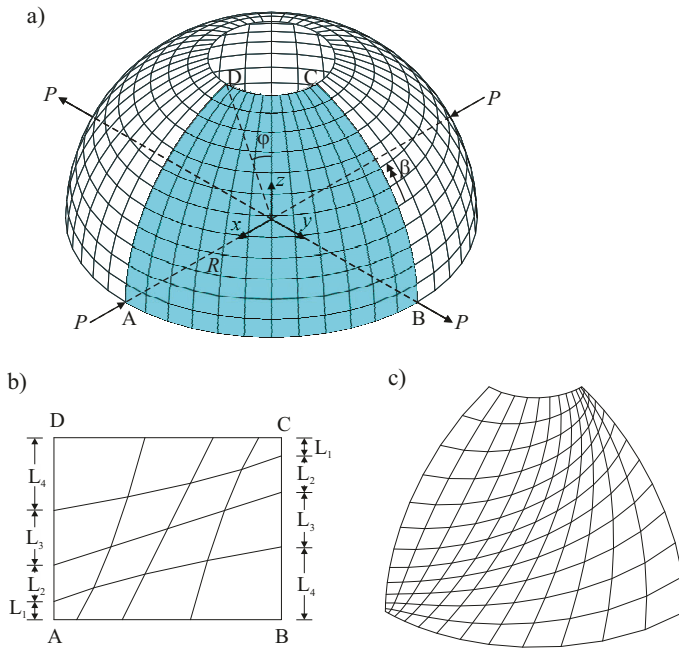


Fig. 9.1. Hemispherical shell: a) system and 12×12 uniform mesh, b) principal mesh distortion for 4×4 mesh, c) 12×12 distorted mesh

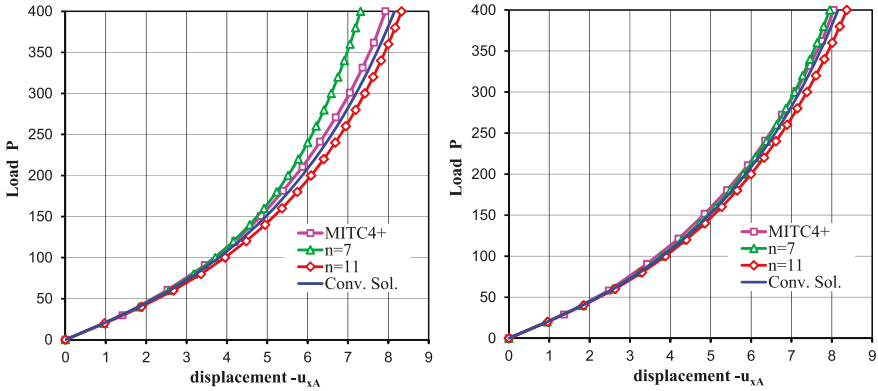


Fig. 9.2. Hemispherical shell: $P - u_{x_A}$ for the uniform 8×8 (left) and 12×12 (right) meshes

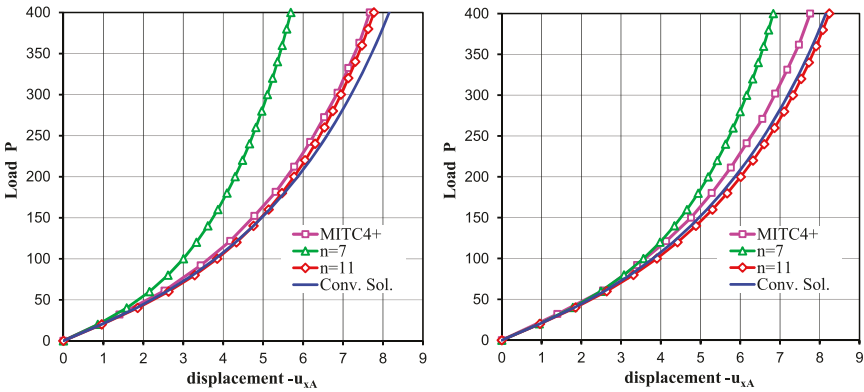


Fig. 9.3. Hemispherical shell: $P - u_{x_A}$ for the distorted 8×8 (left) and 12×12 (right) meshes

9.4.3 Cylindrical Shell Segment

In this subsection we examine a cylindrical shell segment, e.g. Bathe et al (1984), subjected to a uniform bending moment $M = M_0 \cdot h^3$ along \overline{BC} . The shell segment is fully clamped at \overline{DE} (Fig. 9.4). Geometrical and material data are chosen to $R = 20$, $L = 10$, thickness $h = R/10000$, $\theta = 30^\circ$ and $E = 2.1 \cdot 10^6$, $\nu = 0$.

Figure 9.5 depicts load displacement curves for point A and uniform meshes. A 128×128 uniform mesh is utilized for the defined converged solution. In addition, Fig. 9.6 shows results for distorted meshes. Here, the principal mesh distortion is described in Fig. 9.4b for a 4×4 mesh. Left and right edge are discretized using the aspect ratios $L_1 : L_2 : L_3 : \dots : L_N = 1 : 2 : 3 : \dots : N$. A 12×12 distorted mesh for the calculation is presented in Fig. 9.4c in a perspective view. Again, improvements can be achieved for distorted meshes when using the quadratic terms in Eq. (9.14) ($n = 11$). For comparison we add results from the element formulation (Lavrenčić

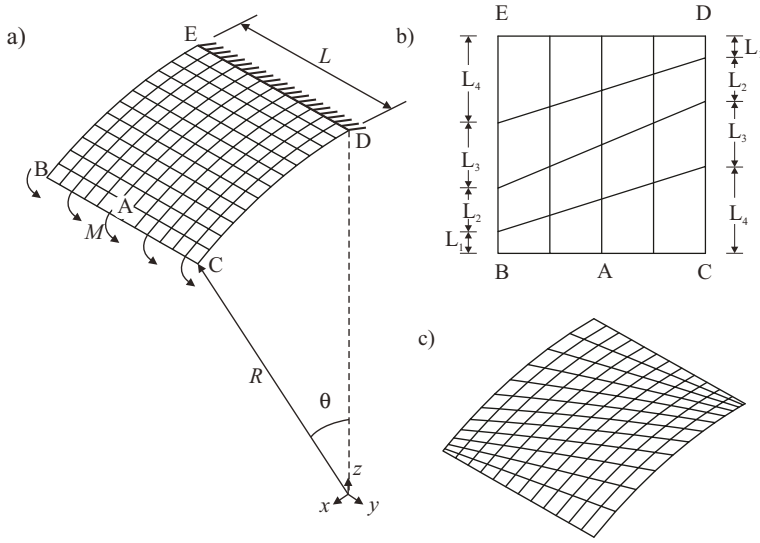


Fig. 9.4. Cylindrical shell segment: a) system and 12×12 uniform mesh, b) principal mesh distortion for 4×4 mesh, c) 12×12 distorted mesh

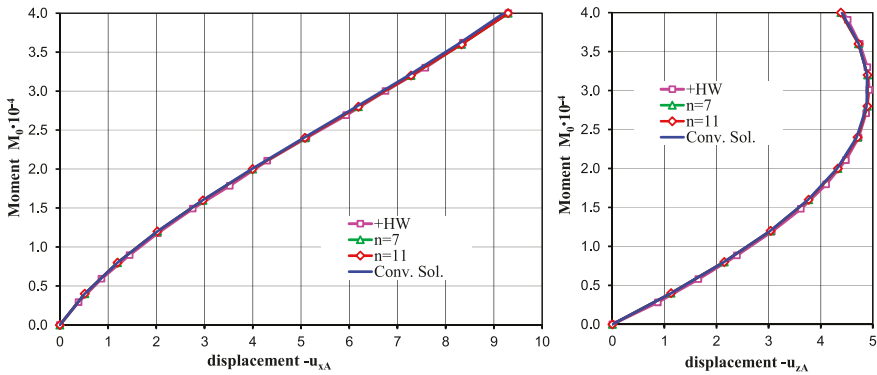


Fig. 9.5. Cylindrical shell segment: $M_0 - u_{xA}$ and $M_0 - u_{zA}$ for the uniform 12×12 mesh

and Brank, 2020) denoted as +HW. The performance of the MITC4+ element (Ko et al, 2017b) is similar.

9.4.4 Twisted Beam

Finally, we consider the twisted beam problem shown in Fig. 9.7, originally introduced in MacNeal and Harder (1985). Geometrical and material data are chosen to

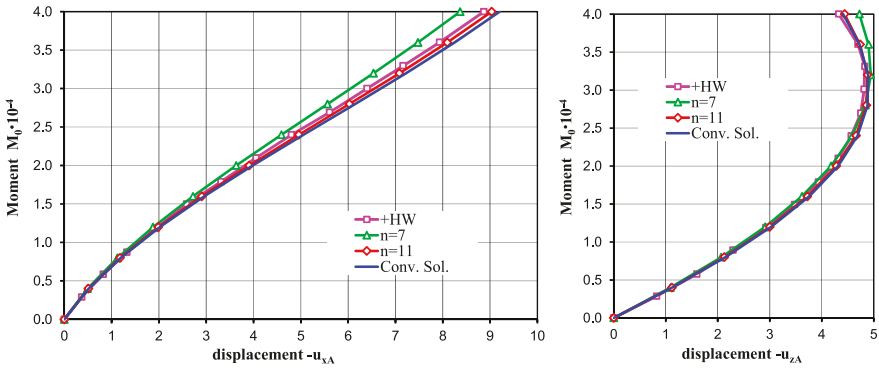
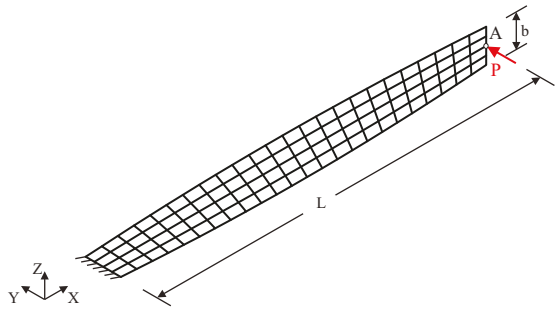


Fig. 9.6. Cylindrical shell segment: $M_0 - u_{xA}$ and $M_0 - u_{zA}$ for the distorted 12×12 mesh

Fig. 9.7 Twisted beam: system and 4×24 uniform mesh



$L = 12$, $b = 1.1$, thickness $h = 0.0032$ and $E = 29 \cdot 10^6$, $\nu = 0.22$, respectively. The cantilever beam is clamped at one end and is loaded by an out-of-plane acting load P at point A. A regular 4×24 mesh is selected for the solution. Figure 9.8 depicts the convergence behavior of the displacements of point A for different parameters n and results using the MITC4+ element (Ko et al, 2017b). Furthermore mesh distortion is investigated. The first distorted mesh is shown in Fig. 9.9a together with a flat projection in Fig. 9.9b, both in a perspective view. A ratio $L_{\max}/L_{\min} = 2$ is chosen, where L_{\max} and L_{\min} denote the longest and shortest element length in the flat projection, respectively. Figure 9.10 depicts the resulting load displacement curves of point A. In both cases we define a converged solution by employing a 32×192 uniform mesh. Very good results can be seen, even for $n = 0$. In addition we investigate a second distorted mesh, where the distortion is introduced in the opposite direction, see Fig. 9.11. Now, Fig. 9.12 illustrates the load displacement curves of point A with respect to the choice of n . Again, the quadratic terms in Eq. (9.14) ($n = 11$) are necessary to produce accurate results. The associated convergence behavior of displacement u_{yA} for the second distorted mesh versus the number of elements N in width direction is presented in Fig. 9.13. It is obvious that $n = 11$ leads to a significant improvement of the element behavior.

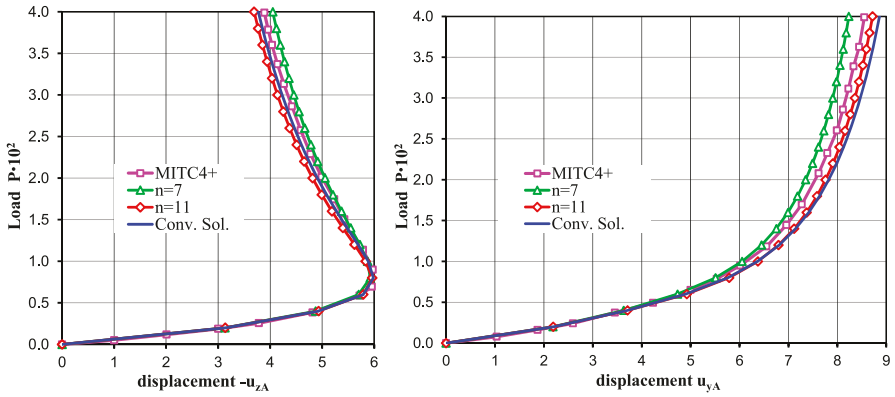


Fig. 9.8. Twisted beam: $P - u_{zA}$ and $P - u_{yA}$ for the regular 4×24 mesh

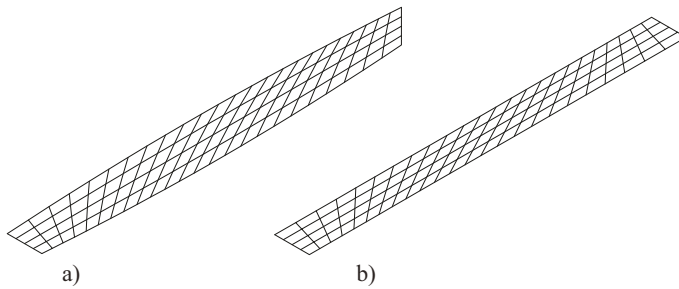


Fig. 9.9. Twisted beam: distorted 4×24 mesh 1, a) perspective view, b) perspective view of the flat projection

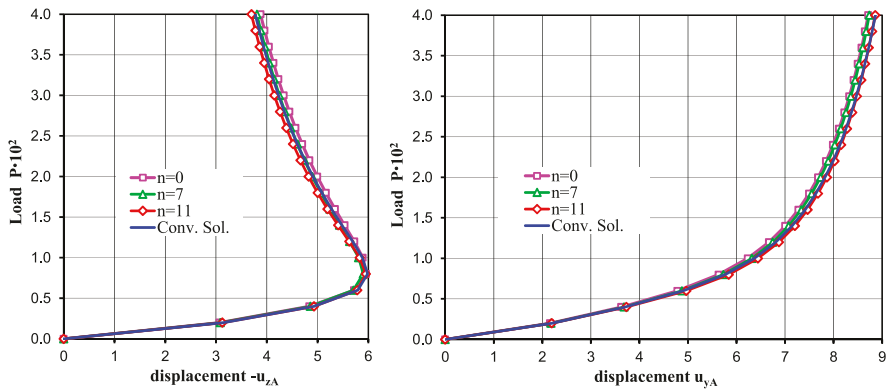


Fig. 9.10. Twisted beam: $P - u_{zA}$ and $P - u_{yA}$ for the distorted 4×24 mesh 1

Fig. 9.11 Twisted beam: distorted 4×24 mesh 2, a) perspective view, b) perspective view of the flat projection

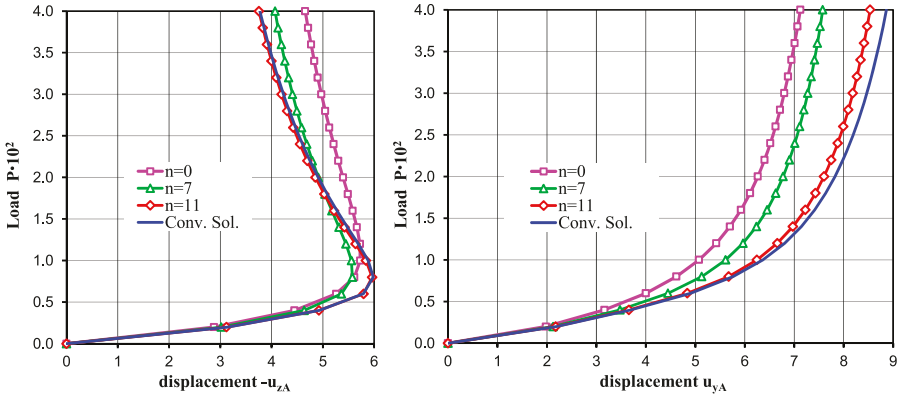
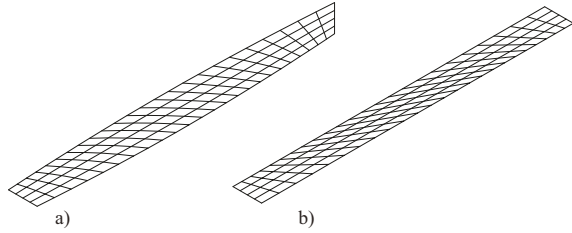
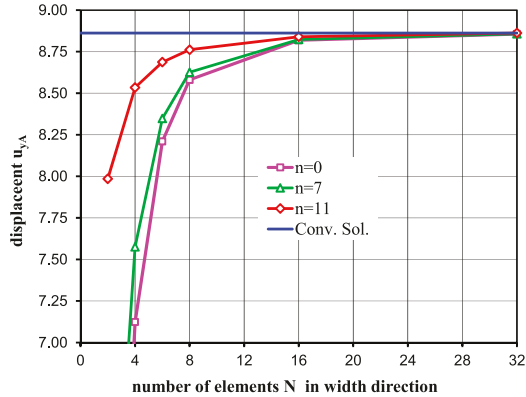


Fig. 9.12. Twisted beam: $P - u_{zA}$ and $P - u_{yA}$ for the distorted 4×24 mesh 2

Fig. 9.13 Twisted beam: $u_{yA} - N$ for distorted mesh 2



9.5 Conclusions

Based on a previous paper on a mixed hybrid quadrilateral shell element the interpolation matrix for the membrane strains are expanded by quadratic shape functions. Thereby membrane locking can be significantly relieved. The shape factor c according to Eq. (9.15) has been chosen by numerical tests. The new terms lead to a considerable improvement of the approximation behavior especially when the

element form deviates from a square or for distorted elements. Further systematic investigations using the proposed ansatz, like eigenvalue computations of the element stiffness matrix, should be topic of future research. For pure membrane problems the interpolation matrix leads to results which are too soft and thus is not applicable in the presented form. A well-known feature of present element formulation is the remarkable robustness in nonlinear applications. It allows very large load steps in comparison to element formulations based on the displacement method.

References

- Bathe KJ, Dvorkin E, Ho LW (1984) Our discrete-Kirchhoff and isoparametric shell elements for nonlinear analysis - an assessment. *Computer & Structures* 16(1):89–98
- Choi CK, Paik JG (1996) An effective four node degenerated shell element for geometrically nonlinear analysis. *Thin-Walled Structures* 24(3):261 – 283
- Cook RD, Malkus DS, Plesha ME (1989) *Concepts and Applications of Finite Element Analysis*. John Wiley & Sons
- Dvorkin E, Bathe KJ (1984) A continuum mechanics based four node shell element for general nonlinear analysis. *Engineering Computations* 1:77–88
- Gruttmann F, Wagner W (2005) A linear quadrilateral shell element with fast stiffness computation. *Computer Methods in Applied Mechanics and Engineering* 194:4279–4300
- Gruttmann F, Wagner W (2006) Structural analysis of composite laminates using a mixed hybrid shell element. *Computational Mechanics* 37:479–497
- Gruttmann F, Wagner W, Wriggers P (1992) A nonlinear quadrilateral shell element with drilling degrees of freedom. *Archive of Applied Mechanics* 62(7):474–486
- Hughes TJR, Tezduyar TE (1981) Finite elements based upon mindlin plate theory with particular reference to the four-node bilinear isoparametric element. *Transactions ASME Journal of Applied Mechanics* 48(3):587–596
- Ko Y, Lee PS, Bathe KJ (2017a) A new MITC4+ shell element. *Computers & Structures* 182:404–416
- Ko Y, Lee PS, Bathe KJ (2017b) The MITC4+ shell element in geometric nonlinear analysis. *Computers & Structures* 185:1–14
- Koschnick F, Bischoff M, Camprubí N, Bletzinger KU (2005) The discrete strain gap method and membrane locking. *Computer Methods in Applied Mechanics and Engineering* 194:2444–2463
- Kulikov GM, Plotnikova SV (2002) Efficient mixed Timoshenko–Mindlin shell elements. *International Journal for Numerical Methods in Engineering* 55(10):1167–1183
- Kulikov GM, Plotnikova SV (2010) A family of ANS four-node exact geometry shell elements in general convected curvilinear coordinates. *International Journal for Numerical Methods in Engineering* 83(10):1376–1406

- Lavrenčič M, Brank B (2019) Hybrid-mixed shell finite elements and implicit dynamic schemes for shell post-buckling. In: Altenbach, H and Chróścielewski, J and Eremeyev, V A and Wiśniewski, K (ed) *Recent Developments in the Theory of Shells*, Springer, *Advanced Structured Materials*, vol 110, pp 383–412
- Lavrenčič M, Brank B (2020) Hybrid-mixed shell quadrilateral that allows for large solution steps and is low-sensitive to mesh distortion. *Computational Mechanics* 65:177–192
- MacNeal RH (1978) A simple quadrilateral shell element. *Computers & Structures* 8(2):175 – 183
- MacNeal RH, Harder RL (1985) A proposed standard set of problems to test finite element accuracy. *Finite Elements in Analysis and Design* 1(1):3 – 20
- Pian THH, Sumihara K (1984) Rational approach for assumed stress finite elements. *International Journal for Numerical Methods in Engineering* 20(9):1685–1695
- Simo JC, Rifai MS (1990) A class of mixed assumed strain methods and the method of incompatible modes. *International Journal for Numerical Methods in Engineering* 29(8):1595–1638
- Simo JC, Fox DD, Rifai MS (1990) On a stress resultant geometrically exact shell model. Part III: Computational aspects of the nonlinear theory. *Computer Methods in Applied Mechanics and Engineering* 79(1):21–70
- Sze KY, Chow CL (1991) A mixed formulation of a four-node mindlin shell/plate with interpolated covariant transverse shear strains. *Computers & Structures* 40(3):775–784
- Taylor RL (2020) FEAP. <http://www.ce.berkeley.edu/projects/feap/>
- Wagner W, Gruttmann F (2005) A robust non-linear mixed hybrid quadrilateral shell element. *International Journal for Numerical Methods in Engineering* 64(5):635–666
- Wiśniewski K, Turska E (2008) Improved four-node Hellinger–Reissner elements based on skew coordinates. *International Journal for Numerical Methods in Engineering* 76(6):798–836
- Wiśniewski K, Turska E (2009) Improved 4-node Hu–Washizu elements based on skew coordinates. *Computers & Structures* 87(7):407–424
- Wiśniewski K, Wagner W, Turska E, Gruttmann F (2010) Four-node Hu–Washizu elements based on skew coordinates and contravariant assumed strain. *Computers & Structures* 88(21):1278–1284



Chapter 10

Development of a Method for Determining One of the Additional Elastic Moduli of Curvilinear Rods

Elena A. Ivanova and Valentina A. Timoshenko

Abstract In this paper we suggest a method for determining one of the additional elastic moduli in curvilinear rod theory. The method is based on the comparison of the analytical solution of the problem of static curvilinear rod bending with the numerical solution of the corresponding 3D problem. The method can be used for rods with any section shape and any microstructure.

Key words: Curvilinear rods · Thin-walled structures · Elastic moduli · Numerical experiment

10.1 Introduction

The rod model has been known for a long time and is widely used in engineering analysis. However, there are still a lot of unsolved problems in the rod theory. An overview of investigations in modern rod theory can be found in Ghuku and Saha (2017). The research of statics, dynamics and stability of curvilinear rods is one of the most significant research directions (Ghuku and Saha, 2016; Satō, 1959; Tarn and Tseng, 2012; Sugiyama et al, 2006; Shiva Shankar and Vijayarangan, 2006; Gummadi and Palazotto, 1998; Erkmén and Bradford, 2009; Pippard, 1990; François et al, 2010). It is well known that two approaches are used for the formulation of

Elena A. Ivanova

Higher School of Theoretical Mechanics, Peter the Great St.Petersburg Polytechnic University, Polytechnicheskaya, 29, 195251, Saint-Petersburg & Institute for Problems in Mechanical Engineering of Russian Academy of Sciences, Bolshoy pr. V.O., 61, 199178, Saint-Petersburg, Russia
e-mail: elenaivanova239@gmail.com

Valentina A. Timoshenko

Higher School of Theoretical Mechanics, Peter the Great St.Petersburg Polytechnic University, Polytechnicheskaya, 29, 195251, Saint-Petersburg, Russia
e-mail: alya.tim.2012@mail.ru

the rod theory equations. They are the asymptotic one Berdichevskii (1981); Rubin (2000); Tiba and Vodak (2005); Meunier (2008); Jurak and Tambača (2001) and the direct one Svetlitsky (2000, 2005); Zhilin (2006, 2007); Altenbach et al (2006, 2012, 2013). If we consider the asymptotic approach, the formulae for the elastic moduli are obtained during the formulation of the basic equations, and this is an advantage of the approach. On the other hand, it is evident that if the rod has a complex configuration or complex internal structure, the use of mentioned approach becomes quite problematic. For the direct approach, the complexity of the configuration and internal structure do not influence the formulation of the basic equations, but in this case the determination of the elastic moduli becomes the separate research. A method for determining the elastic moduli and in the simplest cases the elastic moduli themselves are well known for straight rods. The situation is completely different with curvilinear rods. In addition to those elastic moduli that straight rods have, there are several additional elastic moduli in curvilinear rod theory Zhilin (2006, 2007); Altenbach et al (2006, 2012, 2013). The additional moduli can be neglected if the rod is thin enough. But the additional elastic moduli can be important in the case of thick rods. Consequently, the development of a method for their determination is an important problem. In this paper we suggest the method for determining one of the additional elastic moduli of curvilinear rods.

10.2 Basic Equations of the Linear Theory of Curvilinear Rods

In this section we consider the basic equations of the linear theory of curvilinear rods, which has been suggested in Zhilin (2006, 2007) and further developed in Altenbach et al (2006, 2012, 2013). The model of the curvilinear rod is the directed curve. Reference configuration is defined by the position vector $\mathbf{r}(s)$, where s is the coordinate along the curve. Further we consider two triples: natural triple $\mathbf{t}, \mathbf{n}, \mathbf{b}$ and additional triple $\mathbf{d}_1, \mathbf{d}_2, \mathbf{d}_3$. Vectors \mathbf{t}, \mathbf{n} and \mathbf{b} are the unit vectors of tangent, normal and binormal respectively. The triple of mutually perpendicular unit vectors $\mathbf{d}_1, \mathbf{d}_2, \mathbf{d}_3$ associated with the cross-section of the rod. Vector \mathbf{d}_3 coincides with the direction of tangent vector \mathbf{t} , and vectors $\mathbf{d}_1, \mathbf{d}_2$ are placed in the cross-section plane (see Fig. 10.1).

In the linear theory the motion equations are

$$\mathbf{T}' + \rho_0 \mathbf{f} = \rho_0 \dot{\mathcal{K}}_1, \quad \mathbf{M}' + \mathbf{t} \times \mathbf{T} + \rho_0 \mathbf{m} = \rho_0 \dot{\mathcal{K}}_2. \tag{10.1}$$

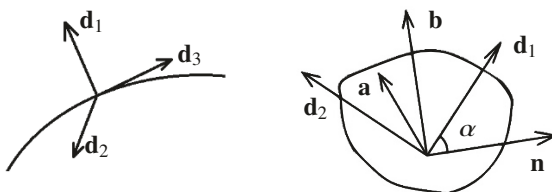


Fig. 10.1 The directed curve and position of the triple vectors in the cross-section

Here the prime represents the derivative with respect to the spatial coordinate, the dot represents the time derivative, \mathbf{T} and \mathbf{M} are the force and the moment in the cross-section, ρ_0 is the linear density of mass in the reference configuration, \mathbf{f} and \mathbf{m} are the external force and the external moment per unit mass, \mathcal{K}_1 and \mathcal{K}_2 are the linear momentum vector and the angular momentum vector per unit mass.

The kinetic energy per unit mass is

$$\mathcal{K} = \frac{1}{2} \mathbf{v} \cdot \mathbf{v} + \mathbf{v} \cdot \boldsymbol{\theta}_1 \cdot \boldsymbol{\omega} + \frac{1}{2} \boldsymbol{\omega} \cdot \boldsymbol{\theta}_2 \cdot \boldsymbol{\omega}, \quad (10.2)$$

where \mathbf{v} is the velocity vector, $\boldsymbol{\omega}$ is the angular velocity vector, $\boldsymbol{\theta}_1$ and $\boldsymbol{\theta}_2$ are the inertia tensors per unit mass. The tensors $\boldsymbol{\theta}_1$ and $\boldsymbol{\theta}_2$ are time independent in the linear theory, but can be dependent on the spartial coordinate. The linear momentum vector and the angular momentum vector per unit mass are defined as partial derivatives of the kinetic energy per unit mass with respect to the velocity and angular velocity vectors respectively:

$$\mathcal{K}_1 = \frac{\partial \mathcal{K}}{\partial \mathbf{v}} = \mathbf{v} + \boldsymbol{\theta}_1 \cdot \boldsymbol{\omega}, \quad \mathcal{K}_2 = \frac{\partial \mathcal{K}}{\partial \boldsymbol{\omega}} = \mathbf{v} \cdot \boldsymbol{\theta}_1 + \boldsymbol{\theta}_2 \cdot \boldsymbol{\omega}. \quad (10.3)$$

The linear density of mass ρ_0 and the inertia tensors per unit length $\rho_0 \boldsymbol{\theta}_1$, $\rho_0 \boldsymbol{\theta}_2$ are

$$\rho_0 = \int_{(\mathcal{F})} \rho^{(3)} \mu d\mathcal{F}, \quad \rho_0 \boldsymbol{\theta}_1 = -\mathbf{E} \times \int_{(\mathcal{F})} \rho^{(3)} \mathbf{a} \mu d\mathcal{F}, \quad \rho_0 \boldsymbol{\theta}_2 = \int_{(\mathcal{F})} \rho^{(3)} (\mathbf{a} \cdot \mathbf{a} \mathbf{E} - \mathbf{a} \mathbf{a}) \mu d\mathcal{F}, \quad (10.4)$$

with

$$\mu = 1 + \frac{1}{R_c} \mathbf{n} \cdot \mathbf{a}.$$

Here $\rho^{(3)}$ is the mass density per unit volume, \mathcal{F} is a cross-section area, \mathbf{E} is the unit tensor, R_c is the radius of curvature, \mathbf{a} is a vector, which connects the centre and some point of the cross-section (see Fig. 10.1).

The internal energy is the quadratic form of the deformation vectors in the linear theory:

$$\rho_0 \mathcal{U} = \frac{1}{2} \boldsymbol{\mathcal{E}} \cdot \mathbf{A} \cdot \boldsymbol{\mathcal{E}} + \boldsymbol{\mathcal{E}} \cdot \mathbf{B} \cdot \boldsymbol{\Phi} + \frac{1}{2} \boldsymbol{\Phi} \cdot \mathbf{C} \cdot \boldsymbol{\Phi}. \quad (10.5)$$

Here \mathcal{U} is the internal energy per unit mass, $\boldsymbol{\mathcal{E}}$ is the vector of extension-shear deformation, $\boldsymbol{\Phi}$ is the vector of bending-twisting deformation, \mathbf{A} , \mathbf{B} , \mathbf{C} are the elasticity tensors. Tensor \mathbf{A} is responsible for extension and transverse shear, tensor \mathbf{C} is responsible for bending and twisting, tensor \mathbf{B} characterizes the mutual influence of the extension-shear deformations and the bending-twisting deformations. If we consider the straight rod and the natural twisting is absent, the tensor \mathbf{B} is equal to zero. The tensors \mathbf{A} , \mathbf{B} , \mathbf{C} are time independent in the linear theory, but can be dependent on spartial coordinate. The deformation vectors are

$$\boldsymbol{\mathcal{E}} = \mathbf{u}' + \mathbf{t} \times \boldsymbol{\psi}, \quad \boldsymbol{\Phi} = \boldsymbol{\psi}', \quad (10.6)$$

where \mathbf{u} is the displacement vector, $\boldsymbol{\psi}$ is the rotation vector. The constitutive equations have the form

$$\mathbf{T} = \frac{\partial(\rho_0 \mathcal{U})}{\partial \boldsymbol{\varepsilon}} = \mathbf{A} \cdot \boldsymbol{\varepsilon} + \mathbf{B} \cdot \boldsymbol{\Phi}, \quad \mathbf{M} = \frac{\partial(\rho_0 \mathcal{U})}{\partial \boldsymbol{\Phi}} = \boldsymbol{\varepsilon} \cdot \mathbf{B} + \mathbf{C} \cdot \boldsymbol{\Phi}. \quad (10.7)$$

The elasticity tensors have the following structure for curvilinear rods without the natural twisting:

$$\begin{aligned} \mathbf{A} &= A_1 \mathbf{d}_1 \mathbf{d}_1 + A_2 \mathbf{d}_2 \mathbf{d}_2 + A_3 \mathbf{d}_3 \mathbf{d}_3, \\ \mathbf{C} &= C_1 \mathbf{d}_1 \mathbf{d}_1 + C_2 \mathbf{d}_2 \mathbf{d}_2 + C_3 \mathbf{d}_3 \mathbf{d}_3, \\ \mathbf{B} &= \frac{1}{R_c} \left[(B_{23} \mathbf{d}_2 \mathbf{d}_3 + B_{32} \mathbf{d}_3 \mathbf{d}_2) \cos \alpha + (B_{13} \mathbf{d}_1 \mathbf{d}_3 + B_{31} \mathbf{d}_3 \mathbf{d}_1) \sin \alpha \right] \\ &\quad + \frac{1}{R_t} (B_1 \mathbf{d}_1 \mathbf{d}_1 + B_2 \mathbf{d}_2 \mathbf{d}_2 + B_3 \mathbf{d}_3 \mathbf{d}_3), \end{aligned} \quad (10.8)$$

where R_t is the radius of torsion, α is an angle between the vectors \mathbf{d}_1 , \mathbf{d}_2 and the vectors \mathbf{n} , \mathbf{b} (see Fig. 10.1). Other scalar coefficients in Eq. (10.8) represent the elastic moduli. The elastic moduli A_k and C_k are determined during the experiments with straight rods. The elastic moduli B_{ij} can be determined during the experiments with plane curvilinear rods. The elastic moduli B_k can be determined during the experiments with spatially curved rods.

We need formulae relating the characteristics of stress-strain state of the rod and the three-dimensional body for interpretation of the data from physical and numerical experiments. In the linear theory the force and moment vectors in the cross-section of the rod are the integral characteristics of stress in cross-section of the three-dimensional body. The corresponding formulae are generally accepted. Different authors determine the relationships between the kinematic characteristics differently. In considered theory for comparison of the kinematic characteristics we use the assumption that the linear momentum vector and the angular momentum vector of the rod and the three-dimensional body must be the same. The mentioned relationships are easily integrated over time, as a result we get the relationship between the displacement vector, the rotation vector and the integral characteristics of the displacement vector of three-dimensional body. This way we get the following relationships:

$$\begin{aligned} \mathbf{T} &= \int_{(\mathcal{F})} \mathbf{t} \cdot \boldsymbol{\tau} \, d\mathcal{F}, \quad \mathbf{M} = \int_{(\mathcal{F})} \mathbf{a} \times (\mathbf{t} \cdot \boldsymbol{\tau}) \, d\mathcal{F}, \\ \rho_0 (\mathbf{u} + \boldsymbol{\Theta}_1 \cdot \boldsymbol{\psi}) &= \int_{(\mathcal{F})} \rho^{(3)} \mathbf{u}^{(3)} \, \mu \, d\mathcal{F}, \\ \rho_0 (\mathbf{u} \cdot \boldsymbol{\Theta}_1 + \boldsymbol{\Theta}_2 \cdot \boldsymbol{\psi}) &= \int_{(\mathcal{F})} \rho^{(3)} \mathbf{a} \times \mathbf{u}^{(3)} \, \mu \, d\mathcal{F}. \end{aligned} \quad (10.9)$$

Here τ is the stress tensor, $\mathbf{u}^{(3)}$ is the displacement vector in the 3D-theory. Eq. (10.9) form the method of the numerical experiment.

10.3 Formulation and Solution of the Model Problem

The aim of this research is to formulate the model problem, which solution provides the opportunity of determination of the elastic modulus B_{32} . In this section we discuss the formulation and numerical solution of the model problem within the rod theory, the formulation of the corresponding problem within the 3D-theory and the relationships that allow us to compare the solutions of mentioned problems.

We consider the plane curvilinear rod, which has a form of $3/4$ of the circle with the radius R . We also assume that the principal axes of inertia of the cross-section coincide with the vectors of the natural triple. This way $\alpha = 0, R_t = \infty$. It is obviously that the use of cylindrical coordinate system r, θ, z (see Fig. 10.2) is convenient for the model problem. The following relationships occur:

$$s = r\theta, \quad \mathbf{d}_1 = \mathbf{n} = -\mathbf{e}_r, \quad \mathbf{d}_2 = \mathbf{b} = \mathbf{k}, \quad \mathbf{d}_3 = \mathbf{t} = \mathbf{e}_\theta, \quad R_c = -R. \quad (10.10)$$

We consider the static deformation of the rod. One end of the rod is rigidly fixed and another end is loaded only by the moment, which deforms the rod without taking it out the plane. External forces and moments distributed along the length of the rod are absent. In the rod theory we formulate this problem as

$$\begin{aligned} \mathbf{T}' &= 0, \quad \mathbf{M}' + \mathbf{t} \times \mathbf{T} = 0, \quad \boldsymbol{\varepsilon} = \mathbf{u}' + \mathbf{t} \times \boldsymbol{\psi}, \quad \boldsymbol{\Phi} = \boldsymbol{\psi}', \\ \mathbf{T} &= \mathbf{A} \cdot \boldsymbol{\varepsilon} + \mathbf{B} \cdot \boldsymbol{\Phi}, \quad \mathbf{M} = \boldsymbol{\varepsilon} \cdot \mathbf{B} + \mathbf{C} \cdot \boldsymbol{\Phi}, \\ \mathbf{u}|_{s=0} &= 0, \quad \boldsymbol{\psi}|_{s=0} = 0, \quad \mathbf{T}|_{s=0} = 0, \quad \mathbf{M}|_{s=l} = M_0 \mathbf{k}, \end{aligned} \quad (10.11)$$

where M_0 is the external moment. Taking into account the structure of the tensors from Eq. (10.8), we obtain the solution of Eq. (10.11):

$$\mathbf{u} = u_n \mathbf{n} + u_t \mathbf{t}, \quad \boldsymbol{\psi} = \psi_b \mathbf{b}, \quad (10.12)$$

where

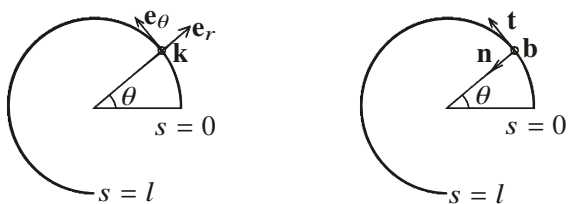


Fig. 10.2 The natural triple and the cylindrical coordinate system

$$\begin{aligned}
 u_n &= M_0 R^2 \left(C_2 - \frac{B_{32}^2}{R^2 A_3} \right)^{-1} \left(1 - \frac{B_{32}}{R^2 A_3} \right) \left(1 - \cos \frac{s}{R} \right), \\
 u_t &= M_0 R^2 \left(C_2 - \frac{B_{32}^2}{R^2 A_3} \right)^{-1} \left(\frac{s}{R} - \left(1 - \frac{B_{32}}{R^2 A_3} \right) \sin \frac{s}{R} \right), \\
 \psi_b &= M_0 s \left(C_2 - \frac{B_{32}^2}{R^2 A_3} \right)^{-1}.
 \end{aligned}
 \tag{10.13}$$

From Eqs. (10.12), (10.13), it follows that the rod is deformed in the plane and the solution depends on three elastic moduli. These moduli are the extension elastic modulus A_3 , the bending elastic modulus C_2 and the additional elastic modulus B_{32} . It is important that the solution of the model problem depends on only one unknown elastic modulus. If the elastic modulus $B_{32} = 0$, Eq. (10.13) simplifies and has the form

$$\begin{aligned}
 u_n^c &= \frac{M_0 R^2}{C_2} \left(1 - \cos \frac{s}{R} \right), \\
 u_t^c &= \frac{M_0 R^2}{C_2} \left(\frac{s}{R} - \sin \frac{s}{R} \right), \\
 \psi_b^c &= \frac{M_0 s}{C_2}.
 \end{aligned}
 \tag{10.14}$$

Comparison of the solutions of Eqs. (10.13) and (10.14) shows that the elastic modulus B_{32} has an effect on the solution of the problem and also provides the effect of the elastic modulus A_3 .

Figure 10.3 illustrates the formulation of the corresponding problem in 3D-theory. We consider the body, which is 3/4 of the hollow cylinder. The height of the cylinder is b , the difference between the internal and external radii is a , the radius of the midline, i.e. the line passing through the centres of the sections, is equal to the radius R of the rod. The surface of the cylinder $\theta = 0$ is rigidly fixed. There is a distributed load on the surface $\theta = 3\pi/2$, which causes the resultant force equal to zero and the resultant moment M_0 . The other cylinder surfaces are free. As a result

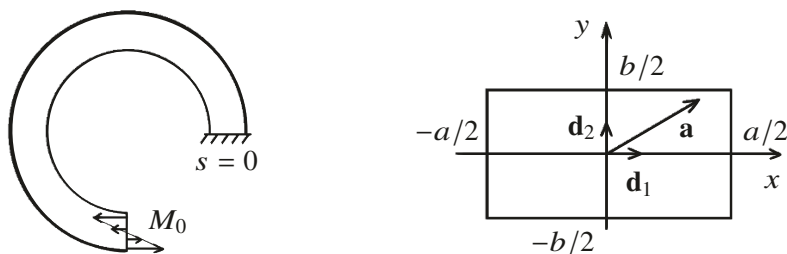


Fig. 10.3. Boundary conditions and the local coordinate system in the cross-section

of numerical solution we determine the displacement field $\mathbf{u}^{(3)}$ in the cylindrical coordinate system:

$$\mathbf{u}^{(3)} = u_r^{(3)} \mathbf{e}_r + u_\theta^{(3)} \mathbf{e}_\theta + u_z^{(3)} \mathbf{k}. \quad (10.15)$$

Taking into account Eqs. (10.4), (10.9) and writing vector \mathbf{a} (see Fig. 10.3) as

$$\mathbf{a} = x\mathbf{d}_1 + y\mathbf{d}_2, \quad (10.16)$$

we get the following integral relationships between the components of the displacement and rotation vectors in the rod theory and the components of the displacement vector in the 3D-theory

$$\begin{aligned} u_n &= -\frac{1}{ab} \int_{-\frac{a}{2}}^{\frac{a}{2}} \int_{-\frac{b}{2}}^{\frac{b}{2}} u_r^{(3)} \left(1 - \frac{x}{R}\right) dx dy, \\ u_t &= \frac{1}{ab} \left(1 - \frac{a^2}{12R^2}\right)^{-1} \int_{-\frac{a}{2}}^{\frac{a}{2}} \int_{-\frac{b}{2}}^{\frac{b}{2}} u_\theta^{(3)} \left(1 - \frac{x^2}{R^2}\right) dx dy, \\ \psi_b &= -\frac{1}{abR} \left(1 - \frac{a^2}{12R^2}\right)^{-1} \int_{-\frac{a}{2}}^{\frac{a}{2}} \int_{-\frac{b}{2}}^{\frac{b}{2}} u_\theta^{(3)} \left(1 + \frac{12Rx}{a^2}\right) \left(1 - \frac{x}{R}\right) dx dy. \end{aligned} \quad (10.17)$$

Thus, if we get the numerical solution of the 3D-problem, we can calculate components u_n , u_t and ψ_b in current cross-section of the rod using Eq. (10.17). After their substitution into Eq. (10.13), we get three expressions for determining the elastic modulus B_{32} . From the theoretical point of view the value of the modulus B_{32} should be independent of the choice of the expression. This value also should be independent of the cross-section position. However, the elastic modulus B_{32} depends on the position of the cross-section and the chosen equation in fact. It is the reason why the choice of the method for determining the elastic modulus B_{32} is very important. We choose the method with respect to the less dependency on the cross-section position.

10.4 Method for Determining the Elastic Modulus B_{32}

In this section we consider three methods for determining the elastic modulus B_{32} . For better presentation of the difference between the methods for determining the elastic modulus we perform the calculations for the body, which is not very similar to the rod. This body has the radius of the midline $R = 0,5$ m, its cross-section is the square with the sides length $a = b = 0,2$ m. We choose the steel with Young's

modulus $E = 2 \cdot 10^{11}$ N/m² and Poisson's ratio $\nu = 0.33$ as a material. For the chosen body:

$$A_3 = Ea^2 = 8 \cdot 10^9 \text{ N}, \quad A_3 R^2 = 2 \cdot 10^9 \text{ Nm}^2, \quad C_2 = \frac{Ea^2}{12} = 2.67 \cdot 10^7 \text{ N}. \quad (10.18)$$

In this section and further all values of the elastic moduli are in the SI. The external moment equals $M_0 = 150000$ N·m. The calculations are done with a software application ABAQUS. We use cubic finite element with the side length 0,005 m. The investigation of the convergence shows that the numerical solution converges even for coarse mesh. Decrease of the mesh element length increases the accuracy of the calculations of the integrals from Eq. (10.17). We use the displacements and rotation angles from Eq. (10.17) in three cross-sections $\theta = 3\pi/4$, $\theta = \pi$, $\theta = 5\pi/4$ (it also is necessary to consider the cross-section $\theta = \pi/2$ for one calculation series) for determining the elastic modulus B_{32} . The choice of the cross-sections is explained by the fact that their positions are quite far from each other and the boundaries (see Fig. 10.4).

- *The first method* uses the coefficient

$$\left(C_2 - \frac{B_{32}^2}{R^2 A_3} \right)^{-1} \left(1 - \frac{B_{32}}{R^2 A_3} \right).$$

According to Eq. (10.13), there are two ways to calculate the mentioned coefficient. The first one uses the value of the component u_n in the cross-section s_* as

$$\left(C_2 - \frac{B_{32}^2}{R^2 A_3} \right)^{-1} \left(1 - \frac{B_{32}}{R^2 A_3} \right) = \frac{u_n(s_*)}{M_0 R^2 (1 - \cos(s_*/R))} \quad (10.19)$$

and the second one uses the value of the difference $u_t - R\psi_b$ in the cross-section s_* as

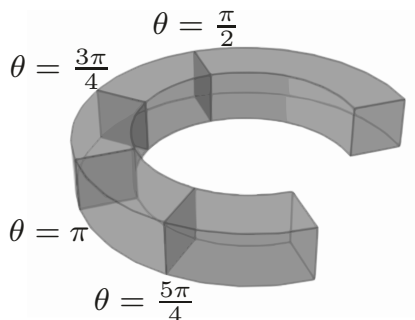


Fig. 10.4 The position and angles of chosen cross-sections

$$\left(C_2 - \frac{B_{32}^2}{R^2 A_3}\right)^{-1} \left(1 - \frac{B_{32}}{R^2 A_3}\right) = \frac{R\psi_b(s_*) - u_t(s_*)}{M_0 R^2 \sin(s_*/R)}. \tag{10.20}$$

The calculation results are presented in Table 10.1. Obviously we cannot calculate the coefficient using the values $u_t - R\psi_b$, but the way of calculation using the values of the component u_n is highly accurate. However, solving Eq. (10.19) we obtain complex values of the modulus B_{32} , the imaginary parts of which are comparable to the real parts. It means that this method of determining the elastic modulus B_{32} is unacceptable.

- **The second method** supposes the use of the coefficient

$$\left(C_2 - \frac{B_{32}^2}{R^2 A_3}\right)^{-1}.$$

According to Eq. (10.13), this coefficient can be calculated in three ways. The first one uses the value of the component ψ_b in the cross-section s_* as

$$\left(C_2 - \frac{B_{32}^2}{R^2 A_3}\right)^{-1} = \frac{\psi_b(s_*)}{M_0 R s_*}, \tag{10.21}$$

the second one uses the value of the component u_t in the cross-section with $s_* = \pi R$ as

$$\left(C_2 - \frac{B_{32}^2}{R^2 A_3}\right)^{-1} = \frac{u_t(s_*)}{M_0 R^2 s_*}, \tag{10.22}$$

and the third one uses the value of the sum $u_n + u_t$ in the cross-section $s_* = \pi R/2$, i.e. the cross-section, where

$$1 - \cos \frac{s}{R} = \sin \frac{s}{R},$$

as

Table 10.1

Coefficient values $\left(C_2 - \frac{B_{32}^2}{R^2 A_3}\right)^{-1} \left(1 - \frac{B_{32}}{R^2 A_3}\right)$

Cross-section	Using u_n	Error, using u_n	Using $u_t - R\psi_b$	Error, using $u_t - R\psi_b$
$3\pi/4$	$3,67 \cdot 10^{-8}$	0,90%	$4,8 \cdot 10^{-8}$	52,84%
π	$3,65 \cdot 10^{-8}$	0,41%	-	-
$5\pi/4$	$3,59 \cdot 10^{-8}$	1,31%	$1,48 \cdot 10^{-8}$	52,84%

$$\left(C_2 - \frac{B_{32}^2}{R^2 A_3} \right)^{-1} = \frac{u_n(s_*) + u_t(s_*)}{M_0 R s_*}. \tag{10.23}$$

The calculation results are presented in Table 10.2. It is evident that the way based on the use of the values of the component ψ_b is highly accurate. The value calculated using the sum $u_n + u_t$ corresponds the general tend to decreasing of the value as the cross-section gets closer to the fixed end. The coefficient value calculated using the component u_t is smaller than other values, and we suppose it to be questionable.

From the theoretical point of view the elastic modulus B_{32} can be positive or negative. It is clear that the suggested method allows us to determine the absolute value of modulus B_{32} . In Table 10.3 we present positive values of the modulus B_{32} . An analysis of the results shows that the method for determining the elastic modulus B_{32} using Eq. (10.21) allows us to obtain the values, which slightly depend on the choice of the cross-section. Thus this method is acceptable. It has the only disadvantage that we cannot determine the sign of the elastic modulus B_{32} .

- **The third method** uses the values of the coefficient

$$\left(1 - \frac{B_{32}}{R^2 A_3} \right).$$

According to Eq. (10.13), we can calculate this coefficient in three ways. The first one consists in the use of the ratio u_n/u_t in the cross-section s_* as

Table 10.2

Coefficient values $\left(C_2 - \frac{B_{32}^2}{R^2 A_3} \right)^{-1}$

Cross-section	Using $u_n + u_t$	Using u_t	Using ψ_b	Error, using ψ_b
$\pi/2$	$3,91 \cdot 10^{-8}$	-	-	-
$3\pi/4$	-	-	$4,08 \cdot 10^{-8}$	1,18%
π	-	$3,76 \cdot 10^{-8}$	$4,14 \cdot 10^{-8}$	0,18%
$5\pi/4$	-	-	$4,17 \cdot 10^{-8}$	1,00%

Table 10.3

The elastic modulus B_{32} calculated using $\left(C_2 - \frac{B_{32}^2}{R^2 A_3} \right)^{-1}$

Cross-section	Using $u_n + u_t$	Using u_t	Using ψ_b	Error, using ψ_b
$\pi/2$	$4,67 \cdot 10^7$	-	-	-
$3\pi/4$	-	-	$6,56 \cdot 10^7$	5,99%
π	-	$1,19 \cdot 10^7$	$7,05 \cdot 10^7$	1,04%
$5\pi/4$	-	-	$7,32 \cdot 10^7$	4,95%

$$1 - \frac{B_{32}}{R^2 A_3} = \frac{u_n(s_*)s_*}{R[u_t(s_*)(1 - \cos(s_*/R)) + u_n(s_*)\sin(s_*/R)]}, \tag{10.24}$$

the second one consists in the use of the ratio u_n/ψ_b in the cross-section s_* as

$$1 - \frac{B_{32}}{R^2 A_3} = \frac{u_n(s_*)s_*}{R^2\psi_b(s_*)[1 - \cos(s_*/R)]} \tag{10.25}$$

and the third one consists in the use of the ratio u_t/ψ_b in the cross-section s_* as

$$1 - \frac{B_{32}}{R^2 A_3} = \frac{[R\psi_b(s_*) - u_t(s_*)]s_*}{R^2\psi_b(s_*)\sin(s_*/R)}. \tag{10.26}$$

The calculation results are presented in Table 10.4. It is evident that the way based on the use of the ratio u_t/ψ_b is unacceptable at all. Others demonstrate the same dependency of the cross-section choice, but give different average values of the coefficient.

The results of calculation of the elastic modulus are presented in Table 10.5. An analysis of the results shows the noticeable difference between the values of the modulus B_{32} calculated using the ratio u_n/u_t and the values calculated using the ratio u_n/ψ_b . The substitution of the average values into the coefficient

$$\left(C_2 - \frac{B_{32}^2}{R^2 A_3}\right)^{-1}$$

Table 10.4

Coefficient values $\left(1 - \frac{B_{32}}{R^2 A_3}\right)$

Cross-section	Using u_n/u_t	Error, using u_n/u_t	Using u_n/ψ_b	Error, using u_n/ψ_b	Using u_t/ψ_b
$3\pi/4$	0,981	1,54%	0,899	2,02%	1,18
π	0,970	0,47%	0,883	0,21%	-
$5\pi/4$	0,946	2,01%	0,860	2,31%	0,36

Table 10.5

The elastic modulus B_{32} , calculated using $\left(1 - \frac{B_{32}}{R^2 A_3}\right)$

Cross-section	Using u_n/u_t	Error, using u_n/u_t	Using u_n/ψ_b	Error, using u_n/ψ_b
$3\pi/4$	$3,85 \cdot 10^7$	43,6%	$2,02 \cdot 10^8$	15,44%
π	$5,91 \cdot 10^7$	13,4%	$2,35 \cdot 10^8$	1,58%
$5\pi/4$	$10,7 \cdot 10^7$	56,9%	$2,79 \cdot 10^8$	17,02%

shows that this expression is positive if the modulus B_{32} is calculated using the ratio u_n/u_t , and the expression is negative if we substitute the values calculated using the ratio u_n/ψ_b . Consequently, the way of determining the modulus B_{32} using the ratio u_n/ψ_b is unacceptable.

Thus the only method for determining the sign of the elastic modulus consists in determining this modulus using the ratio u_n/u_t . From Table. 10.5 we see that this way gives the values dependent on the cross-section choice. However, the average value $B_{32} = 6,82 \cdot 10^7$ is close to the average value $B_{32} = 6,98 \cdot 10^7$ which is calculated using the components ψ_b . The relative difference between them is equal to 2,32%.

10.5 Discussion

As a result of our study we conclude that considered model problem can be used for determining the elastic modulus B_{32} by the numerical experiment. The best of considered methods for determining this modulus is the method which uses Eq. (10.21). We can also use the method based on Eq. (10.24) for additional verification and determining the sign of modulus B_{32} .

In Zhilin (2007) the author considers the method for determining the elastic modulus B_{32} , based on the solution of a problem of the deformation of a closed circular rod under the action of a uniformly distributed radial load. The balance equations have the form

$$\mathbf{T}' + f\mathbf{n} = 0, \quad \mathbf{M}' + \mathbf{t} \times \mathbf{T} = 0. \quad (10.27)$$

Due to axial symmetry the solution has the following structure:

$$\begin{aligned} \mathbf{u} &= u_n \mathbf{n}, & \psi &= 0, \\ \mathcal{E} &= \mathcal{E}_t \mathbf{t}, & \Phi &= 0, \\ \mathbf{T} &= A_3 \mathcal{E}_t \mathbf{t}, & \mathbf{M} &= \frac{B_{32}}{R_c} \mathcal{E}_t \mathbf{b}. \end{aligned} \quad (10.28)$$

This model problem is interesting with the fact that the corresponding 3D-problem allows to find the analytical solution in the case if the height of the cylinder is small enough to allow us to consider the stress-strain state to be plane. The comparison of the 1D-problem solution and the 3D-problem solution leads to the simple formula $B_{32} = C_2$.

The calculated above value of B_{32} coincides with $B_{32} = C_2$ in an order of magnitude. However, the calculated value is about 2,5 times higher. Taking into account the specifics of the model problem considered in Zhilin (2007) and the fact that three-dimensional body used in our study is not very similar to the rod, we can consider the coincidence of the results as quite good.

The developed method can be used for determining the elastic modulus B_{32} in the case of curvilinear rods, which have different shapes of the cross-section and the arbitrarily complex internal structure.

References

- Altenbach H, Naumenko K, Zhilin PA (2006) A direct approach to the formulation of constitutive equations for rods and shells. In: Pietraszkiewicz W, Szymczak C (eds) *Shell Structures: Theory and Applications*, Taylor and Francis, London, pp 87–90
- Altenbach H, Birsan M, Eremeyev V (2012) On a thermodynamic theory of rods with two temperature fields. *Acta Mechanica* 223:1583–1596
- Altenbach H, Birsan M, Eremeyev V (2013) Cosserat-type rods. In: Altenbach H, Eremeyev V (eds) *Generalized Continua – from the theory to Engineering Applications*, Springer, Wien, CISM International Centre for Mechanical Sciences, vol 541, pp 179–248
- Berdichevskii V (1981) On the energy of an elastic rod. *Journal of Applied Mathematics and Mechanics* 45(4):518 – 529
- Erkmen RE, Bradford MA (2009) Nonlinear elastic analysis of composite beams curved in-plan. *Engineering Structures* 31(7):1613 – 1624
- François MLM, Semin B, Auradou H (2010) Identification of the shape of curvilinear beams and fibers. In: *Advances in Experimental Mechanics VII*, Trans Tech Publications Ltd, Applied Mechanics and Materials, vol 24-25, pp 359–364
- Ghuku S, Saha KN (2016) A theoretical and experimental study on geometric nonlinearity of initially curved cantilever beams. *Engineering Science and Technology, an International Journal* 19(1):135 – 146
- Ghuku S, Saha KN (2017) A review on stress and deformation analysis of curved beams under large deflection. *International Journal of Engineering and Technologies* 11:13–39
- Gummadi L, Palazotto A (1998) Large strain analysis of beams and arches undergoing large rotations. *International Journal of Non-Linear Mechanics* 33(4):615 – 645
- Jurak M, Tambača J (2001) Linear curved rod model: General curve. *Mathematical Models and Methods in Applied Sciences* 11(7):1237–1252
- Meunier N (2008) Recursive derivation of one-dimensional models from three-dimensional nonlinear elasticity. *Mathematics and Mechanics of Solids* 13(2):172–194
- Pippard AB (1990) The elastic arch and its modes of instability. *European Journal of Physics* 11(6):359–365
- Rubin MB (2000) *Cosserat Theories: Shells, Rods, and Points*. Kluwer Academic Publishers, Dordrecht
- Satō K (1959) Large deflection of a circular cantilever beam with uniformly distributed load. *Ingenieur-Archiv* 27(3):195 – 200

- Shiva Shankar GS, Vijayarangan S (2006) Mono composite leaf spring for light weight vehicle—design, end joint analysis and testing. *Materials Science* 12(3):220–225
- Sugiyama H, Shabana AA, Omar MA, Loh WY (2006) Development of nonlinear elastic leaf spring model for multibody vehicle systems. *Computer Methods in Applied Mechanics and Engineering* 195(50):6925 – 6941
- Svetlitsky VA (2000) *Statics of Rods*. Foundations of Engineering Mechanics, Springer, Berlin-Heidelberg
- Svetlitsky VA (2005) *Dynamics of Rods*. Foundations of Engineering Mechanics, Springer, Berlin-Heidelberg
- Tarn JQ, Tseng WD (2012) Exact analysis of curved beams and arches with arbitrary end conditions: A Hamiltonian state space approach. *Journal of Elasticity* 107(1):39–63
- Tiba D, Vodak R (2005) A general asymptotic model for Lipschitzian curved rods. *Advances in Mathematical Sciences and Applications* 15:137–198
- Zhilin PA (2006) Nonlinear theory of thin rods. In: Indeitsev DA, Ivanova EA, Krivtsov AM (eds) *Advanced Problems in Mechanics*, Instit. Problems Mech. Eng. R.A.S. Publ, St. Petersburg, vol 2, pp 227–249
- Zhilin PA (2007) *Applied Mechanics. Theory of Thin Elastic Rods (in Russ.)*. Politekh. Univ. Publ., St. Petersburg



Chapter 11

Beam Dynamics Using a Generalized Beam Theory Based on the Solution of a Reference Beam Problem

Stephan Kugler, Peter A. Fotiu, and Justin Murín

Abstract Mechanical properties of slender, prismatic structures are typically analyzed based on classical beam mechanics (Timoshenko's shear force bending, Vlasov's theory of warping torsion, . . .). There it is assumed that the cross-section remains rigid in its projection plane and in-plane distortional deformations of the cross-section are neglected. Such a model is predictive in case of static gradually distributed loading, and solid cross-sections, however, in case of thin-walled cross-sections and dynamic loading severe deviations might occur. Therefore, a generalized beam theory is proposed, where warping fields and accompanied distortional fields of the cross-section are axially distributed each based on one generalized degree of freedom. The evaluation of pairs of warping and distortional fields in ascending order of importance is performed using a specific reference beam problem (RBP), where three-dimensional elasticity theory is applied in connection with semi-analytical finite elements (SAFE). Convergence of the resulting formulation is ensured by increasing the number of contributing pairs of warping and distortional fields. The resulting formulation yields significantly better results compared to classical beam mechanics especially in the dynamic regime.

Key words: Generalized beam theory · Reference beam problem · Torsion-distortion-coupling · Warping · Functionally graded material

Stephan Kugler and Peter A. Fotiu

Department of Applied and Numerical Mechanics, University of Applied Sciences in Wiener Neustadt, Johannes Gutenberg-Straße 3, 2700 Wiener Neustadt, Austria
e-mail: kugler@fhwn.ac.at, fotiu@fhwn.ac.at

Justin Murín

Department of Applied Mechanics and Mechatronics, IAMM FEI, STU Bratislava, Ilkovicova 3, 812 19 Bratislava, Slovakia
e-mail: justin.murin@stuba.sk

11.1 Introduction, Motivation and State of the Art

Classical beam mechanics (CBM) is frequently applied in engineering practice to analyze the mechanical properties of slender structures. The main advantages of CBM are without any claim to completeness the small number of degrees of freedom, a decoupled analysis of different load cases (axial, shear force bending and warping torsion), less modeling time due to simple modeling of supports and junctions and the possibility of analytic analyses in connection with parametric results without the construction of multiple models. Specific homogenization procedures allow the application of CBM even in case of composite or functionally graded material beam structures (see e.g. Murin et al, 2016). However, the gain of these advantages requires the following specific assumptions whose validity depends mostly on the slenderness of the structure and on the cross-sectional shape:

- *Rigid cross-section:* CBM assumes that the cross-section moves rigidly in space based on three displacement and three rotational degrees of freedom. If transverse shear is included shear correction factors have to be established which account for the mismatch between true non-linear shear strains and constant assumed strains, i.e. any warping due to shear is smoothed in Timoshenko's theory. The hypotheses of a rigid cross-section has to be weakened in case of non-uniform warping torsion, where out of plane warping deformations have to be included. This typically causes an additional degree of freedom in the beam model. In Vlasov's theory of torsion (Vlasov, 1961) the axial displacements in the shaft are related to a warping function $\omega(y, z)$ depending on the cross-sectional coordinates times the twist $\varphi'_x(x)$. The introduction of a dependent additional degree of freedom seems to be artificial and can be weakened according to a theory due to Bencoter (1954), where warping is described by an independent degree of freedom $F(x)$ ¹. After all, the hypothesis of a rigid cross-section is responsible for the small number of degrees of freedom and the efficiency of CBM.
- *Decoupling of different load cases:* Axial, transverse and torsional load cases can be typically analyzed in a decoupled manner if they refer to beam coordinate systems originated at specific locations of the cross-section. It is well known that axial and transverse load cases will decouple if the origin of the coordinate system is located at the centroid of a homogeneous cross-section.

A decoupled analyses of transverse loading with respect to two specific transverse directions is somewhat questionable: There, it is typically assumed that the cross-section has principal directions which are related to the bending stiffness tensor. Such an assumption, however, requires that a tensor of transverse shear stiffnesses (with shear correction factors included) has the same principal axis, which is not true in an arbitrary unsymmetrical case. In an example of Sect. 11.4.1 it is shown that a single cantilever with unsymmetrical cross-section loaded by an end force directed into a principal direction of the bending stiffness tensor, exhibits side-

¹ Modern applications of a Bencoter related theory of torsion are discussed in recent proceedings by Kugler et al (2018b, 2019) which indicate slightly more accuracy compared to Vlasov and improvements regarding the corresponding finite element equations.

way deflections transversely to the load direction. This effect, which decreases with increasing slenderness, has been reported by Schramm et al (1994) and is discussed in Dong et al (2013) (note the corrigendum Dong et al, 2015). A suitable finite beam element formulation is proposed by Pilkey et al (1995). In most applications these side-way deflections are small and can be neglected for the sake of efficiency. Then, shear correction factors have to be evaluated with respect to the principal directions of the bending stiffness tensor (see e.g. Kugler et al, 2018a).

A decoupling of transverse and torsional loading requires the origin of the beam's coordinate system to be located at the shear center. This location is typically assumed to be congruent with the drill center, i.e. the pivot point of in-plane rigid body rotation due to torsion, see e.g. Barretta (2012), where it is proved that the shear center coincides with the St. Venant drill center. However, the definition of the shear center is not unique, see Schmidrathner (2019), where between the kinematic shear center and the energetic shear center is distinguished. Torsional and flexural vibrations always couple, except when the cross-section has two orthogonal axes of symmetry (i.e. drill-center and centroid are congruent). This well known fact (see e.g. Weaver et al, 1990) is shown in Subsect. 11.4.3, where resonance curves of a shaft with an unsymmetrical cross-section are calculated. The results show a slight amplification of the torsional angle at eigenfrequencies of a bending mode.

Clearly, CBM requires stiffness quantities which are typically evaluated by cross-sectional integration. For axial and bending stiffnesses this integration can be carried out analytically. However, in an arbitrary case quantities like transverse shear stiffnesses and stiffness quantities for non-uniform warping torsion can only be evaluated numerically based on a discretized cross-section². The definition of transverse shear stiffnesses requires the knowledge of transverse shear stresses due to shear forces, which cannot be given analytically in an arbitrary case (see e.g. Gruttmann and Wagner, 2001, for a corresponding procedure). The evaluation of torsion stiffnesses requires a warping function $\omega(y,z)$ which is the solution of a Laplace equation $\Delta\omega = \omega_{,yy} + \omega_{,zz} = 0$, which cannot be solved analytically in an arbitrary case. Therefore, any new formulations based on discretized cross-sections will not add a substantial amount of complexity.

Deficiencies of CBM are typically reported in case of buckling problems of short members in connection with thin-walled cross-sections (see e.g. Sapountzakis and Argyridi, 2018, and the references therein). In order to motivate our following approach, we consider the torsional resonance curves of a prismatic shaft with a homogeneous rectangular box type cross-section (see Subsect. 11.4.2, Fig. 11.10): Fig. 11.1 displays considerable discrepancies between continuum models and CBM formulations (Vlasov's or Bencoter's theory of warping torsion, Kugler et al, 2018b, 2019). Even though the shaft seems to be slender (length to height ratio of ten) CBM

² In Kugler et al (2018a,b) a new numerical approach for the evaluation of these quantities is proposed, which is based on the solution of a reference beam problem and, therefore, is physically interpretable and easy to understand.

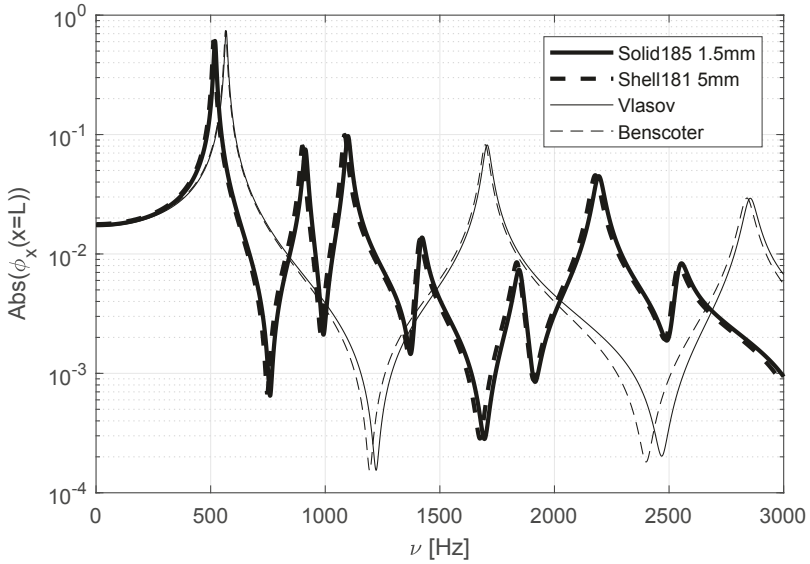


Fig. 11.1. Resonance curve of problem Fig. 11.10. Comparison of FEM solutions and torsion theories

reproduces only the first resonance spike accurately, whereas the higher frequency spectrum does not come close to FEM results (Fig. 11.1).

The major limitations of CBM are due to the neglect of in-plane distortions which is also indicated by observing the first two relevant mode shapes of the problem (Fig. 11.2). The inclusion of in-plane distortions necessitates higher order

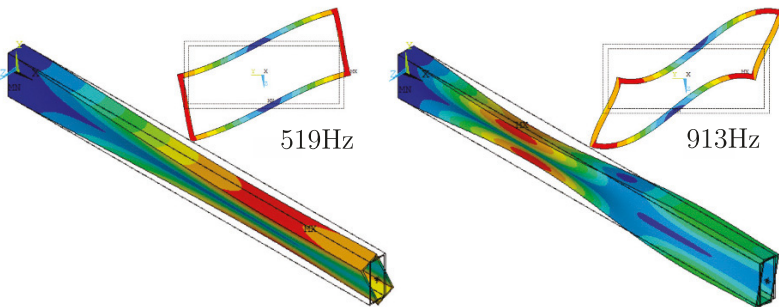


Fig. 11.2. Two mode shapes of continuum model

beam theories or generalized beam theories (GBT)³. A comprehensively written paper discussing the state of the art in GBT is due to Sapountzakis and Argyridi (2018). There, it is pointed out that the majority of research focused on thin-walled profiles with pronounced distortion and warping. Schardt (1989) introduces GBT to the analysis of linear static and buckling problems of thin-walled open cross-sections which are assumed to be unbranched. A generalization to branched profiles or closed sections leads to much more involved formulations (e.g. Dinis et al, 2006; Goncalves et al, 2009).

After all, GBT is a two-step algorithm consisting of a *cross-sectional analysis* defining warping and distortional fields, followed by a *member analysis*, where those deformation fields are weighted axially along the beam. According to Sapountzakis and Argyridi (2018) most approaches in that field perform the cross-sectional analysis in two stages, first defining the warping modes and then the distortional modes found from Vlasov's zero shear stress conditions. Ranzi and Luongo (2011) propose a reversed procedure starting with an eigenvalue decomposition of a planar discretized cross-section, where the eigenvectors define the distortional fields. Then, the warping modes are evaluated from conditions enforced on the shear strain. Warping and distortional fields are found simultaneously in Genoese et al (2014) where an eigenvalue cross-sectional problem is developed. Finally, Dikaros and Sapountzakis (2017); Argyridi and Sapountzakis (2018, 2019) developed a very advanced beam formulation based on a so-called sequential equilibrium scheme where within the cross-sectional analysis the boundary element method is employed. This formulation is not restricted to thin-walled cross-sections and does not stand on any corresponding assumption.

In Sect. 11.2 we discuss the basic idea of our present approach, where we focus on plane beam problems. In Sect. 11.3 we discuss our approach in a more rigorous manner, where the cross-sectional analysis (Subsect. 11.3.1) and the member analysis (Subsect. 11.3.2) refer to three-dimensional structures. No a priori assumptions regarding the cross-sectional shape or regarding the applied coordinate system are taken, however, we restrict ourselves to constitutive relations with point-wise isotropy. Finally, in Sect. 11.4 the performance of the proposed solution strategy will be investigated.

11.2 Preliminaries and Basic Idea of Present Approach

In the following we briefly introduce our approach to analyze isotropic prismatic structures where distortions and warping deformations cannot be neglected. The procedure is related to GBT and identifies warping and distortions from a vibration analysis of a reference beam followed by a member analysis, where the beam kinematics from the first step is weighted axially. For the sake of clarity in this

³ Alternatively to GBT, the finite strip method is also a possibility to introduce distortional and warping effects in slender members (see Ádány and Schafer, 2006a,b), however, the finite strip method is not directly related to a beam theory.

section we discuss a two dimensional plane stress problem here (see Fig. 11.3): The crucial idea is the extraction of warping and distortions from a dynamic analysis of a reference beam problem (RBP) with length l_{RB} . According to Fig. 11.3(a), we

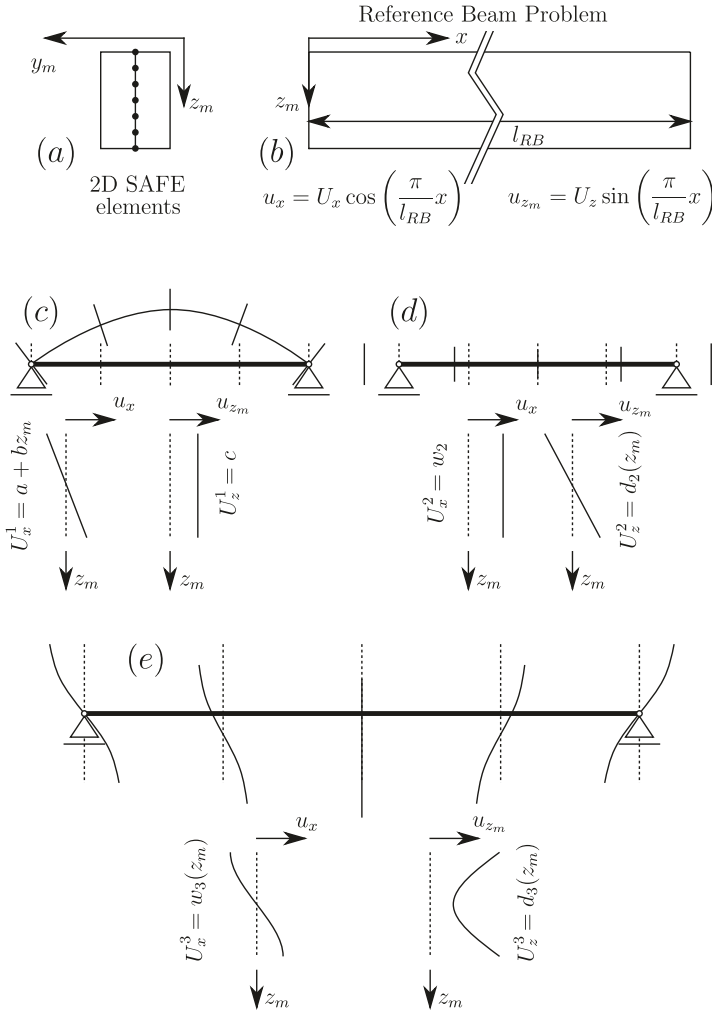


Fig. 11.3. Principle of present approach:

- (a) Two noded line elements discretize the cross-section in plane problems. Nodal degrees of freedom are the amplitudes of (b)
- (b) Simply supported reference beam of length l_{RB} - axial distribution of u_x and u_{z_m} is due to **one** cosine and sine function, respectively.
- (c) Physical flexural mode of simply supported beam.
- (d) Physical axial mode of unrestrained truss.
- (e) Artificial third mode to trigger warping and distortions.

start by discretizing the cross-section with semi-analytical finite elements (SAFE), where displacements u_i with $i = x, z_m$ are interpolated using finite element type shape functions within the cross-section, while analytical functions are applied axially (Zienkiewicz and Taylor, 2000): In Fig. 11.3 the reference beam is assumed to deform in the x - z_m plane only, which enables one to use simple two noded line elements over the cross-sectional height. The variation of the components u_x and u_{z_m} along the x -direction is modeled by a Fourier series, i.e. the application of,

$$u_x = \sum_{n=1}^{\infty} U_x^{(n)}(z_m) \cos\left(\frac{n\pi}{l_{RB}} x\right) \quad \text{and} \quad u_{z_m} = \sum_{n=1}^{\infty} U_z^{(n)}(z_m) \sin\left(\frac{n\pi}{l_{RB}} x\right), \quad (11.1)$$

defines the kinematic boundary conditions of the reference beam, we chose a simply supported reference beam problem here. The amplitudes of the sine and cosine functions in (11.1), $U_i^{(n)}(z_m)$ for $i = x, z$, are interpolated based on classical shape functions, and we may write on element level,

$$U_i^{(n)e}(z_m) = [N_1(z_m) \ N_2(z_m)] \begin{bmatrix} U_{i1}^{(n)e} \\ U_{i2}^{(n)e} \end{bmatrix} = \mathbf{N}(z_m) \mathbf{U}_i^{(n)e}. \quad (11.2)$$

Now, the key in the present approach lies in recognizing that it is sufficient to include only the **first** wave number $n = 1$ in the analysis, and from (11.1) and (11.2) we get with $\alpha = \pi/l_{RB}$ on element level,

$$\begin{bmatrix} u_x^e(x, z_m) \\ u_{z_m}^e(x, z_m) \end{bmatrix} = \begin{bmatrix} \mathbf{N}(z_m) \cos(\alpha x) & \mathbf{0} \\ \mathbf{0} & \mathbf{N}(z_m) \sin(\alpha x) \end{bmatrix} \begin{bmatrix} \mathbf{U}_x^e \\ \mathbf{U}_z^e \end{bmatrix}. \quad (11.3)$$

The displacement interpolations (11.3) are introduced into the principle of virtual work⁴,

$$\int_{V_{RB}} \sigma_{ij} \delta \epsilon_{ij} dV + \int_{V_{RB}} \rho \ddot{u}_i \delta u_i dV = 0. \quad (11.4)$$

There, σ_{ij} and ϵ_{ij} denote the stress and strain tensor (Einstein sum convention is understood), a superscript double dot refers to the second partial time derivative, ρ represents the density of the material while δ is the variation symbol. The strain tensor is found from (11.3) based on classical strain-displacement relations (a comma in the index refers to a partial derivative), and the stress tensor is subsequently evaluated using the linear elastic constitutive relation,

$$\epsilon_{ij} = \frac{1}{2} (u_{i,j} + u_{j,i}) \quad \text{and} \quad \sigma_{ij} = f(\epsilon_{ij}). \quad (11.5)$$

Using classical finite element assembly procedures, we obtain for steady state vibration,

⁴ Note, that any integration with respect to the axial coordinate x can be carried out analytically due to the sine and cosine functions in (11.3).

$$\left(\mathbf{K} - \omega^2 \mathbf{M}\right) \boldsymbol{\Gamma} = \mathbf{0}, \quad (11.6)$$

where \mathbf{K} and \mathbf{M} denote the global stiffness and mass matrix, respectively, $\boldsymbol{\Gamma} = [\mathbf{U}_x \ \mathbf{U}_z]^T$ refers to the eigenvector consisting of the nodal amplitudes from (11.3), while $\omega = \omega_1, \omega_2, \dots$ denote the resonance frequencies in ascending order. Any vibration mode amplitude vector $\boldsymbol{\Gamma}_k$ can be decomposed into axial displacements \mathbf{U}_x^k and accompanied transverse displacements \mathbf{U}_z^k , which are related by l_{RB} . It is important to note that only the first two eigenvalues represent a physical solution of the RBP if l_{RB} is large compared to a characteristic cross-section dimension (see Fig. 11.3(c) and (d)): The first resonance frequency ω_1 is due to transverse vibration of a simply supported beam (analytical vibration mode based on a shear rigid Euler-Bernoulli beam theory, which is valid for a slender RBP): The axial displacement amplitude vector \mathbf{U}_x^1 represents the rigid body rotation about the centroid of the cross-section, while the transverse amplitude vector \mathbf{U}_z^1 refers to rigid body translation (see Fig. 11.3(c)). Although, shape changing warping and distortions decrease for increasing values of l_{RB} , we suggest a true rigid body mode extraction by simple linear fitting. Note, that the orders of \mathbf{U}_x^1 and \mathbf{U}_z^1 are related by l_{RB} , i.e. $l_{RB} \max(\mathbf{U}_x^1) \sim \max(\mathbf{U}_z^1)$. This can be explained by the Euler-Bernoulli constraint, where the bending angle is proportional to the first derivative of transverse displacement. However, both the axial and the transverse displacement amplitude vector can be scaled independently (such that each maximum value is related to a characteristic cross-section dimension) to arrive at the first pair of GBT kinematics.

The second resonance frequency $\omega_2 > \omega_1$ refers to axial vibration of an unrestrained truss. There, \mathbf{U}_x^2 corresponds to approximate axial rigid body motion of the cross-section, while \mathbf{U}_z^2 refers to the accompanied Poisson contraction (again a linear fitting operation is proposed to extract true rigid body motion). After independent scaling of \mathbf{U}_x^2 and \mathbf{U}_z^2 we obtain the second pair of GBT kinematics. Note, that \mathbf{U}_z^2 is the first shape changing distortion mode of the cross-section, which is typically not present in CBM.

All resonance frequencies ω_k for $k = 3, 4, 5, \dots$ cannot be interpreted as physical steady state vibration modes of the RBP (see the third artificial mode in Fig. 11.3(e)), since we restrict ourselves to only the first wave number $n = 1$ in (11.3). This is done as an artifice to trigger warping and accompanied distortion fields of the cross-section. Again each mode $\boldsymbol{\Gamma}_k$ for $k \geq 3$ is decomposed into the corresponding axial displacement amplitude vector (shape changing warping mode \mathbf{U}_x^k) and into the accompanied transverse displacement amplitude vector (shape changing distortion mode \mathbf{U}_z^k). Subsequently, they are scaled independently in order to avoid bad conditioning due to small numbers, and they contribute pair-wise to the GBT kinematics. Note, that the resonance frequencies ω_k are used in the cross-sectional analysis to order the corresponding pairs of warping and distortion modes, i.e. larger pair numbers k contribute to the results of GBT to a lesser extent. In a plane problem at least \mathbf{U}_x^1 , \mathbf{U}_z^1 and \mathbf{U}_x^2 have to be introduced in the GBT formulation. The proposed linear fitting operations are important to achieve the required rigid body criteria within GBT. Additional higher pairs of warping and distortion modes enhance the accuracy of the resulting GBT formulation.

Once, the independently scaled pairs of warping and distortion modes are found, we introduce them in the member analysis of our GBT formulation as corresponding kinematical fields. We assume the following separation Ansatz based on K pairs of warping and distortion modes,

$$u_x(x, z_m) = \sum_{k=1}^K U_x^k(z_m) \alpha_k(x), \quad u_z(x, z_m) = \sum_{k=1}^K U_z^k(z_m) \beta_k(x), \quad (11.7)$$

where the generalized degrees of freedom α_k and β_k interpolate the corresponding warping and distortional fields by finite element shape functions⁵. Then, the GBT strain fields are evaluated from the strain-displacement relations (11.5), and the GBT stress fields are found by the constitutive relation. Subsequently, these tensors are put into the principle of virtual work (11.4)⁶, where all displacement amplitude vectors couple with each other due to a product of sums. A somewhat laborious collection of terms detailed in Subsect. 11.3.2 enables the integration with respect to the cross-section, while the axial integration can be carried out subsequently. Without giving any mathematical details here, it has to be pointed out that within the cross-sectional integration some of the following terms will arise: Denoting the Young's modulus by E we get

$$\int E \left(\mathbf{U}_x^1(z_m) \right)^T \mathbf{U}_x^1(z_m) dA$$

and

$$\int E \left(\mathbf{U}_x^2(z_m) \right)^T \mathbf{U}_x^2(z_m) dA$$

which are recognized as being proportional (see footnote 5) to the bending stiffness and the axial or membrane stiffness, respectively, since according to Fig. 11.3(c) and (d) \mathbf{U}_x^1 is a linear field while \mathbf{U}_x^2 is a constant field.

Note, that our briefly introduced approach relies on a cross-section discretization, thus, the proposal is applicable for cross-sections made of inhomogeneous multi-layer composites or functionally graded materials (FGM). In such a case clearly both the cross-sectional and the member analysis has to be performed based on $E(z_m)$ where E is constant within one element.

⁵ Strictly speaking, α_1 is proportional to the bending angle, β_1 is related to cross-sectional shape preserving transverse displacements, while α_2 is proportional to cross-sectional shape preserving axial displacements. The factor of proportionality depends on the above-mentioned scaling operation where the maximum amplitude of \mathbf{U}_i^k is related to characteristic cross-sectional dimension in order to avoid numerical issues.

⁶ Volume integration is now with respect to the beam element member V_m .

11.3 Generalized Beam Model Based on the Reference Beam Problem

In this section we discuss the new approach to derive beam models for prismatic structures which are capable to cover in-plane distortions of cross-sections leading to more predictive solutions in dynamic problems according to Fig. 11.1. The procedure is suitable to arbitrary cross-section shapes and inhomogeneous material distributions. In what follows we restrict ourselves to constitutive relations that are isotropic at each material point. Basically, the idea of our approach is the separation Ansatz with a multiplicative decomposition of the displacement field,

$$u_i(x, y, z) = f(y, z)g(x). \quad (11.8)$$

This is a typical approach also for classical first order beam theory (CBM). In addition we assume that the functions $f(y, z)$ do not depend on the beam's boundary conditions, i.e. $f(y, z)$ might be prescribed regardless of any restraints to the global prismatic structure. Hence, we can evaluate $f(y, z)$ from a suitably chosen Reference Beam Problem (RBP), where global boundary conditions are elected such that three dimensional elasticity theory can be applied at minimum computational costs. In this respect the present work is a generalization of the procedures discussed in Kugler et al (2018a) where the RBP was used to identify stiffness properties of classical beam mechanics where cross-sections remain plane in their projection area.

The present approach is carried out in two steps: At first the RBP is used to evaluate the relevant warping and distortion modes (cross-sectional analysis), and, secondly, these modes are weighted axially by generalized degrees of freedom to arrive at a generalized beam element (member analysis).

11.3.1 Reference Beam Problem for the Cross-sectional Analysis

Consider a prismatic structure of arbitrary length $l = l_{RB}$ described in a Cartesian base where x directs along the axis while y_m and z_m are Cartesian cross-section coordinates with arbitrary origin (see Fig. 11.4). The mechanical behavior of such a structure can be analyzed efficiently by semi-analytical finite elements (SAFE), where the cross-section is discretized using a standard quadrilateral⁷ FE approach with local coordinates $\xi - \eta$ (see e.g. Zienkiewicz and Taylor, 2000). The displacement components are interpolated by finite element shape functions with respect to the cross-section coordinates, and their axial interpolation is carried out using Fourier series (Kugler et al, 2018a). The boundary conditions at $x = 0$ and $x = l_{RB}$ define the specific form of the expansion, where we assume for the in-plane displacements

⁷ Some authors in that field apply quadratic Serendipity or Lagrangian elements to avoid locking, however, since functionally graded material (FGM) cross-sections are in the scope of this text (where fine meshes have to be applied in order to capture the variation of the constitutive model) we prefer to apply quadrilateral low order finite elements.

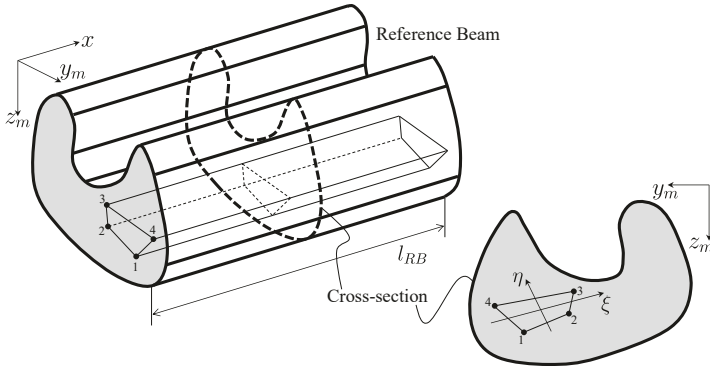


Fig. 11.4. Application of SAFE to analyze the RBP

$$u_{y_m}(x = 0) = u_{z_m}(x = 0) = u_{y_m}(x = l_{RB}) = u_{z_m}(x = l_{RB}) = 0, \quad (11.9)$$

together with arbitrary axial displacements at both beam ends. The resulting RBP is

- simply supported for transverse action,
- double sided fork supported for torsional action,
- and unsupported for axial action.

In order to satisfy (11.9) we apply the following Fourier series expansion

$$u_x \sim \cos\left(\frac{n\pi}{l_{RB}}x\right), \quad (11.10)$$

$$u_{y_m} \sim \sin\left(\frac{n\pi}{l_{RB}}x\right), \quad u_{z_m} \sim \sin\left(\frac{n\pi}{l_{RB}}x\right), \quad (11.11)$$

with $n = 1, 2, 3, \dots$ denoting the number of harmonic and l_{RB} referring to the length of the reference beam. Thus, we propose⁸ on element level

$$\begin{bmatrix} u_x(x, \xi, \eta) \\ u_{y_m}(x, \xi, \eta) \\ u_{z_m}(x, \xi, \eta) \end{bmatrix} = \sum_n \begin{bmatrix} \mathbf{N} \cos(\alpha_n x) & \mathbf{0} & \mathbf{0} \\ \mathbf{0} & \mathbf{N} \sin(\alpha_n x) & \mathbf{0} \\ \mathbf{0} & \mathbf{0} & \mathbf{N} \sin(\alpha_n x) \end{bmatrix} \begin{bmatrix} \mathbf{U}_x^{(e)n} \\ \mathbf{U}_{y_m}^{(e)n} \\ \mathbf{U}_{z_m}^{(e)n} \end{bmatrix}, \quad (11.12)$$

with the bilinear shape functions $\mathbf{N}(\xi, \eta)$ and the nodal displacements

$$\mathbf{U}_i^{(e)n} = \left[U_i^{(1)n} \dots U_i^{(4)n} \right]^T$$

depending on the number of harmonic n , while $\alpha_n = n\pi/l_{RB}$. It can be shown that different wave numbers n remain uncoupled in case of a point-wise isotropic constitutive relation (see Kugler et al, 2018a). By introducing (11.12) into the principle of

⁸ Equation (11.12) is also based on the Separation Ansatz.

virtual work (11.4) in connection with the strain displacement relations (11.5) and the constitutive relation

$$\begin{bmatrix} \sigma_{xx} \\ \sigma_{y_m y_m} \\ \sigma_{z_m z_m} \end{bmatrix} = \frac{E}{(1 + \nu^*)(1 - 2\nu^*)} \begin{bmatrix} 1 - \nu^* & \nu^* & \nu^* \\ & 1 - \nu^* & \nu^* \\ & & 1 - \nu^* \end{bmatrix} \begin{bmatrix} \epsilon_{xx} \\ \epsilon_{y_m y_m} \\ \epsilon_{z_m z_m} \end{bmatrix}, \quad (11.13)$$

$$\begin{bmatrix} \tau_{xy_m} \\ \tau_{xz_m} \\ \tau_{y_m z_m} \end{bmatrix} = \frac{E}{2(1 + \nu)} \begin{bmatrix} 1 & 0 & 0 \\ & 1 & 0 \\ & & 1 \end{bmatrix} \begin{bmatrix} \gamma_{xy_m} \\ \gamma_{xz_m} \\ \gamma_{y_m z_m} \end{bmatrix}, \quad (11.14)$$

with $\gamma_{ij} = 2\epsilon_{ij}$ and $\nu^* = \kappa\nu$ ($\kappa \leq 1$) defining the amount of coupling of the normal components, we are able to define elemental mass- and stiffness matrices depending on the length of the reference beam l_{RB} and the number of harmonic n . There, the required volume integration is done analytically in axial direction and numerically (2×2 Gauss points) in $\xi - \eta$. A subsequent assembly to global matrices is straight forward and has to be carried out for each harmonic n leading to a global system of differential equations describing the dynamic behavior of the RBP. By using element-wise constant material properties, FGM or multi-layer composite structures can be modeled easily.

By assuming (see Sect. 11.2) that only one wave number ($n = 1$) contributes and l_{RB} is large compared to a characteristic cross-section dimension, we perform a steady state vibrational analysis (see (11.6)) leading to resonance frequencies $\omega_i = \omega_1, \omega_2, \dots$ in connection with the eigenvectors \boldsymbol{T}_i consisting of nodal amplitudes $\mathbf{U}_k^{(i)}$ with $k = x, y_m, z_m$. The resonance frequencies are used to order the eigenvectors ascendingly, and it can be assumed that lower ones contribute more in the upcoming member-analysis. Note that due to $n = 1$ only the first four resonance frequencies are related to physical vibration modes of the RBP:

1. The lowest resonance frequency is related to a flexural mode about the weak principal direction of the cross-section (e.g. the z -axis in Fig. 11.7). The solution is exact compared to CBM and analytical considerations since for large reference beam lengths transverse shear can be neglected, i.e. the transverse displacement mode is proportional to a sine function and the bending angle (related to axial displacements) is proportional to a cosine function in the first bending mode (see (11.12)) of a simply supported beam.
2. The second resonance frequency corresponds to the flexural mode about the stiff principal direction of the cross-section (e.g. the y -axis in Fig. 11.7) and the above considerations. In that sense engineering quantities like the principal directions and the elastic center (centroid in homogeneous cross-sections) can be extracted based on fitting operations.
3. The third resonance frequency is due to torsion of a double sided fork supported shaft. According to Gere (1954) (see Blevins, 1979) warping can be neglected in vibrational analysis even in thin-walled open cross-sections if $t l_{RB} > 10D^2$, where t is the minimum wall thickness and D denotes the diameter of the cross-section, i.e. the relation of u_{y_m} and u_{z_m} to torsional angle $\varphi_x(x) \sim \sin(\pi x/l_{RB})$ is consistent to analytical considerations of Vlasov's theory of torsion, while axial

motion $u_x \sim \varphi'_x \sim \cos(\pi x/l_{RB})$ is proportional to the warping function ω (which is typically defined from the St. Venant problem as $\omega_{,y_m y_m} + \omega_{,z_m z_m} = 0$) if l_{RB} is large.

4. The fourth resonance frequency is related to steady state vibration of an unsupported truss. There, axial motion proportional to a cosine function is consistent to analytical considerations, and in-plane displacements based on Poisson-breathing are proportional to $v\epsilon_{x,x} = v u_{x,x} \sim \sin(\pi x/l_{RB})$.

The eigenvectors Γ_i can be split up according to couples consisting of warping modes,

$$\mathbf{w}^{(i)} = \mathbf{U}_x^{(i)}, \quad (11.15)$$

and distortion modes,

$$\mathbf{d}^{(i)} = \begin{bmatrix} \mathbf{d}_{y_m}^{(i)} \\ \mathbf{d}_{z_m}^{(i)} \end{bmatrix} = \begin{bmatrix} \mathbf{U}_{y_m}^{(i)} \\ \mathbf{U}_{z_m}^{(i)} \end{bmatrix}, \quad (11.16)$$

for each mode number $i = 1, \dots, i_{\max}$ ⁹ which are scaled in a way that maximum nodal displacements in (11.15) separately from (11.16) are e.g. one tenth of a characteristic cross-section dimension χ . If the length of the reference beam is large compared to χ (i.e. $l_{RB} > 100\chi$) we expect approximate rigid body modes for $1 \leq i \leq 4$, i.e. $i = 1$ and $i = 2$ lead to bending modes with respect to the principal axes of the cross-section, $i = 3$ leads to torsion (the nodal warping function $\omega(y_m, z_m)$ is represented by $\mathbf{w}^{(3)}$ while rigid in-plane rotation is represented by $\mathbf{d}^{(3)}$ while $\mathbf{w}^{(4)}$ is devoted to the axial mode and $\mathbf{d}^{(4)}$ is Poisson's mode for axial vibration. All further modes ($i > 4$) contribute to higher order beam mechanics¹⁰.

At this stage a linear fitting operation is useful to extract the real rigid body modes (see footnote 10) from the approximate ones (Fig. 11.5 for a challenging unsymmetrical thin-walled multi-cell cross-section made of steel, see Fig. 11.15): If the difference between approximate and true rigid body motion is small, we expect to have chosen the right reference beam length l_{RB} , in case of nonphysical behavior (e.g. bending is not directed into the principal direction) l_{RB} might be too large and some numerical issues related to the eigenvalue problem are encountered, and if the cross-section changes significantly its shape except $\mathbf{w}^{(3)}$ and $\mathbf{d}^{(4)}$, l_{RB} was selected too short. Some of the ascending higher order mode shapes ($5 \leq i \leq 8$) are depicted in Fig. 11.6. These mode shapes represent the $f(y, z)$ in the separation Ansatz (11.8), and we develop our beam finite elements subsequently in the following section.

⁹ $i_{\max} \geq 4$ can be selected and represents a convergence parameter in the upcoming beam model.

¹⁰ At a rigid load sharing plate being able to move rigidly through space only $\mathbf{w}^{(1)}$, $\mathbf{w}^{(2)}$, $\mathbf{w}^{(4)}$ and $\mathbf{d}^{(1)}$, $\mathbf{d}^{(2)}$, $\mathbf{d}^{(3)}$ remain, while all other modes have to be restrained. In that sense, $\mathbf{w}^{(3)}$ and $\mathbf{d}^{(4)}$ also count to higher order beam mechanics.

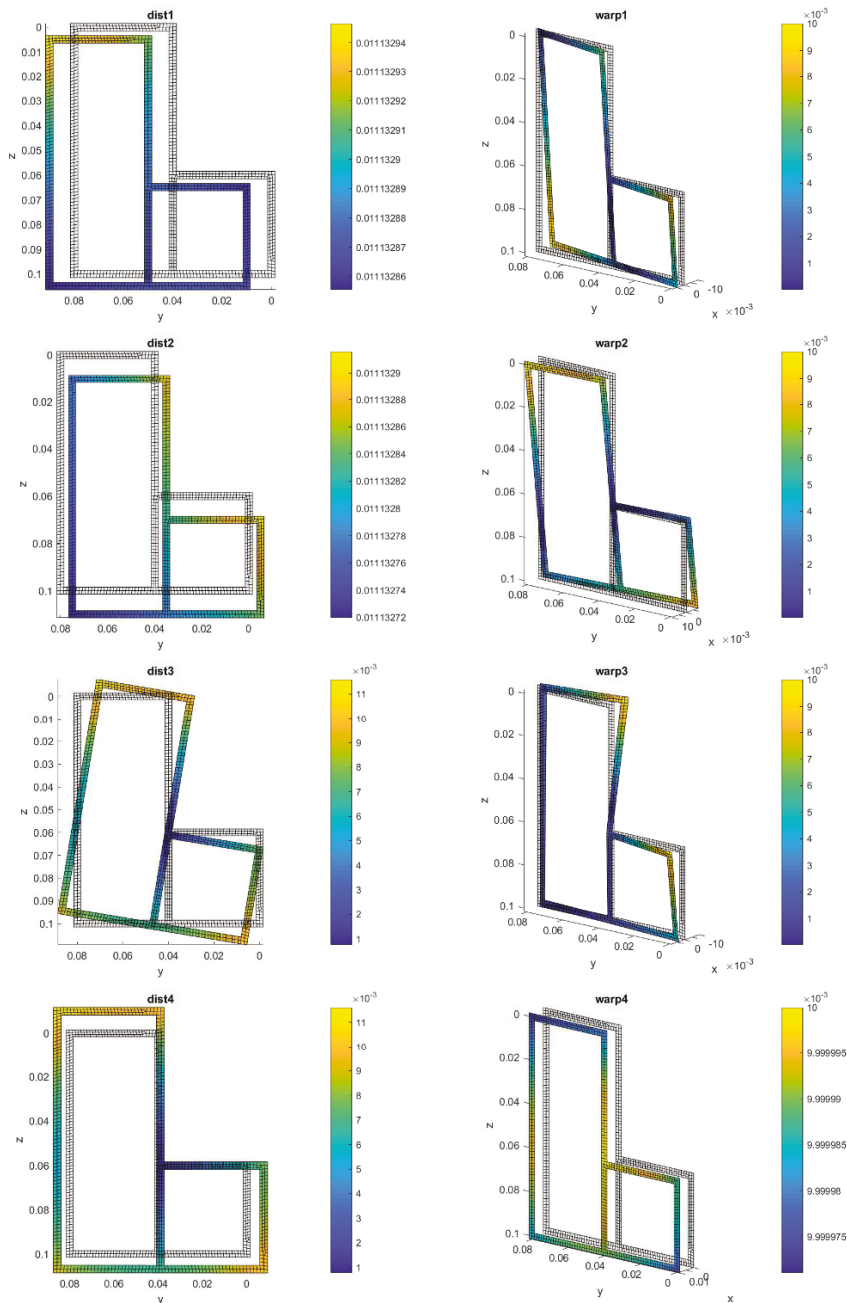


Fig. 11.5. Modes before rigid body extraction $I_{RB} = 50$ m, $\nu^* = \nu$

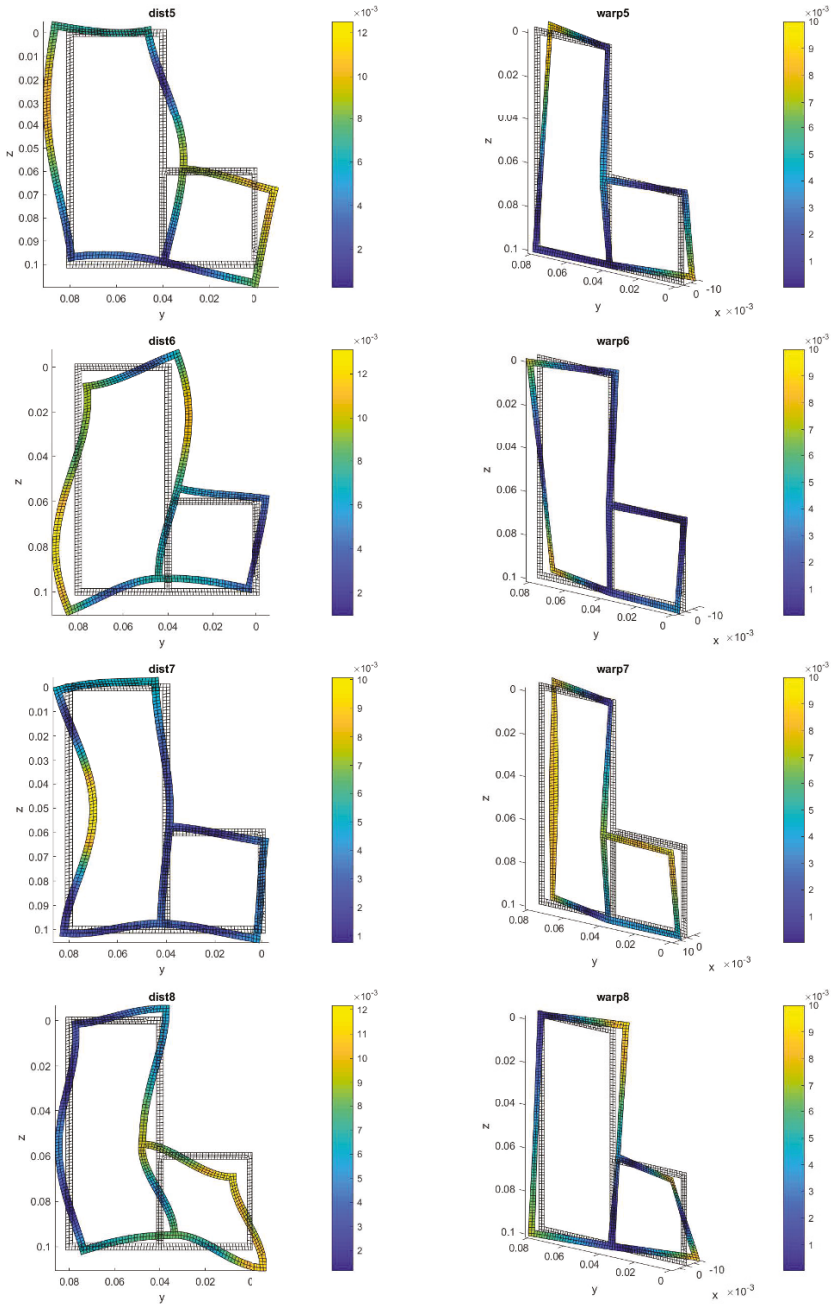


Fig. 11.6. Higher order mode shapes $l_{RB} = 50$ m, $\nu^* = \nu$

11.3.2 Member Analysis Based on Generalized Beam Finite Elements

At this stage of the derivation we have the mode shapes describing warping and distortion based on the separation Ansatz (11.8) within the considered cross-section. The terms warping and distortion could be misleading for the first four mode couples since there rigid body modes (except $\mathbf{w}^{(3)}$ and $\mathbf{d}^{(4)}$) are delivered, however, we call any out of plane motion (shape preserving displacements or shape changing deformations) a warping mode, while all in-plane motions are called distortional modes. In this section we start weighing them in axial direction. For each SAFE element e in the cross-section we have,

$$u_x^{(i)}(\xi, \eta, x) = \mathbf{N}(\xi, \eta) \mathbf{w}_e^{(i)} \alpha_i(x), \quad (11.17)$$

$$u_{y_m}^{(i)}(\xi, \eta, x) = \mathbf{N}(\xi, \eta) \mathbf{d}_{y_m e}^{(i)} \beta_i(x), \quad (11.18)$$

$$u_{z_m}^{(i)}(\xi, \eta, x) = \mathbf{N}(\xi, \eta) \mathbf{d}_{z_m e}^{(i)} \beta_i(x), \quad (11.19)$$

where each warping mode is weighted with one degree of freedom (α_i), while each distortional mode is weighted using another degree of freedom (β_i). The matrix $\mathbf{N} = [N_1 \ N_2 \ N_3 \ N_4]$ represents classical finite element shape functions for the quadrilateral element and the index e in the column vectors $\mathbf{w}_e^{(i)}$ and $\mathbf{d}_{k_e}^{(i)}$ for $k = y_m, z_m$ denotes the extraction of the elemental nodal displacements from the global warping and distortion modes found in Sect. 11.3.1. Equations (11.17)-(11.19) can be reformulated in matrix notation,

$$\mathbf{u}_e^{(i)}(\xi, \eta, x_e) = \begin{bmatrix} \mathbf{u}_{x_e}^{(i)} \\ \mathbf{u}_{y_m e}^{(i)} \\ \mathbf{u}_{z_m e}^{(i)} \end{bmatrix} = \mathbf{N}_{3D} \mathbf{u}_u^{(i)}, \quad (11.20)$$

with

$$\mathbf{N}_{3D} = \underbrace{\begin{bmatrix} \mathbf{N}(\xi, \eta) & \mathbf{0} & \mathbf{0} \\ \mathbf{0} & \mathbf{N}(\xi, \eta) & \mathbf{0} \\ \mathbf{0} & \mathbf{0} & \mathbf{N}(\xi, \eta) \end{bmatrix}}_{3 \times 12} \quad (11.21)$$

and

$$\begin{aligned} \mathbf{u}_u^{(i)} &= \mathbf{N}_{u e}^{(i)} \mathbf{N}_{B u} \mathbf{\Xi}_e^{(i)} = \\ &= \underbrace{\begin{bmatrix} \mathbf{w}_e^{(i)} & \mathbf{0} & \mathbf{0} \\ \mathbf{0} & \mathbf{d}_{y_m e}^{(i)} & \mathbf{0} \\ \mathbf{0} & \mathbf{0} & \mathbf{d}_{z_m e}^{(i)} \end{bmatrix}}_{12 \times 3} \underbrace{\begin{bmatrix} \mathbf{N}_B(x_e) & \mathbf{0} \\ \mathbf{0} & \mathbf{N}_B(x_e) \\ \mathbf{0} & \mathbf{N}_B(x_e) \end{bmatrix}}_{3 \times 2k} \underbrace{\begin{bmatrix} \mathbf{A}^{(i)} \\ \mathbf{B}^{(i)} \end{bmatrix}}_{2k \times 1} \end{aligned} \quad (11.22)$$

where x_e denotes the beam element's axial direction $0 \leq x_e \leq l_e$ with l_e denoting the beam's element length. In (11.20) we use a k -noded beam element ($k \geq 2$)

and classical finite element shape functions \mathbf{N}_B of order $k - 1$ (we additionally assume that the distance between nodes is kept equal in each beam finite element) and the beam element's degrees of freedom $\mathbf{A}^{(i)}$ and $\mathbf{B}^{(i)}$, i.e. $\alpha_i(x_e) = \mathbf{N}_B(x_e)\mathbf{A}^{(i)}$ and $\beta_i(x_e) = \mathbf{N}_B(x_e)\mathbf{B}^{(i)}$. The interpolated strains are found according to the strain displacement relations (11.5) in connection with (11.20) and we get by laborious suitable rearrangement,

$$\boldsymbol{\epsilon}_e^{(i)}(\xi, \eta, x_e) = \begin{bmatrix} \epsilon_{xxe}^{(i)} \\ \epsilon_{yyme}^{(i)} \\ \epsilon_{zmez}^{(i)} \\ \gamma_{xye}^{(i)} \\ \gamma_{xze}^{(i)} \\ \gamma_{yze}^{(i)} \end{bmatrix} = \mathbf{B}\mathbf{u}_e^{(i)}, \quad (11.23)$$

with

$$\mathbf{B} = \underbrace{\begin{bmatrix} \mathbf{0} & \mathbf{N} & \mathbf{0} & \mathbf{0} & \mathbf{0} & \mathbf{0} \\ \mathbf{0} & \mathbf{0} & \mathbf{N}_{,ym} & \mathbf{0} & \mathbf{0} & \mathbf{0} \\ \mathbf{0} & \mathbf{0} & \mathbf{0} & \mathbf{0} & \mathbf{N}_{,zm} & \mathbf{0} \\ \mathbf{N}_{,ym} & \mathbf{0} & \mathbf{0} & \mathbf{N} & \mathbf{0} & \mathbf{0} \\ \mathbf{N}_{,zm} & \mathbf{0} & \mathbf{0} & \mathbf{0} & \mathbf{0} & \mathbf{N} \\ \mathbf{0} & \mathbf{0} & \mathbf{N}_{,zm} & \mathbf{0} & \mathbf{N}_{,ym} & \mathbf{0} \end{bmatrix}}_{6 \times 24}, \quad (11.24)$$

and

$$\begin{aligned} \mathbf{u}_e^{(i)} &= \mathfrak{N}_{\epsilon e}^{(i)} \mathbf{N}_B \boldsymbol{\epsilon}_e^{(i)} = \\ &= \underbrace{\begin{bmatrix} \mathbf{w}_e^{(i)} & \mathbf{0} & \mathbf{0} & \mathbf{0} & \mathbf{0} & \mathbf{0} \\ \mathbf{0} & \mathbf{w}_e^{(i)} & \mathbf{0} & \mathbf{0} & \mathbf{0} & \mathbf{0} \\ \mathbf{0} & \mathbf{0} & \mathbf{d}_{yme}^{(i)} & \mathbf{0} & \mathbf{0} & \mathbf{0} \\ \mathbf{0} & \mathbf{0} & \mathbf{0} & \mathbf{d}_{yme}^{(i)} & \mathbf{0} & \mathbf{0} \\ \mathbf{0} & \mathbf{0} & \mathbf{0} & \mathbf{0} & \mathbf{d}_{zme}^{(i)} & \mathbf{0} \\ \mathbf{0} & \mathbf{0} & \mathbf{0} & \mathbf{0} & \mathbf{0} & \mathbf{d}_{zme}^{(i)} \end{bmatrix}}_{24 \times 6} \underbrace{\begin{bmatrix} \mathbf{N}_B & \mathbf{0} \\ \mathbf{N}_{B,x_e} & \mathbf{0} \\ \mathbf{0} & \mathbf{N}_B \\ \mathbf{0} & \mathbf{N}_{B,x_e} \\ \mathbf{0} & \mathbf{N}_B \\ \mathbf{0} & \mathbf{N}_{B,x_e} \end{bmatrix}}_{6 \times 2k} \underbrace{\begin{bmatrix} \mathbf{A}^{(i)} \\ \mathbf{B}^{(i)} \end{bmatrix}}_{2k \times 1}. \end{aligned} \quad (11.25)$$

From the strains (11.23) we find stresses according to the constitutive relation (11.13) and (11.14) with $\nu^* = 0$ representing a decoupled one-dimensional material law $\boldsymbol{\sigma} = \mathbf{C}_{red}\boldsymbol{\epsilon}$. By using element-wise (with respect to cross-section discretization) constant material properties, FGM or multi-layer composite structures can be modeled easily. Introducing that into the principle of virtual work (11.4) leads to

$$\begin{aligned}
& \delta \Xi_e^{(j)T} \int_{l_e} \mathbf{N}_{Bu}^T \mathbf{N}_{ue}^{(j)T} \underbrace{\sum_e \int_{A_e} \rho \mathbf{N}_{3D}^T \mathbf{N}_{3D} dA \mathbf{N}_{ue}^{(i)} \mathbf{N}_{Bu}}_{\mathbf{M}_{ij}^e} dx_e \ddot{\Xi}_e^{(i)} + \\
& \underbrace{\mathbf{M}_{ij}^e}_{\mathbf{M}_{Bij}^e} \\
& + \delta \Xi_e^{(j)T} \int_{l_e} \mathbf{N}_{Be}^T \mathbf{N}_{\epsilon e}^{(j)T} \underbrace{\sum_e \int_{A_e} \mathbf{B}^T \mathbf{C}_{red} \mathbf{B} dA \mathbf{N}_{\epsilon e}^{(i)} \mathbf{N}_{Be}}_{\mathbf{K}_{ij}^e} dx_e \Xi_e^{(i)} = \delta W_{ext}. \quad (11.26) \\
& \underbrace{\mathbf{K}_{ij}^e}_{\mathbf{K}_{Bij}^e}
\end{aligned}$$

There, $\mathbf{M}_{inner}^e = 3N \times 3N$ (integrated analytically with respect to A_e) and $\mathbf{K}_{inner}^e = 6N \times 6N$ (integrated with 2×2 Gauss integration) are assembled to global matrices based on cross-section discretization with N nodes. The modal coupling based on $\mathbf{N}_u^{(i)}$ and $\mathbf{N}_\epsilon^{(i)}$ to arrive at four dimensional arrays $\mathbf{M}_{ij}^e = 3 \times 3 \times i \times j$ and $\mathbf{K}_{ij}^e = 6 \times 6 \times i \times j$ for $i = 1 \dots i_{max}$ and $j = 1 \dots i_{max}$ is carried out on global level and the final integration in axial direction to evaluate $\mathbf{M}_{Bij}^e = 2k \times 2k \times i \times j$ and $\mathbf{K}_{Bij}^e = 2k \times 2k \times i \times j$ is carried out using a full Gaussian integration with two integration points for $k = 2$ (linear beam element), with three points for $k = 3$ (quadratic beam element) and with four points for $k = 4$ (cubic beam element), respectively, where k denotes the number of beam element's nodes. Next, a rearrangement of the four dimensional arrays \mathbf{M}_{Bij}^e and \mathbf{K}_{Bij}^e to beam elemental matrices $\mathbf{M}_B^e = 2ki_{max} \times 2ki_{max}$ and $\mathbf{K}_B^e = 2ki_{max} \times 2ki_{max}$ is performed and, finally, the beam elemental matrices are assembled to global matrices \mathbf{M}_B and \mathbf{K}_B ,

$$\mathbf{M}_B \ddot{\Xi}^{(i)} + \mathbf{K}_B \Xi^{(i)} = \mathbf{F}_B, \quad (11.27)$$

with $2i_{max}$ of generalized degrees of freedom at each node. The force vector \mathbf{F}_B has to be established consistently according to the principle of virtual work. Now, boundary conditions of the beam structure can be introduced by canceling the corresponding generalized degrees of freedom. Then, the resulting dynamic properties of beam structures (11.27) now converge due to mesh refinement of the cross-section discretization, due to the number of mode couples i_{max} ¹¹, due to the polynomial order $k - 1$ of the beam element's shape functions and due to the number of beam elements discretizing the entire prismatic structure.

¹¹ Note, that $i = 1 \dots i_{max}$ does not necessarily have to be applied. If some mode shapes obviously do not contribute, i.e. they are not excited by the applied loading, they can be skipped.

11.4 Examples

In this section we check the performance of the proposed solution strategy (Sect. 11.3) and discuss its convergence characteristics. The first example (Sect. 11.4.1) considers elasto-statics of a short single cantilever with an unsymmetrical thin-walled cross-section. As discussed in the introduction some side-way deflections occur even if the cantilever is transversely loaded into its principal direction, and we prove that our present procedure is capable to cover such an effect. The remaining examples firstly introduced in Kugler et al (2019) focus on harmonic analyses of torsional shafts of length l which are fully clamped at $x = 0$ and a harmonic torsion moment is applied on a massless rigid load sharing plate at $x = l$ (see Fig. 11.10). The results are compared to classical torsion theories where cross-section distortions are assumed to vanish and the issues discussed in Sect. 11.1 occur. The analysis of the problem using three-dimensional continuum elements and (if possible) shell elements is called an exact solution if fine meshes are used.

11.4.1 Static Analysis of Single Cantilever with an Unsymmetrical Thin-walled Cross-section

Consider a single cantilever of length l made of an unsymmetrical thin-walled open cross-section shown in Fig. 11.7, where $x = 0$ is fully clamped while an end force $F_z = 3EI_y/l^3$ (wall thickness t) is applied onto a rigid load sharing plate at $x = l$ (vanishing distortions and warping) such that no torsion occurs. There, $I_y = 1.1332 \cdot 10^{-2} \text{ m}^4$ refers to the stiff principal second moment of area, and the end

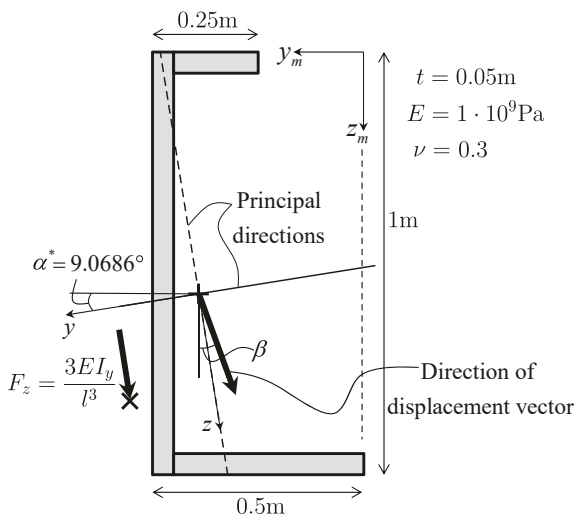


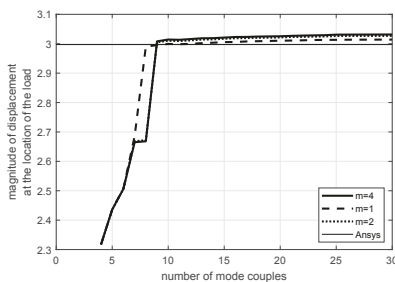
Fig. 11.7 Unsymmetrical C-profile

force is selected such that transverse tip displacement into z -direction equals one if l is large (Euler-Bernoulli solution). Due to transverse shear the tip displacement increases for decreasing beam lengths, and this effect is covered in CBM based on a shear correction factor which influences the transverse shear stiffness. As discussed in Sect. 11.1 plane behavior with respect to the principal axis is typically assumed, thus, CBM delivers typically no side-way deflection even in short beams ($\beta = \alpha^*$). However, Pilkey et al (1995); Schramm et al (1994) report side-way deflections ($\beta \neq \alpha^*$) in that kind of problems and Table 11.1 shows the corresponding amount based on Ansys continuum solutions. The application of the present GBT solution algorithm requires the discretization of the cross-section using a regular mesh of m elements in wall-thickness direction. The cross-sectional analysis (Sect. 11.3.1) is carried out with a reference beam length of $l_{RB} = 400$ m, however, it turns out that the results do not depend on l_{RB} if $l_{RB} \geq 40$ m. The member analysis (Sect. 11.3.2) is done based on 30 cubic $k = 4$ GBT elements to discretize the cantilever. Figure 11.8 shows the corresponding outcome for $l = 1$ m with respect to the total number of contributing mode couples i_{max} . The magnitude of tip displacement converges smoothly to values slightly above the Ansys reference (see Fig. 11.8 (a)), while the corresponding direction converges non-monotonic to the Ansys reference (see Fig.

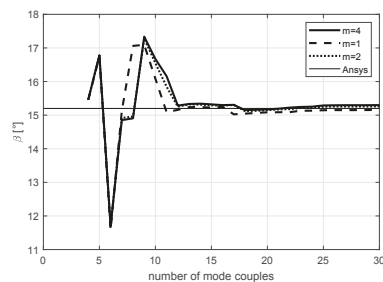
Table 11.1

Convergence study using an Ansys continuum formulation with respect to the length of the single cantilever

l [m]	u_{y_m} [m]	u_{z_m} [m]	magnitude [m]	$\beta = \arctan \frac{ u_{y_m} }{u_{z_m}}$ [°]
1	-0.78672	2.8921	2.9972	15.2
1.5	-0.45337	1.8381	1.8932	13.9
2	-0.32714	1.4656	1.5017	12.6
3	-0.23345	1.1985	1.2210	11.0
4	-0.19997	1.1051	1.1230	10.3
5	-0.18439	1.0620	1.0779	9.8
10	-0.16372	1.0051	1.0183	9.3



(a) Magnitude of displacement



(b) Direction of displacement

Fig. 11.8. Magnitude and side-way deflection of single cantilever of length $l = 1$ with respect to the total number of active mode couples

11.8 (b)). It turns out that accurate solutions require at least $i_{\max} = 12$ contributing mode couples, while the discretization parameter m of the cross-section introduces only a minor dependency of the results (virtually no difference between $m = 2$ and $m = 4$). Figure 11.9 illustrates the magnitude and side-way deflection of a single cantilever with respect to l , where the lines refer to the GBT solution while the circles denote the Ansys reference solution. Accurate values of the magnitude require $i_{\max} \geq 9$ (Fig. 11.9 (a)), while the corresponding direction calls for $i_{\max} \geq 12$ to be accurate (Fig. 11.9 (b)). After all it turns out that the proposed GBT formulation behaves well and converges to accurate solutions.

11.4.2 Homogeneous Rectangular Hollow Cross-section

In this example - used as a motivation in Sect. 11.1 (Fig. 11.1) - we analyze the dynamic behavior of a prismatic shaft of length $l = 1$ m made of a homogeneous thin-walled closed cross-section (wall-thickness t) shown in Fig. 11.10. The left hand side of the shaft $x = 0$ is fully clamped while a harmonic torsional moment (excitation frequency ν , amplitude $M_0 = 1000$ Nm) is applied onto a rigid massless load sharing plate, i.e. any warping deformations or any distortions are prohibited $x = l$. We evaluate resonance curves (amplitude of steady state vibration of torsional angle at $x = l$, modal damping $\zeta = 0.01$) of this problem (see Fig. 11.1) by applying Ansys continuum or shell elements to discretize the structure and compare the results to

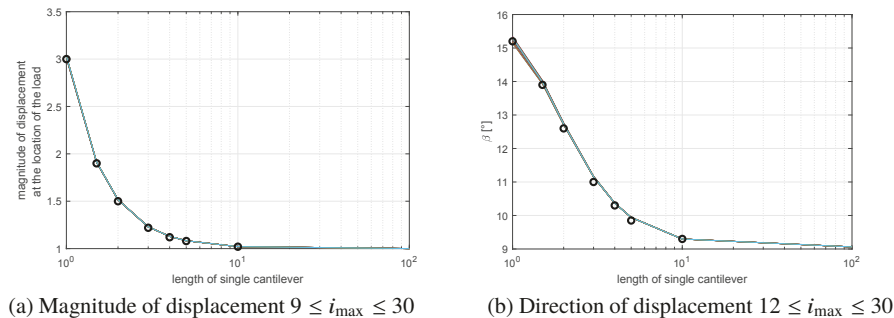


Fig. 11.9. Magnitude and side-way deflection of single cantilever with respect to l and the total number of active mode couples. The circles refer to the Ansys reference solution

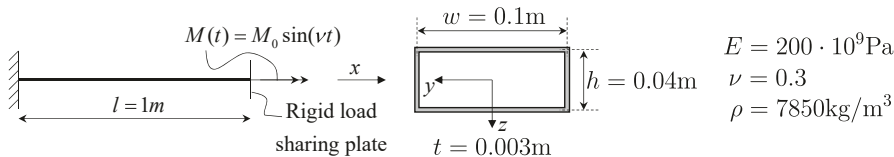


Fig. 11.10. Shaft with box type cross-section under harmonic load

CBM solutions (Vlasov’s non-uniform warping torsion or a Bescotter related theory, Kugler et al, 2018b, 2019). Now, we add the results of the present procedure to the problem. There, we regularly discretize the cross-section with either two elements in wall-thickness direction (coarse mesh) or with five elements (fine mesh), respectively. The analysis of the reference beam problem is performed by assigning a reference beam length of $l_{RB} = 50$ m. Figure 11.11 depicts the superior over all performance of the proposed method, where 30 cubic beam elements ($k = 4$) in connection with the first 30 mode couples ($i = 1, 2, 3, \dots, 30$) are applied. The model $\nu^* = \nu$ fits very well at higher frequencies (observe sixth and seventh spike in 11.11 (a)), while some deviations are observed at the second and third spike (relative error of plus three percent in location of the spike for the coarse mesh). In contrast, the model $\nu^* = 0.01\nu$ tends to weaker responses which according to the coarse mesh fits nicely at second and third spike, however, at higher frequencies (seventh spike) a relative error of minus 1.5 percent occurs. Overall, the fine mesh with $\nu^* = \nu$ performs nearly perfectly compared to 3D continuum elements and discretization stiffening (some locking phenomenon of coarse meshes) could be reduced by applying $\nu^* < \nu$. The convergence characteristic for different numbers of mode couples in use is shown in Fig. 11.12, where the fine cross-section discretization mesh is applied ($\nu^* = \nu$) with thirty cubic ($k = 4$) beam elements. The application of only the third mode

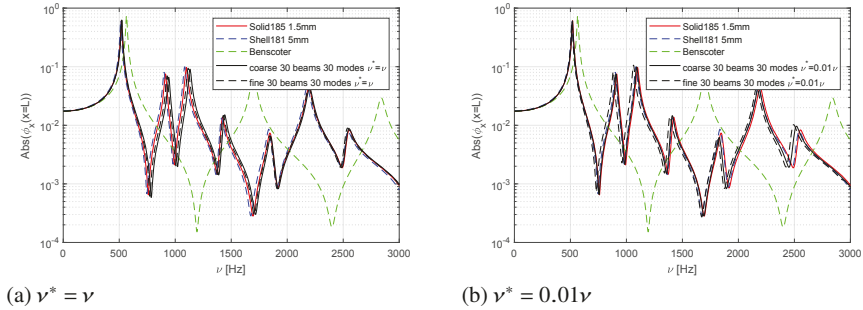


Fig. 11.11. 30 cubic beam elements ($k = 4$), first 30 mode couples

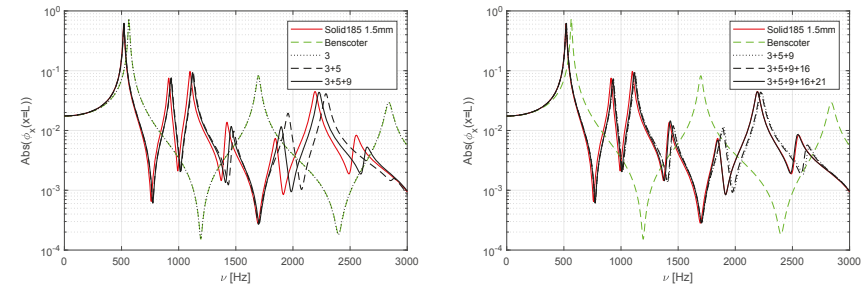


Fig. 11.12. Variable number of mode couples

couple leads to results identical to Bescoter's theory of torsion. The addition of the fifth mode couple enhances the performance significantly and the accuracy of the first four spikes is nice both in amplitude and location. More accuracy in higher frequency bands requires the addition of the ninth, 16th and 21st mode couple. All other mode couples are not excited by the applied torsion moment and, thus, do not contribute. Those higher order mode couples are depicted graphically in Fig. 11.13, where we used to coarse mesh for clarity in the plot. The convergence characteristic with respect to the polynomial order of the beam element's shape function is shown in Fig. 11.14 where the fine cross-section discretization mesh in connection with $\nu^* = \nu$ and mode couples 3,5,9,16,21 are used. There, we observe severe locking for $k = 2$ (linear shape functions), where the results depend significantly on the number of beam elements (Fig. 11.14(a)). Locking is much more moderate for quadratic shape functions ($k = 3$) (see Fig. 11.14(b)), while nearly perfect results are obtained using cubic shape functions ($k = 4$) since locking within the beam element is nearly overcome (see Fig. 11.14(c)).

11.4.3 Homogeneous Unsymmetrical Thin-walled Multi-cell Cross-section

In this example we use a homogeneous unsymmetrical thin-walled multi-cell cross-section (see Fig. 11.15) with wall-thickness t where the profile center-lines are dimensioned. We apply two different discretizations of the cross-section (free coarse (Fig. 11.15) and fine mesh with two and five elements in wall-thickness direction, respectively). The amplitude of the harmonic excitation is $M_0 = 1000 \text{ Nm}$ and the length of the considered shaft is again $l = 1 \text{ m}$. The cross-section analysis (Sect. 11.3.1) is carried out using a length of the RBP $l_{\text{RB}} = 50 \text{ m}$. Some of the cross-section mode shapes are depicted in Figs. 11.5 and 11.6 and we analyze the dynamic behavior using 30 cubic beam elements ($k = 4$) in connection with the first 30 mode couples ($i_{\text{max}} = 30$). The harmonic answer of the system is found based on the eigenvalues and -vectors in an interval of $0 < f < 4000 \text{ Hz}$ in connection with modal damping $\zeta = 0.01$. The parameters of classic torsion theories are $C_\omega = 1.762 \cdot 10^{-10} \text{ m}^6$, $I_T = 1.083 \cdot 10^{-6} \text{ m}^4$, $K_1 = -K_2 = 1.1525 \cdot 10^5 \text{ Nm}^2$ and $K_3 = 1.971 \cdot 10^5 \text{ Nm}^2$, which are extracted using the procedures discussed in Kugler et al (2018a). The corresponding resonance curves are shown in Fig. 11.16, where the exact solution is evaluated using Shell181 elements, indicating a very complex behavior due to geometrical unsymmetry of the cross-section. Vlasov's and Bescoter's theory of torsion (no coupling between bending and torsion is considered) leads to significantly erroneous results, while the present approach is more predictive. There, the application of $\nu^* = \nu$ leads to some stiffening and the peaks slightly shift to the right. This shift is more severe for the coarse mesh compared to finer one. Using a weaker coupling within the cross-section analysis ($\nu^* = 0.01 \nu$) cures that phenomenon and the fine mesh delivers very accurate response curves. In contrast to double symmetric cross-sections, where only some cross-sectional modes contribute to the load case of torsion (and others

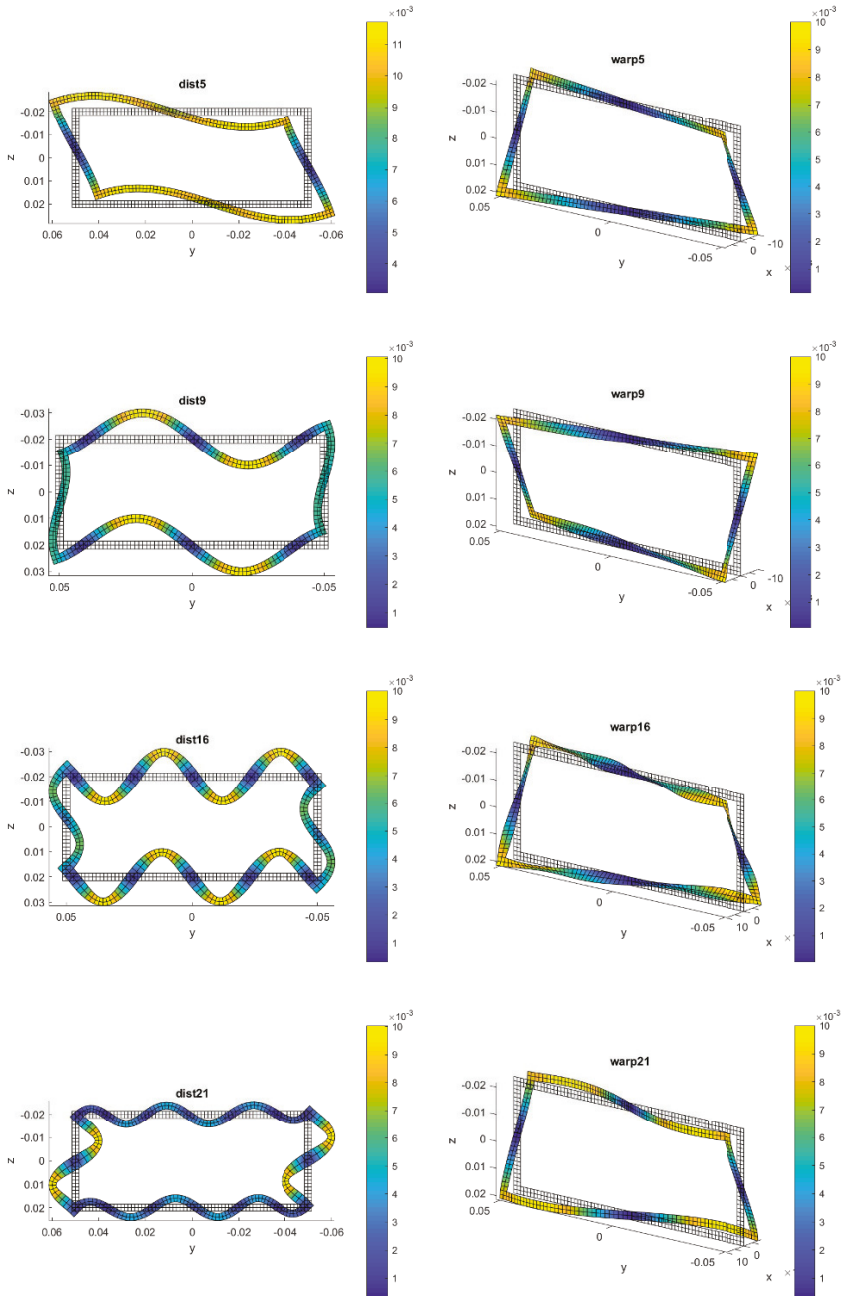


Fig. 11.13. Higher order mode shapes $l_{RB} = 50$ m, $\nu^* = \nu$

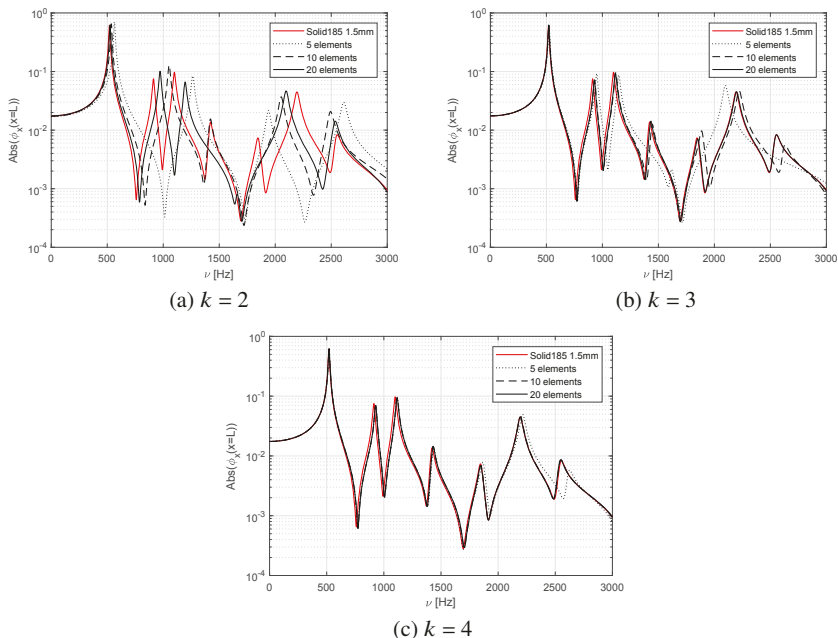


Fig. 11.14. Convergence characteristic with respect to k

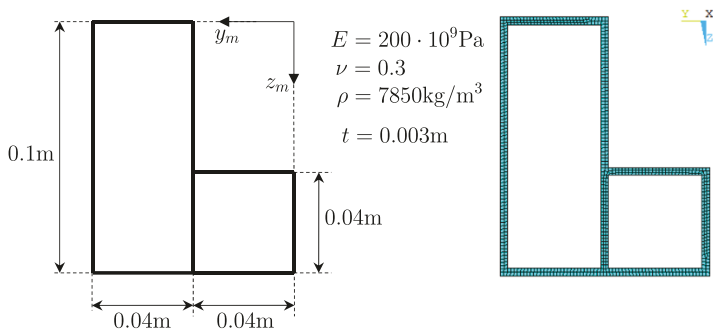
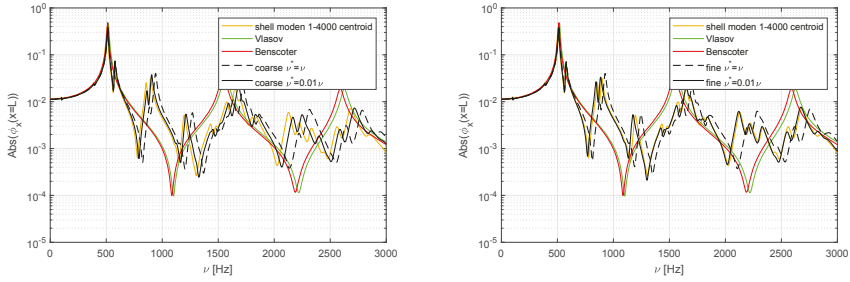


Fig. 11.15. Homogeneous unsymmetrical thin-walled multi-cell cross-section

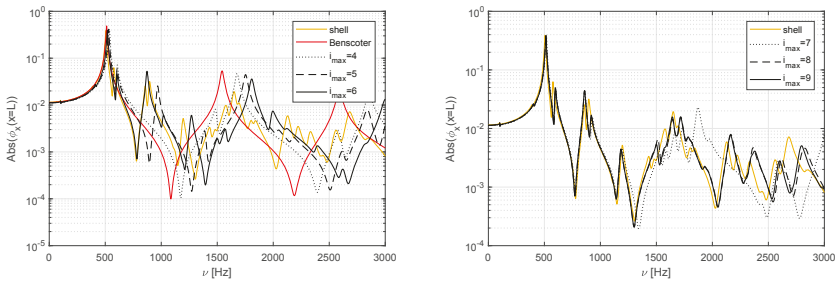
can be skipped), here, all mode shapes couple and contribute altogether (we have to apply $i = 1, 2, 3, 4, \dots i_{\max}$). This is shown in Fig. 11.17 where smooth convergence with respect to increasing i_{\max} is observed.



(a) Coarse mesh

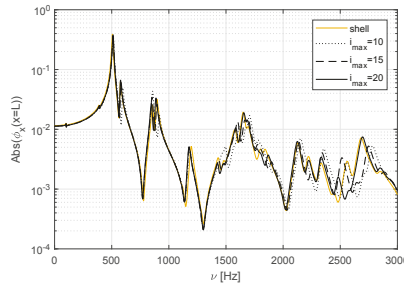
(b) Fine mesh

Fig. 11.16. 30 cubic beam elements ($k = 4$), first 30 mode couples



(a) Low number of modes

(b) Medium number of modes



(c) High number of modes

Fig. 11.17. 30 cubic beam elements ($k = 4$) with variable i_{max} ($\nu^* = 0.01\nu$, fine mesh)

11.4.4 Hollow Thin-walled Box Cross-section made of Functionally Graded Material

In the third example we check the performance of the proposed procedure regarding inhomogeneous cross-sections. We consider a double symmetric hollow box cross-section depicted in Fig. 11.18, where the outer surface consists of pure TiC ($E_{TiC} = 480$ GPa, $\nu_{TiC} = 0.2$, $\rho_{TiC} = 4920$ kg/m³) while the inner surface consists of pure Aluminum ($E_{Al} = 69$ GPa, $\nu_{Al} = 0.33$, $\rho_{Al} = 2700$ kg/m³).

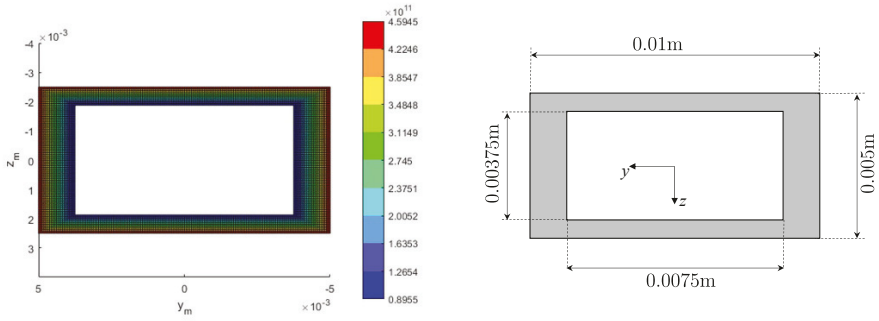


Fig. 11.18. Hollow thin-walled box cross-section made of functionally graded material

The spatial variations of the material properties is assumed to be linear in wall-thickness direction as shown for $E(y,z)$ in Fig. 11.18, where we use a regular mesh with ten layers each with constant constitutive properties. The length of the considered shaft (30 cubic beam elements) is $l = 0.1$ m and the amplitude of the harmonic end-moment is $M_0 = 1$ Nm. The results regarding classical theories of torsion require torsion properties, which are again found with the strategies discussed in Kugler et al (2018a) and a reference beam length of $l_{RB} = 5$ m ($E_T C_\omega = 9.011 \cdot 10^{-5}$ Nm⁴, $G_T I_T = 22.15$ Nm², $K_1 = -K_2 = 21.32$ Nm², $K_3 = 43.47$ Nm², $m_\omega = 1.4115 \cdot 10^{-6}$ kgm³, $m_\varphi = 1.17 \cdot 10^{-12}$ kgm). The cross-section analysis for extracting the mode couples for present approach (Sect. 11.3.1) is done using $l_{RB} = 2$ m. The harmonic answer is found based on a modal decomposition of the considered shaft in an interval $0 < f < 80000$ Hz, and a constant modal damping $\zeta = 0.01$ is applied. The resulting resonance curves are depicted in Fig. 11.19, for $v^*(y,z) = v(y,z)$, where the “exact” solution is found with linear enhanced strain Solid185 elements and quadratic reduced integrated Solid186 elements in ANSYS (2019), indicating no difference. The application of the third mode couple only leads to Bencsoter’s classical theory which is way off the exact solution. Introducing additionally the fifth mode couple delivers considerably more predictive quality and

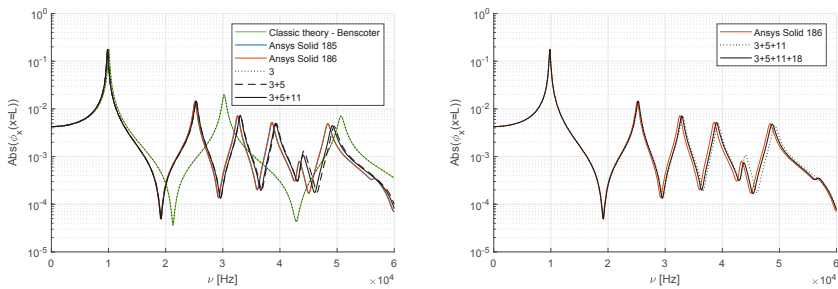


Fig. 11.19. Variable number of mode couples ($v^*(y,z) = v(y,z)$)

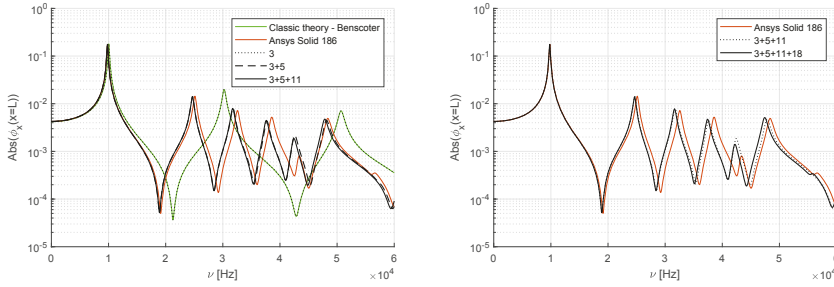


Fig. 11.20. Variable number of mode couples ($v^*(y, z) = 0.01v(y, z)$)

only slight deviation occur in higher frequency bands (two percent error in location of the sixth peak). There, the eleventh and 18th mode enhances the performance and the results converge to the exact solution, however, being slightly stiffer. In contrast, if we apply $v^*(y, z) = 0.01v(y, z)$ in the cross-section analysis leads to weaker responses, i.e. the spikes are slightly shifted to left (see Fig. 11.20) with minus two percent error in location of the sixth spike. Note that our cross-sectional analysis is carried out using 18.000 degrees of freedom (see Fig. 11.19), and the member analysis with 30 cubic elements and four relevant mode couples has 728 degrees of freedom. The gain in efficiency of our theory becomes obvious since the Ansys continuum results require at least more than one million degrees of freedom.

11.5 Conclusion

This contribution introduces a generalized beam theory (GBT) to cover effects due to higher order beam mechanics, where cross-sectional warping and distortions influence the results considerably. While most literature regarding GBT state that warping and distortions influence buckling loads, we show that these effects also contribute to beam dynamics especially regarding torsion of thin-walled box type cross-sections. There, the resonance curves due to harmonic loading indicate significant qualitative and quantitative discrepancies compared to “exact” solutions evaluated using 3D continuum elements or shell elements. In order to overcome these issues a new procedure is proposed where distortion and warping modes of the cross-section are evaluated with the aid of a reference beam problem RBP. These mode couples are introduced in a herein proposed generalized beam theory, where their axial distribution is weighted by generalized degrees of freedom. Then, the resulting mechanical properties of beam structures converge due to mesh refinement of the cross-section discretization, due to the number of mode couples, due to the polynomial order of the beam element’s shape functions and due to the number of beam elements discretizing the entire prismatic structure. The predictive quality of the outcome is

significantly better compared to classical beam mechanics CBM, and homogeneous and inhomogeneous cross-sections can be analyzed.

Acknowledgements The authors gratefully acknowledge financial support by the Slovak Grant Agency of the project VEGA No. 1/0102/18 and VEGA No. 1/0081/18.

References

- Ádány S, Schafer B (2006a) Buckling mode decomposition of single-branched open cross-section members via finite strip method: Application and examples. *Thin-Walled Structures* 44(5):585 – 600
- Ádány S, Schafer BW (2006b) Buckling mode decomposition of single-branched open cross-section members via finite strip method: Derivation. *Thin-Walled Structures* 44(5):563 – 584
- ANSYS (2019) Ansys v16 documentation
- Argyridi AK, Sapountzakis EJ (2018) Higher order beam theory for linear local buckling analysis. *Engineering Structures* 177:770 – 784
- Argyridi AK, Sapountzakis EJ (2019) Advanced analysis of arbitrarily shaped axially loaded beams including axial warping and distortion. *Thin-Walled Structures* 134:127 – 147
- Barretta R (2012) On the relative position of twist and shear centres in the orthotropic and fiberwise homogeneous Saint–Venant beam theory. *International Journal of Solids and Structures* 49(21):3038 – 3046
- Benscoter S (1954) A theory of torsion bending for multicell beams. *Trans ASME Journal of Applied Mechanics* 21:25 – 34
- Blevins R (1979) *Formulas for Natural Frequency and Mode Shape*. Krieger Publishing Company
- Dikaros IC, Sapountzakis EJ (2017) Distortional analysis of beams of arbitrary cross section using BEM. *Trans ASCE Journal of Engineering Mechanics* 143(10):04017,118
- Dinis PB, Camotim D, Silvestre N (2006) Gbt formulation to analyse the buckling behaviour of thin-walled members with arbitrarily ‘branched’ open cross-sections. *Thin-Walled Structures* 44(1):20 – 38
- Dong SB, Carbas S, Taciroglu E (2013) On principal shear axes for correction factors in Timoshenko beam theory. *International Journal of Solids and Structures* 50(10):1681 – 1688
- Dong SB, Carbas S, Taciroglu E (2015) Corrigendum to “On principal shear axes for correction factors in Timoshenko beam theory” [*Int. J. Solids Struct.* 50 (2013) 1681–1688]. *International Journal of Solids and Structures* 62:274
- Genoese A, Genoese A, Bilotta A, Garcea G (2014) A generalized model for heterogeneous and anisotropic beams including section distortions. *Thin-Walled Structures* 74:85 – 103

- Gere J (1954) Torsional vibration of beams of thin-walled open section. *Trans ASCE J Appl Mech Div* 21:381 – 387
- Goncalves R, Dinis PB, Camotim D (2009) Gbt formulation to analyse the first-order and buckling behaviour of thin-walled members with arbitrary cross-sections. *Thin-Walled Structures* 47(5):583 – 600
- Gruttmann F, Wagner W (2001) Shear correction factors in Timoshenko's beam theory for arbitrary shaped cross-sections. *Computational Mechanics* 27(3):199–207
- Kugler S, Fotiu P, Murin J (2018a) The application of safe to extract relevant stiffness quantities for efficient modelling of FGM beam structures - axial deformations and shear force bending. In: 13th World Congress on Computational Mechanics (WCCM XIII) and 2nd Pan American Congress on Computational Mechanics (PANACM II), New York
- Kugler S, Fotiu P, Murin J (2018b) On non-uniform torsion in fgm beam structures and the extraction of relevant stiffness quantities based on safe. In: 13th World Congress on Computational Mechanics (WCCM XIII) and 2nd Pan American Congress on Computational Mechanics (PANACM II), New York
- Kugler S, Fotiu P, Murin J (2019) On the deficiencies of classical theories in predicting torsional frequencies of prismatic shafts. In: 14th International Conference on Vibration Problems
- Murin J, Aminbaghai M, Hrabovsky J, Gogola R, Kugler S (2016) Beam finite element for modal analysis of fgm structures. *Engineering Structures* 121:1 – 18
- Pilkey WD, Kang W, Schramm U (1995) New structural matrices for a beam element with shear deformation. *Finite Elements in Analysis and Design* 19(1):25 – 44
- Ranzi G, Luongo A (2011) A new approach for thin-walled member analysis in the framework of gbt. *Thin-Walled Structures* 49(11):1404 – 1414
- Sapountzakis E, Argyridi A (2018) Influence of in-plane deformation in higher order beam theories. *Strojnícky casopis – Journal of Mechanical Engineering* 68(3):77 – 94
- Schardt R (1989) *Verallgemeinerte Technische Bigetheorie*. Springer, Berlin, Heidelberg
- Schmidrathner C (2019) Validation of Bredt's formulas for beams with hollow cross sections by the method of asymptotic splitting for pure torsion and their extension to shear force bending. *Acta Mechanica* 230:4035–4047
- Schramm U, Kitis L, Kang W, Pilkey WD (1994) On the shear deformation coefficient in beam theory. *Finite Elements in Analysis and Design* 16(2):141 – 162
- Vlasov V (1961) *Thin Walled Elastic Beams*. Israel Program for Scientific Translations, Jerusalem
- Weaver W, Timoshenko S, Young D (1990) *Vibration Problems in Engineering*, 5th edn. John Wiley & Sons
- Zienkiewicz OC, Taylor RL (2000) *Finite Element Method, vol 2: Solid Mechanics*, 5th edn. Butterworth-Heinemann, Oxford et al.



Chapter 12

Free Vibration of Flexomagnetic Nanostructured Tubes Based on Stress-driven Nonlocal Elasticity

Mohammad Malikan and Victor A. Eremeyev

Abstract A framework for the flexomagneticity influence is here considered extending the studies about this aspect on the small scale actuators. The developed model accommodates and composes linear Lagrangian strains, Euler-Bernoulli beam approach as well as an extended case of Hamilton's principle. The nanostructured tube should subsume and incorporate size effect; however, for the sake of avoiding the staggering costs of experiments, here, via stress-driven nonlocal elasticity theory, the desired influence is captured. A given section is dedicated to reveal the accuracy of the achieved model. In view of solution, the numerical results are generated analytically. We receive the conclusion that in nanoscale tubes the diameter can affect fundamentally the performance of the flexomagnetic effect.

Key words: Flexomagneticity · Nanotube · Magnetoelasticity · Hamilton's principle

12.1 Introduction

As a new-discovered material's phenomenon, flexomagneticity absorbs the engineering researchers to study this physical occurrence when materials subject to static and dynamics states. Indeed, flexomagneticity results from strain gradients. This manner

Mohammad Malikan

Department of Mechanics of Materials and Structures, Faculty of Civil and Environmental Engineering, Gdansk University of Technology, 80-233, Gdansk, Poland
e-mail: mohammad.malikan@pg.edu.pl

Victor A. Eremeyev

Department of Mechanics of Materials and Structures, Faculty of Civil and Environmental Engineering, Gdansk University of Technology, 80-233, Gdansk, Poland & Don State Technical University, Gagarina sq., 1, Rostov on Don 344000, Russia
e-mail: victor.eremeev@pg.edu.pl, eremeyev.victor@gmail.com

can be named as the direct impact of flexomagnetivity. In a reverse impact, one can observe the flexo-effect during existence of an outer magnetic field gradient. This effect would not be absolutely and solely in actuators and smart materials, but even can occur in all materials and crystalline structures, see Eliseev et al (2009); Lukashhev and Sabirianov (2010); Zhang et al (2012); Zhou et al (2014); Kabychenkov and Lisovskii (2019); Eliseev et al (2019).

Since discovering of flexomagnetivity effect, a very few publications have been observed on the statics and dynamics responses of small scale actuators and sensors which incorporate the effect, see Sidhardh and Ray (2018); Zhang et al (2019). Within these articles, Zhang et al (2019) entirely focused on the effect of flexomagnetic during bending of a nano actuator beam. By means of Euler-Bernoulli beam theory, the static bending equation was formulated. Moreover, the consideration has been carried out by use of surface elasticity. A variety boundary conditions were investigated on the basis of both converse and direct magnetizations. From their result, one can find that the flexomagnetic is a size-dependent material property. On the other hand, Sidhardh and Ray (2018) studied the static bending of a piezomagnetic-flexomagnetic Euler-Bernoulli nanosize beam based on the clamped-free ends conditions. Both inverse and direct effects of magnetization were discussed. The surface elasticity aided to examine the size-dependency into the small beam. With a quantitative evaluation, they showed the scale-dependent behavior of flexomagnetivity and identified the significance of such the effect into nanostructures even with disregarding the piezomagnetivity.

As far as we are aware, no research work is found yet in terms of investigating of natural frequencies of a nano-actuator tube composing the flexomagnetic. We aim to study the flexomagnetivity effect on the natural frequencies of a nanostructured tube and intend to evaluate the small scale behavior on the basis of the stress-driven nonlocal model of elasticity. The numerical outcomes pertain to an analytical solution. The magneto-mechanical model is extended by illustrating some drawn graphs during variations in significant and particular criterions.

12.2 Applied Mathematical Model

Here a right-handed Cartesian coordinate system is attached to the schematic domain of the flexomagnetic nanotube as presented by Fig. 12.1. To this, we define L and r , for length and radius of the specimen, respectively.

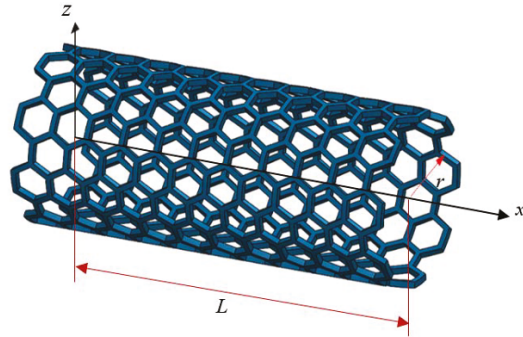
Assuming that the nanostructured tube contains flexomagnetivity influence give the constitutive equations as in Sidhardh and Ray (2018); Zhang et al (2019)

$$\sigma_{xx} = C_{11}\varepsilon_{xx} - q_{31}H_z, \quad (12.1)$$

$$\xi_{xxz} = g_{31}\eta_{xxz} - f_{31}H_z, \quad (12.2)$$

$$B_z = a_{33}H_z + q_{31}\varepsilon_{xx} + f_{31}\eta_{xxz}, \quad (12.3)$$

Fig. 12.1 Pictured geometry of a nanostructured tube presented schematically in the Cartesian coordinates



in which g_{31} illustrates the influence of the sixth-order gradient elasticity tensor, H_z and B_z exhibit the component of magnetic field and the magnetic flux, respectively, ξ_{xxz} is the component of the higher-order hyper stress tensor and is an induction of coverse flexomagnetic effect, q_{31} depicts the component of the third-order piezomagnetic tensor, a_{33} represents the component of the second-order magnetic permeability tensor, f_{31} denotes the component of the fourth-order flexomagnetic coefficients tensor, σ_{xx} is the axial stress, C_{11} is the elastic modulus, ε_{xx} and η_{xxz} are the axial elastic strain and its gradient.

To have a movement for each node of body of the applied model after deformation, the Euler-Bernoulli hypothesis is used as in Song and Li (2007); Reddy (2010); Malikan and Eremeyev (2020)

$$u_1(x, z, t) = u(x, t) - z \frac{\partial w(x, t)}{\partial x}, \quad u_3(x, z, t) = w(x, t), \quad (12.4)$$

in which the general movements along x and z directions are shown by u_i ($i = 1, 3$) and the movements of the middle plane of the thickness along the aforementioned directions there have been used as u and w , respectively. More importantly, we employ z to dedicate the thickness coordinate. Axial strain and the related gradient by means of linear Lagrangian strains as well as Eqs. (12.4), are attained as

$$\varepsilon_{xx} = \frac{\partial u}{\partial x} - z \frac{\partial^2 w}{\partial x^2}, \quad \eta_{xxz} = \frac{\partial \varepsilon_{xx}}{\partial z} = -\frac{\partial^2 w}{\partial x^2}. \quad (12.5)$$

To yield the equation which governs the domain subjected to vibrational state, the Hamiltonian can be extended and nominated as

$$\delta \int_{t_1}^{t_2} (\Pi_K - \Pi_U + \Pi_W) dt = 0 \quad (12.6)$$

for which the total internal strain energy, work of external forces and the kinetic energy are introduced by Π_U , Π_W and Π_K . To determine the total strain energy, one

should collect the strain energy by mechanics and the magnetic strain energy which lead to

$$\delta\Pi_U = \int_V (\sigma_{xx}\delta\varepsilon_{xx} + \xi_{xxz}\delta\eta_{xxz} - B_z\delta H_z) dV. \quad (12.7)$$

In a magnetic-mechanical coupling problem for a beam, the resultants of stress can be defined as

$$N_x = \int_{-h/2}^{h/2} \sigma_{xx} dz, \quad (12.8)$$

$$M_x = \int_{-h/2}^{h/2} \sigma_{xx} z dz, \quad (12.9)$$

$$T_{xxz} = \int_{-h/2}^{h/2} \xi_{xxz} dz. \quad (12.10)$$

To write a relation between the transverse component of the magnetic field and magnetic potential Ψ , one can show that

$$H_z + \frac{\partial\Psi}{\partial z} = 0. \quad (12.11)$$

Here we assume a closed circuit state for the modeled system giving the boundary conditions for the magnetic potential as

$$\Psi\left(+\frac{h}{2}\right) = \psi, \quad \Psi\left(-\frac{h}{2}\right) = 0. \quad (12.12)$$

To determine the magnetic potential which is externally applied on the model as a result of the existence magnetic field, we symbolize ψ .

A mathematical combination of Eqs. (12.3), (12.7), (12.11) and (12.12), we can obtain the magnetic potential along the thickness and the magnetic field as below, see Sidhardh and Ray (2018); Zhang et al (2019) for details,

$$\Psi = -\frac{q_{31}}{2a_{33}} \left(z^2 - \frac{h^2}{4} \right) \frac{\partial^2 w}{\partial x^2} + \frac{\psi}{h} \left(z + \frac{h}{2} \right), \quad (12.13)$$

$$H_z = z \frac{q_{31}}{a_{33}} \frac{\partial^2 w}{\partial x^2} - \frac{\psi}{h}. \quad (12.14)$$

Therefore, one can insert Eqs. (12.13) and (12.14) into Eqs. (12.1)-(12.3) to harvest the magnetic induction and stress also higher-order moment stress component as follows

$$\sigma_{xx} = C_{11} \frac{\partial u}{\partial x} - z \left(C_{11} + \frac{q_{31}^2}{a_{33}} \right) + \frac{q_{31}\psi}{h}, \quad (12.15)$$

$$\xi_{xxz} = - \left(g_{31} + \frac{q_{31}f_{31}z}{a_{33}} \right) \frac{\partial^2 w}{\partial x^2} + \frac{f_{31}\psi}{h}, \quad (12.16)$$

$$B_z = -f_{31} \frac{\partial^2 w}{\partial x^2} - \frac{a_{33}\psi}{h}. \quad (12.17)$$

Thus, the magnetic-mechanical stress resultants can be developed as

$$M_x = -I_z \left(C_{11} + \frac{q_{31}^2}{a_{33}} \right) \frac{\partial^2 w}{\partial x^2}, \quad (12.18)$$

$$T_{xz} = -g_{31}h \frac{\partial^2 w}{\partial x^2} + f_{31}\psi, \quad (12.19)$$

where the general form of the area moment of inertia is as

$$I_z = \int_A z^2 dA.$$

The general form of kinetic energy is displayed below

$$\Pi_K = \frac{1}{2} \int_{-h/2}^{h/2} \int_A \rho(z) \left[\left(\frac{\partial u_1}{\partial t} \right)^2 + \left(\frac{\partial u_3}{\partial t} \right)^2 \right] dA dx. \quad (12.20)$$

The first variation of kinetic energy leads to

$$\delta \Pi_K = \int_0^L \left(I_2 \frac{\partial^4 w}{\partial t^2 \partial x^2} - I_0 \frac{\partial^2 w}{\partial t^2} \right) \delta w dx, \quad (12.21)$$

where the mass moment of inertias are given by

$$I_0, I_2 = \int_{-h/2}^{h/2} \rho(z)(1, z^2) dz.$$

We consider the general case of established work by external forces as

$$\Pi_W = \frac{1}{2} \int_0^L N_x^0 \left(\frac{\partial w}{\partial x} \right)^2 dx, \quad (12.22)$$

which its first variational case will be

$$\delta\Pi_W = \int_0^L N_x^0 \frac{\partial \delta w}{\partial x} \frac{\partial w}{\partial x} dx, \quad (12.23)$$

in which N_x^0 depicts the axial load. In this paper, we investigate the axial magnetic force as the in-plane axial resultant. To this,

$$N_x^0 = \psi q_{31}. \quad (12.24)$$

Eventually, based on the above formulation the local governing equation which gives the natural frequencies of the flexomagnetic nanotube can be taken as

$$\frac{\partial^2 M_x}{\partial x^2} + \frac{\partial^2 T_{xxz}}{\partial x^2} + N_x^0 \frac{\partial^2 w}{\partial x^2} = I_0 \frac{\partial^2 w}{\partial t^2} - I_2 \frac{\partial^4 w}{\partial x^2 \partial t^2}. \quad (12.25)$$

Here, we employ the stress-driven nonlocal elasticity model (NDM). It stands here differentially as below in Apuzzo et al (2017); Sedighi and Malikan (2020)

$$\frac{\partial^2 \chi(x)}{\partial x^2} - \frac{1}{L_c^2} \chi(x) = -\frac{1}{DL_c^2} M_x(x), \quad (12.26)$$

in which L_c shows a nonlocal characteristic length. And for $\chi(x)$ we have

$$\chi(x) = \frac{\partial^2 w}{\partial x^2}. \quad (12.27)$$

Consequently,

$$D \left(L_c^2 \frac{\partial^6 w}{\partial x^6} - \frac{\partial^4 w}{\partial x^4} \right) = B \frac{\partial^4 w}{\partial x^4} + N_x^0 \frac{\partial^2 w}{\partial x^2} - I_0 \frac{\partial^2 w}{\partial t^2} + I_2 \frac{\partial^4 w}{\partial x^2 \partial t^2}, \quad (12.28)$$

where $B = -g_{31}h$ and

$$D = I_z \left(C_{11} + \frac{q_{31}^2}{a_{33}} \right).$$

It is required to solve the above characteristic equation to obtain the natural frequencies of the flexomagnetic nanotube.

12.3 Solution of the Equation

The methodology here comprises the analytical solution as in Malikan et al (2020)

$$w(x,t) = \sum_{m=1}^{\infty} \sin\left(\frac{m\pi}{L}x\right) \exp\{i\omega_n t\}. \quad (12.29)$$

The above-mentioned series can satisfy the conditions for pinned-pinned beams.

To compute and present the numerical values of the natural frequencies of the flexomagnetic nanostructured tube, we apply Eq. (12.28) on Eq. (12.29). Finally, the characteristic equation of frequency would be

$$\omega_n = \sqrt{\frac{-DL_c^2\alpha_m^6 - (D+B)\alpha_m^4 - \Psi q_{31}}{I_0 + I_2\alpha_m^2}}, \quad (12.30)$$

where $\alpha_m = m\pi/L$.

12.4 Results and Discussions

12.4.1 Results' Validation

This section associates a comparison for the present formulation. The examination of formulation is based on the ignoring piezo-flexomagnetic features. Table 12.1 is prepared to estimate natural frequencies in dimensionless quantities with respect to Barretta et al (2018) in which one can observe the evaluations for stress-driven nonlocal integral model (SDM) and strain gradient theory (SGT). As it is clear, slight differences are seen between NDM and SDM when the characteristic parameter λ is sufficiently small. However, increasing this dimensionless characteristic parameter results in further conflicts. Nevertheless, it is so far easier to use the NDM vis-à-vis the SDM and results can be acceptable. Here we assume that

$$\Omega = \omega_n L^2 \sqrt{\frac{\rho A}{C_{11} I_z}}, \quad \lambda = \frac{L_c}{L}, \quad E = 30 \times 10^6, \quad \nu = 0.3, \quad \frac{L}{h} = 10, \quad \rho = 1.$$

12.4.2 Computational Model

This section devotes some tabulated results for natural frequencies of the nanotube in the presence and absence of the flexomagneticity impact. To do this, the Table 12.2 aids us in Sidhardh and Ray (2018); Zhang et al (2019). Additionally, the results are shown for a non-dimensional manner of natural frequency as

$$\Omega = \omega_n L^2 \sqrt{\frac{\rho A}{C_{11} I_z}}.$$

We initially evaluate the effect of length scale parameter variations in accordance with the Table 12.3. The nanotube is assumed in two states. The former has been

Table 12.1

Evaluation of natural frequencies of a nanobeam. SDM and SGT relate to Barretta et al (2018), whereas column NDM present current research

λ	SDM	SGT	NDM
0	9.82927	9.8293	9.82927
0.01	9.83402	9.8339	9.8341
0.02	9.84787	9.8471	9.8486
0.03	9.87022	9.8676	9.8728
0.04	9.90042	9.8943	9.9066
0.05	9.93783	9.9259	9.9498
0.06	9.98183	9.9614	10.0024
0.07	10.0318	9.9997	10.0641
0.08	10.0871	10.0398	10.1349
0.09	10.1472	10.0810	10.2146
0.1	10.2115	10.1223	10.3029

investigated with regard to the effects of flexomagnetic and the latter without considering the effect and merely under piezomagnetic conditions. It is important to note

Table 12.2

Material specifications of an assumed piezo-actuator nanotube

C_{11}	286×10^9	N/m ²
f_{31}	10^{-10}	N/A
q_{31}	580.3	N/A·m
a_{33}	1.57×10^{-4}	N/A ²
L	$15d$	
d	1	nm
h	0.34	nm

Table 12.3

Dimensionless natural frequencies in variations of the length scale parameter ($\Psi = 1\mu A$)

L_c nm	Piezomagnetic nanotube with considering flexomagneticity	Piezomagnetic nanotube
0	14.4114	14.4303
0.25	14.4307	14.4496
0.5	14.4886	14.5074
0.75	14.5845	14.6032
1	14.7177	14.7362
1.25	14.8872	14.9055
1.5	15.0918	15.1099
1.75	15.3301	15.3479
2	15.6006	15.6180
2.5	16.2312	16.2480
3	16.9702	16.9863
3.5	17.8041	17.8194
4	18.7202	18.7347

that the flexomagnetic effect makes the natural frequencies smaller. It is also worth mentioning that the larger the values of L_c , the higher the natural frequencies. It can be observed that while the value of L_c is set to be zero in contrast to the when its value is at 4, give further difference for natural frequencies of the mentioned tubes. It can be stated that this decreasing behavior in the difference of results of both cases can be because the length scale parameter increases the strength of the tubes and as far as the flexomagnetic effect makes the material more flexible, hence, in higher values of the length scale the influence of flexomagnetism is slighter. More significantly, as the variation of the length scale parameter creates differences between results of a piezomagnetic nanotube against a flexo-piezomagnetic one, this behavior can confirm that the flexomagnetism is a size-dependent phenomenon similar to the flexoelectricity, see Yudin and Tagantsev (2013); Wang et al (2019); Nguyen et al (2013); Eremeyev et al (2020) and the reference therein.

Tables 12.4 and 12.5 give the numerical values of natural frequencies for the both aforementioned cases of nanotubes in variations of diameter and length of the tubes. Again here the size dependency behavior of flexomagnetism can be seen. The increase in the diameter leads to decrease of the discrepancy between response

Table 12.4

Dimensionless natural frequencies in variations of the diameter ($L_c = 0.5 \text{ nm}, \Psi = 1\mu A$)

d nm	Piezomagnetic nanotube with considering flexomagnetism	Piezomagnetic nanotube
0.7	10.6768	10.7023
1	14.4886	14.5074
1.2	16.6303	16.6467
1.5	19.5766	19.5905
2	24.2887	24.2999
2.5	29.2463	29.2556
3	34.8146	34.8224
3.5	41.2301	41.2367
4	48.6422	48.6478

Table 12.5

Dimensionless natural frequencies in variations of the length ($L_c = 0.5 \text{ nm}, \Psi = 1\mu A$)

L/d	Piezomagnetic nanotube with considering flexomagnetism	Piezomagnetic nanotube
10	14.4471	14.4660
15	14.4886	14.5074
20	14.8129	14.8313
25	15.5244	15.5420
30	16.7575	16.7737
35	18.6175	18.6321
40	21.1582	21.1710
45	24.3866	24.3977
50	28.2822	28.2919

of the two tubes. Howbeit it is noteworthy that the reducing effect in Table 12.3 is further remarkable than the Table 12.2. In addition, it seems that the diminishing effect as a result of enlarging diameter is more noticeable than the lessening effect of the length scale parameter as the previous Table. Accordingly, it is important to say that the diameter plays as a crucial factor to study size-dependent response of nanotubes possessing flexomagnetism.

In Table 12.6 the natural frequencies of both cases of nanotubes are tabulated in order to exhibit whether the magnetic field affects a flexo-piezomagnetic nanotube more than a piezomagnetic one or not. As can be observed, there is no highlight

Table 12.6

Dimensionless natural frequencies in variations of the magnetic potential ($L_c = 0.5 \text{ nm}$)

$\Psi(\mu A)$	Piezomagnetic nanotube with considering flexomagnetism	Piezomagnetic nanotube
-2	13.9794	13.9989
-1	14.1512	14.1704
0	14.3209	14.3399
1	14.4886	14.5074
2	14.6544	14.6730
3	14.8183	14.8367
4	14.9805	14.9987
5	15.1409	15.1589
6	15.2996	15.3174
7	15.4567	15.4743
8	15.6122	15.6297
9	15.7662	15.7835
10	15.9187	15.9358

difference among the two tubes, although a very little difference can be seen. The meaning of difference is here about difference between results of two cases when the magnetic potential is chosen as minimum against when it is selected as maximum in the Table. As a matter of fact, it can be said that the magnetic field has approximately identical influence on the two tubes. Furthermore, it is substantial that the values of the external potential are insignificant, but their effect is major. In fact, it is concluded that the effect of outer magnetic potential on the natural frequencies of a nanoscale actuator tube having piezo-flexomagnetic influences is momentous.

12.5 Conclusions

In this paper, we successfully combined the flexomagnetic effect with elasticity relations to consider this impact on the natural frequencies of a nanotube. We further considered the nanosize effects based on the stress-driven nonlocal elasticity model. The extended Hamiltonian demonstrated governing equation in a magnetic-

mechanical coupling. We verified our results regarded to a nanotube and correspond well to the open literature. In an analytical framework, we established some tabulated results to show the flexomagnetic effect. Based on our numerical exercises, it was found that the variation of diameter is more notable to show the effect of flexomagnetism. And the lesser the diameter, the larger the flexomagnetic effect. Likewise, the smaller the length of the tube, the greater the flexomagnetism effect. It can confirm that the flexomagnetism is a size-dependent feature of materials, and its impact is more considerable in nanoscale.

Acknowledgements V.A. Eremeyev acknowledges the support of the Government of the Russian Federation (contract No. 14.Z50.31.0046).

References

- Apuzzo A, Barretta R, Luciano R, de Sciarra FM, Penna R (2017) Free vibrations of Bernoulli-Euler nano-beams by the stress-driven nonlocal integral model. *Composites Part B: Engineering* 123:105–111
- Barretta R, Faghidian SA, Luciano R, Medaglia CM, Penna R (2018) Free vibrations of FG elastic Timoshenko nano-beams by strain gradient and stress-driven nonlocal models. *Composites Part B: Engineering* 154:20–32
- Eliseev EA, Morozovska AN, Glinchuk MD, Blinc R (2009) Spontaneous flexoelectric/flexomagnetic effect in nanoferroics. *Physical Review B* 79(16):165,433
- Eliseev EA, Morozovska AN, Khist VV, Polinger V (2019) Chapter six – effective flexoelectric and flexomagnetic response of ferroics. In: Stamps RL, Schultheiß H (eds) *Recent Advances in Topological Ferroics and their Dynamics*, Solid State Physics, vol 70, Academic Press, pp 237–289
- Eremeyev VA, Ganghoffer JF, Konopińska-Zmysłowska V, Uglov NS (2020) Flexoelectricity and apparent piezoelectricity of a pantographic micro-bar. *International Journal of Engineering Science* 149:103,213
- Kabychenkov AF, Lisovskii FV (2019) Flexomagnetic and flexoantiferromagnetic effects in centrosymmetric antiferromagnetic materials. *Technical Physics* 64(7):980–983
- Lukashev P, Sabirianov RF (2010) Flexomagnetic effect in frustrated triangular magnetic structures. *Physical Review B* 82(9):094,417
- Malikan M, Eremeyev VA (2020) Post-critical buckling of truncated conical carbon nanotubes considering surface effects embedding in a nonlinear Winkler substrate using the Rayleigh-Ritz method. *Materials Research Express* 7:025,005
- Malikan M, Krasheninnikov M, Eremeyev VA (2020) Torsional stability capacity of a nano-composite shell based on a nonlocal strain gradient shell model under a three-dimensional magnetic field. *International Journal of Engineering Science* 148:103,210
- Nguyen TD, Mao S, Yeh YW, Purohit PK, McAlpine MC (2013) Nanoscale flexoelectricity. *Advanced Materials* 25(7):946–974

- Reddy JN (2010) Nonlocal nonlinear formulations for bending of classical and shear deformation theories of beams and plates. *International Journal of Engineering Science* 48(11):1507–1518
- Sedighi HM, Malikan M (2020) Stress-driven nonlocal elasticity for nonlinear vibration characteristics of carbon/boron-nitride hetero-nanotube subject to magneto-thermal environment. *Physica Scripta* DOI <http://iopscience.iop.org/10.1088/1402-4896/ab7a38>
- Sidhardh S, Ray MC (2018) Flexomagnetic response of nanostructures. *Journal of Applied Physics* 124(24):244,101
- Song X, Li SR (2007) Thermal buckling and post-buckling of pinned–fixed Euler–Bernoulli beams on an elastic foundation. *Mechanics Research Communications* 34(2):164–171
- Wang B, Gu Y, Zhang S, Chen LQ (2019) Flexoelectricity in solids: Progress, challenges, and perspectives. *Progress in Materials Science* 106:100,570
- Yudin PV, Tagantsev AK (2013) Fundamentals of flexoelectricity in solids. *Nanotechnology* 24(43):432,001
- Zhang JX, Zeches RJ, He Q, Chu YH, Ramesh R (2012) Nanoscale phase boundaries: a new twist to novel functionalities. *Nanoscale* 4(20):6196–6204
- Zhang N, Zheng S, Chen D (2019) Size-dependent static bending of flexomagnetic nanobeams. *Journal of Applied Physics* 126(22):223,901
- Zhou H, Pei Y, Fang D (2014) Magnetic field tunable small-scale mechanical properties of nickel single crystals measured by nanoindentation technique. *Scientific Reports* 4(4583):1–6



Chapter 13

Coupled, Thermo-elastic, Large Amplitude Vibration of Bi-material Beams

Emil Manoach, Simona Doneva, and Jerzy Warminski

Abstract The main goal of this work is to develop a theoretical and numerical approach, to study the geometrical nonlinear vibration of bi-material beams under the combined action of mechanical and thermal loads. The geometrically nonlinear version of the Timoshenko beam theory is used to describe the theoretical model of the problem. Starting from the geometrical, constitutive and equilibrium equations of each layer the governing equations of the bi-material beam are derived. The beam is subjected to heat flux and dynamic mechanical loading. The influence of the elevated temperature or the heat propagation along the beam length and thickness on the response of the beam was studied.

Key words: Bi-material · Timoshenko beam · Large amplitude vibration · Heat propagation

13.1 Introduction

The usage of composites materials in many engineering fields has grown in recent years. Among the most popular composite structures the bi-material structures and especially the bi-material beams are frequently used in different branches in industry.

Emil Manoach
Institute of Mechanics, BAS, Acad. G. Bochev Str. Bl. 4, 1113 Sofia, Bulgaria
e-mail: e.manoach@imbm.bas.bg

Simona Doneva
Institute of Mechanics, BAS, Acad. G. Bochev Str. Bl. 4, 1113 Sofia, Bulgaria & Lublin University of Technology, Nadbystrzycka 36, 20-618 Lublin, Poland
e-mail: s.doneva@imbm.bas.bg

Jerzy Warminski
Lublin University of Technology, Nadbystrzycka 36, 20-618 Lublin, Poland
e-mail: j.warminski@pollub.pl

When the bi-material beam is subjected to different fields including mechanical and thermal loading the modelling of their behavior could be very complex. Most of the studies of the thermomechanical behaviour of the beams are devoted to their static states. Some consideration of the bending of bi-material beams can be found as early as in 1960 in Boley and Weiner (1960). Later many studies appear about the deformation, stresses and temperature distribution in bi-metallic beams. A subject of interest is the thermoelastic behavior of such beams because of the different elastic and thermal properties of the layers which lead to more complex behavior of the structures. The static thermoelastic deformation of composite beams was studied, for example in Shang et al (2013); Carpinteri and Pugno (2006); Carpinteri and Paggi (2008); Srinivasan and Spearing (2008).

Generally, the most of the studies of the dynamic response of the thermally loaded beam consider that the structure gets elevated temperature instantly, and the heat propagation is not included in model. The elevated temperature can lead the structures to buckle and several authors studied the buckling and postbuckling behaviour of structures subjected to mechanical loads at elevated temperatures (Mei et al, 1999; Shi et al, 1999, etc).

Many years ago, however, it was shown, in Boley (1956) that the intensive thermal loading (thermal shocks) can result to a transient vibration in structures. For such cases the simultaneous consideration of the heat propagation and the structure vibration is important. Such studies are performed in Karagiozova and Manoach (1992); Manoach (2003); Manoach and Ribeiro (2004).

Recently, deep and complicated studies of nonlinear behaviour of structures subjected to thermal and mechanical loading have been done in the works of Saetta and Rega (2014, 2016, 2017); Settimi et al (2018). They used reduced models to study the local and global dynamics of the coupled and uncoupled thermoelastic nonlinear vibration of structures.

The dynamic instabilities and transient vibrations of a bimaterial beam with alternating magnetic fields and thermal loads are investigated in Wu (2009). The authors used the Hamilton principle to deduce the equation of the beam vibration on the base of the Euler-Bernoulli theory. The equation of motion and the solution of thermal effect are obtained by superposing certain fundamental linear elastic stress states.

The goal of the present work is to derive the equations of the geometrically nonlinear vibration of bi-material beam with non-symmetric layers according to the Timoshenko beam theory and to study the coupled nonlinear vibration of the beam. An influence of the heat propagation during the vibration will also be analysed.

13.2 Basic Equations

A beam with length l width b and thickness h is considered. The beam consists of two layers made of different materials (Material 1 and 2) with thickness h_1 and h_2 ($h = h_1 + h_2$). The geometrical scheme of the beam is shown in Fig. 13.1.

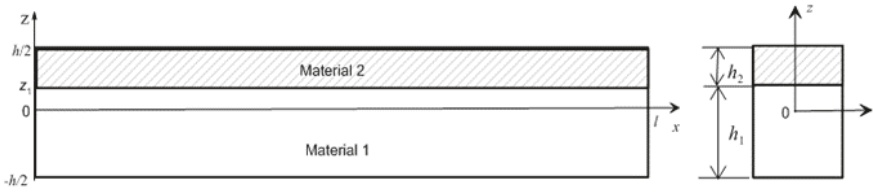


Fig. 13.1. The geometrical scheme of the beam model

13.2.1 Geometrical Relationships

The strain and curvature-displacements relationships associated with the mid-axes of the beam, which consider large displacements $u(x,t)$ and $w(x,t)$ in x and z directions, respectively, and the angle rotation $\psi(x,t)$ of the cross-section effect, take the form:

$$\varepsilon_x^0 = \frac{\partial u}{\partial x} + \frac{1}{2} \left(\frac{\partial w}{\partial x} \right)^2, \quad \varepsilon_{xy}^0 = \frac{\partial w}{\partial x} - \psi, \quad \kappa^0 = -\frac{\partial \psi}{\partial x}, \quad (13.1)$$

and the strain vector is expressed as follows:

$$\boldsymbol{\varepsilon} = \{ \varepsilon_x^0 + z\kappa^0, f(z)\varepsilon_{xy}^0 \}, \quad (13.2)$$

where $f(z)$ is a function describing the distribution of the shear strain along the beam thickness.

13.2.2 Constitutive Equations

Assuming that the beam material is linear elastic and isotropic the relations between the component of the stresses and the strains are:

$$\sigma_x^{(i)} = E^{(i)} \left[\varepsilon_x - \alpha_T^{(i)}(T - T_0) \right], \quad \sigma_{xy}^{(i)} = G^{(i)} \varepsilon_{xy}, \quad i = 1, 2, \quad (13.3)$$

where $E^{(i)}$ is the Young modulus and $G^{(i)}$ is the shear modulus of the i^{th} layer and $\alpha_T^{(i)}$ is the coefficient of thermal expansion of the corresponding layer.

The bending moment M , the shear force Q and the in-plane stress resultant per unit length N are expressed by the stresses as follows:

$$\begin{aligned}
 M &= b \left(\int_{-h/2}^{z_1} \sigma_x z dz + \int_{z_1}^{h/2} \sigma_x z dz \right), \\
 Q &= b \left(\int_{-h/2}^{z_1} \sigma_{xy} dz + \int_{z_1}^{h/2} \sigma_{xy} dz \right), \\
 N &= b \left(\int_{-h/2}^{z_1} \sigma_x dz + \int_{z_1}^{h/2} \sigma_x dz \right)
 \end{aligned} \tag{13.4}$$

13.3 Field Equations

13.3.1 Governing Equations

The equations describing the coupled problem of the temperature distribution and the beam vibrations as a result of the action of a heat flow with intensity $q(x,t)$ and of mechanical load with intensity $p(x,t)$ are ($i = 1,2$):

$$\begin{aligned}
 \frac{c_p^{(i)}}{\lambda_T^{(i)}} \frac{\partial T}{\partial t} &= \frac{\partial^2 T}{\partial x^2} + \frac{\partial^2 T}{\partial z^2} - \frac{\alpha_T^{(i)} E^{(i)} T_0}{\lambda_T^{(i)}} \frac{\partial \varepsilon^{(i)}}{\partial t}, \\
 \frac{\partial N}{\partial x} - c_1^{(i)} \frac{\partial u}{\partial t} - \rho^{(i)} b h^{(i)} \frac{\partial^2 u}{\partial t^2} &= 0, \\
 -\frac{\partial M}{\partial x} - c_2^{(i)} \frac{\partial \psi}{\partial t} - \rho^{(i)} I^{(i)} \frac{\partial^2 \psi}{\partial t^2} &= 0, \\
 \frac{\partial Q}{\partial x} + N \frac{\partial^2 w}{\partial x^2} + \frac{\partial N}{\partial x} \frac{\partial w}{\partial x} - c_1^{(i)} \frac{\partial w}{\partial x} - \rho^{(i)} b h^{(i)} \frac{\partial^2 w}{\partial t^2} &= -p(x,t),
 \end{aligned} \tag{13.5}$$

where $I^{(i)}$ is the inertia moment of i^{th} layer, $\rho^{(i)}$ is the density of the i^{th} material, $T(x,z,t)$ is current temperature, T_0 is the initial constant temperature, $\lambda_T^{(i)}$ is the thermal conductivity of i^{th} material and $c_p^{(i)}$ is the heat capacity per unit volume, $w(x,t)$ is the transverse displacement, $\psi(x,t)$ is the rotation angle and

$$\varepsilon^{(i)} = -z \frac{\partial \psi}{\partial x} + \alpha_T^{(i)} (T - T_0) + \frac{\partial u}{\partial x} + \frac{1}{2} \left(\frac{\partial w}{\partial x} \right)^2$$

Neglecting the longitudinal inertia effect and by using the geometrical and constitutive equations Eqs. (13.5) can be rewritten in the form:

$$\begin{aligned}
(Eh)^* \frac{\partial^2 u}{\partial x^2} &= G_u + G_u^T, \\
(EI)^* \frac{\partial^2 \psi}{\partial x^2} - (Gh)^* k^2 \left(\frac{\partial w}{\partial x} - \psi \right) - (\rho I)^* \ddot{\psi} &= G_1^L + G_1^T, \\
(Gh)^* k^2 \left(\frac{\partial^2 w}{\partial x^2} - \frac{\partial \psi}{\partial x} \right) - c_1 \frac{\partial w}{\partial x} - (\rho F)^* \frac{\partial^2 w}{\partial t^2} &= -p(x,t) + G_2^L + G_2^T,
\end{aligned} \tag{13.6}$$

where

$$\begin{aligned}
G_u &= -(E^{(1)}h^{(1)} + E^{(2)}h^{(2)}) \left(\frac{\partial w}{\partial x} \frac{\partial^2 w}{\partial x^2} \right) - (E^{(1)} - E^{(2)}) \frac{h^{(1)}h^{(2)}}{2} \frac{\partial^2 \psi}{\partial x^2}, \\
G_u^T &= - \left(E^{(1)}\alpha_T^{(1)} \frac{\partial \gamma_T^{(1)}}{\partial x} + E^{(2)}\alpha_T^{(2)} \frac{\partial \gamma_T^{(2)}}{\partial x} \right), \\
G_1^L &= - \frac{E^{(2)} - E^{(1)}}{2} h^{(1)}h^{(2)} \left(\frac{\partial^2 u}{\partial x^2} + \frac{\partial w}{\partial x} \frac{\partial^2 w}{\partial x^2} \right), \\
G_1^T &= - \left(E^{(1)}\alpha_T^{(1)} \frac{\partial \chi_T^{(1)}}{\partial x} + E^{(2)}\alpha_T^{(2)} \frac{\partial \chi_T^{(2)}}{\partial x} \right), \\
G_2^L &= - \left[(E^{(1)}h^{(1)} + E^{(2)}h^{(2)}) \left(\frac{\partial u}{\partial x} + 0.5 \left(\frac{\partial w}{\partial x} \right)^2 \right) - (E^{(1)} - E^{(2)}) \frac{h^{(1)}h^{(2)}}{2} \frac{\partial \psi}{\partial x} \right] \frac{\partial^2 w}{\partial x^2}, \\
G_2^T &= - \left(E^{(1)}\alpha_T^{(1)}\gamma_T^{(1)} + E^{(2)}\alpha_T^{(2)}\gamma_T^{(2)} \right) \frac{\partial^2 w}{\partial x^2}.
\end{aligned} \tag{13.7}$$

Here the nonlinear terms due to the large deflections and the thermal loading are moved to the right hand side of the equations, thus forming pseudo-load vectors $\mathbf{G}^L(G_1^L, G_2^L)$, $\mathbf{G}^T(G_1^T, G_2^T)$.

In these equations the following notations are introduced:

$$\begin{aligned}
(Eh)^* &= (E^{(1)}h^{(1)} + E^{(2)}h^{(2)}), & (Gh)^* &= (G^{(1)}h^{(1)} + G^{(2)}h^{(2)}), \\
I^{(1)} &= \frac{1}{3}E^{(1)} \left(z_1^3 + \frac{h^3}{8} \right), & I^{(2)} &= E^{(2)} \left(\frac{h^3}{8} - z_1^3 \right), \\
(EI)^* &= (E^{(1)}I^{(1)} + E^{(2)}I^{(2)}), & (\rho I)^* &= (\rho^{(1)}I^{(1)} + \rho^{(2)}I^{(2)}), \\
\gamma_T^{(1)} &= \int_{-h/2}^{z_1} T dz, & \gamma_T^{(2)} &= \int_{z_1}^{h/2} T dz, \\
\chi_T^{(1)} &= \int_{-h/2}^{z_1} T z dz, & \chi_T^{(2)} &= \int_{z_1}^{h/2} T z dz.
\end{aligned} \tag{13.8}$$

It is seen that the different properties of the composing materials lead to appearance of new terms in the governing equations which do not exist in the case of one-material beam. The greater is the difference in material properties, the greater the influence of the shear forces on the beam behavior. This fact shows that for analyzes of composite beams it is important to use at least first-order beam theory, such as Timoshenko's theory.

13.3.2 Boundary and Initial Conditions

Assuming that the upper surface and the surfaces at $x = 0$ and $x = l$ are heat isolated and a heat flow $q(x, t)$ acts on the lower beam surface, the boundary conditions for the equation describing the heat propagation are:

$$\frac{\partial T}{\partial z} = \begin{cases} \lambda_T^{(1)-1} q(x, t) & \text{if } t \leq t_0 \\ 0 & \text{if } t > t_0 \end{cases} \quad (13.9)$$

The beam is considered clamped, in-axis fixed, i.e.:

$$u(0, t) = u(l, t) = w(0, t) = w(l, t) = 0, \quad \psi(0, t) = \psi(l, t) = 0. \quad (13.10)$$

The initial conditions are accepted as:

$$\begin{aligned} w(x, 0) = 0, \quad \dot{w}(x, 0) = 0, \quad \psi(x, 0) = 0, \quad \dot{\psi}(x, 0) = 0, \\ T(x, z, 0) = T_0, \quad x \in [0, l], z \in [-h/2, h/2]. \end{aligned} \quad (13.11)$$

13.3.3 Dimensionless Variables

The derived partial differential equations and associated boundary conditions have been transformed to dimensionless form by following transformations:

$$\bar{u} = u/l, \quad \bar{w} = w/l, \quad \bar{z} = z/h, \quad \bar{t} = t \frac{c}{l}, \quad c^2 = \frac{(Eh)^*}{(\rho I)^*}, \quad \theta = \frac{T - T_0}{T_0}. \quad (13.12)$$

Omitting the bars above the dimensionless variables the equations of the beam dynamics can be rewritten in the form:

$$\begin{aligned} \frac{\partial^2 u}{\partial x^2} &= G_u + G_u^T, \\ \frac{\partial^2 \psi}{\partial x^2} - \alpha \beta \left(\frac{\partial w}{\partial x} - \psi \right) - \ddot{\psi} &= G_1^L + G_1^T, \\ \beta \left(\frac{\partial^2 w}{\partial x^2} - \frac{\partial \psi}{\partial x} \right) - d_1 \frac{\partial w}{\partial x} - \frac{(\rho E)^*}{(Eh)^*} \frac{\partial^2 w}{\partial t^2} &= -p(x,t) + G_2^L + G_2^T, \end{aligned} \quad (13.13)$$

The nonlinear terms (13.7) from Eqs. (13.6) get the form

$$\begin{aligned} G_u &= - \left(\frac{\partial w}{\partial x} \frac{\partial^2 w}{\partial x^2} \right) - \frac{E^{(1)} - E^{(2)}}{(Eh)^*} \frac{h^{(1)} h^{(2)}}{2l} \frac{\partial^2 \psi}{\partial x^2}, \\ G_u^T &= \left(E^{(1)} \alpha_T^{(1)} \frac{\partial \gamma_\theta^{(1)}}{\partial x} + E^{(2)} \alpha_T^{(2)} \frac{\partial \gamma_\theta^{(2)}}{\partial x} \right) \frac{h}{(Eh)^*}, \\ G_1^L &= - \frac{E^{(2)} - E^{(1)}}{2} \frac{h^{(1)} h^{(2)} l}{(EI)^*} \left(\frac{\partial^2 u}{\partial x^2} + \frac{\partial w}{\partial x} \frac{\partial^2 w}{\partial x^2} \right), \\ G_1^T &= - \left(E^{(1)} \alpha_T^{(1)} \frac{\partial \chi_\theta^{(1)}}{\partial x} + E^{(2)} \alpha_T^{(2)} \frac{\partial \chi_\theta^{(2)}}{\partial x} \right) \frac{lh^2}{(EI)^*}, \\ G_2^L &= - \left[\left(\frac{\partial u}{\partial x} + 0.5 \left(\frac{\partial w}{\partial x} \right)^2 \right) - \frac{(E^{(1)} - E^{(2)}) h^{(1)} h^{(2)}}{2(Eh)^* l} \frac{\partial \psi}{\partial x} \right] \frac{\partial^2 w}{\partial x^2}, \\ G_2^T &= - \left(E^{(1)} \alpha_T^{(1)} \gamma_T^{(1)} + E^{(2)} \alpha_T^{(2)} \gamma_T^{(2)} \right) \frac{\partial^2 w}{\partial x^2}, \\ \beta &= k^2 \frac{(Gh)^*}{(Eh)^*}, \quad \alpha = \frac{(Eh)^* l^2}{(EI)^*}, \\ d_1 &= c_1 l^2 / [b(Eh)^*], \quad d_2 = c_2 l^2 / (EI)^*, \quad p_1(x,t) = \frac{lp(x,t)}{(Eh)^*} \end{aligned} \quad (13.14)$$

Here, k^2 characterizes the distribution of the shear stresses along the beam cross-section (shear correction factor). It is assumed that the damping coefficients are equal for both layers.

13.4 Numerical Approach

13.4.1 Discretization of the Equation for the Heat Transfer

For the solution of the equation for the heat propagation (13.5)₁ the finite difference method is applied for the space discretization. The central difference formulas were used and this equation becomes:

$$\begin{aligned} \dot{\theta}_{i,j} = & b_1(\theta_{i+1,j} - 2\theta_{i,j} + \theta_{i-1,j})/\Delta x^2 - b_2(\theta_{i+1,j} - 2\theta_{i,j} + \theta_{i-1,j})/\Delta z^2 \\ & + b_3 z_{i,j}(\dot{\psi}_{i+1} - \dot{\psi}_{i-1})/(2\Delta x) - b_4(w_{i+1} - w_{i-1})(\dot{w}_{i+1} - \dot{w}_{i-1})/(4\Delta x^2), \end{aligned} \quad (13.15)$$

where $i = 1, \dots, N_x, j = 1, \dots, N_z, \Delta x = 1/(N_x - 1), \Delta z = 1/(N_z - 1)$. N_x and N_z are numbers of points taken along the axes x and z , respectively and

$$\begin{aligned} b_1^{(j)} &= \left[c l^2 \left(a_1^{(j)} + a_2^{(j)} \right) \right]^{-1}, & b_2^{(j)} &= l \left[c h^{(j)2} \left(a_1^{(j)} + a_2^{(j)} \right) \right]^{-1}, \\ b_3^{(j)} &= \alpha_T^{(j)} T_0 E^{(j)} h^{(j)} \left[\lambda_{T(i)}^{(j)} l \left(a_1^{(j)} + a_2^{(j)} \right) \right]^{-1}, & b_4^{(j)} &= \alpha_T^{(j)} E^{(j)} \left[\lambda_{T(i)}^{(j)} l \left(a_1^{(j)} + a_2^{(j)} \right) \right]^{-1}, \\ a_1^{(j)} &= c_p^{(j)} / \lambda_T^{(j)}, & a_2^{(j)} &= \alpha_T^{(j)2} T_0 E^{(j)} / \lambda_T^{(j)}, & j &= 1, 2. \end{aligned}$$

It must be noted that the discretization step along the thickness Δz of the beam is equal for both layers.

The discretized initial condition is:

$$t = 0 : \theta_{i,j} = 0$$

The discretized boundary conditions are:

$$\begin{aligned} \theta_{0,j} = \theta_{2,j}, \quad \theta_{N+1,N_z} = \theta_{N-1,N_z}, \quad \theta_{i,N_z+1} = \theta_{i,N_z-1}, \\ \theta_{i,0} = \theta_{i,2} + 2q_i(t)h\Delta z / (\lambda_T^{(k)} T_0) & \text{if } t \leq t_0 \\ \theta_{i,1} = \theta_{i,2} & \text{if } t > t_0 \end{aligned} \quad (13.16)$$

The thermomechanical coupling effects are defined by the coefficients a_2, b_3 and b_4 . Case $a_2 = 0$ and $b_3 = b_4 = 0$ is referred to the uncoupled problem.

13.4.2 Algorithm for the Solution of the Beam Vibration Problem

The algorithm to solve the Eqs. (13.13) is very similar to the one used in Manoach and Ribeiro (2004) and only briefly is reported here.

- First, the eigenvalue problem was solved by considering the Eqs. (13.13)₂, (13.13)₃ with zero right hand sides.
- Then using the pseudo-normal mode superposition method (see Manoach and Ribeiro, 2004) the generalized displacements vector $\mathbf{v} = \{\alpha\psi, w\}^T$ is expanded as a sum of the product of the vectors of pseudo-normal modes v_n and time dependent functions $q_n(t)$ as

$$\mathbf{v}(x,t) = \sum_{n=1}^{N_f} \mathbf{v}_n(x) q_n(t) \quad (13.17)$$

and the partial differential equations are transformed in the following coupled system of ordinary differential equations:

$$\ddot{q}_n(t) + 2\xi_n \dot{q}_n(t) + \omega_n^2 q_n(t) = F_n(t), \quad (13.18)$$

where n are the natural frequencies of the linear elastic (undamped) bi-material Timoshenko beam, ξ_n are modal damping parameters and

$$F_n(t) = \int_0^1 \mathbf{v}_n^T(x) [\mathbf{P}(x,t) + \mathbf{G}(x,t)] dx, \quad \mathbf{P}(x,t) = (0, -\bar{p})^T, \quad \mathbf{G} = \mathbf{G}_L + \mathbf{G}_T \quad (13.19)$$

In (13.19) by \mathbf{G}_L and \mathbf{G}_T are denoted the vectors $\mathbf{G}_L(G_1^L, G_2^L)$ and $\mathbf{G}_T(G_1^T, G_2^T)$ (see Eqs. (13.14)) and $\mathbf{P}(x,t)$ is the force vector. In (13.17) it is assumed that the transverse displacements and the rotation angle have the same time dependent amplitudes q_n .

The algorithm is based on the successive solution of the equations for the mechanical vibrations of the beam and for the heat transfer. The detailed description of the algorithm could be found in Manoach and Ribeiro (2004).

13.5 Numerical Examples

The numerical examples given here aim to illustrate the application of the numerical approach described above and to verify the equations deduced her for thermoelastic vibration of bi-materials Timoshenko beams. The considered beam consists of two materials (aluminium and copper) with the following parameters:

$$\begin{aligned} E^{(1)} &= 7 \times 10^7 \text{N/m}^2, & E^{(2)} &= 12.8 \times 10^7 \text{N/m}^2, & \nu^{(1)} &= \nu^{(2)} = 0.34, \\ \rho^{(1)} &= 2778 \text{kg/m}^3, & \rho^{(2)} &= 8960 \text{kg/m}^3, & c_p^{(1)} &= 2484 \text{N/(m}^2\text{K)}, & c_p^{(2)} &= 1018 \text{N/(m}^2\text{K)}, \\ \lambda_T^{(1)} &= 207 \text{N/(sK)}, & \lambda_T^{(2)} &= 385 \text{N/(sK)}, & l &= 0.5 \text{m}, & b &= 0.025 \text{m} \end{aligned}$$

Two cases of the geometry of the beam were considered: (i) $h/l = 0.1$ and (ii) $h/l = 0.05$. In the first case $z_1 = 0.007$ m and in the second case $z_1 = 0.003125$ m. In both cases the beam cross-section was discretized with 9 nodes along the thickness, i.e. $N_z = 9, N_z^{(1)} = 6$ and $N_z^{(2)} = 4$ (the interface layer was counted 2 times). For the interface layer ($N_z = 6$) the coefficients in Eqs. (13.12) were calculated using the average values of the physical parameters, i.e.

$$E^* = \frac{E^{(1)} + E^{(2)}}{2}, \quad \alpha_T^* = \frac{\alpha_T^{(1)} + \alpha_T^{(2)}}{2}, \quad \text{etc.}$$

The beam was discretized with 41 nodes along its length - $N_x = 41$. The results of calculations with 81 nodes show almost identical results with the ones with 41. In all calculations five terms were chosen in the expansion of Eq. (13.17) ($N_f = 5$).

13.5.1 Eigenfrequencies

The natural frequencies and normal modes of the bi-material Timoshenko beam were calculated using the same approach as in Manoach and Karagiozova (1993). The natural frequencies and normal nodes were calculated for a beam with the “averaged” properties

$$(Eh)^* = 5.73 \times 10^7 \text{N/m}^2, \quad \nu = 0.34, \quad (\rho h)^* = 3981.2 \text{kg/m}^3$$

by using the general purpose FE program MSC NASTRAN. The beam was discretized with 40 linear beam elements. The obtained frequencies are shown in Table 13.1.

The “averaging” of the material properties is an approximation of the real modelling of the bi-material beam. For example, the inertia moment for the equivalent beam is different from the one obtained by the present model. There are other discrepancies between two models so we accept that the relative differences in the calculated frequencies according to the two models are acceptable and the present model can be applied for the further studies.

13.5.2 Beam at Elevated Temperature

The first considered case is the beam at an elevated temperature. We consider that the beam with $h/l = 0.1$ gets an elevated temperature ΔT instantly. The beam is subjected to harmonic loading $p = p_0 \sin \omega_e t$, where ω_e denotes the excitation frequency. It is accepted that the mechanical loading is uniformly distributed along the beam length. The results for vibration of centre of the beam in time for four different temperatures are shown in Fig. 13.2. The dimensionless excitation frequency is $\bar{\omega}_e = 0.4$ ($\bar{\omega}_1 = 0.61$). As can be expected the elevated temperatures lead to vibrations with larger amplitudes. In all cases vibrations are periodic and symmetric around the mid-axis of the beam. Because the beam is quite thick for this parameter of the loading more complex phenomena like buckling or non-periodic response have not been observed. The non-symmetric vibration around the mid-axis of the beam is not

Table 13.1
The natural frequencies of the beam

Frequency number	Present model, rad/s	MSC NASTRAN, rad/s	Relative difference, %
1	4934	5041	2.10
2	12579	12878	2.32
3	22628	23206	2.49
4	34221	35146	2.63
5	46839	48162	2.75

observed for the selected geometrical parameters of the beam. Such phenomenon was observed for thinner beams (not shown here).

13.5.3 Beam Subjected to Heat Impact

The next considered case is a thinner beam ($h/l = 0.05$) subjected to a harmonic loading and heat impact. In this case the beam made of the same two materials (with $z_1 = 0.003125$ m) is subjected to a short heat pulse acting on the lower beam surface, distributed along the beam length according to the sin function and its amplitude decreases in time as:

$$\bar{q}(\bar{x}, \bar{t}) = \begin{cases} \bar{q}_0 \left(1 - \frac{\bar{t}}{\bar{t}_0}\right) \sin(\pi \bar{x}) & \text{for } 0 \leq \bar{t} \leq \bar{t}_0 \\ 0 & \text{for } \bar{t} > \bar{t}_0 \end{cases}$$

The thermal loading changes dramatically the beam response. The intensive short thermal pulse force the beam to buckle. After the initial peak of the response, with

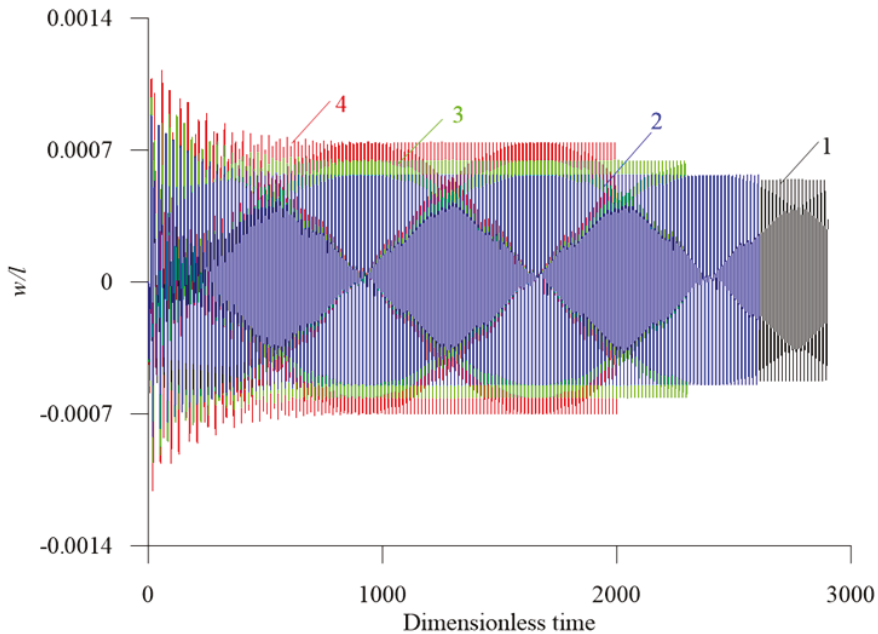


Fig. 13.2. Time-history diagrams of the response of the beam subjected to harmonic loading at elevated temperature ($p = 8 \cdot 10^5$ N/m, $\omega_e = 3284.2$ rad/s): 1 - $\Delta T = 10$ K, 2 - $\Delta T = 20$ K, 3 - $\Delta T = 30$ K, 4 - $\Delta T = 60$ K

decreasing and ceasing of the thermal loading the maximal deflections of the beam decrease and the beam continue to vibrate around a buckle state which changes with time. This can be seen in Fig. 13.2 where the response of the beam subjected to mechanical loading and thermal shock are shown.

The results concerning the heat propagation along the beam length and thickness can be seen in Figs. 13.3 and 13.4. These figures compared with Fig. 13.5 clearly show the different velocity of the heat propagation and beam elastic vibrations. As it is known the heat propagation is much slower process. It is seen that after tens periods of elastic vibrations the temperature still continues to propagate along the beam cross-section.

At the first contour plot of the temperature distribution (Fig. 13.3a) the temperature propagates only at the first layers of the beam and it even has not reached the middle of the beam cross-section. At the same time the beam oscillates more than 40 times along its mid axis. At later moment, $\bar{t} = 1277$, the temperature propagation has reached the whole beam cross section but still has not reached a uniform value. The speed of the heat propagation is different for the different layers because of the different thermal properties of the materials.

The influence of the speed of the heat propagation can be judged and from Fig. 13.4 where the change of the temperature in time at three different layers along z axis is shown. The bottom layer (layer 1), its adjacent layer (layer 2) and interface

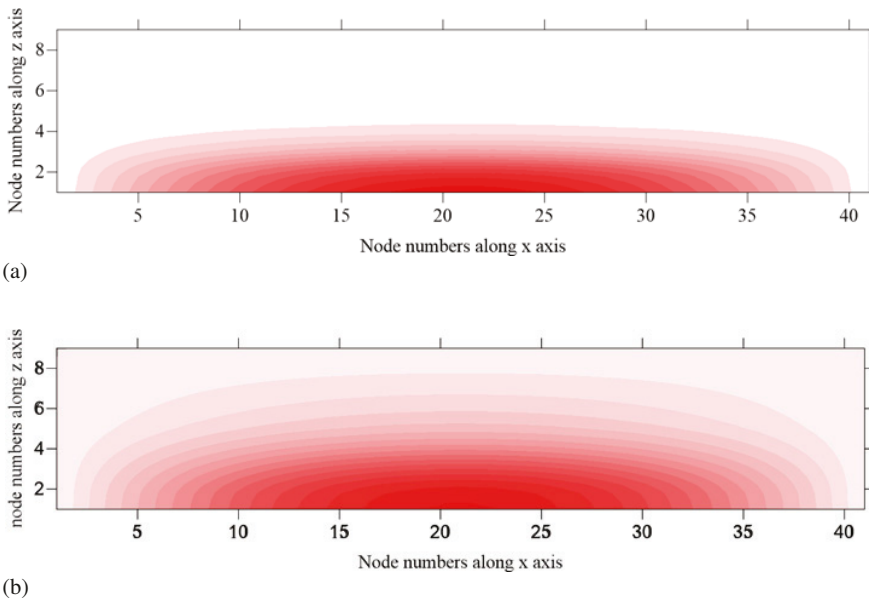


Fig. 13.3. Distribution of the temperature along the beam cross-section and the beam length: (a) - $\bar{t} = 827$; (b) - $\bar{t} = 1277$

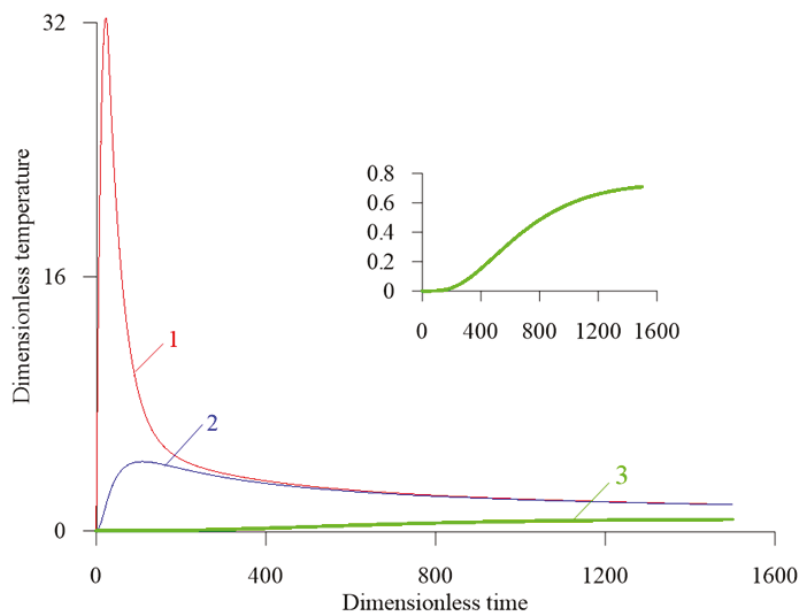


Fig. 13.4. Variation of the temperature at the beam center at the first layer – 1 (red colour), at the second layers - 2 (blue colour), and at 6th (interface) layer (green colour) of the beam cross-section

layer (layer 6) are chosen. In order the process of the heat propagation to be more visible, a small figure showing the heat evolution at layer 6 is added.

13.6 Discussion and Conclusions

The large amplitude vibrations of bi-material Timoshenko beams subjected to mechanical load and thermal loading are studied in this work. The deduced equations of the beam motion include nonlinear terms which do not appear in the equation of motion of homogeneous beams. These terms are G_1^L and G_1^T . The other nonlinear terms in the right hand side of the Eqs. (13.13) are more complex than the ones obtained for the single-material Timoshenko beam model. The equations of the beam motion are coupled with the equation of the heat propagation. The different properties of the beam material along the beam cross-section are also considered in the solution of this equation. The considered equations include full coupling of the mechanical and thermal fields, i.e. the thermal field influences the beam motion and the beam motion influence the heat propagation.

The considered numerical examples aim to check the applicability and the correctness of the deduced equations and the methods developed to solve them. The

obtained results demonstrate that temperature loading and short heat pulses can have a big influences on the beam behavior.

Of course the influence of the mechanical vibration on the heat propagation is much weaker and often negligible. In some cases, for example, for bi-material micro structures,) the beam motion could have some influence on the heat propagation process. In the considered case only at the initial stage of the process small differences between the coupled and uncoupled solution could be observed – see Fig. 13.6.

The small difference at the beginning of the process becomes negligible in time.

The influence of the nonlinear terms due to different layers on the beam response as well as the influences of the coupled terms on the beam vibration and heat propagation will be studied in our further works. The heat pulse parameters (pulse shape, pulse duration and the heat flux value) are also objects of interests and will be studied.

Acknowledgements This work has been accomplished with the financial support of Grant DN 02-7/2016 from the Bulgarian research fund and of the Bulgarian Ministry of Education and Science, Grant No. D01-221/03.12.2018 for NCDSC – part of the Bulgarian National Roadmap on RIs. The third author has been financed within the framework of the project Lublin University of Technology-Regional Excellence Initiative, funded by the Polish Ministry of Science and Higher Education (Contract No. 030/RID/2018/19).

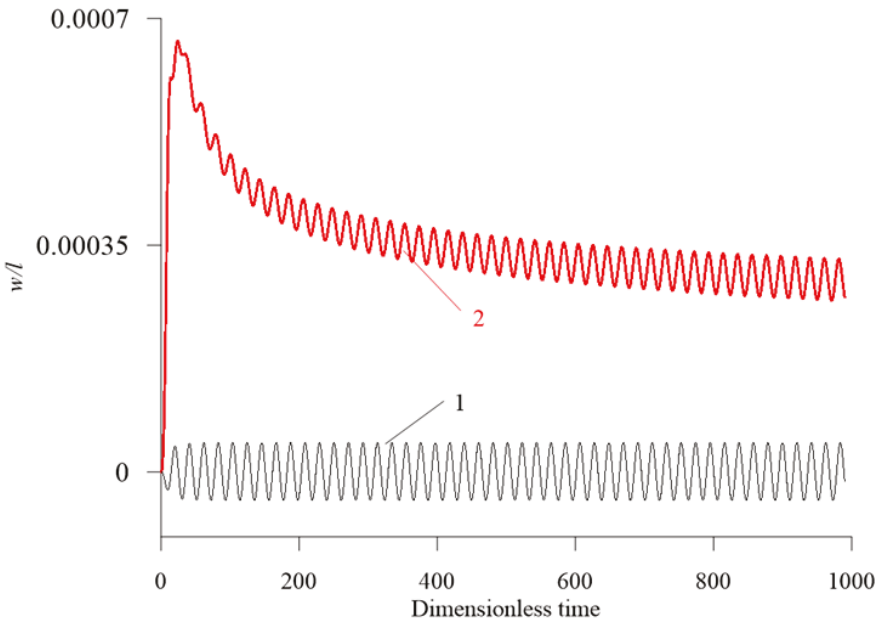


Fig. 13.5. Time history of the response of the beam subjected to thermal loading and harmonic loading with $p = 1000$ N/m, $\omega_e = 2468.8$ rad/s ($\omega_1 = 2651$ rad/s), $h/l = 0.05$: 1 – $q_0 = 0$ W/m², 2 – $q_0 = 9000$ W/m², $\bar{t}_0 = 30$

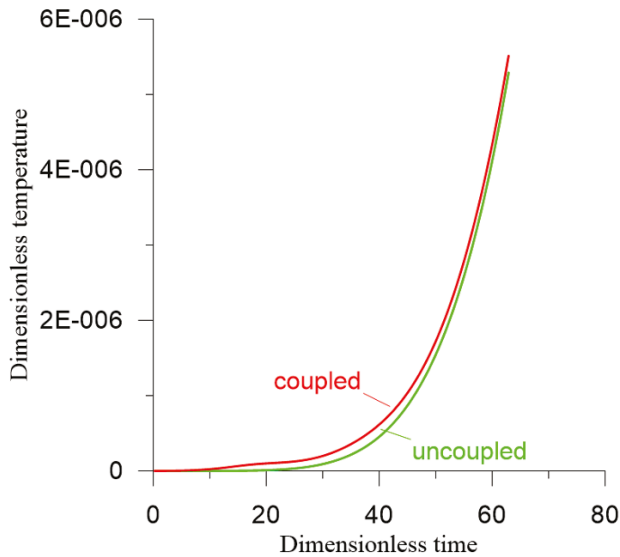


Fig. 13.6. Variation of the temperature at the beam center at 6th, interface layer of the beam cross-section ($q_0 = 22500 \text{ W/m}^2$, $\bar{t}_0 = 120$). Red colour – coupled solution; green colour – uncoupled solution.

References

- Boley B, Weiner J (1960) *Theory of Thermal Stresses*. Wiley, New York
- Boley BA (1956) Thermally induced vibrations of beams. *Journal of Aeronaut Sci* 23:179–181
- Carpinteri A, Paggi M (2008) Thermoelastic mismatch in nonhomogeneous beams. *Journal of Engineering Mathematics* 61:371–384
- Carpinteri A, Pugno N (2006) Thermal loading in multi-layered and/or functionally graded materials: Residual stress field, delamination, fatigue and related size effects. *International Journal of Solids and Structures* 43(3):828–841
- Karagiozova D, Manoach E (1992) Coupling effects in an elastic-plastic beam subjected to heat impact. *Nuclear Engineering and Design* 135(3):267–276
- Manoach E (2003) Large amplitude vibrations of Timoshenko beams subjected to thermal loading. In: *Proceedings of 8th International Conference on Recent Advances in Structural Dynamics*, Southampton, UK, CD-paper 39
- Manoach E, Karagiozova D (1993) Dynamic response of thick elastic-plastic beams. *International Journal of Mechanical Sciences* 35(11):909–919
- Manoach E, Ribeiro P (2004) Coupled, thermoelastic, large amplitude vibrations of timoshenko beams. *International Journal of Mechanical Sciences* 46(11):1589–1606
- Mei C, Abdel-Motagaly K, Chen R (1999) Review of Nonlinear Panel Flutter at Supersonic and Hypersonic Speeds. *Applied Mechanics Reviews* 52(10):321–332

- Saetta E, Rega G (2014) Unified 2D continuous and reduced order modeling of thermomechanically coupled laminated plate for nonlinear vibrations. *Meccanica* 49(8):1723–1749
- Saetta E, Rega G (2016) Modeling, dimension reduction, and nonlinear vibrations of thermomechanically coupled laminated plates. *Procedia Engineering* 144:875–882, international Conference on Vibration Problems 2015
- Saetta E, Rega G (2017) Third order thermomechanically coupled laminated plate: 2D nonlinear modeling, minimal reduction, and transient/post-buckled dynamics under different thermal excitations. *Composite Structures* 174:420–441
- Settimi V, Saetta E, Rega G (2018) Local and global nonlinear dynamics of thermomechanically coupled composite plates in passive thermal regime. *Nonlinear Dynamics* 93:167–187
- Shang Y, Ye X, Feng J (2013) Theoretical analysis and simulation of thermoelastic deformation of bimorph microbeams. *Science China Technological Sciences* 56:1715–1722
- Shi Y, Lee RYY, Mei C (1999) Thermal postbuckling of composite plates using the finite element modal coordinate method. *Journal of Thermal Stresses* 22(6):595–614
- Srinivasan P, Spearing SM (2008) Effect of heat transfer on materials selection for bimaterial electrothermal actuators. *Journal of Microelectromechanical Systems* 17(3):653–667
- Wu GY (2009) The analysis of dynamic instability of a bimaterial beam with alternating magnetic fields and thermal loads. *Journal of Sound and Vibration* 327(1):197–210



Chapter 14

Effect of Longitudinal Variation of Material Properties in Warping Torsion of FGM Beams

Justín Murín, Juraj Hrabovsky, Stephan Kugler, Vladimír Kutíš,
and Mehdi Aminbaghai

Abstract In this paper, the influence of longitudinal variation of material properties on the deformation and stresses of thin-walled non-uniformly twisted Functionally Graded Material (FGM) beams is investigated. The longitudinal variation is described by a polynomial. Secondary deformations, resulting from the angle of twist, are considered. The transfer relations are derived and used for establishing finite element equations for non-uniformly twisted FGM beams in local coordinate systems. The warping part of the first derivative of the twist angle, caused by the bimoment, is considered as an additional degree of freedom at the nodes of the beam elements. The numerical investigation is performed with consideration of the Secondary Torsional Moment Deformation Effect (STMDE). It is focused on elastostatic analysis of straight cantilever FGM beams with doubly symmetric open as well as closed cross-sections. A very strong effect of the longitudinal variation of material properties on the twist angle and bimoment normal stresses is originally studied and presented. The results are compared with the ones obtained by a very fine mesh of standard solid and shell as well as warping beam finite elements.

Key words: Functionally graded material beams · Longitudinally varying material properties · Non-uniform torsion

Justín Murín · Juraj Hrabovsky · Vladimír Kutíš
Department of Applied Mechanics and Mechatronics, IAMM FEI, STU Bratislava, Ilkovicova 3,
812 19 Bratislava, Slovakia
e-mail: justin.murin@stuba.sk, juraj.hrabovsky@stuba.sk, vladimir.kutis@stuba.sk
Stephan Kugler
University of Applied Sciences, Johannes Gutenberg-Strasse 3, 2700 Wiener Neustadt, Austria
e-mail: kugler@fhwn.ac.at
Mehdi Aminbaghai
Vienna University of Technology, Institute for Mechanics of Materials and Structures, Karlsplatz 13,
1040 Vienna, Austria
e-mail: mehdi.aminbaghai@tuwien.ac.at

14.1 Introduction

The effect of non-uniform torsion may be significant in structural elastostatic and elastodynamic analysis of thin-walled beams with open as well as closed cross-sections and with constant material properties. The maximum normal stress resulting from the bimoment occurs at the points of action of the external torques (except for free ends of beams) and at cross-sections of restrained warping (e.g. clamped cross-sections). A comprehensive overview of the literature dealing with the issue of non-uniform torsion of thin-walled beams made of homogeneous material can be found, e.g., in Aminbaghai et al (2016); Dikaros et al (2016). Commercial Finite Element Method (FEM) codes allow for elastostatic torsional analysis by 3D finite beam elements without as well as with consideration of the warping effect (ANSYS, 2019; ADINA, 2013; ABAQUS, 2018; Przemieniecki, 1992; Murín et al, 2014). For uniform torsion, frequently an improved Saint-Venant theory is used. In non-uniform torsion, the bicurvature is very often chosen as an additional warping degree of freedom, and the Secondary Torsion Moment Deformation Effect (STMDE) is not considered. Most recent research results have shown, however, that for non-uniform torsion of beams with closed cross-sections the influence of the STMDE (Murín et al, 2014) and of the distortion of the cross-section (Tsiptsis and Sapountzakis, 2017b) is particularly significant. The effect of the axial force on torsional warping is investigated in Aminbaghai et al (2017). A common feature of the cited articles is that constant material properties of the beams are assumed.

In material science, one of the ground-breaking technologies are functionally graded materials (FGMs). Natural biomaterials often possess the structure of FGMs. This enables them to satisfy requirements such as corrosion resistance, thermal conductivity, strength, elastic stability, fatigue durability, dynamic stability, etc. Fabrication of such materials is complicated. However, in recent years a progress in this area has been significant. A FGM consists of a mixture of two or more constituents of almost the same form and the same dimensions. Plasma spraying, powder metallurgy, 3D printing, and other technologies are used for fabrication of such materials. From a macroscopic point of view, FGMs are isotropic at each material point, but the material properties can vary continuously or discontinuously in one, two, or three directions. The variation of the macroscopic material properties can be realized by varying the volume fractions of the constituents or their material properties. An important class of structural components, made of FGMs, are beams. Thin-walled beams play an important role not only in structural applications, but also in thermal, electro-thermal, and electro-thermo-structural systems (e.g. Micro-Electro-Mechanical-Systems (MEMS), sensors and actuators), as well as in mechatronics. In all of these applications, FGMs can greatly improve the effectiveness of the systems concerned (Shoghmand and Ahmadian, 2018; Fariborz and Batra, 2019).

For mechanical investigations of FGM beams, semi-analytical and numerical methods of analysis of planar beams with a predominantly transverse variability of the material properties were first developed. Intensive activities in the area of uniform (Saint-Venant) torsion are presently in full swing. A list of scientific articles on modelling of FGM beams can be found e.g. in Murin et al (2016). In this article, a

3D FGM beam finite element with a spatial variation of the material properties was presented, considering Saint-Venant torsion. Uniform torsion of FGM beams was also investigated in Shen et al (2016); Kim and Lee (2016); Barretta et al (2018). In Barretta et al (2015), closed-form solutions of FGM beams, subjected to non-uniform torsion, were presented. In Yoon et al (2015), nonlinear finite element formulations for 3D analysis of FGM beams were presented. A power law distribution of the material properties in the transverse direction was considered.

In Aminbaghai et al (2016); Murín et al (2014), a new 3D Timoshenko finite beam element including warping torsion of open and closed cross-sections with constant material properties was presented. In Murin et al (2018) and Aminbaghai et al (2019), this beam element was extended for non-uniform torsional modal and elastostatic analysis of FGM beams with a polynomial form of variation of the material properties in the longitudinal direction. This form of longitudinal variability of the material properties allows for a wide range of practical applications. Moreover, it facilitates structural analysis of such composite beams. In many cases, the spatial validation of the material properties of FGM beams can be reduced to a longitudinal variation (e.g. Murín et al, 2014; Kutis et al, 2011). From the finite element equations, established for such partially homogenized beams, the primary variables in form, e.g., of nodal displacements are obtained. The stresses, however, must be computed for the real beam.

The main body of the present paper consists of the theoretical part and the numerical evaluation of the developed elastostatic warping torsion theory for thin-walled beams with longitudinally varying material properties. Doubly symmetric open and closed cross-sections of straight FGM beams are considered. In Sect. 14.2, a summary of the differential equations for non-uniform torsional deformations is presented. The part of the bicurvature, caused by the bimoment, is taken into account as the warping degree of freedom. The STMDE is also considered. A general semi-analytical solution of the differential equation is presented. Furthermore, the transfer matrix relation is presented, from which the finite element equations for two-node straight warping torsion beams (FGM-WT) are derived. Section 14.3 contains the numerical investigation. The results from elastostatic analysis of cantilever beams with open I cross-sections and rectangular hollow cross-sections are presented and compared with results obtained from commercial FEM codes. The effect of the longitudinally varying material properties is quantified. A final assessment of the proposed method is contained in the conclusions. A very strong effect of the longitudinal variation of material properties on the twist angle and bimoment normal stresses in the field of the beams is originally studied and presented.

14.2 Non-uniform Torsion FGM Beam Finite Element

In the following, the differential equations, with variable parameters, for torsional elastostatic analysis of FGM beams with doubly symmetric open or closed cross-sections will be shortly presented. The material properties in the longitudinal direc-

tion of the beams are assumed to vary in a polynomial form. The solution of the differential equations is based on the concept of transfer functions. After derivation of the transfer matrix, the finite element equations for local coordinate systems for non-uniform torsion are established.

The stiffness matrix of the developed finite element is based on a semi-analytical solution of the differential equation for non-uniformly twisted FGM beams, derived by the authors. In this way, the longitudinal variability of the material properties is considered with great accuracy. Thus, in a system consisting of several beams, with a polynomial form of variability of the material properties, each beam can be modelled by a single finite element. It is, of course, possible to divide the beam into several finite elements of the proposed kind, but this has no significant influence on the accuracy of the numerical solution. This is seen as a strong advantage of the proposed finite element. However, for a longitudinally discontinuous change of the cross-section or of the material properties of the beam, a subdivision into several finite elements is necessary.

Figure 14.1 refers to the determination of the deformation of a FGM beam, subjected to non-uniform torsion. It shows the torsional moment $M_T(x)$ as the sum of the primary torsional moment $M_{Tp}(x)$, the secondary torsional moment $M_{Ts}(x)$ and the bimoment $M_\omega(x)$ according to the definitions of positive values of these quantities in the framework of the Transfer Matrix Method (TMM). Figure 14.1 also shows the angle of twist, $\psi(x)$, corresponding to $M_{Tp}(x)$. It is equal to the sum of the angle of twist from the primary deformation, $\psi_M(x)$, and of the one from the secondary deformation, $\psi_S(x)$.

Figure 14.2 illustrates the beam element. It is loaded by the torsional line moment $m_T(x)$. The equilibrium equations are obtained as

$$M'_T(x) = -m_T(x), \tag{14.1}$$

where

$$m_T(x) = \sum_{k=0}^{\max k} \eta_{mT,k} x^k$$

is the polynomial representation of the torsional moment with the parameters $\eta_{mT,k}$. According to Murin et al (2018),

$$M'_\omega(x) = M_T(x) - M_{Tp}(x) + m_\omega(x) = M_{Ts} + m_\omega(x), \tag{14.2}$$

where

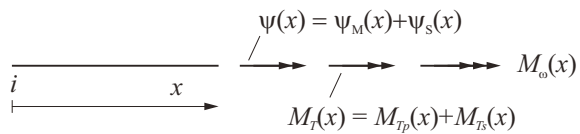


Fig. 14.1 Non-uniform torsion: torsional moment, bimoment, and angle of twist.

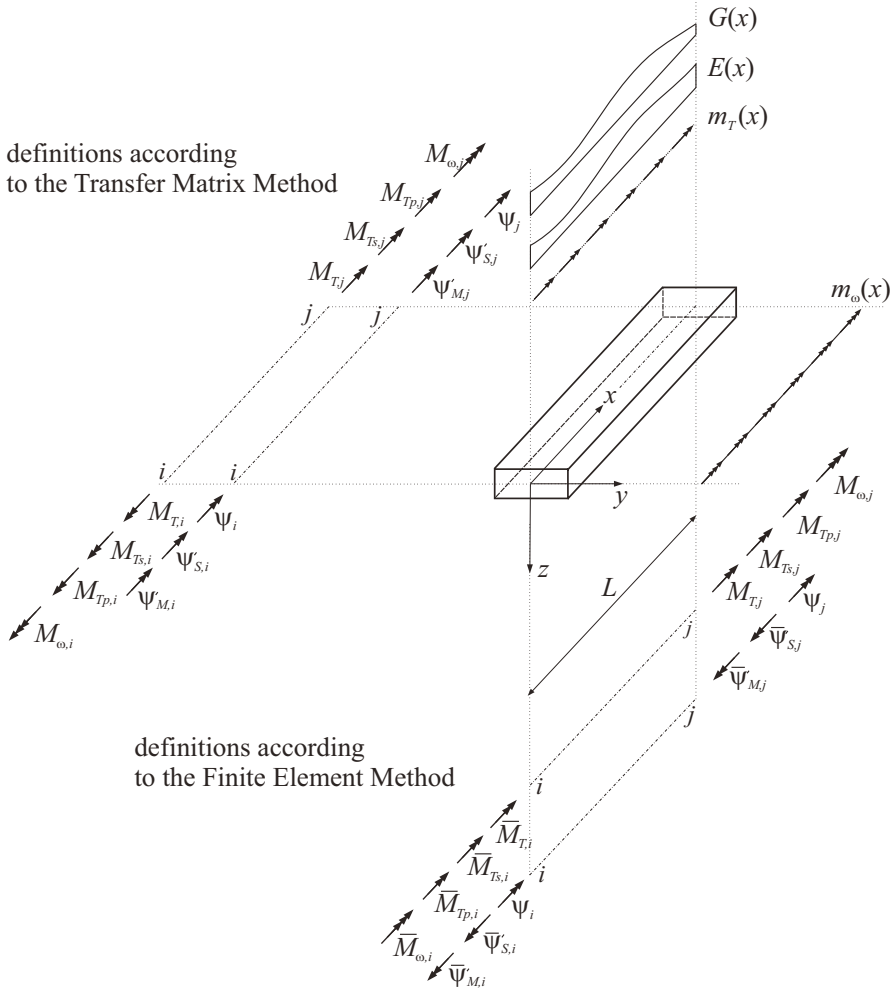


Fig. 14.2. Definitions of positive torsional moments and rotation angles at the element nodes for the TMM and the FEM in the local coordinate system.

$$m_{\omega}(x) = \sum_{k=0}^{\max k} \eta_{m_{\omega},k} x^k$$

is the polynomial representation of the warping moment with the parameters $\eta_{m_{\omega},k}$ and

$$M_T(x) = M_{Tp}(x) + M_{Ts}(x). \tag{14.3}$$

According to Aminbaghai et al (2016),

$$\psi''_M(x) = -\frac{M_\omega(x)}{EI_\omega(x)} \quad (14.4)$$

and

$$\psi'(x) = \psi'_M(x) + \psi'_S(x), \quad (14.5)$$

with

$$\psi'_P(x) = \frac{M_{Tp}(x)}{GI_T(x)} \quad (14.6)$$

and

$$\psi'_S(x) = \frac{M_{Ts}(x)}{GI_{Ts}(x)}, \quad (14.7)$$

where I_{Ts} denotes the secondary torsion constant and $E(x)$ and $G(x)$ stand for the longitudinally varying effective elasticity modulus and shear modulus, respectively. Multiplication of the polynomial representation of the shear modulus, i.e. of $G(x)$, by I_{Ts} yields $G(x)I_{Ts}$. For convenience, it will be written in the following as GI_{Ts} . Multiplication of the polynomial representation of the modulus of elasticity, i.e. of $E(x)$, by I_ω yields EI_ω .

According to Murin et al (2018), differentiation of Eq. (14.7) with respect to x and multiplication by EI_ω gives

$$M_\omega + \frac{EI_\omega(M_{Ts}GI'_{Ts}) + GI_{Ts}(-M'_{Ts} + GI_{Ts}\psi'')}{GI_{Ts}^2} = 0. \quad (14.8)$$

Differentiation of Eq. (14.8) with respect to x , multiplication by EI_ω^2 , and use of Eq. (14.7) yields

$$\frac{EI_\omega^2}{GI_{Ts}^3} \left(\begin{array}{c} -2EI_\omega M_{Ts} (GI'_{Ts})^2 M_{Ts} \\ +GI_{Ts} (GI'_{Ts} (2EI_\omega M'_{Ts} + EI'_\omega M_{Ts}) + EI_\omega) GI''_{Ts} M_{Ts} \\ -(GI_{Ts})^2 (EI'_\omega M'_{Ts} + EI_\omega M''_{Ts}) \\ +GI_{Ts}^3 (M_{Ts} + m_\omega + EI'_\omega \psi'' + EI_\omega \psi''') \end{array} \right) = 0. \quad (14.9)$$

Substituting Eq. (14.6) into Eq. (14.3) gives

$$M_{Ts} = M_T - M_{Tp} = M_T - GI_T \psi'. \quad (14.10)$$

The first and the second derivative of Eq. (14.10) with respect to x are inserted into Eq. (14.9). This yields the following expression for the torsional moment:

$$\begin{aligned}
 & M_T \left(GI_{T_s}^3 + GI_{T_s} EI'_\omega GI'_{T_s} - 2EI_\omega (GI'_{T_s})^3 + EI_\omega GI_{T_s} GI''_{T_s} \right) = \\
 & \frac{(GI_T (GI_{T_s})^3 - (GI_{T_s})^2 E'I_\omega G'I_T + GI_T GI_{T_s} E'I_\omega G'I_{T_s} + 2EI_\omega GI_T G'I_{T_s} - 2EI_\omega GI_T (G'I_{T_s})^2 - EI_\omega (GI_{T_s})^2 G''I_T}{GI_T (GI_{T_s})^3 - (GI_{T_s})^2 E'I_\omega G'I_T + GI_T GI_{T_s} E'I_\omega G'I_{T_s} + 2EI_\omega GI_T G'I_{T_s} - 2EI_\omega GI_T (G'I_{T_s})^2 - EI_\omega (GI_{T_s})^2 G''I_T} \cdot \psi' \\
 & + \frac{EI_\omega GI_T GI_{T_s} G''I_{T_s}}{GI_T (GI_{T_s})^3 - (GI_{T_s})^2 E'I_\omega G'I_T + GI_T GI_{T_s} E'I_\omega G'I_{T_s} + 2EI_\omega GI_T G'I_{T_s} - 2EI_\omega GI_T (G'I_{T_s})^2 - EI_\omega (GI_{T_s})^2 G''I_T} \cdot \psi'' \\
 & - \frac{(EI_\omega GI_T GI_{T_s}^2 + EI_\omega GI_{T_s}^3)}{GI_T (GI_{T_s})^3 - (GI_{T_s})^2 E'I_\omega G'I_T + GI_T GI_{T_s} E'I_\omega G'I_{T_s} + 2EI_\omega GI_T G'I_{T_s} - 2EI_\omega GI_T (G'I_{T_s})^2 - EI_\omega (GI_{T_s})^2 G''I_T} \cdot \psi''' \\
 & - GI_{T_s}^3 m_\omega + (-GI_{T_s}^2 EI'_\omega + 2EI_\omega GI_{T_s} GI'_{T_s}) m_T - EI_\omega GI_{T_s}^2 m'_T.
 \end{aligned} \tag{14.11}$$

Setting M'_T , which follows from Eq. (14.8), equal to $-m_T$, results in the following differential equation of fourth order:

$$\begin{aligned}
 \eta_4(x)\psi''''(x) + \eta_3(x)\psi''''(x) + \eta_2(x)\psi''(x) + \eta_1(x)\psi'(x) + \eta_0(x)\psi(x) = \\
 = \eta_L(x) = \sum_{s=0}^{\max s} \eta_{L,s} x^s.
 \end{aligned} \tag{14.12}$$

The variable polynomial parameters $\eta_0(x) - \eta_4(x)$ are given in Appendix 14.4.

The general semi-analytical solution of Eq. (14.12) can be written as follows:

$$\psi(x) = b_0(x)\psi_i + b_1(x)\psi'_i + b_2(x)\psi''_i + b_3(x)\psi'''_i + \sum_{s=0}^{\max s} \eta_{L,s} b_{s+4}(x). \tag{14.13}$$

In Eq. (14.13), $b_0(x)$, $b_1(x)$, $b_2(x)$, $b_3(x)$ and $b_{s+4}(x)$, $s \in \langle 0, \max s \rangle$ denote the transfer functions. The quantities ψ_i , ψ'_i , ψ''_i , ψ'''_i stand for the integration constants, referred to the starting point i , see Figs. 14.1 and 14.2, (e.g., $\psi_i = \psi(x)$ for $x = 0$, etc.). Equation (14.13) and the first three derivatives of $\psi(x)$ are condensed to the following matrix equation:

$$\begin{bmatrix} \psi(x) \\ \psi'(x) \\ \psi''(x) \\ \psi'''(x) \end{bmatrix} = \begin{bmatrix} b_0(x) & b_1(x) & b_2(x) & b_3(x) \\ b'_0(x) & b'_1(x) & b'_2(x) & b'_3(x) \\ b''_0(x) & b''_1(x) & b''_2(x) & b''_3(x) \\ b'''_0(x) & b'''_1(x) & b'''_2(x) & b'''_3(x) \end{bmatrix} \cdot \begin{bmatrix} \psi_i \\ \psi'_i \\ \psi''_i \\ \psi'''_i \end{bmatrix} + \overset{\Psi^L}{\begin{bmatrix} \sum_{s=0}^{\max s} \eta_{L,s} b_{s+4}(x) \\ \sum_{s=0}^{\max s} \eta_{L,s} b'_{s+4}(x) \\ \sum_{s=0}^{\max s} \eta_{L,s} b''_{s+4}(x) \\ \sum_{s=0}^{\max s} \eta_{L,s} b'''_{s+4}(x) \end{bmatrix}}. \tag{14.14}$$

Equation (14.14) can be written as

$$\begin{array}{c} \mathbf{\Psi} \\ \left[\begin{array}{c} \psi(x) \\ \psi'(x) \\ \psi''(x) \\ \psi'''(x) \\ \hline 1 \end{array} \right] \end{array} = \overbrace{\begin{array}{c} \mathbf{B} \\ \left[\begin{array}{cccc|c} b_0(x) & b_1(x) & b_2(x) & b_3(x) & \sum_{s=0}^{\max} b_{s+4}(x) \\ b'_0(x) & b'_1(x) & b'_2(x) & b'_3(x) & \sum_{s=0}^{\max} b'_{s+4}(x) \\ b''_0(x) & b''_1(x) & b''_2(x) & b''_3(x) & \sum_{s=0}^{\max} b''_{s+4}(x) \\ b'''_0(x) & b'''_1(x) & b'''_2(x) & b'''_3(x) & \sum_{s=0}^{\max} b'''_{s+4}(x) \\ \hline 0 & 0 & 0 & 0 & 1 \end{array} \right] \end{array}} \cdot \begin{array}{c} \mathbf{\Psi}_i \\ \left[\begin{array}{c} \psi_i \\ \psi'_i \\ \psi''_i \\ \psi'''_i \\ \hline 1 \end{array} \right] \end{array} \quad (14.15)$$

In Eq. (14.15), \mathbf{B} is a matrix, containing the solution functions of Eq. (14.13) and their first three derivatives at x . Thus, the so-called transfer functions for torsion with warping, $\mathbf{\Psi}$, represent a vector, containing the angle of twist and its first three derivatives at x . $\mathbf{\Psi}_i$ is a vector, containing the values of the angle of twist and of its first three derivatives at the starting point i , and $\mathbf{\Psi}^L$ is a load vector. Based on the dependence of $\psi'(x)$, $\psi''(x)$, and $\psi'''(x)$ on $M_T(x)$ and $M_\omega(x)$, the following transfer matrix expression is obtained:

$$\begin{array}{c} \mathbf{Z}_x \\ \left[\begin{array}{c} \psi(x) \\ \psi'_M(x) \\ M_\omega(x) \\ M_T(x) \\ \hline 1 \end{array} \right] \end{array} = \overbrace{\begin{array}{c} \mathbf{A} \\ \left[\begin{array}{cccc|c} A_{1,1}(x) & A_{1,2}(x) & A_{1,3}(x) & A_{1,4}(x) & A_{1,5}(x) \\ A_{2,1}(x) & A_{2,2}(x) & A_{2,3}(x) & A_{2,4}(x) & A_{2,5}(x) \\ A_{3,1}(x) & A_{3,2}(x) & A_{3,3}(x) & A_{3,4}(x) & A_{3,5}(x) \\ A_{4,1}(x) & A_{4,2}(x) & A_{4,3}(x) & A_{4,4}(x) & A_{4,5}(x) \\ \hline 0 & 0 & 0 & 0 & 1 \end{array} \right] \end{array}} \cdot \begin{array}{c} \mathbf{Z}_i \\ \left[\begin{array}{c} \psi_i \\ \psi'_{M,i} \\ \psi_{\omega,i} \\ \psi_{T,i} \\ \hline 1 \end{array} \right] \end{array} \quad (14.16)$$

The transfer matrix \mathbf{A} relates the vector \mathbf{Z}_x to the "static vector" \mathbf{Z}_i . Appendix 14.4 contains a detailed description of these terms.

The kinematic and kinetic variables at node i are characterized by the subscript i . By setting $x = L$ in Eq. (14.16), the dependence of the nodal variables at node j on the ones at node i is obtained. Then, by means of appropriate mathematical operations, the finite element equations for non-uniform torsion are obtained as

$$\begin{array}{c} \mathbf{K} \\ \left[\begin{array}{c} \bar{M}_{T,i} \\ \bar{M}_{\omega,i} \\ M_{T,j} \\ M_{\omega,j} \end{array} \right] \end{array} = \overbrace{\begin{array}{c} \mathbf{K} \\ \left[\begin{array}{cccc} K_{1,1} & K_{1,2} & K_{1,3} & K_{1,4} \\ K_{2,1} & K_{2,2} & K_{2,3} & K_{2,4} \\ K_{3,1} & K_{3,2} & K_{3,3} & K_{3,4} \\ K_{4,1} & K_{4,2} & K_{4,3} & K_{4,4} \end{array} \right] \end{array}} \cdot \begin{array}{c} \mathbf{F} \\ \left[\begin{array}{c} \psi_i \\ \bar{\psi}'_{M,i} \\ \psi_j \\ \bar{\psi}'_{M,j} \end{array} \right] \end{array} + \overbrace{\begin{array}{c} \mathbf{F} \\ \left[\begin{array}{c} F_1 \\ F_2 \\ F_3 \\ F_4 \end{array} \right] \end{array}} \quad (14.17)$$

where

$$\bar{M}_{T,i} = -M_{T,i}, \bar{M}_{\omega,i} = -M_{\omega,i}, \bar{M}_{T_p,i} = -M_{T_p,i}, \bar{M}_{T_s,i} = -M_{T_s,i} \quad (14.18)$$

considering the definitions of positive quantities in the framework of the FEM.

A detailed description of establishing of the finite element equations Eq. (14.17) is made in (Aminbaghai et al, 2019). The finite element matrix \mathbf{K} in Eq. (14.17) is symmetric.

The described solution algorithm was implemented into MATHEMATICA (Wolfram, 2012). Elastostatic analyses were performed for selected thin-walled cantilever FGM beams with open and closed cross-sections in Sect. 14.3. The effects of several longitudinal variation of material properties on the deformation and stresses is studied. The results from the numerical experiments are presented and compared with results obtained by means of the available commercial software. After simple modification, the Eq. (14.17) can be also used for Saint-Venant torsion analysis of FGM beams.

14.3 Numerical Investigation

In this section, the results from elastostatic analysis of cantilever FGM beams with I-cross-sections and hollow cross-sections are presented. The length of the beams, L , is equal to 0.1m. The FGM consists of a mixture of Aluminum and Tungsten (denoted with the indexes m and f). The material properties are listed in Table 14.1. To show the effect of the longitudinal variation of material properties, the variable Young's modulus $E(x)$ and Poisson's ratio $\nu(x)$ are chosen for following three cases.

14.3.1 Case 1 - Polynomial Variation

$$E(x) = E_f + (E_m - E_f) \left(\frac{x}{L}\right)^n, \quad (14.19)$$

$$\nu(x) = \nu_f + (\nu_m - \nu_f) \left(\frac{x}{L}\right)^n, \quad (14.20)$$

where n denotes the power of $\left(\frac{x}{L}\right)$. The expression for the shear modulus reads as

$$G(x) = \frac{E(x)}{2(1 + \nu(x))}. \quad (14.21)$$

Table 14.1

Material properties of the FGM constituents.

	Material properties		
Young's modulus	$E_f = 4.8 \times 10^{11}$	$E_m = 0.69 \times 10^{11}$	Pa
Poisson's ratio	$\nu_f = 0.2$	$\nu_m = 0.33$	-
Shear modulus	$G_f = 2.0 \times 10^{11}$	$G_m = 0.26 \times 10^{11}$	Pa

The axial variation of the material properties for the Case 1 is shown in Figs. 14.3 and 14.4 for $n \in \langle 1,5 \rangle$.

14.3.2 Case 2 - Polynomial Variation

$$E(x) = E_m + (E_f - E_m) \left(\frac{x}{L}\right)^n, \tag{14.22}$$

$$\nu(x) = \nu_m + (\nu_f - \nu_m) \left(\frac{x}{L}\right)^n, \tag{14.23}$$

where n denotes the power of $\left(\frac{x}{L}\right)$. The expression for the shear modulus reads as

$$G(x) = \frac{E(x)}{2(1 + \nu(x))}. \tag{14.24}$$

The axial variation of the material properties is shown in Figs. 14.5 and 14.6 for $n \in \langle 1,5 \rangle$.

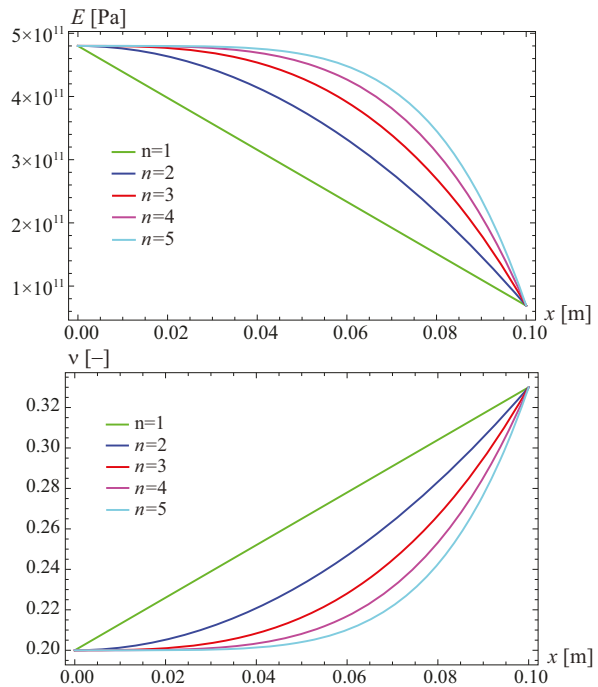


Fig. 14.3 Variation of Young's modulus E and Poisson's ratio ν for different values of n (Case 1).

Fig. 14.4 Variation of the shear modulus G for different values of n (Case 1).

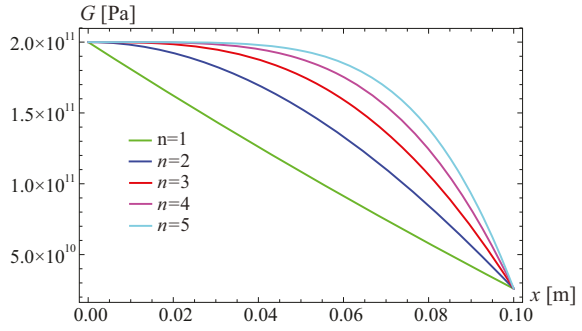
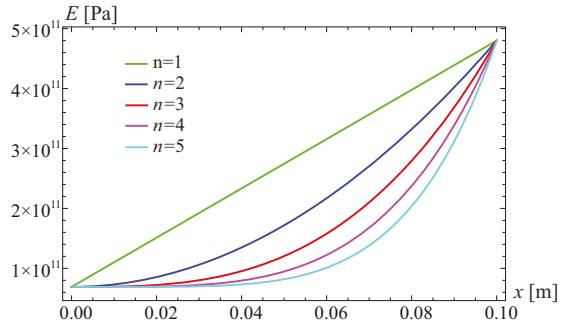


Fig. 14.5 Variation of Young's modulus E for different values of n (Case 2).



14.3.3 Case 3 - Parabolic Variation 1 and 2

For the variation 1, the volume fractions of the constituents are

$$v_f(x) = -400x^2 + 40x, v_m(x) = 400x^2 - 40x + 1. \tag{14.25}$$

Effective Young's modulus E and Poisson's ratio ν is

$$\begin{aligned} E(x) &= E_f v_f(x) + E_m v_m(x) \\ &= 6.9 \times 10^{10} + 1.644 \times 10^{10} x - 1.644 \times 10^{11} x^2 \text{ [Pa]} \\ \nu(x) &= \nu_f v_f(x) + \nu_m v_m(x) = 0.33 + 5.2x + 52x^2 [-]. \end{aligned} \tag{14.26}$$

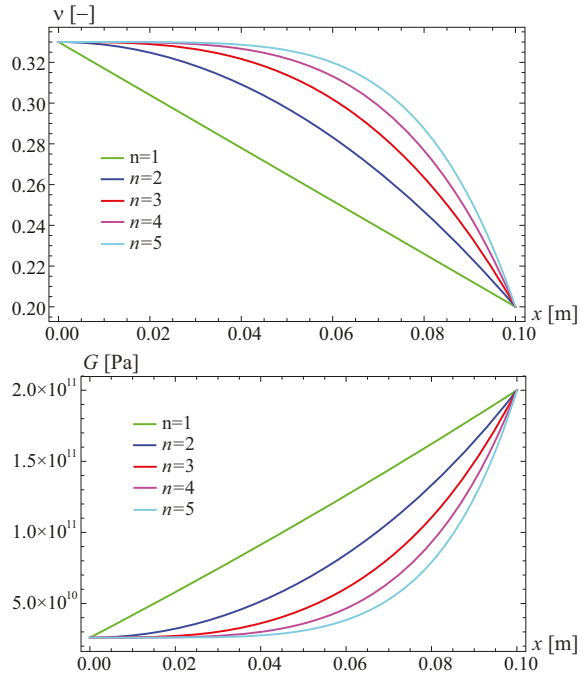
After substitution (14.26) into (14.24), the effective shear modulus G is calculated. The parabolic axial variation of the effective material properties is shown in Figs. 14.7 and 14.8 (blue curves).

For the variation 2, the volume fractions of the constituents are

$$v_m(x) = -400x^2 + 40x, v_f(x) = 400x^2 - 40x + 1. \tag{14.27}$$

Effective Young's modulus E and Poisson's ratio ν is

Fig. 14.6 Variation of the Poisson’s ratio ν and shear modulus G for different values of n (Case 2).



$$\begin{aligned}
 E(x) &= E_f v_f(x) + E_m v_m(x) \\
 &= 4.8 \times 10^{11} + 1.644 \times 10^{10} x - 1.644 \times 10^{11} x^2 \text{ [Pa]} \\
 \nu(x) &= \nu_f v_f(x) + \nu_m v_m(x) = 0.2 + 5.2x - 52x^2 \text{ [-]}.
 \end{aligned}
 \tag{14.28}$$

After substitution (14.28) into (14.24), the effective shear modulus G is calculated. The parabolic axial variation of the effective material properties is shown in Figs. 14.7 and 14.8 (red curves).

Despite the academic nature of the chosen variations of the material properties, it allows for an assessment of the effect of the variability of E and ν on the state of deformation of thin-walled beams, subjected to non-uniform torsion.

14.3.4 Elastostatic Analysis of a Cantilever Beam with an I Cross-section, with Longitudinally Varying Material Properties

The cross-sectional dimensions of the cantilever beam, shown in Fig. 14.9, are given as follows: $b = 0.005$ m, $h_1 = 0.010$ m, $h = h_1 - t = 0.00875$ m, $t = s = 0.00125$ m. In Table 14.2, the cross-sectional parameters required for the analysis are listed. The geometric constants in Table 14.2 were computed by means of ANSYS (ANSYS, 2019), except for the secondary torsion constant and the warping torsion constant,

Fig. 14.7 Variation 1 (blue curve) and 2 (red curve) of Young’s modulus E and Poisson’s ratio ν for Case 3.

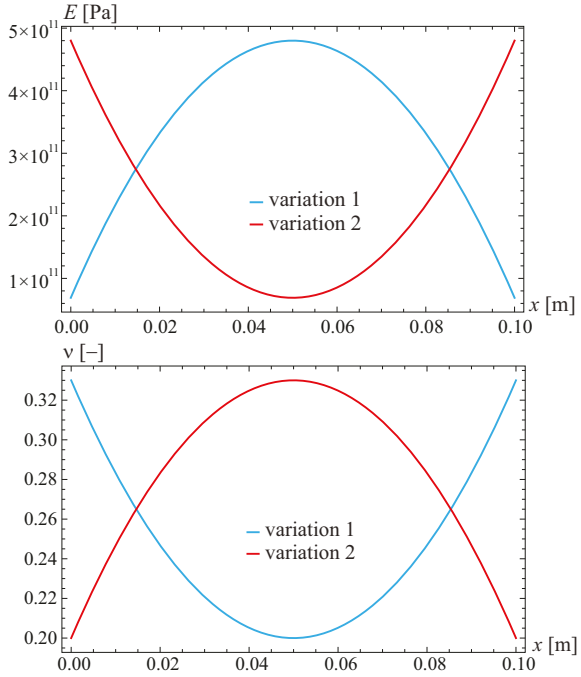
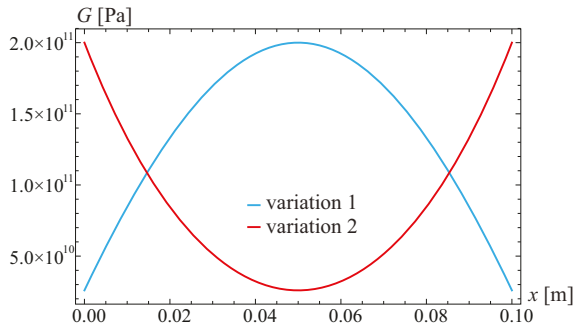


Fig. 14.8 Variation 1 (blue curve) and variation 2 (red curve) of the shear modulus G for the Case 3.



which were calculated by the Thin Tube Theory (TTT) (Rubin, 2005). The beam is loaded by the torsional moment $m_T = Fh = 1 \text{ Nm}$ at point k . The elastostatic torsional analysis of the considered cantilever beam were performed for the three cases of the material properties variation.

The following boundary conditions were specified for warping torsion in Eq. (14.17):

$$\psi|_{x=0} = 0, \quad \psi'_M|_{x=0} = \psi'_{M,i} = 0. \tag{14.29}$$

Remark 14.1. According to the analogy between non-uniform torsion and the Timoshenko beam theory (Rubin, 2005), the following conditions hold at the clamped end of the beam:

- for the case of flexural deformations:

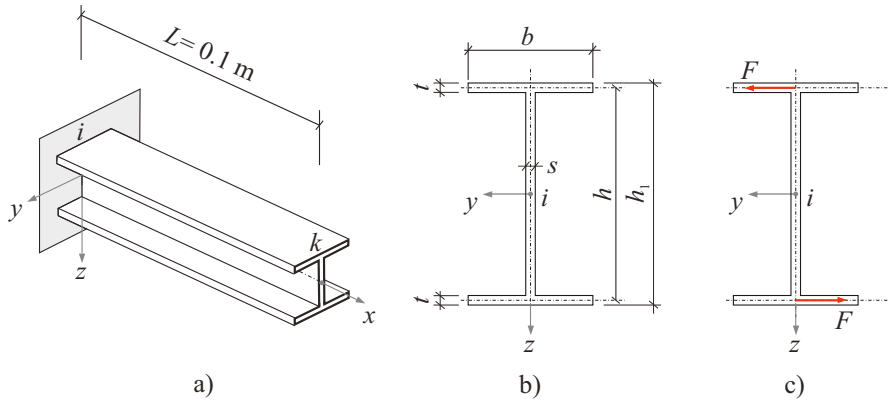


Fig. 14.9. Cantilever beam with an I cross-section: a) system, b) cross-section, c) applied forces ($F = 114.3\text{ N}$).

Table 14.2

Cross-sectional parameters for warping torsion.

Cross-sectional parameters		
Cross-sectional area	$A = 0.21875 \times 10^{-4}$	m^2
Second moment of area about the y-axis	$I_y = 0.28483 \times 10^{-9}$	m^4
Second moment of area about the z-axis	$I_z = 0.27262 \times 10^{-10}$	m^4
Polar moment of area	$I_p = I_y + I_z = 0.31212 \times 10^{-9}$	m^4
Torsional constant	$I_T = 0.1119 \times 10^{-10}$	m^4
Secondary torsion constant	$I_{T_s} = 0.19938 \times 10^{-9}$	m^4
Warping constant	$I_\omega = 0.498 \times 10^{-15}$	m^6

$$\left. \frac{\partial w}{\partial x} \right|_{x=0} = w'_i \neq 0, \text{ but } \varphi|_{x=0} = \varphi_i = 0, \text{ and}$$

- for the case of warping deformations:

$$\left. \frac{\partial \psi}{\partial x} \right|_{x=0} = \psi'_i \neq 0, \text{ but } \left. \frac{\partial \psi'_M}{\partial x} \right|_{x=0} = \psi'_{M,i} = 0,$$

where $w = w(x)$ is the deflection and $\varphi = \varphi(x)$ is the angle of rotation of the cross-section about the y-axis.

14.3.4.1 Elastostatic Analysis of a Cantilever Beam with an I Cross-section, with Longitudinally Varying Material Properties for the Case 1 and Case 2

The elastostatic torsional analyses were performed by means of:

- one warping torsion FGM beam finite element, simplified for Saint-Venant torsion (FGM SV), one warping torsion beam finite element with STMDE (FGM-WT with STMDE) and for warping torsion without STMDE (FGM-WT without STMDE);
- a very fine mesh (500 finite elements) of WT BEAM finite elements, with the STMDE included (Murín et al, 2014) and BEAM 188 WR finite elements with option Warping Restained (ANSYS, 2019), with constant material properties obtained as the average values of their variation over the length of each finite beam element (Figs. 14.3-14.6);
- a very fine mesh of 3D SOLID186 finite elements (850500 finite elements), implemented into the commercial software ANSYS (2019), used for stress evaluation and for comparison of the results with the ones obtained by the FGM-WT beam finite element. In the SOLID186 FE model, all degrees of freedom of the nodes at the clamped end of the beam were restrained. At the free end of the beam, the torsional moment $M_T = Fh = 1 \text{ Nm}$ with $F = 114.3 \text{ N}$ was applied, as shown in Fig. 14.9c;
- a very fine mesh of SHELL181 finite elements (17700 elements), implemented into the commercial software ANSYS (2019). The beam is loaded at its free end in the same way as in Fig. 14.9c.

Results of the analyses for the clamped and the free end of the beam, i.e. at nodes i and k in are drawn in Figs. 14.10-14.14 for the Case 1 and Case 2. Numerical results of the analyses for the Case 1 are listed in Table 14.3.

As shown in Table 14.3, the results for the Case 1, obtained by all of the warping torsion beam finite elements (WT) and SHELL181 elements (ANSYS, 2019), agree very well. The STMDE is marginal for this type of cross-section. The FGM SV solution for the angle of twist gives slightly different results, because the warping torsion effect for open cross-section beams on the stress state is significant, whereas. This fact is verified by the torsional analysis of such beams with constant material properties. Plots of the longitudinal distribution of the angle of twist, ψ [rad], for the case of non-uniform torsion of the investigated cantilever are shown in Figure 14.10. As expected, the variation of material properties influences the angle of twist

Fig. 14.10 Angle of twist, ψ [rad], for non-uniform torsion of the cantilever beam with an I cross-section, ($x \in \langle 0, L \rangle$), for the Case 1 and Case 2 for $n \in \langle 1, 5 \rangle$, and for $n = 0$ (constant material properties equal to the ones of Tungsten for the Case 1 and of Aluminum for the Case 2).

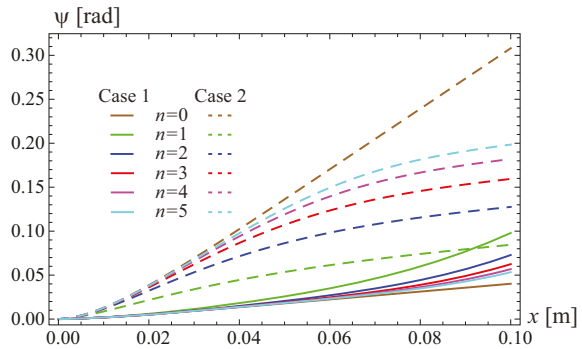


Table 14.3

Angle of twist and internal moments, calculated by FGM-WT with and without STDME, WT BEAM, and SHELL181 finite elements in the expression for the material properties, for the Case 1 with $n \in \langle 1, 5 \rangle$ and for the case of $n = 0$ (constant material properties equal to the ones of Tungsten).

Variables	n	FGM SV	FGM-WT with STMDE/ SHELL181 ANSYS (2019)	WT BEAM Murín et al (2014)	FGM-WT without STMDE
ψ_k [rad]	0	0.044	0.040/0.0420	0.042	0.040
	1	0.108	0.098/0.102	0.098	0.098
	2	0.082	0.073/0.074	0.073	0.072
	3	0.072	0.062/0.064	0.062	0.062
	4	0.066	0.057/0.058	0.057	0.056
	5	0.062	0.053/0.055	0.053	0.053
$\psi'_{M,k}$ [rad/m]	0	-	0.447	0.447	0.477
	1	-	2.169	2.169	2.190
	2	-	1.690	1.690	1.711
	3	-	1.423	1.423	1.442
	4	-	1.250	1.250	1.267
	5	-	1.129	1.129	1.144
$M_{\omega,i}$ [kNm ²]	0	-	-1.006×10^{-5}	-1.006×10^{-5}	1.003×10^{-5}
	1	-	-1.072×10^{-5}	-1.072×10^{-5}	1.099×10^{-5}
	2	-	-1.024×10^{-5}	-1.024×10^{-5}	1.052×10^{-5}
	3	-	-1.012×10^{-5}	-1.012×10^{-5}	-1.039×10^{-5}
	4	-	-1.012×10^{-5}	-1.009×10^{-5}	-1.036×10^{-5}
	5	-	-1.009×10^{-5}	-1.007×10^{-5}	-1.035×10^{-5}
$M_{T\rho,i}$ [kNm]	0	-	5.3140×10^{-5}	5.3141×10^{-5}	0.0
	1	-	5.3141×10^{-5}	5.3141×10^{-5}	0.0
	2	-	5.3141×10^{-5}	5.3141×10^{-5}	0.0
	3	-	5.3140×10^{-5}	5.3141×10^{-5}	0.0
	4	-	5.3141×10^{-5}	5.3141×10^{-5}	0.0
	5	-	5.3141×10^{-5}	5.3141×10^{-5}	0.0
$M_{T\rho,k}$ [kNm]	0	-	9.998×10^{-4}	9.998×10^{-4}	9.999×10^{-4}
	1	-	6.495×10^{-4}	6.530×10^{-4}	6.551×10^{-4}
	2	-	5.177×10^{-4}	5.233×10^{-4}	4.965×10^{-4}
	3	-	4.442×10^{-4}	4.514×10^{-4}	4.185×10^{-4}
	4	-	3.969×10^{-4}	4.052×10^{-4}	3.679×10^{-4}
	5	-	3.635×10^{-4}	3.729×10^{-4}	3.322×10^{-4}
$M_{T\sigma,i}$ [kNm]	0	-	9.469×10^{-4}	9.469×10^{-4}	0.001
	1	-	9.469×10^{-4}	9.469×10^{-4}	0.001
	2	-	9.469×10^{-4}	9.469×10^{-4}	0.001
	3	-	9.469×10^{-4}	9.469×10^{-4}	0.001
	4	-	9.469×10^{-4}	9.469×10^{-4}	0.001
	5	-	9.469×10^{-4}	9.469×10^{-4}	0.001
$M_{T\sigma,k}$ [kNm]	0	-	1.543×10^{-7}	1.543×10^{-7}	1.255×10^{-7}
	1	-	3.505×10^{-4}	3.469×10^{-4}	3.449×10^{-4}
	2	-	4.822×10^{-4}	4.766×10^{-4}	5.034×10^{-4}
	3	-	5.557×10^{-4}	5.486×10^{-4}	5.815×10^{-4}
	4	-	6.031×10^{-4}	5.948×10^{-4}	6.321×10^{-4}
	5	-	6.365×10^{-4}	6.270×10^{-4}	6.678×10^{-4}

Fig. 14.11 Part of the bicurvature, ψ'_M [rad/m], resulting from the bimoment of the cantilever beam of the I cross-section for the Case 1, ($x \in (0, L)$ and $n \in (1, 5)$).

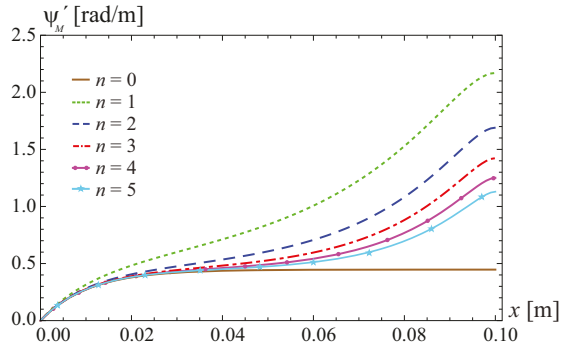


Fig. 14.12 Bimoment M_ω [kNm²] for the cantilever beam with an I cross-section for the Case 1 and Case 2, ($x \in (0, L)$ and $n \in (1, 5)$).

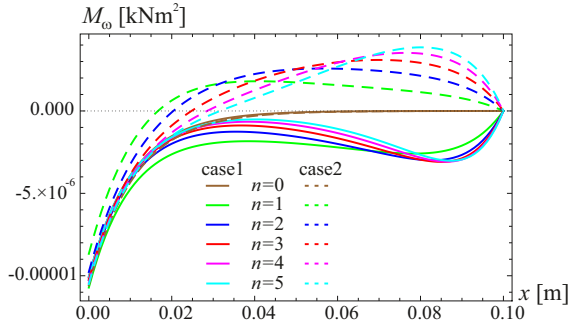
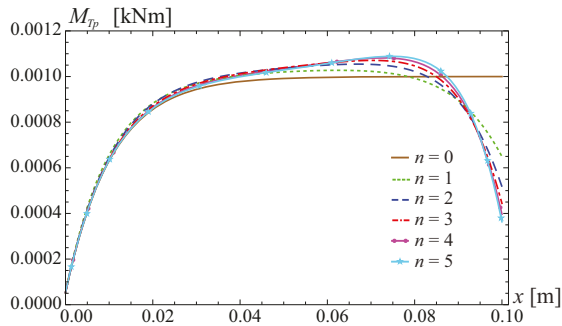


Fig. 14.13 Primary torsional moment, M_{Tp} [kNm], for the cantilever beam with an I cross-section for the Case 1, ($x \in (0, L)$).

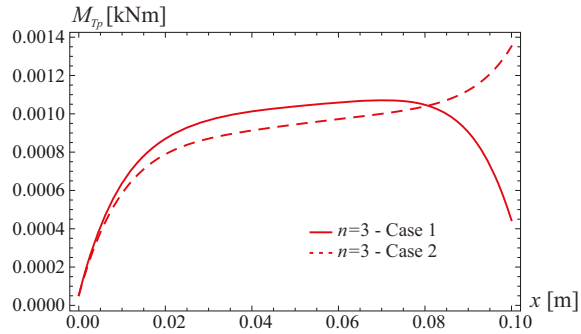


significantly. For the Case 2 and $n = 0$ (the beam is made of Aluminum only), the twist angle exceeds permissible values of only academic significance.

Figure 14.11 shows the longitudinal variation of the part of the bicurvature, ψ'_M [rad/m] for the Case 1, resulting from the bimoment of the cantilever beam of the I cross-section for the Case 1. This quantity was computed by the FGM-WT with STMDE.

Figure 14.12 shows the longitudinal variation of the bimoment, M_ω [kNm²], for the cantilever beam with an I cross-section for the Case 1 and Case 2. This quantity was computed by the FGM-WT with STMDE. The maximum value of the bimoment, which occurs at the clamped end of the beam, is not significantly influenced by the

Fig. 14.14 Primary torsional moment, M_{Tp} [kNm], for the cantilever beam with an I cross-section for the Case 1 and Case 2 and for $n = 3$, ($x \in (0, L)$).



considered variability of the material properties. As shown in Fig. 14.12, longitudinal variation of the material properties increases significantly the bimoment in the field of the beam.

In comparison to the case with constant material properties, i.e. for $n = 0$, the influence of the variability of the material properties increases with increasing distance from the clamped end of the beam (in some parts of the beam field). For the Case 1, the strong increase of the bimoment correlates with the strong decrease of E and G close to the free end of the beam. It holds for the considered case only if the material properties vary such that the warping effect is increased, since warping is increasing along the length. For the Case 2, the strong increase of E and G changes surprisingly the sign of the bimoment in the field of the beam.

Figure 14.13 shows the longitudinal variation of the primary torsional moment, M_{Tp} [kNm], for the cantilever beam with an I cross-section for the Case 1. This quantity was computed by the FGM-WT with STMDE. Figure 14.14 separately shows the longitudinal variation of the primary torsional moment, M_{Tp} [kNm], for the cantilever beam with an I cross-section, computed by the FGM-WT BEAM finite elements with STMDE for the Case 1 and Case 2 for parameter $n = 3$.

Figure 14.15 shows the longitudinal variation of the secondary torsional moment, M_{Ts} [kNm], for the cantilever beam with an I cross-section, computed by the FGM-WT BEAM finite elements with STMDE for the Case 1. Figure 14.16 separately shows the longitudinal variation of the secondary torsional moment, M_{Ts} [kNm],

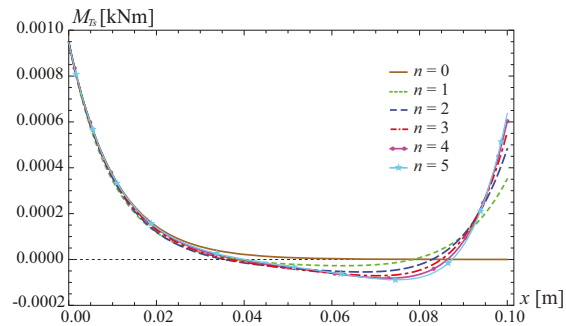
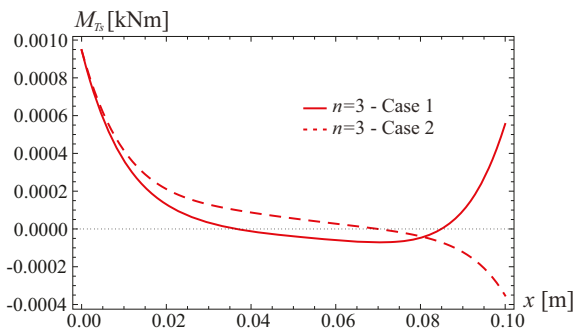


Fig. 14.15 Secondary torsional moment, M_{Ts} [kNm], for the cantilever beam with an I cross-section for the Case 1, ($x \in (0, L)$).

Fig. 14.16 Secondary torsional moment, M_{T_s} [kNm], for the cantilever beam with an I cross-section for the Case 1 and Case 2 and for $n = 3$, ($x \in (0, L)$).



for the cantilever beam with an I cross-section, computed by the FGM-WT BEAM finite elements with STMDE for the Case 1 and Case 2 for parameter $n = 3$.

The maximum value of the primary and secondary torsional moment, which occurs at the clamped end of the beam, is not influenced by the considered variability of the material properties. As shown in Figs. 14.13-14.16, longitudinal variation of the material properties influences significantly the primary and secondary torsional moment in the field of the beam.

For all of the investigated cases, $M_T(x) = M_{T_p}(x) + M_{T_s}(x) = 1 \text{ Nm}$, the variation of the angle of twist and of the internal moments, obtained by the fine mesh of WT BEAM finite elements, is very close to the ones shown in Figs. 14.10-14.16. Therefore, the diagrams concerned are not shown. This confirms the efficiency and the accuracy of the FGM-WT BEAM finite elements with STMDE.

The normal stresses in consequence of the bimoment and the torsional shear stresses, in the cross-section at the clamped end of the beam, were computed by the TTT. For example, as shown in Table 14.3 for $n = 1$ (Case 1), the cross-section at the clamped end i was subjected to the bimoment

$$M_{\omega,i} = -1.072 \times 10^{-5} \text{ kNm}^2 = -0.01072 \text{ Nm}^2,$$

the primary torsional moment

$$M_{T_p,i} = 5.314 \times 10^{-5} \text{ kNm} = 0.05314 \text{ Nm},$$

and the secondary torsional moment

$$M_{T_s,i} = 9.469 \times 10^{-4} \text{ kNm} = 0.9496 \text{ Nm}.$$

According to Rubin (2005), the maximum bimoment normal stress at the corners of the clamped cross-section was obtained as

$$\sigma_{\omega,i} = \pm \frac{M_{\omega,i}}{I_{\omega}} \omega_R = \pm 235.2 \text{ MPa},$$

where

$$|\omega_R| = \frac{bh}{4} = 10.94 \text{ mm}^2$$

is the warping ordinate at these points (Rubin, 2005), Fig. 14.17d. The figure does not explicitly show this quantity. The maximum shear stress, resulting from the secondary torsion moment, was obtained as

$$\tau_{s,1} = 1.5 \frac{M_{T_{s,i}}}{thb} = 25.97 \text{ MPa},$$

Fig. 14.17c. The shear stresses, resulting from the primary torsion moment, were obtained as

$$\tau_{p,1} = \tau_{p,2} = \frac{M_{T_P}}{I_T} t = 5.47 \text{ MPa},$$

Fig. 14.17b. According to Figs. 14.17b and 14.17c, the total shear stresses are given as follows:

$$\tau_1^{\text{total}} = \tau_{s,1} + \tau_{p,1} = 31.44 \text{ MPa}, \tau_2^{\text{total}} = \tau_{p,2} = 5.47 \text{ MPa}.$$

The results for the stresses at the clamped end of the beam have shown that the normal stresses, resulting from warping, are much higher than the torsional shear stresses. The longitudinal variation of the maximum bimoment normal stresses is proportional to the longitudinal variation of the bimoment shown in Fig. 14.12. The longitudinal variation of the maximum bimoment normal stresses along the upper left beam edge for the Case 1, computed by the FGM-WT with STMDE for $n \in (0,5)$, is shown in Fig. 14.18. Almost identical distributions of these stresses are obtained by the WT BEAM finite elements with STMDE (Murín et al, 2014). Figure 14.18 shows that because of the variation of the material properties, the bimoment normal stresses do not only occur at the clamped end of the beam. At the free end of the beam, there is only one material, namely, Aluminum. Its elasticity modulus is much smaller than the one of tungsten. The strong increase of the angle of twist causes

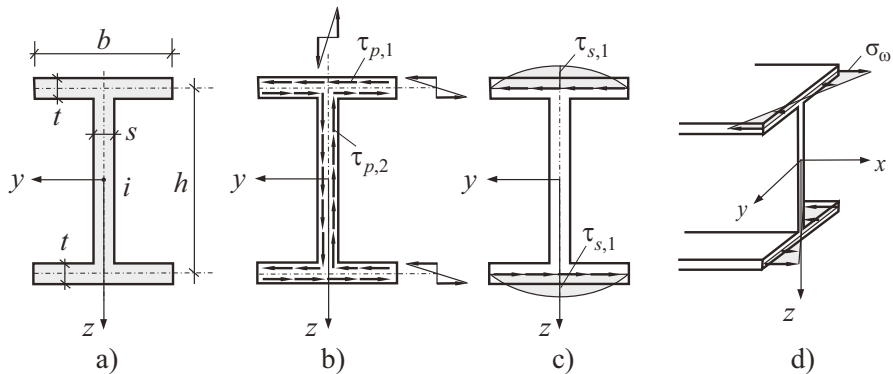
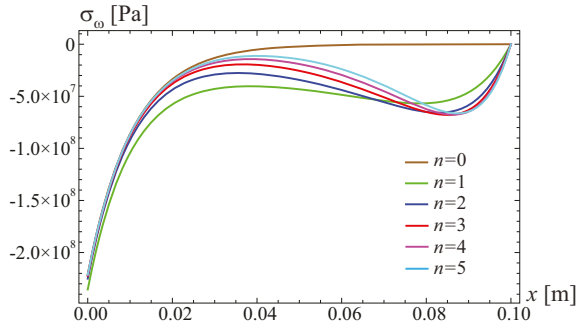


Fig. 14.17. I cross-section: a) Cross-section, b) primary shear stresses, c) secondary shear stresses, d) axial stresses in consequence of warping.

Fig. 14.18 Distribution of the warping normal stresses along the upper left beam edge for Case 1, $n \in \langle 0, 5 \rangle$.



normal stresses resulting from warping also in the vicinity of the free end of the beam. The longitudinal variation of the maximum bimoment normal stresses along the upper left beam edge for the Case 2, computed by the FGM-WT with STMDE for $n \in \langle 0, 5 \rangle$, is shown in Fig. 14.19.

To verify the obtained results, numerical analyses of the beam were performed with very fine meshes of BEAM188 WR finite elements (500 elements), SOLID186 finite elements (85500 elements) and SHELL181 finite elements (17604 elements), ANSYS (2019). The results obtained for the Case 1 and for $n = 1$ are compared in Tables 14.4 and 14.5 and Figs. 14.20-14.21.

Table 14.4 shows that the maximum values of the angle of twist, obtained by different analysis tools, agree very well. For the solid and the shell finite element model, the twist angle at the free end of the beam was computed from the displacements of the points on the symmetry axes of the I-profile.

Fig. 14.19 Distribution of the warping normal stresses along the upper left beam edge for Case 2, $n \in \langle 0, 5 \rangle$.

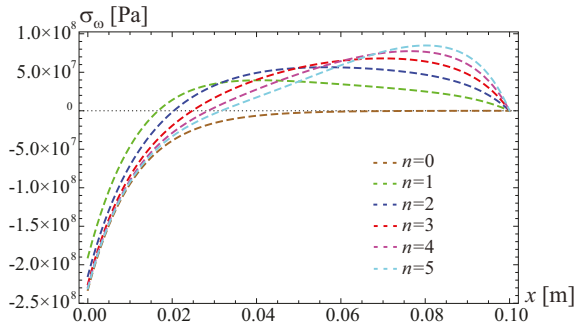


Table 14.4

Comparison of results for the Case 1 and $n = 1$.

Analysis tool	FGM-WT with STMDE	WT BEAM [7]	SOLID186 [3]	SHELL181 [3]
ψ_k [rad]	0.098	0.098	0.096	0.102
$\sigma_{\omega,i}$ [MPa]	± 235.2	± 235.2	$\pm (375.8/244.5)$	$\pm (308.9/232)$

Table 14.5

Maximum values of the normal stresses at both ends of the beam, in MPa, for the Case 1 and $n = 1$.

Case/x [m]	clamped end	free end
Green curve - SOLID186	-339.6	-42.6
Dotted blue curve - SOLID186	-244.5	39.5
Dotted red curve - SOLID186	-375.8	1.6
Dashed orange curve - SHELL181	-308.9/-232.0	3.4
Dashed black curve - FGM-WT with STMDE	-235.2	0

Fig. 14.20 Angle of twist, ψ [rad], for non-uniform torsion of the cantilever beam with an I cross-section, ($x \in (0, L)$), for the Case 1 and $n = 3$.

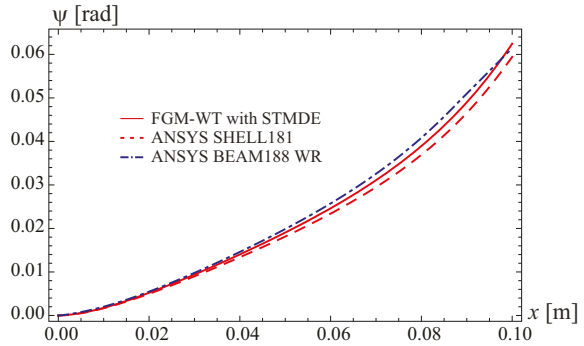
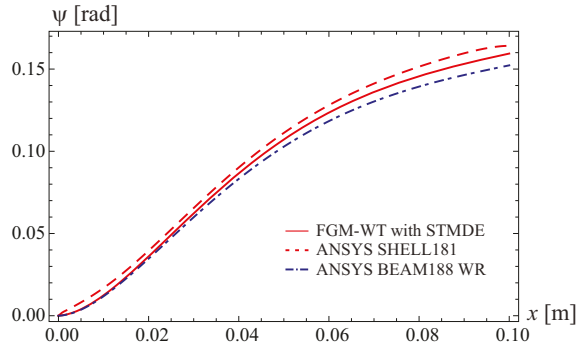


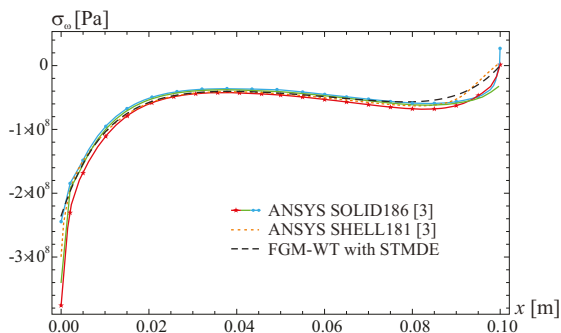
Fig. 14.21 Angle of twist, ψ [rad], for non-uniform torsion of the cantilever beam with an I cross-section, ($x \in (0, L)$), for the Case 2 and $n = 3$.



Figures 14.20-14.21 show distribution of the twist angles for the Case 1 and Case 2 for $n = 3$. They were calculated by a very fine mesh BEAM188 WR finite elements (ANSYS, 2019).

Figure 14.22 shows distributions of the maximum longitudinal normal stresses for the Case 1 and linearly varying material properties ($n = 1$). They were calculated by a very fine mesh of SOLID186 finite elements (ANSYS, 2019). The green curve refers to a line at a distance of 0.1 mm from the edge of the longitudinal upper left flange of the beam; the dotted blue curve refers to the longitudinal middle axis of the flange thickness t ; the dotted red curve refers to the edge of the longitudinal upper left flange of the beam. The maximum warping normal stress distribution,

Fig. 14.22 Distribution of the maximum normal stresses along the upper left side of the beam flange for linearly varying material properties for the Case 1 and $n = 1$.



based on the FGM-WT BEAM finite elements with STMDE, is marked by a dashed black curve. The dashed orange curve shows the normal stress distribution along the longitudinal bottom edge of the left part of the flange, calculated by the SHELL181 finite elements (ANSYS, 2019).

Maximum values of the normal stresses, for the Case 1 and $n = 1$, at both ends of the beam are listed in Table 14.5. Figure 14.22 shows good agreement of the authors' results (dashed black curve) with the ones obtained by the SOLID186 finite elements (dotted blue curve). According to Table 14.5, the percentage difference of the maximum value of the normal stresses at the clamped end (-244.5 for the SOLID 186 element and -235.2 for the authors' element) is less than 4%.

Very good agreement of the normal stresses along the beam was obtained for all of the investigated cases. Small discrepancies of the results occurred in the vicinity of the free end of the beam. Fig. 14.22 shows a significant difference of the results at the clamped end, obtained by the SOLID186 finite elements (dotted red curve) and the SHELL181 finite elements (dashed orange curve).

The maximum value of the normal stress at the sharp corners of the I-profile obtained by the SOLID186 finite elements, (± 375.8 MPa), and the SHELL181 finite elements, (± 308.9), are strongly affected not only by a numerical singularity, but also by the different type of the finite elements and the way of satisfaction of the boundary conditions. Therefore, they are not relevant to the evaluation of the numerical results. As shown in Fig. 14.26, the normal stress in the middle of the flange thickness t , obtained by the SHELL181 finite elements, is above ± 232 MPa. It agrees very well with the authors' FGM-WT with STMDE beam solution. According to Fig. 14.18, the distribution of the warping normal stresses at the clamped end for $n > 1$ is very similar to the distribution for $n = 1$. Figures 14.23-14.24 show the warping normal stress distribution for the Cases 1 and 2, and $n = 3$. Additionally to Fig. 14.22, the solution results (the dot-dashed blue curve), which were obtained by BEAM188 finite element with option warping restrained (ANSYS, 2019), are shown in Fig. 14.23 and Fig. 14.24.

The distribution of the normal stresses for the Case 1 and of linearly varying material properties, calculated by SOLID186 finite elements along the flange width b , is shown in Fig. 14.25. The green curve refers to a line, at a distance of about 0.4 mm from the upper edge of the clamped flange, in the longitudinal direction of

Fig. 14.23 Distribution of the maximum normal stresses along the upper left side of the beam flange for for the Case 1, ($n = 3$).

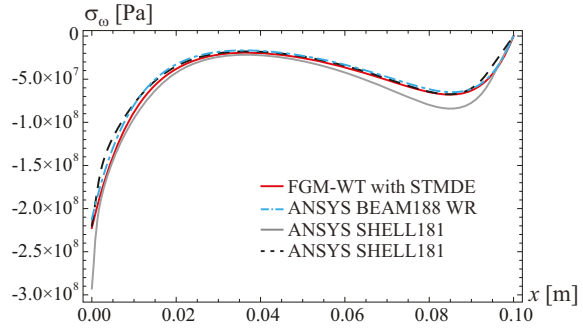


Fig. 14.24 Distribution of the maximum normal stresses along the upper left side of the beam flange for for the Case 2, ($n = 3$).

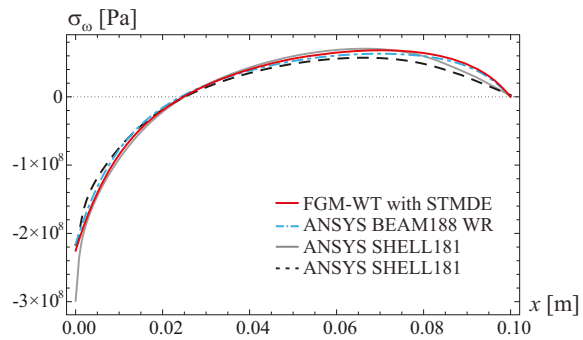
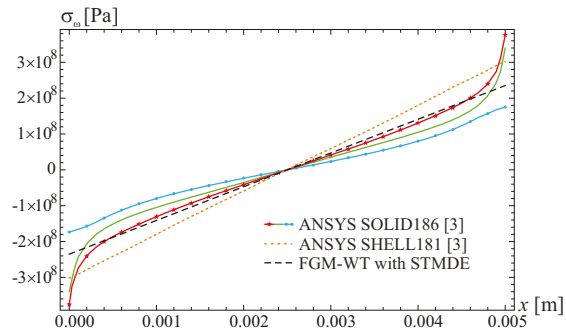


Fig. 14.25 Normal stresses for the Case 1 and $n = 1$ along the width b of the upper flange at the clamped end of the beam.



the beam; the dotted blue curve refers to the middle axis of the flange thickness t ; the dotted red curve refers to the upper edge of the clamped flange. The distribution of the normal stresses along the upper edge of the flange of the clamped end, calculated by SHELL181 finite elements, is illustrated by the dashed orange curve. The stress distributions computed by the SOLID186 finite elements, i.e. the green and the red curves, are non-linear, which is inconsistent with the present assumption of the TTT (see Fig. 14.17d). The linear distribution, obtained by the FGM-WT BEAM finite elements with STMDE, is shown as a black dashed curve, located between the blue and the orange curve. This situation is partially caused by the known fact that the stresses at the sharp corners of the structure, calculated by solid finite elements, are inaccurate. With increasing refinement of the mesh, the discrepancy of the results

for points on sharp corners increases. Another possible reason of the discrepancy is that the boundary conditions of the solid finite elements constrain the transverse and the lateral displacements of the nodes of the cross-sectional area at the clamped end of the beam.

The maximum values of the normal stresses at both ends of the flange width are listed in Table 14.6. Figure 14.26 shows the distribution of the normal stresses at the cross-section of the clamped end of the beam for the Case 1 a $n = 1$, calculated by SHELL181 finite elements. The maximum value of the normal stresses in the middle of the flange thickness is a little smaller than ± 240 MPa. Thus, it is very close to the authors’ result of ± 235.2 MPa, obtained by the FGM-WT beam finite elements.

Finally, the equivalent von Mises stresses at the clamped end of the beam are evaluated by the different finite elements and compared. Figure 14.27 shows the distribution of these stresses, obtained by the SHELL181 finite elements.

If the equivalent von Mises stresses at the sharp corners of the cross-section are not taken into account because of the singularity of the stresses obtained by the SHELL181 finite elements, then the relevant normal stress is the one in the middle of the flange thickness t . It is above 232 MPa. This value corresponds to the average value of the von Mises stresses over the thickness of the flange t .

Table 14.6

Maximum values of the normal stresses, in MPa, for the Case 1 and $n = 1$, along the upper flange width b at the clamped end of the beam.

Case/x [m]	0	0.005
Green curve - SOLID186	-339.6	339.6
Dotted blue curve - SOLID186	-170.4	170.4
Dotted red curve - SOLID186	-375.8	375.8
Dashed orange curve - SHELL181	-308.9	308.9
Dashed black curve - FGM-WT with STMDE	-235.2	235.2

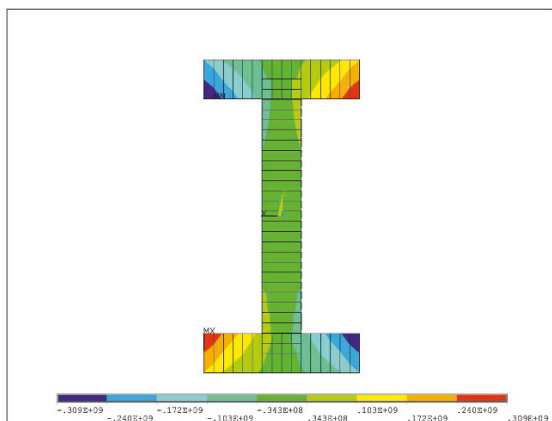
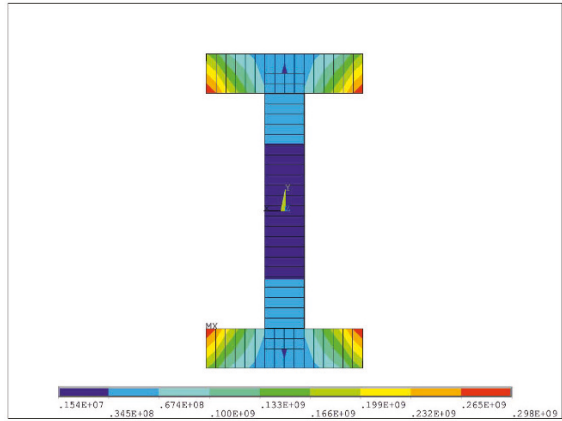


Fig. 14.26 Distribution of the normal stresses computed by SHELL181 finite elements (ANSYS, 2019) for the Case 1 and $n = 1$.

Fig. 14.27 Von Mises stresses at the clamped end of the beam for the Case 1 and $n = 1$.



According to Fig. 14.17, the shear stress at the corners is

$$\tau_{p,1} = \tau_{1,total} = \frac{M_{Tp}}{I_T} t = 5.47 \text{ MPa.}$$

Thus, the maximum value of the von Mises stresses at the corners is obtained as

$$\sigma_s = \sqrt{\sigma_{\omega,i}^2 + 3\tau_{1,total}^2} = 235.4 \text{ MPa.}$$

This comparison shows that the results obtained by the authors' element FGM-WT agree well with the ones obtained by the SHELL181 beam finite elements.

14.3.4.2 Elastostatic Analysis of a Cantilever Beam with an I Cross-section, with Longitudinally Varying Material Properties for the Case 3

The elastostatic torsional analyses were performed by means of

- one warping torsion beam finite element with STMDE (FGM-WT with STMDE);
- a very fine mesh (500 finite elements) of BEAM188 finite elements, with the option warping restrained (WR) (ANSYS, 2019), with constant material properties obtained as the average values of their variation over the length of each finite beam element according Figs. 14.7-14.8;
- a very fine mesh of SHELL181 finite elements (17700 elements), implemented into the commercial software ANSYS (ANSYS, 2019). At the free end of the beam, the torsional moment $M_T = Fh = 1 \text{ Nm}$ with $F = 114.3 \text{ N}$ was applied, as shown in Fig. 14.9c.

Results of the analyses for the clamped and the free end of the beam, i.e. at nodes i and j in are drawn in Figs. 14.28-14.31 for the Case 3 with the variations 1 and

Fig. 14.28 Angle of twist, ψ [rad], for non-uniform torsion of the cantilever beam with an I cross-section, ($x \in (0, L)$), for the Case 3 and the variations 1 and 2.

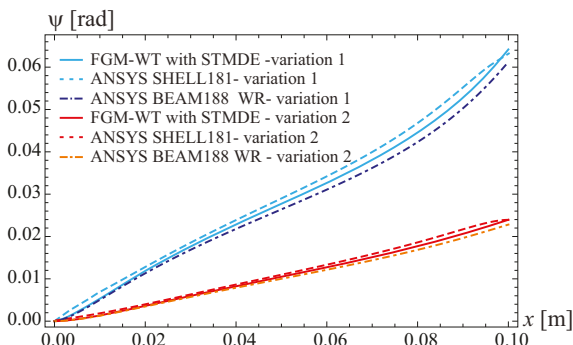


Fig. 14.29 Bimoment M_ω kNm^2 for the cantilever beam with an I cross-section for the Case 3, ($x \in (0, L)$), and the variations 1 and 2.

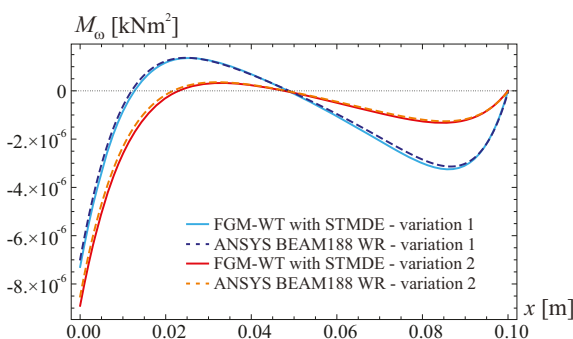
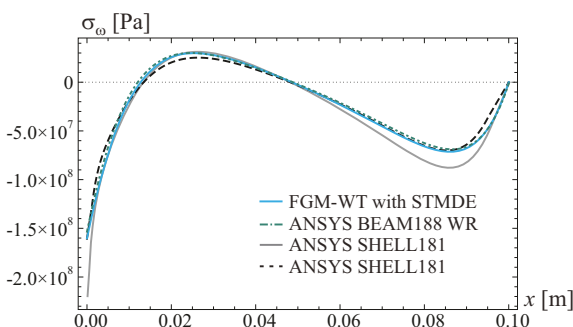


Fig. 14.30 Distribution of the warping normal stresses along the upper left beam edge for Case 3, variation 1.



2. Numerical results of the analyses for the Case 3 are listed in Tables 14.7-14.9. As shown in Tab. 14.7, the results for the maximal twist angle, obtained by all of the warping torsion beam finite elements and SHELL181 elements (ANSYS, 2019), agree very well. Plots of the longitudinal distribution of the angle of twist, ψ [rad], for the case of non-uniform torsion of the investigated cantilever are shown in Figure 14.28. As expected, the variation of material properties influences the angle of twist significantly. A very good agreement of all the distributions is obtained.

Figure 14.29 shows the longitudinal distribution of the bimoment, M_ω kNm^2 , for the cantilever beam with an I cross-section for the Case 3. This quantity was

Fig. 14.31 Distribution of the warping normal stresses along the upper left beam edge for Case 3, variation 2.

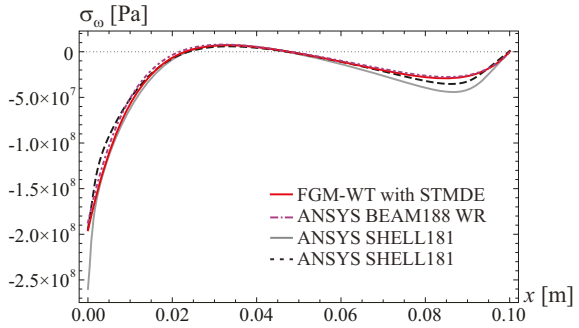


Table 14.7

Angle of twist, calculated by FGM-WT with STDME, BEAM188 WR, and SHELL181 finite elements in the expression for the material properties, for the Case 3.

Twist angle ψ [rad] for:	variation 1	variation 2
FGM-WT with STMDE	0.064	0.024
BEAM188 WR (ANSYS, 2019)	0.061	0.023
SHELL181 (ANSYS, 2019)	0.062	0.024

Table 14.8

Normal stresses, calculated by FGM-WT with STDME, BEAM188 WR, and SHELL181 finite elements for the Case 3, variation 1.

x [m]	0	0.026	0.086	0.1
FGM-WT with STMDE - blue curve	-160.2	29.8	-71.4	0.0
BEAM188 WR - dashed green curve	-153.4	30.0	-68.8	-1.1
SHELL181 - grey curve	-219.4	31.5	-87.6	-0.1
SHELL181 - dashed black curve	-160.6	25.2	-70.0	-0.1

Table 14.9

Normal stresses, calculated by FGM-WT with STDME, BEAM188 WR, and SHELL181 finite elements for the Case 3, variation 2.

x [m]	0	0.033	0.08	0.1
FGM-WT with STMDE - red curve	-195.5	7.14	-29.1	0.0
BEAM188 WR - dashed violet curve	-187.1	7.8	-27.6	-0.5
SHELL181 - grey curve	-259.9	7.4	-44.1	-0.6
SHELL181 - dashed black curve	-194.7	5.9	-35.5	0.8

computed by the FGM-WT with STMDE and BEAM188 WR (ANSYS, 2019). An excellent agreement of all the distributions is obtained.

The normal stresses in consequence of the bimoment and the torsional shear stresses, in the cross-section at the clamped end of the beam, were computed by the

TTT. For example, as shown in Fig. 14.29 for the variation 1, the cross-section at the clamped end i was subjected to the bimoment, calculated by FGM-WT with STMDE, $M_{\omega,i} = -7.293 \times 10^{-6} \text{ kNm}^2 = -0.00729 \text{ Nm}^2$. Its value, calculated by BEAM188 WR, is equal to $-6.84 \times 10^{-6} \text{ kNm}^2$. From our calculations, the primary torsional moment $M_{Tp,i} = 5.314 \times 10^{-5} \text{ kNm} = 0.05314 \text{ Nm}$, and the secondary torsional moment $M_{Ts,i} = 9.469 \times 10^{-4} \text{ kNm} = 0.9469 \text{ Nm}$. The same values of the primary and secondary torsional moment at the clamped end of the beam were obtained as in previously analysed cases.

According to Rubin (2005) and for the bimoment calculated by FGM-WT beam with STMDE, the maximum normal stress at the corners of the clamped cross-section was obtained as,

$$\sigma_{\omega,i} = \pm \frac{M_{\omega,i}}{I_{\omega}} \omega_R = \pm 160.2 \text{ MPa}$$

where

$$|\omega_R| = \frac{bh}{4} = 10.94 \text{ mm}^2$$

is the warping ordinate at these points (Rubin, 2005), Fig. 14.17d. The figure does not explicitly show this quantity. The maximum normal stress, calculated from bimoment obtained by BEAM188 WR, is equal to $\pm 153.4 \text{ MPa}$.

The maximum shear stress, resulting from the secondary torsion moment, was obtained as

$$\tau_{s,1} = 1.5 \frac{M_{Ts,i}}{thb} = 25.97 \text{ MPa},$$

Fig. 14.17c. The shear stresses, resulting from the primary torsion moment, were obtained as,

$$\tau_{p,1} = \tau_{p,2} = \frac{M_{Tp}}{I_T} t = 5.47 \text{ MPa},$$

Fig. 14.17b. According to Figs. 14.17b and 14.17c, the total shear stresses are given as follows:

$$\tau_1^{total} = \tau_{s,1} + \tau_{p,1} = 31.44 \text{ MPa}, \quad \tau_2^{total} = \tau_{p,2} = 5.47 \text{ MPa}.$$

The longitudinal variation of the maximum bimoment normal stresses is proportional to the longitudinal variation of the bimoment shown in Fig. 14.29. The longitudinal variation of the maximum normal stresses along the upper left beam edge for the Case 3 and the variation 1 and 2, computed by the FGM-WT with STDME and BEAM188 WR and SHELL181 finite elements, is shown in Figs. 14.30-14.31.

In Figs. 14.30-14.31, two distributions of the normal stresses, obtained by SHELL181 finite elements, are drawn. Distribution of the normal stresses along the upper left edge of the beam is drawn by the grey colour. The dashed black curve refers to a line, at a distance of about 0.4 mm from the upper edge of the clamped flange, in the longitudinal direction of the beam. The values of the maximum normal stresses, in [MPa], for the variation 1, at several distances x from the clamped cross-section, are read in Table 14.8. The values of the maximum normal stresses,

in [MPa], for the variation 2, at several distances x from the clamped cross-section, are read in Table 14.9.

As shown in Figs. 14.30-14.31 and Tables 14.8-14.9, an acceptable conformity of normal stresses was achieved except for the maximum stress at clamped end of the beam. Because of numerical singularity at the sharp corners, the solution by SHELL181 finite elements, (drawn by grey curves), shows a divergent result at the point of the clamping of the edges of the cross-section. The agreement of the distribution of normal stresses, obtained by only one author’s beam finite element, (FGM-WT with STDME), and the distribution obtained, by the very fine mesh of SHELL181 finite elements that drawn along the little shifted line from the edge of the beam, is excellent.

Finally, the equivalent von Mises stresses at the clamped end of the beam are evaluated by the different finite elements and compared for the variation 1. Figure 14.32 shows the distribution of these stresses, obtained by the SHELL181 finite elements.

If the equivalent von Mises stresses at the sharp corners of the cross-section are not taken into account because of the singularity of the stresses obtained by the SHELL181 finite elements, then the relevant normal stress is the one in the middle of the flange thickness t . It is a little bit more than 164 MPa. This value corresponds to the average value of the von Mises stress at the thickness of the flange t .

According to Fig. 14.17, the shear stress at the corners is

$$\tau_{p,1} = \tau_{1,total} = \frac{M_{Tp}}{I_T} t = 5.47 \text{ MPa.}$$

Thus, the maximum value of the von Mises stresses at the corners is obtained as

$$\sigma_s = \sqrt{\sigma_{\omega,i}^2 + 3\tau_{1,total}^2} = 163.6 \text{ MPa.}$$

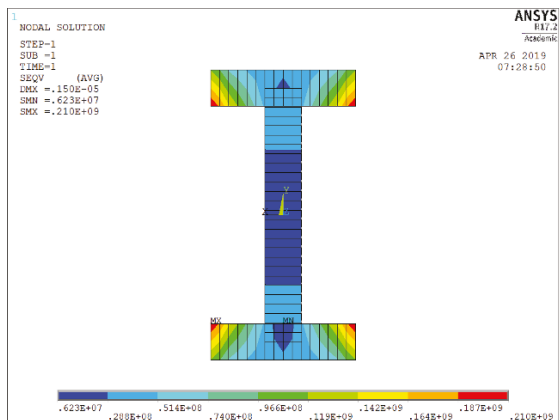


Fig. 14.32 Von Mises stresses at the clamped end of the beam for the Case 3 and the variation 1.

This comparison shows that the results obtained by the authors' beam element FGM-WT with STDME agree very well with the ones obtained by the SHELL181 beam finite elements.

Based on the obtained numerical results, the authors' new beam finite element is considered to be useful for the design of I-beams made of FGM with longitudinally varying material properties. The solution has been obtained with only one FGM-WT with STMDE beam finite element. This is the greatest advantage of this new warping torsion beam finite element.

14.3.5 Elastostatic Analysis of a Cantilever Beam with a Rectangular Hollow Cross-section, with Longitudinally Varying Material Properties

The cross-sectional parameters of the cantilever beam (Fig. 14.33b) are calculated by ANSYS (ANSYS, 2019) and by the TTT (Rubin, 2005). They are listed in Table 14.10. The material properties of the FGM constituents are listed in Table 14.1, and the same longitudinal variations of the material properties and the boundary conditions are considered as in Subsect. 14.3.4.

The elastostatic torsional analyses were performed by means of:

- one warping torsion beam finite element with STMDE (FGM-WT with STMDE) and the FGM SV beam finite elements. The beam is loaded at point k on its free end by a torsional moment $M_T = 1 \text{ Nm}$;
- a very fine mesh (500 finite elements) BEAM188 WR (ANSYS, 2019) and WT BEAM (Murín et al, 2014). The material properties are obtained as average values of their variation over the length of the relevant beam finite element according

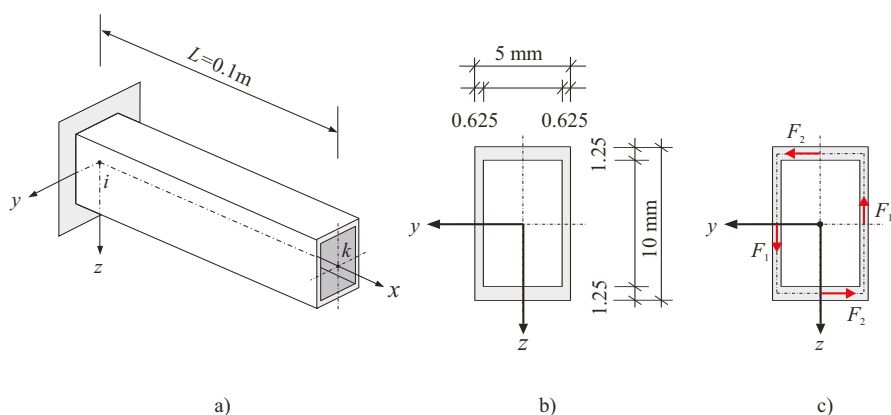


Fig. 14.33. Cantilever beam with a rectangular hollow cross-section: a) system, b) cross-section, c) applied forces: $F_1 = 114.286 \text{ N}$, $F_2 = 57.143 \text{ N}$.

Table 14.10
Cross-sectional parameters for warping torsion of the hollow cross-section.

Cross-sectional parameters		
Cross-sectional area	$A = 0.21875 \times 10^{-4}$	m^2
Second moment of area about the y-axis	$I_y = 0.28483 \times 10^{-9}$	m^4
Second moment of area about the z-axis	$I_z = 0.71208 \times 10^{-10}$	m^4
Polar moment of area	$I_p = I_y + I_z = 0.31209 \times 10^{-9}$	m^4
Torsional constant	$I_T = 0.16748 \times 10^{-9}$	m^4
Secondary torsion constant	$I_{T_s} = 0.717773 \times 10^{-10}$	m^4
Warping constant	$I_\omega = 0.240426 \times 10^{-15}$	m^6

to Figs. 14.3 - 14.8. The beam is loaded at point k on its free end by a torsional moment $M_T = 1 \text{ Nm}$;

- a very fine mesh of SHELL181 elements (16012 elements) of the commercial software ANSYS (2019). The beam is loaded at point k on its free end by a torsional moment $M_T = 1 \text{ Nm}$. M_T is applied as a couple of forces F_1 and F_2 , as shown in Fig. 14.33c.

14.3.5.1 Elastostatic Analysis of a Cantilever Beam with a Rectangular Hollow Cross-section, with Longitudinally Varying Material Properties for the Case 1 and Case 2

Results of the analyses for the angle of twist and the internal moments at the clamped and the free end of the beam, i.e. at nodes i and k , are listed in Table 14.11 and shown in Figs. 14.34-14.38. Table 14.11 also contains results for the angle of twist, obtained by SHELL181 finite elements. As shown in Table 14.11, the twist angle obtained by both the warping beam finite elements and the SHELL181 elements (ANSYS, 2019) agree very well. The STMDE is significant for this type of cross-section. Disregarding the STMDE in the computation by the FGM- WT BEAM

Fig. 14.34 Angle of twist, ψ [rad], for non-uniform torsion of the cantilever beam with a hollow cross-section, ($x \in \langle 0, L \rangle$), for the Case 1 and Case 2 for ($n \in \langle 1, 5 \rangle$), and for $n = 0$ (constant material properties equal to the ones of Tungsten for the Case 1 and of Aluminum for the Case 2).

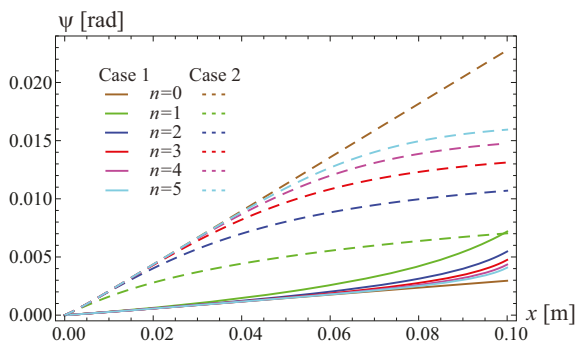


Table 14.11

Angle of twist and internal moments, calculated by FGM-WT with and without STDME, WT BEAM, and SHELL181 finite elements in the expression for the material properties, for the Case 1 with $n \in \langle 1, 5 \rangle$ and for the case of $n = 0$ (constant material properties equal to the ones of Tungsten).

Variables	n	FGM SV	FGM-WT with STMDE/ SHELL181 (ANSYS, 2019)	WT BEAM (Murín et al, 2014)
ψ_k [rad]	0	0.00298	0.00295/0.00290	0.00295
	1	0.00724	0.00719/0.00699	0.00719
	2	0.00552	0.00547/0.00525	0.00547
	3	0.00480	0.00475/0.00453	0.00474
	4	0.00440	0.00434/0.00414	0.00434
	5	0.00415	0.00409/0.00390	0.00408
$\psi'_{M,k}$ [rad/m]	0	-	0.02986	0.02985
	1	-	0.19160	0.19160
	2	-	0.16717	0.16721
	3	-	0.15005	0.14977
	4	-	0.13616	0.13650
	5	-	0.12765	0.12599
$M_{\omega,i}$ [kNm ²]	0	-	-1.01660×10^{-6}	-1.0166×10^{-6}
	1	-	-1.03520×10^{-6}	-1.0351×10^{-6}
	2	-	-1.01875×10^{-6}	-1.0184×10^{-6}
	3	-	-1.01726×10^{-6}	-1.0168×10^{-6}
	4	-	-1.01674×10^{-6}	-1.0166×10^{-6}
	5	-	-1.01675×10^{-6}	-1.0166×10^{-6}
$M_{T_P,i}$ [kNm]	0	-	7.0×10^{-4}	7.0×10^{-4}
	1	-	7.0×10^{-4}	7.0×10^{-4}
	2	-	7.0×10^{-4}	7.0×10^{-4}
	3	-	7.0×10^{-4}	7.0×10^{-4}
	4	-	7.0×10^{-4}	7.0×10^{-4}
	5	-	7.0×10^{-4}	7.0×10^{-4}
$M_{T_P,k}$ [kNm]	0	-	1.000×10^{-3}	1.000×10^{-3}
	1	-	9.497×10^{-4}	9.512×10^{-4}
	2	-	9.178×10^{-4}	9.205×10^{-4}
	3	-	8.955×10^{-4}	8.987×10^{-4}
	4	-	8.774×10^{-4}	8.822×10^{-4}
	5	-	8.663×10^{-4}	8.691×10^{-4}
$M_{T_S,i}$ [kNm]	0	-	3.0×10^{-4}	3.0×10^{-4}
	1	-	3.0×10^{-4}	3.0×10^{-4}
	2	-	3.0×10^{-4}	3.0×10^{-4}
	3	-	3.0×10^{-4}	3.0×10^{-4}
	4	-	3.0×10^{-4}	3.0×10^{-4}
	5	-	3.0×10^{-4}	3.0×10^{-4}
$M_{T_S,k}$ [kNm]	0	-	0	0
	1	-	5.027×10^{-5}	4.876×10^{-5}
	2	-	8.211×10^{-5}	7.942×10^{-5}
	3	-	1.044×10^{-4}	1.012×10^{-4}
	4	-	1.225×10^{-4}	1.177×10^{-4}
	5	-	1.336×10^{-4}	1.308×10^{-4}

Fig. 14.35 Part of the bi-curvature, [rad/m], resulting from the bimoment of the cantilever beam with a hollow cross-section for the Case 1, ($x \in \langle 0, L \rangle$), for ($n \in \langle 1, 5 \rangle$), and for $n = 0$ (constant material properties equal to the ones of Tungsten).

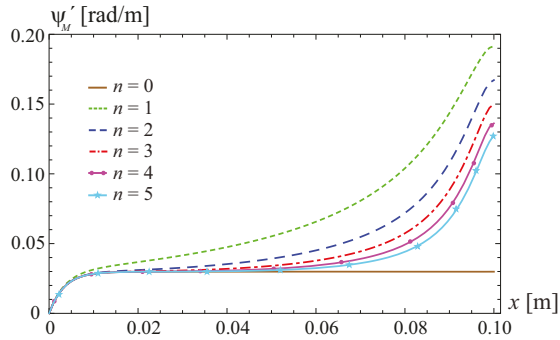


Fig. 14.36 Bimoment M_ω [kNm²] for the cantilever beam with a hollow cross-section section for the Case 1 and Case 2, for ($n \in \langle 1, 5 \rangle$), and for $n = 0$ (constant material properties equal to the ones of Tungsten for the Case 1 and of Aluminum for the Case 2), ($x \in \langle 0, L \rangle$).

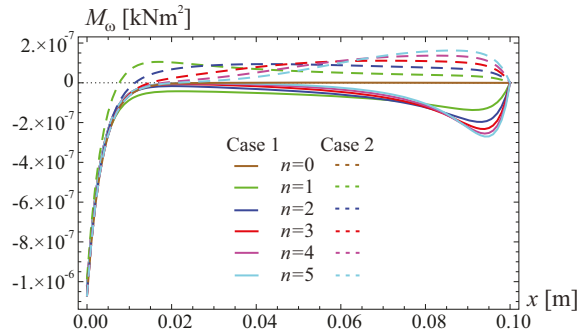
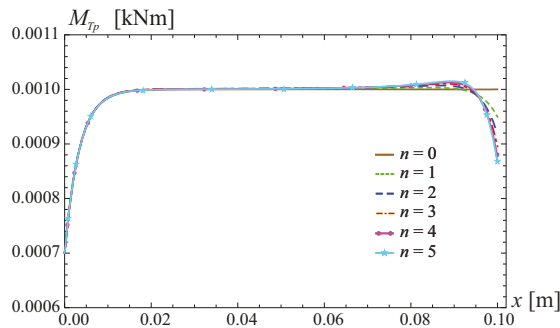
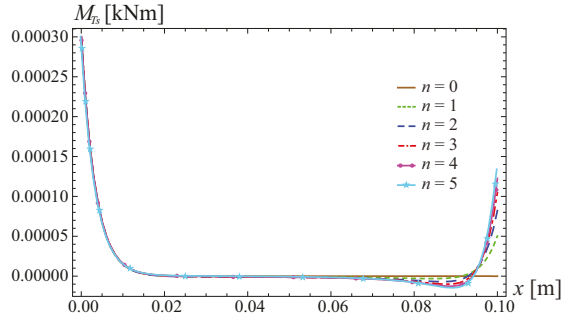


Fig. 14.37 Primary torsional moment, M_{Tp} [kNm], for the cantilever beam with a hollow cross-section, for the Case 1 for $n \in \langle 1, 5 \rangle$, and for $n = 0$ (constant material properties equal to the ones of Tungsten, ($x \in \langle 0, L \rangle$)).



element has provided unrealistic results. Therefore, these results are not contained in Table 14.11. As was also shown in Murín et al (2014), the computation of the angle of twist in the framework of the Saint-Venant (FGM SV) theory paradoxically yields acceptable results. However, as described in Rubin (2005); Murin et al (2018), and as will be shown in the following, neglect of warping by thin-walled closed cross-section FGM beams may lead to an underestimation of the stress state. The longitudinal distribution of the angle of twist, resulting from non-uniform torsion of the cantilever FGM beam with a hollow cross-section, computed by the FGM-WT with STDME beam finite elements for the Case 1 and Case 2, is shown in Fig. 14.34.

Fig. 14.38 Secondary torsional moment, M_{T_s} [kNm], for the cantilever beam with a hollow cross-section, for the Case 1 for $n \in \langle 1, 5 \rangle$, and for $n = 0$ (constant material properties equal to the ones of Tungsten, ($x \in \langle 0, L \rangle$)).



The longitudinal variation of the part of the bicurvature, ψ'_M [rad/m], resulting from the bimoment of the cantilever beam with a hollow cross-section, computed by the FGM-WT beam finite elements with STMDE for the Case 1, is shown in Fig. 14.35. Figure 14.36 shows the longitudinal variation of the bimoment, M_ω [kNm²], of the cantilever beam with a hollow cross-section, for the Case 1 and Case 2. This quantity was computed by the FGM-WT with STMDE. Figure 14.37 illustrates the longitudinal variation of the primary torsional moment, M_{T_p} [kNm], for the cantilever beam with a hollow cross-section, for the Case 1. This quantity was computed by the FGM-WT beam finite elements with STMDE. Fig. 14.38 illustrates the variation of the secondary torsional moment, M_{T_s} [kNm], for the cantilever beam with a hollow cross-section, for the Case 1. This quantity was computed by the FGM-WT BEAM finite elements with STMDE.

Figures 14.39 and 14.40 separately show the longitudinal variation of the primary and secondary torsional moment, M_{T_s} [kNm] and M_{T_p} [kNm], for the cantilever beam with an I cross-section, computed by the FGM-WT beam finite elements with STMDE for the Case 1 and Case 2 and for parameter $n = 3$. For all of the investigated cases, $M_T(x) = M_{T_p}(x) + M_{T_s}(x) = 1 \text{ Nm}$.

The variation of the angle of twist and of the internal moments, obtained by the WT BEAM elements (Murín et al, 2014), is very close to the ones shown in Figs. 14.34-14.40. Therefore, the diagrams concerned are not shown. The significant influence of the variation of the material properties on the angle of twist and the

Fig. 14.39 Primary torsional moment, M_{T_p} [kNm], for the cantilever beam with a hollow cross-section for the Case 1 and Case 2 and for $n = 3$, $x \in \langle 0, L \rangle$.

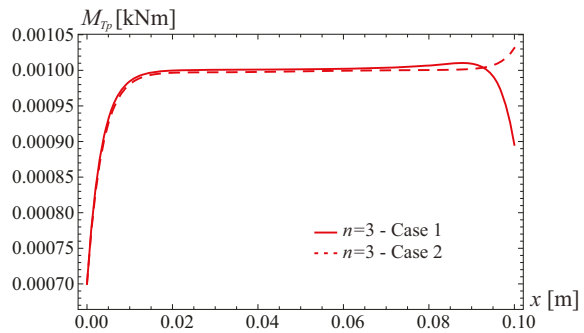
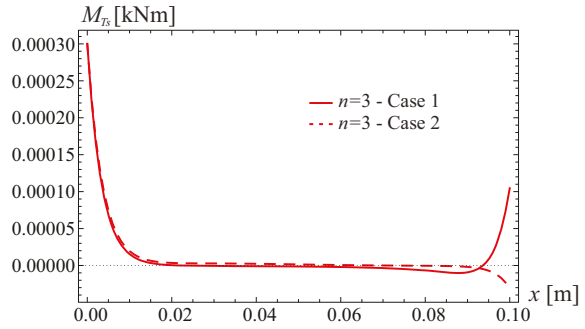


Fig. 14.40 Secondary torsional moment, M_{Ts} [kNm], for the cantilever beam with a hollow cross-section for the Case 1 and Case 2 and for $n = 3, x \in \langle 0, L \rangle$.



internal moments becomes obvious when comparing the results with the ones for the case $n = 0$.

The normal stresses and the torsional shear stresses in consequence of the bimoment, in the cross-section of the clamped end of the beam, were computed analytically for a linear variation of the material properties, i.e. for the Case 1 and for $n = 1$. As shown in Table 14.11, the cross-section at the clamped end of the beam is subjected to the bimoment $M_{\omega,i} = -1.0352 \times 10^{-6} \text{ [kNm}^2\text{]} = -0.010352 \text{ [Nm}^2\text{]}$, the primary torsional moment $M_{Tp,i} = 7.0 \times 10^{-4} \text{ [kNm]} = 0.7 \text{ [Nm]}$, and the secondary torsional moment $M_{Ts,i} = 3.0 \times 10^{-4} \text{ [kNm]} = 0.3 \text{ [Nm]}$.

According to Rubin (2005) and RFEM (2006), the maximum bimoment normal stress at the corners of the cross-section at the clamped end of the beam (Fig. 14.41d) is obtained as

$$\sigma_{\omega,i} = \pm \frac{M_{\omega,i}}{I_{\omega}} \omega_R = \pm 24.72 \text{ MPa}$$

where

$$|\omega_R| = \frac{bh}{4} \frac{bt - bs}{bt + bs} = 5.74 \text{ mm}^2$$

is the warping ordinate at the corners.

According to Rubin (2005) and RFEM (2006), the shear stresses resulting from the secondary torsional moment are given as

$$\begin{aligned} \tau_{s,1} &= \frac{M_{Ts,i}}{tI_{\omega}} S_0 = 3.13 \text{ MPa}, & \tau_{s,2} &= \frac{M_{Ts,i}}{sI_{\omega}} S_0 = 6.27 \text{ MPa}, \\ \tau_{s,3} &= \frac{M_{Ts,i}}{tI_{\omega}} S_1 = 10.90 \text{ MPa}, & \tau_{s,4} &= \frac{M_{Ts,i}}{sI_{\omega}} S_2 = -9.40 \text{ MPa}, \end{aligned}$$

where

$$\begin{aligned} S_0 &= \frac{h^2 - b^2}{6\gamma} \omega_R = 3.130258790 \times 10^{-12} \text{ m}^4, \\ S_1 &= S_0 + A_G \frac{\omega_R}{4} = 1.099090576 \times 10^{-11} \text{ m}^4, \\ S_2 &= S_0 - A_S \frac{\omega_R}{4} = -4.710388182 \times 10^{-12} \text{ m}^4 \end{aligned}$$

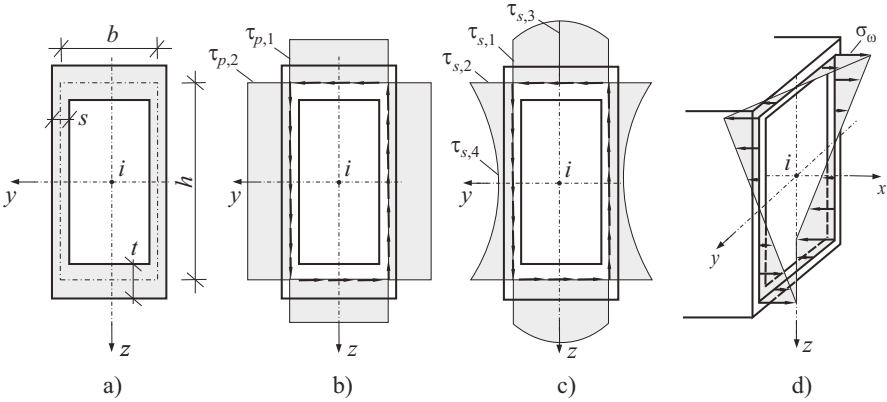


Fig. 14.41. Rectangular cross-section: a) Cross-section, b) primary shear stresses, c) secondary shear stresses, d) axial stresses in consequence of warping.

are auxiliary constants, with the area of the web, A_S , and the area of the flange, A_G , given as $A_S = s h = 5468.75 \times 10^{-9} \text{m}^2$ and $A_G = t b = 5468.75 \times 10^{-9} \text{m}^2$.

The shear stresses resulting from the primary torsional moment are given as

$$\tau_{p,1} = \frac{M_{Tp} s b h}{I_T (h t + b s)} = 7.31 \text{ MPa}, \quad \tau_{p,2} = \frac{M_{Tp} t b h}{I_T (h t + b s)} = 14.63 \text{ MPa}.$$

The total shear stresses at points 1, 2, 3, and 4 are obtained as

$$\begin{aligned} \tau_{1,total} &= \tau_{s,1} + \tau_{p,1} = 10.45 \text{ MPa}, & \tau_{3,total} &= \tau_{s,3} + \tau_{p,1} = 18.28 \text{ MPa}, \\ \tau_{2,total} &= \tau_{s,2} + \tau_{p,2} = 20.89 \text{ MPa}, & \tau_{4,total} &= \tau_{s,4} + \tau_{p,2} = 5.22 \text{ MPa}. \end{aligned}$$

The value of the maximum warping normal stress in the clamped cross-section is comparable to the maximum values of the torsional shear stresses. The longitudinal distribution of the bimoment normal stresses in the x -direction, along the middle line of the cross-section, see Fig. 14.41d, is proportional to the distribution of the bimoment, shown in Fig. 14.36. The distribution of the bimoment normal stresses, computed by the FGM-WT with STMDE for the Case 1 and Case 2, $n \in \langle 0,5 \rangle$, is shown in Fig. 14.42. Similar to the clamped beam with the I-profile, beginning at a small distance from the clamped end, useful results are obtained in the field of the beam, for $n \in \langle 1,5 \rangle$.

To verify the obtained results, numerical analyses of the beam were performed with very fine meshes of BEAM188 WR finite elements, (500 elements) and SHELL181 finite elements (16012 elements), ANSYS (2019). All degrees of freedom of the finite element nodes at the clamped end of the beam were restrained. Figures 14.43-14.44 and Tables 14.12-14.13 show the warping normal stress distribution for the Cases 1 and 2, and $n = 3$. Additionally to Fig. 14.42, the solution results (the green dot-dashed curve) for the Case 1 and for the Case 2, which were obtained

Fig. 14.42 Distribution of the warping normal stresses along the upper left beam edge, for the hollow cross-section and for the Case 1 and Case 2, for $n \in \langle 1, 5 \rangle$, and for $n = 0$ (constant material properties equal to the ones of Tungsten for the Case 1 and of Aluminum for the Case 2), ($x \in \langle 0, L \rangle$).

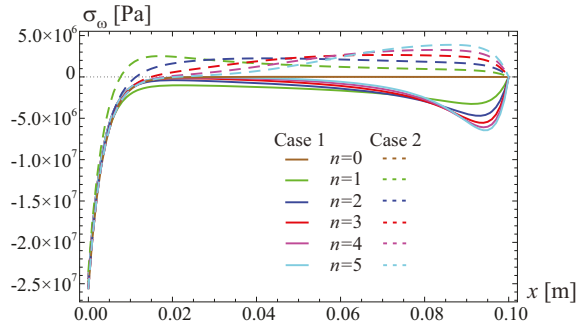


Fig. 14.43 Normal stresses along the outer longitudinal edge of the beam, for the cantilever beam with a hollow cross-section for the Case 1 and for $n = 3$, ($x \in \langle 0, L \rangle$).

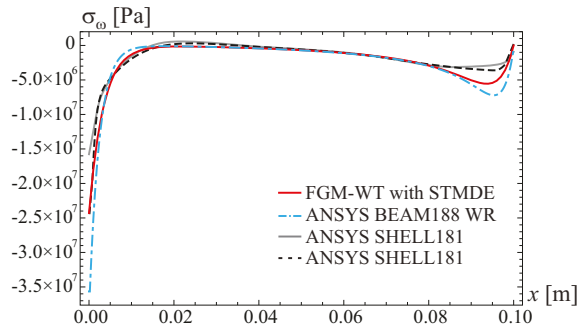
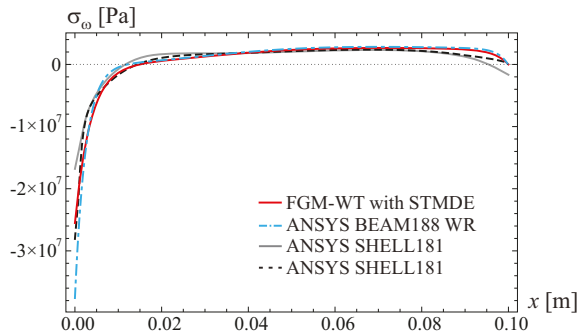


Fig. 14.44 Normal stresses along the outer longitudinal edge of the beam, for the cantilever beam with a hollow cross-section for the Case 2 and for $n = 3$, ($x \in \langle 0, L \rangle$).



by BEAM188 finite element with option warping restrained (ANSYS, 2019), are shown in Fig. 14.43 and Fig. 14.44.

In Figs. 14.43-14.44, two distributions of the normal stresses, obtained by SHELL181 finite elements, are drawn. Distribution of the normal stresses along the upper left edge of the beam is drawn by the grey colour. The dashed black curve refers to a line, at a distance of about 0.4 mm from the upper edge of the clamped flange, in the longitudinal direction of the beam. The maximum normal stresses, resulting from warping, computed by the authors' FGM-WT beam finite elements with STMDE, are shown as a red curve. A very good agreement of the normal stresses in the field of the beam was obtained by all the finite elements. However, there are discrepancies of the solutions from the BEAM188 WR and the SHELL

Table 14.12

Normal stresses, calculated by FGM-WT with STDME, BEAM188 WR, and SHELL181 finite elements for the Case 1, $n = 3$.

x [m]	0	0.1
FGM-WT with STMDE - red curve	-24.3	0.0
BEAM188 WR - green dot dashed curve	-35.6	-0.4
SHELL181 - grey curve	-15.7	-0.9
SHELL181 - dashed black cuve	-24.3	0.2

Table 14.13

Normal stresses, calculated by FGM-WT with STDME, BEAM188 WR, and SHELL181 finite elements for the Case 2, $n = 3$.

x [m]	0	0.1
FGM-WT with STMDE - blue curve	-25.5	0.0
BEAM188 WR - dashed green curve	-37.6	0.1
SHELL181 - grey curve	-16.8	-0.5
SHELL181 - dashed black cuve	-28.1	0.2

181 and FGM-WT with STMDE finite elements in the clamped end of the cantilever beam. As mentioned above, the BEAM 188 WR produced, for closed cross sections, relevant results for the angle of twist, but not the bimoment normal stress. The best agreement of the results for the normal stresses at the clamped end of the beam was obtained by WT-BEAM with STMDE (the blue curve) and SHELL181 (the dashed black curve) finite elements.

The values of the maximum normal stresses, in [MPa], for the Case 1 and $n = 3$, at several distances x from the clamped cross-section, are read in Table 14.12.

The values of the maximum normal stresses, in [MPa], for the Case 2 and $n = 3$, at several distances x from the clamped cross-section, are read in Table 14.13.

In Figs. 14.45-14.46, distributions of the twist angle calculated by FGM-WT with STDME (the read curve), SHELL181 (the dashed red curve) and BEAM188 WR finite elements for the Case 2 and $n = 3$. A very good agreement of the results was obtained. The results obtained by the WT BEAM (Murín et al, 2014) agree very well with the ones obtained by the FGM-WT BEAM finite elements with STMDE. Therefore, they are not displayed in the figures presented above.

Additionally, the distribution of the normal stresses, in the cross-section at the clamped end of the beam, obtained by SHELL181 finite elements for the Case 1 and $n = 1$, is shown in Fig. 14.47. An analogous distribution of the normal stresses refers to a cross-section at a distance of 1mm from the clamped end of the beam. It is shown in Fig. 14.48. As follows from Fig. 14.48, the maximum value of the normal stresses in the considered cross-section agrees well with the authors' result, obtained by the FGM-WT beam finite elements with STMDE.

Finally, the von Mises stresses in the cross-section at the clamped end of the beam are computed. The distribution of these stresses, obtained by SHELL181 finite

Fig. 14.45 Twist angles along the longitudinal axis of the beam, for the cantilever beam with a hollow cross-section for the Case 1 and for $n = 3$, ($x \in (0, L)$).

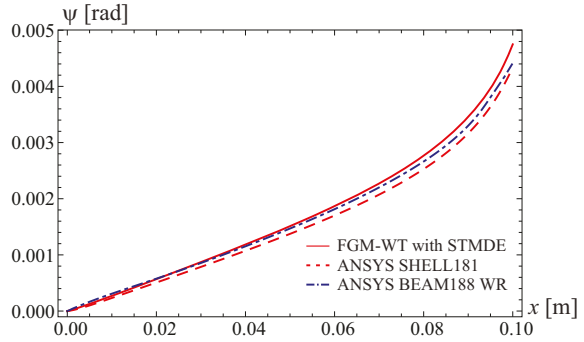


Fig. 14.46 Twist angles along the longitudinal axis of the beam, for the cantilever beam with a hollow cross-section for the Case 2 and for $n = 3$, ($x \in (0, L)$).

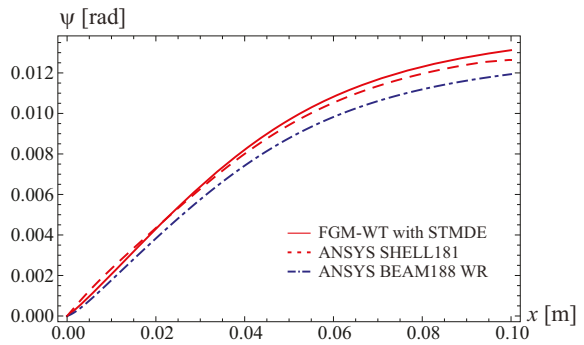
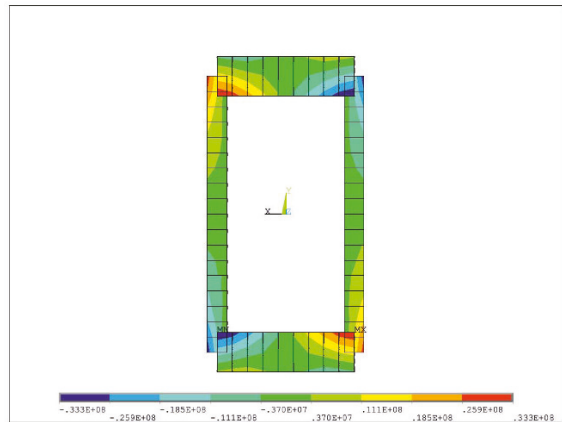


Fig. 14.47 Distribution of the normal stresses in the cross-section at the clamped end of the beam, for the case 1 and for $n = 1$.



elements, is shown in Fig. 14.49. The maximum value of the von Mises stresses is equal to 42.2 MPa. An analogous illustration refers to a cross-section at a distance of 1 mm from the clamped end of the beam, see Fig. 14.50. The maximum value of the von Mises stresses is equal to 40.2 MPa.

As follows from Fig. 14.41, the torsional shear stress, according to the TTT, at the corners of the cross-section, is equal to $\tau_2^{total} = 20.89$ MPa. Then, the maximum value of the von Mises stress in the cross-section at the clamped end of the beam

Fig. 14.48 Distribution of the normal stresses in a cross-section at a distance of 1mm from the clamped end of the beam, for the Case 1 and for $n = 1$.

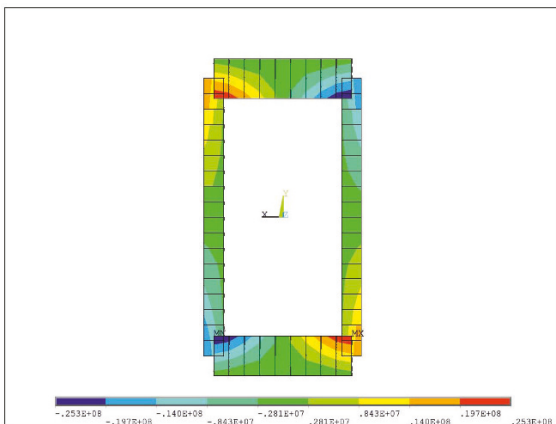
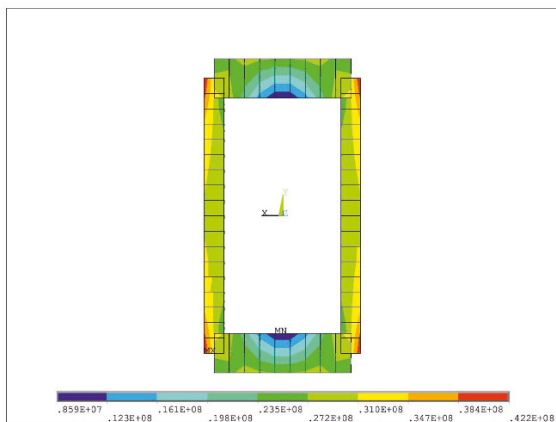
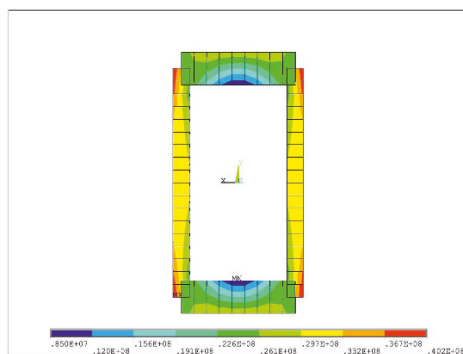


Fig. 14.49 Distribution of the von Mises stresses in the cross-section at the clamped end of the beam, for the Case 1 and for $n = 1$.



is obtained as $\sigma_s = \sqrt{\sigma_{\omega,i}^2 + 3\tau_{2,total}^2} = 43.82 \text{ MPa}$. This shows that the difference

Fig. 14.50 Distribution of the von Mises stresses in a cross-section at a distance of 1 mm from the clamped end of the beam, for the Case 1 and for $n = 1$.



between the authors’ solution and the result by the SHELL181 finite elements is small.

14.3.5.2 Elastostatic Analysis of a Cantilever Beam with a Rectangular Hollow Cross-section, with Longitudinally Varying Material Properties for the Case 3

The elastostatic torsional analyses were performed by means of:

- one warping torsion beam finite element (FGM-WT with STMDE);
- a very fine mesh (500 finite elements) of BEAM188 finite elements, with the option warping restrained (WR) (ANSYS, 2019), with constant material properties obtained as the average values of their variation over the length of each finite beam element according Figs. 14.7-14.8;
- a very fine mesh of SHELL181 elements (16012 elements) of the commercial software ANSYS (ANSYS, 2019). The beam is loaded at point k on its free end by a torsional moment $M_T = 1 \text{ Nm}$. M_T is applied as a couple of forces F_1 and F_2 , as shown in Fig. 14.33c.

Results of the analyses for the clamped and the free end of the beam, i.e. at nodes i and k are drawn in Figs. 14.51-14.54 for the Case 3 with the variations 1 and 2.

Fig. 14.51 Angle of twist, ψ [rad], for non-uniform torsion of the cantilever beam with a hollow cross-section, ($x \in (0, L)$), for the Case 3 and the variations 1 and 2.

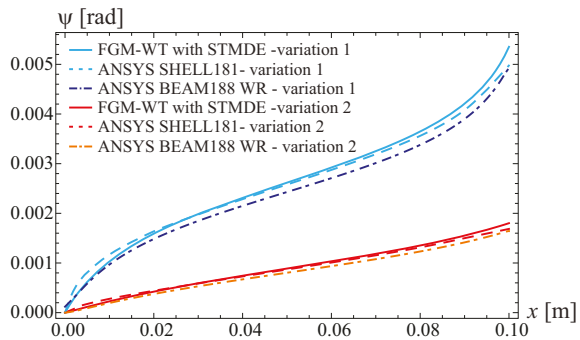


Fig. 14.52 Bimoment $M_\omega \text{ kNm}^2$ for the cantilever beam with a hollow cross-section for the Case 3, ($x \in (0, L)$), and the variations 1 and 2.

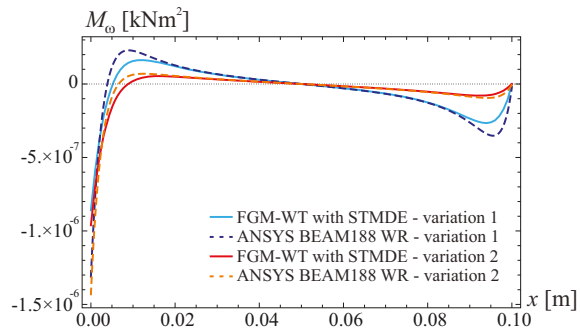


Fig. 14.53 Distribution of the warping normal stresses along the upper left beam edge for Case 3, variation 1.

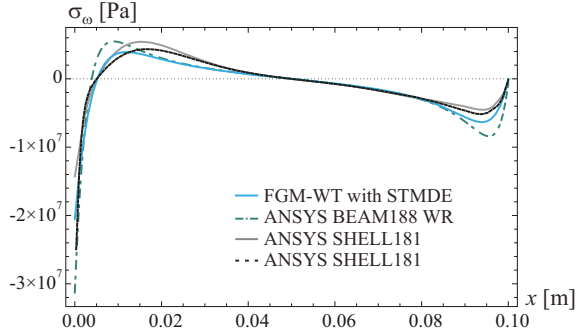
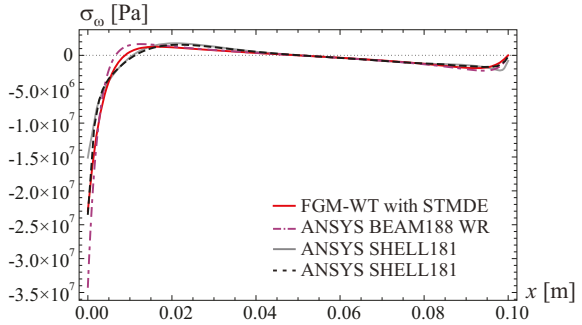


Fig. 14.54 Distribution of the warping normal stresses along the upper left beam edge for Case 3, variation 2.



Numerical results of the analyses for the Case 3 are listed in Tables 14.14-14.16. As shown in Table 14.14, the results for the maximal twist angle, obtained by all of the warping torsion beam finite elements and SHELL181 elements (ANSYS, 2019), agree very well.

Plots of the longitudinal distribution of the angle of twist, ψ [rad], for the case of non-uniform torsion of the investigated cantilever are shown in Figure 14.51. As expected, the variation of material properties influences the angle of twist significantly. A very good agreement of all the distributions is obtained.

Figure 14.52 shows the longitudinal distribution of the bimoment, M_ω [kNm²], for the cantilever beam with a hollow cross-section for the Case 3. This quantity was computed by the FGM-WT with STMDE and BEAM188 WR (ANSYS, 2019). A satisfactory match of all the distributions is obtained in the field of the beam. Similar

Table 14.14

Angle of twist, calculated by FGM-WT with STDME, BEAM188 WR, and SHELL181 finite elements in the expression for the material properties, for the Case 3.

Twist angle ψ [rad] for:	variation 1	variation 2
FGM-WT with STMDE	0.00535	0.00180
BEAM188 (ANSYS, 2019)	0.00493	0.00164
SHELL181 (ANSYS, 2019)	0.00496	0.00169

Table 14.15

Normal stresses in [MPa], calculated by FGM-WT with STDME, BEAM188 WR, and SHELL181 finite elements for the Case 3, variation 1.

x[m]	0	0.012	0.094	0.1
FGM-WT with STMDE - blue curve	-22.5	3.9	-6.3	0.0
BEAM188 WR - dashed green curve	-31.3	5.5	-8.4	-0.5
SHELL181 - grey curve	-14.3	5.4	-4.3	-0.8
SHELL181 - dashed black curve	-24.6	4.33	-5.6	-0.2

Table 14.16

Normal stresses, calculated by FGM-WT with STDME, BEAM188 WR, and SHELL181 finite elements for the Case 3, variation 2.

x[m]	0	0.016	0.092	0.1
FGM-WT with STMDE - red curve	-22.9	1.3	-1.9	0.0
BEAM188 WR - dashed violet curve	-34.2	1.7	-2.3	-1.0
SHELL181 - grey curve	-15.1	1.8	-2.3	-1.0
SHELL181 - dashed black curve	-23.4	1.6	-1.8	-0.2

discrepancies are achieved at the clamped end of the beam, as it was in the above analyzed Cases 1 and 2.

The normal stresses in consequence of the bimoment and the torsional shear stresses, in the cross-section at the clamped end of the beam, were computed by the TTT. For example, as shown in Fig. 14.53 for the variation 1, the cross-section at the clamped end i was subjected to the bimoment, calculated by FGM-WT with STMDE, $M_{\omega,i} = -8.595 \times 10^{-7} \text{ kNm}^2 = -0.000859 \text{ Nm}^2$. Its value, calculated by BEAM188 WR, is equal to $-1.310 \times 10^{-6} \text{ kNm}^2$. From our calculations, the primary torsional moment $M_{T_p,i} = 5.314 \times 10^{-5} \text{ kNm} = 0.05314 \text{ Nm}$, and the secondary torsional moment $M_{T_s,i} = 9.469 \times 10^{-4} \text{ kNm} = 0.9469 \text{ Nm}$. The same values of the primary and secondary torsional moment at the clamped end of the beam were obtained as in previously analyzed cases.

According to Rubin (2005) and for the bimoment calculated by FGM-WT beam with STMDE, the maximum normal stress at the corners of the clamped cross-section was obtained as

$$\sigma_{\omega,i} = \pm \frac{M_{\omega,i}}{I_{\omega}} \omega_R = \pm 20.5 \text{ MPa},$$

where

$$|\omega_R| = 5.74 \text{ mm}^2$$

is the warping ordinate at these points (Rubin, 2005), Fig. 14.17d. The figure does not explicitly show this quantity. The maximum normal stress, calculated from bimoment obtained by BEAM188 WR, is equal to $\pm 31.3 \text{ MPa}$.

The maximum shear stress, resulting from the secondary torsion moment, was obtained in [MPa] as $\tau_{s,1} = 9.9$, $\tau_{s,2} = 19.8$, $\tau_{s,3} = 34.6$, $\tau_{s,4} = -29.7$, MPa, Fig.

14.41c. The shear stresses, resulting from the primary torsion moment, were obtained in [MPa] as $\tau_{p,1} = 0.6$, $\tau_{p,2} = 1.1$, MPa, (Fig. 14.41b). The total shear stresses at points 1, 2, 3, and 4 are obtained as

$$\begin{aligned}\tau_{1,total} &= \tau_{s,1} + \tau_{p,1} = 10.5 \text{ MPa} & \tau_{3,total} &= \tau_{s,3} + \tau_{p,1} = 35.2 \text{ MPa} \\ \tau_{2,total} &= \tau_{s,2} + \tau_{p,2} = 20.9 \text{ MPa} & \tau_{4,total} &= \tau_{s,4} + \tau_{p,2} = -28.6 \text{ MPa}.\end{aligned}$$

As follows from Fig. 14.41, the torsional shear stress, according to the TTT, at the corners of the cross-section, is equal to $\tau_2^{total} = 20.89$ MPa. Then, the maximum value of the von Mises stress in the cross-section at the clamped end of the beam is obtained as $\sigma_s = \sqrt{\sigma_{\omega,i}^2 + 3\tau_{2,total}^2} = 41.6$ MPa.

The longitudinal variation of the maximum bimoment normal stresses is proportional to the longitudinal variation of the bimoment shown in Fig. 14.52. The longitudinal variation of the maximum normal stresses along the upper left beam edge for the Case 3 and the variation 1 and 2, computed by the FGM-WT with STDME and BEAM188 WR and SHELL181 finite elements, is shown in Figs. 14.53-14.54. Almost identical distributions of these stresses are obtained by the WT BEAM finite elements with STMDE (Murín et al, 2014).

In Figs. 14.53-14.54, two distributions of the normal stresses, obtained by SHELL181 finite elements, are drawn. Distribution of the normal stresses along the upper left edge of the beam is drawn by the grey colour. The dashed black curve refers to a line, at a distance of about 0.4 mm from the upper edge of the clamped flange, in the longitudinal direction of the beam. The values of the maximum normal stresses, in [MPa], for the variation 1, at several distances x from the clamped cross-section, are read in Table 14.15. The values of the maximum normal stresses, in [MPa], for the variation 2, at several distances x from the clamped cross-section, are read in Table 14.16.

As shown in Figs. 14.53-14.54 and Tables 14.15-14.16, an acceptable conformity of normal stresses was achieved except for the maximum stress at clamped end of the beam. Because of numerical singularity at the sharp corners, the solution by SHELL181 finite elements, (drawn by grey curves), shows a divergent result at the point of the clamping of the edges of the cross-section. The agreement of the distribution of normal stresses, obtained by only one author's beam finite element, (FGM-WT with STDME), and the distribution obtained, by the very fine mesh of SHELL181 finite elements that drawn along the little shifted line from the edge of the beam, is excellent.

On the other hand, despite of correct evaluation of the twist angle by all the used finite elements, the bimoment normal stress, which was calculated by BEAM188 WR finite elements (there the STMDE is not included and the bicurvature is chosen as a warping degree of freedom), differ significantly from the results obtained by author's FGM-WT with STMDE beam finite element for the hollow cross-section beams. As shown in our previous papers, dealing with non-uniform torsion of the closed cross-sections with constant material properties, the STMDE is significant for this type of cross-section. As the results of our analyzes show, the effect of the longitudinal variability of the material properties on the bimoment normal stress distribution in

the thin-walled FGM beam of the hollow cross-section is less pronounced than in the case of the FGM beam with I-profile.

The results for the stresses at the clamped end of the beam have shown that the normal stresses, resulting from warping, are comparable to the torsional shear stresses. Therefore, their neglecting in design of thin-walled FGM beam structures with hollow cross-section may not be admissible.

14.4 Summary and Conclusions

The differential equations of fourth order for non-uniform torsion of FGM beams with doubly symmetric thin-walled open and closed cross-section were established. For an analysis of torsional warping decoupled from bending, doubly symmetric cross-sections were selected in this work. A polynomial longitudinal variation of the effective material properties was originally considered and its effect on the twist angle and stresses was studied. The longitudinally varying material properties can, e.g., be obtained by homogenization of spatially varying material properties (Kutiš et al. 2011). The general semi-analytical solution of the differential equation (14.12) was presented and the transfer matrix relations were formulated, from which the finite element equations for FGM-WT with STDME beams were obtained. Results from elastostatic analysis of open I cross-section beams and beams with rectangular hollow cross-sections, obtained by the proposed method, were presented and compared with results, obtained by commercial FEM codes. In the theoretical investigation, the secondary torsional moment deformation effect (STDME) was taken into account. A part of the expression for the first derivative of the twist angle was chosen as the warping degree of freedom.

The main conclusions that can be drawn from this investigation are as follows:

1. Torsional elastostatic analysis of a cantilever FGM beam with an I cross-section:
 - The results from elastostatic analysis, using the proposed warping torsion beam finite elements for non-uniform (FGM-WT with STDME), and uniform (SV) torsion of FGM beams with open doubly symmetric cross-sections, have shown considerable differences in the twist angle and significant differences in the stresses. The normal stresses caused by warping significantly outweigh the shear stresses resulting from uniform Saint-Venant torsion. This proves that the warping effect must also be taken into account for beams made of FGM. It was also shown that a strong continuous change in the material properties causes significant bimoment normal stresses in the field of the beam.
 - The proposed approach for elastostatic non-uniform torsional analysis of FGM beams without and with consideration of STMDE produces slightly different results. The STMDE does not reduce the torsional stiffness of the hollow cross-section significantly. However, the results in case of accounting for the STMDE agree better with the ones obtained by 3D solid and shell finite elements.

- The BEAM 188 WR finite element (ANSYS, 2019) produced relevant results for the angle of twist, but not the bimoment normal stress.
 - The proposed warping torsion beam finite element, (FGM-WT with STDME), is very effective, because the FGM beam with a polynomial variation of the material properties can be modelled with only one finite element. The obtained results by such a coarse mesh agree well with the ones from a very fine mesh of 3D SOLID186 and SHELL181 finite elements (ANSYS, 2019).
 - As expected, the results exhibit a significant influence of the variation of the material properties on the deformations of the twisted beam and on the bimoment normal and torsional shear stresses (predominantly in the field of the FGM beam).
2. Torsional elastostatic analysis of a FGM cantilever beam with a rectangular hollow cross-section:
- The degree of agreement of the results obtained by the proposed warping finite beam element (FGM-WT with STMDE) with the ones obtained by SHELL181 shell elements is acceptable. The differences of the results are primarily caused by the way of application of the torsional moment and of specification of the boundary conditions in the numerical model. In reality, the decrease of the torsional stiffness is not only caused by warping and STMDE, but also by the distortion of the cross-section. As shown in Tsiptsis and Sapountzakis (2017b,a); Sapountzakis and Dikaros (2019), the effect of this distortion is significant for very short beams. In the authors' approach, distortion effects are not considered. However, the FGM- WT with STDME beam finite element with only one additional degree of freedom produces acceptable results in comparison with the solution obtained by shell finite elements. Expectedly, the longitudinal variation of the material properties has a significant influence on the beam with a hollow cross-section subjected to non-uniform torsion.

Despite of relatively correct evaluation of the twist angle by all the used finite elements, the bimoment normal stress, which was calculated by BEAM188 WR finite elements (ANSYS, 2019), (there the STMDE is not included and the bicurvature is chosen as a warping degree of freedom), differ significantly from the results obtained by author's FGM-WT with STMDE beam finite element for the hollow cross-section beams. The STMDE is significant for this type of cross-section. As the results of our analyzes show, the effect of the longitudinal variability of the material properties on the bimoment normal stress distribution in the thin-walled FGM beam of the hollow cross-section is less pronounced than in the case of the FGM beam with I-profile.

Appendix

A.1 Variable polynomial parameters in (14.12)

These parameters are given as follows:

$$\eta_0(x) = 0;$$

$$\begin{aligned} \eta_1(x) = & -((-GI_{Ts})^3GI_T + 2EI_\omega GI_T(G'I_{Ts})^2 + (GI_{Ts})^2(E'I_\omega G'I_T + EI_\omega G''I_T) \\ & - GI_{Ts}((GI_T E'I_\omega + 2EI_\omega G'I_T)G'I_T + EI_\omega GI_T G''I_{Ts})) \\ & ((GI_{Ts})^2(3G'I_{Ts}) - G'I_{Ts}(E'I_\omega G'I_{Ts} + 3EI_\omega G''I_{Ts}) \\ & + GI_{Ts}(E'I_\omega G'I_{Ts} + EI_\omega G''I_{Ts})) \\ & + ((GI_{Ts})^3(-G'I_T) + GI_T G'I_{Ts}(E'I_\omega G'I_{Ts} + 3EI_\omega G''I_{Ts}) \\ & + (GI_{Ts})^2(-GI_T 3G'I_{Ts} + G'I_T E''I_\omega + 2E'I_\omega G''I_T + EI_\omega G'''I_T) \\ & - GI_{Ts}(G'I_T(G'I_T(E'I_\omega G'I_{Ts} + 3EI_\omega G''I_{Ts}) + GI_T(G'I_{Ts}E'I_\omega \\ & 2E'I_\omega G''I_{Ts} + EI_\omega G'''I_{Ts})))) \\ & /((GI_{Ts})^3 - 2E'I_\omega(G'I_{Ts})^2 + GI_{Ts}(E'I_\omega G'I_{Ts} + E'I_\omega G''I_{Ts}))^2; \end{aligned}$$

$$\begin{aligned} \eta_2(x) = & -((GI_{Ts}(-((GI_{Ts})^3 - 2EI_\omega(G'I_{Ts})^2 + GI_{Ts}(E'I_\omega G'I_{Ts} + EI_\omega G''I_{Ts})) \\ & (GI_{Ts}(E'I_\omega(4G'I_T + 3G'I_{Ts}) + GI_{Ts}E''I_\omega + EI_\omega 3G''I_T) \\ & - GI_T((GI_{Ts})^2 + E'I_\omega G'I_{Ts} - GI_{Ts}E''I_\omega + 3EI_\omega G''I_{Ts})) \\ & + GI_{Ts}((GI_T + GI_{Ts})E'I_\omega + 2EI_\omega G'I_T) - 2EI_\omega GI_T G'I_{Ts}) \\ & (GI_{Ts}^2(3G'I_{Ts}) - G'I_{Ts}(E'I_\omega G'I_{Ts} + 3EI_\omega G''I_{Ts}) \\ & + GI_{Ts}(G'I_{Ts}E''I_\omega + 2E'I_\omega G''I_{Ts} + EI_\omega G'''I_{Ts})))) \\ & /((GI_{Ts})^3 - 2EI_\omega(G'I_{Ts})^2 + GI_{Ts}(E'I_\omega G'I_{Ts} + EI_\omega G''I_{Ts}))^2; \end{aligned}$$

$$\begin{aligned} \eta_3(x) = & -(GI_{Ts})^2(-2(GI_T + GI_{Ts})E'I_\omega + 3EI_\omega(G'I_T + G'I_{Ts}))((GI_{Ts})^3 \\ & - 2EI_\omega(G'I_{Ts})^2 + GI_{Ts}(E'I_\omega G'I_{Ts} + EI_\omega G''I_{Ts})) \\ & + EI_\omega(GI_T + GI_{Ts})((GI_{Ts})^2 3G'I_{Ts} - G'I_{Ts}(E'I_\omega G'I_{Ts} + 3EI_\omega G''I_{Ts}) \\ & + GI_{Ts}(G'I_{Ts}E''I_\omega + 2E'I_\omega G''I_{Ts} + EI_\omega G'''I_{Ts}))) \\ & /((GI_{Ts})^3 - 2EI_\omega(G'I_{Ts})^2 + GI_{Ts}(E'I_\omega G'I_{Ts} + EI_\omega G''I_{Ts}))^2; \end{aligned}$$

$$\eta_4(x) = \frac{EI_\omega(GI_{Ts})^2(GI_T + GI_{Ts})}{(GI_{Ts})^3 - 2EI_\omega(G'I_{Ts})^2 + GI_{Ts}(E'I_\omega G'I_{Ts} + EI_\omega G''I_{Ts})}.$$

The load polynomial on the right-hand side of Eq. (14.12), for several load conditions, reads as follows:

$$\eta_L(x) = \sum_{s=0}^{\max s} \eta_{L,s} x^s =$$

$$m \neq 0 \quad m_T(-1 - ((GI_{Ts})^3 - 2EI_\omega(G'I_{Ts})^2 + GI_{Ts}(E'I_\omega G'I_{Ts} + EI_\omega G''I_{Ts})) \\ ((GI_{Ts})^2 E''I_\omega - 2EI_\omega((G'I_{Ts})^2 + GI_{Ts}G''I_{Ts})) \\ + GI_{Ts}(GI_{Ts}E'I_\omega - 2EI_\omega G'I_{Ts})(GI_{Ts}^2 3G'I_{Ts} \\ - G'I_{Ts}(E'I_\omega G'I_{Ts} + 3EI_\omega G''I_{Ts})) \\ + GI_{Ts}(G'I_{Ts}E''I_\omega + 2E'I_\omega G''I_{Ts} + EI_\omega G'''I_{Ts}))) \\ /((GI_{Ts})^3 - 2EI_\omega(G'I_{Ts})^2 + GI_{Ts}(E'I_\omega G'I_{Ts} + EI_\omega G''I_{Ts}))^2;$$

$$m'_T \neq 0 \quad m'_T(((GI_{Ts})^2(2(GI_{Ts})^3 E'I_\omega + (GI_{Ts})^2(-3EI_\omega G'I_{Ts}) + 3EI_\omega G'I_{Ts} \\ (-E'I_\omega G'I_{Ts} + EI_\omega G''I_{Ts}) + GI_{Ts}(G'I_{Ts}(2(E'I_\omega)^2 \\ + EI_\omega(-E''I_\omega)) - (EI_\omega)^2 G'''I_{Ts}))) \\ /((GI_{Ts})^3 - 2EI_\omega(G'I_{Ts})^2 + GI_{Ts}(E'I_\omega G'I_{Ts} + EI_\omega G''I_{Ts}))^2;$$

$$m''_T \neq 0 \quad m''_T((EI_\omega(GI_{Ts})^2)/((GI_{Ts})^3 - 2EI_\omega(G'I_{Ts})^2 \\ + GI_{Ts}(E'I_\omega G'I_{Ts} + EI_\omega G''I_{Ts})));$$

$$m_\omega \neq 0 \quad m_\omega(((GI_{Ts})^2(-6EI_\omega(G'I_{Ts})^3 + 2GI_{Ts}G'I_{Ts}(2E'I_\omega G'I_{Ts} + 3EI_\omega G''I_{Ts}) \\ - (GI_{Ts})^2(G'I_{Ts}E''I_\omega + 2E'I_\omega G''I_{Ts} + EI_\omega G'''I_{Ts}))) \\ /((GI_{Ts})^3 - 2EI_\omega(G'I_{Ts})^2 + GI_{Ts}(E'I_\omega G'I_{Ts} + EI_\omega G''I_{Ts}))^2;$$

$$m'_\omega \neq 0 \quad m'_\omega(GI_{Ts})^3 / ((GI_{Ts})^3 - 2EI_\omega(G'I_{Ts})^2 + GI_{Ts}(E'I_\omega G'I_{Ts} + EI_\omega G''I_{Ts})).$$

A.2 Detailed description of the transformation matrix \mathbf{T}

The transformation matrix \mathbf{T} transforms the vector \mathbf{Z}_x to the vector Ψ , i.e. $\Psi = \mathbf{T} \cdot \mathbf{Z}_x$

$$\begin{array}{c} \mathbf{Z}_x \\ \left[\begin{array}{c} \psi(x) \\ \psi'(x) \\ \psi''(x) \\ \psi'''(x) \\ \hline 1 \end{array} \right] \end{array} = \begin{array}{c} \mathbf{A} \\ \left[\begin{array}{ccccc} T_{1,1}(x) & T_{1,2}(x) & T_{1,3}(x) & T_{1,4}(x) & T_{1,5}(x) \\ T_{2,1}(x) & T_{2,2}(x) & T_{2,3}(x) & T_{2,4}(x) & T_{2,5}(x) \\ T_{3,1}(x) & T_{3,2}(x) & T_{3,3}(x) & T_{3,4}(x) & T_{3,5}(x) \\ T_{4,1}(x) & T_{4,2}(x) & T_{4,3}(x) & T_{4,4}(x) & T_{4,5}(x) \\ \hline 0 & 0 & 0 & 0 & 1 \end{array} \right] \end{array} \cdot \begin{array}{c} \mathbf{Z}_i \\ \left[\begin{array}{c} \psi(x) \\ \psi'_M(x) \\ \psi_\omega(x) \\ \psi_T(x) \\ \hline 1 \end{array} \right] \end{array} \quad (14.30)$$

The first line of the transformation matrix \mathbf{T} reads as

$$T_{1,1} = 1, \quad T_{1,2} = 0, \quad T_{1,3} = 0, \quad T_{1,4} = 0, \quad T_{1,5} = 0. \quad (14.31)$$

Substitution of (14.7) into (14.5) gives

$$\psi'(x) = \psi'_M(x) + \psi'_S(x) = \psi'_M(x) + \frac{M_{Ts}(x)}{GI_{Ts}}. \quad (14.32)$$

Inserting the expression for $M_{Tp}(x)$, obtained from (14.6), into (14.3) yields

$$M_{Ts}(x) = M_T(x) - GI_T\psi'(x). \tag{14.33}$$

Substitution of (14.33) into (14.32) gives

$$\psi'(x) = \left(\frac{GI_{Ts}}{GI_{Ts} + GI_T} \right) \psi'_M(x) + \left(\frac{1}{GI_{Ts} + GI_T} \right) M_T(x). \tag{14.34}$$

The second line of the transformation matrix \mathbf{T} reads as

$$T_{2,1} = 0; \quad T_{2,2} = \frac{GI_{Ts}}{GI_{Ts} + GI_T}; \quad T_{2,3} = 0; \quad T_{2,4} = \frac{1}{GI_{Ts} + GI_T}; \quad T_{2,5} = 0. \tag{14.35}$$

Inserting $\psi''_M(x)$, obtained from (14.4), and $M'_T(x)$, following from (14.1), into the expression for $\psi''(x)$, obtained from derivation of (14.34) with respect to x , yields the third line of the transformation matrix:

$$\begin{aligned} T_{3,1} &= -\frac{\omega^2 \rho I_p}{GI_{Ts} + GI_T}; & T_{3,2} &= \frac{-GI_{Ts}GI'_T + GI_TGI'_{Ts}}{(GI_{Ts} + GI_T)^2}; \\ T_{3,3} &= -\frac{GI_{Ts}}{EI_\omega(GI_{Ts} + GI_T)}; & T_{3,4} &= -\frac{GI'_T + GI'_{Ts}}{(GI_{Ts} + GI_T)^2}; & T_{3,5} &= -\frac{m_T}{GI_{Ts} + GI_T}. \end{aligned} \tag{14.36}$$

The fourth line of the transformation matrix is obtained from the second derivative of (14.34) with respect to x . The resulting expression for $\psi'''(x)$ contains $\psi'(x)$, $\psi''(x)$, $M'_\omega(x)$, and $M'_T(x)$. The expressions for $\psi''_M(x)$ and $\psi'_T(x)$ are given in (14.4) and (14.1). Inserting the expressions for $\psi'_M(x)$ and $M_{Ts}(x)$ according to (14.32) and (14.33), respectively, into (14.2), yields $\psi'_\omega(x)$. In this way, the fourth line of the transformation matrix is obtained as follows:

$$\begin{aligned}
T_{4,1} &= 0; \\
T_{4,2} &= \frac{1}{(GI_{Ts} + GI_T)^3} \left(\frac{GI_{Ts}(GI_T + GI_{Ts})(GI_T GI_{Ts})}{EI_\omega} \right. \\
&\quad - GI_{Ts}(-2G'I_T(G'I_{Ts} + G'I_T) + GI_{Ts}G''I_T) \\
&\quad \left. - GI_T(2G'I_{Ts}(G'I_{Ts} + G'I_T) + GI_{Ts}(G''I_T - G''I_{Ts})) + GI_T^2 G''I_{Ts} \right); \\
T_{4,3} &= \frac{(GI_{Ts}((GI_{Ts} + GI_T)Ei'_\omega + 2EI_\omega GI'_T) - 2EI_\omega GI_{Ts}GI'_T)}{EI_\omega^2 (GI_{Ts} + GI_T)^2}; \\
T_{4,4} &= -\frac{(GI_{Ts})^3 - 2EI_\omega(G'I_T + G'I_{Ts})^2 + EI_\omega GI_{Ts}(G''I_T + G''I_{Ts})}{EI_\omega (GI_{Ts} + GI_T)^3} \\
&\quad + \frac{GI_T((GI_{Ts})^2 + EI_\omega(G''I_T + G''I_{Ts}))}{EI_\omega (GI_{Ts} + GI_T)^3}; \\
T_{4,5} &= -\frac{GI_{Ts}m_\omega}{EI_\omega(GI_{Ts} + GI_T)} + \frac{2m_T(GI'_T + GI'_{Ts})}{(GI_{Ts} + GI_T)^2} - \frac{m'_T}{GI_{Ts} + GI_T}.
\end{aligned} \tag{14.37}$$

Next, the load vector, if needed, and the matrix \mathbf{B} in (14.13) are established:
The matrix \mathbf{A} , which is part of (14.16), is obtained as

$$\mathbf{A} = \mathbf{T}^{-1}\mathbf{B}\mathbf{T}\Big|_{x=0} = \mathbf{T}^{-1}\mathbf{B}\mathbf{T}_i. \tag{14.38}$$

A.3 Coefficients of the stiffness matrix \mathbf{K} and the load vector \mathbf{F} in (14.17)

$$\begin{aligned}
K_{1,1} &= \frac{-A_{1,3}A_{2,1} + A_{1,1}A_{2,3}}{A_{1,4}A_{2,3} - A_{1,3}A_{2,4}}; & K_{2,1} &= \frac{-A_{1,4}A_{2,2} - A_{1,2}A_{2,4}}{-A_{1,4}A_{2,3} + A_{1,3}A_{2,4}}; \\
K_{3,1} &= A_{4,1} - \frac{A_{1,1}A_{4,3}}{A_{1,3}} + \frac{A_{1,4}A_{2,1}A_{4,3}}{-A_{1,4}A_{2,3} + A_{1,3}A_{2,4}} - \frac{A_{1,1}A_{1,4}A_{2,3}A_{4,3}}{A_{1,3}(-A_{1,4}A_{2,3} + A_{1,3}A_{2,4})} \\
&\quad - \frac{A_{1,3}A_{2,1}A_{4,4}}{-A_{1,4}A_{2,3} + A_{1,3}A_{2,4}} + \frac{A_{1,1}A_{2,3}A_{4,4}}{-A_{1,4}A_{2,3} + A_{1,3}A_{2,4}};
\end{aligned} \tag{14.39}$$

$$\begin{aligned}
K_{4,1} &= \frac{A_{1,4}A_{2,3}A_{3,1} - A_{1,3}A_{2,4}A_{3,1} - A_{1,4}A_{2,1}A_{3,3} + A_{1,1}A_{2,4}A_{3,3}}{-A_{1,4}A_{2,3} + A_{1,3}A_{2,4}} \\
&\quad + \frac{A_{1,3}A_{2,1}A_{3,4} - A_{1,1}A_{2,3}A_{3,4}}{-A_{1,4}A_{2,3} + A_{1,3}A_{2,4}}; \\
K_{1,2} &= \frac{A_{1,3}A_{2,1} - A_{1,2}A_{2,3}}{-A_{1,4}A_{2,3} + A_{1,3}A_{2,4}}; & K_{2,2} &= \frac{-A_{1,4}A_{2,2} - A_{1,2}A_{2,4}}{-A_{1,4}A_{2,3} + A_{1,3}A_{2,4}}; \\
K_{3,2} &= A_{4,2} - \frac{A_{1,2}A_{4,3}}{A_{1,3}} + \frac{A_{1,4}A_{2,2}A_{4,3}}{-A_{1,4}A_{2,3} + A_{1,3}A_{2,4}} - \frac{A_{1,2}A_{1,4}A_{2,3}A_{4,3}}{A_{1,3}(-A_{1,4}A_{2,3} + A_{1,3}A_{2,4})}; \\
K_{4,2} &= \frac{A_{1,4}A_{2,3}A_{3,2} - A_{1,3}A_{2,4}A_{3,2} - A_{1,4}A_{2,2}A_{3,3} + A_{1,2}A_{2,4}A_{3,3}}{-A_{1,4}A_{2,3} + A_{1,3}A_{2,4}} \\
&\quad + \frac{A_{1,3}A_{2,2}A_{3,4} - A_{1,2}A_{2,3}A_{3,4}}{-A_{1,4}A_{2,3} + A_{1,3}A_{2,4}}; \\
K_{1,3} &= \frac{A_{2,3}}{-A_{1,4}A_{2,3} + A_{1,3}A_{2,4}}; & K_{2,3} &= \frac{A_{2,4}}{-A_{1,4}A_{2,3} + A_{1,3}A_{2,4}}; \\
K_{3,3} &= \frac{A_{4,3}}{A_{1,3}} - \frac{A_{2,3}A_{4,4}}{-A_{1,4}A_{2,3} + A_{1,3}A_{2,4}} + \frac{A_{1,4}A_{2,3}A_{4,3}}{A_{1,3}(-A_{1,4}A_{2,3} + A_{1,3}A_{2,4})}; \\
K_{4,3} &= \frac{-A_{2,4}A_{3,3} + A_{2,3}A_{3,4}}{-A_{1,4}A_{2,3} + A_{1,3}A_{2,4}}; \\
K_{1,4} &= \frac{A_{1,3}}{A_{1,4}A_{2,3} - A_{1,3}A_{2,4}}; & K_{2,4} &= \frac{A_{1,4}}{A_{1,4}A_{2,3} - A_{1,3}A_{2,4}}; \\
K_{3,4} &= \frac{A_{1,4}A_{4,3} + A_{1,3}A_{4,4}}{-A_{1,4}A_{2,3} + A_{1,3}A_{2,4}}; \\
K_{4,4} &= \frac{A_{1,4}A_{3,3}}{-A_{1,4}A_{2,3} + A_{1,3}A_{2,4}} + \frac{A_{1,3}A_{3,4}}{-A_{1,4}A_{2,3} + A_{1,3}A_{2,4}}; \\
F_1 &= \frac{A_{1,5}A_{2,3} - A_{1,3}A_{2,5}}{-A_{1,4}A_{2,3} + A_{1,3}A_{2,4}}; & F_2 &= \frac{A_{1,5}A_{2,4} - A_{1,4}A_{2,5}}{A_{1,4}A_{2,3} - A_{1,3}A_{2,4}}; \\
F_3 &= \frac{A_{1,5}A_{2,4}A_{4,3} - A_{1,4}A_{2,5}A_{4,3} - A_{1,5}A_{2,3}A_{4,4} + A_{1,3}A_{2,5}A_{4,4}}{A_{1,4}A_{2,3} - A_{1,3}A_{2,4}}; \\
F_4 &= \frac{A_{1,5}A_{2,4}A_{4,3} - A_{1,4}A_{2,5}A_{3,3} - A_{1,5}A_{2,3}A_{3,4} + A_{1,3}A_{2,5}A_{3,4}}{-A_{1,4}A_{2,3} - A_{1,3}A_{2,4}} + A_{3,5}.
\end{aligned} \tag{14.40}$$

Acknowledgements The authors gratefully acknowledge financial support by the Slovak Grant Agency of the project VEGA No. 1/0102/18.

References

- ABAQUS (2018) ABAQUS/CAE, Version 6.10-1. Dassault Systems Simulia Corp. Providence, RI, USA
- ADINA (2013) Theory and Modelling Guide. Volume I: ADINA (Version 8.9.4.). ADINA R & D, Inc.
- Aminbaghai M, Murin J, Hrabovsky J, Mang HA (2016) Torsional warping eigenmodes including the effect of the secondary torsion moment on the deformations. *Engineering Structures* 106:299–316
- Aminbaghai M, Murin J, Balduzzi G, Hrabovsky J, Hochreiner G, Mang HA (2017) Second-order torsional warping theory considering the secondary torsion-moment deformation-effect. *Engineering Structures* 147:724–739
- Aminbaghai M, Murin J, Kutis V, Hrabovsky J, Kostolani M, Mang HA (2019) Torsional warping elastostatic analysis of fgm beams with longitudinally varying material properties. *Engineering Structures* 200:109,694
- ANSYS (2019) Release R 3. Swanson Analysis System, Inc., 201 Johnson Road, Houston, PA 15342/1300, USA
- Barretta R, Feo L, Luciano R (2015) Some closed-form solutions of functionally graded beams undergoing nonuniform torsion. *Composite Structures* 123:132–136
- Barretta R, Diaco M, Feo L, Luciano R, de Sciarra FM, Penna R (2018) Stress-driven integral elastic theory for torsion of nano-beams. *Mechanics Research Communications* 87:35–41
- Dikaros IC, Sapountzakis EJ, Argyridi AK (2016) Generalized warping effect in the dynamic analysis of beams of arbitrary cross section. *Journal of Sound and Vibration* 369:119–146
- Fariborz J, Batra R (2019) Free vibration of bi-directional functionally graded material circular beams using shear deformation theory employing logarithmic function of radius. *Composite Structures* 210:217–230
- Kim NI, Lee J (2016) Theory of thin-walled functionally graded sandwich beams with single and double-cell sections. *Composite Structures* 157:141–154
- Kutis V, Murin J, Belák R, Paulech J (2011) Beam element with spatial variation of material properties for multiphysics analysis of functionally graded materials. *Computers & Structures* 89(11):1192–1205
- Murin J, Aminbaghai M, Hrabovsky J, Gogola R, Kugler S (2016) Beam finite element for modal analysis of FGM structures. *Engineering Structures* 121:1–18
- Murin J, Aminbaghai M, Hrabovsky J, Balduzzi G, Dorn M, Mang HA (2018) Torsional warping eigenmodes of FGM beams with longitudinally varying material properties. *Engineering Structures* 175:912–925
- Murin J, Aminbaghai M, Kutis V, Královic V, Sedlár T, Goga V, Mang H (2014) A new 3D Timoshenko finite beam element including non-uniform torsion of open and closed cross sections. *Engineering Structures* 59:153–160
- Przemieniecki JS (1992) Theory of Matrix Structural Analysis. McGraw-Hill
- RFEM (2006) 5.07. Ingenieur - Software Dlubal GmbH, Tiefenbach

- Rubin H (2005) Wölbkrafttorsion von durchlaufträgern mit konstantem querschnitt unter berücksichtigung sekundärer schubverformungen. *Stahlbau* 74(11):826–842
- Sapountzakis EJ, Dikaros IC (2019) Advanced 3-D beam element including warping and distortional effects for the analysis of spatial framed structures. *Engineering Structures* 188:147–164
- Shen Y, Yongjie C, Li L (2016) Torsion of a functionally graded material. *International Journal of Engineering Science* 109:14–28
- Shoghmand A, Ahmadian MT (2018) Dynamics and vibration analysis of an electrostatically actuated FGM microresonator involving flexural and torsional modes. *International Journal of Mechanical Sciences* 148:422–441
- Tsiptsis I, Sapountzakis E (2017a) Distortional analysis of beams with isogeometric methods. *Archive of Applied Mechanics* p 233–252
- Tsiptsis IN, Sapountzakis EJ (2017b) Generalized warping and distortional analysis of curved beams with isogeometric methods. *Computers & Structures* 191:33–50
- Wolfram (2012) *Mathematica 12.0.0.0*. Wolfram Research
- Yoon K, Lee PS, Kim DN (2015) Geometrically nonlinear finite element analysis of functionally graded 3D beams considering warping effects. *Composite Structures* 132:1231–1247



Chapter 15

Laminated Plates with Non-linear Visco-elastic Interlayer: The Governing Equations

Konstantin Naumenko and Holm Altenbach

Abstract Laminated glass panels are widely used in civil, automotive and photovoltaic industries. Polymeric interlayers exhibit time-dependent deformation even at room temperature. Therefore, inelastic deformation of the core layer should be identified from appropriate bending tests and taken into account in the analysis of laminated structures. The aim of this paper is to derive governing differential equations to describe non-linear visco-elastic behaviour of the panel based on the layer-wise plate theory. To this end equilibrium conditions, kinematical relations and constitutive equations for individual layers are introduced. With appropriate compatibility conditions, a system of linear twelfth order partial differential equations is derived.

Key words: Laminated glass · Layer-wise theory · Visco-elasticity · Transverse shear

15.1 Introduction

Laminated flat and curved panels with glass skin layers and a soft core layer from polymers are widely used in the civil engineering, automotive and photovoltaic industry (Ivanov, 2006; Corrado and Paggi, 2013; ABmus et al, 2016; ABmus, 2018, 2019). Crystalline or thin film photovoltaic modules are laminates with front glass layer, solar cell layer embedded in a polymeric encapsulant and a back sheet from glass or polymer (Paggi et al, 2011; Schulze, 2011; Schulze et al, 2012; Weps, 2012; Weps et al, 2013).

Konstantin Naumenko · Holm Altenbach
Lehrstuhl für Technische Mechanik., Institut für Mechanik, Otto-von-Guericke-Universität Magdeburg, 39106 Magdeburg, Germany
e-mail: konstantin.naumenko@ovgu.de, holm.altenbach@ovgu.de

Several models of structural mechanics are available for the analysis of laminated plates. The widely used approach is the first order shear deformation theory (FSDT). As shown in Eisenträger et al (2015a) this theory is well applicable for laminates with relatively stiff interlayer. An advantage of FSDT is the possibility to derive analytical solutions for deflections, strains and stresses in rectangular plates subjected to various loading configurations and boundary conditions (Naumenko et al, 2001; Altenbach et al, 2016). A problem in the FSDT is to derive effective transverse shear stiffness of the laminate based on the properties of layers. Solutions are available for layers from materials with linear-elastic properties (Reissner, 1944; Mindlin, 1951; Altenbach, 2000; Altenbach et al, 2015; Gruttmann and Wagner, 2017). However, for materials undergoing creep numerical iterative procedures are required to compute time-dependent transverse shear deformations (Altenbach and Naumenko, 2002). Furthermore, for very soft interlayers the FSDT fails to predict the behaviour of the plate accurately (Naumenko and Eremeyev, 2014; Eisenträger et al, 2015b).

Recently, higher-order shell theories were developed and applied to the analysis of laminated glass structures and photovoltaic modules. An approach applied in many works is the zig-zag approximation of displacements with respect to the thickness coordinate. Applying the variational methods or asymptotic approaches the governing equations of the three-dimensional elasticity theory can be reduced to a two-dimensional shell theory (Carrera, 2003; Filippi et al, 2018).

In contrast, within the layer-wise theory (LWT), balance equations and constitutive models are formulated independently for each layer. Applying constitutive assumptions for interaction forces and/or compatibility conditions between the layers, a model for the laminate can be developed. An advantage of LWT over a zig-zag theory is that the load transfer between the layers can be considered explicitly. Furthermore, delamination can be analyzed applying local or non-local traction-separation laws (Nase et al, 2016; Gao and Oterkus, 2019; Nordmann et al, 2019). In many cases a LWT leads to robust equations such that analytical solutions can be derived. In Naumenko and Eremeyev (2014); Eisenträger et al (2015b) closed-form analytical solutions are presented for rectangular plates with various boundary conditions. In Eisenträger et al (2015b) a finite element is developed and utilized inside Abaqus finite element code for the analysis of laminates.

Polymers like polyvinyl butyral (PVB) or ethylen vinylacetat (EVA) exhibit time-dependent deformation even at room temperature. Therefore, for the analysis of glass and photovoltaic laminates, inelastic deformation of the core layer should be taken into account. In Paggi et al (2011); Zemanová et al (2017); Zemanova et al (2018) linear visco-elasticity is applied to model creep of interlayers. Although the assumption of linear viscosity is suitable for several polymers at low stress values, in general both amorphous and crystalline polymers exhibit non-linear, in many cases exponential dependence of inelastic strain rate on the stress level (Mulliken and Boyce, 2006).

The aim of this paper is to derive governing equations describing non-linear inelastic behavior of glass laminates based on LWT. Towards this goal basic kinematics assumptions, equilibrium and compatibility conditions for layers are introduced following (Naumenko and Eremeyev, 2017). For skin layers we assume linear-elastic

material properties, while for the interlayer the non-linear visco-elastic material behavior is introduced. For the analysis of bending of symmetric laminates the LWT is reduced to a system of two coupled partial differential equations. The first one is linear and of the fourth order with respect to the plate deflection function. The second one is with respect to the relative in-plane displacement vector of skin layers. This equation is of the second order and includes the vector of inelastic shear strains, defined by the evolution equation.

15.2 Equilibrium Conditions

Figure 15.1 illustrates a rectangular three-layered plate. The Cartesian base vectors $\mathbf{i}_1, \mathbf{i}_2, \mathbf{n}$ and the corresponding coordinates x_1, x_2 and z are used to specify the position vectors in the reference state. l_1 and l_2 designate the length and the width of the plate while $h_T, h_C,$ and h_B denote the thicknesses of the top, core and bottom layers, respectively. In what follows all quantities related to the top, core and bottom layers, will be denoted by subscripts $T, C,$ and $B,$ respectively. The origin for the z coordinate is placed in the midplane of the core layer as shown in Fig. 15.1, such that

$$-h_B - \frac{h_C}{2} \leq z \leq \frac{h_C}{2} + h_T.$$

Figure 15.2 shows free-body diagrams for individual layers. The Cartesian components of stress resultant vectors and second order tensors are shown in Fig. 15.2a. They include the in-plane force tensor $\mathbf{N}_k = N_{k\alpha\beta} \mathbf{i}_\alpha \otimes \mathbf{i}_\beta,$ the shear force vector $\mathbf{Q}_k = Q_{k\alpha} \mathbf{i}_\alpha$ and the bending/twisting moment tensor $\mathbf{M}_k = -M_{k\alpha\beta} \mathbf{i}_\alpha \otimes \mathbf{i}_\beta \times \mathbf{n}$ for the k th layer with $k = T, C, B.$ The stress resultants can be obtained by the through-the-thickness integration of the stress tensor $\boldsymbol{\sigma}$ as follows, e.g. Lebedev et al (2010)

$$\mathbf{T}_k = \langle \mathbf{P} \cdot \boldsymbol{\sigma} \rangle_k = \mathbf{N}_k + \mathbf{Q}_k \otimes \mathbf{n}, \tag{15.1}$$

$$\mathbf{M}_k = -\langle z \mathbf{P} \cdot \boldsymbol{\sigma} \times \mathbf{n} \rangle_k, \tag{15.2}$$

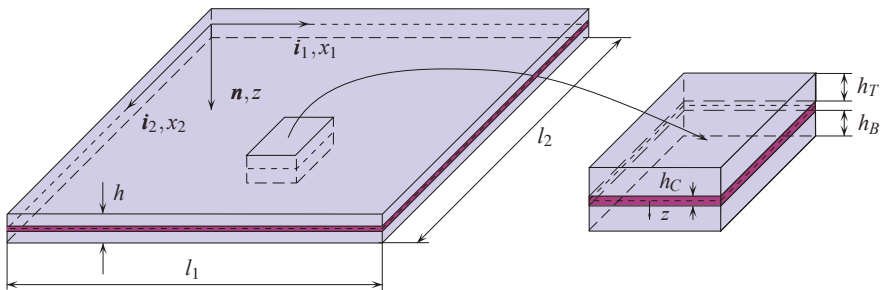


Fig. 15.1. Geometry of the layered plate

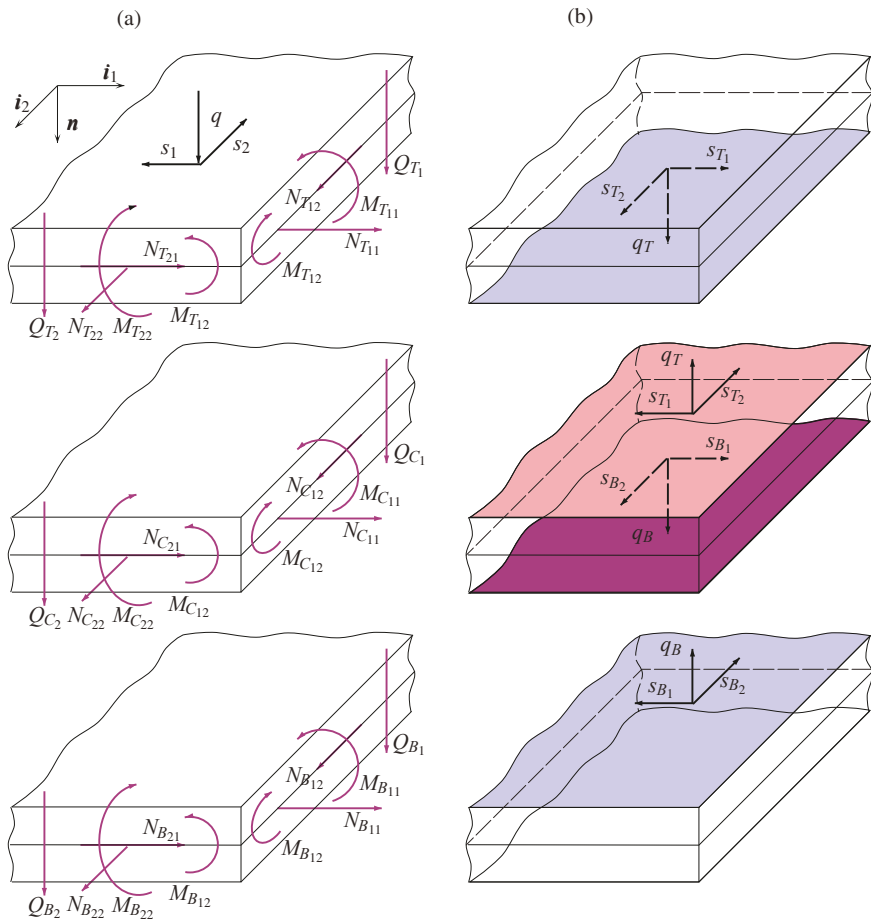


Fig. 15.2. Free-body-diagrams for layers. (a) Stress resultants, (b) interaction forces

$$N_{k\alpha\beta} = \langle \sigma_{\alpha\beta} \rangle_k, \quad Q_{k\alpha} = \langle \sigma_{\alpha 3} \rangle_k, \quad M_{k\alpha\beta} = \langle z \sigma_{\alpha\beta} \rangle_k,$$

$$\mathbf{P} = \mathbf{i}_\alpha \otimes \mathbf{i}_\alpha, \quad \langle \dots \rangle_k = \int_{-h_k/2}^{h_k/2} (\dots) dz, \quad k = T, C, B,$$

where \mathbf{P} is the projector.

The interaction force vectors between the layers include the tangentially distributed forces $\pm \mathbf{s}_T$ (interactions between the layers T and C) and $\pm \mathbf{s}_B$ (interaction between the layers C and B) as well as the corresponding normally distributed forces $\pm q_T \mathbf{n}$ and $\pm q_B \mathbf{n}$, Fig. 15.2b. We assume that the top face of the plate is subjected to the distributed lateral $\mathbf{q} = q \mathbf{n}$ and tangential \mathbf{s} loads, while the bottom face is load-free.

The equilibrium equations for the plate layer can either be derived from the equilibrium conditions for the stress tensor, e.g. Lebedev et al (2010); Libai and Simmonds (2005) or by applying the direct approach, i.e. by considering an infinitesimal plate element with stress resultants (Altenbach et al, 2005; Naumenko and Eremeyev, 2017). The equilibrium conditions are

$$\nabla \cdot \mathbf{T}_T + (q_T + q)\mathbf{n} + \mathbf{s}_T + \mathbf{s} = \mathbf{0}, \quad \nabla \cdot \mathbf{M}_T + \mathbf{T}_{T \times} + \mathbf{m}_T = \mathbf{0}, \quad (15.3)$$

$$\nabla \cdot \mathbf{T}_C + (q_B - q_T)\mathbf{n} + \mathbf{s}_B - \mathbf{s}_T = \mathbf{0}, \quad \nabla \cdot \mathbf{M}_C + \mathbf{T}_{C \times} + \mathbf{m}_C = \mathbf{0}, \quad (15.4)$$

$$\nabla \cdot \mathbf{T}_B - q_B \mathbf{n} - \mathbf{s}_B = \mathbf{0}, \quad \nabla \cdot \mathbf{M}_B + \mathbf{T}_{B \times} + \mathbf{m}_B = \mathbf{0}, \quad (15.5)$$

where

$$\nabla = \mathbf{i}_\alpha \frac{\partial}{\partial x_\alpha}$$

is the nabla (Hamilton) operator, \mathbf{T}_\times denotes the Gibbs cross or vectorial invariant of the stress resultant tensor \mathbf{T} , and

$$\mathbf{m}_T = \frac{h_T}{2} \mathbf{n} \times (\mathbf{s} + \mathbf{s}_T), \quad \mathbf{m}_C = \frac{h_C}{2} \mathbf{n} \times (\mathbf{s}_T + \mathbf{s}_B), \quad \mathbf{m}_B = \frac{h_B}{2} \mathbf{n} \times \mathbf{s}_B \quad (15.6)$$

With Eqs. (15.3)₁–(15.5)₁ the equilibrium conditions for the in-plane force tensor and the shear force vector can be derived as follows

$$\nabla \cdot \mathbf{N}_T + \mathbf{s}_T + \mathbf{s} = \mathbf{0}, \quad \nabla \cdot \mathbf{Q}_T + q_T + q = 0, \quad (15.7)$$

$$\nabla \cdot \mathbf{N}_C + \mathbf{s}_B - \mathbf{s}_T = \mathbf{0}, \quad \nabla \cdot \mathbf{Q}_C + q_B - q_T = 0, \quad (15.8)$$

$$\nabla \cdot \mathbf{N}_B - \mathbf{s}_B = \mathbf{0}, \quad \nabla \cdot \mathbf{Q}_B - q_B = 0 \quad (15.9)$$

Instead of axial moment tensors \mathbf{M}_k the polar moment tensors \mathbf{L}_k can be introduced as follows $\mathbf{L}_k = \mathbf{M}_k \times \mathbf{n} = M_{k\alpha\beta} \mathbf{i}_\alpha \otimes \mathbf{i}_\beta$. With \mathbf{L}_k the equilibrium conditions (15.3)₂–(15.5)₂ can be formulated as follows

$$\nabla \cdot \mathbf{L}_T - \mathbf{Q}_T + \frac{h_T}{2} (\mathbf{s}_T + \mathbf{s}) = \mathbf{0}, \quad (15.10)$$

$$\nabla \cdot \mathbf{L}_C - \mathbf{Q}_C + \frac{h_C}{2} (\mathbf{s}_B + \mathbf{s}_T) = \mathbf{0}, \quad (15.11)$$

$$\nabla \cdot \mathbf{L}_B - \mathbf{Q}_B + \frac{h_B}{2} \mathbf{s}_B = \mathbf{0} \quad (15.12)$$

15.3 Constitutive Equations

15.3.1 Skin Layers

For skin layers the linear-elastic behavior can be assumed. The constitutive equations for the stress resultants are formulated as follows (Naumenko and Eremeyev, 2017)

$$\mathbf{N}_k = \mathbf{C}_k \cdot \boldsymbol{\varepsilon}_k, \quad \mathbf{L}_k = \mathbf{D}_k \cdot \boldsymbol{\chi}_k, \quad k = T, B \quad (15.13)$$

where

$$\boldsymbol{\varepsilon}_k = \frac{1}{2} \left(\nabla \mathbf{u}_k + (\nabla \mathbf{u}_k)^T \right), \quad \boldsymbol{\chi}_k = \frac{1}{2} \left(\nabla \boldsymbol{\varphi}_k + (\nabla \boldsymbol{\varphi}_k)^T \right) \quad (15.14)$$

In Eqs. (15.13) $\boldsymbol{\varepsilon}_k$ is the strain tensor, \mathbf{u}_k is the in-plane displacement vector, $\boldsymbol{\varphi}_k$ is the normal rotation vector and $\boldsymbol{\chi}_k$ is the curvature change tensor of the k -th layer. \mathbf{C}_k and \mathbf{D}_k are fourth-order in-plane and bending stiffness tensors.

The skin layers of laminated glass and photovoltaic panels are usually made from isotropic materials. An exception is the light-weight design proposed in Weps et al (2013), where the bottom layer is produced from a short-fiber thermoplastic by injection molding. For short-fiber composites anisotropic and inhomogeneous material properties as a result of the manufacturing should be considered, e.g. Altenbach et al (2003). Here we assume isotropic and homogeneous material behavior. The stiffness tensors for the skin layers are represented as follows

$$\mathbf{C}_k = \frac{E_k \nu_k h_k}{1 - \nu_k^2} \mathbf{P} \otimes \mathbf{P} + \frac{E_k h_k}{2(1 + \nu_k)} (\mathbf{i}_\alpha \otimes \mathbf{P} \otimes \mathbf{i}_\alpha + \mathbf{i}_\alpha \otimes \mathbf{i}_\beta \otimes \mathbf{i}_\alpha \otimes \mathbf{i}_\beta), \quad k = T, B, \quad (15.15)$$

$$\mathbf{D}_k = \frac{E_k \nu_k h_k^3}{12(1 - \nu_k^2)} \mathbf{P} \otimes \mathbf{P} + \frac{E_k h_k^3}{24(1 + \nu_k)} (\mathbf{i}_\alpha \otimes \mathbf{P} \otimes \mathbf{i}_\alpha + \mathbf{i}_\alpha \otimes \mathbf{i}_\beta \otimes \mathbf{i}_\alpha \otimes \mathbf{i}_\beta), \quad k = T, B, \quad (15.16)$$

where E_k is the Young modulus and ν_k is the Poisson ratio of the k th skin layers.

Following many works on laminated glass, for example Ivanov (2006); Foraboschi (2012); Schulze et al (2012); Weps et al (2013), we assume that skin layers are shear-rigid. Applying the Kirchhoff kinematic hypothesis (straight normal hypothesis) we obtain

$$\boldsymbol{\varphi}_T = -\nabla w_T, \quad \boldsymbol{\varphi}_B = -\nabla w_B \quad (15.17)$$

With the kinematical constraints the shear force vectors \mathbf{Q}_T and \mathbf{Q}_B are not defined by the constitutive equations but should be computed from equilibrium conditions.

15.3.2 Core Layer

For the core layer the following constitutive equation for the shear force is assumed

$$\mathbf{Q}_C = \Gamma_C (\boldsymbol{\gamma}_C - \boldsymbol{\gamma}_C^{\text{in}}) \quad (15.18)$$

with the following transverse shear stiffness

$$\Gamma_C = \kappa G_C h_C \quad (15.19)$$

where G_C is the shear modulus and κ is some shear correction factor. The transverse shear strain is computed as follows

$$\boldsymbol{\gamma}_C = \nabla w_C + \boldsymbol{\varphi}_C \quad (15.20)$$

The inelastic part of the transverse shear strain vector is defined by the following rate equation

$$\begin{aligned} \dot{\boldsymbol{\gamma}}_C^{\text{in}} &= \mathbf{g}(\mathbf{Q}_C, \boldsymbol{\gamma}_C^{\text{in}}, \boldsymbol{s}_i, \dot{\boldsymbol{s}}_i), \quad i = 1, \dots, n, \\ \dot{\boldsymbol{s}}_i &= \mathbf{h}_i(\mathbf{Q}_C, \boldsymbol{\gamma}_C^{\text{in}}, \dot{\boldsymbol{\gamma}}_C^{\text{in}}, \boldsymbol{s}_j), \quad j = 1, \dots, n \end{aligned} \quad (15.21)$$

The variables \boldsymbol{s}_i include hardening, softening or other internal state variables and can be scalars and/or vectors. For the inelastic strain as well as for the set of internal state variables, the initial conditions must be specified

$$\boldsymbol{\gamma}_C^{\text{in}} \Big|_{t=0} = \boldsymbol{\gamma}_{C_0}^{\text{in}}, \quad \boldsymbol{s}_i \Big|_{t=0} = \boldsymbol{s}_{i_0} \quad (15.22)$$

where $\boldsymbol{\gamma}_{C_0}^{\text{in}}$ and \boldsymbol{s}_{i_0} are initial values of the inelastic strain tensor and internal state variables.

15.4 Compatibility Conditions and Constraints

From Eqs. (15.14) the compatibility condition for the in-plane strain tensors $\boldsymbol{\varepsilon}_k$ of individual layers can be derived as follows

$$\nabla \cdot (\nabla \cdot \boldsymbol{\varepsilon}_k) = \Delta \text{tr} \boldsymbol{\varepsilon}_k, \quad (15.23)$$

where $\Delta = \nabla \cdot \nabla$ is the Laplace operator. For the in-plane displacement vectors \mathbf{u}_k and vectors of cross section rotations $\boldsymbol{\varphi}_k$ the following relations can be assumed

$$\mathbf{u}_T + \frac{h_T}{2} \boldsymbol{\varphi}_T = \mathbf{u}_C - \frac{h_C}{2} \boldsymbol{\varphi}_C, \quad (15.24)$$

$$\mathbf{u}_B - \frac{h_B}{2} \boldsymbol{\varphi}_B = \mathbf{u}_C + \frac{h_C}{2} \boldsymbol{\varphi}_C \quad (15.25)$$

Furthermore, we assume that the layers have the same deflections

$$w_B = w_C = w_T = w \quad (15.26)$$

The kinematical constraints (15.24) – (15.26) imply that the layers are rigidly connected on interfaces, Fig. 15.3. Sliding and delamination between the layers are not allowed. With Eq. (15.26) it follows

$$\boldsymbol{\varphi}_T = \boldsymbol{\varphi}_B = -\nabla w \quad (15.27)$$

and the cross section rotations of the skin layers are the same. The curvature tensors take the following form

$$\chi_T = \chi_B = -\nabla\nabla w \tag{15.28}$$

With $\varphi_T = \varphi_B$ Eqs. (15.24) can be transformed to

$$\mathbf{u}_T + \mathbf{u}_B - \frac{h_T - h_B}{2} \nabla w = 2\mathbf{u}_C, \tag{15.29}$$

$$\mathbf{u}_T - \mathbf{u}_B - \frac{h_T + h_B}{2} \nabla w = -h_C \varphi_C \tag{15.30}$$

15.5 Model Reduction

Equations (15.3) - (15.28) can be used for the creep analysis of three-layer plates with soft core layer. With several simplifying assumptions these equations can be reduced to a system of three partial differential equations. The in-plane stiffness of the laminate is primarily determined by the in-plane stiffness of the skin layers. Furthermore, the core layer does not support bending moments and can be assumed to be moments-free. In the equilibrium condition (15.11) the tensor \mathbf{L}_C can be neglected. As a result the following relationship can be obtained

$$\mathbf{Q}_C = \frac{h_C}{2} (\mathbf{s}_T + \mathbf{s}_B) \tag{15.31}$$

Following Naumenko and Eremeyev (2014) let us derive the governing equations with respect to the following primary unknowns: the in-plane force tensor

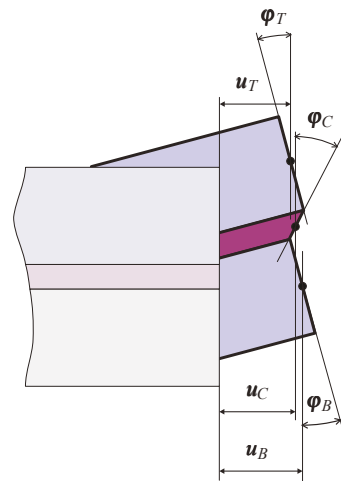


Fig. 15.3 In-plane displacements and cross section rotations of layers

$$\mathbf{N} = \mathbf{N}_T + \mathbf{N}_C + \mathbf{N}_B, \quad (15.32)$$

the relative in-plane displacement vector of the skin layers

$$\mathbf{u}_\delta = \mathbf{u}_T - \mathbf{u}_B \quad (15.33)$$

and the deflection function of the laminate w .

For the sake of brevity let us consider symmetric laminates such that $h_T = h_B$, $\mathbf{C}_T = \mathbf{C}_B$ and $\mathbf{D}_T = \mathbf{D}_B$. With the new variables $\boldsymbol{\varepsilon} = \boldsymbol{\varepsilon}_T + \boldsymbol{\varepsilon}_B$ and $\boldsymbol{\varepsilon}_\delta = \boldsymbol{\varepsilon}_T - \boldsymbol{\varepsilon}_B$ we obtain

$$\boldsymbol{\varepsilon}_\delta = \frac{1}{2} \left(\nabla \mathbf{u}_\delta + (\nabla \mathbf{u}_\delta)^T \right) \quad (15.34)$$

Taking the gradient of Eq. (15.29) and computing its symmetric part we arrive at the following relation

$$\boldsymbol{\varepsilon} = 2\boldsymbol{\varepsilon}_C \quad (15.35)$$

With the introduced variables and Eq. (15.28) we can express the strain tensors of individual layers as follows

$$2\boldsymbol{\varepsilon}_T = \boldsymbol{\varepsilon} + \boldsymbol{\varepsilon}_\delta, \quad 2\boldsymbol{\varepsilon}_B = \boldsymbol{\varepsilon} - \boldsymbol{\varepsilon}_\delta, \quad 2\boldsymbol{\varepsilon}_C = \boldsymbol{\varepsilon} \quad (15.36)$$

With Eqs. (15.13), (15.32) and (15.36) the following relation can be obtained

$$\mathbf{C} \cdot \boldsymbol{\varepsilon} = 2\mathbf{N}, \quad (15.37)$$

where $\mathbf{C} = \mathbf{C}_T + \mathbf{C}_B$ is the effective in-plane stiffness tensor of the laminate which can be computed as follows

$$\mathbf{C} = 2 \frac{E_T \nu_T h_T}{1 - \nu_T^2} \mathbf{P} \otimes \mathbf{P} + \frac{E_T h_T}{1 + \nu_T} (\mathbf{i}_\alpha \otimes \mathbf{P} \otimes \mathbf{i}_\alpha + \mathbf{i}_\alpha \otimes \mathbf{i}_\beta \otimes \mathbf{i}_\alpha \otimes \mathbf{i}_\beta) \quad (15.38)$$

With Eqs. (15.37) and (15.38) the following relation can be obtained

$$\boldsymbol{\varepsilon} = \frac{1 + \nu_T}{E_T h_T} \mathbf{N} - \frac{\nu_T}{E_T h_T} \mathbf{P} \operatorname{tr} \mathbf{N} \quad (15.39)$$

To derive the governing equation for the in-plane force tensor we add the equilibrium conditions (15.7)₁, (15.8)₁ and (15.9)₁. As a result the equilibrium condition for \mathbf{N} takes the familiar form

$$\nabla \cdot \mathbf{N} + \mathbf{s} = \mathbf{0} \quad (15.40)$$

For the sake of brevity let us neglect the tangential forces. Introducing the Airy function θ

$$\mathbf{N} = \Delta \theta \mathbf{P} - \nabla \nabla \theta \quad (15.41)$$

the equilibrium condition (15.40) is identically satisfied. The in-plane strain tensor (15.39) can now be expressed by the stress function and the force potential as follows

$$\boldsymbol{\varepsilon} = \frac{1}{E_T h_T} \Delta \Theta \mathbf{P} - \frac{1 + \nu_T}{E_T h_T} \nabla \nabla \Theta \quad (15.42)$$

With the compatibility conditions for in-plane strain tensors of skin layers (15.23) the compatibility condition for $\boldsymbol{\varepsilon}$ is

$$\nabla \cdot (\nabla \cdot \boldsymbol{\varepsilon}) = \Delta \operatorname{tr} \boldsymbol{\varepsilon} \quad (15.43)$$

Inserting (15.42) into (15.43) provides the governing equation for the stress function

$$\Delta \Delta \Theta = 0 \quad (15.44)$$

With the kinematical constraint (15.29)₁ the constitutive equations for the shear force of the core layer (15.18) can be expressed through the primary variables as follows

$$\mathbf{Q}_C = \frac{\Gamma_C}{h_C} \left(H \nabla w - \mathbf{u}_\delta - h_C \boldsymbol{\gamma}_C^{\text{in}} \right), \quad H = h_C + \frac{h_T + h_B}{2} \quad (15.45)$$

Subtracting the Eq. (15.7)₁ from (15.8)₁ and taking into account Eq. (15.31) we obtain

$$\frac{2}{h_C} \mathbf{Q}_C + \nabla \cdot \mathbf{N}_\delta = \mathbf{0}, \quad \mathbf{N}_\delta = \mathbf{N}_T - \mathbf{N}_B \quad (15.46)$$

With Eqs. (15.36)_{1,2} the constitutive equations for in-plane force tensors of skin layers (15.13)₁ take the form

$$\mathbf{N}_T = \frac{1}{2} \mathbf{C}_T \cdot \cdot (\boldsymbol{\varepsilon} + \boldsymbol{\varepsilon}_\delta), \quad \mathbf{N}_B = \frac{1}{2} \mathbf{C}_B \cdot \cdot (\boldsymbol{\varepsilon} - \boldsymbol{\varepsilon}_\delta) \quad (15.47)$$

Therefore

$$\mathbf{N}_\delta = \frac{1}{2} (\mathbf{C}_T - \mathbf{C}_B) \cdot \cdot \boldsymbol{\varepsilon} + \frac{1}{2} \mathbf{C} \cdot \cdot \boldsymbol{\varepsilon}_\delta \quad (15.48)$$

For symmetric laminates Eq. (15.48) can be simplified as follows

$$\mathbf{N}_\delta = \frac{E_T \nu_T h_T}{1 - \nu_T^2} \operatorname{tr} \boldsymbol{\varepsilon}_\delta \mathbf{P} + \frac{E_T h_T}{1 + \nu_T} \boldsymbol{\varepsilon}_\delta \quad (15.49)$$

Inserting Eqs. (15.45) and (15.49) into Eq. (15.46) and taking into account Eq. (15.34) we obtain the governing equation for the relative in-plane displacement vector

$$\frac{E_T h_T h_C^2}{4 \Gamma_C (1 - \nu_T)} \nabla \nabla \cdot \mathbf{u}_\delta + \frac{E_T h_T h_C^2}{4 \Gamma_C (1 + \nu_T)} \Delta \mathbf{u}_\delta + H \nabla w - \mathbf{u}_\delta - h_C \boldsymbol{\gamma}_C^{\text{in}} = \mathbf{0} \quad (15.50)$$

Following Naumenko and Eremeyev (2014) the moment tensor of the laminate can be introduced as follows

$$\mathbf{L} = \mathbf{L}_T + \mathbf{L}_B + \frac{1}{2} (h_C + h_B) \mathbf{N}_B - \frac{1}{2} (h_C + h_T) \mathbf{N}_T \quad (15.51)$$

With Eqs. (15.10) – (15.12) and (15.7) – (15.9) the following equilibrium conditions of the laminate can be derived

$$\nabla \cdot \mathbf{L} = \mathbf{Q}, \quad \nabla \cdot \mathbf{Q} + q = 0, \quad \mathbf{Q} = \mathbf{Q}_T + \mathbf{Q}_C + \mathbf{Q}_B \quad (15.52)$$

Applying the divergence operator to Eq. (15.52)₁ and with Eq. (15.52)₂ we obtain the familiar equation for the moment tensor

$$\nabla \cdot (\nabla \cdot \mathbf{L}) + q = 0 \quad (15.53)$$

For symmetric laminates Eq. (15.51) simplifies to

$$\mathbf{L} = \mathbf{L}_T + \mathbf{L}_B - \frac{1}{2} H \mathbf{N}_\delta \quad (15.54)$$

With Eqs. (15.13)₂, (15.16) and (15.54) we obtain

$$\mathbf{L} = \frac{E_T h_T^3}{6(1 + \nu_T)} \left(\boldsymbol{\chi} + \frac{\nu_T}{1 - \nu_T} \text{tr} \boldsymbol{\chi} \mathbf{P} \right), \quad (15.55)$$

where

$$\boldsymbol{\chi} = \frac{1}{2} \left(\nabla \boldsymbol{\varphi} + (\nabla \boldsymbol{\varphi})^T \right), \quad \boldsymbol{\varphi} = \nabla w - 3 \frac{H}{h_T^2} \mathbf{u}_\delta$$

Inserting Eqs. (15.55) into the equilibrium condition (15.53) the governing equation with respect to the deflection function can be derived

$$\Delta \Delta w + 3 \frac{H}{h_T^2} \Delta (\nabla \cdot \mathbf{u}_\delta) = \frac{q}{2D_T}, \quad D_T = \frac{E_T h_T^3}{12(1 - \nu_T^2)} \quad (15.56)$$

15.6 Discussion

The aim of this paper was to derive the governing equations for the analysis of three-layer laminated glass panels with a non-linear visco-elastic interlayer. The derived Eqs. (15.44), (15.50) and (15.56) include three basic unknown functions: the Airy stress function Θ , the relative displacement vector \mathbf{u}_δ and the deflection w . With the given field of the residual transverse shear strain vector $\boldsymbol{\gamma}_C^{\text{in}}$ at a certain time step, Eqs. (15.44), (15.50) and (15.56) provide a system of linear twelfth order partial differential equations. The solution with appropriate boundary conditions can be applied to evaluate the shear force in the core layer as a function of coordinates based on Eq. (15.45). With the constitutive model (15.21) the rate of the inelastic shear strain vector can be computed for the given stress state in the core layer. Applying a time-integration procedure the residual shear strain vector can be evaluated for the next time step. The step-by-step numerical procedure can be utilized providing the deflection of the plate as a function of time. The robust and efficient numerical

method would provide a way to identify the non-linear visco-elastic properties of the interlayer based on three and/or four point bending tests on laminates.

References

- Altenbach H (2000) On the determination of transverse shear stiffnesses of orthotropic plates. *Journal of Applied Mathematics and Physics (ZAMP)* 51:629–649
- Altenbach H, Naumenko K (2002) Shear correction factors in creep-damage analysis of beams, plates and shells. *JSME International Journal Series A, Solid Mechanics and Material Engineering* 45:77–83
- Altenbach H, Naumenko K, L'vov G, Pilipenko S (2003) Numerical estimation of the elastic properties of thin-walled structures manufactured from short-fiber-reinforced thermoplastics. *Mechanics of Composite Materials* 39(3):221–234
- Altenbach H, Naumenko K, Zhilin PA (2005) A direct approach to the formulation of constitutive equations for rods and shells. In: Pietraszkiewicz W, Szymczak C (eds) *Shell Structures: Theory and Applications*, Taylor & Francis, Leiden, pp 87–90
- Altenbach H, Eremeyev VA, Naumenko K (2015) On the use of the first order shear deformation plate theory for the analysis of three-layer plates with thin soft core layer. *ZAMM-Journal of Applied Mathematics and Mechanics/Zeitschrift für Angewandte Mathematik und Mechanik* 95(10):1004–1011
- Altenbach H, Altenbach J, Naumenko K (2016) *Ebene Flächentragwerke*. Springer, Berlin
- Aßmus M (2018) *Globale Strukturanalyse an Photovoltaik-Modulen - Theorie, Numerik, Anwendung*. Dissertation, Fakultät Maschinenbau, Otto-von-Guericke-Universität Magdeburg, Magdeburg
- Aßmus M (2019) *Structural Mechanics of Anti-Sandwiches*. SpringerBriefs in Continuum Mechanics, Springer
- Aßmus M, Naumenko K, Altenbach H (2016) A multiscale projection approach for the coupled global–local structural analysis of photovoltaic modules. *Composite Structures* 158:340–358
- Carrera E (2003) Historical review of Zig-Zag theories for multilayered plates and shells. *Applied Mechanics Review* 56(2):287–308
- Corrado M, Paggi M (2013) A multi-physics and multi-scale numerical approach to microcracking and power-loss in photovoltaic modules. *Composite Structures* 95:630–638
- Eisenträger J, Naumenko K, Altenbach H, Köppe H (2015a) Application of the first-order shear deformation theory to the analysis of laminated glasses and photovoltaic panels. *International Journal of Mechanical Sciences* 96:163–171
- Eisenträger J, Naumenko K, Altenbach H, Meenen J (2015b) A user-defined finite element for laminated glass panels and photovoltaic modules based on a layer-wise theory. *Composite Structures* 133:265–277

- Filippi M, Carrera E, Valvano S (2018) Analysis of multilayered structures embedding viscoelastic layers by higher-order, and zig-zag plate elements. *Composites Part B: Engineering* 154:77–89
- Foraboschi P (2012) Analytical model for laminated-glass plate. *Composites Part B: Engineering* 43(5):2094–2106
- Gao Y, Oterkus S (2019) Fully coupled thermomechanical analysis of laminated composites by using ordinary state based peridynamic theory. *Composite Structures* 207:397–424
- Gruttmann F, Wagner W (2017) Shear correction factors for layered plates and shells. *Computational Mechanics* 59(1):129–146
- Ivanov IV (2006) Analysis, modelling, and optimization of laminated glasses as plane beam. *International Journal of Solids and Structures* 43:6887–6907
- Lebedev LP, Cloud MJ, Eremeyev VA (2010) *Tensor Analysis with Applications in Mechanics*. World Scientific, New Jersey
- Libai A, Simmonds JG (2005) *The Nonlinear Theory of Elastic Shells*. Cambridge University Press
- Mindlin RD (1951) Influence of rotatory inertia and shear on flexural motions of isotropic, elastic plates. *Trans ASME J Appl Mech* 18(2):31 – 38
- Mulliken A, Boyce M (2006) Mechanics of the rate-dependent elastic–plastic deformation of glassy polymers from low to high strain rates. *International Journal of Solids and Structures* 43(5):1331–1356
- Nase M, Rennert M, Naumenko K, Eremeyev VA (2016) Identifying traction–separation behavior of self-adhesive polymeric films from in situ digital images under T-peeling. *Journal of the Mechanics and Physics of Solids* 91:40–55
- Naumenko K, Eremeyev VA (2014) A layer-wise theory for laminated glass and photovoltaic panels. *Composite Structures* 112:283–291
- Naumenko K, Eremeyev VA (2017) A layer-wise theory of shallow shells with thin soft core for laminated glass and photovoltaic applications. *Composite Structures* 178:434–446
- Naumenko K, Altenbach J, Altenbach H, Naumenko VK (2001) Closed and approximate analytical solutions for rectangular Mindlin plates. *Acta Mechanica* 147:153–172
- Nordmann J, Naumenko K, Altenbach H (2019) A damage mechanics based cohesive zone model with damage gradient extension for creep-fatigue-interaction. *Key Engineering Materials* 794:253–259
- Paggi M, Kajari-Schröder S, Eitner U (2011) Thermomechanical deformations in photovoltaic laminates. *The Journal of Strain Analysis for Engineering Design* 46(8):772–782
- Reissner E (1944) On the theory of bending of elastic plates. *J Math Phys* 23:184 – 191
- Schulze S (2011) *Charakterisierung polymerer Zwischenschichten in Verbundglas-Solarmodulen*. Dissertation, Zentrum für Ingenieurwissenschaften, Martin-Luther-Universität Halle-Wittenberg, Halle

- Schulze S, Pander M, Naumenko K, Altenbach H (2012) Analysis of laminated glass beams for photovoltaic applications. *International Journal of Solids and Structures* 49(15 - 16):2027–2036
- Weps M (2012) Ein Beitrag zur Charakterisierung unsymmetrischer Dreischichtverbunde mit schubweicher Zwischenschicht. Dissertation, Zentrum für Ingenieurwissenschaften, Martin-Luther-Universität Halle-Wittenberg, Halle
- Weps M, Naumenko K, Altenbach H (2013) Unsymmetric three-layer laminate with soft core for photovoltaic modules. *Composite Structures* 105:332–339
- Zemanová A, Zeman J, Šejnoha M (2017) Comparison of viscoelastic finite element models for laminated glass beams. *International Journal of Mechanical Sciences* 131:380–395
- Zemanova A, Zeman J, Janda T, Sejnoha M (2018) Layer-wise numerical model for laminated glass plates with viscoelastic interlayer. *Structural Engineering and Mechanics* 65(4):369–380



Chapter 16

Open Circular Hole in a Finite Plate Under Tension Treated by Airy Stress Function Method

Minh Nguyen-Hoang and Wilfried Becker

Abstract Open circular holes are an essential design feature and are often placed in narrow plates for reasons of limited space raising high stress concentrations. To create lightweight optimal structures precise analysis tools are vital, which can be based on analytical means providing efficient computation. That is why focus of the present paper is the determination of the stress field for the isotropic finite-width open-hole problem under uniform tension using the Airy stress function. This is performed by taking the stress field of corresponding infinite domain problem and supplementing it with auxiliary functions enabling to continuously model traction-free edges. The results are eventually validated against Finite Element analyses.

Key words: Open-hole · Finite dimensions · Stress analysis · Airy stress function

16.1 Introduction

Open circular holes are an important design feature e.g. to connect parts using bolted joints. The overall structural assessment begins with the mechanical idealisation. In many cases the thickness is much smaller than the longitudinal and lateral dimensions and a plate model is eligible. Its stresses are then numerically or analytically determined and a failure analysis is conducted. Corresponding concepts to predict brittle fracture can be distinguished in between local and non-local criteria. The former has been applied to many problems (Neuber, 1933, 1934, 2013; Peterson and Wahl, 1936) and involves the evaluation of the stress concentration directly at the hole edge. Contrary, the latter requires evaluation of the stresses at or averaged within a certain distance to the hole boundary and is capable to model the hole size effect. In the frame of Theory of Critical Distances (TCD, Whitney and Nuismer,

Minh Nguyen-Hoang · Wilfried Becker

Fachgebiet Strukturmechanik, TU Darmstadt, Franziska-Braun-Str. 7, 64287 Darmstadt, Germany
e-mail: nguyen-hoang@fsm.tu-darmstadt.de, becker@fsm.tu-darmstadt.de

1974) this length is referred to the experimentally determined characteristic distance and assumed to be invariant to the absolute value of the defect size. Furthermore, it has been identified as structural and not as material parameter since a dependency on geometric properties such as finite boundaries is evident (Camanho and Lambert, 2006). The recent state of the art non-local failure prediction concept Finite Fracture Mechanics established by Leguillon (2002) and successfully applied to many problems (Weißgraber et al, 2015) including the open-hole (Camanho et al, 2012; Rosendahl et al, 2017) and filled-hole (Catalanotti and Camanho, 2013) postulates failure, in particular the initiation of a finite-sized crack, if both stress and energy release rate yield a corresponding critical value (Cornetti et al, 2006). This generally leads to an optimisation problem to determine the failure load as well as the crack length revealing the latter being dependant of the hole diameter's absolute value. For a lightweight optimal design sufficiently exploiting the material non-local criteria being capable to capture the hole size effect shall be used. These criteria require not only the stress concentration at the hole edge but also its decay. By analytical tools the stress at any point can be easily calculated without any interpolation function. Furthermore one can profit by quickly implementable code and generated results, which is beneficial in preliminary design. That is why analytical solutions shall be focus of the present paper.

The stress analysis of open-holes was treated by many scientists with different levels of complexity such as material anisotropy, shape of the hole, finite width as well as loading along the outer boundaries. An extensive review can be found in Sevenois and Koussios (2014). The stress field of an isotropic, infinite-sized plate with central circular hole under uniform tension was found by Kirsch (1898) using the Airy stress function. The elliptical hole in an infinite, isotropic plate was treated by Savin (1961) for various load cases by means of complex potentials of Muskhelishvili (1963). Solutions regarding anisotropic plate material were found using Lekhnitskii (1968) complex potential formalism. The anisotropic ellipse without bending extension coupling in an infinite plate under uniform tension, biaxial loading and shearing is documented in Lekhnitskii (1968). Corresponding problem with bending extension coupling is treated in Becker (1993); Ukadgaonker and Rao (2000a) for arbitrary hole shape and arbitrarily oriented constant loading as well as Ukadgaonker and Rao (2000b) including arbitrarily oriented loading functions. Regarding finite width modelling the existing solutions can be classified in heuristic approaches and calculi aiming to fulfil prescribed boundary conditions of the finite setting. Concerning the former Tan (1988) suggests correction factors which scale the infinite solution for an ellipse under uniform tension by Lekhnitskii (1968) such that its integrated stresses over the actual width of the finite problem equilibrate the external load yielding good correlation regarding the stress concentrations and the decay in the hole vicinity (Tan and Kim, 1990). Solutions aiming to model finite dimensions by fulfilling the boundary conditions are mostly based on boundary collocation technique involving an overdetermined equation system. The determination of its coefficients then is performed by minimising their least square errors in the prescribed boundary conditions. For instance Ogonowski (1980) obtains agreement with the stress concentration factors of Pilkey and Pilkey (2008) for a quasi-isotropic laminate

within the width to diameter ratio range $2 \leq w/d \leq 12$ and in the circumferential stresses for a $[50^\circ/40^\circ/10^\circ]_s$ laminate and a rather large value of $w/d = 8$ with FE values. Lin and Ko (1988) provide failure predictions based on analytical stresses and TCD for both open-hole under uniform and biaxial tension for up to $w/d \geq 7.25$ leading to good agreement with experiments. Note that assessing if finite width effects on the stress field are accurately modelled using failure loads may be unsuitable since its deviations can be also due to inaccuracies in the failure prediction concept being just an idealisation of real physical mechanisms. Furthermore the small ratio of $w/d \geq 7.25$ involves rather slight finite width effects. Hufenbach and Kroll (1999) model finite dimensions including mechanical and hygrothermal load yielding good results in comparison to FE for $w/d = 6$ in an unbalanced laminate of $[30^\circ]$ and $[60^\circ]$. In Hufenbach et al (2010) good results are obtained compared to strains from the experiment for $w/d = \{2; 5\}$. Furthermore Hufenbach et al (2013) additionally implement non-constant tractions along the straight edges as well as arbitrary orientation of the elliptical hole in the plate. The uniform tension case leads to accurate results of an elliptical hole with the properties $w/(2a) = 1.67, b/a = 3$ where a represents the semi-major axis and b the semi-minor axis.

The present paper aims to model finite width by continuously fulfilling the vanishing stress boundary conditions and not only at given points. This is implemented by supplementing the infinite solution with auxiliary functions, which are capable to continuously model violations enabling their cancellation. Beneficial of this approach is that minimisation problems in overdetermined equation systems of boundary collocation approaches are not necessary. For the sake of simplicity the calculus shall be developed for the open circular hole problem under uniform tension applied at infinity. The plate material is chosen isotropic and the problem can be then solved using the Airy stress function. Once the methodology has been proven to be feasible one may extend it for more complicated settings such as orthotropic laminates using complex potentials or external loading functions.

16.2 Determination of the Stress Field

The stress field for an isotropic open-hole problem with finite width w and hole diameter d as shown in Fig. 16.1 is determined. Herein, the quantity σ_0 denotes the tensile load applied at infinity in y -direction. The stresses of this boundary value problem are determined by means of the Airy stress function.

16.2.1 Fundamentals of the Airy Stress Function

Let us assume a two-dimensional plane stress or plane strain state with linear elastic and isotropic material behaviour. Then the governing equations equilibrium, compatibility and Hooke's law can be reduced to one single differential equation using

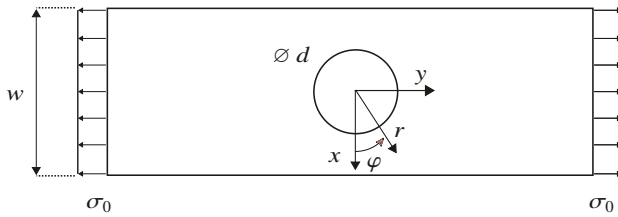


Fig. 16.1. Problem setting of finite width plate under uniform tension at infinity and circular, central opening.

the Airy stress function F . For a plane stress problem with vanishing body forces the function F needs to obey the following biharmonic equation (Timoshenko and Goodier, 1951; Sadd, 2005):

$$\Delta\Delta F = 0 \quad \text{with}$$

$$\Delta = \begin{cases} \frac{\partial^2 F}{\partial x^2} + \frac{\partial^2 F}{\partial y^2} & \text{in cartesian coordinates,} \\ \frac{\partial^2}{\partial r^2} + \frac{1}{r} \frac{\partial}{\partial r} + \frac{1}{r^2} \frac{\partial^2}{\partial \varphi^2} & \text{in polar coordinates.} \end{cases} \quad (16.1)$$

Functions F obeying the biharmonic equation are called biharmonic functions and were addressed by Michell (1899). The plane stress components are derived using

$$\sigma_x = \frac{\partial^2 F}{\partial y^2}, \quad \sigma_y = \frac{\partial^2 F}{\partial x^2}, \quad \tau_{xy} = -\frac{\partial^2 F}{\partial x \partial y}, \quad (16.2)$$

$$\sigma_r = \frac{1}{r} \frac{\partial F}{\partial r} + \frac{1}{r^2} \frac{\partial^2 F}{\partial \varphi^2}, \quad \sigma_\varphi = \frac{\partial^2 F}{\partial r^2}, \quad \tau_{r\varphi} = -\frac{\partial}{\partial r} \left(\frac{1}{r} \frac{\partial F}{\partial \varphi} \right). \quad (16.3)$$

Stress functions F are now to be chosen in such a way that the corresponding stresses satisfy the given stress boundary conditions. With $R = d/2$ being the hole radius these then read

$$\lim_{y \rightarrow \pm\infty} \sigma_y(x, y) = \sigma_0, \quad \sigma_r(R, \varphi) = \tau_{r\varphi}(R, \varphi) = 0, \quad (16.4)$$

$$\sigma_x(\pm w/2, y) = \tau_{xy}(\pm w/2, y) = 0. \quad (16.5)$$

16.2.2 Overview of Used Stress Functions

The open-hole problem containing an infinite domain with the corresponding boundary conditions in Eq. (16.4) was solved by Kirsch (1898). To determine the stress field of the finite width problem the solution of the infinite domain setting shall be taken

and supplemented by three types of auxiliary functions such that the stress boundary conditions in Eq. (16.5) are fulfilled in addition and finite width is modelled.

The first type of the auxiliary functions is dedicated to cancel non-zero tractions $\tau_{xy}(\pm w/2, y)$ in load direction along the straight edges. The second type of the auxiliary functions is dedicated to eliminate non-zero tractions $\sigma_x(\pm w/2, y)$ perpendicular to it and the third type mitigates deviations in the hole boundary conditions, which may arise due to the other two.

16.2.3 Stress Function F^{inf} Modelling the Infinite Dimension Problem

The determination of F_{inf} describing the infinite-sized open-hole problem according to Kirsch (1898); Timoshenko and Goodier (1951) is summarised. Let us investigate the stress state in sufficient large hole distance $r = R^* \gg R$. Due to St. Venant's principle it has to yield the stress components of uniform tension. Corresponding tractions are given by

$$\sigma_r(R^*, \varphi) = \frac{\sigma_0}{2} (1 - \cos 2\varphi), \quad \tau_{r\varphi}(R^*, \varphi) = \frac{\sigma_0}{2} \sin 2\varphi, \quad (16.6)$$

which can be described by the sum of one axisymmetric and one non-axisymmetric stress function. In particular,

$$F^{\text{inf}} = F^{\text{inf},1} + F^{\text{inf},2}, \quad (16.7)$$

where the former represents uniform radial tension of the amount $\sigma_0/2$ given by the stress function

$$F^{\text{inf},1} = \frac{\sigma_0}{4} \left(r^2 - 2R^2 \ln \frac{r}{R} \right) \quad (16.8)$$

while the latter can be described by that of the general form

$$F^{\text{inf},2} = f(r) \cos 2\varphi. \quad (16.9)$$

Inserting $F^{\text{inf},2}$ into the biharmonic equations Eq. (16.1) yields the ordinary differential equation

$$\left(\frac{d^2}{dr^2} + \frac{1}{r} \frac{d}{dr} - \frac{4}{r^2} \right) \left(\frac{d^2 f}{dr^2} + \frac{1}{r} \frac{df}{dr} - \frac{4f}{r^2} \right) = 0 \quad (16.10)$$

with the general solution

$$f(r) = Ar^2 + Br^4 + C \frac{1}{r^2} + D. \quad (16.11)$$

Inserting into Eq. (16.7), calculating its polar stresses using Eq. (16.3) and taking into account the vanishing tractions along the hole boundary enables the calculation of the free constants and eventually

$$F^{\text{inf}} = \underbrace{\frac{\sigma_0}{4} \left(r^2 - 2R^2 \ln \frac{r}{R} \right)}_{= F^{\text{inf},1}} + \underbrace{\frac{\sigma_0}{4} \frac{(r^2 - R^2)^2}{r^2} \cos 2\varphi}_{= F^{\text{inf},2}}. \quad (16.12)$$

Its stress components read

$$\sigma_r^{\text{inf}} = \frac{\sigma_0}{2} \left[1 - \frac{R^2}{r^2} - \left(1 - 4 \frac{R^2}{r^2} + 3 \frac{R^4}{r^4} \right) \cos 2\varphi \right], \quad (16.13)$$

$$\sigma_\varphi^{\text{inf}} = \frac{\sigma_0}{2} \left[1 + \frac{R^2}{r^2} + \left(1 + 3 \frac{R^4}{r^4} \right) \cos 2\varphi \right], \quad (16.14)$$

$$\tau_{r\varphi}^{\text{inf}} = \sigma_0 \left(1 + 2 \frac{R^2}{r^2} - 3 \frac{R^4}{r^4} \right) \cos \varphi \sin \varphi. \quad (16.15)$$

Let us use the infinite geometry solution to develop that of the finite open-hole problem. The stress field of F^{inf} incorporates non-zero tractions at $x = \pm w/2$ where the edges of the finite width problem are located. Auxiliary functions shall now be determined and superimposed such that these tractions vanish.

16.2.4 Cancellation of Tractions in Load Direction Along Straight Edges

Auxiliary functions of the first type aiming to cancel non-zero tractions $\tau_{xy}^{\text{inf}}(\pm w/2, y)$ of F^{inf} are developed. These show in load direction and their elimination is vital to equilibrate the external load by the net section stresses alone and therefore are a necessary condition to obtain an adequate solution. Hence, a robust cancellation method needs to be found, which is provided by the following mirror technique.

Let us superimpose virtual auxiliary plates created by shifting the stress field of the infinite domain problem F^{inf} and arrange them around it as illustrated in Fig. 16.2. For vanishing shear stresses F_1^{inf} is horizontally mirrored creating F_2^{inf} and F_3^{inf} . Since the left auxiliary plate does not only cancel the shear stresses at $x = -w/2$ but also affects those at the opposite edge $x = w/2$ and vice versa for the right auxiliary plate and its opposite edge at $x = -w/2$ there will be a remaining shear traction at both edges. Its magnitude depends on the number of auxiliary plates in use, which vanishes if a periodic row of auxiliary plates is superimposed. For the specific open-hole problem the shear stresses τ_{xy} are only due to the non-axisymmetric part $F^{\text{inf},2}$ since $F^{\text{inf},1}$ represents the plain plate under uniform tension. Therefore, only $F^{\text{inf},2}$

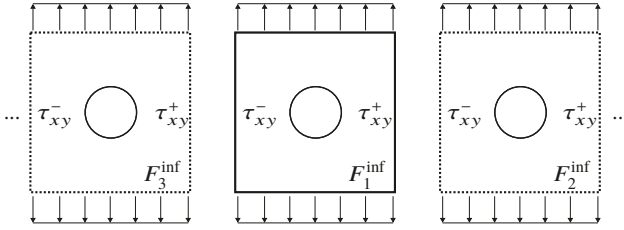


Fig. 16.2. Schematic how to arrange virtual auxiliary plates of $F_1^{\text{inf}} = F^{\text{inf}}$. For a better understanding the whole infinite open hole problem is shown although in fact only its part $F^{\text{inf},2}$ is mirrored

needs to be taken into account when mirroring. The arrangement for F^{inf} is then calculated using

$$F_i^{\text{inf}}(x,y) = \begin{cases} F^{\text{inf}}(x,y) & \text{for } i = 1, \\ F^{\text{inf},2}(x_i,y) & \text{for } i > 1, \end{cases} \quad (16.16)$$

$$\begin{aligned} \text{with } [x_i] &= [x_1 \ x_2 \ x_3 \ x_4 \ \dots] \\ &= [x \ x - w \ x + w \ x - 2w \ \dots]. \end{aligned} \quad (16.17)$$

The superimposed mirrored field is eventually obtained by

$$M(F^{\text{inf}}) = \sum_{i=1}^{n_x} F_i^{\text{inf}}. \quad (16.18)$$

The quantity n_x represents the total number of plates in use. For the present problem n_x is regarded as sufficiently large if there is less than 1 % inaccuracy in the load transfer due to remaining shear stresses along the straight edges in the superimposed field. This is expressed by

$$\psi_{\tau_{xy}^{\text{inf}}} = \frac{4}{P_y} \left| \int_0^\infty \sum_{i=1}^{n_x} \tau_{xy,i}^{\text{inf}}(\pm w/2,y) dy \right| \leq 0.01 \quad \text{with } P_y = \sigma_0 \cdot w, \quad (16.19)$$

and the smallest n_x obeying Eq. (16.19) eventually leads to $n_{x,\text{min}}$.

Note that this mirror technique can be applied to satisfy the vanishing tractions in load direction of any other plane problem involving free straight edges in a finite domain if the setup has at least one symmetry axis. In Nguyen-Hoang and Becker (2020) quasi-isotropic bolted joints are treated to name an example. Herein, the corresponding infinite geometry problem is described by a stress function requiring many terms contrary to the open-hole. Heuristic approaches equally scaling the coefficients of the net section stresses $\sigma_y^{\text{inf}}(x,0)$ of an infinite domain problem such that its integrated stresses transfer the whole external load then are unlikely to coincide with that of the actual finite boundary value problem. However, the mirror technique

provides a robust and physically motivated means for load transfer modelling no matter how complex the infinite dimensions stress field is.

16.2.5 Cancellation of Tractions Perpendicular to the Load Direction Along Straight Edges

Non-zero tractions $\sigma_x(\pm w/2)$ perpendicular to the load direction of the superimposed mirrored auxiliary field $M(F^{\text{inf}})$ shall be cancelled. This is achieved by the stress function $F_k^{\text{SE}\perp}$ developing the undesirable deviations in a Fourier series. The index k denotes a placeholder for any arbitrary stress function for which those non-zero tractions shall be eliminated. The procedure to derive $F_k^{\text{SE}\perp}$ is adapted from that of Timoshenko and Goodier (1951). A more detailed investigation can be found in Filon (1903). Taking into account the double symmetry of the present problem then the Fourier series expansion of the deviation $\sigma_{x,k}^{\text{dev}}(\pm w/2, y)$ over the wave length l_k is

$$\sigma_{x,k}^{\text{SE}\perp}(\pm w/2, y)/\sigma_0 = \frac{f_{k,0}^{\sigma_x}}{2} + \sum_{n_k=1}^{N_k} f_{k,n}^{\sigma_x} \cos \alpha_{k,n} y \quad \text{with} \quad (16.20)$$

$$\alpha_{k,n} = \frac{2n\pi}{l_k}, \quad f_{k,n}^{\sigma_x} = \frac{2}{l_k} \int_0^{l_k} \sigma_{x,k}^{\text{dev}}(\pm w/2, y) \cos \alpha_{k,n} y dy. \quad (16.21)$$

Note that the expansion is periodic over l_k and Gibbs' phenomenon to be expected due to jump discontinuities, for instance $\sigma_{x,k}^{\text{dev}}(\pm w/2, 0) \neq \sigma_{x,k}^{\text{dev}}(\pm w/2, \pm l_k)$. This is a discrepancy since the actual deviations continuously decay with increasing distance to the load introduction. That is why the correction function of the type $F_k^{\text{SE}\perp}$ is considered as less robust than the mirror technique and shall not be used to simultaneously also cancel the load transfer relevant shear stresses being necessary condition for the overall solution accuracy. Furthermore additional shear stresses elimination by $F_k^{\text{SE}\perp}$ would require another Fourier series expansion which is more expensive than their cancellation by mirroring only involving translation of stress fields. To mitigate the effect of periodicity and Gibbs' phenomenon on the characteristic stresses nearby the hole the length $l_k = 40d$ is chosen sufficiently large and a uniaxial stress state in the far-field $|y| \gg d$ establishes.

Furthermore the correction function shall not cause non-zero shear stresses at $x = \pm w/2$ expressed by

$$\tau_{xy,k}^{\text{SE}\perp}(\pm w/2, y) = 0. \quad (16.22)$$

The Airy stress function modelling these boundary conditions in Eq. (16.20) and (16.22) is given by

$$F_k^{SE\perp}/\sigma_0 = a_k y^2 + \sum_{n=1}^{N_k} \phi_{k,n}(x) A_{k,n} \cos \alpha_{k,n} y \quad \text{with} \quad (16.23)$$

$$\phi_{k,n}(x) = C_1^{\phi_{k,n}} \cosh \alpha_{k,n} x + C_2^{\phi_{k,n}} \sinh \alpha_{k,n} x +$$

$$C_3^{\phi_{k,n}} x \cosh \alpha_{k,n} x + C_4^{\phi_{k,n}} x \sinh \alpha_{k,n} x.$$

Its stress components are derived using Eq. (16.2) and read

$$\sigma_{x,k}^{SE\perp}/\sigma_0 = 2a_k - \sum_{n=1}^{N_k} \alpha_{k,n}^2 \phi_{k,n}(x) A_{k,n} \cos \alpha_{k,n} y, \quad (16.24)$$

$$\sigma_{y,k}^{SE\perp}/\sigma_0 = \sum_{n=1}^{N_k} \frac{d^2 \phi_{k,n}}{dx^2} A_{k,n} \cos \alpha_{k,n} y, \quad (16.25)$$

$$\tau_{xy,k}^{SE\perp}/\sigma_0 = \sum_{n=1}^{N_k} \alpha_{k,n} \frac{d\phi_{k,n}}{dx} A_{k,n} \sin \alpha_{k,n} y \quad (16.26)$$

with

$$\frac{d\phi_{k,n}}{dx} = \alpha_{k,n} \left(C_1^{\phi_{k,n}} \sinh \alpha_{k,n} x + C_2^{\phi_{k,n}} \cosh \alpha_{k,n} x \right) +$$

$$C_3^{\phi_{k,n}} \left(\alpha_{k,n} x \sinh \alpha_{k,n} x + \cosh \alpha_{k,n} x \right) +$$

$$C_4^{\phi_{k,n}} \left(\alpha_{k,n} x \cosh \alpha_{k,n} x + \sinh \alpha_{k,n} x \right), \quad (16.27)$$

$$\frac{d^2 \phi_{k,n}}{dx^2} = \alpha_{k,n}^2 \left(C_1^{\phi_{k,n}} \cosh \alpha_{k,n} x + C_2^{\phi_{k,n}} \sinh \alpha_{k,n} x \right) +$$

$$C_3^{\phi_{k,n}} \left(\alpha_{k,n}^2 x \cosh \alpha_{k,n} x + 2\alpha_{k,n} \sinh \alpha_{k,n} x \right) +$$

$$C_4^{\phi_{k,n}} \left(\alpha_{k,n}^2 x \sinh \alpha_{k,n} x + 2\alpha_{k,n} \cosh \alpha_{k,n} x \right). \quad (16.28)$$

The coefficients $C_i^{\phi_{k,n}}$ are calculated using

$$\phi_{k,n}(\pm w/2) = 1, \quad (16.29)$$

$$\tau_{xy,k}^{SE\perp}(\pm w/2, y) = 0 \quad \Rightarrow \quad \left. \frac{d\phi_{k,n}}{dx} \right|_{x=\pm w/2} = 0. \quad (16.30)$$

Note that setting Eq. (16.29) to one is only due to computational convenience and eventually

$$C_1^{\phi_{k,n}} = \frac{2 \sinh w/2 \alpha_{k,n} + \alpha_{k,n} w \cosh w/2 \alpha_{k,n}}{\sinh w \alpha_{k,n} + w \alpha_{k,n}}, \quad (16.31)$$

$$C_2^{\phi_{k,n}} = C_3^{\phi_{k,n}} = 0, \quad (16.32)$$

$$C_4^{\phi_{k,n}} = -\frac{2 \alpha_{k,n} \sinh w/2 \alpha_{k,n}}{\sinh w \alpha_{k,n} + w \alpha_{k,n}}. \quad (16.33)$$

Equating the coefficients in Eq. (16.20), (16.24) and taking into account Eq. (16.29) yields

$$a_k = \frac{f_{k,0}^{\sigma_x}}{4}, \quad A_{k,n} = -\frac{f_{k,n}^{\sigma_x}}{\alpha_{k,n}^2}. \quad (16.34)$$

With that all stress functions to cancel non-zero tractions along the edges $x = \pm w/2$ are fully determined. At this stage $F_k^{\text{SE}\perp}$ is applied to $M(F^{\text{inf}})$ the mirrored field of the infinite domain setting. Since both mirroring and $F_k^{\text{SE}\perp}$ interfere with the boundary conditions along the hole a corresponding mitigation stress function needs to be developed.

16.2.6 Cancellation of Tractions Along Hole Boundary

Let $\sigma_{r,k}^{\text{dev}}(R, \varphi), \tau_{r\varphi,k}^{\text{dev}}(R, \varphi)$ be the given stress deviations along the hole boundary to be eliminated. Taking into account the double symmetry of the open-hole problem their Fourier expansion reads

$$\sigma_{r,k}(R, \varphi)/\sigma_0 = \frac{f_{k,0}^{\sigma_r}}{2} + \sum_{n=1}^{N_k^*} f_{k,n}^{\sigma_r} \cos n\varphi \quad (16.35)$$

$$\tau_{r\varphi,k}(R, \varphi)/\sigma_0 = \sum_{n=1}^{N_k^*} g_{k,n}^{\tau_{r\varphi}} \sin n\varphi. \quad (16.36)$$

with the Fourier coefficients

$$\begin{aligned} f_{k,n}^{\sigma_r} &= \frac{1}{\pi} \frac{1}{\sigma_0} \int_0^{2\pi} \sigma_{r,k}^{\text{dev}}(R, \varphi) \cos n\varphi \, d\varphi, \\ g_{k,n}^{\tau_{r\varphi}} &= \frac{1}{\pi} \frac{1}{\sigma_0} \int_0^{2\pi} \tau_{r\varphi,k}^{\text{dev}}(R, \varphi) \sin n\varphi \, d\varphi. \end{aligned} \quad (16.37)$$

Taking into account that for the specific symmetric problem uneven coefficients vanish then the stress function modelling the deviations expanded in Eq. (16.35), (16.36) has the general form

$$F_k^{\text{HBC}} = R^2 \left[b_k^{\sigma_r} \ln \frac{r}{R} + \sum_{n=1}^{N_k} \left\{ B_{k,n} \left(\frac{R}{r} \right)^{2n} + C_{k,n} \left(\frac{R}{r} \right)^{2n-2} \right\} \cos 2n\varphi \right] \sigma_0. \quad (16.38)$$

Its stress components are

$$\sigma_{r,k}^{\text{HBC}} = \left[b_k^{\sigma_r} \left(\frac{R}{r} \right)^2 - 2 \sum_{n=1}^{N_k} \left\{ n(2n+1) B_{k,n} \left(\frac{R}{r} \right)^{2n+2} + (n+1)(2n-1) C_{k,n} \left(\frac{R}{r} \right)^{2n} \right\} \cos 2n\varphi \right] \sigma_0, \quad (16.39)$$

$$\sigma_{\varphi,k}^{\text{HBC}} = \left[-b_k^{\sigma_r} \left(\frac{R}{r} \right)^2 + 2 \sum_{n=1}^{N_k} \left\{ n(2n+1) B_{k,n} \left(\frac{R}{r} \right)^{2n+2} + (n-1)(2n-1) C_{k,n} \left(\frac{R}{r} \right)^{2n} \right\} \cos 2n\varphi \right] \sigma_0, \quad (16.40)$$

$$\tau_{r\varphi,k}^{\text{HBC}} = -2 \left[\sum_{n=1}^{N_k} \left\{ n(2n+1) B_{k,n} \left(\frac{R}{r} \right)^{2n+2} + n(2n-1) C_{k,n} \left(\frac{R}{r} \right)^{2n} \right\} \sin 2n\varphi \right] \sigma_0. \quad (16.41)$$

Equating the coefficients in Eq. (16.35), (16.39) and Eq. (16.36), (16.41) leads to

$$b_k^{\sigma_r} = \frac{1}{2} f_{k,0}^{\sigma_r}, \quad B_{k,n} = -\frac{1}{n(2n+1)} \left[\frac{1}{2} g_{k,2n}^{\tau_{r\varphi}} + n(2n-1) C_{k,n} \right], \quad (16.42)$$

$$C_{k,n} = \frac{1}{2} \frac{g_{k,2n}^{\tau_{r\varphi}} - f_{k,2n}^{\sigma_r}}{2n-1}$$

and the stress function to mitigate the deviating hole boundary conditions is fully determined. With that all means to address the boundary conditions of the finite domain problem are developed. However, each of the correction function is dedicated to the tractions along just one of the boundaries, in particular straight vertical edges or circular hole edge, and even may interfere the others. This is further explained in the next section and an iterative calculation scheme suggested to nevertheless take into account all boundary conditions simultaneously.

16.2.7 Overall Iterative Calculation Procedure

The capability of the correction functions to fulfil the tractions along one boundary as well as their potential interference with other edges is summarised in Table 16.1. To satisfy all boundary conditions simultaneously it is required to iteratively apply the correction functions until the remaining deviations are negligibly small. This procedure is illustrated in Fig. 16.3. After assembling the mirrored auxiliary field $M(F^{inf})$ of the infinite open-hole problem, the correction functions $F_k^{SE\perp}, F_k^{HBC}$ are applied for the first time. Since F_k^{HBC} is only dedicated to cancel non-zero traction along the hole boundary violations of those at $x = \pm w/2$ are to be expected. This is cured by mirroring the correction field F_k^{HBC} as performed for F^{inf} and then by superimposing another field $F_{k+1}^{SE\perp}$ to eliminate newly arisen $\sigma_x(\pm w/2, y)$ along the straight edges, which will slightly violate the hole boundary conditions again. Note that any field $F_k^{SE\perp}$ does not require mirroring since the condition in Eq. (16.22) assures its vanishing shear stresses. Iterating this procedure will lead to vanishing deviations along all boundaries provided by the full solution

$$F = \underbrace{\sum_{i=1}^{n_{x,\min}} F_i^{inf}}_{\text{mirrored field of } F^{inf}} + \sum_{k=1}^K \left\{ F_k^{SE\perp} + \underbrace{\sum_{i=1}^{n_{x,\min}} F_{k,i}^{HBC}}_{\text{mirrored field of } F_k^{HBC}} \right\}. \tag{16.43}$$

Herein, the quantity K denotes the number of iterations leading to sufficiently fulfilled boundary conditions, which is quantitatively assured using the following criteria:

Table 16.1

List of correction functions.

	fulfils	interferes with
$M(F^{inf})$	$\tau_{xy}(\pm w/2, y)$	Hole BCs, $\sigma_x(\pm w/2, y)$
$F_k^{SE\perp}$	$\sigma_x(\pm w/2, y)$	Hole BCs
F_k^{HBC}	Hole BCs	$\sigma_x(\pm w/2, y), \tau_{xy}(\pm w/2, y)$

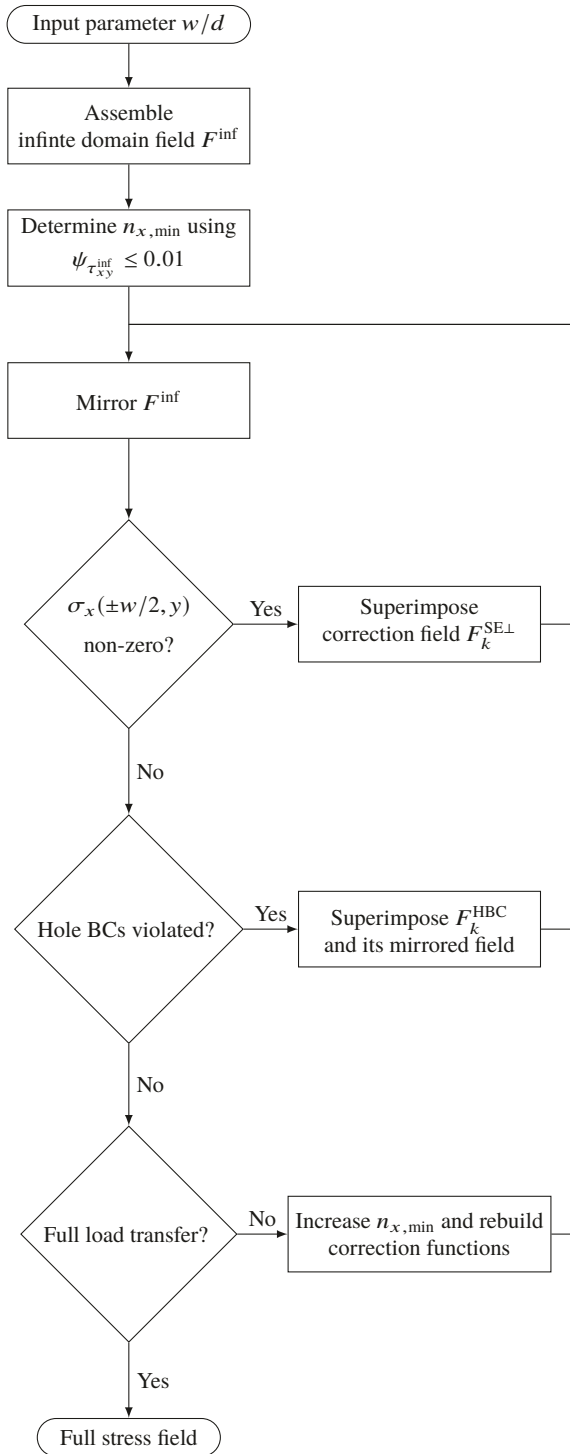


Fig. 16.3. Flowchart of the open-hole calculation method.

$$\begin{aligned}
\psi_{\sigma_r} &= \frac{R}{P_y} \int_0^{2\pi} \sqrt{\sigma_r(R, \varphi)^2} \sin \varphi \, d\varphi && \leq 0.01, \\
\psi_{\tau_{r\varphi}} &= \frac{R}{P_y} \int_0^{2\pi} \sqrt{\tau_{r\varphi}(R, \varphi)^2} \cos \varphi \, d\varphi && \leq 0.01, \\
\psi_{\sigma_x} &= \frac{4}{P_y} \int_0^{l_k/2} \sqrt{\sigma_x(\pm w/2, y)^2} \, dy && \leq 0.01, \\
\psi_{\tau_{xy}} &= \frac{4}{P_y} \int_0^\infty \sqrt{\tau_{xy}(\pm w/2, y)^2} \, dy && \leq 0.01, \\
\psi_{\sigma_y^{\text{inf}}} &= \frac{2}{P_y} \int_0^{w/2} \sqrt{(\sigma_y(x, \pm l_k/2) - \sigma_0)^2} \, dx && \leq 0.01, \\
\chi_{\sigma_y^{\text{NS}}} &= \frac{2}{P_y} \int_R^{w/2} \sigma_y(x, 0) \, dx && \leq 0.99.
\end{aligned} \tag{16.44}$$

To high values of $\psi_{\sigma_r}, \psi_{\tau_{r\varphi}}, \psi_{\sigma_x}, \psi_{\tau_{xy}}$ indicate that the corresponding non-zero stress boundary condition is not fulfilled, which requires further iterations K . Since cancellation of $\sigma_x(\pm w/2, y)$ involves periodic Fourier series expansion the upper boundary of the integral in ψ_{σ_x} is chosen at the finite value $y = l_k/2$ conservatively assuming that along half of the wave length l_k Gibbs' phenomenon has hardly an impact and a uniaxial stress state $\sigma_y(x, \pm l_k/2)$ has incorporated. This is assured by $\psi_{\sigma_y^{\text{inf}}}$ and a too high value is mitigated by increasing K and/or l_k . The fact that a value of $\psi_{\sigma_y^{\text{inf}}} \leq 0.01$ is accepted also means that an external load slightly different to $P_y = \sigma_0 \cdot w$ may be actually introduced. This shall be corrected by scaling the full stress field by

$$\frac{P_y}{P_y^*} = \frac{P_y}{2 \int_0^{w/2} \sigma_y(x, \pm l_k) \, dx}. \tag{16.45}$$

A too small value of the load transfer ratio χ_{σ_y} is due to non-vanishing force flux through the hole boundary and/or an insufficient shear stress cancellation along $x = \pm w/2$. The latter can be cured by increasing the number of auxiliary plates $n_{x,\text{min}}$. Note that the correction functions have then to be recalculated since the stress deviations depend on $n_{x,\text{min}}$. For the configurations $w/d \geq 3$ investigated $K \geq 3$, $n_{x,\text{min}} \geq 5$ have revealed to provide accurate results. These quantities generally decrease the wider w/d is chosen since deviations decay stronger. Table 16.2 lists for the correction functions of an iteration step from which stress field the deviation to cancel originates. With that all means to build the full solution are determined. Results for different geometry ratios w/d are presented and verified using Finite Element analysis in the next section.

16.3 Discussion of the Stress Results

The results for geometrical dimensions in the range $w/d = \{3, 10\}$ are presented and verified using a Finite Element model implemented in ABAQUS. The mesh contains CPS8 continuum plane stress elements with 8 nodes. The external load $\sigma_0 = 1$ MPa is applied at the hole distance $y = 20d$. Convergence in the stresses is reached for 72 elements along the hole boundary. Figure 16.4 shows an excerpt of the FE model for $w/d = 3$ and introduces the dimensionless coordinate

$$\xi = \frac{x - R}{w/2 - R}, \tag{16.46}$$

with $\xi = 0$ at the hole boundary and $\xi = 1$ at the free straight edge. To qualitatively

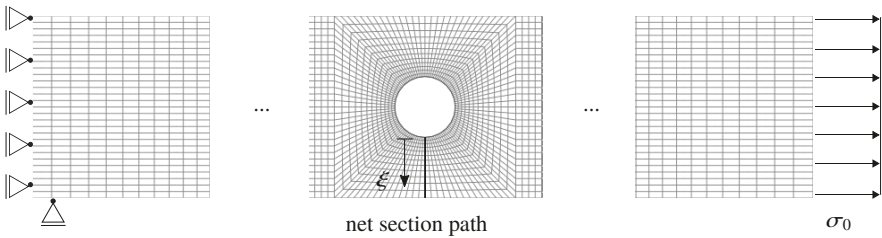


Fig. 16.4. Excerpt of Finite Element model for $w/d = 3$.

analyse the impact of the virtual auxiliary plates on the load transfer let us exemplarily plot the force flux using the stress vector

$$\vec{t}_y = \begin{bmatrix} \sigma_x & \tau_{xy} \\ \tau_{xy} & \sigma_y \end{bmatrix} \cdot \begin{bmatrix} 0 \\ 1 \end{bmatrix} = \begin{bmatrix} \tau_{xy} \\ \sigma_y \end{bmatrix}, \tag{16.47}$$

for $w/d = 3$ shown in Fig. 16.5. The force flux of the present solution is tangent to the straight edges and to the hole boundary as in the FE solution and thus provides a physical load transfer. Furthermore for the open-hole configurations investigated the present calculus leads to load transfer ratios within the range

Table 16.2

Correction function input.

stress function	corrects deviations by
$F_1^{SE\perp}$	$M(F^{inf})$
F_1^{HBC}	$M(F^{inf}) + F_1^{SE\perp}$
$F_{k>1}^{SE\perp}$	$M(F^{inf}) + \sum_{j=1}^{k-1} F_j^{SE\perp} + \sum_{j=1}^{k-1} M(F_j^{HBC})$
$F_{k>1}^{HBC}$	$M(F^{inf}) + \sum_{j=1}^k F_j^{SE\perp} + \sum_{j=1}^{k-1} M(F_j^{HBC})$

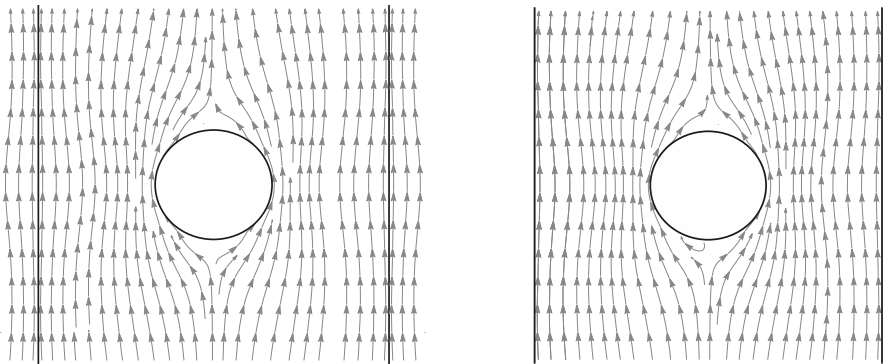
$$\chi_{\sigma_y} \geq 0.99, \quad \psi_{\sigma_x}, \psi_{\tau_{xy}}, \psi_{\sigma_y^{\text{inf}}} < 0.01, \quad \psi_{\sigma_r}, \psi_{\tau_{r\varphi}} \ll 0.001 \quad (16.48)$$

fulfilling the requirements defined in Eq. (16.44) and therefore confirming the methodology.

Let us investigate the circumferential as well as the net section stresses in Fig. 16.6. For comparison the net section stresses calculated by the heuristic approach of Tan (1988) are also shown. These are derived by taking σ_y^{inf} of the infinite geometry solution and scaling in such a way that its integrated stresses carry the whole external load and can be analytically expressed by

$$\begin{aligned} \sigma_y^{\text{Tan}}(\xi, 0) &= \frac{K_T^{\text{Tan}}}{K_T^{\text{inf}}} \sigma_y^{\text{inf}}(\xi, 0) \quad \text{with} \\ \frac{K_T^{\text{Tan}}}{K_T^{\text{inf}}} &= \frac{2}{2 - (d/w)^2 - (d/w)^4}, \\ \sigma_y^{\text{inf}}(\xi, 0) &= 1 + \frac{1}{2R^2 \left[1 + \xi(w/d - 1) \right]^2} + \frac{3}{2R^4 \left[1 + \xi(w/d - 1) \right]^4}. \end{aligned} \quad (16.49)$$

The present solution shows coincidence with the FE reference in the characteristic stresses. Note that for $w/d = 10$ the infinite domain solution by Kirsch (1898) is taken yielding a maximum error of 2 % at $\xi = 1$ in the net section stresses relevant for crack initiation assessment. Hence, a problem setting bounded by $w/d \geq 10$ can be treated as within an infinite domain. Concerning $w/d = 3$ its normalised deviations are within the order of 1 %. Those by Tan (1988) yield errors up to 36 %. However, non-local failure criteria applied to technical relevant diameter ranges require the



(a) Present finite geometry solution with influence of mirrored auxiliary plates.

(b) FE solution.

Fig. 16.5. Force flux of stress vectors \vec{t}_y with $w/d = 3$.

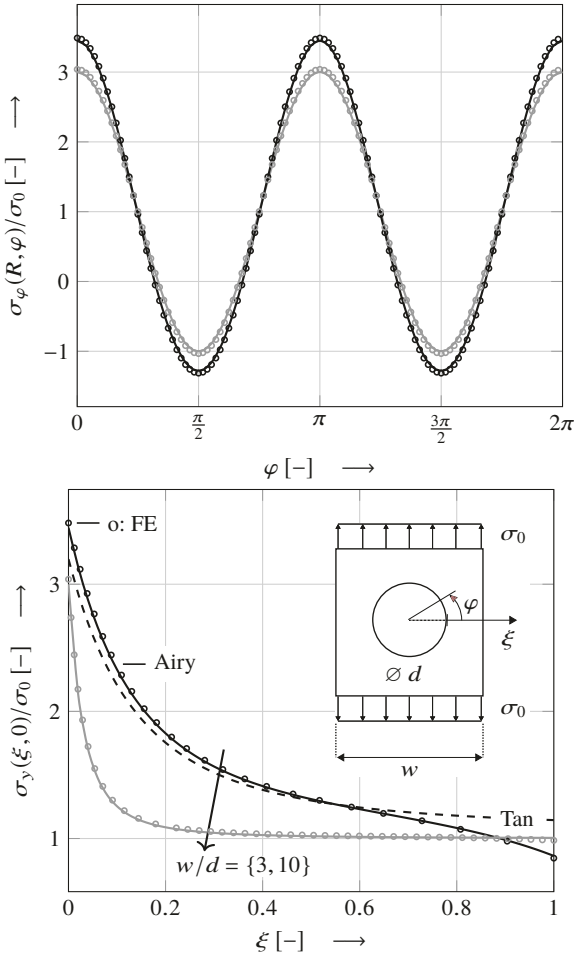


Fig. 16.6. Circumferential and net section stresses.

stress evaluation in the vicinity of the hole boundary (Whitney and Nuismer, 1974; Camanho et al, 2012) and hence limiting the actual area of interest. Let us roughly estimate it to be within the range $0 \leq \xi \leq 0.2$ then the maximum stress error by Tan (1988) is 8.3 % and that of the present solution 1.5 %. All in all the present calculus provides rather accurate results and can be used not only in preliminary but also in detail analysis where precise assessment tools matter for lightweight-optimal design.

16.4 Conclusion

In the present paper the stress field for the isotropic and finite domain open-hole problem under uniform tension is derived by analytical means of the Airy stress function. This is performed by taking the solution of the corresponding problem within an infinite domain and supplementing it with auxiliary functions to fulfil vanishing tractions along the straight edges of the actual finite width problem. Those functions include Fourier series to continuously model the deviations enabling their cancellation and mirrored arrangements of the infinite open-hole problem. The results reveal coincidence with FE net section stresses relevant for brittle fracture assessment using non-local criteria as Theory of Critical Distance with errors in the order of only 1 %.

References

- Becker W (1993) Complex method for the elliptical hole in an unsymmetric laminate. *Archive of Applied Mechanics* 63:159–169
- Camanho P, Lambert M (2006) A design methodology for mechanically fastened joints in laminated composite materials. *Composites Science and Technology* 66:3004–3020, DOI 10.1016/j.compscitech.2006.02.017
- Camanho P, Ercin G, Catalanotti G, Mahdi S, Linde P (2012) A finite fracture mechanics model for the prediction of the open-hole strength of composite laminates. *Composites Part A: Applied Science and Manufacturing* 43(8):1219 – 1225, DOI <https://doi.org/10.1016/j.compositesa.2012.03.004>
- Catalanotti G, Camanho P (2013) A semi-analytical method to predict net-tension failure of mechanically fastened joints in composite laminates. *Composites Science and Technology* 76:69–76, DOI 10.1016/j.compscitech.2012.12.009
- Cornetti P, Pugno N, Carpinteri A, Taylor D (2006) Finite fracture mechanics: A coupled stress and energy failure criterion. *Engineering Fracture Mechanics* 73(14):2021 – 2033
- Filon LNG (1903) On an approximate solution for the bending of a beam of rectangular cross-section under any system of load, with special reference to points of concentrated or discontinuous loading. *Philosophical Transactions of the Royal Society of London, Series A* 201:63–155, DOI 10.1098/rsta.1903.0014
- Hufenbach W, Kroll L (1999) Stress analysis of notched anisotropic finite plates under mechanical and hygrothermal loads. *Archive of Applied Mechanics* 69(3):145–159
- Hufenbach W, Grüber B, Gottwald R, Lepper M, Zhou B (2010) Analytical and experimental analysis of stress concentration in notched multilayered composites with finite outer boundaries. *Mechanics of Composite Materials* 46(5):531–538
- Hufenbach W, Grüber B, Lepper M, G R, Zhou B (2013) An analytical method for the determination of stress and strain concentrations in textile-reinforced gf/pp

- composites with elliptical cutout and a finite outer boundary and its numerical verification. *Archive of Applied Mechanics* 83:125–135
- Kirsch G (1898) Die Theorie der Elastizität und die Bedürfnisse der Festigkeitslehre. *Zeitschrift des Vereins deutscher Ingenieure* 42:797–807
- Leguillon D (2002) Strength or toughness? A criterion for crack onset at a notch. *European Journal of Mechanics - A/Solids* 21(1):61 – 72
- Lekhnitskii S (1968) *Anisotropic plates*. Gordon and Breach Science Publishers
- Lin CC, Ko CC (1988) Stress and strength analysis of finite composite laminates with elliptical holes. *Journal of Composite Materials* 22(4):373–385
- Michell JH (1899) On the direct determination of stress in an elastic solid with application to the theory of plates. *Proceedings of the London Mathematical Society* 31:100–124
- Muskhelishvili N (1963) Some basic problems of the mathematical theory of elasticity. Noordhoff, Groningen 17404
- Neuber H (1933) Elastisch-strengelösungen zur Kerbwirkung bei Scheiben und Umdrehungskörpern. *ZAMM* 13:439–442
- Neuber H (1934) Zur Theorie der Kerbwirkung bei Biegung und Schub. *Ingenieur-Archiv* 5(3):238–244
- Neuber H (2013) *Kerbspannungslehre: Theorie der Spannungskonzentration. Genaue Berechnung der Festigkeit*. Springer-Verlag
- Nguyen-Hoang M, Becker W (2020) Tension failure analysis for bolted joints using a closed-form stress solution. *Composite Structures* p 111931
- Ogonowski J (1980) Analytical study of finite geometry plates with stress concentrations. In: 21st Structures, Structural Dynamics, and Materials Conference, p 778
- Peterson R, Wahl A (1936) Two and three dimensional cases of stress concentration and comparison with fatigue tests. *Trans ASME* 58:A15
- Pilkey WD, Pilkey DF (2008) *Peterson's stress concentration factors*. John Wiley & Sons
- Rosendahl P, Weißgraeber P, Stein N, Becker W (2017) Asymmetric crack onset at open-holes under tensile and in-plane bending loading. *International Journal of Solids and Structures* 113-114:10 – 23
- Sadd MH (2005) *Elasticity: Theory, Applications, and Numerics - Second Edition*. Elsevier Butterworth-Heinemann
- Savin G (1961) *Stress Concentration Around Holes*. Pergamon Press
- Sevenois R, Koussios S (2014) Analytic methods for stress analysis of two-dimensional flat anisotropic plates with notches: An overview. *Applied Mechanics Reviews* 66:060,802
- Tan SC (1988) Finite-width correction factors for anisotropic plate containing a central opening. *Journal of Composite Materials* 22(11):1080–1097
- Tan SC, Kim RY (1990) Strain and stress concentrations in composite laminates containing a hole. *Experimental Mechanics* 30(4):345–351
- Timoshenko S, Goodier JN (1951) *Theory of Elasticity*. McGraw-Hill Book Company, Inc.

- Ukadgaonker V, Rao D (2000a) A general solution for stress resultants and moments around holes in unsymmetric laminates. *Composite Structures* 49(1):27 – 39
- Ukadgaonker V, Rao D (2000b) A general solution for stresses around holes in symmetric laminates under inplane loading. *Composite Structures* 49(3):339 – 354
- Weißgraeber P, Leguillon D, Becker W (2015) A review of finite fracture mechanics: Crack initiation at singular and non-singular stress-raisers. *Archive of Applied Mechanics* 86:375–401
- Whitney JM, Nuismer RJ (1974) Stress fracture criteria for laminated composites containing stress concentrations. *Journal of Composite Materials* 8:253–265, DOI 10.1177/002199837400800303



Chapter 17

Theory of Flexible Mesh-Type Shallow Kirchhoff-Love Structures Based on the Modified Couple Stress Theory

Irina V. Papkova, Jan Awrejcewicz, Anton V. Krysko, Ekatarina Yu. Krylova, and Vadim A. Krysko

Abstract In this work a generalization of the Pshenichnov theory is introduced which is devoted to study of rectangular in plane structures composed of meshed shells with two families of mutually perpendicular ribs. It is based on an account of higher order couple stresses while employing the classical modified couple stress theory. The considerations are based on the Kirchhoff-Love theory including von Kármán geometric nonlinearity. The worked out algorithms are aimed on reduction of the governing PDEs to ODEs using the FDM (finite difference method) of the second order. The obtained Cauchy problem is solved with a help of the 4th order Runge-Kutta method, whereas the static problems are solved using the set-up method. Convergence of the proposed computational scheme is validated with regard to spatial and time coordinates. Computational examples are provided.

Key words: Theory of mesh structures · Kirchhoff-Love models · Couple stress theory · Runge-Kutta methods · Geometric nonlinearity

Irina V. Papkova · Vadim A. Krysko
Department of Mathematics and Modeling, Saratov State Technical University, Politeknicheskaya 77, 410054 Saratov, Russian Federation
e-mail: ikravzova@mail.ru,tak@san.ru

Jan Awrejcewicz
Department of Automation, Biomechanics and Mechatronics, Lodz University of Technology, 1/15 Stefanowski St., 90-924 Łódź, Poland
e-mail: jan.awrejcewicz@p.lodz.pl

Anton V. Krysko
Department of Applied Mathematics and Systems Analysis, Saratov State Technical University, 77 Politeknicheskaya Str., 41005 Saratov, Russian Federation
e-mail: anton.krysko@gmail.com

Ekatarina Yu. Krylova
Department of Mathematic and Computer Modeling, Saratov State University, 83 Astrakhanskaya St., 410012 Saratov, Russian Federation
e-mail: kat.krylova@bk.ru83

17.1 Introduction

Micro- and nano-sized mesh shells are widely used in various branches of industry and beyond including production of electromechanical systems, in medicine for fabrication of biologically compatible implants, in design of various by-passes for cardiac surgeries, in solving complex problems of stability of heated objects embedded in supersonic gas flows (Belostochny and Myltcina, 2018) and in the temperature field (Belostochny and Myltcina, 2015), in a study of complex fluctuation of flexible panels and plates under longitudinal load and additive white noise (Awrejcewicz et al, 2016b; Krysko et al, 2018; Krysko-Jr. et al, 2019) as well as in many problems dealing with an account of piezoelectric effects (Krysko et al, 2013; Awrejcewicz and Krysko, 2003b). On the other hand, investigations devoted to modelling and analysis of mesh type constructions with an account of size dependent behaviour are rarely reported in the available literature (Sarkisjan, 2005).

Rapid development of MEMS/NEMS devices in mechanical and biomechanical engineering, robotics, medicine, aerospace engineering, and other, implied a wide application of micro- and nano-shells as the structural members. However, the industrial expectation require safe, reliable and accurate working regimes of size dependent mesh structures which cannot be achieved without a proper mathematical modelling of the mentioned micro/nano size dependent mechanical objects. As it has been shown in the recently published papers, the micropolar couple stress theory stands as a strong tool to solve this challenging problem (Awrejcewicz et al, 2016a; Belostochny and Myltcina, 2018; Wang, 1990).

It should be emphasized that in majority of the papers devoted to study of the so far mentioned mechanical objects rather linear models are used (Zhou and Wang, 2012). However, the experimental results exhibit the need to account of nonlinear effects while modelling of the mentioned micro- and nanosized structures.

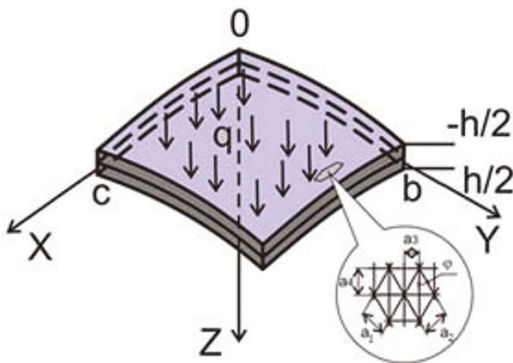
17.2 Problem Statement

In this work we investigate a shallow rectangular in plane shell composed of two families of densely distributed ribs made from one material and subjected to a constant normal continuous load (Fig. 17.1). In the rectangular system of coordinates the shell is defined as follows:

$$\Omega = \left\{ x \in [0, c]; y \in [0, b]; -\frac{h}{2} \leq z \leq \frac{h}{2} \right\}, \quad 0 \leq t \leq \infty.$$

In order to include the size effects, the corresponding mathematical model of vibrations of the mentioned mechanical system is constructed based on the micropolar (non-symmetric, couple stress) theory with inclusion of constrained rotation of particles and the von Kármán geometric nonlinearity. Owing to the continuous model proposed by Pshenichnov (1982), a regular system of ribs can be substituted

Fig. 17.1 Computational scheme of the shallow shell reinforced by two families of ribs.



by its counterpart continuous layer. The latter approach allows for quantifying of stresses occurred in the equivalent smooth panel yielded by the stresses in ribs with regard to their position measured by angles φ_j in the following way:

$$\begin{aligned}
 \sigma_{xx} &= \sum_{j=1}^2 \frac{\sigma_x^j \delta_j \cos^2 \varphi_j}{a_j}, & \sigma_{yy} &= \sum_{j=1}^2 \frac{\sigma_x^j \delta_j \sin^2 \varphi_j}{a_j}, \\
 \sigma_{xy} &= \sum_{j=1}^2 \frac{\sigma_x^j \delta_j \cos \varphi_j \sin \varphi_j}{a_j}, & m_{xx} &= \sum_{j=1}^2 \frac{m_x^j \delta_j \cos^2 \varphi_j}{a_j}, \\
 m_{yy} &= \sum_{j=1}^2 \frac{m_x^j \delta_j \sin^2 \varphi_j}{a_j}, & m_{xy} &= \sum_{j=1}^2 \frac{m_x^j \delta_j \cos \varphi_j \sin \varphi_j}{a_j}, \\
 m_{xz} &= \sum_{j=1}^2 \frac{m_{zx}^j \delta_j \cos \varphi_j}{a_j}, & m_{yz} &= \sum_{j=1}^2 \frac{m_{zx}^j \delta_j \sin \varphi_j}{a_j}.
 \end{aligned}
 \tag{17.1}$$

Here a_j denotes distance between ribs of the j -th family ($j = 1; 2$); δ_j stands for a thickness of j -th family; φ_j is the angle between the axis OX and the axis of ribs of j -th family; σ_{xx} , σ_{yy} , σ_{xy} and m_{xx} , m_{yy} , m_{xy} , m_{xz} , m_{yz} are components of stress tensor and tensor of couple stresses of the modified (smooth) shell, respectively. Physical relations for the mesh-type panel are defined based on the method of the Lagrange multipliers, i.e. we have

$$\begin{aligned}
 \sigma_x^j &= \sigma_{xx} \cos^2 \varphi_j + \sigma_{yy} \sin^2 \varphi_j + \sigma_{xy} \cos \varphi_j \sin \varphi_j, \\
 \tau^j &= \sigma_{xz} \cos \varphi_j + \sigma_{yz} \sin \varphi_j, \\
 m_x^j &= m_{xx} \cos^2 \varphi_j + m_{yy} \sin^2 \varphi_j + m_{xy} \cos \varphi_j \sin \varphi_j, \\
 m_z^j &= m_{xz} \cos \varphi_j + m_{yz} \sin \varphi_j.
 \end{aligned}
 \tag{17.2}$$

In the case of the shell material, the following relations hold

$$\sigma_{xx} = \frac{E}{1-\nu^2} [e_{xx} + \nu e_{yy}], x \leftrightarrow y, \quad \sigma_{xy} = \frac{E}{(1+\nu)} e_{xy}, \quad (17.3)$$

$$(m_{xx}, m_x, m_{zx}) = \frac{El^2}{1+\nu} (\chi_{xx}, \chi_x, \chi_{zx}),$$

where: E - Young modulus, ν - Poisson's coefficient, l - additional size dependent length parameter coupled with the tensor of bending-rotation χ . Components of the tensor of deformations e_{xx}, e_{yy}, e_{xy} with an account of the kinematic Kirchhoff-Love hypotheses take the following form

$$\begin{aligned} e_{xx} &= \frac{\partial u}{\partial x} + \frac{1}{2} \left(\frac{\partial w}{\partial x} \right)^2 - k_x w - z \frac{\partial^2 w}{\partial x^2}, \\ e_{yy} &= \frac{\partial v}{\partial y} + \frac{1}{2} \left(\frac{\partial w}{\partial y} \right)^2 - k_y w - z \frac{\partial^2 w}{\partial y^2}, \\ e_{xy} &= \frac{1}{2} \left(\frac{\partial u}{\partial y} + \frac{\partial v}{\partial x} + \frac{\partial w}{\partial x} \frac{\partial w}{\partial y} \right) - z \frac{\partial^2 w}{\partial x \partial y}. \end{aligned} \quad (17.4)$$

Components of the χ tensor, assuming that the fields of displacements and rotations depend on each other, are as follows

$$\begin{aligned} \chi_{xx} &= \frac{\partial^2 w}{\partial x \partial y}, \quad \chi_{yy} = -\frac{\partial^2 w}{\partial y \partial x}, \quad \chi_{xy} = \frac{1}{2} \left(\frac{\partial^2 w}{\partial y^2} - \frac{\partial^2 w}{\partial x^2} \right), \\ \chi_{xz} &= \frac{1}{4} \left(\frac{\partial^2 v}{\partial x^2} - \frac{\partial^2 u}{\partial x \partial y} \right), \quad \chi_{yz} = \frac{1}{4} \left(\frac{\partial^2 v}{\partial y \partial x} - \frac{\partial^2 u}{\partial y^2} \right), \end{aligned} \quad (17.5)$$

where: w - deflection; u, v - axial displacements of middle shell surface in directions of x, y , respectively; k_x, k_y - curvature parameters in directions of x, y , respectively.

17.3 Governing Equations

The governing equations of dynamics of the smooth shell, and the boundary and initial conditions are yielded by the variational Hamilton principle. Namely, a comparison of two neighbourhood motions of the system material points beginning in time instant t_0 into another system position in time instant t_1 in the case of real motion allows to define the following relation

$$\int_{t_0}^{t_1} (\delta K - \delta U + \delta W_\varepsilon + \delta W_q) dt = 0, \quad (17.6)$$

where: K - kinetic energy; U - potential energy; W - external work associated with the continuous forces W_q and dissipation energy W_ε .

An account of the couple stress theory yields the following equation governing the potential energy accumulation in an elastic body subjected to infinite small deformations:

$$U = \frac{1}{2} \int_{\Omega} (\sigma_{xx}e_{xx} + 2\sigma_{xy}e_{xy} + \sigma_{yy}e_{yy} + m_{xx}\chi_{xx} + m_{yy}\chi_{yy} + 2m_{xy}\chi_{xy} + 2m_{zx}\chi_{zx} + 2m_{zy}\chi_{zy}) dv. \tag{17.7}$$

The kinetic energy is

$$K = \frac{1}{2}\rho \int_{\Omega} \left[\left(\frac{\partial u}{\partial t} \right)^2 + \left(\frac{\partial v}{\partial t} \right)^2 + \left(\frac{\partial w}{\partial t} \right)^2 \right] dv, \tag{17.8}$$

whereas the work of external forces takes the following forms

$$W_{\varepsilon} = \int_{\Omega} \left[\varepsilon \rho \left(\frac{\partial u}{\partial t} u + \frac{\partial v}{\partial t} v + \frac{\partial w}{\partial t} w \right) \right] dv, \quad W_q = \int_0^b \int_0^c q(x, y, t) w dx dy, \tag{17.9}$$

where: ε - dissipation coefficient; ρ - density of shell material; $q(x, y, t)$ - external normal load.

We substitute relations for the potential energy (17.7) with account of (17.2)-(17.5), kinetic energy (17.8) with account of (17.1), and the work of external forces (17.9) into the energetic Hamilton principle (17.6). Variation along the variables u, w, v and integration by parts, and next comparison of the terms standing by $\delta u, \delta w, \delta v$ to zero yield the governing equations (17.13). All quantities appeared in PDEs (17.13) are defined for the counterpart smooth shell, and have the following form

$$\begin{aligned} (N_{xx}, N_{yy}, T) &= \int_{-\frac{h}{2}}^{\frac{h}{2}} (\sigma_{xx}, \sigma_{yy}, \sigma_{xy}) dz, \\ (M_{xx}, M_{yy}, H) &= \int_{-\frac{h}{2}}^{\frac{h}{2}} (\sigma_{xx}, \sigma_{yy}, \sigma_{xy}) z dz, \\ Y_{xx} &= \int_{-\frac{h}{2}}^{\frac{h}{2}} m_{xx} dz, Y_{xy} = \int_{-\frac{h}{2}}^{\frac{h}{2}} m_{xy} dz, Y_{xz} = \int_{-\frac{h}{2}}^{\frac{h}{2}} m_{xz} dz, x \overleftrightarrow{=} y \end{aligned} \tag{17.10}$$

and

$$\begin{aligned}
& \frac{\partial N_{xx}}{\partial x} + \frac{\partial T}{\partial y} + \frac{1}{2} \frac{\partial^2 Y_{yz}}{\partial y^2} + \frac{1}{2} \frac{\partial^2 Y_{xz}}{\partial x \partial y} = 2\rho h \frac{\partial^2 u}{\partial t^2} + 2\varepsilon \rho h \frac{\partial u}{\partial t}, \\
& \frac{\partial N_{yy}}{\partial y} + \frac{\partial T}{\partial x} - \frac{1}{2} \frac{\partial^2 Y_{xz}}{\partial x^2} - \frac{1}{2} \frac{\partial^2 Y_{yz}}{\partial x \partial y} = 2\rho h \frac{\partial^2 v}{\partial t^2} + 2\varepsilon \rho h \frac{\partial v}{\partial t}, \\
& \frac{\partial N_{xx}}{\partial x} \frac{\partial w}{\partial x} + N_{xx} \frac{\partial^2 w}{\partial x^2} + \frac{\partial N_{yy}}{\partial y} \frac{\partial w}{\partial y} + N_{yy} \frac{\partial^2 w}{\partial y^2} + k_y N_{yy} \\
& + k_x N_{xx} + \frac{\partial^2 M_{xx}}{\partial x^2} + \frac{\partial^2 M_{yy}}{\partial y^2} + 2 \frac{\partial^2 H}{\partial x \partial y} + \frac{\partial T}{\partial x} \frac{\partial w}{\partial y} + \frac{\partial T}{\partial y} \frac{\partial w}{\partial x} \\
& + 2T \frac{\partial^2 w}{\partial x \partial y} - \frac{\partial^2 Y_{xx}}{\partial y \partial x} + \frac{\partial^2 Y_{yy}}{\partial y \partial x} - \frac{\partial^2 Y_{xy}}{\partial y^2} + \frac{\partial^2 Y_{xy}}{\partial x^2} \\
& = 2\rho h \frac{\partial^2 w}{\partial t^2} - \frac{h^3}{6} \rho \frac{\partial^4 w}{\partial x^2 \partial t^2} - \frac{h^3}{6} \rho \frac{\partial^4 w}{\partial y^2 \partial t^2} + 2\varepsilon \rho h \frac{\partial w}{\partial t} - 2q.
\end{aligned} \tag{17.11}$$

The boundary conditions are as follows

$$\delta w = 0$$

or

$$\begin{aligned}
& \left\{ N_{xx} \frac{\partial w}{\partial x} + \frac{\partial M_x}{\partial x} + T \frac{\partial w}{\partial y} + \frac{\partial Y_{xy}}{\partial x} + 2 \frac{\partial H}{\partial y} - \frac{\partial Y_{xx}}{\partial y} + \frac{\partial Y_{yy}}{\partial y} - \frac{\partial Y_{xy}}{\partial x} \right\}_{n_x} \\
& + \left\{ N_{yy} \frac{\partial w}{\partial y} + \frac{\partial M_y}{\partial y} + T \frac{\partial w}{\partial x} + 2 \frac{\partial H}{\partial x} - \frac{\partial Y_{xx}}{\partial x} + \frac{\partial Y_{yy}}{\partial x} - \frac{\partial Y_{xy}}{\partial y} \right\}_{n_y} = 0, \\
& \frac{\partial \delta w}{\partial x} = 0 \text{ or } \{M_{xx} - Y_{xy}\}_{n_x} + \{-2H + Y_{xx} - Y_{yy}\}_{n_y} = 0, \\
& \frac{\partial \delta w}{\partial y} = 0 \text{ or } \{-2H + Y_{xx} - Y_{yy}\}_{n_x} + \{-M_{yy} + Y_{xy}\}_{n_y} = 0, \\
& \delta u = 0 \text{ or } \left\{ N_{xx} - \frac{1}{2} \frac{\partial Y_{xz}}{\partial y} \right\}_{n_x} + \left\{ T - \frac{1}{2} \frac{\partial Y_{yz}}{\partial y} - \frac{1}{2} \frac{\partial Y_{xz}}{\partial x} \right\}_{n_y} = 0, \\
& \frac{\partial \delta u}{\partial x} = 0 \text{ or } \left\{ \frac{1}{2} Y_{xz} \right\}_{n_y} = 0, \\
& \frac{\partial \delta u}{\partial y} = 0 \text{ or } \left\{ \frac{1}{2} Y_{xz} \right\}_{n_x} + \left\{ \frac{1}{2} Y_{yz} \right\}_{n_y} = 0, \\
& \delta v = 0 \text{ or } \left\{ N_{xy} - \frac{1}{2} \frac{\partial Y_{xz}}{\partial x} - \frac{1}{2} \frac{\partial Y_{yz}}{\partial y} \right\}_{n_x} + \left\{ N_{yy} - \frac{1}{2} \frac{\partial Y_{yz}}{\partial x} \right\}_{n_y} = 0, \\
& \frac{\partial \delta v}{\partial x} = 0 \text{ or } \left\{ \frac{1}{2} Y_{xz} \right\}_{n_x} + \left\{ \frac{1}{2} Y_{yz} \right\}_{n_y} = 0, \\
& \frac{\partial \delta v}{\partial y} = 0 \text{ or } \left\{ \frac{1}{2} Y_{yz} \right\}_{n_x} = 0.
\end{aligned} \tag{17.12}$$

Substitution of (17.11) with an account of (17.1)-(17.2), and (17.3)-(17.5) yields the following PDEs governing motion of the equivalent mesh-type shell:

$$\begin{aligned}
& A_{40} \frac{\partial N_{xx}}{\partial x} + A_{22} \frac{\partial N_{yy}}{\partial x} + A_{31} \frac{\partial T}{\partial x} + A_{31} \frac{\partial N_{xx}}{\partial y} + A_{13} \frac{\partial N_{yy}}{\partial y} + A_{22} \frac{\partial T}{\partial y} \\
& + \frac{1}{2} \left(A_{11} \frac{\partial^2 Y_{xz}}{\partial y^2} + A_{02} \frac{\partial^2 Y_{yz}}{\partial y^2} + A_{01} \frac{\partial^2 Y_{zz}}{\partial y^2} + A_{20} \frac{\partial^2 Y_{\alpha z}}{\partial x \partial y} + A_{11} \frac{\partial^2 Y_{\beta z}}{\partial x \partial y} \right. \\
& \left. + A_{10} \frac{\partial^2 Y_{zz}}{\partial x \partial y} \right) = \rho h \frac{\partial^2 u}{\partial t^2} + \varepsilon \rho h \frac{\partial u}{\partial t}, \\
& A_{22} \frac{\partial N_{xx}}{\partial y} + A_{04} \frac{\partial N_{yy}}{\partial y} + A_{13} \frac{\partial T}{\partial y} + A_{31} \frac{\partial N_{xx}}{\partial x} + A_{13} \frac{\partial N_{yy}}{\partial x} + A_{22} \frac{\partial T}{\partial x} \\
& - \frac{1}{2} \left(A_{20} \frac{\partial^2 Y_{xz}}{\partial x^2} + A_{11} \frac{\partial^2 Y_{yz}}{\partial x^2} + A_{10} \frac{\partial^2 Y_{zz}}{\partial x^2} + A_{11} \frac{\partial^2 Y_{xz}}{\partial x \partial y} + A_{02} \frac{\partial^2 Y_{yz}}{\partial x \partial y} \right. \\
& \left. + A_{01} \frac{\partial^2 Y_{zz}}{\partial x \partial y} \right) = \rho h \frac{\partial^2 v}{\partial t^2} + \varepsilon \rho h \frac{\partial v}{\partial t}, \\
& A_{40} \frac{\partial^2 M_{xx}}{\partial x^2} + A_{22} \frac{\partial^2 M_{yy}}{\partial x^2} + A_{31} \frac{\partial^2 H}{\partial x^2} + A_{22} \frac{\partial^2 M_{xx}}{\partial y^2} + A_{04} \frac{\partial^2 M_{yy}}{\partial y^2} \\
& + A_{13} \frac{\partial^2 H}{\partial y^2} + 2A_{31} \frac{\partial^2 M_{xx}}{\partial x \partial y} + 2A_{13} \frac{\partial^2 M_{yy}}{\partial x \partial y} + 2A_{22} \frac{\partial^2 H}{\partial x \partial y} + A_{40} \frac{\partial N_{xx}}{\partial x} \frac{\partial w}{\partial x} \\
& + A_{22} \frac{\partial N_{yy}}{\partial x} \frac{\partial w}{\partial x} + A_{31} \frac{\partial T}{\partial x} \frac{\partial w}{\partial x} + A_{40} N_{xx} \frac{\partial^2 w}{\partial x^2} + A_{22} N_{yy} \frac{\partial^2 w}{\partial x^2} \\
& + A_{31} T \frac{\partial^2 w}{\partial x^2} + A_{22} \frac{\partial N_{xx}}{\partial y} \frac{\partial w}{\partial y} + A_{04} \frac{\partial N_{yy}}{\partial y} \frac{\partial w}{\partial y} + A_{13} \frac{\partial T}{\partial y} \frac{\partial w}{\partial y} \\
& + A_{22} N_{xx} \frac{\partial^2 w}{\partial y^2} + A_{04} N_{yy} \frac{\partial^2 w}{\partial y^2} + A_{13} T \frac{\partial^2 w}{\partial y^2} + A_{31} \frac{\partial N_{xx}}{\partial x} \frac{\partial w}{\partial y} \\
& + A_{13} \frac{\partial N_{yy}}{\partial x} \frac{\partial w}{\partial y} + A_{22} \frac{\partial T}{\partial x} \frac{\partial w}{\partial y} + A_{31} \frac{\partial N_{xx}}{\partial y} \frac{\partial w}{\partial x} + A_{13} \frac{\partial N_{yy}}{\partial y} \frac{\partial w}{\partial x} \\
& + A_{22} \frac{\partial T}{\partial y} \frac{\partial w}{\partial x} + 2A_{31} N_{xx} \frac{\partial^2 w}{\partial x \partial y} + 2A_{13} N_{yy} \frac{\partial^2 w}{\partial x \partial y} + 2A_{22} T \frac{\partial^2 w}{\partial x \partial y} \\
& - A_{04} \frac{\partial^2 Y_{xx}}{\partial x \partial y} - A_{22} \frac{\partial^2 Y_{yy}}{\partial x \partial y} - A_{31} \frac{\partial^2 Y_{xy}}{\partial x \partial y} + A_{22} \frac{\partial^2 Y_{xx}}{\partial y \partial x} + A_{04} \frac{\partial^2 Y_{yy}}{\partial y \partial x} + A_{13} \frac{\partial^2 Y_{xy}}{\partial y \partial x} \\
& + A_{31} \left(\frac{\partial^2 Y_{xx}}{\partial x^2} - \frac{\partial^2 Y_{yy}}{\partial y^2} \right) + A_{13} \left(\frac{\partial^2 Y_{yy}}{\partial x^2} - \frac{\partial^2 Y_{yy}}{\partial y^2} \right) + A_{22} \left(\frac{\partial^2 Y_{xy}}{\partial x^2} - \frac{\partial^2 Y_{xy}}{\partial y^2} \right) \\
& = 2\rho h \frac{\partial^2 w}{\partial t^2} - \frac{h^3}{6} \rho \frac{\partial^4 w}{\partial x^3 \partial t^2} - \frac{h^3}{6} \rho \frac{\partial^4 w}{\partial y^2 \partial t^2} + 2\varepsilon \rho h \frac{\partial w}{\partial t} - 2q,
\end{aligned} \tag{17.13}$$

where $A_{sk} = \sum_{j=1}^n \frac{\delta_j \cos^s \varphi_j \sin^k \varphi_j}{a_j}$.

We consider, widely met in application, a case study where the shell is clamped along its contour assuming $\delta_1 = \delta_2 = \delta$, $a_1 = a_2 = a$, $\varphi_1 = 45^\circ$, $\varphi_2 = 135^\circ$. The following nondimensional governing PDEs are obtained for the case of micropolar shallow rectangular in plane shell composed of two the same and mutually perpendicular families of ribs

$$\begin{aligned}
 & 2(\nu-1) \frac{\partial^2 u}{\partial y^2} - 2(3+\nu) \frac{\partial^2 v}{\partial x \partial y} - 4(\nu+1) \lambda^2 \frac{\partial^2 u}{\partial x^2} \\
 & + 4(k_x + k_y)(\nu+1) \frac{\partial w}{\partial x} + 2(\nu-1) \frac{\partial^2 w}{\partial y^2} \frac{\partial w}{\partial x} \\
 & - 2(3+\nu) \frac{\partial w}{\partial y} \frac{\partial^2 w}{\partial x \partial y} - 4(1+\nu) \lambda^2 \frac{\partial w}{\partial x} \frac{\partial^2 w}{\partial x^2} \\
 & + l^2(\nu-1) \left(-\frac{h^2}{b^2} \frac{\partial^4 u}{\partial y^4} + \frac{h^2}{b^2} \frac{\partial^4 v}{\partial x \partial y^3} - \frac{h^2}{c^2} \frac{\partial^4 u}{\partial x^2 \partial y^2} + \frac{h^2}{c^2} \frac{\partial^4 v}{\partial x^3 \partial y} \right) \\
 & = \frac{8a(\nu^2-1)}{\delta} \frac{\partial^2 u}{\partial t^2}, \\
 & 4(k_x + k_y)(1+\nu) \frac{\partial w}{\partial y} - 4(1+\nu) \frac{\partial^2 v}{\partial y^2} - 2(3+\nu) \lambda^2 \frac{\partial^2 u}{\partial x \partial y} \\
 & + 2(1-\nu) \lambda^2 \frac{\partial^2 v}{\partial x^2} - 4(\nu+1) \frac{\partial w}{\partial y} \frac{\partial^2 w}{\partial y^2} - 2(3+\nu) \lambda^2 \frac{\partial w}{\partial x} \frac{\partial^2 w}{\partial y \partial x} \\
 & + 2(\nu-1) \lambda^2 \frac{\partial w}{\partial y} \frac{\partial^2 w}{\partial x^2} + l^2(\nu-1) \left(\frac{h^2}{c^2} \frac{\partial^4 u}{\partial x \partial y^3} - \frac{h^2}{c^2} \frac{\partial^4 v}{\partial x^2 \partial y^2} \right. \\
 & \left. + \frac{h^2}{c^2} \lambda^2 \frac{\partial^4 u}{\partial x^3 \partial y} - \frac{h^2}{c^2} \lambda^2 \frac{\partial^4 v}{\partial x^4} \right) = \frac{8a(\nu^2-1)}{\delta} \frac{\partial^2 v}{\partial t^2}, \\
 & \left([1+\nu] + 6l^2[1-\nu] \right) \frac{c}{\lambda h} \frac{\partial^4 w}{\partial y^4} + 4(1+3l^2[\nu-1]) \frac{1}{\lambda^2} \frac{\partial^4 w}{\partial x^2 \partial y^2} \\
 & + \left([1+\nu] + 6l^2[1-\nu] \right) \lambda^2 \frac{\partial^4 w}{\partial x^4} + 12k_y(k_x + k_y)(1+\nu) \frac{1}{\lambda^2} w \\
 & - 12k_y(1+\nu) \frac{c}{\lambda h} \frac{\partial v}{\partial y} - 12k_y(1+\nu) \frac{b^2}{h^2} \frac{\partial u}{\partial x} \\
 & + 6(2k_x + k_y)(1+\nu) \frac{c}{h\lambda} \left(\frac{\partial w}{\partial y} \right)^2 - 12(1+\nu) \frac{1}{\lambda^2} \frac{\partial w}{\partial y} \frac{\partial^2 v}{\partial y^2} \\
 & + 12(k_x + k_y)(1+\nu) \frac{c}{h\lambda} w \frac{\partial^2 w}{\partial y^2} - 12(1+\nu) \frac{1}{\lambda^2} \frac{\partial v}{\partial y} \frac{\partial^2 w}{\partial y^2} \\
 & - 18(1+\nu) \left(\frac{\partial w}{\partial y} \right)^2 \frac{\partial^2 w}{\partial y^2} - 12(\nu+1) \frac{\partial^2 w}{\partial y^2} \frac{\partial u}{\partial x} + 6(\nu-1) \frac{\partial^2 u}{\partial y^2} \frac{\partial w}{\partial x}
 \end{aligned} \tag{17.14}$$

$$\begin{aligned}
 &+ 6(2k_x + k_y)(\nu + 1) \frac{b}{h} \left(\frac{\partial w}{\partial x} \right)^2 - 12 \frac{\partial^2 w}{\partial y^2} \left(\frac{\partial w}{\partial x} \right)^2 - 6(3 + \nu) \frac{\partial w}{\partial y} \frac{\partial^2 u}{\partial x \partial y} \\
 &- 6(3 + \nu) \frac{\partial w}{\partial x} \frac{\partial^2 v}{\partial x \partial y} + 12(\nu - 1) \frac{\partial u}{\partial y} \frac{\partial^2 w}{\partial x \partial y} + 12(\nu - 1) \frac{\partial v}{\partial x} \frac{\partial^2 w}{\partial x \partial y} \\
 &- 48 \frac{\partial w}{\partial y} \frac{\partial w}{\partial x} \frac{\partial^2 w}{\partial x \partial y} - 12(1 + \nu) \frac{b^2}{c^2} \frac{\partial w}{\partial x} \frac{\partial^2 u}{\partial x^2} + 6(\nu - 1)\lambda \frac{\partial w}{\partial y} \frac{\partial^2 v}{\partial x^2} \\
 &+ 12(k_x + k_y)(\nu + 1) \frac{b}{h} w \frac{\partial^2 w}{\partial x^2} - 12(\nu + 1) \frac{1}{\lambda^2} \frac{\partial v}{\partial y} \frac{\partial^2 w}{\partial x^2} \\
 &- 12 \left(\frac{\partial w}{\partial y} \right)^2 \frac{\partial^2 w}{\partial x^2} - 12(1 + \nu) \frac{\partial u}{\partial x} \frac{\partial^2 w}{\partial x^2} \\
 &- 18(1 + \nu)\lambda^2 \left(\frac{\partial w}{\partial x} \right)^2 \frac{\partial^2 w}{\partial x^2} = \frac{24a(\nu^2 - 1)}{\delta} \left(\frac{\partial^2 w}{\partial t^2} + \varepsilon \frac{\partial w}{\partial t} - 2q \right)
 \end{aligned}$$

The following initial conditions are taken

$$u = v = w = 0, \quad \frac{\partial w}{\partial t} = 0, \quad \frac{\partial u}{\partial t} = 0, \quad \frac{\partial v}{\partial t} = 0 \quad (t = 0), \tag{17.15}$$

whereas the boundary conditions are as follows

$$\begin{aligned}
 u = v = w = 0, \quad \frac{\partial u}{\partial x} = 0, \quad \frac{\partial u}{\partial y} = 0, \quad \frac{\partial v}{\partial x} = 0, \quad \frac{\partial v}{\partial y} = 0, \\
 \frac{\partial w}{\partial x} = 0, \quad \frac{\partial w}{\partial y} = 0 \quad \text{for } x = 0; 1, \quad y = 0; 1.
 \end{aligned} \tag{17.16}$$

The following relations hold for dimensional and nondimensional parameters:

$$\begin{aligned}
 x = c\bar{x}, \quad y = b\bar{y}, \quad w = h\bar{w}, \quad u = \frac{h^2}{c}\bar{u}, \quad v = \frac{h^2}{b}\bar{v}, \quad \delta = h\bar{\delta}, \quad a = h\bar{a}, \\
 l = h\bar{l}, \quad k_x = \frac{h}{c^2}\bar{k}_x, \quad k_y = \frac{h}{b^2}\bar{k}_y, \quad t = \frac{cb}{h}\sqrt{\frac{\rho}{E}}\bar{t}, \quad \varepsilon = \frac{h}{cb}\sqrt{\frac{E}{\rho}}\bar{\varepsilon}, \\
 q = \frac{Eh^4}{c^2b^2}\bar{q}, \quad \lambda = \frac{b}{c}.
 \end{aligned} \tag{17.17}$$

Here c, b stand for the linear dimension of the panel with regard to x and y , respectively, and ε is the dissipation coefficient.

In order to reduce the problem governed by nonlinear PDEs (17.3) to its counterpart Cauchy problem, the method of FDM of the second order is employed, which yields

$$\begin{aligned}
 &2(\nu - 1)\Lambda_{yy}^2 u - 2(3 + \nu)\Lambda_{xy}^2 v - 4(\nu + 1)\lambda^2 \Lambda_{yy}^2 u + 4(k_x + k_y)(\nu + 1)\Lambda_y^1 u \\
 &+ 2(\nu - 1)\Lambda_{yy}^2 w \Lambda_x^1 w - 2(3 + \nu)\Lambda_y^1 w \Lambda_{xy}^2 w - 4(1 + \nu)\lambda^2 \Lambda_x^1 w \Lambda_{xy}^2 w
 \end{aligned}$$

$$\begin{aligned}
 &+ l^2(\nu - 1) \left(-\frac{h^2}{b^2} \Lambda_{yyyy}^4 w \right) + l^2(\nu - 1) \left(\frac{h^2}{b^2} \Lambda_{xyyy}^4 w \right) \\
 &+ l^2(\nu - 1) \left(-\frac{h^2}{c^2} \Lambda_{xxyy}^4 u + \frac{h^2}{c^2} \Lambda_{xxxy}^4 v \right) = \frac{8a(\nu^2 - 1)}{\delta} \ddot{u}, \\
 &4(k_x + k_y)(1 + \nu) \Lambda_{yy}^2 w - 4(1 + \nu) \Lambda_{yy}^2 v - 2(3 + \nu) \lambda^2 \Lambda_{xy}^2 u \\
 &+ 2(1 - \nu) \lambda^2 \Lambda_{xx}^2 v - 4(\nu + 1) \Lambda_y^1 w \Lambda_{yy}^2 w - 2(3 + \nu) \lambda^2 \Lambda_x^1 w \Lambda_{xy}^2 w \\
 &+ 2(\nu - 1) \lambda^2 \Lambda_y^1 w \Lambda_{yy}^2 w + l^2(\nu - 1) \left(-\frac{h^2}{c^2} \Lambda_{xxyy}^4 v - \frac{h^2}{c^2} \lambda^2 \Lambda_{xxxx}^4 v \right. \\
 &\left. + \frac{h^2}{c^2} \Lambda_{xyyy}^4 u + \frac{h^2}{c^2} \lambda^2 \Lambda_{xxxy}^4 u \right) = \frac{8a(\nu^2 - 1)}{\delta} \ddot{v}, \tag{17.18} \\
 &([1 + \nu] + 6l^2[1 - \nu]) \frac{c}{\lambda h} \Lambda_{yyyy}^4 w + 4(1 + 3l^2[\nu - 1]) \frac{1}{\lambda^2} \Lambda_{xxyy}^4 w \\
 &+ ([1 + \nu] + 6l^2[1 - \nu]) \lambda^2 \Lambda_{xxxx}^4 w + 12k_y(k_x + k_y)(1 + \nu) \frac{1}{\lambda^2} w_i \\
 &- 12k_y(1 + \nu) \frac{c}{\lambda h} \Lambda_y^1 v - 12k_y(1 + \nu) \frac{b^2}{h^2} \Lambda_x^1 u + 6(2k_x + k_y)(1 + \nu) \frac{c}{h\lambda} (\Lambda_y^1 w)^2 \\
 &- 12(1 + \nu) \frac{1}{\lambda^2} \Lambda_y^1 v \Lambda_{yy}^2 w - 18(1 + \nu) (\Lambda_y^1 w)^2 \Lambda_{yy}^2 w - 12(\nu + 1) \Lambda_{yy}^2 w \Lambda_y^1 v \\
 &+ 6(\nu - 1) \Lambda_{yy}^2 u \Lambda_x^1 w + 6(2k_x + k_y)(\nu + 1) \frac{b}{h} (\Lambda_x^1 w)^2 \\
 &- 12\Lambda_{yy}^2 w (\Lambda_x^1 w)^2 - 6(3 + \nu) \Lambda_y^1 w \Lambda_{xy}^2 u - 6(3 + \nu) \Lambda_x^1 w \Lambda_{xy}^2 v \\
 &+ 12(\nu - 1) \Lambda_y^1 u \Lambda_{xy}^2 w + 12(\nu - 1) \Lambda_x^1 v \Lambda_{xy}^2 w - 48\Lambda_y^1 w \Lambda_x^1 w \Lambda_{xy}^2 w \\
 &- 12(1 + \nu) \frac{b^2}{c^2} \Lambda_x^1 w \Lambda_{xx}^2 u + 6(\nu - 1) \lambda \Lambda_y^1 w \Lambda_{xx}^2 v \\
 &+ 12(k_x + k_y)(\nu + 1) \frac{b}{h} w_i \Lambda_{xx}^2 w - 12(\nu + 1) \frac{1}{\lambda^2} \Lambda_y^1 v \Lambda_{xx}^2 w \\
 &- 12(\Lambda_y^1 w)^2 \Lambda_{xx}^2 w - 12(1 + \nu) \Lambda_x^1 u \Lambda_{xx}^2 w \\
 &- 18(1 + \nu) \lambda^2 (\Lambda_x^1 w)^2 \Lambda_{xx}^2 w = \frac{24a(\nu^2 - 1)}{\delta} (\ddot{w} + \varepsilon \dot{w} - 2q).
 \end{aligned}$$

The associated boundary conditions take the following difference form

$$\begin{aligned}
 &u_{0,j} = v_{0,j} = w_{0,j} = 0, \quad u_{-1,j} = u_{1,j}, \quad v_{-1,j} = v_{1,j}, \quad w_{-1,j} = w_{1,j}, \\
 &u_{n,j} = v_{n,j} = w_{n,j} = 0, \quad u_{n+1,j} = u_{n-1,j}, \quad v_{n+1,j} = v_{n-1,j}, \quad w_{n+1,j} = w_{n-1,j}, \\
 &u_{i,0} = v_{i,0} = w_{i,0} = 0, \quad u_{i,-1} = u_{i,1}, \quad v_{i,-1} = v_{i,1}, \quad w_{i,-1} = w_{i,1}, \\
 &u_{i,n} = v_{i,n} = w_{i,n} = 0, \quad u_{i,n+1} = u_{i,n-1}, \quad v_{i,n+1} = v_{i,n-1}, \quad w_{i,n+1} = w_{i,n-1},
 \end{aligned} \tag{17.19}$$

where:

$$\begin{aligned}
A_x^1(f) &= \frac{f_{i+1,j} - f_{i-1,j}}{2h}; \\
A_y^1(f) &= \frac{f_{i,j+1} - f_{i,j-1}}{2h}; \\
A_{yy}^2(f) &= \frac{f_{i,j+1} - 2f_{i,j} + f_{i,j-1}}{h^2}; \\
A_{xx}^2(f) &= \frac{f_{i+1,j} - 2f_{i,j} + f_{i-1,j}}{h^2}; \\
A_{xy}^2(f) &= \frac{f_{i+1,j+1} - f_{i+1,j-1} - f_{i-1,j+1} + f_{i-1,j-1}}{h^2}; \\
A_{yyyy}^4(f) &= \frac{f_{i,j+2} - 4f_{i,j+1} + 6f_{i,j} - 4f_{i,j-1} + f_{i,j-2}}{h^4}; \\
A_{xyyy}^4(f) &= \frac{f_{i+1,j+2} - 2f_{i+1,j+1} + 2f_{i+1,j-1} - f_{i+1,j-2} - f_{i-1,j+2}}{h^4} \\
&\quad + \frac{2f_{i-1,j+1} - 2f_{i-1,j-1} + f_{i-1,j-2}}{4h^4}; \\
A_{xxyy}^4(f) &= \frac{f_{i+1,j+1} - 2f_{i+1,j} + f_{i+1,j-1} - 2(f_{i,j+1} - 2f_{i,j} + 2f_{i,j-1})}{h^4} \\
&\quad + \frac{f_{i-1,j+1} - 2f_{i-1,j} + f_{i-1,j-1}}{h^4}; \\
A_{xxxy}^4(f) &= \frac{f_{i+2,j+1} - f_{i+2,j-1} - 2(f_{i+1,j+1} - f_{i+1,j-1})}{4h^4} \\
&\quad + \frac{2(f_{i-1,j+1} - f_{i-1,j-1}) - f_{i-2,j+1} + f_{i-2,j-1}}{4h^4},
\end{aligned} \tag{17.20}$$

and $f_{i,j}$ describe the corresponding functions of deflection w and displacements u, v .

17.4 Computational Results

Traditionally, the static problems in theory of plates and shells were solved by employment of various approximate methods which allow to reduce the system of PDEs into a corresponding system of nonlinear AEs (algebraic equations). In our work, a solution of the static problem is found with a help of the set-up method (see Awrejcewicz and Krysko, 2003a, and references therein). The latter approach was validated by numerical investigations in Awrejcewicz et al (2006); Krysko et al (2005, 2017). In the set-up method, a solution to PDEs is reduced to the Cauchy problem of ODEs, which initially depends on time in a linear way. The mentioned approach possesses numerous benefits. First, it exhibits a high accuracy, since the employed method is a member of iteration methods family, it relies on computations of solution after the introduced time step based on the previous solution approximation. Second, the set-up method is not sensitive to the initial approximation choice. Third, branches of various static solution can be obtained in a relative simple way.

Solving the Cauchy problem under $\varepsilon = \varepsilon_{cr}$ for a series of the parameter of normal constant load q_i yields a series of deflection w_i . Based on the obtained data, the dependence $w(q)$ can be constructed as well as the stress-strain shell state can be analysed.

As an example, we consider a clamped cylindrical panel composed of two families of mutually perpendicular ribs made from aluminium with the following fixed parameters: length and width $b = c = 0.01$ m, thickness $h = 0.0002$ m, distance between ribs $a = 0.0002$ m, Young’s modulus $E = 71.456 \cdot 10^9$ N/m², Poisson modulus $\nu = 0.3$, ribs width $\delta = 2 \cdot 10^{-4}$ m, and the parameters of curvature $k_x = 0, k_y = 48$. Furthermore, we investigate the problem related to stability loss of the micropolar mesh-type cylindrical panel. As it has been already mentioned, in order to solve the problem of statics, the governing PDEs are reduced to the Cauchy problem of ODEs, by using FDM of the second order.

Next, the Cauchy problem is solved by using the 4th order Runge-Kutta method. The carried out numerical experiments yields the value of $\varepsilon_{cr} = 10$ which allows to reduce a number of iterations while solving the problem with a help of the set-up method. In order to obtain the reliable results, we have analysed convergence of the solution with regard to spatial and time co-ordinates. We have found that the optimal choice is obtained for the computational mesh $n \times n = 16 \times 16$. Figure 17.2 presents the computational results for the case of fixed nondimensional parameters $\bar{k}_x = 0, \bar{k}_y = 24$ as the functions $\bar{q}(\bar{w}(0.5;0.5)), \bar{w}(t;0.5;0.5)$ for certain values of the size dependent parameter $\bar{l} = 0;0.1;0.3;0.5; 0.7$. Analysis of the results allows to conclude that a character of the critical load is changed beginning from a rapid increase of the deflection under infinite small change of the load ($\bar{l} = 0;0.1;0.3;0.5$) up to the critical point of deflection ($\bar{l} = 0.7$). In other words, increase of l implied increase of the critical load.

17.5 Concluding remarks

Based on the carried out investigations, the following general conclusions can be formulated.

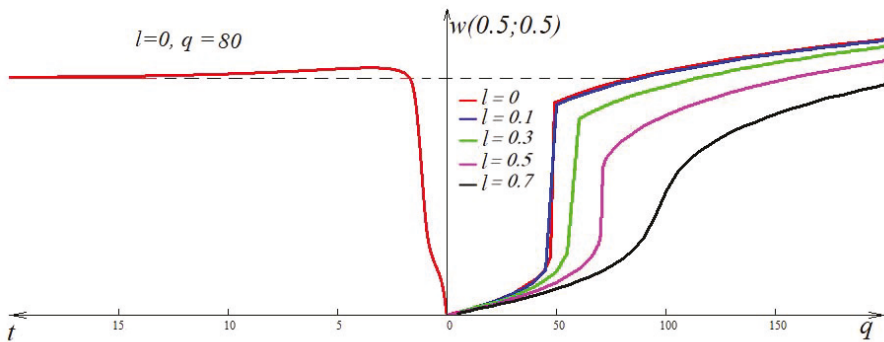


Fig. 17.2. Diagrams of the load-deflections nondimensional dependencies $\bar{q}(\bar{w}(0.5;0.5)), \bar{w}(t;0.5;0.5)$ for the cylindrical panel ($\bar{k}_x = 0, \bar{k}_y = 24$)

1. We have extended and modified the Kirchhoff-Love theory of shallow flexible mesh structures with a help of the modified couple stress theory.
2. There are worked out algorithms of investigation of stability and stress-strain states of mesh-type flexible shell structures based on the mathematical models of nano-sized effects.
3. The problem governed by nonlinear PDEs has been reduced to the Cauchy problem through employment of the 2nd order of accuracy of the finite difference method (FDM). The latter problem has been solved by using Runge-Kutta methods of various orders of the Prince-Dormand method of the 8th order, and the Newmark method. The best choice with respect to the computational time was offered the 4th order Runge-Kutta method. The results have been analysed by comparison of the coincidence of the functions and their derivatives up to the 2nd order inclusively versus the number n of the used spatial variable parts.
4. The stationary problem has been solved using the set-up method which is computationally stable and exhibits a high accuracy while solving a set of algebraic equations (Krysko et al, 2005).
5. It has been demonstrated that increase of the size-dependent parameter l yields the qualitative change in increase of the critical load values, i.e. we have detected rapid deflection increase under introduction of the very small change of the load parameter ($\bar{l} = 0; 0.1; 0.3; 0.5$) up to the point of the curve deflection ($l = 0.7$).

Acknowledgements This work has been carried out with financial support of the Russian Science Foundation RSF No 19-19-00215.

References

- Awrejcewicz J, Krysko VA (2003a) Nonclassic Thermoelastic Problems in Nonlinear Dynamics of Shells. Springer, Berlin
- Awrejcewicz J, Krysko VA (2003b) Nonlinear coupled problems in dynamics of shells. *International Journal of Engineering Science* 41(6):587–607
- Awrejcewicz J, Krysko VA, Kravtsova IV (2006) Dynamics and statics of flexible axially-symmetric shallow shells. *Math Prob Eng* 2006:ID35,672
- Awrejcewicz J, Krysko VA, Papkova IV, Krysko AV (2016a) Deterministic Chaos in One-Dimensional Continuous Systems. World Scientific, Singapore
- Awrejcewicz J, Krysko-Jr VA, Yakovleva TV, Krysko VA (2016b) Noisy contact interactions of multi-layer mechanical structures coupled by boundary conditions. *Journal of Sound and Vibration* 369:77–86
- Belostochny GN, Myltcina OA (2015) The geometrical irregular plates under the influence of the quick changed on the time coordinate forces and temperature effects (in Russ.). *News Saratov Univ Ser: Math Mech Comput Sci* 5(4):442–451
- Belostochny GN, Myltcina OA (2018) Dynamic stability of heated geometrically irregular cylindrical shell in supersonic gas flow (in Russ.). *J Samara St Tech Univ, Ser Phys Math Sci* 22(4):750–761

- Krysko AV, Awrejcewicz J, Zhigalov MV, Pavlov SP, Krysko VA (2017) Nonlinear behaviour of different flexible size-dependent beams models based on the modified couple stress theory. Part 1: Governing equations and static analysis of flexible beams. *International Journal of Non-Linear Mechanics* 93:96–105
- Krysko VA, Awrejcewicz J, Komarov SA (2005) Nonlinear deformations of spherical panels subjected to transversal load action. *Computer Methods in Applied Mechanics and Engineering* 194(27):3108–3126
- Krysko VA, Awrejcewicz J, Kutepov IE, Zagniboroda NA, Papkova IV, Serebryakov AV, Krysko AV (2013) Chaotic dynamics of flexible beams with piezoelectric and temperature phenomena. *Physics Letters A* 377(34):2058–2061
- Krysko VA, Awrejcewicz J, Krylova EY, Papkova IV, Krysko AV (2018) Non-symmetric forms of non-linear vibrations of flexible cylindrical panels and plates under longitudinal load and additive white noise. *Journal of Sound and Vibration* 423:212–229
- Krysko-Jr VA, Awrejcewicz J, Yakovleva TV, Kirichenko AV, Szymanowska O, Krysko VA (2019) Mathematical modeling of MEMS elements subjected to external forces, temperature and noise, taking account of coupling of temperature and deformation fields as well as a nonhomogenous material structure. *Communications in Nonlinear Science and Numerical Simulation* 72:39–58
- Pshenichnov G (1982) *Theory of Thin Elastic Meshed Shells and Plates* (in Russ.). Nauka, Moscow
- Sarkisjan SO (2005) Micropolar theory of thin rods, plates and shells. *Proc Nat Acad Sci Armenia Mech* 58(2):84–95
- Wang FY (1990) On the solutions of Eringen's micropolar plate equations and of other approximate equations. *International Journal of Engineering Science* 28(9):919–925
- Zhou X, Wang L (2012) Vibration and stability of micro-scale cylindrical shells conveying fluid based on modified couple stress theory. *Micro & Nano Letters* 7(7):679–684



Chapter 18

Buckling of the Nonuniformly Compressed Plate with Dislocations and Disclinations

Isa M. Peshkoev and Alexander M. Stolyar

Abstract The buckling problem of the elastic rectangular plate, which is compressed by the nonuniformly distributed along the edges external loads, is considered. This plate contains continuously distributed sources of internal stresses and is found under the action of a small normal load. The components of the external loads are the given continuous functions and act in direction, which is parallel to the coordinate axes. The coordinate system has its beginning in the center of the plate. The study is based on a modified system of elastic plates' nonlinear von Káráan equations, which take into account influence of dislocations and disclinations or other sources of intrinsic stresses. The boundary conditions correspond to the free clamped plates' edges or their movable hinge support. The considered problem is reduced to a sequence of three linear boundary value problems for determining the forms of the stress functions, which correspond to internal sources and two components of compressive forces, and a system of nonlinear equations with a trivial solution. Numerical parameters characterizing the intensity of stresses caused by internal sources and components of external loads are introduced. The critical buckling load is defined as the solution of the linearized nonlinear problem on a trivial solution. The stability loss problem is reduced to a parametric eigenvalue boundary value problem. The problem of eigenvalues is solved by the variational method. To study the post-critical behavior of a compressed plate, the Lyapunov–Schmidt method is used in combination with numerical methods for calculating the coefficients of the system of the branching equations. The cases of equilibrium branching of a compressed plate with one and two eigenforms are considered. Asymptotic formulas of new equilibria in the vicinity of the bifurcation point are constructed in the case when a small normal load acts and without it as well. It is obtained that the presence

Isa M. Peshkoev
Don State Technical University, Rostov-on-Don, Russian Federation
e-mail: peshkoev@gmail.com

Alexander M. Stolyar
Southern Federal University, Rostov-on-Don, Russian Federation
e-mail: ajoiner@mail.ru

of a small normal load does not reduce the bearing capacity of the plate in the case of even forms of the incompatibility function and even forms of distribution along the edges of the compressive forces.

Key words: Elastic plate · Critical load · Internal stresses · Stability of equilibrium · Ramification of equilibrium · Lyapunov-Schmidt method · Ramification equation

18.1 Introduction

Method of solution of the compressed elastic rectangular plate stability problem was proposed in Polubarinova-Kochina (1936) as a small parameter power series construction. This method was later proved by Vorovich (1956). For the case of the critical value of the compressive load the first study of the problem for a circular plate with radial symmetry and without normal load was carried out by Friedrichs and Stoker (1941). Using the variational method, they showed the origin of a pair of new solutions when the parameter of the compressive load gets over the critical value. Berger and Fife (1968) transferred this result to the case of a plate of arbitrary shape when the normal load was absent; they assumed that the boundary forces depend on one parameter and used the M. A. Krasnosel'ky topological theorem on bifurcation (Krasnosel'skij, 1956).

Some time earlier, in 1955–1958, Vorovich (1958) used the theory of eigenvalues of nonlinear odd operators along with variational and topological methods to study the general problems of the nonlinear theory of shallow shells and gave a qualitative study of the behavior of plates and shells after loss of stability.

Besides I. Vorovich used the Lyapunov-Schmidt method (Vorovich, 1956) to consider the post-critical behavior of an annular circular plate in the presence of normal load and a variety of boundary conditions (Vorovich, 1955). The Lyapunov-Schmidt method for nonlinear equations in Banach spaces was developed by Trenogin (1958) and applied by Srubshchik and Trenogin (1968) for studying the problem of the effect of a small transverse load on the buckling and post-buckling behavior of a plate of arbitrary shape under compressive boundary forces, parallel to the axes of coordinates. The effects of a nonlinearly elastic base on the buckling and the initial post-buckling behavior of an infinite plate with small geometric imperfections were studied by Reissner (1970) in case of a momentless plane-stressed state. The buckling problem of the thin compressed plate of a strictly convex shape with a free edge was considered by Srubshchik (1981, 1985).

Zubov (2007) obtained the modified von Kármán system of the elastic plates nonlinear equations which took into account the presence of dislocations and disclinations as well as other sources of intrinsic stresses. The bending problem of a free of external loads thin plate (membrane) which takes place due to the relaxation of the internal stresses caused by defects has been considered. The stress state problem of the thin elastic plate containing dislocations and disclinations is considered within the framework of the classical Kirchhoff theory in Zubov and Stolpovskii (2008). The

problem of annular plate bending caused by helical dislocation and torsion deflection is solved. The theory of thin plates with distributed dislocations and disclinations is constructed. Solutions of bending problems of circular and elliptic plates with continuously distributed disclinations are obtained. An analogy is established between the plate with defects bending problem and the plane problem of elasticity theory with mass forces, as well as between the plane problem with dislocations and disclinations and the plate with given distributed loads bending problem. The effect of continuously distributed disclinations or heat sources on the deflections and stress state of acircular flexible plate, loaded with a transverse pressure has been studied in Zubov and Fam (2010).

Asymptotic and numerical analysis of the problems of vibrations of narrow elastic rectangular plates, cylindrical panels, shallow elastic-plastic arches, panels and spherical shells has been carried out in Stolyar (2014). In particular, for the problem of oscillations of elastic long rectangular plates, in which the long edges are free of loading and the short edges are freely supported, an asymptotic transition to the beam problem of oscillations has been established. The limit transition in the problems of vibrations and dynamic buckling of elastic and elastic-plastic cylindrical panels has been established as well.

The critical loads of the compressed elastic plate with dislocations and disclinations were considered in Peshkoev (2016). The effect of initial imperfections, shaped as small transverse loads, on the loss of stability and the post-critical behavior of a compressed elastic rectangular plate lying on a nonlinearly elastic foundation has been considered in Peshkoev and Sobol' (2016). The post-buckling behavior of the plate has been investigated with some asymptotic formulas derived for the new equilibria in the neighborhood of critical loads. Some relations between the values of the parameters of the base, where its bearing capacity is preserved in the neighborhood of the classical value of the critical load, have been established for the variety of values of the parameters of compressive loads and the parameter of internal stresses.

In Sidorov et al (2002) an overview of some results of applying the Lyapunov-Schmidt methods in combination with other methods obtained by Russian mathematicians.

In Altenbach and Eremeyev (2010) within the framework of the direct approach to the plate theory the infinitesimal deformations of a plate made of hyper elastic materials taking into account the non-homogeneously distributed initial stresses have been considered. Here the plate as a material surface with 5 degrees of freedom (3 translations and 2 rotations) is considered. The influence of initial stresses in the bulk material on the plate behavior is considered.

Forms of stability loss of a compressed infinite plate lying on a soft elastic foundation has been considered in Morozov and Tovstik (2012). Class of binary-periodic forms of loss of stability has been investigated. By the analysis of the potential energy density of the post-critical deformation it was established that the preference should be given to the staggered form.

In Eremeev and Zubov (2017) within the framework of nonlinear elasticity instability of a uniformly compressed circular two-layered plate with an initially com-

pressed or stretched layer has been analyzed. The incompressible neo-Hookean model has been used as a constitutive relation of the material. It has been assumed that the lower layer was subjected to radial tension or compression. As a result initial strains and stresses appeared in this layer. The two-layered plate was subjected to a uniform lateral compression. Stability of the plate has been studied using of the static Euler method. Within the method loading parameters were determined for which the linearized boundary-value problem had non-trivial solutions. The three-dimensional linearized equilibrium equations for each layer have been derived. The solutions of the latter equations were obtained with the help of the Fourier method. The equation for critical strains was derived. Analysis of dependence of critical stress resultants on the initial strains and stiffness parameters was presented.

Altenbach and Eremeyev (2017) present mathematical and mechanical aspects of the theory of plates and shells, applications in civil, aero-space and mechanical engineering, as well in other areas. The focus relates to the following problems: comprehensive review of the most popular theories of plates and shells, relations between three-dimensional theories and two-dimensional ones, presentation of recently developed new refined plates and shells theories (for example, the micropolar theory or gradient-type theories), modeling of coupled effects in shells and plates related to electromagnetic and temperature fields, phase transitions, diffusion, etc., applications in modeling of non-classical objects like, for example, nanostructures, presentation of actual numerical tools based on the finite element approach.

In Altenbach and Eremeyev (2018) the bending deformations of a three-layered plate taking into account surface and interfacial stresses has been considered. The first-order shear deformation plate theory and the Gurtin-Murdoch model of surface stresses are considered and the formulae for stiffness parameters of the plate are derived. Their dependence on surface elastic moduli has been analyzed.

The significance of this work is in the study of the post-critical behavior of the nonuniformly compressed plates, containing the sources of internal stresses as well as the application of the Lyapunov–Schmidt method to the modified nonlinear system of von Kármán equations obtained by Zubov and Fam (2010).

18.2 Governing Equations

Let us consider the equilibrium equations of a thin elastic rectangular plate which contains continuously distributed edge dislocations and wedge disclinations. Our plate is found under a small normal load of intensity $\xi G(X, Y)$ and edge pressure with axial components $P(Y)$ and $Q(X)$ respectively. Then the equilibrium equations system is written as (Srubshchik and Trenogin, 1968; Timoshenko and Woinowsky-Krieger, 1959; Washizu, 1982; Zubov, 2007)

$$D\Delta^2 W = [\Psi, W] + \xi G(X, Y), \quad \Delta^2 \Psi + \frac{1}{2} Eh[W, W] = Eh\mu \quad (18.1)$$

$$D = \frac{Eh^3}{\gamma^2}, \quad \gamma^2 = 12(1 - \nu^2), \quad [\Psi, W] \equiv W_{XX}\Psi_{YY} - 2W_{XY}\Psi_{XY} + W_{YY}\Psi_{XX}$$

Here $\mu(X, Y)$ is the scalar measure of incompatibility which is expressed in terms of dislocation and disclination densities (Zubov, 2007), $W(X, Y)$ is the plate deflection, $\Psi(X, Y)$ is the Airy stress function, h is the plate thickness, ν is the Poisson's ratio, E is the Young's modulus, X, Y are rectangular coordinates with the origin at the center of the plate and axes parallel to its edges, ξ is the small numeric parameter.

System (18.1) is considered together with the boundary conditions of one of the following types

$$\begin{cases} W = W_X = \Psi_{XY} = 0, & \Psi_{YY} = -P(Y), & |X| = a/2, |Y| < b/2 \\ W = W_Y = \Psi_{XY} = 0, & \Psi_{XX} = -Q(X), & |Y| = b/2, |X| < a/2 \end{cases} \quad (18.2)$$

$$\begin{cases} W = W_{XX} = \Psi_{XY} = 0, & \Psi_{YY} = -P(Y), & |X| = a/2, |Y| < b/2 \\ W = W_{YY} = \Psi_{XY} = 0, & \Psi_{XX} = -Q(X), & |Y| = b/2, |X| < a/2 \end{cases} \quad (18.3)$$

$$\begin{cases} W = W_X = \Psi_{XY} = 0, & \Psi_{YY} = -P(Y), & |X| = a/2, |Y| < b/2 \\ W_{YY} + \nu W_{XX} = W_{YY} + (2 - \nu)W_{XXY} = \Psi_{XY} = \Psi_{XX} = 0, & & |Y| = b/2, |X| < a/2 \end{cases} \quad (18.4)$$

$$\begin{cases} W = W_{XX} = \Psi_{XY} = 0, & \Psi_{YY} = -P(Y), & |X| = a/2, |Y| < b/2 \\ W_{YY} + \nu W_{XX} = W_{YY} + (2 - \nu)W_{XXY} = \Psi_{XY} = \Psi_{XX} = 0, & & |Y| = b/2, |X| < a/2 \end{cases} \quad (18.5)$$

Here the subscript denotes differentiation with respect to the corresponding variable. The boundary conditions (18.2) correspond to free pinching and (18.3) correspond to the movable hinge support of the edges. We assume that $P(Y)$ and $Q(X)$ are the continuous functions up to the second-order derivatives on the segments $|Y| \leq b/2$ and $|X| \leq a/2$ respectively. Compressive forces $P(Y)$ and $Q(X)$ are applied to the edges $X = \pm a/2$ and $Y = \pm b/2$ respectively. The boundary conditions (18.4) and (18.5) correspond to free edges.

Let us obtain the homogeneous boundary conditions. Let

$$\Psi = \Phi - P(Y)\alpha(Y) - Q(X)\beta(X),$$

where $\alpha(Y)$ and $\beta(X)$ satisfy the differential equations

$$(P(Y)\alpha(Y))_{YY} = P(Y), \quad |Y| < b/2; \quad (Q(X)\beta(X))_{XX} = Q(X), \quad |X| < a/2 \quad (18.6)$$

Φ satisfies the homogeneous boundary conditions $\Phi_{XY} = \Phi_{YY} = 0$ at $|X| = a/2$, $|Y| < b/2$, $\Phi_{XY} = \Phi_{XX} = 0$ at $|Y| = b/2$, $|X| < a/2$. Replacing these equalities by the equivalent $\Phi = \Phi_X = 0$ along the $|X| = a/2$, $|Y| < b/2$ and $\Phi = \Phi_Y = 0$ along $|Y| = b/2$, $|X| < a/2$, we obtain the boundary conditions using (18.2)–(18.5)

$$\begin{cases} W = W_X = \Phi = \Phi_X = 0, & |X| = a/2, |Y| < b/2 \\ W = W_Y = \Phi = \Phi_Y = 0, & |Y| = b/2, |X| < a/2 \end{cases} \quad (18.7)$$

$$\begin{cases} W = W_{XX} = \Phi = \Phi_X = 0, & |X| = a/2, |Y| < b/2 \\ W = W_{YY} = \Phi = \Phi_Y = 0, & |Y| = b/2, |X| < a/2 \end{cases} \quad (18.8)$$

$$\begin{cases} W = W_X = \Phi = \Phi_X = 0, & |X| = a/2, |Y| < b/2 \\ W_{YY} + \nu W_{XX} = W_{YY} + (2 - \nu)W_{XX} = \Phi = \Phi_Y = 0, & |Y| = b/2, |X| < a/2 \end{cases} \quad (18.9)$$

$$\begin{cases} W = W_{XX} = \Phi = \Phi_X = 0, & |X| = a/2, |Y| < b/2 \\ W_{YY} + \nu W_{XX} = W_{YY} + (2 - \nu)W_{XX} = \Phi = \Phi_Y = 0, & |Y| = b/2, |X| < a/2 \end{cases} \quad (18.10)$$

Substituting $\Psi = \Phi - P(Y)\alpha(Y) - Q(X)\beta(X)$ in (18.1) with regard to (18.6), we obtain

$$\begin{cases} D\Delta^2 W - [W, \Phi] + P(Y)W_{XX} + Q(X)W_{YY} = \xi G(X, Y) \\ \Delta^2 \Phi + \frac{1}{2} Eh[W, W] = (P(Y))_{YY} + (Q(X))_{XX} + Eh\mu \end{cases} \quad (18.11)$$

Equations (18.11) may be written in the following dimensionless form

$$\begin{cases} \Delta_\alpha^2 w - \alpha[w, \bar{F}] + r_p p \alpha w_{xx} + r_q q w_{yy} = \xi g(x, y) \\ \frac{1}{2} \Delta_\alpha^2 \bar{F} + \alpha[w, w] = r_\mu \bar{\mu} + r_p p_{yy} + r_q q_{xx} \end{cases} \quad (18.12)$$

$$\Delta_\alpha(\cdot) \equiv (\cdot)_{yy} + \alpha(\cdot)_{xx}, \quad \Delta_\alpha^2 = \Delta_\alpha \Delta_\alpha$$

in $\Omega = \{(x, y): |x| < 1/2, |y| < 1/2\}$. The given functions and coefficients are connected with dimensionless values by the following relations: $X = ax, Y = by, W(X, Y) = w(x, y)h/\gamma, \alpha = b^2/a^2, \Phi(X, Y) = D\bar{F}(x, y), P(Y) = r_p Dp(y)/b^2, Q(X) = r_q Dq(x)/(\alpha a^2), \mu(X, Y) = r_\mu \bar{\mu}(x, y)\gamma^2/h^2, G(X, Y) = hDg(x, y)/(\gamma b^4)$, where $r_\mu \bar{\mu}(x, y)$ is the measure of incompatibility, $r_p p(y)$ is component of the compressive load along the axis $x, r_q q(x)$ is component of the compressive load along the axis y , coefficients r_μ, r_p, r_q are the so-called intensity parameters of the corresponding stress sources, $\bar{\mu}(x, y)$ is the incompatibility measure, $p(y)$ is the compressive load on the edges $x = \pm 1/2, q(x)$ is the compressive load on the edges $y = \pm 1/2$. We assume that the functions $\bar{\mu}(x, y), p(y)$ and $q(x)$ are fixed and have the identity norm which is defined as the maximum of the module in the domain of definition.

Let the dimensionless Airy stress function in (18.12) be written in such a way

$$\bar{F} = F + r_\mu F_\mu + r_p F_p + r_q F_q \quad (18.13)$$

where functions F_μ, F_p and F_q are defined as solutions of the following boundary value problems

$$\Delta_\alpha^2 F_\mu = \bar{\mu}(x, y), (x, y) \in \Omega \text{ and } F_\mu = (F_\mu)_n = 0 \text{ on the border of area } \Omega \quad (18.14)$$

$$\Delta_\alpha^2 F_p = p_{yy}(y), (x, y) \in \Omega \text{ and } F_p = (F_p)_n = 0 \text{ on the border of area } \Omega \quad (18.15)$$

$$\Delta_\alpha^2 F_q = q_{xx}(x), (x, y) \in \Omega \text{ and } F_q = (F_q)_n = 0 \text{ on the border of area } \Omega \quad (18.16)$$

Index n in (18.14)–(18.16) and further on designates derivative in the direction which is normal to the boundary.

Now the boundary problem (18.1) with one of the boundary conditions (18.2)–(18.5) is reduced to solution of the linear boundary problems (18.14)–(18.16) and nonlinear boundary value problem as follows

$$\begin{cases} \Delta_\alpha^2 w + r_p p \alpha w_{xx} + r_q q w_{yy} = \alpha[w, F] + r_\mu \alpha[w, F_\mu] + r_p \alpha[w, F_p] \\ \quad + r_q \alpha[w, F_q] + \xi g \\ \Delta_\alpha^2 F + \alpha[w, w]/2 = 0, \quad (x, y) \in \Omega \end{cases} \quad (18.17)$$

with one of the following boundary conditions

$$w = w_n = 0, \quad F = F_n = 0 \quad \text{on the border of area } \Omega, \quad (18.18)$$

$$w = w_{nn} = 0, \quad F = F_n = 0 \quad \text{on the border of area } \Omega, \quad (18.19)$$

$$\begin{cases} w = w_x = F = F_x = 0, \quad |x| = 1/2, \quad |y| < 1/2 \\ w_{yy} + \nu \alpha w_{xx} = w_{yyy} + (2 - \nu) \alpha w_{xxy} = F = F_y = 0, \quad |y| = 1/2, \quad |x| < 1/2, \end{cases} \quad (18.20)$$

$$\begin{cases} w = w_{xx} = F = F_x = 0, \quad |x| = 1/2, \quad |y| < 1/2 \\ w_{yy} + \nu \alpha w_{xx} = w_{yyy} + (2 - \nu) \alpha w_{xxy} = F = F_y = 0, \quad |y| = 1/2, \quad |x| < 1/2 \end{cases} \quad (18.21)$$

Here formula (18.13) defines the general stress function \bar{F} , which corresponds to the stresses caused by the combined action of internal sources and external compressive loads.

18.3 Critical Loads

Let E^2 be the Hilbert space which is the closure of the set of vector functions $f = (f_1, f_2), g = (g_1, g_2)$ with the norm defined by the scalar product

$$\langle f, g \rangle_{E^2} = \iint_{\Omega} (f_1 g_1 + f_2 g_2) dx dy;$$

E^1 is the closure of a linear set of infinitely differentiable in a rectangular domain $\Omega = \{(x, y): |x| < 1/2, |y| < 1/2\}$ vector-functions $u = (w, F)$ which satisfy one of the boundary conditions (18.18)–(18.21), with the finite norm generated by the scalar product

$$\langle u, v \rangle_{E^1} = \left\langle \sum_{i+j \leq 4} \partial^{i+j} u / \partial x^i \partial y^j, \partial^{i+j} v / \partial x^i \partial y^j \right\rangle_{E^2}.$$

Let $g(x, y)$ be sufficiently smooth in the domain Ω . Thus we consider the boundary value problem (18.17) with one of the conditions (18.18)–(18.21) as a nonlinear operator equation

$$M_0u = \Pi u + \xi R, \quad u = (w, F) \in E^1, \quad R = \begin{pmatrix} g \\ 0 \end{pmatrix} \tag{18.22}$$

$$M_0u \equiv \begin{pmatrix} \Delta_\alpha^2 w - r_\mu \alpha[w, F_\mu] + r_q(qw_{yy} - \alpha[w, F_q]) + r_p \alpha(pw_{xx} - [w, F_p]) \\ \Delta_\alpha^2 F \end{pmatrix}$$

$$\Pi u \equiv \begin{pmatrix} \alpha[w, F] \\ \alpha[w, w]/2 \end{pmatrix}$$

Morozov (1957) and Vorovich (1989) show that operators M_0 and Π act from the space E^1 into space E^2 . Equation (18.22) has a trivial solution $u_* = (w_*, F_*) = (0, 0)$, when $r_\mu = 0, r_p = 0, r_q = 0, \xi = 0$. Bifurcation point (r_μ, r_p, r_q) of the nonlinear equation (18.22) is defined in Trenogin (1958) as the eigenvalue of the boundary value problem $M_0u = 0$, which is obtained by linearization of the Eq. (18.22) on a trivial solution. Using the definition of the operator M_0 one can obtain that the second component of the eigenvector function $u = (\omega, \psi)$ is equal to zero while the first one is determined from the following linear boundary value problem:

One must find such a value of parameter r_p that there exists nontrivial solution of the problem

$$\Delta_\alpha^2 \omega - r_\mu \alpha[\omega, F_\mu] + r_q(q\omega_{yy} - \alpha[\omega, F_q]) = -r_p \alpha(p\omega_{xx} - [\omega, F_p]) \tag{18.23}$$

for the given parameters r_μ, r_q , where functions F_μ, F_p, F_q are the solutions of problems (18.14)–(18.16) and ω satisfies one of the following boundary conditions

$$\omega = \omega_n = 0 \text{ on the border of area } \Omega, \tag{18.24}$$

$$\omega = \omega_{nn} = 0 \text{ on the border of area } \Omega, \tag{18.25}$$

$$\begin{cases} w = w_x = 0, & |x| = 1/2, |y| < 1/2 \\ w_{yy} + \nu \alpha w_{xx} = w_{yyy} + (2 - \nu) \alpha w_{xxy} = 0, & |y| = 1/2, |x| < 1/2 \end{cases} \tag{18.26}$$

$$\begin{cases} w = w_{xx} = 0, & |x| = 1/2, |y| < 1/2 \\ w_{yy} + \nu \alpha w_{xx} = w_{yyy} + (2 - \nu) \alpha w_{xxy} = 0, & |y| = 1/2, |x| < 1/2 \end{cases} \tag{18.27}$$

Stress functions F_μ, F_p and F_q are caused by the action of internal sources and external loads. Numbers r_μ, r_p, r_q can be called parameters of intensity of these stresses because of the linearity of the problems (18.14)–(18.16). We are going to investigate further on the influence of the form of distribution of internal stress sources $\bar{\mu}(x, y)$ and forms of distribution of compressive loads $p(y), q(x)$ on the critical values of the intensity parameters r_μ, r_p, r_q .

Let us write Eq. (18.23) in operator form

$$A\omega = r_p B\omega, \tag{18.28}$$

$$A\omega \equiv \Delta_\alpha^2 \omega - r_\mu \alpha[\omega, F_\mu] + r_q(q\omega_{yy} - \alpha[\omega, F_q]), \quad B\omega \equiv -\alpha(p\omega_{xx} - [\omega, F_p])$$

and consider the properties of operators A and B . Let $H(\Omega)$ be a subspace of the Sobolev space W_2^4 and consist of functions u and v , which satisfy one of the boundary conditions (18.24)–(18.27) and have norm generated by the scalar product

$$(u, v) \equiv \iint_{\Omega} uv \, dx \, dy.$$

Using the change of variables $x = x_1, y = y_1\sqrt{\alpha}$, one can reduce operator Δ_{α}^2 which acts in $H(\Omega)$ to biharmonic operator Δ^2 which acts in $H(\Omega_1)$,

$$\Omega_1 = \{|x_1| \leq \frac{1}{2}, |y_1| \leq \frac{\sqrt{\alpha}}{2}\}.$$

Therefore properties of operator Δ^2 are easily transferred on operator Δ_{α}^2 .

The properties of the biharmonic operator Δ^2 have been investigated in Mikhlin (1970), where it was actually shown that Δ^2 acted from $H(\Omega_1)$ into $L_2(\Omega_1)$ and was positive definite. Two inequalities follow from Friedrich’s inequality (Mikhlin, 1970):

$$\iint_{\Omega} \Delta_{\alpha}^2 \omega \omega \, dx \, dy \geq C_1 \iint_{\Omega} \omega^2 \, dx \, dy, \quad C_1 > 0, \tag{18.29}$$

$$\iint_{\Omega} \Delta_{\alpha}^2 \omega \omega \, dx \, dy \geq C_2 \iint_{\Omega} \omega_y^2 \, dx \, dy, \quad C_2 > 0. \tag{18.30}$$

Applying (18.29), (18.30), we deduce inequality

$$(\Delta_{\alpha}^2 \omega + r_q q \omega_{yy}, \omega) \geq C_1 \left(1 - \frac{r_q m_q}{C_2}\right) \iint_{\Omega} \omega^2 \, dx \, dy \tag{18.31}$$

where $m_q = \max_x q(x)$.

Operators $-p(y)(\)_{xx}$ and $-q(x)(\)_{yy}$ are both symmetric and nonnegative when $p(y) \geq 0$ and $q(x) \geq 0$:

$$(-p(y)\omega_{xx}, \omega) = \iint_{\Omega} p(y)\omega_x^2 \, dx \, dy \geq 0, \quad (-q(x)\omega_{yy}, \omega) = \iint_{\Omega} q(x)\omega_y^2 \, dx \, dy \geq 0$$

It is easy to check the equality

$$\iint_{\Omega} [\omega, F]\phi \, dx \, dy = \iint_{\Omega} [\phi, F]\omega \, dx \, dy \tag{18.32}$$

using integration by parts, when ω and ϕ satisfy one of the boundary conditions (18.24)–(18.27) and F satisfies the conditions $F = F_n = 0$. It means that operator $D\omega \equiv [\omega, F]$ which acts in $H(\Omega)$ is symmetric and therefore bounded (Lyusternik and Sobolev, 1966), so the following inequalities are valid:

$$\iint_{\Omega} [\omega, F_{\mu}]\omega \, dx \, dy \leq C_{\mu} \iint_{\Omega} \omega^2 \, dx \, dy, \quad C_{\mu} > 0, \tag{18.33}$$

$$\iint_{\Omega} [\omega, F_q] \omega \, dx \, dy \leq C_q \iint_{\Omega} \omega^2 \, dx \, dy, \quad C_q > 0. \tag{18.34}$$

Taking into account (18.31), (18.33), (18.34) one can prove the boundedness from below of the operator A :

$$(A\omega, \omega) \geq \left(C_1 \left(1 - \frac{r_q m_q}{C_2} \right) - r_\mu \alpha C_\mu - r_q \alpha C_q \right) \int_{-1/2}^{1/2} \int_{-1/2}^{1/2} \omega^2 \, dx \, dy. \tag{18.35}$$

Thus one can state that operator B in equation (18.27) is symmetric.

The eigenvalue problem (18.23) is reduced to the functional minimum problem (Mikhlin, 1970):

$$J(\omega) \equiv (A\omega, \omega) / (B\omega, \omega). \tag{18.36}$$

Problem (18.36) is solved numerically. The method used here is a generalization of the algorithm (Bauer and Reiss, 1972) which was used for solving the eigenvalue problem for a biharmonic equation in a rectangle.

We would like to formulate some conclusions which one can do on the basis of analysis of problems (18.14), (18.15), (18.16) and problem (18.23) with one of the boundary conditions (18.24)–(18.27). The solution of problem (18.14) allows us to state that the presence of internal sources ($\bar{\mu}(x, y) \neq 0$) leads to internal stresses ($F_\mu \neq 0$) in the plate. The analysis of problems (18.15), (18.16) shows that the stress functions F_p and F_q are nonzero when conditions $p_{yy}(y) \neq 0$ and $q_{xx}(x) \neq 0$ take place respectively. Hence one can state that non-zero stresses appear ($F_p \neq 0, F_q \neq 0$) in plate with any (non-zero) value of the intensity parameters r_p and r_q , if compressive loads $p(y)$ and $q(x)$ are nonlinearly distributed along the boundaries. If the compressive loads are uniformly or linearly distributed along the edges of the plate, then stresses F_p and F_q are equal to zero for any value of the stress intensity parameters r_p and r_q .

Integrals $(A\omega, \omega)$ and $(B\omega, \omega)$ contain terms of the form

$$\iint_{\Omega} [\omega, F] \omega \, dx \, dy$$

which are equal to zero if one of the functions (ω or F) is odd with respect to one variable and even or odd for another variable, and the other function is even or odd with respect to both variables. Due to the symmetry of the boundary conditions, the solution of each of the problems (18.14), (18.15) and (18.16) is odd with respect to one variable and even or odd for another variable, if the right part is odd with respect to one variable and even or odd for another one. Therefore the corresponding internal stresses with any intensity r_μ do not affect the critical value r_p if the incompatibility function $\bar{\mu}(x, y)$ is odd with respect to one variable and even or odd for another variable.

Similarly if the compressive load $q(x)$ is an odd function, then the corresponding stresses also do not affect the critical value r_p for any intensity r_q . If the OX -axis compressive load is an odd function, then problem (18.23) has no solution. If the

incompatibility function $\mu(x, y)$ is even with respect to both variables, $p(y)$ and $q(x)$ are even functions, then the eigenfunctions of problem (18.23) with one of the boundary conditions (18.24)–(18.27) are even or odd for each variable.

Let us rewrite equation (18.23) as

$$\Delta_a^2 \omega + r_p \alpha(p\omega_{xx} - [\omega, F_p]) + r_q(q\omega_{yy} - \alpha[\omega, F_q]) = r_\mu \alpha[\omega, F_\mu] \tag{18.37}$$

Analysis of the problem (18.37) with one of the boundary conditions (18.24)–(18.27) shows that the loss of stability of the plate can occur without compressive loads ($r_p = 0, r_q = 0$) as well caused by internal stress sources action only. Note that the same conclusion was obtained in Zubov and Fam (2010) for the stability problem of a circular plate with continuously distributed disclinations. We are not considering the eigenvalue problem (18.37) further on.

18.4 Behavior of Plate After Loss of Stability

We consider the post-critical behavior of a compressed plate using the Lyapunov-Schmidt method (Vajnberg and Trenogin, 1969). Let $(r_{\mu 0}, r_{p 0}, r_{q 0})$ be the bifurcation point of the nonlinear equation (18.22), that is, $r_p = r_{p 0}$ be the eigenvalue of the problem (18.23) with one of the boundary conditions (18.24)–(18.27) and the given values $r_\mu = r_{\mu 0}, r_q = r_{q 0}$.

Let $r_\mu = r_{\mu 0} + \lambda_1, r_p = r_{p 0} + \lambda_2, r_q = r_{q 0} + \lambda_3, w = w_* + \omega = \omega, F = F_* + \psi = \psi$. We write the equation for small perturbations $\lambda_1, \lambda_2, \lambda_3, u = (\omega, \psi)$ in the following form

$$M_0 u = \Pi u + \sum_{i=1}^3 \lambda_i C_i u + \xi R, \tag{18.38}$$

$$C_1 u \equiv \begin{pmatrix} \alpha(p(y)\omega_{xx} - [\omega, F_p]) \\ 0 \end{pmatrix}, \quad C_2 u \equiv \begin{pmatrix} q(x)\omega_{yy} - [\omega, F_q] \\ 0 \end{pmatrix},$$

$$C_3 u \equiv \begin{pmatrix} -\alpha[\omega, F_\mu] \\ 0 \end{pmatrix}, \quad C_i : E^1 \rightarrow E^2, \quad i = 1, 2, 3.$$

Let $r_{p 0}$ be a double eigenvalue of problem (18.23) with one of the boundary conditions (18.24)–(18.27) and the fixed values $r_\mu = r_{\mu 0}, r_q = r_{q 0}$ with two corresponding eigenfunctions ω_1 and ω_2 . Then the vector-eigenfunctions of the equation $M_0 u = 0$ have the form $\phi_1 = (\omega_1, \psi_1), \phi_2 = (\omega_2, \psi_2)$, where $\psi_1 = \psi_2 = 0$.

We construct the Schmidt operator (Vajnberg and Trenogin, 1969) in the following form

$$M_1 u \equiv M_0 u + \sum_{i=1}^2 a_i \mu_i \phi_i, \mu_i = \langle u, \phi_i \rangle_{E^1}, \quad a_i \iint_{\Omega} \omega_i^2 dx dy = 1, \quad i = 1, 2. \tag{18.39}$$

Taking into account (18.39) the nonlinear equation (18.22) may be reduced to the equation

$$M_1 u = u + \sum_{i=1}^2 a_i \mu_i \phi_i + \sum_{i=1}^3 \lambda_i C_i u + \xi R \tag{18.40}$$

We construct the solution of equation (18.40) as a power series

$$u = \sum_{i+j+k+l+m+n \geq 1} u_{ijklmn} \mu_1^i \mu_2^j \lambda_1^k \lambda_2^l \lambda_3^m \xi^n, \quad u_{ijklmn} = (\omega_{ijklmn}, \psi_{ijklmn}). \tag{18.41}$$

Then we substitute (18.41) in (18.40) and gather coefficients standing near powers $\mu_1^i \mu_2^j \lambda_1^k \lambda_2^l \lambda_3^m \xi^n$ of the same degree and derive the equations

$$M_1 u_{ijklmn} = f_{ijklmn}. \tag{18.42}$$

Problems (18.42) are solvable by virtue of the generalized Schmidt Lemma (Vajnberg and Trenogin, 1969). Functions f_{ijklmn} are found using the right side of (18.40). We successively solve the problems (18.42) are express solution by eigenfunctions ω_1 and ω_2 of problems (18.23) with one of the boundary conditions (18.24)–(18.27):

$$\begin{aligned} f_{100000} &= a_1 \phi_1 = \begin{pmatrix} a_1 \omega_1 \\ 0 \end{pmatrix}, \quad f_{010000} = a_1 \phi_1 = \begin{pmatrix} a_2 \omega_2 \\ 0 \end{pmatrix}, \\ f_{001000} &= f_{000100} = f_{000010} = \begin{pmatrix} 0 \\ 0 \end{pmatrix}, \quad f_{000001} = \begin{pmatrix} g \\ 0 \end{pmatrix}, \\ f_{200000} &= \begin{pmatrix} 0 \\ -\frac{\alpha}{2} [\omega_1, \omega_1] \end{pmatrix}, \quad f_{020000} = \begin{pmatrix} 0 \\ -\frac{\alpha}{2} [\omega_1, \omega_1] \end{pmatrix}, \quad f_{110000} = \begin{pmatrix} 0 \\ -\alpha [\omega_1, \omega_2] \end{pmatrix} \\ f_{002000} &= f_{000200} = f_{000020} = f_{000002} = \begin{pmatrix} 0 \\ 0 \end{pmatrix}, \\ f_{101000} &= \begin{pmatrix} \alpha([\omega_1, F_p] - p(y)\omega_{1,xx}) \\ 0 \end{pmatrix} \\ f_{100100} &= \begin{pmatrix} ([\omega_1, F_q] - q(x)\omega_{1,yy}) \\ 0 \end{pmatrix}, \quad f_{011000} = \begin{pmatrix} \alpha([\omega_2, F_p] - p(y)\omega_{2,xx}) \\ 0 \end{pmatrix} \\ f_{100010} &= \begin{pmatrix} [\omega_1, F_\mu] \\ 0 \end{pmatrix}, \quad f_{010100} = \begin{pmatrix} ([\omega_2, F_q] - q(x)\omega_{2,yy}) \\ 0 \end{pmatrix}, \quad f_{010010} = \begin{pmatrix} [\omega_2, F_\mu] \\ 0 \end{pmatrix} \\ f_{210000} &= \begin{pmatrix} \alpha([\omega_2, \psi_{200000}] + [\omega_1, \psi_{110000}]) \\ 0 \end{pmatrix}, \\ f_{120000} &= \begin{pmatrix} \alpha([\omega_1, \psi_{020000}] + [\omega_2, \psi_{110000}]) \\ 0 \end{pmatrix} \\ f_{300000} &= \begin{pmatrix} \alpha[\omega_1, \psi_{200000}] \\ 0 \end{pmatrix}, \quad f_{030000} = \begin{pmatrix} \alpha[\omega_2, \psi_{020000}] \\ 0 \end{pmatrix}. \end{aligned} \tag{18.43}$$

Equalities (18.42), (18.43) allow to get the boundary value problems concerning functions $\psi_{200000}, \psi_{020000}, \psi_{110000}$

$$A_\alpha^2 \psi_{200000} = -\frac{\alpha}{2} [\omega_1, \omega_1], \quad \psi_{200000} = (\psi_{200000})_n = 0 \quad \text{on the border area } \Omega, \quad (18.44)$$

$$A_\alpha^2 \psi_{020000} = -\frac{\alpha}{2} [\omega_2, \omega_2], \quad \psi_{020000} = (\psi_{020000})_n = 0 \quad \text{on the border area } \Omega, \quad (18.45)$$

$$A_\alpha^2 \psi_{110000} = -\alpha [\omega_1, \omega_2], \quad \psi_{110000} = (\psi_{110000})_n = 0 \quad \text{on the border area } \Omega. \quad (18.46)$$

Taking into account the solution expansion (18.41) we obtain the ramification equations (Vajnberg and Trenogin, 1969) using the second equation (18.39)

$$\sum_{i+j+k+l+m+n \geq 1} L_{ijklmn}^{(t)} \mu_1^i \mu_2^j \lambda_1^k \lambda_2^l \lambda_3^m \xi^n = \mu_t, \quad t = 1, 2. \quad (18.47)$$

Coefficients of ramification equations (18.47) are calculated as follows

$$L_{ijklmn}^{(t)} = \langle f_{ijklmn}, \phi_t \rangle_{E^2}, \quad t = 1, 2. \quad (18.48)$$

Taking into account the orthogonality of the eigenfunctions ω_1, ω_2 and the third equality in (18.39), we obtain coefficients of the ramification equations system using formulas (18.48):

$$\begin{aligned} L_{100000}^{(1)} &= \langle f_{100000}, \phi_1 \rangle_{E^2} = \langle a_1 \phi_1, \phi_1 \rangle_{E^2} = a_1 \iint_{\Omega} \omega_1^2 dx dy = 1, \\ L_{100000}^{(2)} &= L_{010000}^{(1)} = 0, \quad L_{010000}^{(2)} = 1, \\ L_{001000}^{(t)} &= L_{000100}^{(t)} = L_{000010}^{(t)} = 0, \quad L_{000001}^{(t)} = \iint_{\Omega} g \omega_t dx dy, \\ L_{002000}^{(t)} &= L_{000200}^{(t)} = L_{000020}^{(t)} = L_{000002}^{(t)} = 0, \\ L_{101000}^{(t)} &= \alpha \iint_{\Omega} ([\omega_1, F_p] - p(y) \omega_{1,xx}) \omega_t dx dy, \\ L_{100100}^{(t)} &= \alpha \iint_{\Omega} ([\omega_1, F_q] - q(x) \omega_{1,yy}) \omega_t dx dy, \\ L_{100010}^{(t)} &= \iint_{\Omega} [\omega_1, F_\mu] \omega_t dx dy, \quad L_{011000}^{(t)} = \alpha \iint_{\Omega} ([\omega_2, F_p] - p(y) \omega_{2,xx}) \omega_t dx dy, \\ L_{010100}^{(t)} &= \alpha \iint_{\Omega} ([\omega_2, F_q] - q(x) \omega_{2,yy}) \omega_t dx dy, \\ L_{010010}^{(t)} &= \iint_{\Omega} [\omega_2, F_\mu] \omega_t dx dy, \quad t = 1, 2. \end{aligned} \quad (18.49)$$

Taking into account (18.32), (18.44)–(18.46) we obtain

$$\begin{aligned}
 L_{210000}^{(1)} &= \iint_{\Omega} \alpha([\omega_2, \psi_{200000}] + [\omega_1, \psi_{110000}])\omega_1 \, dx \, dy \\
 &= -3 \iint_{\Omega} \Delta_{\alpha}\psi_{200000}\Delta_{\alpha}\psi_{110000} \, dx \, dy, \\
 L_{210000}^{(2)} &= -2 \iint_{\Omega} \Delta_{\alpha}\psi_{200000}\Delta_{\alpha}\psi_{020000} \, dx \, dy - \iint_{\Omega} (\Delta_{\alpha}\psi_{110000})^2 \, dx \, dy, \\
 L_{120000}^{(1)} &= L_{210000}^{(2)}, \\
 L_{120000}^{(2)} &= -3 \iint_{\Omega} \Delta_{\alpha}\psi_{020000}\Delta_{\alpha}\psi_{110000} \, dx \, dy, \\
 L_{300000}^{(1)} &= -2 \iint_{\Omega} (\Delta_{\alpha}\psi_{200000})^2 \, dx \, dy < 0, \\
 L_{300000}^{(2)} &= - \iint_{\Omega} \Delta_{\alpha}\psi_{110000}\Delta_{\alpha}\psi_{200000} \, dx \, dy, \\
 L_{030000}^{(1)} &= - \iint_{\Omega} -\Omega\Delta_{\alpha}\psi_{110000}\Delta_{\alpha}\psi_{020000} \, dx \, dy, \\
 L_{030000}^{(2)} &= -2 \iint_{\Omega} (\Delta_{\alpha}\psi_{020000})^2 \, dx \, dy.
 \end{aligned} \tag{18.50}$$

Let us assume the incompatibility function $\mu(x, y)$ and the normal load function $g(x, y)$ be the even functions with respect to both variables, $p(y)$ and $q(x)$ be also even functions. Therefore the eigenfunctions of the problem (18.23) with one of the boundary conditions (18.24)-(18.27) are even or odd with respect to each variable.

Let us assume the eigenfunction ω_1 be even with respect to both variables and ω_2 be odd with respect to one variable and even or odd for the other variable. In this case some of coefficients (18.49), (18.50) are equal to zero and the ramification equations system has the form

$$\begin{aligned}
 \Phi_1(\mu_1, \mu_2) &\equiv (a_1\mu_1^2 + b_1\mu_2^2 + \Lambda_1)\mu_1 + d_1\xi = 0, \\
 \Phi_2(\mu_1, \mu_2) &\equiv (a_2\mu_1^2 + b_2\mu_2^2 + \Lambda_2)\mu_2 = 0
 \end{aligned} \tag{18.51}$$

with

$$\begin{aligned}
 a_1 &= L_{300000}^{(1)} < 0, \quad b_1 = L_{120000}^{(1)}, \quad a_2 = L_{210000}^{(2)}, \quad b_2 = L_{030000}^{(2)} < 0, \quad d_1 = L_{000001}^{(1)}, \\
 \Lambda_1 &= L_{101000}^{(1)}\lambda_1 + L_{100100}^{(1)}\lambda_2 + L_{100010}^{(1)}\lambda_3, \quad \Lambda_2 = L_{011000}^{(2)}\lambda_1 + L_{010100}^{(2)}\lambda_2 + L_{010010}^{(2)}\lambda_3.
 \end{aligned}$$

Let r_{p0} be a simple eigenvalue of the problem (18.23) with one of the boundary conditions (18.24)–(18.27) for the fixed values $r_{\mu} = r_{\mu 0}$, $r_q = r_{q 0}$ with the corresponding eigenfunction ω . Then we have the only ramification equation

$$\Phi(\mu) \equiv a\mu^3 + \mu\Lambda + d\xi = 0 \tag{18.52}$$

with

$$a = L_{300000}, \quad \Lambda = L_{110000}\lambda_1 + L_{101000}\lambda_2 + L_{100100}\lambda_3, \quad d = L_{000001}$$

and

$$L_{30000} = -2 \iint_{\Omega} (\Delta_{\alpha} \psi_{20000})^2 dx dy < 0, \quad L_{11000} = \alpha \iint_{\Omega} ([\omega, F_p] - p(y)\omega_{xx})\omega dx dy,$$

$$L_{10100} = \alpha \iint_{\Omega} ([\omega, F_q] - q(x)\omega_{yy})\omega dx dy, \quad L_{10010} = \iint_{\Omega} [\omega, F_{\mu}]\omega dx dy.$$

Let us firstly consider the case of the absence of a small transverse load. Solving (18.51) system relative to μ_1 and μ_2 when $\xi = 0$ and using (18.36) expansion of the nonlinear equations system (18.41) solution we derive the following statement.

Theorem 18.1. *Let the incompatibility function $\mu(x, y)$ and the normal load function $g(x, y)$ be the even functions with respect to both variables, $p(y)$ and $q(x)$ be the even functions and $\xi = 0$. Let r_{p0} be the double eigenvalue of the problem (18.23) with one of the boundary conditions (18.24)–(18.27) and the given values of the parameters $r_{\mu} = r_{\mu0}$, $r_q = r_{q0}$. Let the first corresponding eigenfunction $\omega_1(x, y)$ be the even function with respect to both variables and the second eigenfunction $\omega_2(x, y)$ be the odd function with respect to one variable and even or odd function for another variable. Then the nonlinear equation (18.22) has eight new solutions with asymptotic representations in the small neighborhood of the bifurcation point $(r_{\mu0}, r_{p0}, r_{q0})$:*

$$\tilde{u} = \pm \sqrt{\frac{\Lambda_2 b_1 - \Lambda_1 b_2}{a_1 b_2 - a_2 b_1}} \pm \sqrt{\frac{\Lambda_1 a_2 - \Lambda_2 a_1}{a_1 b_2 - a_2 b_1}} + O(|\Lambda_1| + |\Lambda_2|) \tag{18.53}$$

- if λ_1, λ_2 and λ_3 satisfy the conditions

$$\frac{\Lambda_2 b_1 - \Lambda_1 b_2}{a_1 b_2 - a_2 b_1} > 0, \quad \frac{\Lambda_1 a_2 - \Lambda_2 a_1}{a_1 b_2 - a_2 b_1} > 0;$$

$$\tilde{u} = \pm \sqrt{-\Lambda_2/b_2} + O(|\Lambda_2|) \tag{18.54}$$

- if λ_1, λ_2 and λ_3 satisfy the condition $\Lambda_2 > 0$;

$$\tilde{u} = \pm \sqrt{-\Lambda_1/a_1} + O(|\Lambda_1|) \tag{18.55}$$

- if λ_1, λ_2 and λ_3 satisfy the condition $\Lambda_1 > 0$.

Solving equation (18.52) relative to μ with $\xi = 0$ and using the (18.41) expansion we obtain the following theorem:

Theorem 18.2. *Let in the conditions of theorem 18.1 r_{p0} be a simple eigenvalue of problem (18.23) with one of the boundary conditions (18.24)–(18.27) for the fixed values of $r_{\mu} = r_{\mu0}$, $r_q = r_{q0}$ with the corresponding to one eigenfunction ω which is even with respect to both variables. Then the nonlinear equation (18.22) has in the small neighborhood of the bifurcation point $(r_{\mu0}, r_{p0}, r_{q0})$ two new solutions with asymptotic representations*

$$\tilde{u} = \pm \sqrt{-\Lambda/a} + O(|\Lambda|) \tag{18.56}$$

if λ_1, λ_2 and λ_3 satisfy the condition $\Lambda > 0$.

If there is an imperfection in the form of a small transverse load ($\xi \neq 0, \xi \ll 1$), then the bifurcation point $(r_{\mu 0}, r_{p 0}, r_{q 0})$ becomes a critical load $(r_{\mu s}, r_{p s}, r_{q s})$. We denote

$$(\lambda_{1s}, \lambda_{2s}, \lambda_{3s}) = (r_{\mu s} - r_{\mu 0}, r_{p s} - r_{p 0}, r_{q s} - r_{q 0}).$$

We should use the system of branching equations (18.51) with the branching equation (18.52) as well as the condition of loss of stability (Suchy et al, 1985; Friedrichs and Stoker, 1941)

$$\left\| \frac{\partial \Phi_i}{\partial \mu_j} \right\| = \frac{\partial \Phi_1}{\partial \mu_1} \frac{\partial \Phi_2}{\partial \mu_2} - \frac{\partial \Phi_2}{\partial \mu_1} \frac{\partial \Phi_1}{\partial \mu_2} = 0 \quad \left(\frac{d\Phi}{d\mu} = 0 \right) \tag{18.57}$$

in order to obtain $(\lambda_1, \lambda_2, \lambda_3) = (\lambda_{1s}, \lambda_{2s}, \lambda_{3s})$.

Theorem 18.3. *Let in the conditions of theorem 18.1 $\xi \neq 0, \xi \ll 1$. Then the following formulas for the critical value*

$$\Lambda_{1s} = L_{101000}^{(1)} \lambda_{1s} + L_{100100}^{(1)} \lambda_{2s} + L_{100010}^{(1)} \lambda_{3s}$$

and asymptotic representations of new solutions of nonlinear equation (18.22) take place

$$\Lambda_{1s} = -3 \sqrt[3]{\frac{d_1^2 \xi^2 a_1}{4}} > 0, \quad \tilde{u} = \pm \frac{1}{3} \sqrt{\frac{-3\Lambda_{1s}}{a_1}} \phi_1 + \xi u_{000001} + O(|\Lambda_{1s}|), \tag{18.58}$$

$$\Lambda_{1s} = \frac{3}{b_1 - b_2} \sqrt[3]{\frac{d_1^2 \xi^2 b_2^2 (a_1 b_2 - a_2 b_1)}{4}}, \tag{18.59}$$

$$\tilde{u} = \pm \sqrt{\tau_1 \Lambda_{1s}} \phi_1 \pm \sqrt{\tau_2 \Lambda_{1s}} \phi_2 + \xi u_{000001} + O(|\Lambda_{1s}|),$$

if

$$\tau_1 = \frac{b_1 - b_2}{3(a_1 b_2 - a_2 b_1)} > 0, \quad \tau_2 = -\frac{3a_1 b_2 - 2a_2 b_1 - a_2 b_2}{3b_2(a_1 b_2 - a_2 b_1)} > 0.$$

In this case $\lambda_{1s}, \lambda_{2s}$ and λ_{3s} in (18.58), (18.59) are combined by the relation $\Lambda_{2s} = \Lambda_{1s}$. The vector function $u_{000001} = (\omega_{000001}, \psi_{000001})$ is defined by (18.42), so $\psi_{000001} = 0$. We find the function ω_{000001} from the problem $\Delta_a^2 \omega_{000001} = g(x, y)$ where ω_{000001} satisfies one of the boundary conditions (18.24)–(18.27) on the boundary Ω .

Proof. To prove theorem 18.3 we require parameters λ_1, λ_2 and λ_3 to satisfy a condition $\Lambda_2 = \Lambda_1$. Then we consider the ramification equations system (18.51) together with the stability loss condition (18.57) and derive the formulas (18.58), (18.59). Theorem 18.3 is proved.

Similarly, the solution of the branching equation (18.52) together with the stability loss condition (18.57) proves the following theorem:

Theorem 18.4. *Let under the conditions of theorem 18.2 $\xi \neq 0$, $\xi \ll 1$. Then for the critical value*

$$\Lambda_s = L_{11000}\lambda_{1s} + L_{10100}\lambda_{2s} + L_{10010}\lambda_{3s}$$

and asymptotic representations of new solutions of nonlinear equation (18.22) the following formulas take place

$$\Lambda_s = -3\sqrt[3]{\frac{d^2\xi^2a}{4}} > 0, \quad \tilde{u} = \pm\sqrt{\frac{-3\Lambda_s}{a}}\phi + \xi u_{00001} + O(|\Lambda_s|) \tag{18.60}$$

In this case $u_{00001} = (\omega_{00001}, 0)$, and ω_{00001} is defined from the problem $\Delta_\alpha^2\omega_{00001} = g(x, y)$ with one of the boundary conditions (18.24)–(18.27) on the boundary Ω .

Remark 18.1. Taking into account the replacement (18.13) we should note that the bifurcation point $(r_{\mu 0}, r_{p0}, r_{q0})$ along with one or two eigenfunctions of problem (18.23) correspond to the Airy stress function $\bar{F} = r_{\mu 0}F_\mu + r_{p0}F_p + r_{q0}F_q$, which gives the second component of the asymptotic formulas of new solutions of the initial nonlinear problem (18.12) found above.

We note that firstly Koiter (1963) and then Budiansky (1974); Budiansky and Hutchinson (1966) pointed to the fact that in the case of a small imperfection ($\xi \neq 0$, $\xi \ll 1$), the bifurcation point can move to the limit point.

18.5 Numerical Results

Example 18.1. Loss of stability in two eigenforms. We consider the case of a square plate $\alpha = b^2/a^2 = 1$. Let in problems (18.14), (18.15), (18.16) and (18.23) with boundary condition (18.24) functions be given as follows

$$\begin{aligned} \bar{\mu}(x, y) &= 256[(x + 1/2)(x - 1/2)(y + 1/2)(y - 1/2)]^2, \quad p(y) = \sin(\pi(y + 1/2)), \\ q(x) &= \sin(\pi(x + 1/2)), \quad g(x, y) = 16(x + 1/2)(x - 1/2)(y + 1/2)(y - 1/2). \end{aligned}$$

It is obtained that for $r_{\mu 0} = 550$ and $q_{p0} = -20$ (stretching along the OY axis) the smallest eigenvalue of the problem (18.23) with the boundary conditions (18.24) is equal to $r_{p0} = 142.6$. Two eigenfunctions correspond to eigenvalue found: ω_1 is even with respect to both variables and ω_2 is even with respect to one variable and odd for the second variable. Solution of the ramification equations system (18.51) allowed to obtain the following values of coefficients

$$\begin{aligned} a_1 &= -8.913, \quad b_1 = -11.740, \quad a_2 = -11.740, \quad b_2 = -20.742, \quad d_1 = 0.180, \\ \Lambda_1 &= 1.599\lambda_1 + 1.066\lambda_2 + 0.028\lambda_3, \quad \Lambda_2 = 6.610\lambda_1 + 0.731\lambda_2 + 0.062\lambda_3. \end{aligned}$$

Let $\xi = 0$. As it follows from requirements of theorem 18.1 the small values λ_1 , λ_2 and λ_3 must satisfy the inequality

$$1.277\lambda_1 + 1.141\lambda_2 + 0.012\lambda_3 > 0.$$

Therefore the asymptotic solutions (18.53) exist for small positive values λ_1 , λ_2 and λ_3 . It is also easy to verify that there are small values λ_1 , λ_2 and λ_3 for which solutions (18.54) and (18.55) exist respectively.

Let $\xi \neq 0$. Calculating the values of τ_1 and τ_2 from theorem 18.3 shows that they are positive. It confirms the existence of solutions (18.58), (18.59). We also note that in addition to the eigenfunctions ω_1 and ω_2 the even Airy stresses function

$$\bar{F} = r_{\mu 0}F_{\mu} + r_{p 0}F_p + r_{q 0}F_q$$

corresponds to initial nonlinear problem (18.12). One can see graphs of eigenfunctions ω_1 , ω_2 and Airy stresses function \bar{F} at Fig. 18.1 and the graphs of the components of the Cauchy stress tensor $\sigma_x = \bar{F}_{yy}$, $\sigma_y = \bar{F}_{xx}$ and $\sigma_{xy} = -\bar{F}_{xy}$ at Fig. 18.2.

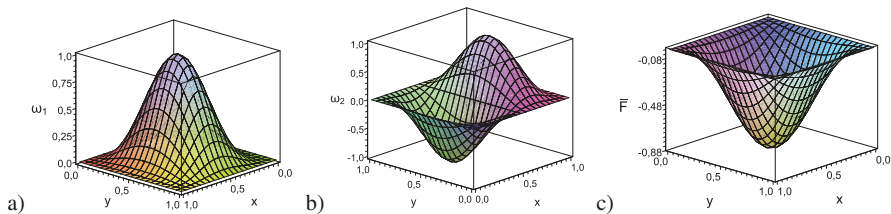


Fig. 18.1. Graphs of eigenfunctions: a) ω_1 , b) ω_2 ; c) graph of stress function \bar{F}

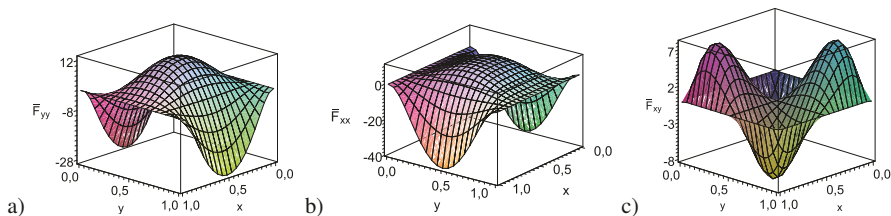


Fig. 18.2. Stresses graphs: a) $\bar{F}_{yy} = \sigma_x$, b) $\bar{F}_{xx} = \sigma_y$, c) $\bar{F}_{xy} = -\sigma_{xy}$

Example 18.2. Let us consider problems (18.14), (18.15), (18.16) and (18.23) with boundary condition (18.25) for rectangular plate $\alpha = b^2/a^2 = 1/4$ and with the given functions

$$\bar{\mu}(x,y) = 4(1/2 - x)(1/2 - y), \quad p(y) = 1, \quad q(x) = (2(1/2 - x))^4, \quad g(x,y) = 1.$$

It is obtained that the smallest eigenvalue $r_{p0} = 33.03$ of the problem (18.23) with boundary conditions of the hinge support (18.25) for $r_{\mu 0} = 100$, $q_{p0} = 20$ corresponds

to one eigenfunction ω_1 (Fig. 18.3). The ramification equation has the form (18.52)

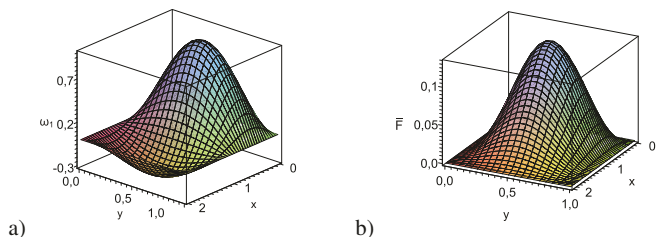


Fig. 18.3. Graphics: a) eigenfunction ω_1 , b) of Airy stress function \bar{F}

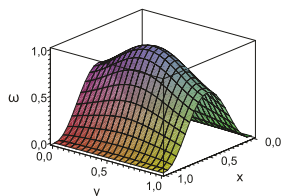
and its coefficients are equal to

$$a = -3.936, \quad d = 0.345, \quad \Lambda = 2.393\lambda_1 + 0.948\lambda_2 + 0.015\lambda_3.$$

Let $\xi = 0$. Using theorem 18.2 we find that asymptotic solutions (18.56) exist for small positive values λ_1, λ_2 and λ_3 . Let $\xi \neq 0$. The existence of solutions (18.60) is obvious. Note that in addition to the eigenfunction ω_1 , the initial nonlinear problem (18.12) has the Airy stress function $\bar{F} = r_{\mu 0}F_{\mu} + r_{q 0}F_q$, since in this case the solution of problem (18.15) is zero ($F_p = 0$). One can see graphs of eigenfunction ω_1 and Airy stress function Fig. 18.3.

Example 18.3. Loss of stability along one eigenform. Let us consider the square plate $\alpha = b^2/a^2 = 1$. Let functions $\bar{\mu}(x, y) = 1, p(y) = 1, q(x) = 0, g(x, y) = 16x^2y^2$ be given while solving problems (18.14), (18.15), (18.16) and (18.23) with boundary condition (18.26). It is obtained that for $r_{\mu 0} = 1000$ and $q_{p 0} = 0$ the smallest eigenvalue of the problem (18.23) with the boundary conditions (18.26) is equal to $r_{p 0} = 37.21$ and the corresponding eigenfunction ω is even with respect to both variables (Fig. 18.4). The following coefficients were obtained for the ramification equation (18.52): $a = -0.318, d = 0.622, \Lambda = 3.66\lambda_1 - 0.0178\lambda_3$.

Fig. 18.4 Graph of the eigenfunction ω



Let $\xi = 0$. Using theorem 18.2 we find that asymptotic solutions (18.56) exist for small values $\lambda_1 > 0$ and $\lambda_3 < 0$. Let $\xi \neq 0$. The existence of solutions (18.60) is

obvious. Note that in addition to the eigenfunction ω_1 , the initial nonlinear problem (18.12) has the Airy stress function $\bar{F} = r_{\mu 0} F_{\mu}$.

18.6 Conclusion

Problem of stability loss and post-critical behavior of an nonuniformly compressed plate with internal stress sources is considered in the paper. Parameters which characterize the intensity of stresses caused by internal sources and components of external loads are introduced and critical values of these parameters are determined. The influence of parity/oddness properties on critical loads of the forms of distribution of internal stress sources in the plate and the forms of distribution of compressive loads on the edges of the plate is established. Asymptotic formulas of new solutions in the vicinity of the bifurcation point for the case of absence of a small normal load are constructed. For the case of a small normal load the asymptotic formulas for new equilibria corresponding to the limit load, formulas of the limit load in which the bifurcation point transfer are constructed.

Acknowledgements This research has been financed by the Russian Foundation for Basic Research (Project 19-08-00074).

References

- Altenbach H, Eremeyev V (2017) Thin-walled structural elements: Classification, classical and advanced theories, new applications. In: Altenbach H, Eremeyev V (eds) Shell-like Structures: Advanced Theories and Applications, CISM International Centre for Mechanical Sciences, vol 572, Springer International Publishing, Cham, pp 1–62
- Altenbach H, Eremeyev V (2018) Bending of a three-layered plate with surface stresses. In: Altenbach H, Carrera E, Kulikov G (eds) Analysis and Modelling of Advanced Structures and Smart Systems, Advanced Structured Materials, vol 81, Springer, Singapore, pp 1–10
- Altenbach H, Eremeyev VA (2010) On the effective stiffness of plates made of hyperelastic materials with initial stresses. *International Journal of Non-Linear Mechanics* 45(10):976–981
- Bauer L, Reiss EL (1972) Block five diagonal matrices and the fast numerical solution of the biharmonic equation. *Mathematics of Computation* 26(118):311–326
- Berger MS, Fife PC (1968) Von Kármán's equations and the buckling of a thin elastic plate, II Plate with general edge conditions. *Communications on Pure and Applied Mathematics* 21(3):227–241
- Budiansky B (1974) Theory of buckling and post-buckling behavior of elastic structures. In: Yih CS (ed) *Advances in Applied Mechanics*, vol 14, Elsevier, pp 1–65

- Budiansky B, Hutchinson JW (1966) A survey of some buckling problems. *AIAA Journal* 4(9):1505–1510
- Eremeev VV, Zubov LM (2017) Buckling of a two-layered circular plate with a prestressed layer. *Mathematics and Mechanics of Solids* 22(4):773–781
- Friedrichs KO, Stoker JJ (1941) The non-linear boundary value problem of the buckled plate. *American Journal of Mathematics* 63(4):839–887
- Koiter WT (1963) Contribution elastic stability and post-buckling behavior. In: Langer RE (ed) *Nonlinear Problems. Proc. Symp. Univ. of Wisconsin, University of Wisconsin Press, Madison, WI*, pp 257–275
- Krasnosel'skij MA (1956) *Topological Methods in the Theory of Nonlinear Integral Equations (in Russ.)*. Gostekhizdat, Moscow
- Lyusternik LA, Sobolev VI (1966) *Elements of Functional Analysis (in Russ.)*. Fizmatgiz, Moscow
- Mikhlin SG (1970) *Variational Methods in Mathematical Physics (in Russ.)*. Nauka, Moscow
- Morozov NF (1957) On the nonlinear theory of thin plates (in Russ.). *Dokl AN SSSR* 114(5):668–671
- Morozov NF, Tovstik PE (2012) Buckling forms of a compressed plate on an elastic foundation. *Doklady Physics* 57(9):335–339
- Peshkoev IM (2016) Critical loads of a compressed elastic rectangular plate with dislocations and disclinations (in Russ.). *Vestnik DGTU* 84:43–51
- Peshkoev IM, Sobol' BV (2016) Buckling and post-critical behavior of a compressed rectangular plate with internal stresses lying on a nonlinear elastic base (in Russ.). *Problemy Prochnosti i Plastichnosti* 81(2):137–145
- Polubarinova-Kochina PY (1936) On the question of the stability of the plate (in Russ.). *Prikladnaya Matematika i Mekhanika* 3(1):16–22
- Reissner E (1970) On postbuckling behavior and imperfection sensitivity of thin elastic plates on a non-linear elastic foundation. *Studies in Applied Mathematics* 49(1):45–57
- Sidorov N, Loginov B, Sinitsyn A, Falaleev M (2002) *Lyapunov-Schmidt Methods in Nonlinear Analysis and Applications, Mathematics and Its Applications*, vol 550. Springer Nature
- Srubshchik LS (1981) *Buckling and Post-critical Behavior of Shells (in Russ.)*. Izd-vo Rostov. un-ta, Rostov on Don
- Srubshchik LS (1985) Edge effect and bulging of thin plates on a nonlinear elastic base (in Russ.). *Differentsial'nye uravneniya XXI*(10):1790–1794
- Srubshchik LS, Trenogin VA (1968) On the buckling of flexible plates. *Journal of Applied Mathematics and Mechanics* 32(4):747–754
- Stolyar AM (2014) *Behavior of Narrow Panels and Spherical Shells Under Static and Dynamic Loading Conditions. Asymptotic and Numerical Analysis (in Russ.)*. Izdatel'stvo SFEDU, Rostov on Don
- Suchy H, Troger H, Weiss R (1985) A numerical study of mode jumping of rectangular plates. *ZAMM - Journal of Applied Mathematics and Mechanics / Zeitschrift für Angewandte Mathematik und Mechanik* 65(2):71–78

- Timoshenko S, Woinowsky-Krieger S (1959) *Theory of Plates and Shells*. McGraw-Hill, New York
- Trenogin VA (1958) Branching solutions of nonlinear equations in Banach space (in Russ.). *Uspekhi matematicheskikh nauk* 13(4):197–203
- Vajnberg MM, Trenogin VA (1969) *Branching Theory of Solutions of Nonlinear Equations* (in Russ.). Nauka, Moscow
- Vorovich II (1955) On the behavior of a round plate after loss of stability (in Russ.). *Uch zap Rostovsk un-ta* 32(4):55–60
- Vorovich II (1956) On some direct methods in nonlinear shell theory (in Russ.). *Prikladnaya Matematika i Mekhanika* 20(4):449–474
- Vorovich II (1958) Some questions about the stability of shells in a large (in Russ.). *Doklady AN SSSR* 122(1):37–40
- Vorovich II (1989) *Mathematical Problems of the Nonlinear Theory of Flat Shells* (in Russ.). Nauka, Moscow
- Washizu K (1982) *Variational Methods in Elasticity and Plasticity*. Pergamon Press, Oxford-New York
- Zubov LM (2007) Von Kármán equations for an elastic plate with dislocations and disclinations. *Doklady Physics* 52(1):67–70
- Zubov LM, Fam TH (2010) Strong bending of a round plate with continuously distributed disclinations (in Russ.). *Izvestiya vuzov Severo-Kavkazskij region Estestvennye nauki* 4:28–33
- Zubov LM, Stolpovskii AV (2008) A theory of dislocations and disclinations in elastic plates. *Journal of Applied Mathematics and Mechanics* 72(6):724–737



Chapter 19

On Null-Lagrangian Energy and Plate Paradoxes

Paolo Podio-Guidugli

Abstract At variance, but not in contrast, with the accepted view that the source of plate paradoxes is located in the way the boundary conditions are imposed, it is argued that paradoxes, not only in the case of plate-like bodies, may be caused by the way the null-lagrangian contribution to stored energy is evaluated.

Key words: Null Lagrangians · Plate paradoxes · Linear elasticity

19.1 Introduction

Here is how plate paradoxes are described in the abstract of Babuška and Pitkäranta (1990):

This paper studies the plate-bending problem with hard and soft simple support. It shows that in the case of hard support, the plate paradox, which is known to occur in the Kirchhoff model, is also present in the three-dimensional model and the Reissner-Mindlin model. The paradox consists of the fact that, on a sequence of convex polygonal domains converging to a circle, the solutions of the corresponding plate-bending problems with a fixed uniform load do not converge to the solution of the limit problem. The paper also shows that the paradox is not present when soft simple support is assumed.

And, in the introductory section one reads that the aim of Babuška and Pitkäranta (1990)

... is to locate the source of the paradox,

and that

Paolo Podio-Guidugli
Accademia Nazionale dei Lincei, Palazzo Corsini – Via della Lungara, 10, 00165 Roma, Italy
e-mail: p.podioguidugli@gmail.com

... it is the way the *boundary conditions* are imposed in the Kirchhoff model that causes the paradox.

Now, according to a standard dictionary, a paradox is *a seemingly absurd or contradictory statement or proposition which when investigated may prove to be well founded or true*. More to it, the conceptual framework of an accepted theory is indispensable, firstly, to perceive a given statement as absurd or contradictory; secondly, to classify it as paradoxical when proved well founded or true; thirdly, to try and find the cause(s) of one's initial bafflement.

When framed within the Kirchhoff-Love theory, the plate paradox consists in the unexpected finding that the transverse displacement of a simply supported, circular plate acted upon by uniform transversal loads is larger when computed directly than when estimated numerically for a sequence of approximating polygonal plates; no doubt, within the Kirchhoff-Love theory, the source of the paradox resides in the manner support boundary conditions are formulated.

In this paper, I take an alternative and, in my opinion, more illuminant point of view: I use the equilibrium theory of linear elasticity as a framework, and I show that there are good reasons to locate the source of the plate paradox in a deficient account of the *null-Lagrangian energy*, that is, of the portion of stored energy admitting a representation as a surface integral; a similar point of view, albeit less explicit, less general, and argued mathematically in a different manner, has been proposed in Simmonds (2010). In principle, paradoxes of identical source are to be expected also for body shapes that are not plate-like, say, when a sequence of convex polygonal domains converges to a spherical ball. I explore the possibility of such paradoxes in case of the *exact Levinson-type solutions*, studied in Nardinocchi and Podio-Guidugli (2003), to a class of equilibrium problems for three-dimensional right cylinders made of a linearly elastic, transversely isotropic material. Levinsonian solutions are of special interest because they work for not necessarily short cylinders of *arbitrary cross section*, not only when the mantle is simply supported but also when two other boundary conditions prevail, described in Nardinocchi and Podio-Guidugli (2003) as, respectively, a *sliding clamp* and an *elastic support*.

19.2 Null-Lagrangian Energy in Linear Elasticity

As detailed in Lancia et al (1995); Podio-Guidugli (2000), the elasticity tensor \mathbb{C} may be split additively into the *Cauchy's* pseudo elasticity tensor $\widetilde{\mathbb{C}}$ and the *null-Lagrangian* tensor $\widehat{\mathbb{C}}$:

$$\mathbb{C} = \widetilde{\mathbb{C}} + \widehat{\mathbb{C}}, \quad 2\widetilde{\mathbb{C}}_{ijhk} = \mathbb{C}_{ijhk} + \mathbb{C}_{ikhj}, \quad 2\widehat{\mathbb{C}}_{ijhk} = \mathbb{C}_{ijhk} - \mathbb{C}_{ikhj}; \quad (19.1)$$

a relevant property of $\widehat{\mathbb{C}}$ is

$$\widehat{\mathbb{C}}_{ijhk} = -\widehat{\mathbb{C}}_{ikhj}. \quad (19.2)$$

For a fully anisotropic material, the independent components of \mathbb{C} are 21, those of $\widetilde{\mathbb{C}}$ are 15, and those of $\widehat{\mathbb{C}}$ are 6; these numbers reduce to, respectively, 5, 3, and 2, in case of transversely isotropic material response. Both $\widetilde{\mathbb{C}}$ and $\widehat{\mathbb{C}}$ have the major symmetry $ij \leftrightarrow hk$ required for an elasticity tensor, but none has the minor symmetries $ij \leftrightarrow ji$ and $hk \leftrightarrow kh$ and hence none qualifies in general as an elasticity tensor, except when $\widehat{\mathbb{C}}$ is taken null and Cauchy's *rariconstant elasticity theory* obtains.

For \mathbf{u} and

$$\mathbf{E}(\mathbf{u}) = \frac{1}{2} [\nabla \mathbf{u} + (\nabla \mathbf{u})^T],$$

respectively, the displacement and strain fields, the stored-energy functional may be split according to (19.1)₁:

$$\frac{1}{2} \int_{\Omega} \mathbf{E}(\mathbf{u}) \cdot \mathbb{C}[\mathbf{E}(\mathbf{u})] = \frac{1}{2} \int_{\Omega} \mathbf{E}(\mathbf{u}) \cdot \widetilde{\mathbb{C}}[\mathbf{E}(\mathbf{u})] + \frac{1}{2} \int_{\Omega} \mathbf{E}(\mathbf{u}) \cdot \widehat{\mathbb{C}}[\mathbf{E}(\mathbf{u})], \quad (19.3)$$

into the Cauchy energy plus a null-Lagrangian contribution, that is, a quadratic functional admitting an alternative representation as a surface integral:

$$\int_{\Omega} \nabla \mathbf{u} \cdot \widehat{\mathbb{C}}[\nabla \mathbf{u}] = \int_{\partial \Omega} \nabla \mathbf{u} \cdot \widehat{\mathbb{C}}[\mathbf{u} \otimes \mathbf{n}] = \int_{\partial \Omega} \widehat{\gamma}(\mathbf{u}, \nabla^s \mathbf{u}, \mathbf{n}) \quad (19.4)$$

with

$$\nabla^s \mathbf{u} = \nabla \mathbf{u} - \partial_{\mathbf{n}} \mathbf{u} \otimes \mathbf{n}.$$

The boundary operator associated to the surface potential $\widehat{\gamma}$ may be interpreted as a fairly general type of configuration-dependent surface load (Podio-Guidugli and Vergara Caffarelli, 1990); when it comes to its evaluation, paradoxical occurrences may follow from one or another combination of prescriptions about

- (a) the constitutive information embodied in $\widehat{\mathbb{C}}$ and
- (b) the class of admissible displacements and their boundary restriction, including their tangential gradient.

19.3 Null-Lagrangian Energy and Plate Paradoxes

On leaving more complex situations for a future study, I here let the integration domain $\Omega \equiv \mathcal{P} \times [-h, +h]$ be *plate-like* – that is, the Cartesian product of a finite flat two-dimensional region \mathcal{P} with piece-wise smooth boundary $\partial \mathcal{P}$ and the interval $[-h, +h]$ of a straight line of direction \mathbf{z} orthogonal to \mathcal{P} . Plate-like regions are said *softly supported* when their boundary fibres are imposed no \mathbf{z} -displacement; for \mathbf{t} and \mathbf{m} the tangent and outward normal vectors at a point of $\partial \mathcal{P}$, standard additional impositions on boundary fibres integrate a *hard support* \equiv no rotation of axis \mathbf{m} about $(x, 0)$ and a *clamped support* \equiv no rotation of axis \mathbf{t} about $(x, 0)$.

I now proceed to show that, no matter how small the ratio $2h/\text{diam}(\mathcal{P})$, paradoxes may occur when the material response is chosen spatially uniform and *transversely isotropic* with respect to the direction \mathbf{z} of the normal to the plane of \mathcal{P} .

For (x, ζ) a typical point of $\overline{\mathcal{P}} \times [-h, +h]$, I let the admissible displacement fields have the form considered by Levinson (1985), namely,

$$\mathbf{u}_L(x, \zeta) = f(\zeta)w(x)\mathbf{z} - g(\zeta)\nabla w(x) \tag{19.5}$$

(see Nicotra et al, 1985; Nardinocchi and Podio-Guidugli, 2003). Note that the Kirchhoff-Love’s *Ansatz*

$$\mathbf{u}_{KL}(x, \zeta) = w(x)\mathbf{z} - \zeta\nabla w(x)$$

is recovered both from Levinson’s – on choosing $f(\zeta) = 1$ and $g(\zeta) = \zeta$ in (19.5) – and from Reissner-Mindlin’s *Ansatz*

$$\mathbf{u}_{RM}(x, \zeta) = w(x)\mathbf{z} + \zeta\varphi(x), \quad \varphi(x) \cdot \mathbf{z} = 0,$$

on choosing $\varphi = -\nabla w$ (recall that $\varphi(x)$ prescribes the rotation about its center of the vertical fibre through x and that a Reissner-Mindlin’s plate is insensitive to in-plane stretching).

For brevity, I here concentrate on Levinson’s case and omit all proofs. With a view toward evaluating the null-Lagrangian integral in (19.3)₂, I notice that

- the only nonnull components of the *null-Lagrangian* tensor are

$$\widehat{\mathbb{C}}_{1122}$$

and

$$\widehat{\mathbb{C}}_{1133} = \widehat{\mathbb{C}}_{2233}$$

(no sign restrictions are required to guarantee positivity of the stored-energy density);

- under the assumption that the parameter function f be even,

$$\int_{\partial\Omega} = \int_{\mathcal{P} \times \{-h, +h\}} + \int_{-h}^{+h} \int_{\partial\mathcal{P}} = \int_{-h}^{+h} \int_{\partial\mathcal{P}}$$

and hence the null-Lagrangian integral in (19.4) becomes

$$\int_{\Omega} \nabla \mathbf{u} \cdot \widehat{\mathbb{C}}[\nabla \mathbf{u}] = \int_{-h}^{+h} \int_{\partial\mathcal{P}} \nabla \mathbf{u} \cdot \widehat{\mathbb{C}}[\mathbf{u} \otimes \mathbf{m}];$$

- under the assumption that the parameter function g be odd,

$$\int_{-h}^{+h} \int_{\partial\mathcal{P}} \nabla \mathbf{u} \cdot \widehat{\mathbb{C}}[\mathbf{u} \otimes \mathbf{m}] \propto \int_{-h}^{+h} g^2 \int_{\partial\mathcal{P}} \Delta w \partial_{\mathbf{m}} w = O(h^3) \int_{\partial\mathcal{P}} \Delta w \partial_{\mathbf{m}} w.$$

I conclude that paradoxes are indeed predictable (in a sense, inducible), depending on

- (i) what boundary conditions are imposed in addition to the support condition

$$w|_{\partial\mathcal{P}} = 0$$

and on

- (ii) how the contour curve $\partial\mathcal{P}$ is approximated.

19.4 Conclusions

I have shown that paradoxes closely resembling to the standard plate paradoxes are to be expected when dealing *à la* Levinson with a class of equilibrium problems for transversely isotropic linearly elastic cylinders.

Acknowledgements Part of the above summarized results was obtained years ago in collaboration with Professor Antonino Favata and remained unpublished. I gratefully acknowledge his kind permission to report on them here.

This paper is dedicated to George Jaiani in the occasion of his 75th birthday.

References

- Babuška I, Pitkäranta J (1990) The plate paradox for hard and soft simple support. *SIAM Journal on Mathematical Analysis* 21(3):551–576
- Lancia MR, Vergara Caffarelli G, Podio-Guidugli P (1995) Null Lagrangians in linear elasticity. *Mathematical Models and Methods in Applied Sciences* 4:415–427
- Levinson M (1985) The simply supported rectangular plate: An exact, three dimensional, linear elasticity solution. *Journal of Elasticity* 7:283–291
- Nardinocchi P, Podio-Guidugli P (2003) Levinson-type benchmarks for slide-clamped and elastically supported plates. *Journal of Elasticity* 73:211–220
- Nicotra V, Podio-Guidugli P, Tiero A (1985) Exact equilibrium solutions for linearly elastic plate-like bodies. *Journal of Elasticity* 56:231–245
- Podio-Guidugli P (2000) *A Primer in Elasticity*. Kluwer Academic Publishers, Dordrecht

- Podio-Guidugli P, Vergara Caffarelli G (1990) Surface interaction potentials in elasticity. *Archive for Rational Mechanics and Analysis* 109:343–383
- Simmonds J (2010) A simple energetic explanation of the polygon-circle paradox for classical (Kirchhoff) plate theory. *Journal of Elasticity* 99:113–116



Chapter 20

A Shell Finite Element Model for Superelasticity of Shape Memory Alloys

Luka Porenta, Boštjan Brank, Jaka Dujc, Miha Brojan, and Jaka Tušek

Abstract A finite element formulation for the analysis of large strains of thin-walled shape memory alloys is briefly presented. For the shell model we use a seven-kinematic-parameter model for large deformations and rotations, which takes into account the through-the-thickness stretch and can directly incorporate a fully 3D inelastic constitutive equations. As for the constitutive model, we use a large strain isotropic formulation that is based on the multiplicative decomposition of the deformation gradient into the elastic and the transformation part and uses the transformation deformation tensor as an internal variable. Numerical examples are presented to illustrate the approach.

Key words: Shape memory alloys · Superelasticity · 3D-shell model · Finite elements

20.1 Introduction

Shape memory alloys (SMAs) are used for numerous applications (see for example Jani et al, 2014, for a recent review), especially in medicine, where the Ni-Ti alloy is used for stents, bone implants and surgical tools, see for example Brojan et al (2008); Petrini and Migliavacca (2011), in robotics, where SMAs are used as actuators,

Luka Porenta

University of Ljubljana, Faculty of Mechanical Engineering, Aškerčeva c. 6, Ljubljana, Slovenia
e-mail: luka.porenta@fs.uni-lj.si

Boštjan Brank · Jaka Dujc

University of Ljubljana, Faculty of Civil and Geodetic Engineering, Jamova c. 2, Ljubljana, Slovenia
e-mail: bbrank@fgg.uni-lj.si, jaka.dujc@fgg.uni-lj.si

Miha Brojan and Jaka Tušek

University of Ljubljana, Faculty of Mechanical Engineering, Aškerčeva c. 6, Ljubljana, Slovenia
e-mail: miha.brojan@fs.uni-lj.si, jaka.tusek@fs.uni-lj.si

see e.g. Coral et al (2012)), and aeronautics, where SMAs are used for vibration damping, seals, deployment mechanisms and morphing wings, see e.g. McDonald Schetky (1991); Hartl et al (2009); Sofla et al (2010). Applications in energy and process engineering are also under development, e.g. in thermal engineering for heat engines and for elastocaloric cooling technology, see e.g. Kaneko and Enomoto (2011); VHK and ARMINES (2016); Tušek et al (2016).

Shape memory alloys have two important properties:

- i) the ability to remember its original shape when a deformed SMA part is subjected to a high temperature (called the shape memory effect) and
- ii) the ability to withstand large strains (up to 8%) without permanent plastic deformation (known as superelasticity), see Fig. 20.1 (left).

Both properties are attributed to the fact that SMAs are found in two different phases, Fig. 1 (right). The high temperature parent phase is called austenite or austenitic phase (A) and the low temperature product phase is called martensite or martensitic phase (M). The crystal structure of A is highly symmetric, which is why it can be only in one variant. On the other hand, M can be found in a large number of variants due to the lower symmetry of its crystal structure. Twinned or self-accommodated martensite (M^t), which is stable at low stress state, occurs in different variants. At a stress state higher than the critical, a process of detwinning starts, which results in detwinned (or stress induced) martensite (M^d), i.e. the variant with the preferable orientation for a given stress state. In the phase diagram in Fig.1 (right), areas with stable crystal lattices and transformation regions are shown schematically.

When a SMA in the M phase is subjected to mechanical loading, it deforms and a detwinning process of martensite variants occurs. At the macroscopic scale, this is a change of shape, while at the micro-scale, martensite variants are oriented in a more preferable way. During unloading the martensite variants do not change, therefore pseudo-plastic deformations are present at zero load. At this stage, shape recovery can be achieved by subjecting the SMA material to a temperature above the austenitic transformation finish temperature (A_f), where only A phase is stable. During the temperature rise, a phase transformation from M to A begins at the austenitic transformation start temperature (A_s) and is completed at A_f . On the other hand, cooling of SMA causes martensitic transformation with formation of self-accommodated martensite variants. The transformation begins at martensitic transformation start temperature (M_s) and ends at martensitic transformation finish temperature (M_f). In contrast to heating, where a shape recovery occurs, cooling of SMA to its initial temperature does not cause any change in shape. It is worth noting that shape recovery is only possible up to a certain degree of deformation.

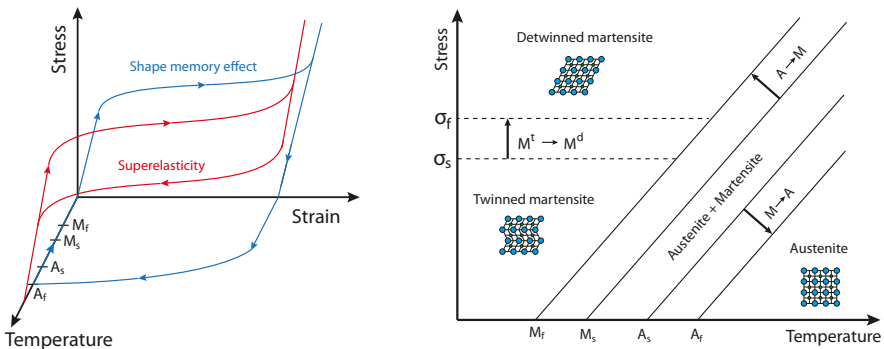


Fig. 20.1. Left: shape memory effect and superelasticity. Right: phase diagram.

Superelasticity (also called pseudoelasticity) is exhibited for a temperature above A_f , where the loading/unloading response is characterised by a nonlinear behaviour with hysteresis. During loading, a stress-induced martensite is formed during the exothermic martensite transformation. At the macroscopic level, this is observed as a large deformation. During unloading an endothermic reverse martensite transformation from martensite to austenite takes place and the deformation vanishes. The mechanism is not elastic because a transformation (change of the crystal lattice) takes place. Depending on the strain rate and heat exchange between the SMA material and the environment, the material may heat up or cool down during the transformation.

A number of 3D SMA material models were proposed. For implementation within the framework of the finite element (FE) method, macroscale phenomenological SMA models are a preferable choice. These models differ in various aspects, but the biggest difference is whether they are designed to solve small strain or large strain problems. The large strain models assume a multiplicative decomposition of the deformation gradient. One of the first large strain SMA models was developed by Auricchio and Taylor (1997) and numerically implemented in Auricchio (2001). Stupkiewicz and Petryk (2013) showed how to reformulate a small strain model for the finite strain regime, for superelasticity with tension-compression asymmetry and anisotropy. In Reese and Christ (2008) the deformation gradient is decomposed into elastic and transformation parts and the latter is further divided into a recoverable and a plastic part.

In this work, we apply a version of the large strain SMA model proposed in Arghavani et al (2011); Souza et al (1998); Evangelista et al (2010). The model can predict the superelastic response and the shape memory effect of polycrystalline SMA. It assumes isothermal transformations and neglects the tension-compression asymmetry as well as functional fatigue due to cyclic loading. In the framework of the finite element method, the 3D SMA material models are usually incorporated into the 3D solid finite elements. A FE implementation of an SMA model in a plate or shell finite element formulation is very rare. One of the reasons is that the standard shell theories of Kirchhoff and Reissner-Mindlin type cannot directly include 3D constitutive models because the plane stress constraint has to be enforced (and this is not a trivial task for an inelastic model, see e.g. Dujc and Brank (2012)). There are, however, the 3D-shell finite elements and the solid-shell finite elements, which are designed in such a way that they can directly use 3D constitutive equations without modification, see for example Brank et al (2002); Brank (2005); Brank et al (2008). In this work we rely on a 3D shell model proposed in Brank (2005). Our numerical formulation, which is presented below, can be used to simulate the nonlinear behaviour (due to mechanical loading) of (very) thin-walled shape memory alloys. They can undergo large deformations, large rotations (the formulation described in Brank and Ibrahimbegovic (2001); Ibrahimbegovic et al (2001) is used) and large strains.

20.2 Constitutive Model for SMA

In this section we revisit the 3D constitutive model for SMA that was originally developed by Souza et al (1998) for small strains and later extended to finite strains by Evangelista et al (2010); Arghavani et al (2011). Similar to the finite strain

plasticity (see e.g. Ibrahimbegovic, 2009), a multiplicative decomposition of the deformation gradient into elastic and transformation parts is postulated:

$$\mathbf{F} = \mathbf{F}_e \mathbf{F}_t \quad (20.1)$$

With Eq. (20.1), the initial (i.e. undeformed), intermediate and current (i.e. deformed) configurations are introduced. In this work, the total Lagrangian formulation is used to describe large deformations of a shell, which requires the derivation of constitutive equations with respect to the initial configuration. To achieve this goal, however, we also use the tensors defined at the intermediate configuration. One such tensor is $\mathbf{C}_e = \mathbf{F}_e^T \mathbf{F}_e$, while $\mathbf{C}_t = \mathbf{F}_t^T \mathbf{F}_t$ is defined at the initial configuration. The Cauchy-Green deformation tensor and the Green-Lagrange strain tensor are:

$$\mathbf{C} = \mathbf{F}^T \mathbf{F} = \mathbf{F}_t^T \mathbf{C}_e \mathbf{F}_t, \quad \mathbf{E} = \frac{1}{2} (\mathbf{C} - \mathbf{1}) \quad (20.2)$$

respectively, where $\mathbf{1}$ is the unit tensor. The velocity gradient tensor $\mathbf{L} = \dot{\mathbf{F}} \mathbf{F}^{-1}$ and its symmetric part (i.e. rate of deformation) $\mathbf{d} = \frac{1}{2} (\mathbf{L} + \mathbf{L}^T)$ are also used. The dot stands for the (pseudo-)time derivative. The relation between \mathbf{d} and the strain rate $\dot{\mathbf{E}}$ is:

$$\dot{\mathbf{E}} = \mathbf{F}^T \mathbf{d} \mathbf{F} \quad (20.3)$$

According to experimental observations, the transformation in SMA is (almost) isochronic, which is expressed by $\det(\mathbf{F}_t) = 1$ that yields $\text{tr}(\mathbf{d}_t) = 0$.

The Helmholtz free energy ψ must depend on \mathbf{F}_e only through \mathbf{C}_e in order to satisfy material objectivity. It is assumed that ψ depends also on \mathbf{C}_t or yet the transformation strain tensor

$$\mathbf{E}_t = \frac{1}{2} (\mathbf{C}_t - \mathbf{1}) \quad (20.4)$$

temperature T , and that it can be additively decomposed into elastic part ψ_e and transformation part ψ_t :

$$\psi = \psi(\mathbf{C}_e, \mathbf{E}_t, T) = \psi_e(\mathbf{C}_e) + \psi_t(\mathbf{E}_t, T) \quad (20.5)$$

We assume material isotropy and choose a neo-Hooke type of hyperelastic strain energy function:

$$\psi_e(\mathbf{C}_e) = \frac{1}{2} \mu (I_1 - 3 - \log(I_3)) + \frac{1}{4} \lambda (I_3 - 1 - \log(I_3)) \quad (20.6)$$

where μ and λ are Lamé's coefficients, and I_1 and I_3 are the first and third invariants of \mathbf{C}_e , respectively. It can be shown that these invariants equal the first and third invariants of $\mathbf{C} \mathbf{C}_t^{-1}$, which enables writing the strain energy function (20.6) in terms of tensors from the initial configuration, i.e. $\psi_e(\mathbf{C}_e) = \tilde{\psi}_e(\mathbf{C}, \mathbf{C}_t)$. The transformation part of free energy is chosen as (after Arghavani et al, 2011; Souza et al, 1998):

$$\psi_t(\mathbf{E}_t, T) = \tau_M(T) \|\mathbf{E}_t\| + \frac{1}{2} h \|\mathbf{E}_t\|^2 + \mathcal{J}(\|\mathbf{E}_t\|) \quad (20.7)$$

Here, $\tau_M(T) = \beta \langle T - T_0 \rangle$ provides temperature dependency of material response, h , β and T_0 are the material parameters of the SMA model, $\langle \cdot \rangle$ are Macaulay brackets and $\|\cdot\|$ is standard tensor norm. In Eq. (20.7), a step function

$$\mathcal{J}(\|\mathbf{E}_t\|) = \begin{cases} 0 & \|\mathbf{E}_t\| \leq \varepsilon_L \\ \infty & \text{otherwise} \end{cases} \quad (20.8)$$

is introduced in order to enable a (computational) enforcement of the limit of transformation strains ε_L . This is another material parameter that can be obtained experimentally from the uniaxial test as the absolute value of the maximum transformation strain.

The Clausius-Duhem inequality form of the second law of thermodynamics states:

$$\mathcal{D} = \mathbf{S} : \frac{1}{2} \dot{\mathbf{C}} - (\dot{\psi} + \eta \dot{T}) \geq 0 \quad (20.9)$$

where \mathbf{S} is the second Piola-Kirchhoff stress tensor and η is entropy. Substituting (20.5) into (20.9), we obtain:

$$\mathcal{D} = \mathbf{S} : \underbrace{\frac{1}{2} \dot{\mathbf{C}} - \frac{\partial \psi_e}{\partial \mathbf{C}_e} : \dot{\mathbf{C}}_e}_{\textcircled{1}} - \underbrace{\frac{\partial \psi_t}{\partial \mathbf{E}_t} : \dot{\mathbf{E}}_t - \frac{\partial \psi_t}{\partial T} : \dot{T}}_{\textcircled{2}} - \eta \dot{T} \geq 0 \quad (20.10)$$

It can be shown that $\textcircled{1}$ can be expanded as:

$$\left(\mathbf{S} - 2 \mathbf{F}_t^{-1} \frac{\partial \psi_e}{\partial \mathbf{C}_e} \mathbf{F}_t^{-T} \right) : \frac{1}{2} \dot{\mathbf{C}} + 2 \mathbf{C}_e \frac{\partial \psi_e}{\partial \mathbf{C}_e} : \mathbf{L}_t \quad (20.11)$$

where $\mathbf{L}_t = \dot{\mathbf{F}}_t \mathbf{F}_t^{-1}$. For an elastic case with no change in transformation and temperature, the expression for the stress tensor follows from (20.10) and (20.11) as:

$$\mathcal{D} = 0, \dot{\mathbf{E}}_t = \mathbf{L}_t = \mathbf{0}, \dot{T} = 0 \Rightarrow \mathbf{S} = 2 \mathbf{F}_t^{-1} \frac{\partial \psi_e}{\partial \mathbf{C}_e} \mathbf{F}_t^{-T} = 2 \frac{\partial \tilde{\psi}_e}{\partial \mathbf{C}} \quad (20.12)$$

For a case of a temperature change with no change in transformation, the expression for entropy is obtained from (20.10) as:

$$\mathcal{D} = 0, \dot{\mathbf{E}}_t = \mathbf{L}_t = \mathbf{0} \Rightarrow \eta = - \frac{\partial \psi_t}{\partial T} \quad (20.13)$$

It is assumed that the relations (20.12) and (20.13) are also valid in the case of transformation, which is the only case that still has to be considered. To this end, it can be shown that the derivatives in $\textcircled{2}$ can be expressed as:

$$\frac{\partial \psi_t}{\partial \mathbf{E}_t} = \mathbf{X} = h \mathbf{E}_t + (\tau_M(T) + \gamma) \mathbf{N} \quad (20.14)$$

where

$$\mathbf{N} = \frac{\mathbf{E}_t}{\|\mathbf{E}_t\|}$$

is a normalized transformation tensor, and

$$\gamma = \begin{cases} \geq 0 & \|\mathbf{E}_t\| = \varepsilon_L \\ 0 & \text{otherwise} \end{cases} \quad (20.15)$$

is a penalty-like parameter that results from sub-differential of the indicator function

$$\frac{\partial \mathcal{I}(\|\mathbf{E}_t\|)}{\partial \mathbf{E}_t} = \gamma \mathbf{N}.$$

Using equations (20.12), (20.13) and (20.14), the dissipation at the transformation case is obtained from (20.10) as:

$$\underbrace{\mathcal{D}^t}_{\mathbf{P}} = 2 \mathbf{C}_e \frac{\partial \psi_e}{\partial \mathbf{C}_e} : \mathbf{L}_t - \mathbf{X} : \dot{\mathbf{E}}_t \geq 0 \quad (20.16)$$

Some mathematical manipulations and (20.3) yield the equality $\mathbf{X} : \dot{\mathbf{E}}_t = \mathbf{F}_t \mathbf{X} \mathbf{F}_t^T : \mathbf{d}_t$. Moreover, a decomposition of \mathbf{L}_t into a symmetric and a skew-symmetric parts, \mathbf{d}_t and \mathbf{w}_t , respectively, leads to equality $\mathbf{P} : \mathbf{L}_t = \mathbf{P} : \mathbf{d}_t$. By further using the notation $\mathbf{K} = \mathbf{F}_t \mathbf{X} \mathbf{F}_t^T$ and $\mathbf{Z} = \mathbf{P} - \mathbf{K}$, where \mathbf{K} plays a role of the back-stress tensor, the inequality of the dissipation at transformation can be rewritten as:

$$\mathcal{D}^t = \mathbf{Z} : \mathbf{d}_t \geq 0 \quad (20.17)$$

It can be shown by some mathematical manipulations that \mathbf{Y} , which plays the role of an effective stress tensor, can be expressed in terms of tensors defined at initial configuration as:

$$\mathbf{Y} = \mathbf{C} \mathbf{S} - \mathbf{C}_t \mathbf{X} \quad (20.18)$$

By choosing a transformation function $f(\mathbf{Z}) \leq 0$ and assuming that the transformation case corresponds to the stress state giving $f(\mathbf{Z}) = 0$, the evolution equation for the transformation case can be obtained. We postulate that among all admissible states of transformation, we choose the one that renders maximum dissipation \mathcal{D}^t or yet minimum of $-\mathcal{D}^t$. Recasting the original problem into the unconstrained minimization problem can be done by using the Lagrange multiplier method and by defining the Lagrange function as:

$$\mathcal{L}(\mathbf{Z}, \dot{\zeta}) = -\mathcal{D}^t(\mathbf{Z}) + \dot{\zeta} f(\mathbf{Z}) \quad (20.19)$$

where $\dot{\zeta}$ is Lagrange multiplier. In order to find minimum of $\mathcal{L}(\mathbf{Z}, \dot{\zeta})$, the stationarity, primal feasibility, dual feasibility and complementary slackness conditions (also known as Kuhn-Tucker conditions and loading/unloading conditions) must hold:

$$\frac{\partial \mathcal{L}(\mathbf{Z}, \dot{\xi})}{\partial \mathbf{Z}} = 0, \quad f(\mathbf{Z}) \leq 0, \quad \dot{\xi} \geq 0, \quad \dot{\xi} f(\mathbf{Z}) = 0 \quad (20.20)$$

From the stationarity condition (20.20)₁, the evolution equation for the rate of transformation deformation \mathbf{d}_t is obtained as:

$$-\mathbf{d}_t + \dot{\xi} \frac{\partial f(\mathbf{Z})}{\partial \mathbf{Z}} = 0 \Rightarrow \mathbf{d}_t = \dot{\xi} \frac{\partial f(\mathbf{Z})}{\partial \mathbf{Z}} \quad (20.21)$$

In this work we choose the following transformation function (according to Arghavani et al, 2011; Souza et al, 1998), which resembles classical yield functions for metals:

$$f(\mathbf{Z}) = \|\mathbf{Z}^D\| - R \quad (20.22)$$

where \mathbf{Z}^D is the deviatoric part of \mathbf{Z} , and R is elastic region radius, which is another parameter of the material model that has to be evaluated experimentally. Finally, combining (20.21) and (20.22) yields the following form of the evolution equation:

$$\mathbf{d}_t = \dot{\xi} \frac{\mathbf{Z}^D}{\|\mathbf{Z}^D\|} \quad (20.23)$$

which can be replaced (in a consistent manner) by another evolution equation, which is more suitable for numerical implementation based on the total Lagrangian formulation:

$$\dot{\mathbf{C}}_t = 2\dot{\xi} \frac{\mathbf{Y}^D}{\sqrt{\mathbf{Y}^D : \mathbf{Y}^{D^T}}} \mathbf{C}_t \quad (20.24)$$

This concludes a short derivation of the SMA material model used in this work. The equations that define the above SMA large strain constitutive model are: the chosen Helmholtz free energy function defined by (20.5), (20.6) and (20.7); the stress tensors that can be computed by (20.12), (20.14) and (20.18); the transformation function (20.22); the loading/unloading conditions (20.20); and the evolution equation (20.24). We will omit discussing its numerical implementation.

20.3 Seven-parameter Shell Model

In this section, we briefly present a 3D-shell model that can incorporate a 3D constitutive model without a modification. Let the position vector to the material point of the initial shell configuration be defined as:

$$\boldsymbol{\varphi}(\xi^1, \xi^2, \xi^3) = \boldsymbol{\varphi}_0(\xi^1, \xi^2) + \xi^3 \mathbf{A}(\xi^1, \xi^2), \quad \|\mathbf{A}\| = 1 \quad (20.25)$$

where ξ^1 and ξ^2 are curvilinear coordinates that parameterize the shell mid-surface \mathcal{A} , $\xi^3 \in [-\frac{h}{2}, \frac{h}{2}]$ is a straight through-the-thickness coordinate, h is the initial shell thickness and \mathbf{A} is the shell director vector. In what follows, we will omit showing

functions and functional dependency on the convective coordinates we introduced above for the sake of brevity. The position vector to the material point of the deformed shell configuration is assumed as:

$$\bar{\boldsymbol{\varphi}} = \boldsymbol{\varphi}_0 + \mathbf{u} + (\xi^3 \lambda + (\xi^3)^2 q) \mathbf{a}, \quad \|\mathbf{a}\| = 1 \quad (20.26)$$

where \mathbf{u} is the mid-surface displacement vector, \mathbf{a} is the rotated shell director that preserves the original unit length and the parameters λ and q define a constant and linear through-the-thickness stretching, respectively. The rotation of \mathbf{A} into \mathbf{a} is described by a singularity-free formulation that uses two large rotation parameters, i.e., $\mathbf{a} = \mathbf{a}(\theta^1, \theta^2)$; we refer to e.g. Brank and Ibrahimbegovic (2001); Ibrahimbegovic et al (2001) for details. Equation (20.26) introduces seven kinematic parameters of the adopted shell model, which can be collected in a vector as $\boldsymbol{\Phi} = \{\mathbf{u}, \theta^1, \theta^2, \lambda, q\}$.

The components of the Green-Lagrange strain tensor can be defined with respect to the above introduced curvilinear coordinates as:

$$\mathbf{E} = E_{ij} \mathbf{G}^i \otimes \mathbf{G}^j \quad (20.27)$$

where \mathbf{G}^i is the contravariant base vector defined as $\mathbf{G}^i \cdot \mathbf{G}_k = \delta_k^i$. The covariant base vector is given as:

$$\mathbf{G}_k = \frac{\partial \boldsymbol{\varphi}}{\partial \xi^k} \quad (20.28)$$

and δ_j^i is the Kronecker delta symbol. The strains E_{ij} are polynomials up to the fourth order with respect to ξ^3 . In this work, we neglect the terms of orders three and four because, as our numerical experiments show, they have a negligible influence on the results. On the other hand, it is important that all strains have non-zero terms of order one and two. This allows the implementation of a fully 3D constitutive equations without modelling errors, which is not possible with many other shell models due to the inherent 2D character of the description of the shell kinematics.

The virtual work equation (i.e. the weak form of the equilibrium equations) is the starting point for finite element discretization. It can be written as:

$$G(\delta \boldsymbol{\Phi}, \boldsymbol{\Phi}, \mathbf{C}_t) = \underbrace{\int_{\mathcal{A}} \int_{-h/2}^{h/2} \delta \mathbf{E}(\delta \boldsymbol{\Phi}, \boldsymbol{\Phi}) : \mathbf{S}(\boldsymbol{\Phi}, \mathbf{C}_t) d\xi^3 d\mathcal{A}}_{G_{int}(\delta \boldsymbol{\Phi}, \boldsymbol{\Phi}, \mathbf{C}_t)} - G_{ext}(\delta \boldsymbol{\Phi}) = 0 \quad (20.29)$$

where G_{int} is the virtual work of the internal forces, G_{ext} is virtual work of the external forces acting on the shell, $\delta \mathbf{E}$ is variation of the strain tensor field that can be obtained as

$$\delta \mathbf{E} = \frac{d}{d\epsilon} \mathbf{E}(\boldsymbol{\Phi} + \epsilon \delta \boldsymbol{\Phi})|_{\epsilon=0},$$

where ϵ is a scalar parameter, and $\delta \boldsymbol{\Phi}$ represents the variation of the fields of seven kinematic parameters of the model. It is worth noting that the 2nd Piola-Kirchhoff

stress tensor field depends on shell kinematics as well as on the internal variable of the above described SMA constitutive model, which is C_t . The linearization of Eq. (20.29) yields:

$$\text{Lin}[G] = G + \Delta G \quad (20.30)$$

where

$$\Delta G = \int_{\mathcal{A}} \int_{-h/2}^{h/2} [\mathbf{S} : \Delta \delta \mathbf{E} + \delta \mathbf{E} : \mathbb{C} \Delta \mathbf{E}] d\xi^3 d\mathcal{A} \quad (20.31)$$

Here,

$$\Delta \delta \mathbf{E} = \frac{d}{d\epsilon} \delta \mathbf{E}(\delta \boldsymbol{\Phi}, \boldsymbol{\Phi} + \epsilon \Delta \boldsymbol{\Phi})|_{\epsilon=0}$$

contributes to the stiffness due to geometric effects, and

$$\mathbb{C} = \frac{\partial \mathbf{S}}{\partial \mathbf{E}}$$

is a consistent material operator, which is the fourth order tensor.

After the introduction of discretization and interpolation in the framework of the finite element method, Eq. (20.29) yields a system of highly nonlinear equations (due to the arbitrariness of $\delta \boldsymbol{\Phi}$), where the unknowns are kinematic parameters at nodes and internal variables at Gauss integration points. The solution of such a system is based on an operator-split technology, which is applied within an incremental-iterative Newton-Raphson solution method. Namely, at each iteration the computation of the Gauss point internal variable C_t (and consequently the computation of the Gauss point stresses \mathbf{S} and the consistent material tangent operator \mathbb{C}) is split from the computation of the nodal kinematic parameters. This is achieved by applying two sequential procedures, where the results of the first procedure are immediately used in the second procedure. Namely, the constitutive equations are first enforced at the integration points by updating the internal variables of the constitutive model. This local update is followed by the solution of the system of equations for an update of nodal kinematic parameters using the consistent tangent stiffness matrix resulting from (20.31).

The numerical examples in the next section are computed using a four node element with the assumed natural strain treatment of the transverse shear strains and through-the-thickness strains in order to avoid transverse shear and thickness lockings. The element has four integration points over the mid-surface and three through-the-thickness integration points, all of which are of the Gaussian type. In order to facilitate the implementation of the SMA constitutive model described in the previous section, a local Cartesian frame is introduced at each integration point.

20.4 Numerical Examples

The material and shell models described above were implemented into the finite element code using AceFEM (Korelc and Wriggers, 2016) by using a generator of the finite element code AceGen, see e.g. Korelc and Stupkiewicz (2014); Hudobivnik and Korelc (2016).

Three examples are presented below. The first and the second example show that our results are in in good agreement with the reference results presented in Arghavani et al (2011). The third example is somehow more demanding and illustrates the ability of the derived formulation to predict a superelastic response of a thin-walled curved structure. The material parameters typical for NiTi are applied for all considered examples:

$$\begin{aligned} E = 51700 \text{ MPa}, \quad \nu = 0.3, \quad h = 750 \text{ MPa}, \quad R = 140 \text{ MPa} \\ \varepsilon_L = 0.075, \quad \beta = 5.6 \text{ MPa}^\circ\text{C}, \quad T_0 = -25^\circ\text{C} \end{aligned} \quad (20.32)$$

To obtain the superelastic response, the ambient temperature T is set to 37°C . The following figures show the components of the second Piola-Kirchhoff stress tensor and the components of the Green-Lagrange strain tensor.

20.4.1 Square Wall Under Uniaxial Loading

A square wall with an edge length of $a = 10 \text{ mm}$ and a thickness of $t = 0.01 \text{ mm}$ is subjected to uniaxial tension and compression. The mesh (5×5 elements), the boundary conditions that allow a homogeneous uniaxial stress state over the wall and the load are shown in Fig. 20.2. The load is $q_1 = \lambda q$ and $q_2 = 0$, where $q = 14 \text{ N/mm}$ and λ is the load multiplier. Loading and unloading in tension was applied first, followed by loading and unloading in compression. Figure 20.3 shows computed uniaxial superelastic response at a Gauss point. Our results (almost) exactly match the results from reference Arghavani et al (2011). The reason for a very small discrepancy at large load levels is the use of Saint-Venant Kirchhoff strain energy function in Arghavani et al (2011), while our choice is the Neo-Hookean strain energy function.

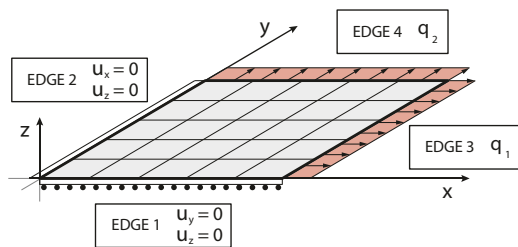
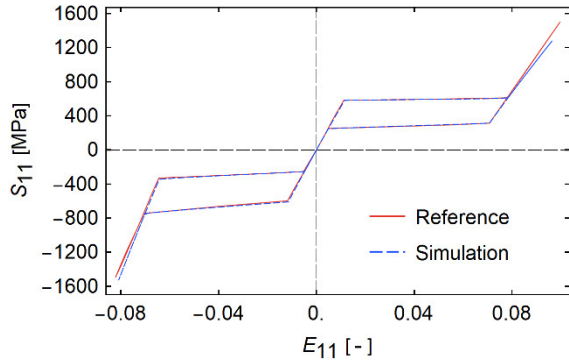


Fig. 20.2 Square wall: boundary and loading conditions.

Fig. 20.3 Square wall: superelastic response at a Gauss point for uniaxial loading.



20.4.2 Square Wall Under Biaxial Loading

Geometry, boundary conditions (which allow a homogenous stress state over the wall) and mesh for this example remain the same as for the previous one, see Fig. 20.2. However, the load is now $q_1 = \lambda_1 q$ and $q_2 = \lambda_2 q$ where $q = 7 \text{ N/mm}$, and λ_1 and λ_2 are load multipliers. The load is therefore non-proportional, with $F_1 = q_1 a$ and $F_2 = q_2 a$ changing in a butterfly-like pattern as shown in Fig. 20.4. The loading was applied in five steps:

- (i) λ_1 and λ_2 increase from 0 to 1,
- (ii) λ_1 decreases to -1 at $\lambda_2 = 1$,
- (iii) λ_1 increases to 1 and λ_2 decreases to -1 ,
- (iv) λ_1 decreases to -1 at $\lambda_2 = -1$, and
- (v) λ_1 and λ_2 go to 0.

The curve in Fig. 20.5 explains how the relation between the in-plane normal strains is changing during the loading. The agreement with the solution found in Arghavani

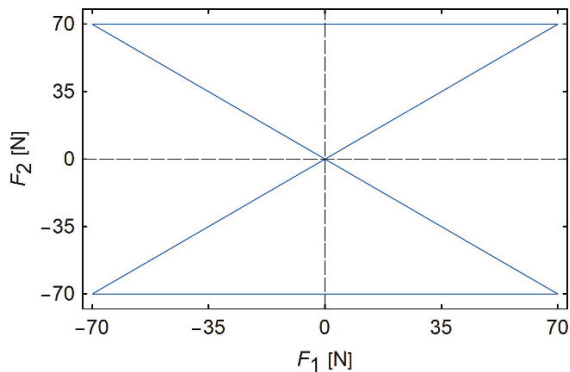
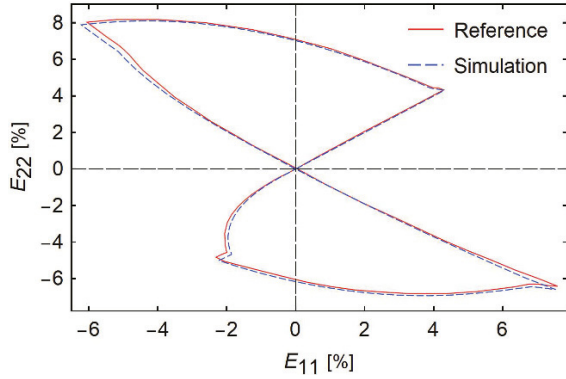


Fig. 20.4 Square wall: non-proportional loading path.

Fig. 20.5 Square wall: relation between the in-plane normal strains at a Gauss point.



et al (2011) is very good. We would like to point out that our load application was different from the one in Arghavani et al (2011). In our case, the mesh with edge loads was considered, while in Arghavani et al (2011) a single Gauss-point algorithm was tested under a butterfly-like stress control (with missing details how it was applied for a strain-driven update algorithm). This is the reason for a difference between our results and the reference results in Fig. 20.6, which shows the relation between the in-plane normal stresses during loading. Part of the difference may also be due to the use of different strain energy functions.

It is worth noting that for the first two examples the plane stress condition is completely reproduced by the derived shell model due to the small thickness to edge ratio $t/a = 10^{-3}$.

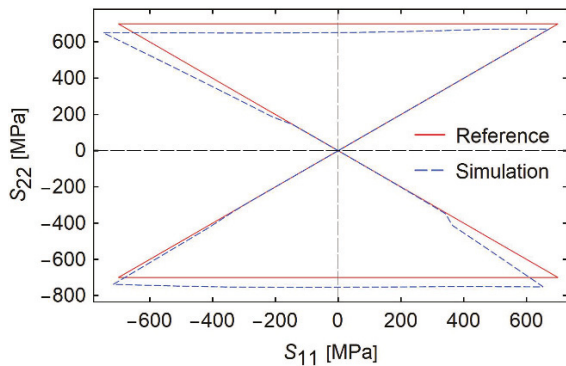


Fig. 20.6 Square wall: relation between the in-plane normal stresses at a Gauss point.

20.4.3 Compression of a Twisted Beam

Twisted beam with length $L = 12$ mm, width $w = 2$ mm and thickness $t = 0.25$ mm, see Fig. 20.7, is clamped at one end and subjected at the opposite end to imposed compressive axial displacements $u = \lambda u_0$, where $u_0 = 1.1$ mm and λ is load multiplier, which goes from 0 to 1 and back to 0. The mesh consists of 16 elements in the longitudinal and 8 elements in the transverse direction. Figure 20.8 shows deformed mesh at $\lambda = 1$, with coloured contours representing $\|\mathbf{E}_t\|$ at the mid-surface (the red colour denotes the largest transformation and the blue colour the smallest). At the final configuration, where λ is back to 0, the stresses are zero and no transformation is observed. The initial shape is fully recovered and the superelastic response is obtained. This can be nicely seen from the diagram in Fig. 20.9, which shows the reaction force at edge 1 as a function of the imposed compressive axial displacement of edge 2.

20.5 Conclusions

The aim of this work was to derive a finite element formulation that can be used for large deformation and stability analysis of curved thin-walled shape memory

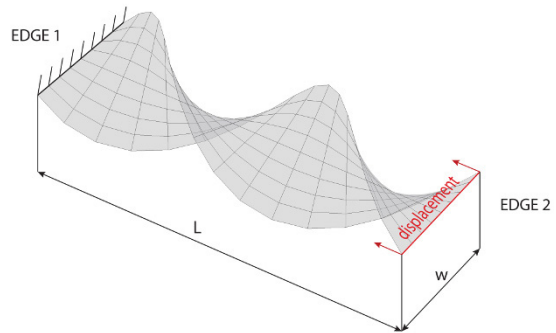


Fig. 20.7 Twisted beam: geometry, mesh, boundary and loading conditions.

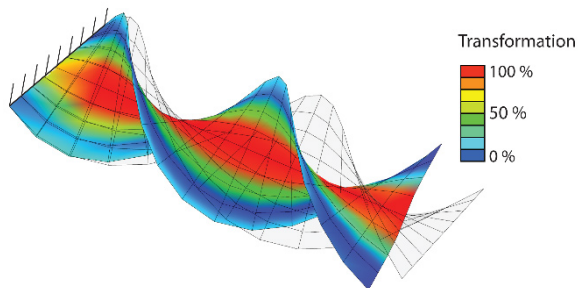
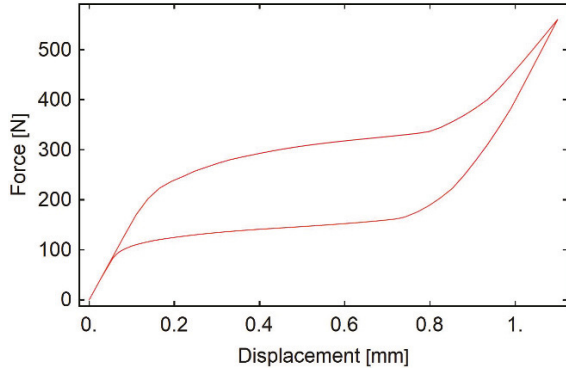


Fig. 20.8 Twisted beam: initial and deformed geometry at $\lambda = 1$.

Fig. 20.9 Superelastic response of twisted beam.



alloys. It is well documented in the finite element literature that for thin shell-like structures the 3D-solid finite element models are inappropriate, because they are very likely introducing a considerable modelling error. For this purpose we have revisited a seven-parameter large deformations and large rotations shell model (that can be used for thin and thick shells), and use it as a framework for implementation of a 3D finite strain material model for shape memory alloys. Several presented numerical examples illustrate a very satisfying performance of resulting finite element formulation.

Questions on the numerical implementation of the considered SMA material model, a comparison with experimental results, further development of the finite element formulation in order to be able to perform large solution steps and to be insensitive to mesh distortions (following Lavrenčič and Brank, 2020; Brank, 2008) and the simulation of the buckling process of shape memory alloys (using Stanić and Brank, 2017) will be answered and shown in a separate publication.

Acknowledgements This work was supported by European research Council (ERC) under Horizon 2020 research and innovation program (ERC Starting Grant No. 803669), and by the Slovenian Research Agency (P2-0210).

References

- Arghavani J, Auricchio F, Naghdabadi R, Reali A (2011) On the robustness and efficiency of integration algorithms for a 3D finite strain phenomenological SMA constitutive model. *International Journal for Numerical Methods in Engineering* 85(1):107–134
- Auricchio F (2001) A robust integration-algorithm for a finite-strain shape-memory-alloy superelastic model. *International Journal of Plasticity* 17(7):971–990

- Auricchio F, Taylor RL (1997) Shape-memory alloys: modelling and numerical simulations of the finite-strain superelastic behavior. *Computer Methods in Applied Mechanics and Engineering* 143(1):175–194
- Brank B (2005) Nonlinear shell models with seven kinematic parameters. *Computer Methods in Applied Mechanics and Engineering* 194(21):2336–2362
- Brank B (2008) Assessment of 4-node EAS-ANS shell elements for large deformation analysis. *Computational Mechanics* 42:39–51
- Brank B, Ibrahimbegovic A (2001) On the relation between different parametrizations of finite rotations for shells. *Engineering Computations: Int J for Computer-Aided Engineering* 18(7):950–973
- Brank B, Korelc J, Ibrahimbegović A (2002) Nonlinear shell problem formulation accounting for through-the-thickness stretching and its finite element implementation. *Computers & Structures* 80(9):699–717
- Brank B, Ibrahimbegovic A, Bohinc U (2008) On prediction of 3D stress state in elastic shell by higher-order shell formulations. *Comput Model Eng Sci* 33:85–108, DOI 10.3970/cmesci.2008.033.085
- Brojan M, Bombač D, Kosel F, Videnič T (2008) Shape memory alloys in medicine. *RMZ – Materials and Geoenvironment* 55:173–189
- Coral W, Rossi C, Colorado J, Lemus D, Barrientos A (2012) Sma-based muscle-like actuation in biologically inspired robots: A state of the art review. In: Berselli G, Verthey R, Vassura G (eds) *Smart Actuation and Sensing Systems*, IntechOpen, Rijeka, chap 3
- Dujc J, Brank B (2012) Stress resultant plasticity for shells revisited. *Computer Methods in Applied Mechanics and Engineering* 247–248:146–165
- Evangelista V, Marfia S, Sacco E (2010) A 3D SMA constitutive model in the framework of finite strain. *International Journal for Numerical Methods in Engineering* 81(6):761–785
- Hartl DJ, Mooney JT, Lagoudas DC, Calkins FT, Mabe JH (2009) Use of a ni60ti shape memory alloy for active jet engine chevron application: II. experimentally validated numerical analysis. *Smart Materials and Structures* 19(1):015,021
- Hudobivnik B, Korelc J (2016) Closed-form representation of matrix functions in the formulation of nonlinear material models. *Finite Elements in Analysis and Design* 111:19–32
- Ibrahimbegovic A (2009) *Nonlinear Solid Mechanics*. Springer, Dordrecht
- Ibrahimbegovic A, Brank B, Courtois P (2001) Stress resultant geometrically exact form of classical shell model and vector-like parameterization of constrained finite rotations. *International Journal for Numerical Methods in Engineering* 52(11):1235–1252
- Jani JM, Leary M, Subic A, Gibson MA (2014) A review of shape memory alloy research, applications and opportunities. *Materials & Design* 56:1078–1113
- Kaneko K, Enomoto K (2011) Development of reciprocating heat engine using shape memory alloy. *Journal of Environment and Engineering* 6(1):131–139
- Korelc J, Stupkiewicz S (2014) Closed-form matrix exponential and its application in finite-strain plasticity. *International Journal for Numerical Methods in Engineering* 98(13):960–987

- Korelc J, Wriggers P (2016) *Automation of Finite Element Methods*. Springer
- Lavrenčič M, Brank B (2020) Hybrid-mixed shell quadrilateral that allows for large solution steps and is low-sensitive to mesh distortion. *Computational Mechanics* 65:177–192
- McDonald Schetky L (1991) Shape memory alloy applications in space systems. *Materials & Design* 12(1):29 – 32
- Petrini L, Migliavacca F (2011) Biomedical applications of shape memory alloys. *Journal of Metallurgy* 2011:ID 501,483
- Reese S, Christ D (2008) Finite deformation pseudo-elasticity of shape memory alloys – Constitutive modelling and finite element implementation. *International Journal of Plasticity* 24(3):455–482
- Sofla AYN, Meguid SA, Tan KT, Yeo WK (2010) Shape morphing of aircraft wing: Status and challenges. *Materials & Design* 31(3):1284–1292
- Souza AC, Mamiya EN, Zouain N (1998) Three-dimensional model for solids undergoing stress-induced phase transformations. *European Journal of Mechanics - A/Solids* 17(5):789–806
- Stanić A, Brank B (2017) A path-following method for elasto-plastic solids and structures based on control of plastic dissipation and plastic work. *Finite Elements in Analysis and Design* 123:1–8
- Stupkiewicz S, Petryk H (2013) A robust model of pseudoelasticity in shape memory alloys. *International Journal for Numerical Methods in Engineering* 93(7):747–769
- Tušek J, Engelbrecht K, Eriksen D, Dall’Olio S, Tusek J, Pryds N (2016) A regenerative elastocaloric heat pump. *Nature Energy* 1:1–6
- VHK, ARMINES (2016) Household refrigeration technology roadmap. https://www.eup-network.de/fileadmin/user_upload/Household_Refrigeration_Review_TECHNOLOGY_ROADMAP_FINAL_20160304.pdf

Open Access This chapter is licensed under the terms of the Creative Commons Attribution 4.0 International License (<http://creativecommons.org/licenses/by/4.0/>), which permits use, sharing, adaptation, distribution and reproduction in any medium or format, as long as you give appropriate credit to the original author(s) and the source, provide a link to the Creative Commons license and indicate if changes were made.

The images or other third party material in this chapter are included in the chapter’s Creative Commons license, unless indicated otherwise in a credit line to the material. If material is not included in the chapter’s Creative Commons license and your intended use is not permitted by statutory regulation or exceeds the permitted use, you will need to obtain permission directly from the copyright holder.





Chapter 21

Validity of the Reduced Bending Stiffness Method for Stacked Laminates

Jakob C. Schilling and Christian Mittelstedt

Abstract Unsymmetrical laminates are unavoidable in practical applications of composite materials. Fuselages require a smooth surface on the outside and can be typically only stiffened by attaching reinforcements on the inside. Here, the stringer feet are often stacked on top of the skin surface. In those cases, the reduced bending stiffness (RBS) method has been applied to avoid more complex computational methods for the approximation of critical buckling loads. However, the validity of the RBS method has not been evaluated for stacked laminates but for single unsymmetrical laminates only. This topic is addressed in the present work by investigating a stacked laminate consisting of two by itself symmetrical cross-ply laminates under uniaxial compression. The panel is simply supported. The effects of prebuckling deformation are neglected. The results show perfect agreement for the special case investigated; thus, the utilisation of the reduced bending stiffness method can be recommended.

Key words: Reduced bending stiffness · Buckling · Stability · Stacked laminate · Extensional-bending coupling · Cross-ply laminate

21.1 Introduction

In the development of highly efficient computational models for composite structures, different approximate methods are used and combined. One of these is the reduced bending stiffness (RBS) method that first appeared in Reissner and Stavsky (1961). They developed a plate model for unsymmetric angle ply laminates where the effect of extensional-bending coupling is included. This was achieved by the partial inversion of the constitutive relations, i.e. by expressing the strains in terms of normal

Jakob C. Schilling · Christian Mittelstedt
Technische Universität Darmstadt, Institute for Lightweight Construction and Design, Otto-Berndt-Straße 2, 64287 Darmstadt, Germany
e-mail: jakob.schilling@klub.tu-darmstadt.de, christian.mittelstedt@klub.tu-darmstadt.de

stress resultants and the moments in terms of curvatures. An Airy stress function is introduced and the system of the three coupled partial differential equations reduced to a set of two. To obtain accurate results the compatibility equations have to be fulfilled. The authors, however, give results in which this requirement is neglected and show that reasonable agreement is still achieved. This simplification is introduced by Chamis (1969) as “reduced rigidities”. The author derived an approximate model for the buckling of anisotropic plates based on the principle of the stationary value of the elastic potential. The field equation is solved using the Galerkin method. An experimental study shows good agreement with the approximate model. The idea of the new approximate model is detailed further by Ashton (1969) who coins the term “reduced bending stiffness method”. He argues that the neglect of the coupling in case of the previously reduced relationship delivers more accurate results than the neglect of the original extensional-bending stiffnesses. Also, he concludes that the RBS method gives the minimum stiffness in every direction and not in regard of an arbitrary reference plane, such as the geometrical mid-plane. The work of the mentioned authors is the starting point for numerous investigations of the applicability of the new method that avoids the solution of the more complex constitutive behaviour of unsymmetric laminates.

The more complex behaviour that is approximated by the means of the RBS method are the extensional-bending coupling effects. They couple the partial differential equations of the in-plane with the out-of-plane deformation. In many studies that follow the works of Reissner and Stavsky, Chamis and Ashton, the prebuckling deformation is not considered. This is only physically sound for certain boundary conditions which are clarified by Leissa (1986). Depending on the lay-up, loading and boundary conditions additional edge moments are necessary to allow a panel to remain flat. The stability behaviour of unsymmetrical laminated panels with varying boundary conditions is further detailed by Qatu and Leissa (1993). Therefore, finite element studies were performed to show the stability behaviour when prebuckling deformation is admitted. When suitable edge moments are not in place, no bifurcation occurs; thus, theories that describe the buckling of antisymmetric, simply supported cross-ply laminates are inadmissible. In a more recent work of Diaconu and Weaver (2006), the stability behaviour is assessed for long unsymmetrical laminated plates. This is in contrast to the work of Qatu and Leissa (1993) who only considered short plates. Here, the conclusion is drawn that classical bifurcation still occurs in the interior of the plate and large prebuckling deformations are observed only close to the supports. Additionally, the RBS method is used in the authors proposed model for the postbuckling behaviour. Hence, the approximative method might still be an reasonable assumption, although not fully physically sound.

The results of studies based on inadmissible configurations, e.g. simply supported plates with unsymmetric cross-ply configuration, are still valuable as guidelines for the use of the RBS method and to estimate the error that is introduced by its application. A brief overview of those studies is given in the present work together with physically sound studies of simply supported angle-ply laminates. Whitney (1969) obtains results for the shear buckling loads of unsymmetrical cross-ply laminates and finds reasonable agreement between the the solution based on Galerkin’s method

with and without the utilisation of the RBS method. Closed-form solutions for bending, vibration and buckling are derived by Whitney and Leissa (1969) in the case of antisymmetric angle- and cross-ply laminates with simply supported boundary conditions. The effect of the extensional-bending coupling is investigated and it is found that it is vanishing with increasing number of layers. This is again shown by Whitney and Leissa (1970) but it is advised that the RBS method is to be used carefully and is not able to deliver reasonably accurate results for all different laminate configurations. The issue of boundary conditions in the context of the RBS method is raised by Whitney (1970) with the focus on clamped boundary conditions with unsatisfying results of values obtained by the RBS method and by Danielson and Tielking (1988) with the focus on membrane boundary conditions who points out that the approximation is only valid for special cases. Furthermore, Ashton and Whitney (1970) describe the effects of the RBS on the total elastic potential and discuss the validity of the method for the example of cylindrical bending. This is presented in combination with a more detailed review of the RBS method in the monograph of Whitney (1987). Jones (1973) treats the problem of unsymmetric laminates with a closed-form solution that solves classical buckling for simply supported cross-ply plates with arbitrary ply thickness and stacking sequence. In his monograph (Jones, 1999) the same author points out that the expectation to obtain reasonable results for generally unsymmetric laminates using the approximation is not justified when only based on experience with antisymmetric laminates. Furthermore, he criticises the lack of studies for more general laminates. In the an extensive study by Ewing et al (1988) bending, vibration and buckling of antisymmetric angle- and cross-ply laminates are investigated. The approximation with the RBS method is considered acceptable for antisymmetric cross-ply laminates.

The usage of the RBS method is also discussed in the context of postbuckling by Diaconu and Weaver (2006). Turvey (1977) investigates moderately thick symmetric and unsymmetric laminates. Different thickness ratios of angle-ply and cross-ply laminates were studied. It is concluded that the results for symmetric laminates are superior to those obtained for unsymmetric ones. Hereby, the non-existent influence of the RBS method, when no extensional-bending coupling exists was not acknowledged.

Despite the controversy about the prebuckling deformation the RBS method is commonly used in the context of stiffened skin structures. Coburn et al (2015) presented a Rayleigh-Ritz based computational model for the buckling analysis of blade stiffened variable stiffness panels. The influence of the stringer foot that is stacked on top of the skin is modelled by considering the area as subplate; thus, the discontinuity in the stiffness of the panel can be captured. The stiffness of this distinct plate is approximated using the RBS method and leads to an underestimation of the critical buckling loads compared to finite element analyses although energy based approximative methods usually do not converge conservatively. This is also concluded by Schilling and Mittelstedt (2020) who investigated the buckling of omega-stringer-stiffened composite panels and employed the same stringer foot modelling strategy as Coburn et al (2015) in their closed-form approximate analytical solution. In the semi-analytical approach of Vescovini and Bisagni (2015) omega-stringer-stiffened

panels are investigated as well. The RBS method is again used but only included in the computation of the elastic potential and not as the material properties of a discrete plate. The effect of the overlapping width of the stringer foot is not investigated by comparing the results to FEA but just a simple approximate model. Thus, it is not conceivable if the underestimation of the critical buckling load is significant in their work. The authors also published computational models for blade stiffened panels (Vescovini and Bisagni, 2017). The RBS method was also used by Mittelstedt and Beerhorst (2009) in their buckling analysis of omega-stringer stiffened panels, where the panel was modelled as elastically restrained plate. Herencia et al (2007) employ the RBS method in an optimization study of a panel consisting of several plates of varying thicknesses and properties. Hereby, also stacked laminates are considered but the reference plane is assumed mid-plane symmetric.

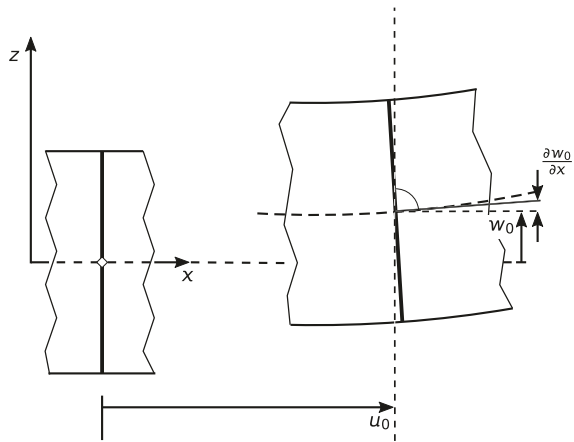
In most cases, the mentioned studies do not account for prebuckling deformation; thus, a possible error introduced by the RBS method can be approximated using solutions for simply supported unsymmetric laminates even though the necessary edge moments are not included. The case of stacked laminates where the extensional-bending coupling results from the change of reference plane has to the knowledge of the authors not been investigated thoroughly in the context of the RBS method. Therefore, the present work establishes new results on the validity of the RBS method within the practical application of composite materials.

In the following section, the classical laminated plate theory (CLPT) is briefly discussed including the relevant coupling effects. Within the framework of the CLPT, the procedure regarding the change of the reference plane is outlined. Also, the RBS method is explained. After introducing the analytical solution of unsymmetrical cross-ply laminates, the presentation of numerical results follows, which are discussed and consequently summarized in the conclusion.

21.2 Classical Laminated Plate Theory

The classical laminated plate theory (CLPT) is valid for thin composite panels, as shear deformation is neglected in this equivalent single layer theory. The kinematics are based on the assumptions of the Kirchoff plate theory and they are depicted for a plate cut in the xz -plane in Fig 21.1. The normal material line is assumed to remain straight before and after deformation whilst staying perpendicular to the mid-plane of the laminate, both when it is deformed or undeformed. The laminate is furthermore considered to be inextensible in thickness direction. Also, geometric linearity and the two dimensional plane stress state are part of the theory's framework. The displacement field resulting from the described assumptions is shown in Eqs. (21.1)-(21.3). The in-plane displacements are depending on the rotations of the mid-plane $\frac{\partial w_0}{\partial x}$ and $\frac{\partial w_0}{\partial y}$ as well as the through thickness coordinate z .

Fig. 21.1 Kinematics of the classical laminated plate theory exemplarily shown for a plate cut in the xz -plane. Depicted are the mid-plane displacement w_0 and the in-plane displacement u_0 as well as the slope $\frac{\partial w_0}{\partial x}$



$$u(x, y, z) = u_0(x, y) - z \frac{\partial w_0}{\partial x} \tag{21.1}$$

$$v(x, y, z) = v_0(x, y) - z \frac{\partial w_0}{\partial y} \tag{21.2}$$

$$w(x, y, z) = w_0(x, y) \tag{21.3}$$

The linear strains ϵ_{xx} , ϵ_{yy} and γ_{xy} and curvatures κ_{xx} , κ_{yy} and κ_{xy} are expressed in Eq. (21.4). The actual strains and curvatures are computed by inserting Eqs. (21.1)-(21.3) into Eq. (21.4).

$$\begin{pmatrix} \epsilon_{xx}^0 \\ \epsilon_{yy}^0 \\ \gamma_{xy}^0 \\ \kappa_{xx}^0 \\ \kappa_{yy}^0 \\ \kappa_{xy}^0 \end{pmatrix} = \begin{pmatrix} \frac{\partial u_0}{\partial x} \\ \frac{\partial v_0}{\partial y} \\ \frac{\partial u_0}{\partial y} + \frac{\partial v_0}{\partial x} \\ -\frac{\partial^2 w_0}{\partial x^2} \\ -\frac{\partial^2 w_0}{\partial y^2} \\ -2\frac{\partial^2 w_0}{\partial x \partial y} \end{pmatrix} \tag{21.4}$$

The constitutive relation formulated in Eq. (21.5) relates the strains and curvatures to the force resultants N_{xx}^0 , N_{yy}^0 and N_{xy}^0 and moment resultants M_{xx}^0 , M_{yy}^0 and M_{xy}^0 via the stiffnesses A_{ij} , B_{ij} and D_{ij} .

$$\begin{pmatrix} N_{xx}^0 \\ N_{yy}^0 \\ N_{xy}^0 \\ M_{xx}^0 \\ M_{yy}^0 \\ M_{xy}^0 \end{pmatrix} = \begin{bmatrix} A_{11} & A_{12} & A_{16} & B_{11} & B_{12} & B_{16} \\ A_{12} & A_{22} & A_{26} & B_{12} & B_{22} & B_{26} \\ A_{16} & A_{26} & A_{66} & B_{16} & B_{26} & B_{66} \\ B_{11} & B_{12} & B_{16} & D_{11} & D_{12} & D_{16} \\ B_{12} & B_{22} & B_{26} & D_{12} & D_{22} & D_{26} \\ B_{16} & B_{26} & B_{66} & D_{16} & D_{26} & D_{66} \end{bmatrix} \begin{pmatrix} \epsilon_{xx}^0 \\ \epsilon_{yy}^0 \\ \gamma_{xy}^0 \\ \kappa_{xx}^0 \\ \kappa_{yy}^0 \\ \kappa_{xy}^0 \end{pmatrix} \tag{21.5}$$

Relevant in the context of the present work are the extensional-bending stiffnesses B_{ij} . They couple the in-plane behaviour with the out-of-plane behaviour leading to instant deformation when the laminate is under inplane load (Jensen and Lagace, 1988; Vasiliev, 1993). The investigation in this paper is limited to cross-ply laminates; consequently, no shear coupling ($A_{16} = A_{26} = 0$) and no bending-twisting coupling ($D_{16} = D_{26} = 0$) occurs. For this special type of laminate lay-up also the extensional-twisting coupling is not present ($B_{16} = B_{26} = 0$) and only the extensional-bending coupling ($B_{11}, B_{12}, B_{22} \neq 0$) and the extensional shear coupling ($B_{66} \neq 0$) do not vanish. The stiffnesses are computed according to Eqs. (21.6)-(21.8).

$$A_{ij} = \sum_{k=1}^N \int_{z_{k-1}}^{z_k} \bar{Q}_{ij}^{(k)} dz = \sum_{k=1}^N \bar{Q}_{ij}^{(k)} (z_k - z_{k-1}) \tag{21.6}$$

$$B_{ij} = \sum_{k=1}^N \int_{z_{k-1}}^{z_k} \bar{Q}_{ij}^{(k)} z dz = \frac{1}{2} \sum_{k=1}^N \bar{Q}_{ij}^{(k)} (z_k^2 - z_{k-1}^2) \tag{21.7}$$

$$D_{ij} = \sum_{k=1}^N \int_{z_{k-1}}^{z_k} \bar{Q}_{ij}^{(k)} z^2 dz = \frac{1}{3} \sum_{k=1}^N \bar{Q}_{ij}^{(k)} (z_k^3 - z_{k-1}^3) \tag{21.8}$$

Therein, \bar{Q}_{ij} is the transformed reduced stiffness of a single layer. The single layer is depicted in Fig. 21.2 with its dedicated local coordinate system consisting of the 1-, 2- and 3-axis. The 1-axis points in the direction of the fibre. Consequently, the transformation takes the laminate lay-up into account. The relationship between the reduced and transformed reduced stiffness is shown in Eq. (21.9), where T_{ij} is the commonly known matrix for coordinate transformation for a rotation about the 3-axis. It transforms the local reduced stiffness with respect to the global laminate coordinate system.

$$\bar{Q}_{ij} = T_{ij} Q_{ij} T_{ij}^T \tag{21.9}$$

where

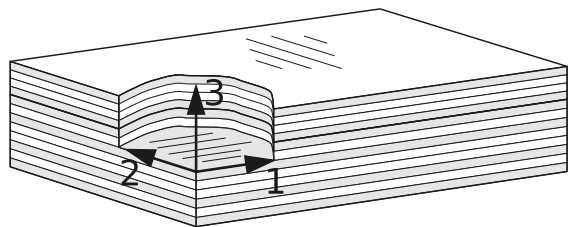


Fig. 21.2 Sketch of the stacked laminate with a cut-out depicting the local coordinate system (1-, 2-, 3-axis) of a single layer; the 1-axis points in the direction of the fibre

$$\begin{aligned}
 Q_{11} &= \frac{E_1}{1 - \nu_{12}\nu_{21}} \\
 Q_{22} &= \frac{E_2}{1 - \nu_{12}\nu_{21}} \\
 Q_{12} &= \frac{\nu_{12} E_2}{1 - \nu_{12}\nu_{21}} \\
 Q_{66} &= G_{12}
 \end{aligned}$$

A more detailed description and derivation of the CLPT can be found in various textbooks (Reddy, 2004; Jones, 1999; Mittelstedt and Becker, 2016). When the laminates are symmetric, the bending stretching coupling vanishes completely. However, by the stacking of laminates and therefore a change of reference plane, the extensional-bending coupling is reintroduced in the constitutive relations.

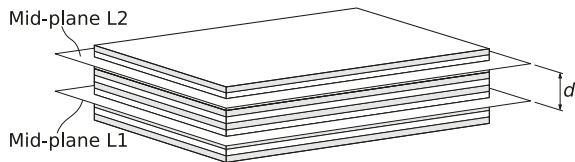
21.3 Change of Reference Plane

The respective reference planes of two different laminates can be referenced to just one; thus, the eccentrically attached laminate is referenced to the base laminate as shown in Fig. 21.3. The procedure of changing the reference plane is presented in more detail in the textbook of Mittelstedt and Becker (2016). The main steps are recapitulated in the following. First the matrices A_{ij} , B_{ij} and D_{ij} (or in short the ABD -matrix) are obtained for each of the two studied laminates separately. Then, the reinforcing laminate is referenced to the base laminate by taking the distance between the reference planes into account. The new combined ABD -matrix is computed according to Eq. (21.10). The base laminate is denoted with the index s and the reinforcing laminate with the index f .

$$\begin{aligned}
 \begin{bmatrix} A_{ij} & B_{ij} \\ B_{ij} & D_{ij} \end{bmatrix} &= \begin{bmatrix} A_{ij,s} & B_{ij,s} \\ B_{ij,s} & D_{ij,s} \end{bmatrix} \\
 &+ \begin{bmatrix} A_{ij,f} & B_{ij,f} + d A_{ij,f} \\ B_{ij,f} + d A_{ij,f} & D_{ij,f} + 2d B_{ij,f} + d^2 A_{ij,f} \end{bmatrix} \quad (21.10)
 \end{aligned}$$

This means that even for the combination of two by itself symmetric laminates ($B_{ij} = 0$) coupling effects are necessarily to be taken into account. One possibility is to approximate these effects with the RBS method.

Fig. 21.3 Sketch of a stacked laminate with the mid-planes of the base laminate (L1) and their reinforcing laminate (L2) and the distance between the two d



21.4 Reduced Bending Stiffness Method

The reduced bending stiffness method is derived from the semi-inverse constitutive relations shown in Eq. (21.11).

$$\begin{pmatrix} \epsilon_{xx}^0 \\ \epsilon_{yy}^0 \\ \gamma_{xy}^0 \\ M_{xx}^0 \\ M_{yy}^0 \\ M_{xy}^0 \end{pmatrix} = \left[\begin{array}{c|c} A_{ij}^* & B_{ij}^* \\ \hline C_{ij}^* & D_{ij}^* \end{array} \right] \begin{pmatrix} N_{xx}^0 \\ N_{yy}^0 \\ N_{xy}^0 \\ \kappa_{xx}^0 \\ \kappa_{yy}^0 \\ \kappa_{xy}^0 \end{pmatrix} \quad (21.11)$$

where

$$\begin{aligned} A_{ij}^* &= A_{ij}^{-1} \\ B_{ij}^* &= -A_{ij}^{-1} B_{ij} \\ C_{ij}^* &= B_{ij} A_{ij}^{-1} \\ D_{ij}^* &= D_{ij} - B_{ij} A_{ij}^{-1} B_{ij} \end{aligned}$$

To simplify the computations B_{ij}^* and C_{ij}^* are neglected and the uncoupled problem can be treated with the reduced bending stiffness D_{ij}^* only. Ashton (1969) indicates a reason for the surprising accuracy of the method by contemplating the elastic potential of a laminated plate. It is given in general form in Eq. (21.12).

$$\Pi = \frac{1}{2} \iint_A \left(\vec{\epsilon}^T \mathbf{A} \vec{\epsilon} + 2 \vec{\epsilon}^T \mathbf{B} \vec{\kappa} + \vec{\kappa}^T \mathbf{D} \vec{\kappa} \right) dA \quad (21.12)$$

When the relationship for the strains $\vec{\epsilon}$ as described in Eq. (21.11) is used and inserted in the expression for the elastic potential, the stress resultants \vec{N} are decoupled from the curvatures. Thus, the coupling between extension and bending is only enforced by the compatibility equations. The elastic potential derived in this way is presented in Eq. (21.13).

$$\Pi = \frac{1}{2} \iint_A \left(\vec{N}^T \mathbf{A} \vec{N} + \vec{\kappa}^T [\mathbf{D} - \mathbf{B} \mathbf{A}^{-1} \mathbf{B}] \vec{\kappa} \right) dA \quad (21.13)$$

In the present case a solution for the coupled problem exists. Thus, the approximation can be compared and evaluated. The analytical solution of the coupled problem is shown in the following section.

21.5 Analytical Solution

For stacked laminates consisting of cross-ply laminates, a solution of the field equation exists for simply supported plates. The solution is discussed and derived in detail in the textbooks (Jones, 1999; Reddy, 2004) and earlier in a paper by (Jones, 1973). The Navier solution is valid for laminates under biaxial compression as indicated in Fig. 21.4. The axial compressive loads are related by the factor k .

$$N_{yy} = k N_{xx} \tag{21.14}$$

So for example for $k = 0$, only uniaxial compression in the direction of the x -axis is present. Hereby, the boundary conditions are presented in Eqs. (21.15-21.18) for $x = 0, a$ and in Eqs. (21.19-21.22) for $y = 0, b$. They are valid for the case that $A_{16} = A_{26} = B_{16} = B_{26} = D_{16} = D_{26} = 0$. Since there is extensional-bending coupling all five boundary conditions per edge are given, as they can be derived e.g. by the principle of the minimum of the elastic potential. The force resultants N_{xx}^0, N_{yy}^0 (see Sect. 21.2 Eq. (21.5)) do not represent the applied loads and have to vanish in the deformed buckled state of the laminate.

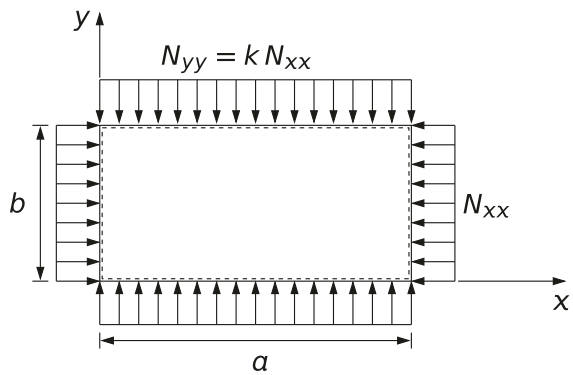


Fig. 21.4 Loading and boundary conditions of the considered laminate with the length a and width b

$$w_0 = v_0 = 0 \quad (21.15)$$

$$\frac{\partial w_0}{\partial y} = 0 \quad (21.16)$$

$$N_{xx}^0 = A_{11} \frac{\partial u_0}{\partial x} + A_{12} \frac{\partial v_0}{\partial y} - B_{11} \frac{\partial^2 w_0}{\partial x^2} - B_{12} \frac{\partial^2 w_0}{\partial y^2} = 0 \quad (21.17)$$

$$M_{xx}^0 = B_{11} \frac{\partial u_0}{\partial x} + B_{12} \frac{\partial v_0}{\partial y} - D_{11} \frac{\partial^2 w_0}{\partial x^2} - D_{12} \frac{\partial^2 w_0}{\partial y^2} = 0 \quad (21.18)$$

$$w_0 = u_0 = 0 \quad (21.19)$$

$$\frac{\partial w_0}{\partial x} = 0 \quad (21.20)$$

$$N_{yy}^0 = A_{12} \frac{\partial u_0}{\partial x} + A_{22} \frac{\partial v_0}{\partial y} - B_{12} \frac{\partial^2 w_0}{\partial x^2} - B_{22} \frac{\partial^2 w_0}{\partial y^2} = 0 \quad (21.21)$$

$$M_{yy}^0 = B_{12} \frac{\partial u_0}{\partial x} + B_{22} \frac{\partial v_0}{\partial y} - D_{12} \frac{\partial^2 w_0}{\partial x^2} - D_{22} \frac{\partial^2 w_0}{\partial y^2} = 0 \quad (21.22)$$

For this set of boundary conditions the Navier solution for the assumed classical buckling problem is shown in Eq. (21.23). Consequently the critical buckling load N_{cr} is depending on the stiffness of the laminate expressed by the elements of the ABD -matrix, geometrical properties such as the length a and width b of the considered plate and the half-wave numbers m and n in the direction of the x - and y -axis. The correct solution for the critical buckling load is the minimal value depending on varying integer half-wave numbers.

$$N_{cr} = \frac{d_{mn}}{a_0 (\alpha^2 + k\beta^2)} \quad (21.23)$$

where

$$\begin{aligned} \alpha &= \frac{m\pi}{a} \\ \beta &= \frac{n\pi}{b} \\ d_{mn} &= \begin{vmatrix} \hat{c}_{11} & \hat{c}_{12} & \hat{c}_{13} \\ \hat{c}_{12} & \hat{c}_{22} & \hat{c}_{23} \\ \hat{c}_{13} & \hat{c}_{23} & \hat{c}_{33} \end{vmatrix} \\ a_0 &= \hat{c}_{11}\hat{c}_{22} - \hat{c}_{12}\hat{c}_{12} \\ \hat{c}_{11} &= (A_{11}\alpha^2 + A_{66}\beta^2) \\ \hat{c}_{12} &= (A_{12} + A_{66})\alpha\beta \\ \hat{c}_{13} &= -B_{11}\alpha^3 - (B_{12} + 2B_{66})\alpha\beta^2 \\ \hat{c}_{22} &= (A_{66}\alpha^2 + A_{22}\beta^2) \\ \hat{c}_{23} &= -(B_{12} + 2B_{66})\alpha^2\beta - B_{22}\beta^3 \\ \hat{c}_{33} &= D_{11}\alpha^4 + 2(D_{12} + 2D_{66})\alpha^2\beta^2 + D_{22}\beta^4 \end{aligned}$$

In the next section this solution is used to obtain numerical results for a buckling analysis based on the reduced bending stiffness as well as on the accurate *ABD*-matrix.

21.6 Results and Discussion

In the present study a stacked laminate with the fixed thickness *h* is considered. The geometry is sketched in Fig. 21.5. The thickness *t_{f,s}* of each of the two sub laminates is varied by introducing the ratio between the thickness of the reinforcing layer and the overall height of the laminate $\frac{t_f}{h}$. In order to achieve symmetrical laminates, the number of layers is chosen as such that the point where the laminates are joined coincides with the boundary of a layer. The lay-up is denoted as

$$[0^\circ 90^\circ]_{n_s}$$

where *n* is the number of layer pairs that are repeated for the top (*n_f*) and for the bottom laminate (*n_s*), respectively. The laminate code index *s* indicates that the laminate is mirrored and as such symmetric. This also directly enforces a minimum number of overall layers of eight in the combined laminate. The number of pairs for the top *n_f* and the bottom *n_s* can be computed according to Eqs. (21.25) and (21.26). They depend on the ply thickness *t_{ply}* that is resulting from the step size *k_{step}*, see Eq. (21.24), of the investigated ratios $\frac{t_f}{h}$.

$$t_{ply} = \frac{h}{4 \frac{1}{k_{step}}} \tag{21.24}$$

$$n_f = \frac{t_f}{4 t_{ply}} \tag{21.25}$$

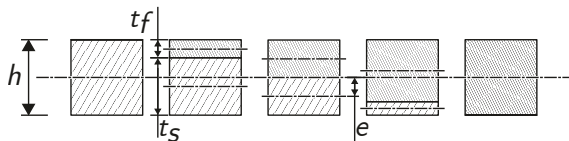
$$n_s = \frac{t_s}{4 t_{ply}} \tag{21.26}$$

As the overall thickness is fixed, the distance between the reference planes is constant with the value of $\frac{h}{2}$. But the eccentricity *e* of the bottom laminate in respect to the geometrical mid-plane increases for increasing ratios $\frac{t_f}{h}$ as shown in Eq. (21.27).

$$e = \frac{h - t_s}{2} = \frac{h}{2} \left(\frac{t_f}{h} \right) \tag{21.27}$$

The elastic moduli are *E₁* = 200000MPa and *E₂* = $\frac{E_1}{40}$. The shear stiffness *G₁₂* is 0.5*E₂*. The Poisson’s ratio *ν₁₂* is 0.25. To ensure thin laminates the ratio $\frac{b}{h}$ is 100.

Fig. 21.5 Sketch of a stacked laminate with their respective reference planes and the eccentricity *e* of the remaining reference plane



21.6.1 Influence of the Ratio $\frac{t_f}{h}$

In a first assessment the aspect ratio $\frac{a}{b}$ is varied for different ratios $\frac{t_f}{h}$. Hereby, the critical buckling load is given for values computed by the analytical exact solution and the reduced bending stiffness method. The results are presented in Fig. 21.6 for the material and geometrical properties given above. The step size k_{step} is 0.01 in order to allow for a thorough investigation of almost arbitrary ratios of $\frac{t_f}{h}$. Following Eqs. (21.24-21.26), the number of layer pairs $n_f + n_s$ is 100 and the layup consists of 400 layers. The results for the critical buckling load with and without the RBS method are not distinguishable; thus they are presented as one plot. The spread between the non-dimensional results for different values of the ratio $\frac{t_f}{h}$ almost completely vanishes once absolute values are considered. Respective numerical results are given in Table 21.1, it becomes apparent that the ratio $\frac{t_f}{h}$ only influences results where the ratio $\frac{a}{b}$ is a rational number. Additionally, the critical buckling load is indifferent to whether the reinforcing or base laminate has a higher thickness as long as the overall lay-up is mirrored. Consequently, exemplary values for $\frac{t_f}{h}$ of 0.2 and 0.8 are identical.

For the special laminate configuration investigated, the expressions for the elements of the ABD -matrix can be simplified. This is the first step towards the assessment of observed results. Hereby, the stiffnesses are expressed depending on the elements of the local reduced stiffness matrix of a single layer Q_{ij} . The extensional stiffness does not take the order of the lay-up into account. Therefore, it does not change its value for the combined cross-ply laminate configuration employed within this study. The extensional stiffness of the base and reinforcing laminate are distributed in accordance with the ratio $\frac{t_f}{h}$. Thus, the following expressions presented in Eq. (21.28) can be determined.

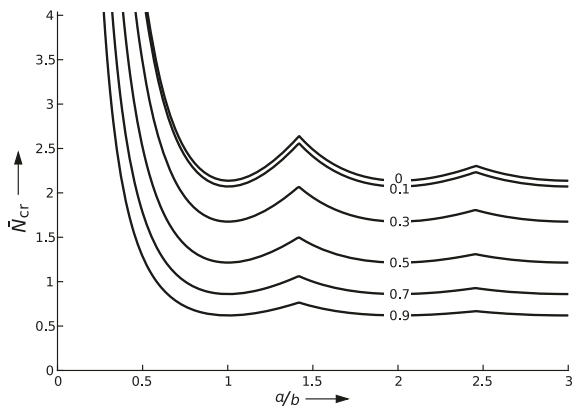


Fig. 21.6 Non-dimensional critical buckling load \bar{N}_{cr} versus the aspect ratio $\frac{a}{b}$ of the panel for different ratios of $\frac{t_f}{h}$ (0, 0.1, 0.3, 0.5, 0.7, 0.9); $E_1 = 200000 \text{ MPa}$, $E_2 = \frac{E_1}{40}$, $G_{12} = 0.5 E_2$, $\nu_{12} = 0.25$, $\frac{b}{h} = 100$ and the laminate consists of 400 layers

Table 21.1

Results for the critical buckling load computed without (N_{cr}) and with ($N_{cr, rbs}$) RBS method for $E_1 = 200000 \text{ MPa}$, $E_2 = \frac{E_1}{40}$, $G_{12} = 0.5 E_2$, $\nu_{12} = 0.25$, $\frac{b}{h} = 100$, and 400 layers.

$\frac{a}{b}$	$\frac{t_f}{h}$	N_{cr} in Nmm^{-1}	$N_{cr, rbs}$ in Nmm^{-1}	Error in %
0.25	0	137.61	137.61	0
	0.2	137.3	137.3	0
	0.4	137.15	137.15	0
	0.6	137.15	137.15	0
	0.8	137.3	137.3	0
0.5	0	37.14	37.14	0
	0.2	37.07	37.07	0
	0.4	37.03	37.03	0
	0.6	37.03	37.03	0
	0.8	37.07	37.07	0
1	0	17.92	17.92	0
	0.2	17.92	17.92	0
	0.4	17.92	17.92	0
	0.6	17.92	17.92	0
	0.8	17.92	17.92	0
2	0	17.92	17.92	0
	0.2	17.92	17.92	0
	0.4	17.92	17.92	0
	0.6	17.92	17.92	0
	0.8	17.92	17.92	0

$$\begin{aligned}
 A_{ij} &= h \frac{t_f}{h} \underbrace{\begin{bmatrix} \frac{Q_{11}+Q_{22}}{2} & Q_{12} & 0 \\ Q_{12} & \frac{Q_{11}+Q_{22}}{2} & 0 \\ 0 & 0 & Q_{66} \end{bmatrix}}_{A_{ij, f}} + h \left(1 - \frac{t_f}{h}\right) \underbrace{\begin{bmatrix} \frac{Q_{11}+Q_{22}}{2} & Q_{12} & 0 \\ Q_{12} & \frac{Q_{11}+Q_{22}}{2} & 0 \\ 0 & 0 & Q_{66} \end{bmatrix}}_{A_{ij, s}} \\
 &= h \begin{bmatrix} \frac{Q_{11}+Q_{22}}{2} & Q_{12} & 0 \\ Q_{12} & \frac{Q_{11}+Q_{22}}{2} & 0 \\ 0 & 0 & Q_{66} \end{bmatrix} \tag{21.28}
 \end{aligned}$$

The extensional-bending coupling stiffness is in this special case only depending on the extensional stiffness A_{ij} as the two bonded laminates are itself symmetric. There is no contribution of $B_{ij, f}$ and $B_{ij, s}$ as indicated in Eq. (21.10). Therefore, the expressions for the elements of B_{ij} are very similar to the expressions for A_{ij} , as shown in Eq. (21.29).

$$\begin{aligned}
 B_{ij} &= \underbrace{B_{ij, s}}_{=0} + \underbrace{B_{ij, f}}_{=0} + d A_{ij, f} = \frac{h^2}{2} \frac{t_f}{h} \begin{bmatrix} \frac{Q_{11}+Q_{22}}{2} & Q_{12} & 0 \\ Q_{12} & \frac{Q_{11}+Q_{22}}{2} & 0 \\ 0 & 0 & Q_{66} \end{bmatrix} \tag{21.29}
 \end{aligned}$$

As it is only depending on one of the laminates, the reinforcing laminate, B_{ij} correlates linearly with the ratio $\frac{t_f}{h}$. Since A_{ij} is independent of the number of layers, this characteristic is also applicable to B_{ij} . The overall effect of different numbers of layers is discussed in the subsequent investigation in Section 21.6.2.

The simplification of the bending stiffness D_{ij} is more difficult as it is in general depending on the number of layers. Thus, interesting findings are shown only for exemplary configurations.

The observation that $\frac{t_f}{h}$ has no influence on the critical buckling load when $\frac{a}{b}$ is not an integer number, is explored more thoroughly. When the results are revisited, the half-wave number n is 1 in the uniaxial loadcase and only m varies with the aspect ratio of the panel. Furthermore, for the phenomenon in question $\frac{a}{b}$ is equal to m . Under this assumption, the expression for the critical buckling load reduces to the form presented in Eq. (21.30). It is obtained by inserting the mentioned simplifications as well as the simplifications that $B_{11} = B_{22}$ and $A_{11} = A_{22}$.

$$N_{cr} = \frac{\pi^2 (A_{12} \gamma_1 - 2 \gamma_2 + A_{22} \gamma_1 + 2 A_{66} \gamma_1)}{b^2 (A_{12} + A_{22} + 2 A_{66})} \quad (21.30)$$

where

$$\gamma_1 = D_{11} + D_{22} + 2 (D_{12} + 2 D_{66}), \quad \gamma_2 = (B_{12} + B_{22} + 2 B_{66})^2$$

Within this simple expression for the critical buckling load the sum of the two stiffnesses D_{11} and D_{22} is included. For this combined term a simple form based on the local stiffness matrix Q_{ij} can be found. This is shown in Eq. (21.31) and (21.32) for the reinforcing and base laminate, respectively.

$$D_{11,f} + D_{22,f} = \frac{h^3 \left(\frac{t_f}{h}\right)^3 (Q_{11} + Q_{22})}{12} \quad (21.31)$$

$$D_{11,s} + D_{22,s} = \frac{h^3 (Q_{11} + Q_{22}) \left(1 - \left(\frac{t_f}{h}\right)\right)^3}{12} \quad (21.32)$$

As can be seen, the new simplified term shows no dependency on the layout configuration as the 0° - and 90° -layers only occur in pairs. The other elements of the bending stiffness matrix are defined and simplified in Eqs. (21.33)-(21.36)

$$D_{12,f} = \frac{Q_{12} h^3 \left(\frac{t_f}{h}\right)^3}{12} \quad (21.33)$$

$$D_{66,f} = \frac{Q_{66} h^3 \left(\frac{t_f}{h}\right)^3}{12} \quad (21.34)$$

$$D_{12,s} = \frac{Q_{12} h^3 \left(1 - \left(\frac{t_f}{h}\right)\right)^3}{12} \quad (21.35)$$

$$D_{66,s} = \frac{Q_{66} h^3 \left(1 - \left(\frac{t_f}{h}\right)\right)^3}{12} \quad (21.36)$$

Now, the combined bending stiffness can be computed according to Eq. (21.10) and the simplified result is shown in Eqs. (21.37)-(21.39)

$$D_{11} + D_{22} = \frac{h^3 (Q_{11} + Q_{22}) \left(3 \left(\frac{t_f}{h} \right)^2 + 1 \right)}{12} \quad (21.37)$$

$$D_{12} = \frac{Q_{12} h^3 \left(3 \left(\frac{t_f}{h} \right)^2 + 1 \right)}{12} \quad (21.38)$$

$$D_{66} = \frac{Q_{66} h^3 \left(3 \left(\frac{t_f}{h} \right)^2 + 1 \right)}{12} \quad (21.39)$$

Finally, it is possible to insert the stiffnesses into Eq. (21.30) leading to the expression presented in Eq. (21.40).

$$N_{cr} = \frac{h^3 \pi^2 (Q_{11} + Q_{22} + 2(Q_{12} + 2Q_{66}))}{12 b^2} \quad (21.40)$$

Consequently, the resulting formula is independent of the ratio $\frac{t_f}{h}$; thus, the behaviour recognizable in the results is explainable by the manner in which the investigated stacked laminate is designed. The contributing $\frac{t_f}{h}$ dependent terms balance out. As the topic of the present paper is to investigate the validity of the RBS method, the critical buckling load will be derived under the same simplifying assumptions employing the RBS method and compared to Eq. (21.40).

As the idea is to be able to compute the critical buckling load using the simple formula for orthotropic and symmetric plates, Eq. (21.41) is the starting point of this comparison.

$$N_{cr} = \frac{\pi^2}{b^2} \left(D_{11} \frac{m^2}{b^2} + 2(D_{12} + 2D_{66}) + D_{22} \frac{a^2}{b^2 m^2} \right) \quad (21.41)$$

It can be immediately concluded that for $\frac{a}{b} = m$ the expression simplifies to a form where, again, D_{11} and D_{22} appear as a sum. Before further evaluation, the RBS matrix must be computed according to Section 21.4. The relevant reduced bending stiffnesses D_{ij}^* are presented in Eqs. (21.42).

$$D_{11}^* + D_{22}^* = \frac{h^3 (Q_{11} + Q_{22})}{12}, \quad D_{12}^* = \frac{Q_{12} h^3}{12}, \quad D_{66}^* = \frac{Q_{66} h^3}{12} \quad (21.42)$$

The influence of the ratio $\left(\frac{t_f}{h} \right)$ vanishes. It is now easily seen, that by inserting Eqs. (21.42) into Eq. (21.41), Eq. (21.40) is obtained. So, in fact, the solution with or without RBS method is in this case identical and the RBS method is consequently valid.

The phenomenon observed in the results for rational values of $\frac{a}{b}$, where the critical buckling load shows symmetric behaviour as values are the same for example for $\frac{t_f}{h} = 0.2$ and $\frac{t_f}{h} = 0.8$. This is investigated in the same fashion, but with different

simplifying assumptions. Still, it is set that obviously $B_{11} = B_{22}$ and $A_{11} = A_{22}$, but now, as mentioned, $\frac{t_f}{h}$ is set to be 0.2 and 0.8, respectively. Also the panel length a is defined as $a = \frac{a}{b}b$. The half-wave number n is 1 and m remains undefined as a parameter.

Then the bending stiffnesses D_{11} and D_{22} can be computed according to the laminate lay-up for the reinforcing laminate ($[0^\circ 90^\circ]_s$) and the base laminate ($[0^\circ 90^\circ]_{4s}$). Their expressions are presented in Eqs. (21.43)-(21.44) for $\frac{t_f}{h} = 0.2$.

$$\begin{aligned} D_{11} &= \frac{h^3 \left(\frac{t_f}{h}\right)^3 (7Q_{11} + Q_{22})}{96} - \frac{h^3 (19Q_{11} + 13Q_{22}) \left(\left(\frac{t_f}{h}\right) - 1\right)^3}{384} \\ &\quad + \frac{h^3 \left(\frac{t_f}{h}\right) (Q_{11} + Q_{22})}{8} \\ &= \frac{h^3 (611Q_{11} + 509Q_{22})}{12000} \quad \text{for} \quad \frac{t_f}{h} = 0.2 \end{aligned} \quad (21.43)$$

$$\begin{aligned} D_{22} &= \frac{h^3 \left(\frac{t_f}{h}\right)^3 (Q_{11} + 7Q_{22})}{96} - \frac{h^3 (13Q_{11} + 19Q_{22}) \left(\left(\frac{t_f}{h}\right) - 1\right)^3}{384} \\ &\quad + \frac{h^3 \left(\frac{t_f}{h}\right) (Q_{11} + Q_{22})}{8} \\ &= \frac{h^3 (509Q_{11} + 611Q_{22})}{12000} \quad \text{for} \quad \frac{t_f}{h} = 0.2 \end{aligned} \quad (21.44)$$

Similarly, this is done for $\frac{t_f}{h} = 0.8$ and the following Eqs. (21.45)-(21.46) are obtained. Again, the laminate lay-up for the reinforcing laminate ($[0^\circ 90^\circ]_{4s}$) and the base laminate ($[0^\circ 90^\circ]_s$) are taken into account.

$$\begin{aligned} D_{11} &= \frac{h^3 \left(\frac{t_f}{h}\right) (Q_{11} + Q_{22})}{8} + \frac{h^3 \left(\frac{t_f}{h}\right)^3 (19Q_{11} + 13Q_{22})}{384} \\ &\quad - \frac{h^3 (7Q_{11} + Q_{22}) \left(\left(\frac{t_f}{h}\right) - 1\right)^3}{96} \\ &= \frac{h^3 (1511Q_{11} + 1409Q_{22})}{12000} \quad \text{for} \quad \frac{t_f}{h} = 0.8 \end{aligned} \quad (21.45)$$

$$\begin{aligned} D_{22} &= \frac{h^3 \left(\frac{t_f}{h}\right) (Q_{11} + Q_{22})}{8} + \frac{h^3 \left(\frac{t_f}{h}\right)^3 (13Q_{11} + 19Q_{22})}{384} \\ &\quad - \frac{h^3 (Q_{11} + 7Q_{22}) \left(\left(\frac{t_f}{h}\right) - 1\right)^3}{96} \\ &= \frac{h^3 (1409Q_{11} + 1511Q_{22})}{12000} \quad \text{for} \quad \frac{t_f}{h} = 0.8 \end{aligned} \quad (21.46)$$

The bending stiffnesses are different for the different values of $\frac{t_f}{h}$. This means that the contributions of other stiffnesses cancel out the differences. This is in fact the case as is shown in Eq. (21.47), where the critical buckling load N_{cr} is given for the two values of $\frac{t_f}{h}$ and is identical.

$$N_{cr} = \frac{h^3 \pi^2}{12 \left(\frac{a}{b}\right)^2 b^2 m^2} \left[\left(0.449 \left(\frac{a}{b}\right)^4 + 0.551 m^4 \right) Q_{11} \right. \tag{21.47}$$

$$\left. + \left(0.551 \left(\frac{a}{b}\right)^4 + 0.449 m^4 \right) Q_{22} + 2 Q_{12} \left(\frac{a}{b}\right)^2 m^2 + 4 Q_{66} \left(\frac{a}{b}\right)^2 m^2 \right]$$

Furthermore, it can be noted that within this general formula, the previously derived Eq. (21.40) is included as special case, when m is set to be equal to $\frac{a}{b}$. To assess the validity of the RBS method, it is tested under the same conditions and compared to expression Eq. (21.47) above. The reduced bending stiffness matrix is calculated according to Eq. (21.11), as already previously explained. Then, the resulting expressions and the assumptions are inserted into Eq. (21.41) and the expression is simplified. The acquired formula is identical to Eq. (21.47) and suggests perfect agreement of the approximate and exact solution.

21.6.2 Influence of the Number of Layers

It has been indicated in the previous section, that for $\frac{a}{b} = m$ the values of the critical buckling load become independent of the number of layers. This will be briefly detailed in this section. In Fig. 21.7 the phenomenon is visible, where buckling curves generated for configurations with 8, 16 and 32 layers are depicted. They intersect where the aspect ratio is equal to the half-wave number. Additionally, the identical value for the critical buckling load is obtained, which is not the minimum of all curves presented. The more layer the configuration has, the closer the intersection point to the minimum value of the respective curve. The reasons for this behaviour are already explained in the previous section where it is pointed out, that the bending stiffnesses D_{11} and D_{22} become independent of the number of layers. Under the condition $\frac{a}{b} = m$, the two terms are summed without any cofactors. This is presented

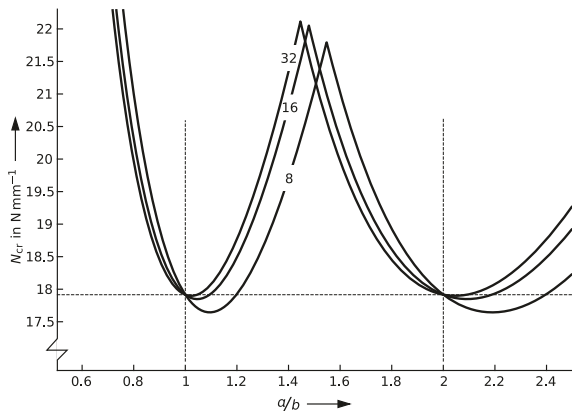


Fig. 21.7 Critical buckling load versus the aspect ratio $\frac{a}{b}$ for different numbers of layers (8, 16 and 32); $\frac{t}{h} = 0.5, E_1 = 200000\text{MPa}, E_2 = \frac{E_1}{40}, G_{12} = 0.5 E_2, \nu_{12} = 0.25,$ and $\frac{b}{h} = 100$

in Eq. (21.37). The simplification is possible since the 0° and 90° layers are stacked in pairs. The curves given are both, the solution with and without the employment of the RBS method. That the RBS method results in identical expressions is shown in Section 21.6.1 for $\frac{t_f}{h} = 0.2$ and $\frac{t_f}{h} = 0.8$. It can be shown also for $\frac{t_f}{h} = 0.5$, for which the data of Fig. 21.7 is obtained. Therefore, the procedure is equivalent and is for brevity not again detailed within this section.

21.6.3 Influence of the Ratio $\frac{E_1}{E_2}$

Another parameter of interest for the assessment of the validity of the RBS method is the ratio between the moduli of elasticity. It influences the degree of orthotropy of the panel. In Table 21.2 results are presented for the ratios $\frac{E_1}{E_2}$ of 10, 20, 40, and 80 for different ratios $\frac{t_f}{h}$. With increasing ratio $\frac{E_1}{E_2}$, the critical buckling load decreases. As the aspect ratio and the half-wave number are equally 2, no influence of the ratio $\frac{t_f}{h}$ is to be expected. Furthermore, as in the previously derived Eqs. (21.40) and (21.47) the critical buckling load is defined depending on the local reduced stiffness elements Q_{ij} , the RBS method is valid for every ratio $\frac{E_1}{E_2}$ when the special case of the present work is considered. This is reflected in the numerical data of Table 21.2.

Table 21.2

Results for the critical buckling load computed without (N_{cr}) and with ($N_{cr, rbs}$) RBS method for $E_1 = 200000 \text{ MPa}$, $E_2 = \frac{E_1}{E_2}$, $G_{12} = 0.5 E_2$, $\nu_{12} = 0.25$, $\frac{b}{h} = 100$, $\frac{a}{b} = 2$, and 40 layers

$\frac{t_f}{h}$	$\frac{E_1}{E_2}$	N_{cr} in Nmm^{-1}	$N_{cr, rbs}$ in Nmm^{-1}	Error in %
0	10	22.33	22.33	0
	20	19.38	19.38	0
	40	17.92	17.92	0
	80	17.18	17.18	0
0.3	10	22.33	22.33	0
	20	19.38	19.38	0
	40	17.92	17.92	0
	80	17.18	17.18	0
0.6	10	22.33	22.33	0
	20	19.38	19.38	0
	40	17.92	17.92	0
	80	17.18	17.18	0
0.9	10	22.33	22.33	0
	20	19.38	19.38	0
	40	17.92	17.92	0
	80	17.18	17.18	0

21.7 Conclusion

The investigation has shown that for the lay-up configurations evaluated, the RBS method is identical to the exact solution. In special cases both approaches result in identical formulas. Consequently, the RBS method is valid not only for the variation of the thicknesses of stacked laminates but also for the variation of the ratios between moduli of elasticity and the number of layers. Despite indications that the RBS method might deliver significant errors when the bending-stiffness coupling is a result of a change of reference plane, it is shown that the opposite is the case. This suggests that the method can be used in the context of larger approximative models without being a contributor to the overall error of those methods. However, within this work only the special case of a simply supported panel has been considered and different boundary conditions need to be investigated in future works. Furthermore, other load cases should be investigated and evaluated, e.g. shear and combined loading conditions. Although inadmissible boundary conditions are used in regard of the prebuckling deformation the present results can serve as guidelines for the implementations of unsymmetric structures such as stringer feet in stiffened panels. Therefore, the present work is a first step in the direction of clarifying, if the RBS method is responsible for any underestimation of the critical buckling load in larger structures.

Acknowledgements Gratitude is expressed to the financial support of the German Research Foundation DFG [project number 399128978].

References

- Ashton JE (1969) Approximate solutions for unsymmetrically laminated plates. *Journal of Composite Materials* 3(1):189–191
- Ashton JE, Whitney JM (1970) *Theory of Laminated Plates*, Progress in materials science series, vol 4. Technomic Publishing, Stamford, Connecticut
- Chamis CC (1969) Buckling of anisotropic composite plates. *Trans ASCE Journal of the Structural Division* 95(ST 10):2119–2139
- Coburn BH, Wu Z, Weaver P (2015) Buckling analysis and optimization of blade stiffened variable stiffness panels, American Institute of Aeronautics and Astronautics, pp 1–25
- Danielson KT, Tielking JT (1988) Membrane boundary condition effects on unsymmetric laminates. *Journal of Engineering Mechanics* 114(12):2158–2172
- Diaconu CG, Weaver PM (2006) Postbuckling of long unsymmetrically laminated composite plates under axial compression. *International Journal of Solids and Structures* 43(22):6978–6997
- Ewing MS, Hinger RJ, Leissa AW (1988) On the validity of the reduced bending stiffness method for laminated composite plate analysis. *Composite Structures*

9(4):301–317

- Herencia JE, Weaver PM, Friswell MI (2007) Optimisation of anisotropic plates that vary in thicknesses and properties. In: 16th International Conference on Composite Materials, Kyoto, Japan, 8-13 July 2007, pp 1–10
- Jensen DW, Lagace PA (1988) Influence of mechanical couplings on the buckling and postbuckling of anisotropic plates. *AIAA Journal* 26(10):1269–1277
- Jones RM (1973) Buckling and vibration of unsymmetrically laminated cross-ply rectangular plates. *AIAA Journal* 11(12):1626–1632
- Jones RM (1999) *Mechanics of Composite Materials*, 2nd edn. Taylor & Francis, Philadelphia, Pa.
- Leissa AW (1986) Conditions for laminated plates to remain flat under inplane loading. *Composite Structures* 6(4):261–270
- Mittelstedt C, Becker W (2016) *Strukturmechanik ebener Laminate*. Studienbereich Mechanik, Technische Universität Darmstadt, Darmstadt
- Mittelstedt C, Beerhorst M (2009) Closed-form buckling analysis of compressively loaded composite plates braced by omega-stringers. *Composite Structures* 88(3):424–435
- Qatu MS, Leissa AW (1993) Buckling or transverse deflections of unsymmetrically laminated plates subjected to in-plane loads. *AIAA Journal* 31(1):189–194
- Reddy JN (2004) *Mechanics of Laminated Composite Plates and Shells: Theory and Analysis*, 2nd edn. CRC Press, Boca Raton
- Reissner E, Stavsky Y (1961) Bending and stretching of certain types of heterogeneous aeolotropic elastic plates. *Journal of Applied Mechanics* 28(3):402–408
- Schilling JC, Mittelstedt C (2020) Local buckling analysis of omega-stringer-stiffened composite panels using a new closed-form analytical approximate solution. *Thin-Walled Structures* 147:106,534
- Turvey GJ (1977) Biaxial buckling of moderately thick laminated plates. *The Journal of Strain Analysis for Engineering Design* 12(2):89–96
- Vasiliev VV (1993) *Mechanics of Composite Structures*. Taylor & Francis, Washington, D.C.
- Vescovini R, Bisagni C (2015) Semi-analytical buckling analysis of omega stiffened panels under multi-axial loads. *Composite Structures* 120:285–299
- Vescovini R, Bisagni C (2017) Buckling and Postbuckling Analysis of Composite-Stiffened Panels Using a Semi-Analytical Approach, World Scientific, chap Chapter 6, pp 173–207
- Whitney JM (1969) Shear buckling of unsymmetrical cross-ply plates. *Journal of Composite Materials* 3(2):359–363
- Whitney JM (1970) The effect of boundary conditions on the response of laminated composites. *Journal of Composite Materials* 4(2):192–203
- Whitney JM (1987) *Structural Analysis of Laminated Composites*. Technomic Publishing, Lancaster, Pa.
- Whitney JM, Leissa AW (1969) Analysis of Heterogeneous Anisotropic Plates. *Journal of Applied Mechanics* 36(2):261–266
- Whitney JM, Leissa AW (1970) Analysis of a simply supported laminated anisotropic rectangular plate. *AIAA Journal* 8(1):28–33



Chapter 22

Asymptotic Estimate of the Potential Energy of a Plastically Deformed Thin Shell

Milad Shirani and David J. Steigmann

Abstract We derive an asymptotic expression for the potential energy of a thin elastic shell that has undergone prior plastic deformation.

Key words: Plastic deformation · Thin shells · Asymptotic model · Potential energy

22.1 Introduction

The kinematical basis of most modern theories of elastic-plastic deformation relies on the decomposition (Noll, 1967; Epstein and Elzanowski, 2007; Sadik and Yavari, 2017; Steigmann, 2020) $\tilde{\mathbf{H}} = \tilde{\mathbf{F}}\tilde{\mathbf{K}}(\tilde{\mathbf{x}})$, where $\tilde{\mathbf{F}}$ is the usual deformation gradient, $\tilde{\mathbf{H}}$ is its elastic part and $\tilde{\mathbf{K}}(\tilde{\mathbf{x}})$ is a tensor field that effectively maps a neighborhood of a material point to a prescribed reference configuration κ , say. Here and henceforth superposed tildes are used to denote three-dimensional variables. In the case of materially uniform elastic bodies (Noll, 1967) considered here, the mechanical response is presumed to be such that there exists a strain-energy function, a function of $\tilde{\mathbf{H}}$, which does not vary from one material point to another. In applications $\tilde{\mathbf{K}}$ - or more often its inverse $\tilde{\mathbf{G}}$ - is interpreted as the plastic part of the deformation gradient. In this work we adopt the prevalent viewpoint that $\tilde{\mathbf{G}}$ is a map from the reference κ to a *local natural state* in which the material is unstressed. Such states are said to be *undistorted*, in the sense of a standard crystal lattice; for solids the symmetry group of the elastic response function is thus contained in the orthogonal group. As is well known, the theory does not require $\tilde{\mathbf{K}}(\tilde{\mathbf{x}})$ to be the gradient of a vector field, and thus furnishes a framework for the modeling of material defects, or *inhomogeneities* (Noll, 1967; Epstein and Elzanowski, 2007; Steigmann, 2020).

Milad Shirani · David J. Steigmann

Department of Mechanical Engineering, University of California, Berkeley, CA. 94720, USA
e-mail: milad_shirani@berkeley.edu, dsteigmann@berkeley.edu

We focus on equilibrium theory. Accordingly, we regard $\tilde{\mathbf{K}}(\tilde{\mathbf{x}})$ as a fixed field, and seek the optimum expression for the energy of deformation. This assumption is not restrictive in practice. For, the analysis of the evolution of material response may be cast as an *incremental minimization* problem (Del Piero, 2014) in which $\tilde{\mathbf{K}}$ is known from a previous step and used to compute the deformation at the current step; this is then used to predict $\tilde{\mathbf{K}}$ at the next step, and so on. The field $\tilde{\mathbf{K}}(\tilde{\mathbf{x}})$ required in the present work may thus be regarded as being effectively known. Our intention is to extend modern derivations of shell theory based on pure elasticity to accommodate inelastic response.

Our purpose in this brief chapter is to describe a procedure for deriving an explicit expression for the optimal areal energy density of a plastically deformed shell in terms of the deformation of the shell midsurface. This extends a theory for the bending/stretching response of plastically deformed plates discussed in Steigmann (2015). Parallel developments, albeit limited to pure bending theory, are discussed in Bhattacharya et al (2016) in the framework of gamma convergence.

Standard notation is used throughout. Thus boldface is used for vectors and tensors and a dot between bold symbols is used to denote the standard Euclidean inner product; for example, if \mathbf{A}_1 and \mathbf{A}_2 are second-order tensors, then their inner product is

$$\mathbf{A}_1 \cdot \mathbf{A}_2 = \text{tr}(\mathbf{A}_1 \mathbf{A}_2^t),$$

where $\text{tr}(\cdot)$ is the trace and the superscript t is used to denote the transpose. The associated norm is $|\mathbf{A}| = \sqrt{\mathbf{A} \cdot \mathbf{A}}$. The linear operator $\text{Sym}(\cdot)$ yields the symmetric part of its second-order tensor argument, and the notation \otimes identifies the standard tensor product of vectors. We also use Orth^+ to denote the group of rotation tensors. The notations \mathbf{A}^{-1} , \mathbf{A}^* and $J_{\mathbf{A}}$ respectively are used to denote the inverse, the cofactor and the determinant of a tensor \mathbf{A} ; they are connected by $\mathbf{A}^* = J_{\mathbf{A}} \mathbf{A}^{-t}$ if \mathbf{A} is invertible. For a fourth-order tensor \mathcal{A} , the notation $\mathcal{A}[\mathbf{B}]$ stands for the second-order tensor resulting from the linear action of \mathcal{A} on the second-order tensor \mathbf{B} (see Truesdell and Noll, 1965, Eq. (7.10)). Its transpose \mathcal{A}^t is defined by

$$\mathbf{B} \cdot \mathcal{A}^t[\mathbf{A}] = \mathbf{A} \cdot \mathcal{A}[\mathbf{B}],$$

and \mathcal{A} is said to possess major symmetry if $\mathcal{A}^t = \mathcal{A}$. If $\mathbf{A} \cdot \mathcal{A}[\mathbf{B}] = \mathbf{A}^t \cdot \mathcal{A}[\mathbf{B}]$ and $\mathbf{A} \cdot \mathcal{A}[\mathbf{B}] = \mathbf{A} \cdot \mathcal{A}[\mathbf{B}^t]$, then \mathcal{A} is said to possess the minor symmetries. Finally, the notation $(\cdot)_{\mathbf{A}}$ stands for the derivative with respect to tensor or vector \mathbf{A} .

Variables appearing without the tilde are the restrictions of their three-dimensional counterparts to the midsurface Ω of the three-dimensional shell-like body. The body itself occupies the volume $\kappa = \Omega \times [-h/2, h/2]$. Our basic assumption is that the shell is thin in the sense that $h/l \ll 1$, where l is a characteristic length associated with the geometry of Ω , i.e., its minimum local principal radius of curvature or its smallest spanwise dimension. For the sake of notational convenience we adopt l as the unit of length, so that $h \ll 1$, and seek a model for the shell valid to order h^3 , the scaling associated with leading-order bending effects.

22.2 Three-dimensional Theory

The Piola stress of the three-dimensional theory is given by

$$\tilde{\mathbf{P}} = \tilde{\Psi}_{\tilde{\mathbf{F}}}, \quad (22.1)$$

the derivative with respect to the deformation gradient $\tilde{\mathbf{F}}$ of the strain energy, $\tilde{\Psi}(\tilde{\mathbf{F}}; \tilde{\mathbf{x}})$, per unit reference volume. Here $\tilde{\mathbf{x}}$ is the position of a material point in reference configuration κ . We assume that this configuration could, in principle, be occupied by the body and thus impose $J_{\tilde{\mathbf{F}}} > 0$.

We seek the optimal expression for the term E in the expansion

$$\mathcal{E} = E + o(h^3) \quad (22.2)$$

of the potential energy

$$\mathcal{E} = \int_{\kappa} \tilde{\Psi} dV - \int_{\partial\kappa_t} \tilde{\mathbf{t}} \cdot \tilde{\boldsymbol{\chi}} da \quad (22.3)$$

under dead-load conditions, say, where $\tilde{\boldsymbol{\chi}}(\tilde{\mathbf{x}})$ is the deformation and $\partial\kappa_t$ is the part of the boundary where traction $\tilde{\mathbf{t}}$ is assigned. Here and elsewhere we use the Landau symbol small "o(ϵ)" in the sense that

$$\frac{o(\epsilon)}{\epsilon} \longrightarrow 0$$

as $\epsilon \longrightarrow 0$.

The Piola stress is related to the Cauchy stress $\tilde{\mathbf{T}}$ by $\tilde{\Psi}_{\tilde{\mathbf{F}}} = \tilde{\mathbf{T}}\tilde{\mathbf{F}}^*$. In materially-uniform elastic bodies we also have (Steigmann, 2020)

$$\tilde{W}_{\tilde{\mathbf{H}}} = \tilde{\mathbf{T}}\tilde{\mathbf{H}}^*, \quad (22.4)$$

where $\tilde{W}(\tilde{\mathbf{H}})$ is a suitable strain-energy function that does *not* depend explicitly on $\tilde{\mathbf{x}}$, with

$$\tilde{\mathbf{H}} = \tilde{\mathbf{F}}\tilde{\mathbf{K}}. \quad (22.5)$$

We assume that $J_{\tilde{\mathbf{K}}} > 0$ and conclude that $J_{\tilde{\mathbf{H}}} > 0$. Comparison with (22.4), together with $\tilde{\mathbf{H}}^* = \tilde{\mathbf{F}}^*\tilde{\mathbf{K}}^*$, furnishes the connection

$$\tilde{W}_{\tilde{\mathbf{H}}} = (\tilde{\Psi}_{\tilde{\mathbf{F}}})\tilde{\mathbf{K}}^*, \quad (22.6)$$

and integration at fixed $\tilde{\mathbf{K}}$ gives

$$\tilde{\Psi}(\tilde{\mathbf{F}}, \tilde{\mathbf{x}}) = J_{\tilde{\mathbf{K}}}^{-1} \tilde{W}(\tilde{\mathbf{F}}\tilde{\mathbf{K}}(\tilde{\mathbf{x}})), \quad (22.7)$$

apart from an unimportant function of $\tilde{\mathbf{x}}$. The strain-energy function $\tilde{W}(\cdot)$ reflects the intrinsic elastic properties of the material.

We confine attention to energy-minimizing states, and thus restrict our considerations to deformations satisfying the strong-ellipticity condition

$$\mathbf{a} \otimes \mathbf{b} \cdot \tilde{\Psi}_{\tilde{\mathbf{F}}\tilde{\mathbf{F}}}(\tilde{\mathbf{F}}, \tilde{\mathbf{x}})[\mathbf{a} \otimes \mathbf{b}] > 0 \quad \text{for all } \mathbf{a} \otimes \mathbf{b} \neq \mathbf{0}. \quad (22.8)$$

To interpret this in terms of \tilde{W} , we differentiate (22.6) at fixed $\tilde{\mathbf{K}}$ on a one-parameter family $\tilde{\mathbf{H}}(t) = \tilde{\mathbf{F}}(t)\tilde{\mathbf{K}}$, deriving

$$\tilde{W}_{\tilde{\mathbf{H}}\tilde{\mathbf{H}}}[\tilde{\mathbf{F}} \cdot \tilde{\mathbf{K}}] = (\tilde{\Psi}_{\tilde{\mathbf{F}}\tilde{\mathbf{F}}}[\tilde{\mathbf{F}} \cdot])\tilde{\mathbf{K}}^*, \quad (22.9)$$

where the superposed dot is the derivative with respect to t . Scalar multiplication by $\tilde{\mathbf{F}} \cdot \tilde{\mathbf{K}}$ and use of the rule $\mathbf{A} \cdot \mathbf{BC} = \mathbf{B}'\mathbf{A} \cdot \mathbf{C}$, with $\mathbf{B} = \tilde{\mathbf{F}} \cdot$ and $\mathbf{C} = \tilde{\mathbf{K}}$, yields

$$\tilde{\mathbf{F}} \cdot \tilde{\mathbf{K}} \cdot \tilde{W}_{\tilde{\mathbf{H}}\tilde{\mathbf{H}}}[\tilde{\mathbf{F}} \cdot \tilde{\mathbf{K}}] = J_{\tilde{K}} \tilde{\mathbf{F}} \cdot \tilde{\Psi}_{\tilde{\mathbf{F}}\tilde{\mathbf{F}}}[\tilde{\mathbf{F}} \cdot], \quad (22.10)$$

which we apply with $\tilde{\mathbf{F}} \cdot = \mathbf{a} \otimes \mathbf{b}$ to recast inequality (22.8) as

$$\mathbf{a} \otimes \mathbf{m} \cdot \tilde{W}_{\tilde{\mathbf{H}}\tilde{\mathbf{H}}}(\tilde{\mathbf{H}})[\mathbf{a} \otimes \mathbf{m}] > 0 \quad \text{for all } \mathbf{a} \otimes \mathbf{m} \neq \mathbf{0}, \quad \text{with } \mathbf{m} = \tilde{\mathbf{K}}^t \mathbf{b}. \quad (22.11)$$

It follows that $\tilde{\Psi}$ is strongly elliptic at $\tilde{\mathbf{F}}$ if and only if \tilde{W} is strongly elliptic at $\tilde{\mathbf{H}} = \tilde{\mathbf{F}}\tilde{\mathbf{K}}$.

Galilean invariance imposes the restriction $\tilde{\Psi}(\tilde{\mathbf{F}}, \tilde{\mathbf{x}}) = \tilde{\Psi}(\tilde{\mathbf{Q}}\tilde{\mathbf{F}}, \tilde{\mathbf{x}})$ for every rotation $\tilde{\mathbf{Q}}$. From (22.7) this is equivalent to $\tilde{W}(\tilde{\mathbf{H}}) = \tilde{W}(\tilde{\mathbf{Q}}\tilde{\mathbf{H}})$, which, as is well known, is satisfied if and only if \tilde{W} depends on $\tilde{\mathbf{H}}$ via $\tilde{\mathbf{H}}^t\tilde{\mathbf{H}}$, or, equivalently, via the *elastic strain*

$$\tilde{\mathbf{E}} = \frac{1}{2}(\tilde{\mathbf{H}}^t\tilde{\mathbf{H}} - \mathbf{I}), \quad (22.12)$$

where \mathbf{I} is the (referential) identity for 3-space. Accordingly,

$$\tilde{W}(\tilde{\mathbf{H}}) = \tilde{U}(\tilde{\mathbf{E}}), \quad (22.13)$$

say, which implies that

$$\tilde{W}_{\tilde{\mathbf{H}}\tilde{\mathbf{H}}} = \tilde{\mathbf{H}}\tilde{\mathbf{S}}, \quad (22.14)$$

where

$$\tilde{\mathbf{S}} = \tilde{U}_{\tilde{\mathbf{E}}\tilde{\mathbf{E}}} \quad (22.15)$$

is the (symmetric) elastic 2nd Piola-Kirchhoff stress.

Application of the chain rule furnishes the useful connection (Steigmann, 2015)

$$\tilde{W}_{\tilde{\mathbf{H}}\tilde{\mathbf{H}}}(\tilde{\mathbf{H}})[\mathbf{B}] = \mathbf{B}\tilde{\mathbf{S}} + \tilde{\mathbf{H}}\tilde{U}_{\tilde{\mathbf{E}}\tilde{\mathbf{E}}}(\tilde{\mathbf{E}})[\tilde{\mathbf{H}}^t\mathbf{B}] \quad (22.16)$$

for any tensor \mathbf{B} , where $\tilde{U}_{\tilde{\mathbf{E}}\tilde{\mathbf{E}}}$ possesses major symmetry and both minor symmetries.

We impose the normalization $\tilde{W}(\mathbf{I}) = 0$. Galilean invariance then implies that $\tilde{W}(\tilde{\mathbf{H}}) = 0$ if $\tilde{\mathbf{H}} \in \text{Orth}^+$. We assume the converse to be true, and hence that $\tilde{W}(\tilde{\mathbf{H}}) = 0$ if and only if $\tilde{\mathbf{H}} \in \text{Orth}^+$. We further assume that $\tilde{\mathbf{S}} = \mathbf{0}$ if and only if $\tilde{\mathbf{E}} = \mathbf{0}$, i.e., if and only if $\tilde{\mathbf{H}} \in \text{Orth}^+$, and that $C = \tilde{U}_{\tilde{\mathbf{E}}\tilde{\mathbf{E}}}(\mathbf{0})$ - the classical elasticity tensor - is positive definite in the sense that $\mathbf{A} \cdot C[\mathbf{A}] > 0$ for all non-zero symmetric \mathbf{A} . Then,

$$\tilde{\mathbf{S}} = C[\tilde{\mathbf{E}}] + o(|\tilde{\mathbf{E}}|), \quad (22.17)$$

and it follows from (22.16) that

$$\tilde{W}_{\tilde{\mathbf{H}}\tilde{\mathbf{H}}}(\mathbf{I})[\mathbf{B}] = C[\mathbf{B}]. \quad (22.18)$$

Our assumptions yield the classical strong-ellipticity condition at zero strain. It also follows from (22.16) that

$$\tilde{W}_{\tilde{\mathbf{H}}\tilde{\mathbf{H}}}(\mathbf{R})[\mathbf{B}] = \mathbf{R}C[\mathbf{R}'\mathbf{B}], \quad (22.19)$$

where \mathbf{R} is any rotation.

The foregoing assumptions are appropriate for most metallic materials. In our further development we assume the fields $\tilde{\mathbf{F}}(\tilde{\mathbf{x}})$ and $\tilde{\mathbf{K}}(\tilde{\mathbf{x}})$ to be twice differentiable. Indeed a certain degree of regularity of these fields is necessary if any two dimensional model of the kind envisaged is to furnish an approximation to the three-dimensional theory.

22.3 Geometric and Kinematic Formulae

As in conventional shell theories, we seek a model for the shell in which the primary field to be determined is the deformation of a curved base surface Ω . This is facilitated by use of the standard *normal-coordinate* parametrization of three dimensional space in the vicinity of the base surface (Koiter, 1966; Ciarlet, 2005; Steigmann, 2013). Thus,

$$\tilde{\mathbf{x}} = \hat{\mathbf{x}}(\theta^\alpha, z) = \mathbf{x}(\theta^\alpha) + z\mathbf{N}(\theta^\alpha), \quad (22.20)$$

where $\mathbf{x}(\theta^\alpha)$; $\alpha = 1, 2$ is the parametrization of Ω with unit-normal field $\mathbf{N}(\theta^\alpha)$ and z is the coordinate in the direction perpendicular to Ω , the latter corresponding to $z = 0$. The lateral surfaces of the thin three-dimensional body are assumed to correspond to constant values of z . These are separated by the small distance h , the thickness of the shell. For simplicity we assume the thickness to be uniform. Following standard practice, we identify the base surface with the midsurface.

The orientation of Ω is induced by the assumed right-handedness of the coordinate system (θ^α, z) ; thus, $\mathbf{A}_1 \times \mathbf{A}_2 \cdot \mathbf{N} > 0$, where $\mathbf{A}_\alpha = \mathbf{x}_{,\alpha} \equiv \partial \mathbf{x} / \partial \theta^\alpha$ span the tangent plane $T_{\Omega(p)}$ to Ω at the point p with coordinates θ^α . The *curvature* tensor \mathbf{B} of the base surface is the symmetric linear map from $T_{\Omega(p)}$ to itself defined by the Weingarten equation

$$d\mathbf{N} = -\mathbf{B}d\mathbf{x}, \quad (22.21)$$

where $d\mathbf{x} = \mathbf{A}_\alpha d\theta^\alpha$ and $d\mathbf{N} = \mathbf{N}_{,\alpha} d\theta^\alpha$. Accordingly,

$$d\tilde{\mathbf{x}} = d\mathbf{x} + z d\mathbf{N} + \mathbf{N}dz = \mathbf{G}(d\mathbf{x} + \mathbf{N}dz), \quad (22.22)$$

where

$$\mathbf{G} = \boldsymbol{\mu} + \mathbf{N} \otimes \mathbf{N}, \quad \boldsymbol{\mu} = \mathbf{1} - z\mathbf{B}, \quad (22.23)$$

and

$$\mathbf{1} = \mathbf{I} - \mathbf{N} \otimes \mathbf{N} = \mathbf{A}_\alpha \otimes \mathbf{A}^\alpha \quad (22.24)$$

is the projection onto - and the identity map for - $T_{\Omega(p)}$, on which the basis $\{\mathbf{A}^\alpha\}$ is dual to $\{\mathbf{A}_\alpha\}$.

We require the volume measure induced by the coordinates. This is (Koiter, 1966; Ciarlet, 2005; Steigmann, 2013) $dv = \mu dz da$, where da is the area measure on Ω , and

$$\mu = 1 - 2Hz + Kz^2 \quad (22.25)$$

is the (two-dimensional) determinant of $\boldsymbol{\mu}$ in which

$$H = \frac{1}{2} \text{tr} \mathbf{B} \quad \text{and} \quad K = \det \mathbf{B} \quad (22.26)$$

are the mean and Gaussian curvatures of Ω , respectively. The transformation from (θ^α, z) to $\tilde{\mathbf{x}}$ is one-to-one and orientation preserving if and only if $\mu > 0$. Following conventional usage we refer to the region of space in which this condition holds as *shell space*.

Let C^* be the line orthogonal to Ω and intersecting κ at a point with surface coordinates θ^α . Let $\partial\kappa_C = \partial\Omega \times C$, where C is the collection of such curves, be the ruled generating surface of the thin shell-like region κ obtained by translating the points of $\partial\Omega$ along their associated lines C^* . Let s measure arclength on the curve $\partial\Omega$ with unit tangent $\boldsymbol{\tau}$ and rightward unit normal $\boldsymbol{\nu} = \boldsymbol{\tau} \times \mathbf{N}$. The oriented differential surface measure induced by the (s, z) - parametrization of $\partial\kappa_C$, required in the sequel, is $\mathbf{G}^* \boldsymbol{\nu} ds dz$, where \mathbf{G}^* is the cofactor of \mathbf{G} . From this it is possible to develop a formula for the oriented area measure on the ruled generators of the shell-like body which, in turn, facilitates the development of an expression for the potential energy of an edge-loaded shell (Steigmann, 2013).

Our development requires expressions for the three-dimensional deformation gradient and its through-thickness derivatives. Let $\hat{\boldsymbol{\chi}}(\tilde{\mathbf{x}})$ be the three-dimensional deformation with gradient $\hat{\mathbf{F}}(\tilde{\mathbf{x}})$. We define

$$\hat{\boldsymbol{\chi}}(\theta^\alpha, z) = \tilde{\boldsymbol{\chi}}(\mathbf{x}(\theta^\alpha) + z\mathbf{N}(\theta^\alpha)) \quad \text{and} \quad \hat{\mathbf{F}}(\theta^\alpha, z) = \tilde{\mathbf{F}}(\mathbf{x}(\theta^\alpha) + z\mathbf{N}(\theta^\alpha)). \quad (22.27)$$

Then,

$$\hat{\mathbf{F}}(\boldsymbol{\mu} d\mathbf{x} + \mathbf{N} dz) = d\hat{\boldsymbol{\chi}} = \hat{\boldsymbol{\chi}}_{,\alpha} d\theta^\alpha + \hat{\boldsymbol{\chi}}' dz = (\nabla \hat{\boldsymbol{\chi}}) d\mathbf{x} + \hat{\boldsymbol{\chi}}' dz, \quad (22.28)$$

where $d\theta^\alpha = \mathbf{A}^\alpha \cdot d\mathbf{x}$, $\hat{\boldsymbol{\chi}}_{,\alpha} = \partial \hat{\boldsymbol{\chi}} / \partial \theta^\alpha$, $\hat{\boldsymbol{\chi}}' = \partial \hat{\boldsymbol{\chi}} / \partial z$ and

$$\nabla \hat{\boldsymbol{\chi}} = \hat{\boldsymbol{\chi}}_{,\alpha} \otimes \mathbf{A}^\alpha \quad (22.29)$$

is the surfacial deformation gradient. Thus,

$$\hat{\mathbf{F}} \mathbf{1} \boldsymbol{\mu} = \nabla \hat{\boldsymbol{\chi}} \quad \text{and} \quad \hat{\mathbf{F}} \mathbf{N} = \hat{\boldsymbol{\chi}}', \quad (22.30)$$

in which the orthogonal decomposition $\hat{\mathbf{F}} = \hat{\mathbf{F}}\mathbf{1} + \hat{\mathbf{F}}\mathbf{N} \otimes \mathbf{N}$ has been used. If the configuration κ is contained in shell space, as we assume, then $\boldsymbol{\mu}^{-1}$ exists and we have

$$\hat{\mathbf{F}} = (\nabla \hat{\boldsymbol{\chi}})\boldsymbol{\mu}^{-1} + \hat{\boldsymbol{\chi}}' \otimes \mathbf{N}. \tag{22.31}$$

The mid-surface value of $\hat{\mathbf{F}}$, and those of its through-thickness derivatives $\hat{\mathbf{F}}'$ and $\hat{\mathbf{F}}''$, are needed in Sect. 22.4. These, and other variables defined on the midsurface, are identified by the absence of superposed carets. The required expressions are (Steigmann, 2013)

$$\mathbf{F} = \nabla \mathbf{r} + \mathbf{d} \otimes \mathbf{N}, \quad \mathbf{F}' = \nabla \mathbf{d} + (\nabla \mathbf{r})\mathbf{B} + \mathbf{g} \otimes \mathbf{N} \tag{22.32}$$

and

$$\mathbf{F}'' = \nabla \mathbf{g} + 2(\nabla \mathbf{d})\mathbf{B} + 2(\nabla \mathbf{r})\mathbf{B}^2 + \mathbf{h} \otimes \mathbf{N}, \tag{22.33}$$

where

$$\mathbf{r} = \boldsymbol{\chi}, \quad \mathbf{d} = \boldsymbol{\chi}', \quad \mathbf{g} = \boldsymbol{\chi}'' \quad \text{and} \quad \mathbf{h} = \boldsymbol{\chi}''' \tag{22.34}$$

are mutually *independent* functions of θ^α and the operation $\nabla(\cdot)$ is defined by (22.29). The first of these is the mid-surface deformation field and the latter three are the *directors*. Together they furnish the coefficient vectors in the expansion

$$\hat{\boldsymbol{\chi}} = \mathbf{r} + z\mathbf{d} + \frac{1}{2}z^2\mathbf{g} + \frac{1}{6}z^3\mathbf{h} + \dots \tag{22.35}$$

of the three-dimensional deformation. Evidently $\mathbf{r}(\theta^\alpha) = \hat{\boldsymbol{\chi}}(\mathbf{x}(\theta^\alpha))$ is the position of a material point on the deformed image ω of the midsurface Ω ; its gradient $\nabla \mathbf{r}$ maps $T_{\Omega(p)}$ to the tangent plane $T_{\omega(p)}$ to ω at the material point p .

22.4 Expansion of the Three-dimensional Energy

The strain energy of the shell is

$$\int_{\kappa} \tilde{\Psi} dv = \int_{\Omega} S da, \tag{22.36}$$

where

$$S = \int_C \mu \tilde{\Psi}(\hat{\mathbf{F}}; \hat{\mathbf{x}}) dz, \tag{22.37}$$

with $C = [-h/2, h/2]$, is the areal strain-energy density on Ω . For a given deformation we apply Leibniz' rule and a Taylor expansion to this integral, regarded as a function of h . Our smoothness assumptions are then consistent with the expansion (Steigmann, 2013)

$$S = h \left(1 + \frac{1}{12} h^2 K \right) \Psi + \frac{1}{24} h^3 (\Psi'' - 4H\Psi') + o(h^3), \tag{22.38}$$

where (cf. (22.7))

$$\begin{aligned}\Psi &= J_{\bar{K}}^{-1}W, \\ \Psi' &= J_{\bar{K}}^{-1}(W' - J_{\bar{K}}^{-1}J_{\bar{K}}'W), \\ \Psi'' &= J_{\bar{K}}^{-1}\left\{W'' + \left[2(J_{\bar{K}}')^2J_{\bar{K}}^{-2} - J_{\bar{K}}''J_{\bar{K}}^{-1}\right]W - 2J_{\bar{K}}'J_{\bar{K}}^{-1}W'\right\},\end{aligned}\tag{22.39}$$

with

$$\begin{aligned}W &= \tilde{W}(\mathbf{H}), \\ W' &= \tilde{W}_{\bar{\mathbf{H}}}(\mathbf{H}) \cdot \mathbf{H}' \\ W'' &= \tilde{W}_{\bar{\mathbf{H}}}(\mathbf{H}) \cdot \mathbf{H}'' + \mathbf{H}' \cdot \tilde{W}_{\bar{\mathbf{H}}\bar{\mathbf{H}}}(\mathbf{H})[\mathbf{H}'],\end{aligned}\tag{22.40}$$

and

$$\mathbf{H} = \mathbf{F}\mathbf{K}, \quad \mathbf{H}' = \mathbf{F}'\mathbf{K} + \mathbf{F}\mathbf{K}', \quad \text{and} \quad \mathbf{H}'' = \mathbf{F}''\mathbf{K} + 2\mathbf{F}'\mathbf{K}' + \mathbf{F}\mathbf{K}'',\tag{22.41}$$

in which \mathbf{F}, \mathbf{F}' and \mathbf{F}'' are given by (22.32) and (22.33).

In view of the intended application to metallic structures it is appropriate to confine our further attention to plastic incompressibility. Accordingly we assume that $J_{\bar{K}} \equiv 1$ throughout the body. This has the consequence that the through-thickness derivatives of $J_{\bar{K}}$ of all orders vanish identically in the body and hence on the midsurface in particular, yielding the simplifications

$$\Psi = W, \quad \Psi' = W', \quad \text{and} \quad \Psi'' = W'',\tag{22.42}$$

where, in view of (22.13) and (22.15),

$$W' = \mathbf{S} \cdot \mathbf{E}' \quad \text{and} \quad W'' = \mathbf{S} \cdot \mathbf{E}'' + \mathbf{S}' \cdot \mathbf{E}',\tag{22.43}$$

in which \mathbf{S} and \mathbf{S}' respectively are the midsurface values of the elastic 2nd Piola-Kirchhoff stress (cf. (22.15)) and its through-thickness derivative.

Moreover, under low strain-rate conditions the elastic strain $\tilde{\mathbf{E}}$ is invariably small in metals as it is then confined to an elastic range bounded by a yield function. Consequently its restriction to the midsurface, \mathbf{E} , is also small, but of course this does *not* imply the smallness of the midsurface values of its through-thickness derivatives. Nevertheless, because of (22.17) we have the approximations

$$W \simeq \frac{1}{2}\mathbf{E} \cdot \mathbf{C}[\mathbf{E}] \quad \text{and} \quad W'' \simeq \mathbf{E}' \cdot \mathbf{C}[\mathbf{E}'],\tag{22.44}$$

valid to *leading order* in $|\mathbf{E}|$, with

$$\mathbf{E} = \frac{1}{2}(\mathbf{H}'\mathbf{H} - \mathbf{I}) \quad \text{and} \quad \mathbf{E}' = \text{Sym}(\mathbf{R}'\mathbf{H}')\tag{22.45}$$

in which \mathbf{R} is the rotation in the polar factorization of \mathbf{H} . Suppressing the term $h^2 K$ in comparison to unity - again appropriate for sufficiently thin shells - and noting that $|\mathbf{S}|$ (and hence W') is of order $|\mathbf{E}|$, the leading-order areal strain energy is approximated by

$$S = \frac{1}{2} h \mathbf{E} \cdot C[\mathbf{E}] + \frac{1}{24} h^3 \mathbf{E}' \cdot C[\mathbf{E}']. \quad (22.46)$$

This depends, via (22.32) and (22.41), on the midsurface surficial deformation gradient $\nabla \mathbf{r}$, on the midsurface values - \mathbf{d} and \mathbf{g} respectively - of the first and second through-thickness derivatives of the deformation, and on the surficial gradient $\nabla \mathbf{d}$.

Assuming the lateral surfaces of the shell to be traction free, the dead-load potential in (22.3) is found, as in Steigmann (2013), to be

$$\int_{\partial \kappa_t} \tilde{\mathbf{t}} \cdot \tilde{\boldsymbol{\chi}} da = \int_{\partial \Omega_t} \chi ds + o(h^3), \quad (22.47)$$

where

$$\chi = \mathbf{p}_r \cdot \mathbf{r} + \mathbf{p}_d \cdot \mathbf{d} + \mathbf{p}_g \cdot \mathbf{g}, \quad (22.48)$$

and

$$\begin{aligned} \mathbf{p}_r &= h \left(1 + \frac{1}{24} h^2 \tau^2 \right) \mathbf{t} + \frac{1}{24} h^3 (\mathbf{t}'' - 2\kappa_\tau \mathbf{t}'), \\ \mathbf{p}_d &= \frac{1}{12} h^3 (\mathbf{t}' - \kappa_\tau \mathbf{t}), \\ \mathbf{p}_g &= \frac{1}{24} h^3 \mathbf{t}, \end{aligned} \quad (22.49)$$

in which \mathbf{t} , \mathbf{t}' and \mathbf{t}'' are the midsurface values of the assigned Piola traction and its through-thickness derivatives on the edge $\partial \kappa_{C_t} = \partial \Omega_t \times C$ of the shell. These are given by Steigmann (2013)

$$\begin{aligned} \mathbf{t} &= \mathbf{P} \mathbf{1} \boldsymbol{\nu}, \\ \mathbf{t}' - \kappa_\tau \mathbf{t} &= \mathbf{P}' \mathbf{1} \boldsymbol{\nu} + \tau \mathbf{P} \mathbf{1} \boldsymbol{\tau} - \kappa_\tau \mathbf{P} \mathbf{1} \boldsymbol{\nu}, \\ \mathbf{t}'' - 2\kappa_\tau \mathbf{t}' &= \mathbf{P}'' \mathbf{1} \boldsymbol{\nu} + 2(\tau \mathbf{P}' \mathbf{1} \boldsymbol{\tau} - \kappa_\tau \mathbf{P}' \mathbf{1} \boldsymbol{\nu}) - \tau^2 \mathbf{P} \mathbf{1} \boldsymbol{\nu}, \end{aligned} \quad (22.50)$$

in which $\boldsymbol{\nu}$ is the exterior unit normal to the edge $\partial \Omega_t$ lying in the tangent planes of Ω , κ_τ is the normal curvature of $\partial \Omega$ and τ is the twist. The latter formulas follow by expanding the oriented area measure, discussed in the foregoing, on the ruled generators of the shell (Steigmann, 2013). Here \mathbf{P} , \mathbf{P}' and \mathbf{P}'' are the through-thickness derivatives of the Piola stress at the boundary $\partial \Omega_t$ of the midsurface.

For consistency with our expression for the strain energy we estimate the coefficients of h and h^3 to leading order in $|\mathbf{E}|$, obtaining

$$\chi = \mathbf{p}_r \cdot \mathbf{r} + \mathbf{p}_d \cdot \mathbf{d} \quad (22.51)$$

with

$$\mathbf{p}_r = h\mathbf{t} + \frac{1}{24}h^3(\mathbf{t}'' - 2\kappa_\tau\mathbf{t}') \quad \text{and} \quad \mathbf{p}_d = \frac{1}{12}h^3\mathbf{t}' \quad (22.52)$$

in which the small term $h^2\tau^2$ - negligible in a sufficiently thin shell - has been suppressed. Accordingly \mathbf{p}_r and \mathbf{p}_d are to be regarded as assigned data. The total energy E is then approximated at leading order in $|\mathbf{E}|$ by

$$E = \int_{\Omega} S da - \int_{\Omega_t} \chi ds, \quad (22.53)$$

with S and χ given by (22.46) and (22.51), respectively.

22.5 Optimal Energy

The areal strain-energy S is a function of $\nabla\mathbf{r}$, \mathbf{d} , $\nabla\mathbf{d}$ and \mathbf{g} . Let $R(\mathbf{d}) = W(\mathbf{H})$ where, on the right-hand side, all variables in the expression for \mathbf{H} , except for \mathbf{d} , are held fixed. This expression is

$$\mathbf{H} = (\nabla\mathbf{r})\mathbf{K} + \mathbf{d} \otimes \mathbf{L}, \quad \text{where} \quad \mathbf{L} = \mathbf{K}'\mathbf{N}. \quad (22.54)$$

Let $\sigma(t) = R(\mathbf{d}(t))$, where $\mathbf{d}(t)$ is a one-parameter family. Then,

$$\dot{\sigma} = R_{\mathbf{d}} \cdot \dot{\mathbf{d}} = W_{\mathbf{H}} \cdot \dot{\mathbf{d}} \otimes \mathbf{L} = \dot{\mathbf{d}} \cdot (W_{\mathbf{H}})\mathbf{L}, \quad (22.55)$$

where superposed dots identify derivatives with respect to the parameter. Thus,

$$R_{\mathbf{d}} = (W_{\mathbf{H}})\mathbf{L}. \quad (22.56)$$

Further,

$$\ddot{\sigma} = R_{\mathbf{d}} \cdot \ddot{\mathbf{d}} + \dot{\mathbf{d}} \cdot (R_{\mathbf{d}\mathbf{d}})\dot{\mathbf{d}} = \ddot{\mathbf{d}} \cdot (W_{\mathbf{H}})\mathbf{L} + \dot{\mathbf{d}} \otimes \mathbf{L} \cdot W_{\mathbf{H}\mathbf{H}}[\dot{\mathbf{d}} \otimes \mathbf{L}], \quad (22.57)$$

so that

$$\dot{\mathbf{d}} \cdot (R_{\mathbf{d}\mathbf{d}})\dot{\mathbf{d}} = \dot{\mathbf{d}} \otimes \mathbf{L} \cdot W_{\mathbf{H}\mathbf{H}}[\dot{\mathbf{d}} \otimes \mathbf{L}]. \quad (22.58)$$

This is positive for all nonzero $\dot{\mathbf{d}}$ because our hypotheses imply that the strong-ellipticity inequality (22.11) holds. Accordingly, by the implicit function theorem the equation $R_{\mathbf{d}} = \mathbf{0}$ yields a unique solution $\mathbf{d} = \bar{\mathbf{d}}(\nabla\mathbf{r}; \mathbf{K}, \mathbf{N})$ because $R_{\mathbf{d}\mathbf{d}}$ is positive definite.

The relevance of this observation lies in the fact that for the energy (22.53), the Euler equation for the field \mathbf{d} on Ω - necessary for smooth energy minimizers - yields

$$R_{\mathbf{d}} + O(h^2) = \mathbf{0}. \quad (22.59)$$

This implies that \mathbf{d} renders R stationary at leading order in h . Thus $\mathbf{d} = \bar{\mathbf{d}}$, furnishing \mathbf{d} in terms of the surfacial gradient of the midsurface deformation. This is extended by continuity to the boundary $\partial\Omega_t$, furnishing the edge-load potential as a functional of \mathbf{r} and $\nabla\mathbf{r}$ in which the latter is resolved into a part normal to the edge and also a tangential part; the latter being further reduced using integration by parts on the boundary, culminating in a functional of \mathbf{r} and its normal derivative on the boundary together with the values of \mathbf{r} at corners, if any (Koiter, 1966; Steigmann, 2013). Moreover this solution minimizes the energy pointwise, again at leading order in h . Accordingly $\nabla\mathbf{d}$ is determined by the first and second midsurface gradients of the deformation.

It remains to determine the field \mathbf{g} occurring in the energy S . This enters algebraically, via \mathbf{H}' , in the coefficient of h^3 . On the basis of (22.41)₂, (22.45) and (22.46) the Euler equation for \mathbf{g} is found to be

$$(C[\mathbf{E}'])\mathbf{L} = \mathbf{0}, \quad (22.60)$$

which may be reduced to

$$(C[\mathbf{R}'\mathbf{g} \otimes \mathbf{L}])\mathbf{L} + \dots = \mathbf{0}, \quad (22.61)$$

wherein the missing terms do not involve \mathbf{g} . Equivalently,

$$\mathbf{A}(\mathbf{R}'\mathbf{g}) + \dots = \mathbf{0}, \quad (22.62)$$

where the second-order tensor \mathbf{A} , defined by

$$\mathbf{A}\mathbf{v} = (C[\mathbf{v} \otimes \mathbf{L}])\mathbf{L} \quad (22.63)$$

for all \mathbf{v} , is positive definite by virtue of the strong ellipticity of the classical elasticity tensor. Thus $\mathbf{R}'\mathbf{g}$ is determined explicitly. Multiplication of the result by \mathbf{R} , which may be replaced by \mathbf{H} to secure an estimate valid to consistent order in $|\mathbf{E}|$, yields a unique function $\mathbf{g} = \bar{\mathbf{g}}$ of the first and second surfacial gradients of \mathbf{r} and other known parameters. Following Steigmann (2015), it is straightforward to show that this function minimizes the energy with respect to \mathbf{g} .

Our procedure thus yields E as a functional of \mathbf{r} involving its first and second surfacial gradients on Ω , and the restriction of \mathbf{r} , together with that of its normal derivative, to the edge $\partial\Omega_t$. The final Euler equations and natural boundary conditions, if needed, are then accessible via standard arguments (Steigmann, 2018).

Acknowledgements We gratefully acknowledge the support of the US National Science Foundation through grant CMMI-1538228.

References

- Bhattacharya K, Lewicka M, Schaffner M (2016) Plates with incompatible prestrain. *Arch Ration Mech Anal* 221(1):143–181
- Ciarlet PG (2005) *An Introduction to Differential Geometry with Applications to Elasticity*. Springer, Dordrecht
- Del Piero G (2014) *A Variational Approach to Fracture and Other Inelastic Phenomena*. Springer, Dordrecht
- Epstein M, Elzanowski M (2007) *Material Inhomogeneities and their Evolution*. Springer, Berlin
- Koiter WT (1966) On the nonlinear theory of thin elastic shells. *Proc Koninklijke Nederlandse Akademie van Wetenschappen B69*:1–54
- Noll W (1967) Materially uniform simple bodies with inhomogeneities. *Arch Ration Mech Anal* 27(1):1–32
- Sadik S, Yavari A (2017) On the origins of the idea of the multiplicative decomposition of the deformation gradient. *Mathematics and Mechanics of Solids* 22(4):771–772
- Steigmann DJ (2013) Koiter's shell theory from the perspective of three-dimensional nonlinear elasticity. *Journal of Elasticity* 111(1):91–107
- Steigmann DJ (2015) Mechanics of materially uniform thin films. *Mathematics and Mechanics of Solids* 20(3):309–326
- Steigmann DJ (2018) Equilibrium of elastic lattice shells. *J Engineering Mathematics* 109(1):47–61
- Steigmann DJ (2020) A primer on plasticity. In: Merodio J, Ogden R (eds) *Constitutive Modeling of Solid Continua*, Springer Switzerland, *Solid Mechanics and its Applications*, vol 262, pp 125–153
- Truesdell C, Noll W (1965) The nonlinear field theories of mechanics. In: Flügge S (ed) *Handbuch der Physik*, Springer, Berlin, vol III/3, pp 125–153



Chapter 23

On Transverse Shear Strains Treatment in Nine-Node Shell Element MITC9i

Krzysztof Wiśniewski and Ewa Turska

Abstract This chapter concerns a nine-node quadrilateral shell element MITC9i based on the Reissner-Mindlin kinematics and Green strain, which is developed from the potential energy functional extended to include drilling rotations Wisniewski and Turska (2018).

We test an alternative treatment of the transverse shear strains in this element motivated by results of the *Curved cantilever* test of Wisniewski and Turska (2019). In the original MITC9i element, these strains are sampled using the 2×3 and 3×2 -point schemes, with all sampling points in the element's interior. In the tested MITC9i2 element, analogous schemes are used, but 8 of the sampling points are located at the element's boundaries. Both elements use the same MITCi transformations.

Several numerical examples are provided to characterize the performance of MITC9i2 compared with two other nine-node elements MITC9i and 9-EAS11.

Key words: 9-node shell element MITC9i · Two-level approximations of strains · Transverse shear strains · Corrected shape functions · Patch tests · Robustness to shape distortions

23.1 Introduction

The basic (unmodified) nine-node element is excessively stiff and sensitive to shape distortion, therefore, several techniques have been proposed to mitigate these problems.

Krzysztof Wiśniewski

Institute of Fundamental Technological Research, Polish Academy of Sciences, Warsaw, Poland
e-mail: kwisn@ippt.pan.pl

Ewa Turska

Polish Japanese Academy of Information Technology, Warsaw, Poland
e-mail: eturska@pjwstk.edu.pl

1. One of the first methods was Selective Reduced Integration (SRI) (Pawsey and Clough, 1971), which uses different integration schemes for various parts of the strain energy. The strain components are computed at different points, which restricts the range of application of this method.
2. To overcome this problem, two-level approximations of strains were proposed in which strain components are sampled at selected points and interpolated over the element's domain to allow a uniform 3×3 Gauss integration. This method is known as either the *Assumed Strain* (AS) method (Huang and Hinton, 1984, 1986; Huang, 1989) or the *Mixed Interpolation of Tensorial Components* (MITC) method (Bathe and Dvorkin, 1986; Bucelem and Bathe, 1993). When applied to transverse shear strains, also as the *Assumed Natural Strain* (ANS) method, e.g. for the nine-node elements in Jang and Pinsky (1987); Bischoff and Ramm (1997).

In this chapter we consider our nine-node shell element designated MITC9i of Wisniewski and Turska (2018). The original nine-node MITC9 element has good accuracy but does not pass the five-element patch test of Robinson and Blackham (1979) even for regular meshes, i.e. with straight edges and central positions of side nodes and the interior node. In Wisniewski and Panasz (2013), we proposed improved transformations, which resolved this problem for membrane strains. An extension to bending/twisting and transverse shear strains was given in Wisniewski and Turska (2018).

Another problem concerning nine-node elements is to pass the patch test for the mesh distorted by shifts of mid-side and central nodes, see Sect. 23.4.1 for details. Instrumental in solving this problem are the so-called *Corrected Shape Functions* (CSF) of Celia and Gray (1984), where they are tested for an eight-node (serendipity) element for the Laplace equation (heat conduction) and the 4×4 integration rule. We extend them to shells in Wisniewski and Turska (2018), so the MITC9i shell element passes this test for parallel shifts of the midside nodes and arbitrary shifts of the central node. The CSF were shown to be beneficial for several other types of nine-node elements in Panasz et al (2013); Wisniewski and Turska (2019).

In this chapter the focus is on the transverse shear strains in the MITC9i element. This is motivated by the *Curved cantilever* test of Wisniewski and Turska (2019) Sect. 5.2, in which the EAS11/DISP/ANS shell element (our implementation) had performed slightly better than MITC9i. We attribute this to the treatment of transverse shear strains and, for this reason, now, we implement the ANS method in our MITC9i shell element and check how this affects its overall performance - the tested element is designated MITC9i2. Note that for the transverse shear strains, the ANS method of Jang and Pinsky (1987) is identical to the proposed earlier AS method of Huang and Hinton (1986), see the comment in Jang and Pinsky (1987) p. 2390.

23.2 Shell Equations with Drilling Rotation

23.2.1 Two-field Functional

In the present work, we use a two-field extended shell functional depending on displacements and three-parameter rotations,

$$F_2(\chi, \mathbf{Q}_0) \doteq \int_B \mathcal{W}(\mathbf{C}) dV + F_{\text{ext}} + F_{\text{drill}}(\chi, \mathbf{Q}_0), \quad (23.1)$$

where χ is the deformation function and $\mathbf{Q}_0 \in SO(3)$ is the rotation tensor. The strain energy density \mathcal{W} depends on the right Cauchy-Green deformation tensor $\mathbf{C} \doteq \mathbf{F}^T \mathbf{F}$, where $\mathbf{F} \doteq \nabla \chi$ is the deformation gradient. F_{ext} is the potential of external loads. The last component in Eq. (23.1) is added to incorporate the drilling rotation using the penalty method,

$$F_{\text{drill}} \doteq \frac{1}{2} \int_M \gamma c^2 dA, \quad c \doteq \frac{1}{2} [(\mathbf{F}_0 \mathbf{t}_2) \cdot (\mathbf{Q}_0 \mathbf{t}_1) - (\mathbf{F}_0 \mathbf{t}_1) \cdot (\mathbf{Q}_0 \mathbf{t}_2)], \quad (23.2)$$

where c is the (1,2) component of the Rotation Constraint (RC) equation

$$\text{skew}(\mathbf{Q}_0^T \mathbf{F}_0) = \mathbf{0}$$

and $\gamma \in (0, \infty)$ is the regularization parameter. For the second-order shell kinematics based on the RC equation see Wisniewski and Turska (2002). Note that \mathbf{F}_0 and \mathbf{Q}_0 are associated with the reference (middle) shell surface at the initial configuration, and \mathbf{t}_1 and \mathbf{t}_2 are the tangent vectors of the local Cartesian basis on this surface.

23.2.2 Reissner-Mindlin Kinematics

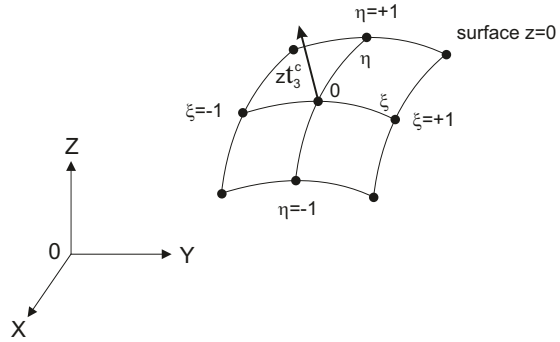
The initial configuration of the shell is parameterized by the natural coordinates $\xi, \eta \in [-1, +1]$ on the reference (middle) surface, and the normal coordinate $z \in [-h/2, +h/2]$, where h is the initial shell thickness, see Fig. 23.1. For the deformed configuration, we use the Reissner-Mindlin kinematical assumptions,

$$\mathbf{x}(\xi, \eta, z) = \mathbf{x}_0(\xi, \eta) + z \mathbf{Q}_0(\xi, \eta) \mathbf{t}_3(\xi, \eta), \quad (23.3)$$

where \mathbf{x} is a position vector at an arbitrary z and \mathbf{x}_0 at $z = 0$. Besides, \mathbf{t}_3 is the unit normal vector in the initial configuration. The rotation tensor \mathbf{Q}_0 is parameterized by the canonical rotation vector ψ ,

$$\mathbf{Q}_0(\psi) \doteq \mathbf{I} + \frac{\sin \omega}{\omega} \tilde{\psi} + \frac{1 - \cos \omega}{\omega^2} \tilde{\psi}^2, \quad (23.4)$$

Fig. 23.1 The reference surface ($z = 0$) of nine-node shell element.



where $\omega = \|\psi\| = \sqrt{\psi \cdot \psi} \geq 0$ and $\tilde{\psi} \doteq \psi \times \mathbf{I}$. This form of \mathbf{Q}_0 is used only within a load step; in the rotation update scheme devised to handle large rotations it is combined with quaternions.

The deformation function $\chi: \mathbf{x} = \chi(\mathbf{X})$ maps the initial (non-deformed) configuration of a shell onto the current (deformed) one. Let us write the deformation gradient as follows:

$$\mathbf{F} \doteq \frac{\partial \mathbf{x}}{\partial \mathbf{X}} = \frac{\partial \mathbf{x}}{\partial \xi} \mathbf{J}^{-1}, \tag{23.5}$$

where $\xi \doteq \{\xi, \eta, z\}$ and the Jacobian matrix $\mathbf{J} \doteq \partial \mathbf{X} / \partial \xi$. The right Cauchy-Green deformation tensor is $\mathbf{C} \doteq \mathbf{F}^T \mathbf{F}$ and the Green strain is defined as $\mathbf{E} \doteq \frac{1}{2}(\mathbf{C} - \mathbf{C}_0)$, where $\mathbf{C}_0 \doteq \mathbf{C}|_{\mathbf{x}=\mathbf{X}} = \mathbf{I}$. The Green strain can be linearized in z ,

$$\mathbf{E}(z) \approx \mathbf{E}_0 + z \mathbf{E}_1, \tag{23.6}$$

where the *0th order* strain \mathbf{E}_0 includes the membrane components $\boldsymbol{\varepsilon}$ and the transverse shear components $\boldsymbol{\gamma}/2$ while the *1st order* strain \mathbf{E}_1 includes the bending/twisting components $\boldsymbol{\kappa}$. The transverse shear part of \mathbf{E}_1 is typically neglected, i.e. $\kappa_{\alpha 3} \approx 0$ ($\alpha = 1, 2$). By Eq. (23.3), the normal shell strains ε_{33} and κ_{33} are equal to zero and in the current work are recovered from the plane stress condition. For details on formulation of our shell finite elements (see Wisniewski, 2010; Wisniewski et al, 2010).

23.3 Characteristics of MITC9i2 Shell Element

A formulation of the MITC9i2 element is similar to that of the MITC9i element described in Wisniewski and Turska (2019). It also uses the Corrected Shape Functions (CSF), which are an important ingredient of the element’s formulation, enabling passing some of the patch tests for distorted elements. Essential in this chapter is a treatment of the transverse shear strains, which differs the tested MITC9i2 from MITC9i.

23.3.1 Corrected Shape Functions for Nine-node Shell Element

The standard isoparametric shape functions for a nine-node element are derived for the side nodes 5,6,7 and 8 located exactly between the corner nodes and the central node 9 exactly at the element’s center. When these nodes are shifted from the middle positions then the parametric lines ($\xi=\text{const.}$ or $\eta=\text{const.}$) are distorted, see e.g. Figs. 13a and 20 in Panasz et al (2013), and the element’s accuracy deteriorates.

To alleviate this problem, the Corrected Shape Functions (CSF) were proposed in Celia and Gray (1984) with six shifts parameters $\alpha, \beta, \gamma, \epsilon, \theta, \kappa \in [-1, +1]$, see Fig. 23.2b. In that paper they are tested for an eight-node (serendipity) element for the Laplace equation (heat conduction) and the 4×4 integration rule. We extended the application range of these functions by considering the nine-node element for plane elasticity with the 3×3 integration, Wisniewski and Panasz (2013); Panasz et al (2013).

The CSF for the nine-node element are defined in two steps. First, the CSF of the 8-node element are defined, which account for shifts of the midside nodes and, next, the basis function for the central node 9 is added hierarchically to them as follows:

$$N_i(\xi, \eta) = \bar{N}_i(\xi, \eta) - \bar{N}_i(\theta, \kappa) N_9(\xi, \eta), \quad i = 1, \dots, 8,$$

$$N_9 \doteq \frac{(\xi^2 - 1)(\eta^2 - 1)}{(\theta^2 - 1)(\kappa^2 - 1)}, \tag{23.7}$$

where $\bar{N}_i(\theta, \kappa) \doteq \bar{N}_i(\xi = \theta, \eta = \kappa)$, see Celia and Gray (1984), Eq. (20). When the shift parameters are equal to zero then the CSF of Eq. (23.7) reduce to the standard isoparametric shape functions.

The shift parameters are computed as proportional to the distance in the physical space, and to determine them, we solve 4 equations with 1 unknown for the midside nodes and 2 equations with 2 unknowns for the central node. These equations are nonlinear but are solved only once, so the time overhead is insignificant.

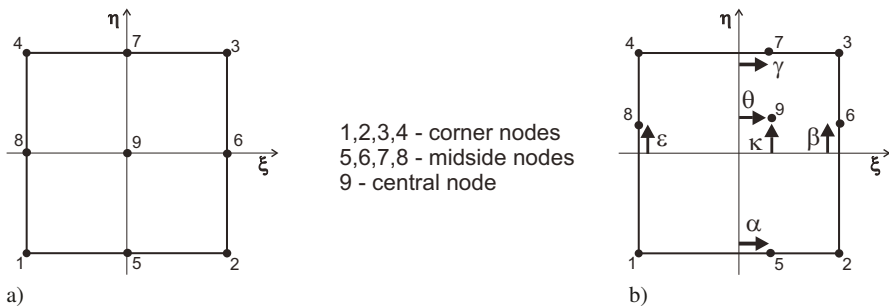


Fig. 23.2. Nine-node element: a) Numbering and naming of nodes, b) Shift parameters for Corrected Shape Functions (CSF).

In Wisniewski and Turska (2018), several extensions of this method of calculating the shift parameters are presented, to enable the use of the CSF to nine-node shell elements located in 3D space; we refer the reader interested in details to this paper. We implemented these extensions in all our nine-node elements. The CSF enable to pass some of the patch tests for elements distorted by shifts of midside and central nodes, see Sect. 23.4.1.

23.3.2 *Alternative Version of MITC_i Method for Transverse Shear Strains*

We consider the MITC (*Mixed Interpolation of Tensorial Components*) method, which is also called the ANS (*Assumed Natural Strain*) method in the literature. The “MITC_i” stands for the *improved* MITC method proposed for 2D elements in Wisniewski and Panasz (2013), and based on modified transformations enabling passing the patch test for a regular mesh. They were directly used to the membrane strains $\boldsymbol{\varepsilon}$ of the shell element MITC9i in Wisniewski and Turska (2018); analogous transformations for the bending/twisting strains $\boldsymbol{\kappa}$ and the transverse shear strains $\boldsymbol{\gamma}$ of this element were given and tested therein.

The transverse shear strains $\boldsymbol{\gamma}$ are treated in the MITC9i element using the two-level approximations and the following transformation steps:

1. The representations in the reference Cartesian basis are transformed to the co-basis at the element center to obtain the COV_c components,

$$\boldsymbol{\gamma}_\xi = \mathbf{j}_c^T \boldsymbol{\gamma}^{\text{ref}}, \quad (23.8)$$

where $\mathbf{j} \doteq [J_{\alpha\beta}]$ ($\alpha, \beta = 1, 2$) is a 2×2 sub-matrix of \mathbf{J} , and the subscript c designates its value at the element center. Note that the components yielded by \mathbf{j}_c instead of \mathbf{j} are not exactly the covariant components; that’s why we designate them by “COV_c”.

2. The two-level approximations of the COV_c components are performed,

$$\boldsymbol{\gamma}_\xi \xrightarrow{\text{MITC}} \tilde{\boldsymbol{\gamma}}_\xi, \quad (23.9)$$

which involves sampling and interpolation, which are described in detail below.

3. The approximated COV_c components $\tilde{\boldsymbol{\gamma}}_\xi$ are transformed back from the co-basis at the element center to the reference Cartesian basis,

$$\tilde{\boldsymbol{\gamma}}^{\text{ref}} = \mathbf{j}_c^{-T} \tilde{\boldsymbol{\gamma}}_\xi. \quad (23.10)$$

The transformations of the first and the third steps are reciprocal and without the second step we would obtain $\tilde{\boldsymbol{\gamma}}^{\text{ref}} = \boldsymbol{\gamma}^{\text{ref}}$. Note that the elemental basis can serve as the reference Cartesian basis.

Let us consider the second step of Eq. (23.9), which involves sampling and interpolation, and describe it separately for MITC9i and for MITC9i2. We consider only $\gamma_{31\xi}$; an analogous reasoning applies to $\gamma_{32\xi}$. In both elements, $a = \sqrt{1/3}$.

23.3.2.1 Scheme of MITC9i

A basis of the sampling strategy used in MITC9i is the scheme, which uses the 2×3 -point scheme for γ_{31} (see Fig. 23.3a) and the 3×2 -point scheme for γ_{32} , totally 12 sampling points. Their position coincides with the integration points for the Selective Reduced Integration (SRI) of strain energy terms of Pawsey and Clough (1971), Table I. They were subsequently used in the MITC element of Bucalem and Bathe (1993) and in the 9-AS element of Panasz and Wisniewski (2008). Note that this sampling does not guarantee continuity of the transverse shear strain components between two adjacent elements.

The transverse shear strains are interpolated as follows:

$$\tilde{\gamma}_{31\xi}(\xi, \eta) = \sum_i R_i(\xi, \eta)(\gamma_{31\xi})_i, \quad \tilde{\gamma}_{32\xi}(\xi, \eta) = \sum_i R_i(\xi, \eta)(\gamma_{32\xi})_i, \quad (23.11)$$

where $i = A, B, C, D, E, F$ is the index of sampling points. The interpolation functions R_i are defined as:

1. for $\gamma_{31\xi}$, the points of Fig. 23.3a are used (2 points in the ξ -direction),

$$\begin{aligned} R_A(\xi, \eta) &= \frac{1}{4} \left(1 - \frac{\xi}{a}\right) \left[\left(\frac{\eta}{b}\right)^2 - \frac{\eta}{b}\right], & R_B(\xi, \eta) &= \frac{1}{4} \left(1 + \frac{\xi}{a}\right) \left[\left(\frac{\eta}{b}\right)^2 - \frac{\eta}{b}\right], \\ R_C(\xi, \eta) &= \frac{1}{4} \left(1 + \frac{\xi}{a}\right) \left[\left(\frac{\eta}{b}\right)^2 + \frac{\eta}{b}\right], & R_D(\xi, \eta) &= \frac{1}{4} \left(1 - \frac{\xi}{a}\right) \left[\left(\frac{\eta}{b}\right)^2 + \frac{\eta}{b}\right], \\ R_E(\xi, \eta) &= \frac{1}{2} \left(1 + \frac{\xi}{a}\right) \left[1 - \left(\frac{\eta}{b}\right)^2\right], & R_F(\xi, \eta) &= \frac{1}{2} \left(1 - \frac{\xi}{a}\right) \left[1 - \left(\frac{\eta}{b}\right)^2\right]. \end{aligned} \quad (23.12)$$

2. for $\gamma_{32\xi}$, analogous points are used (2 points are in the η -direction), and analogous interpolation functions to these of Eq. (23.12) but with ξ and η interchanged.

To reduce the number of evaluations, we proposed a so-called improved sampling strategy for our previous element 9-AS (Panasz and Wisniewski, 2008) and we use it also in MITC9i. The sampling and numerical integration are considered together, which simplifies the code and yields a more efficient implementation.

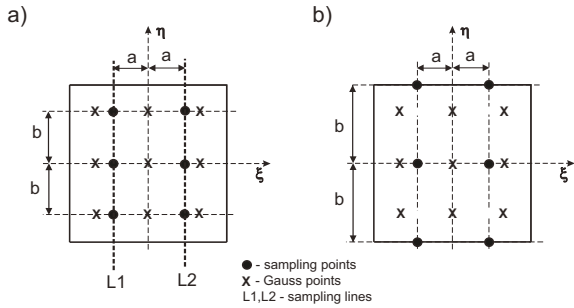
To explain the method, let us consider $\gamma_{31\xi}$, for which the sampling points and the integration points are shown in Fig. 23.3a. We see that both these types of points are located at the same $\eta \in \{-b, 0, +b\}$, where $b = \sqrt{3/5}$. Because, the 3×3 Gauss integration evaluates $\gamma_{31\xi}$ at these values of η , no sampling in the η -direction is needed, and we can sample and interpolate $\gamma_{31\xi}$ only in the ξ -direction,

$$\tilde{\gamma}_{31\xi}(\xi, \eta) = R_{L1}(\xi) \gamma_{31\xi}(-a, \eta) + R_{L2}(\xi) \gamma_{31\xi}(+a, \eta), \quad (23.13)$$

where

$$R_{L1}(\xi) = \frac{1}{2} \left(1 - \frac{\xi}{a}\right), \quad R_{L2}(\xi) = \frac{1}{2} \left(1 + \frac{\xi}{a}\right), \quad (23.14)$$

Fig. 23.3 2×3 -point sampling schemes for $\gamma_{31\xi}$: a) in MITC9i ($b = \sqrt{3/5}$), b) in MITC9i2 ($b = 1$)



The two sampling lines are shown in Fig. 23.3a, where $L1$ is located at $\xi = -a$ and $L2$ at $\xi = a$ ($a = \sqrt{1/3}$).

23.3.2.2 Sampling in MITC9i2

In the tested MITC9i2 element, we use the ANS scheme of Jang and Pinsky (1987); Bischoff and Ramm (1997), which for transverse shear strains is exactly as the scheme proposed earlier within the AS method in Huang and Hinton (1986), see the comment in Jang and Pinsky (1987) p. 2390. It uses the 2×3 -point scheme for γ_{31} and the 3×2 -point scheme for γ_{32} , but now the value $b = 1$ is used, so 8 sampling points are located at element's edges, see Fig. 23.3b. The value of $a = \sqrt{1/3}$ is the same as used in MITC9i. The transverse shear strains are interpolated as in Eq. (23.11) and the interpolation functions R_i are defined as in Eq. (23.12), but now $b = 1$ should be used. Note that the improved sampling strategy of Eqs. (23.13)-(23.14), which was used in MITC9i, cannot be used here.

23.4 Numerical Examples

In this section, we present numerical tests of the nine-node shell element MITC9i2, which is a modified version of the MITC9i of Wisniewski and Turska (2018) with an alternative transverse shear part described in Sect. 23.3.2. The formulation of this element and the reference elements are characterized in Table 23.1; other FEs are also used for comparison in examples. All the shell elements are of the Reissner-Mindlin type and have 6 dofs/node; the drilling rotation is incorporated as specified in eqs. (23.1)-(23.2), for more details see Sects. 2 and 5 of Wisniewski and Turska (2018). Note that in all these elements:

1. the *Corrected Shape Functions* (CSF) are implemented in the version extended to shells in Wisniewski and Turska (2018), Sect. 4,
2. the 3×3 Gauss integration is used, which yields a correct rank (6 zero eigenvalues) of the elements.

Table 23.1

Formulation of nine-node shell elements with drilling rotation.

Element	membrane ϵ	Strains bending κ	transverse shear γ
<i>Tested element</i> MITC9i2	MITCi	MITCi	ANS of Jang and Pinsky (1987)
<i>Reference elements</i>			
MITC9i	MITCi	MITCi	MITCi
Wisniewski and Turska (2018) 9-EAS11 ^a	EAS11	DISP ^b	ANS of Jang and Pinsky (1987)
Bischoff and Ramm (1997), Wisniewski and Turska (2019)			

^a In Wisniewski and Turska (2019), this element is designated 9-EAS11/DISP/ANS.

^b DISP - strain is not modified.

These elements were derived by ourselves using the automatic differentiation program AceGen of Korelc (2002), and were tested within the finite element program FEAP of R.L. Taylor (Zienkiewicz and Taylor, 1989); the use of these programs is gratefully acknowledged. Our parallel multithreaded (OMP) version of FEAP is described in Jarzebski et al (2015).

23.4.1 Patch Tests

We run the five-element patch test of Robinson and Blackham (1979), but also for the mesh distorted by shifts of selected mid-side and central nodes marked in Fig. 23.4. The membrane and bending patch tests are performed as described in Macneal and Harder (1985); the transverse shear test is performed for the load case defined for a nine-node plate in Huang and Hinton (1984), see *Shearing case* in Fig. 2b therein.

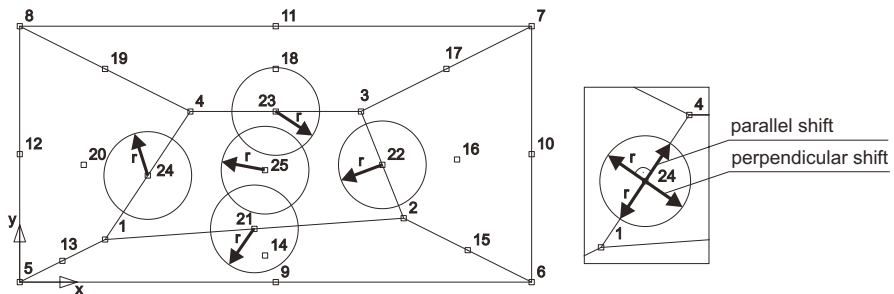


Fig. 23.4. Five-element patch test with shifts of selected nodes (circles not to scale).

Four cases of nodal shifts are considered, see Fig. 23.4: (A) zero shifts (i.e. a regular mesh as in Robinson and Blackham, 1979), (B) arbitrary shifts of node 25, (C) parallel shifts of nodes 21-24, and (D) perpendicular shifts of nodes 21-24, for which edges of the central element become curved. We monitor the level of errors for the analysis with and without the CSF, for more details see Wisniewski and Turska (2018). The conclusions pertaining to performance of the tested MITC9i2 element are as follows:

1. *Membrane patch test.* MITC9i2 performs exactly as MITC9i, because its membrane part is identical. As shown in Wisniewski and Turska (2018), MITC9i passes Case A even for standard shape functions (no CSF), needs the CSF to pass Case B and C, and fails for Case D even with the CSF. The 9-EAS11 element performs better, and passes this test for all cases of nodal shifts using the standard shape functions, see Wisniewski and Turska (2019).
2. *Bending patch test.* For the standard shape functions (no CSF), MITC9i2 passes it for Case A but fails for the other cases. With the CSF, MITC9i2 passes Case B and C; but not D. Recall from Wisniewski and Turska (2019) that the CSF are indispensable also for MITC9i and 9-EAS11, as they enable passing Case B and C, though not D.
3. *Transverse shear patch test.* MITC9i2 passes it for all cases of shifts using the standard shape functions, i.e. the CSF is not needed.

Concluding, we see that MITC9i2 performs similarly to MITC9i, though the errors for the bending patch test and Case D, which is failed, are one order smaller than for MITC9i and the same as for 9-EAS11.

23.4.2 Curved Cantilever

The curved cantilever is fixed at one end and loaded by a moment M_z at the other, see Fig. 23.5. The data is as follows: $E = 2 \times 10^5$, $\nu = 0$, width $b = 0.025$ and radius of curvature $R = 0.1$. The FE mesh consists of 6 nine-node elements, which have either regular (Fig. 23.5a) or distorted shape (Fig. 23.5b); a definition of distortions is given in Koschnick et al (2005) p. 245. For the distorted mesh, this test is very

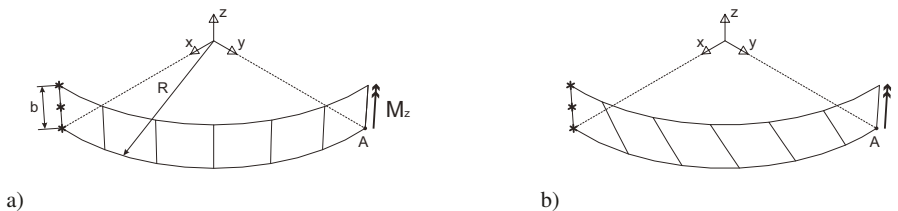


Fig. 23.5. Curved cantilever and two meshes: (a) regular and (b) distorted.

demanding. The side and central nodes of elements are not shifted so the CSF do not affect this test.

In Wisniewski and Turska (2019), Sect. 5.2, we established that the shell element 9-EAS11/DISP/ANS (designated 9-EAS11 in the current chapter) performs slightly better than the MITC9i shell element in this test (when the RBF is not used); now we check how the ANS method applied to transverse shear part affects the performance of MITC9i.

The shell thickness h is varied in the range $[10^{-2}, 10^{-6}]$, and the moment is assumed as $M_z = (R/h)^{-3}$, so the solution of a linear problem should remain constant. The analytical solution for the curved beam subjected to uniform bending is $u_y = M_z R^2 / (EI) = 0.024$, where I is the moment of inertia.

The displacement u_y at point A obtained by a linear analysis are shown in Fig. 23.6, where, for the vertical axis, we use either (a) the standard scale or (b) the logscale,

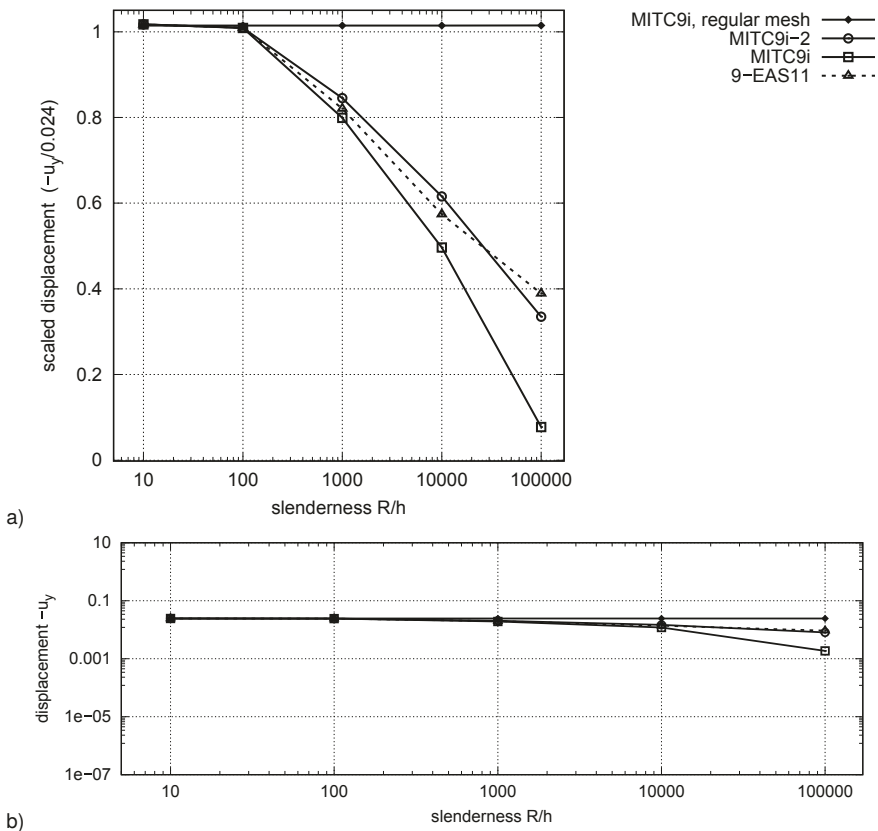


Fig. 23.6. Curved cantilever. Displacement u_y at point A for the distorted mesh and diminishing thickness. $\gamma = G$. a) log-standard scale, b) log-log scale to enable comparisons with Fig. 6 of Koschnick et al (2005).

to enable comparisons with Fig. 6 of Koschnick et al (2005). Additionally, the displacements in Fig. 23.6a are scaled by the analytical solution to quantify the decline of accuracy. We conclude this test as follows:

1. For the regular mesh, the solutions for all tested elements are represented by the horizontal line, which is close to the analytical value. Neither one of the tested elements locks for this mesh despite the curved geometry.
2. For the distorted mesh, all the tested elements lock for $R/h > 100$, and the drop of accuracy for $R/h > 1000$ becomes unacceptable. In the acceptable range, the most accurate is MITC9i2, then 9-EAS11 and MITC9i.
3. Comparing the displacements u_y of our Fig. 23.6b and Fig. 6 of Koschnick et al (2005) (in both these figures the log-log scale is used, and the displacements are not scaled by the analytical solution), we conclude that the element MITC9i2 performs in this test slightly better than Q2-ANS/EAS.

23.4.3 Homogeneous circular shell

The circular shell is shown in Fig. 23.7. The geometrical data is as follows: radius $R = 1000$ mm, thickness $h = 100$ mm and length $L = 100$ mm, see Wagner and Gruttmann (2019). One straight boundary is clamped while the other straight one is free and loaded by the distributed force $P = 100$ N/mm. Note that $R/h = 10$, i.e. this shell is thick. The stresses are reported at $\theta = \pi/4$, using the user's procedure implemented by ourselves in FEAP to define a direction for the strain/stress output in 2D and 3D.

In the circumferential direction, we use either 20 nine-node shell elements or 40 elements of other types. One element is used in the $0Y$ direction.

For a similar 2D problem in the XOZ -plane and the plane stress condition applied in the $0Y$ direction, there exists an analytical stress solution of Timoshenko and Goodier (1951), Sect. 31. The analytical expression (in polar coordinates) for the shear stress is

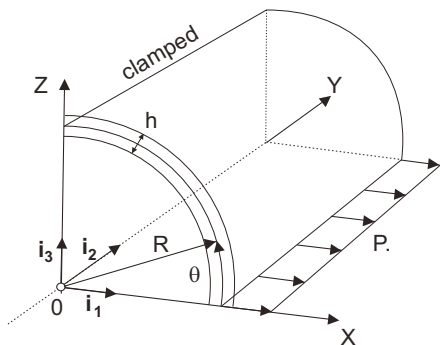


Fig. 23.7 Homogeneous circular shell. Geometry.

$$\sigma_{r\theta}(z, \theta) = -\frac{1}{d} \left[r + \frac{a^2 b^2}{r^3} - \frac{1}{r} (a^2 + b^2) \right] (P \cos \theta), \tag{23.15}$$

where $z \in [-h/2, h/2]$, $r = R + z$, $a = R - h/2$, $b = R + h/2$, and

$$d = a^2 - b^2 + (a^2 + b^2) \log(b/a).$$

Note that an integral over the thickness of the underlined terms is equal to 1, i.e. they characterize a distribution of the shear stress but not its maximum value. The shear stress $\sigma_{r\theta}$ at the cross-section $\theta = \pi/4$ is shown in Fig. 23.8.

The above analytical solution is verified using our 2D 4-node enhanced strain element (EADG4). In the 2D mesh, we use 16 elements in the radial direction (fictive layers of equal thickness) and 40 elements in the circumferential direction. The stress in Eq. (23.15) does not depend on material constants, but in the FE analyses we have to use some values. We assumed $E = 3.8 \cdot 10^5 \text{N/mm}^2$ and $\nu = 0.3$, but for other values, the obtained stress is the same. The shear stress at $\theta = \pi/4$ is shown in Fig. 23.8, and it perfectly matches the analytical $\sigma_{r\theta}$. Both stresses are slightly non-symmetric w.r.t. $z = 0$ due to the curved geometry.

Regarding the Reissner-Mindlin shell elements, the stress resultants are available as a standard in this class of elements, while stresses must be additionally computed. When the shell is curved, we have to specify the orientation vector in an input, and use the shell director to define a basis for the stress resultants' output. In the current example, we use the orientation vector tangent to the reference surface in the X0Z-plane. Having the transverse shear stress resultant N^{31} , we compute a distribution of the transverse shear stress S^{13} and its maximum as follows:

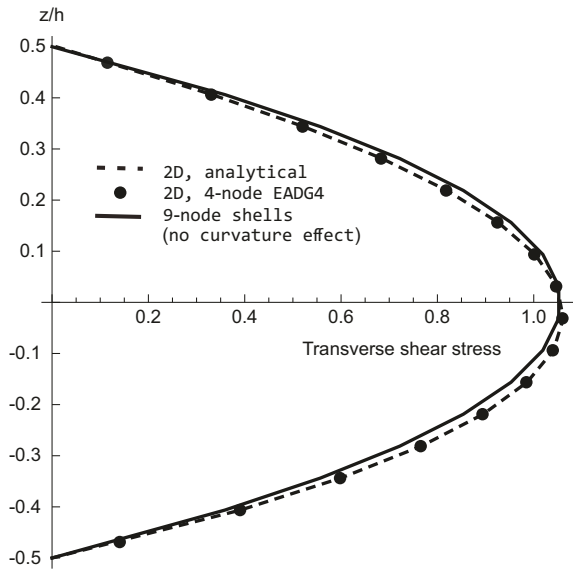


Fig. 23.8 Homogeneous circular shell. Distribution of transverse shear stress at $\theta = \pi/4$.

$$S^{31}(z) = \frac{3}{2h} \left[1 - 2 \left(\frac{z}{h} \right)^2 \right] N^{31}, \quad \max S^{31} = S^{31}(z = 0). \tag{23.16}$$

This standard formula does not account for the shell curvature, so it is symmetric w.r.t. $z = 0$, see Fig. 23.8. The maximum values for the two versions of the MITC9i shell element are given in Table 23.2.

Table 23.2
Homogeneous circular shell. Transverse shear stress resultant and transverse shear stress at $\theta = \pi/4$.

Element	Stress resultant N^{31}	Max stress S^{31} by Eq. (23.15)b
MITC9i2	69.955	1.049
MITC9i	70.13	1.052
Ref. $P \cos(\pi/4)$	70.71	-

Remark 23.1. To include the curvature in a simple way, we note that the resultant N^{31} corresponds to the term $(P \cos \theta)$ in Eq. (23.15) and use the underlined terms in that equation as the distribution function. Then the transverse shear is defined as

$$S^{31}(z) = -\frac{1}{d} \left[r + \frac{a^2 b^2}{r^3} - \frac{1}{r}(a^2 + b^2) \right] N^{31}. \tag{23.17}$$

A difference between the value of N^{31} from Table 23.2 and $P \cos(\pi/4) = 70.71$ causes only a small deviation from the exact non-symmetric distribution yielded by Eq. (23.15). We also see that, compared to the value $P \cos(\pi/4) = 70.71$, the resultant N^{31} for MITC9i is slightly more exact than for MITC9i2.

The displacement components in the OX and OZ direction (u, v) at the straight free boundary obtained for several types of FEs are given in Table 23.3. For all tested nine-node elements, the displacements are almost identical, differing at most by the last digit of the v -displacement. Additionally, the solutions obtained using our 4-node

Table 23.3
Homogeneous circular shell. Displacements at the straight free boundary.

Element	u -displacement	v -displacement
<i>Tested nine-node shell elements</i>		
MITC9i2, MITC92, 9-EAS11	2.4843	1.5796
<i>Reference elements</i>		
2D 4-node EADG4	2.4786	1.5779
Solid-shell 8-node, ours as in Klinkel et al (2006)	2.4745	1.5732
Shell 4-node HW47 (Wisniewski and Turska, 2012)	2.4847	1.5784

shell element HW47 of Wisniewski and Turska (2012) and our implementation of the 8-node solid-shell element of Klinkel et al (2006) are provided.

23.4.4 Twisted Beam

The initial geometry of the beam is shown in Fig. 23.9; it is twisted but the initial strain is equal to zero (Macneal and Harder, 1985). The beam is clamped at one end and loaded by the out-of-plane force P_y at the other. The data is as follows: $E = 2.9 \times 10^7$, $\nu = 0.22$, the length $L = 12$, the width $w = 1.1$ and the twist is 90° . We use the 2×12 -element mesh of nine-node FEs and a very small shell thickness $h = 0.0032$.

The results of a linear analysis for $P_y = 10^{-6}$ are given in Table 23.4, where the displacement $u_y \times 10^3$ at point A is presented. The results for MITC9i2 are slightly

Table 23.4
Twisted beam. Displacement for linear analysis.

Element	$u_y \times 10^3$
MITC9i2	1.2953
MITC9i	1.2948
9-EAS11	1.2952
9 (unmodified)	0.1176
Beam theory (Belytschko et al, 1989)	1.2940

better than for MITC9i and 9-EAS11; they all are a little above the beam theory value. These results are for the regularization parameter for the drilling RC $\gamma = G/1000$; we tested also $\gamma = G$, and the difference was negligible. For this very thin shell, a solution for the unmodified element 9 is very locked (10 times too small), while application of such techniques as the MITC and the EAS is clearly beneficial.

The non-linear load-deflection curves obtained by the arc-length method are shown in Figs. 23.10 and 23.11, where the displacement u_z and u_y at point A are shown, respectively. The initial $\Delta P_y = 10^{-4}$ and the regularization parameter for the drilling RC $\gamma = G/1000$.

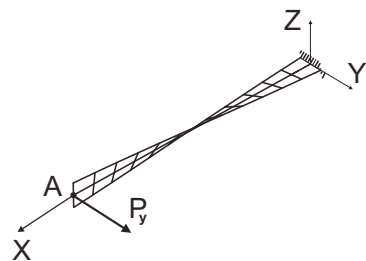


Fig. 23.9 Twisted beam. Geometry and out-of-plane force P_y .

Fig. 23.10 Non-linear twisted beam. Displacement u_z for out-of-plane force.

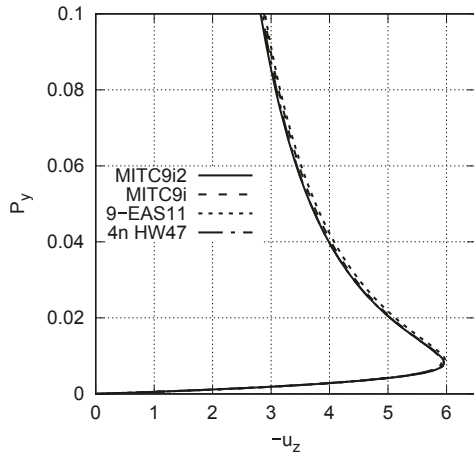
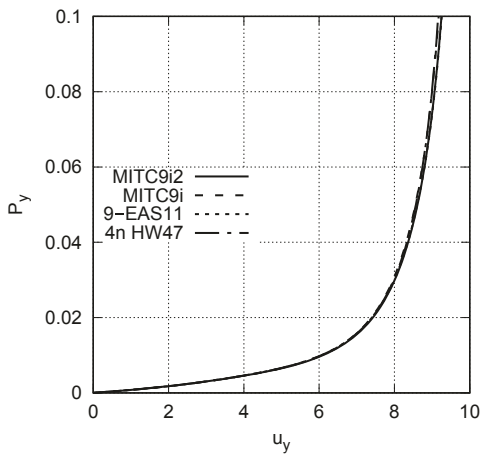


Fig. 23.11 Non-linear twisted beam. Displacement u_y for out-of-plane force.



In Fig. 23.10, which is more indicative, there is almost no difference between the curves for MITC9i2 and MITC9i, and the curve for MITC9i2 nearly coincides with that for the 4-node element HW47 of Wisniewski and Turska (2012). The curve for 9-EAS11 is a little stiffer; it is the curve most to the right after a turning point. As the shell is very thin, similarity of these solutions confirms quality of all these elements.

This example can also be calculated using the load control but the arc-length method enables comparison of the lengths of steps for particular elements. The largest steps are for MITC9i2, then for MITC9i and the shortest for 9-EAS11. For 9-EAS11, the initial $0.5 \Delta P_y$ was used because the element diverged for ΔP_y .

23.4.5 Pinched Hemispherical Shell with Hole

A hemispherical shell with an 18° hole is loaded by two pairs of equal but opposite external forces P applied along the OX and OY axes, see Fig. 23.12. Because of a double symmetry, a quarter of the hemisphere is modeled. In this test, the shell undergoes an almost in-extensional deformation and, because it is very thin (thickness $h = 0.01$), the membrane locking can manifest itself strongly.

The non-linear solutions were obtained using the Newton method; the inward displacement at point A for the 8×8 -element mesh is shown in Fig. 23.13. The differences in solutions are very small; the curves for 9-EAS11 and MITC9i2 fully coincide, while MITC9i is minimally stiffer. On the other hand, we were able to run MITC9i with $\Delta P = 0.2$ for which the other two elements diverged; then $\Delta P = 0.1$ was used. Hence, in this test MITC9i performs better than MITC9i2 and 9-EAS11.

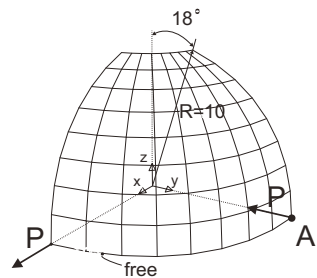


Fig. 23.12 Pinched hemispherical shell with hole. Geometry and load.

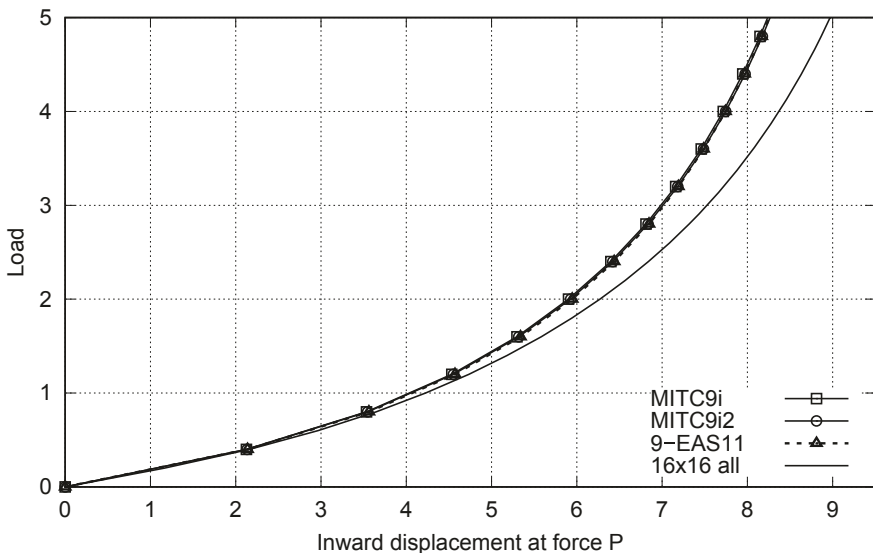


Fig. 23.13. Pinched hemispherical shell with hole. Nonlinear solutions for 8×8 mesh, $\gamma = G/1000$.

23.5 Final remarks

We developed a nine-node quadrilateral shell element MITC9i2 with the transverse shear part different than in the MITC9i element. In both these elements, the 2×3 and 3×2 -point sampling schemes were used, where in the new element 8 of the sampling points are located at element's boundaries. Five numerical examples are computed and their results can be summarized as follows:

1. *Patch tests*: The membrane and transverse shear patch tests are passed by MITC9i2, with no difference compared to MITC9i. Regarding the bending patch test, MITC9i2 with the CSF passes it for Case B and C of nodal shifts, again there is no difference compared to MITC9i. Similarly to the other nine-node elements, MITC9i2 fails the bending patch test with curved elements' edges (Case D of nodal shifts) though the level of errors is one order lower than for MITC9i.
2. *Curved cantilever*: MITC9i2 is slightly more accurate than 9-EAS11 and MITC9i. Results of this test for the EAS11/DISP/ANS element in Wisniewski and Turska (2019) provided the motivation to modify the transverse shear part of MITC9i, and the new MITC9i2 performs in this test better than MITC9i indeed.
3. *Homogeneous circular shell*: Displacements yielded by MITC9i2 are equally accurate as by the other elements, while the transverse shear stress resultant N^{31} is slightly less accurate than by MITC9i.
4. *Twisted beam*: In the linear tests, MITC9i2 is slightly more accurate than MITC9i and 9-EAS11. In the nonlinear test, MITC9i2 and MITC9i perform almost identically, 9-EAS11 is a little stiffer and requires smaller ΔP_y for the arc-length method than the other elements.
5. *Pinched hemisphere*: In this nonlinear test, MITC9i2 and 9-EAS11 are equally exact, while MITC9i is minimally stiffer, although the differences are very small. On the other hand, MITC9i is more robust, as the Newton method runs with $\Delta P = 0.2$ for which the other two elements diverge.

Generally, these preliminary results demonstrate that the tested element MITC9i2 is of a very good quality. In the linear tests, it is slightly more accurate than MITC9i, but in the nonlinear tests, MITC9i seems to have a larger radius of convergence and to be more robust. Further tests are required before a conclusion is drawn as to whether MITC9i2 should replace our best so far MITC9i element.

References

- Bathe KJ, Dvorkin EN (1986) A formulation of general shell elements—the use of mixed interpolation of tensorial components. *International Journal for Numerical Methods in Engineering* 22(3):697–722
- Belytschko T, Wong BL, Stolarski H (1989) Assumed strain stabilization procedure for the 9-node Lagrange shell element. *International Journal for Numerical Methods in Engineering* 28(2):385–414

- Bischoff M, Ramm E (1997) Shear deformable shell elements for large strains and rotations. *International Journal for Numerical Methods in Engineering* 40(23):4427–4449
- Bucalem ML, Bathe KJ (1993) Higher-order MITC general shell elements. *International Journal for Numerical Methods in Engineering* 36(21):3729–3754
- Celia MA, Gray WG (1984) An improved isoparametric transformation for finite element analysis. *International Journal for Numerical Methods in Engineering* 20(8):1443–1459
- Huang HC (1989) *Static and Dynamic Analyses of Plates and Shells*. Springer, London
- Huang HC, Hinton E (1984) A nine node Lagrangian Mindlin plate element with enhanced shear interpolation. *Engineering Computations* 1(4):369–379
- Huang HC, Hinton E (1986) A new nine node degenerated shell element with enhanced membrane and shear interpolation. *International Journal for Numerical Methods in Engineering* 22(1):73–92
- Jang J, Pinsky PM (1987) An assumed covariant strain based 9-node shell element. *International Journal for Numerical Methods in Engineering* 24(12):2389–2411
- Jarzebski P, Wisniewski K, Taylor R (2015) On parallelization of the loop over elements in FEAP. *Computational Mechanics* 56(1):77–86
- Klinkel S, Gruttmann F, Wagner W (2006) A robust non-linear solid shell element based on a mixed variational formulation. *Computer Methods in Applied Mechanics and Engineering* 195(1):179–201
- Korelc J (2002) Multi-language and multi-environment generation of nonlinear finite element codes. *Engineering with Computers* 18(4):312–327
- Koschnick F, Bischoff M, Camprubí N, Bletzinger KU (2005) The discrete strain gap method and membrane locking. *Computer Methods in Applied Mechanics and Engineering* 194(21):2444–2463
- Macneal RH, Harder RL (1985) A proposed standard set of problems to test finite element accuracy. *Finite Elements in Analysis and Design* 1(1):3–20
- Panasz P, Wisniewski K (2008) Nine-node shell elements with 6 dofs/node based on two-level approximations. Part I: Theory and linear tests. *Finite Elements in Analysis and Design* 44(12):784–796
- Panasz P, Wisniewski K, Turska E (2013) Reduction of mesh distortion effects for nine-node elements using corrected shape functions. *Finite Elements in Analysis and Design* 66:83–95
- Pawsey SF, Clough RW (1971) Improved numerical integration of thick shell finite elements. *International Journal for Numerical Methods in Engineering* 3(4):575–586
- Robinson J, Blackham S (1979) *An Evaluation of Lower Order Membranes as Contained in MSC/NASTRAN, ASA and PAFEC FEM Systems*. Robinson and Associates, Dorset, England
- Timoshenko S, Goodier JN (1951) *Theory of Elasticity*. McGraw-Hill
- Wagner W, Gruttmann F (2019) On a simple shell model for thin structures with functionally graded materials. In: Altenbach H, Chróścielewski J, Eremeyev V,

- Wiśniewski K (eds) *Recent Developments in the Theory of Shells*, Springer, Cham, Advanced Structured Materials, vol 110, pp 687–710
- Wisniewski K (2010) *Finite Rotation Shells - Basic Equations and Finite Elements for Reissner Kinematics*. Springer
- Wisniewski K, Panasz P (2013) Two improvements in formulation of nine-node element MITC9. *International Journal for Numerical Methods in Engineering* 93(6):612–634
- Wisniewski K, Turska E (2002) Second-order shell kinematics implied by rotation constraint-equation. *Journal of Elasticity* 67:229–246
- Wisniewski K, Turska E (2012) Four-node mixed hu–washizu shell element with drilling rotation. *International Journal for Numerical Methods in Engineering* 90(4):506–536
- Wisniewski K, Turska E (2018) Improved nine-node shell element MITC9i with reduced distortion sensitivity. *Computational Mechanics* 62:499–523
- Wisniewski K, Turska E (2019) On performance of nine-node quadrilateral shell elements 9-EAS11 and MITC9i. In: Altenbach H, Chróścielewski J, Eremeyev V, Wiśniewski K (eds) *Recent Developments in the Theory of Shells*, Springer, Cham, Advanced Structured Materials, vol 110, pp 710–725
- Wisniewski K, Wagner W, Turska E, Gruttmann F (2010) Four-node Hu–Washizu elements based on skew coordinates and contravariant assumed strain. *Computers & Structures* 88(21):1278–1284
- Zienkiewicz OC, Taylor RL (1989) *The Finite Element Method*, vol I. Basic Formulation and Linear Problems, 4th edn. McGraw-Hill



Chapter 24

Nonlocal Theory of Plates and Shells Based on Legendre's Polynomial Expansion

Volodymyr V. Zozulya

Abstract New nonlocal models of plates and shells based on Legendre's polynomial series expansion have been developed here. The 3-D dynamic equations of the nonlocal elasticity have been presented in an orthogonal system of coordinates. For the development of 2-D models of plates and shells the curvilinear system of coordinates related to the middle surface of the shell has been used along with special hypotheses based on assumptions that take into account the fact that the plate and shells are thin. Higher order theory is based on the expansion of the 3-D equations of the nonlocal theory of elasticity into Fourier series in terms of Legendre polynomials. The stress and strain tensors, as well as vectors of displacements have been expanded into Fourier series in terms of Legendre polynomials with respect to thickness. Thereby, all equations of the nonlocal theory of elasticity have been transformed to the corresponding equations for the Legendre polynomials coefficients. Then, in the same way as in the classical theory of elasticity, a system of differential equations in terms of displacements with initial and boundary conditions for the Legendre polynomials coefficients has been obtained. All equations for higher order theory of nonlocal plates in Cartesian and polar coordinates as well as for cylindrical and spherical shells in coordinates related to the shells geometry have been developed and presented here in detail. The obtained equations can be used for calculating stress-strain and for modelling thin walled structures in macro, micro and nano scale when taking into account size dependent and nonlocal effects.

Key words: Plate · Shell · Nonlocal · Legendre polynomial · Higher order theory

Volodymyr Zozulya

Centro de Investigacion Cientifica de Yucatan, A.C., Calle 43, No 130, Colonia: Chuburna de Hidalgo, C.P. 97200, Merida, Yucatan, Mexico
e-mail: zozulya@cicy.mx

24.1 Introduction

Micro technology and nanotechnology have attracted widespread attention and are a subject of current scientific and technological interest and development due to their broad range of applications (Elishakoff et al, 2012; Ghavanloo et al, 2019; Jha, 2007; Lyshevski, 2005; Peddieson et al, 2003; Voyiadjis, 2019; Wang and Liew, 2007; Wang and Varadan, 2007) etc. Current research has focused on developing new mathematical models which consider physical properties of materials at micro and nanoscales. Microelectro-mechanical systems (MEMS) and nanoelectromechanical systems (NEMS) have been integrated into many small devices and structures because of their superior thermal, mechanical, and electrical properties (Carrera et al, 2011a; Jha, 2007; Lyshevski, 2005; Wang and LI, 2012; Zozulya and Saez, 2014, 2016). The discovery of carbon nanostructures and their successful application in graphene sheets and carbon nanotubes (CNTs) have motivated this interest (Arash and Wang, 2014, 2012; Askari et al, 2017; Hoseinzadeh and Khadem, 2014, 2011; Malikan et al, 2020; Wang and Varadan, 2007). Compared to more conventional materials, these nanomaterials possess superior mechanical, thermal, electrical and electronic properties. The understanding of the mechanical response of nanoscale structures, such as bending, vibration, buckling and wave propagation, is indispensable for the development and accurate design of MEMS and NEMS, which use nanostructures such as CNTs and graphene sheets as constituent elements.

Mathematical modeling and computer simulation of nanostructures such as CNTs, graphene and the MEMS and NEMS are important for an optimum design. The study of nanostructures can be done by experimental methods as well as by theoretical modeling. There are at least three (Ghavanloo et al, 2019; Gopalakrishnan and Narendar, 2013; Karlicic et al, 2016; Voyiadjis, 2019) main approaches for theoretically modeling nanomaterials:

1. atomistic modeling,
2. hybrid atomistic-continuum mechanics,
3. continuum mechanics approach

Continuum theories describe a system in terms of a few variables such as mass, temperature, voltage, stress, deformation, etc., which are highly suited for direct measurements of these variables. Their successes, expediency, and practicality, have been demonstrated and tested throughout the history of science through explaining and predicting diverse physical phenomena. The classical linear theory of elasticity is the most popular and usable in engineering and scientific applications. It is based on the assumption that internal interactions between neighboring elements of an elastic continuum occur locally only by means of the symmetric force-based stress tensor, deformations are determined by the symmetric tensor of deformation and the motion of material particles are described by a position vector. However, the classical theory of elasticity fails to produce acceptable results for materials and structures at nanoscale, because it cannot handle the scale effects observed in numerous experimental studies (Gopalakrishnan and Narendar, 2013; Rogula, 1983; Voyiadjis, 2019).

To explain the fundamental properties and behavior of materials and structures at nanoscale, classical continuum models have been improved and further developed and new mathematical models that take into account nonlocal and micro-continuum effects have been created. The micro-continuum and nonlocal models have been developed in order to model microscopic motions of the material particles and long range material interactions. The micro-continuum (micropolar and couple stress) models of rods, plates and shells have been considered in our previous publications (Carrera and Zozulya, 2019; Zozulya, 1991a,b, 2013a,b). In Altenbach and Eremeyev (2009); Eremeyev and Altenbach (2015) theories of micropolar and second gradient plates have been developed using direct approach. More information and additional references could be found in the review article by Altenbach et al (2010). The nonlocal theory of curved rods has been considered and applied to MEMS/NEMS modeling in our previous publications (Czekanski and Zozulya, 2019; Zozulya, 2007, 2015). Recent state of the art in the case of nonlocal models of plates and shells could be found among other in Altenbach and Eremeyev (2015); Lurie et al (2016); Malikan et al (2020); Zozulya (2017c, 2020).

The classical continuum theories are based on constitutive relations which assume that the stress at a point is a function of strain at that point. On the other hand, nonlocal continuum mechanics assumes that the stress at a point is a function of strain at all points in the continuum. These properties are introduced into the constitutive equations as material parameters in form of integral over the whole area. The nonlocal elasticity has been mostly developed in Eringen's publications: Eringen (1972b,a, 1983, 1976, 2002). The nonlocal theory of elasticity has been used to study lattice dispersion of elastic waves, wave propagation in composites, dislocation and fracture mechanics, etc. Precise mathematical definitions of strong and weak nonlocality were given in (Rogula, 1983). In Eringen (1983) it is proposed a differential model of the nonlocal elasticity which, due to its simplicity is very popular and widely used to study bending, buckling, vibration and wave propagation, modeling size-effects in micro and nano structures, such as CNTs and graphene sheets as well as modeling and simulation MEMS and NEMS. For further reference one can see the following books and reviews: Altenbach and Eremeyev (2015); Arash and Wang (2014, 2012); Chakraverty and Behera (2017); Ghavanloo et al (2019); Gopalakrishnan and Narendar (2013); Karlicic et al (2016); Kil'chevskii (1965); Voyiadjis (2019).

New nonlocal models of rods, plates and shells have been development for mathematical modeling and computer simulation of the materials and structures at nanoscale. In relation to the above we have to mention the following publications (Adali, 2011; Altenbach and Eremeyev, 2015; Ansari et al, 2014; Arefi and Rabczuk, 2019; Czekanski and Zozulya, 2019; Hoseinzadeh and Khadem, 2014, 2011; Hu et al, 2008; Malikan et al, 2020; Wang and Varadan, 2007). A variational approach was developed and applied to the nonlocal theory of elasticity in Polizzotto (2001), nonlocal shell models have been proposed in Adali (2011); Ansari et al (2014); Askari et al (2017); Hoseinzadeh and Khadem (2011); Hu et al (2008), vibration and wave propagation and dynamical nonlocal effects in single-walled and multi-walled CNTs were studied in Ansari et al (2014); Czekanski and Zozulya

(2019); Elishakoff et al (2012); Gopalakrishnan and Narendar (2013); Hoseinzadeh and Khadem (2014, 2011); Hu et al (2008); Wang and LI (2012); Wang and Liew (2007); Wang and Varadan (2007).

There are several approaches to the developed of the theories of thin-walled structures. One consists on the improvement of the classical physical hypothesis and the development of theories that are more accurate. Another approach consists in the expansion of the stress-strain field components into polynomials series in terms of thickness. This approach was first proposed by Cauchy and Poisson and significantly developed by Carrera et al (2011a, 2014, 2011b); Carrera and Zozulya (2019); Khoma (1987); Kil'chevskii (1965); Polizzotto (2001); Vekua (1986). In our previous publications (Carrera and Zozulya, 2019; Czekanski and Zozulya, 2019; Zozulya, 1989, 1991a,b, 2007, 2013a,b, 2015, 2017b,a,c, 2018b,a, 2020; Zozulya and Saez, 2014, 2016; Zozulya and Zhang, 2012) the approach based on the use of Legendre's polynomials series expansion has been applied to the development of high order models of shells, plates and rods. Thermoelastic contact problems of plates and shells when mechanical and thermal conditions are changed during deformation have been considered in Zozulya (1989, 1991a). Then, the proposed approach and methodology were further developed and extended to thermoelasticity of the laminated composite materials with the possibility of delamination along with mechanical and thermal contact in the temperature field in Zozulya (1991b), the pencil-thin nuclear fuel rods modeling in Zozulya (2007), the functionally graded shells in Zozulya (2013a); Zozulya and Zhang (2012), modeling of MEMS and NEMS in Zozulya (2020); Zozulya and Saez (2014, 2016) as well as micropolar beams, curved elastic rods and shells in Carrera and Zozulya (2019); Zozulya (2017b, 2018b), couple stress elastic rods and shells in Wang and Liew (2007); Zozulya (2018a), nonlocal elastic beams and rods in Czekanski and Zozulya (2019); Zozulya (2017c, 2020). An analysis and comparison with the classical theory of elastic and thermoelastic plates and shells has been done in Zozulya (2013a,b). For more information, look over the extended review (Nemish and Khoma, 1993).

In this paper, 2-D high order models of plates and shells based on the nonlocal theory of elasticity have been developed. A special curvilinear system of coordinates related to the middle surface of the shell and special hypothesis based on assumptions that take into account the fact that the shell is thin have been used. High order model is based on the expansion of the equations of the 3-D nonlocal theory of elasticity into Fourier series in terms of Legendre polynomials. First order and second order theories are considered in detail. The obtained equations can be used to calculate stress-strain and to model thin walled structures in micro- and nanoscales by taking into account nonlocal effects. The proposed models can be efficient in MEMS and NEMS modeling as well as in their computer simulations.

24.2 3-D Nonlocal Elasticity in Orthogonal Coordinates

In this study we are developing an approach based on the size dependent material continuum theory and use it to develop higher order theories of plates and shells. This approach is based on the expansion of the 3-D equations of the nonlocal theory of elasticity into Fourier series in terms of Legendre polynomials. For that purpose, let us consider an elastic shell of arbitrary geometry in a 3-D Euclidian space, which occupies the domain $V = \Omega \times [-h, h]$ with a smooth boundary ∂V . Here $2h$ is thickness, Ω is the middle surface of the shell. The boundary of the shell ∂V can be presented in the form $\partial V = S \cup \Omega^+ \cup \Omega^-$, where Ω^+ and Ω^- are the upper and lower sides and S denotes lateral sides.

In nonlocal elasticity, it is assumed that the internal forces (the interaction between adjacent elements) are defined in terms of a stress tensor $\sigma(\mathbf{x}, t) = \sigma_{ij}(\mathbf{x}, t)\mathbf{e}_i \otimes \mathbf{e}_j$, which depend on the strain field not only in vicinity of point \mathbf{x} as it is in classical theory of elasticity, but also on the strain field at every point of the body. The position of each particle during deformation is determined by the displacement vector of the form $\mathbf{u}(\mathbf{x}, t) = u_i(\mathbf{x}, t)\mathbf{e}_i$. Deformations in the nonlocal theory are fully described by the symmetric strain $\varepsilon(\mathbf{x}, t) = \varepsilon_{ij}(\mathbf{x}, t)\mathbf{e}_i \otimes \mathbf{e}_j$ tensor. Natural boundary conditions can be expressed in terms of a traction vector of the form $\mathbf{p}(\mathbf{x}, t) = \sigma(\mathbf{x}, t) \cdot \mathbf{n}$. In a general case all of the above quantities are functions of coordinates and time. They can be presented in the form

$$\sigma_{ij} = \begin{vmatrix} \sigma_{11} & \sigma_{21} & \sigma_{31} \\ \sigma_{12} & \sigma_{22} & \sigma_{32} \\ \sigma_{13} & \sigma_{23} & \sigma_{33} \end{vmatrix}, \quad \varepsilon_{ij} = \begin{vmatrix} \varepsilon_{11} & \varepsilon_{21} & \varepsilon_{31} \\ \varepsilon_{12} & \varepsilon_{22} & \varepsilon_{32} \\ \varepsilon_{13} & \varepsilon_{23} & \varepsilon_{33} \end{vmatrix}, \quad u_i = \begin{vmatrix} u_1 \\ u_2 \\ u_3 \end{vmatrix}, \quad p_i = \begin{vmatrix} p_1 \\ p_2 \\ p_3 \end{vmatrix} \quad (24.1)$$

For the purpose of the theories that have been developed here, we introduce an orthogonal curvilinear system of coordinates $\mathbf{x}(x_1, x_2, x_3)$ in which the position vector of an arbitrary point is equal to $\mathbf{R}(x_1, x_2, x_3) = \mathbf{e}_i x_i$. Unit orthogonal basic vectors and their derivatives with respect to space coordinates are equal to

$$\mathbf{e}_i = \frac{1}{H_i} \frac{\partial \mathbf{R}}{\partial x_i}, \quad \frac{\partial \mathbf{e}_i}{\partial x_j} = \Gamma_{ij}^k \mathbf{e}_k \quad (24.2)$$

where H_i are Lamé coefficients and Γ_{ij}^k are Christoffel symbols. They are calculated by the equations

$$H_i = \left| \frac{\partial \mathbf{R}}{\partial x_i} \right| = \sqrt{\frac{\partial \mathbf{R}}{\partial x_i} \cdot \frac{\partial \mathbf{R}}{\partial x_i}} \quad (24.3)$$

$$\Gamma_{ij}^k = -\frac{1}{H_{ik}} \frac{\partial H_i}{\partial x_j} \delta_{ik} + \frac{1}{2H_i H_k} \left(\delta_{jk} \frac{\partial H_j H_k}{\partial x_i} + \delta_{ik} \frac{\partial H_i H_k}{\partial x_j} - \delta_{ij} \frac{\partial H_i H_j}{\partial x_k} \right) \quad (24.4)$$

From the last equation it follows that $\Gamma_{ij}^k = 0$ for $i \neq j \neq k$ and

$$\Gamma_{ii}^k = -\frac{1}{H_k} \frac{\partial H_i}{\partial x_k}, \quad \Gamma_{ik}^k = \frac{1}{H_i} \frac{\partial H_k}{\partial x_i}, \quad \text{for } i \neq k \quad (24.5)$$

The differential equations of motion can be presented in the form

$$\nabla \cdot \boldsymbol{\sigma} + \mathbf{b} = \rho \ddot{\mathbf{u}}, \quad (24.6)$$

Here \mathbf{b} is a vector of body forces, ρ is a density of material, $\ddot{\mathbf{u}}$ is the acceleration vector. The divergence of the stress tensor in the curvilinear orthogonal system of coordinates has the form

$$\nabla \cdot \boldsymbol{\sigma} = \left(\frac{1}{H_i} \frac{\partial \sigma_{ij}}{\partial x_i} + \frac{\sigma_{kj}}{H_k} \Gamma_{kk}^i + \frac{\sigma_{ik}}{H_i} \Gamma_{ki}^j \right) \mathbf{e}_j \quad (24.7)$$

The kinematic relations have the form

$$\boldsymbol{\varepsilon} = \frac{1}{2} [\nabla \mathbf{u} + (\nabla \mathbf{u})^T] \quad (24.8)$$

The gradient of the displacements vector in the orthogonal curvilinear system of coordinates has the form

$$\nabla \mathbf{u} = \mathbf{e}_i \otimes \mathbf{e}_j \left(\frac{1}{H_i} \frac{\partial u_j}{\partial x_i} + \frac{u_k}{H_i} \Gamma_{ki}^j \right) \quad (24.9)$$

According to the nonlocal elasticity theory developed by Eringen (2002) the stress at point \mathbf{x} in a body is functional of the strain field at every point of the body. Thus, the nonlocal stress tensor $\boldsymbol{\sigma}$ at point \mathbf{x} can be expressed by,

$$\boldsymbol{\sigma}(\mathbf{x}) = \int_V H(|\mathbf{x} - \mathbf{x}'|, \tau_e) \boldsymbol{\sigma}^c(\mathbf{x}') d\mathbf{x}', \quad \tau_e = e_0 a / l_e, \quad \mathbf{x} \in V \quad (24.10)$$

$$\boldsymbol{\sigma}^c = \lambda (tr \boldsymbol{\varepsilon}) \mathbf{I} + 2\mu \boldsymbol{\varepsilon} \quad (24.11)$$

where λ and μ are Lamé constants of classical elasticity, $\boldsymbol{\sigma}$, $\boldsymbol{\sigma}^c$ and $\boldsymbol{\varepsilon}$ are non-local, classical stress, and strain tensors, respectively. The kernel function $H(|\mathbf{x} - \mathbf{x}'|, \tau)$ is the nonlocal modulus incorporated into the constitutive equations the nonlocal effects at the reference point \mathbf{x} , produced by local strain at the source points \mathbf{x}' . The term $|\mathbf{x} - \mathbf{x}'|$ is the Euclidean distance, τ_e is the material constant that depends on internal e_0 (e.g. lattice parameter, granular size and distance between the C-C bonds, etc.), l_e and external characteristic lengths.

Following Eringen (2002) it is assumed that the nonlocal modulus has to meet the following conditions

1. It reaches maximum at $\mathbf{x} = \mathbf{x}'$ attenuating with $|\mathbf{x} - \mathbf{x}'|$.
2. When $\tau \rightarrow 0$, $H|\mathbf{x} - \mathbf{x}'|$ must revert to the Dirac delta function $\delta|\mathbf{x} - \mathbf{x}'|$ for a classical elasticity limit to be satisfied.

For the given material, the nonlocal modulus H can be determined by matching the dispersion curves of plain waves with those of atomic lattice dynamics or experiments. For the 2-D case nonlocal modulus is proposed by Eringen (1983) in the form

$$H(|\mathbf{x}|, \tau) = \frac{1}{2\pi l_e^2 \tau^2} K_0 \left(\frac{\sqrt{\mathbf{x} \cdot \mathbf{x}}}{\tau l_e} \right) \quad (24.12)$$

where K_0 is the modified Bessel function. From Eq. (24.12), it can be seen that the integral of the equation over the domain yields unity. The nonlocal modulus function of Eq. (24.12) is frequently used for the analysis of materials and structures at nanoscale.

The nonlocal constitutive relations in the form (24.10) lead to the governing equations of nonlocal elasticity in the form of integro-differential equations, which are generally difficult to solve. To simplify the situation, Eringen (1983) assumed that the non-local modulus $H(|\mathbf{x} - \mathbf{x}'|, \tau)$ is a Green's function of the linear differential operator

$$L_0[H(|\mathbf{x} - \mathbf{x}'|, \tau)] = \delta(|\mathbf{x} - \mathbf{x}'|) \quad (24.13)$$

Green's function is chosen in conjunction with the properties of the non-local modulus. By applying $L[\square]$ to Eq. (24.10), the following relation can be obtained

$$L_0[\boldsymbol{\sigma}] = \boldsymbol{\sigma}^c \quad (24.14)$$

The differential operator $L_0[\square]$ has different forms for different expressions of the nonlocal modulus. In Eringen (1983, 2002) it was shown that the nonlocal modulus with kernel (24.12) linear differential operator $L_0[\square]$ has the form

$$L_0[\square] = (1 - \tau^2 l_e^2 \nabla^2)[\square] \quad (24.15)$$

Here $\nabla^2 = \nabla \cdot \nabla$ is the Laplace operator of the stress tensor. In the curvilinear orthogonal system of coordinates it can be presented in the form

$$\nabla \cdot \nabla \boldsymbol{\sigma} = \left(\frac{1}{H_i} \frac{\partial}{\partial x_i} \nabla_i \sigma_{jl} + \frac{\nabla_m \sigma_{jil}}{H_m} \Gamma_{mm}^i + \frac{\nabla_i \sigma_{jl}}{H_i} \Gamma_{mi}^j + \frac{\nabla_i \sigma_{jm}}{H_i} \Gamma_{mi}^l \right) \mathbf{e}_j \otimes \mathbf{e}_l \quad (24.16)$$

where $\nabla \boldsymbol{\sigma}$ is a gradient of the stress tensor of the form

$$\nabla \boldsymbol{\sigma} = \nabla_i \sigma_{jl} \mathbf{e}_i \otimes \mathbf{e}_j \otimes \mathbf{e}_l = \left(\frac{1}{H_i} \frac{\partial \sigma_{jl}}{\partial x_i} + \frac{\sigma_{ml}}{H_i} \Gamma_{mi}^j + \frac{\sigma_{jm}}{H_i} \Gamma_{mi}^l \right) \mathbf{e}_i \otimes \mathbf{e}_j \otimes \mathbf{e}_l \quad (24.17)$$

Therefore, according to Eqs. (24.14) and (24.15), the nonlocal constitutive relations (24.10) can be expressed in a differential form as:

$$(1 - \tau^2 l_e^2 \nabla^2) \boldsymbol{\sigma} = \lambda (\text{tr} \boldsymbol{\varepsilon}) \mathbf{I} + 2\mu \boldsymbol{\varepsilon} \quad (24.18)$$

The differential equations of motion in form of displacements can be obtained by substituting kinematic relations (24.8) into the nonlocal constitutive relation (24.18) and the obtained result into the equations of motion (24.6). In vector form, they can be represented as the following

$$\mu \nabla^2 \mathbf{u} + (\lambda + \mu) \nabla (\nabla \cdot \mathbf{u}) + \tilde{\mathbf{b}} = \rho \ddot{\mathbf{u}} - \rho \tau^2 l_e^2 \nabla^2 \ddot{\mathbf{u}} \quad (24.19)$$

where

$$\tilde{\mathbf{b}} = (1 - \tau^2 l_e^2 \nabla^2) \mathbf{b} \quad (24.20)$$

The Laplacian and gradient of divergence operators of the displacements vector in the orthogonal curvilinear system of coordinates have the form

$$\begin{aligned} \nabla^2 \mathbf{u} &= \left(\frac{1}{H_i} \frac{\partial \nabla \cdot \mathbf{u}|_{ij}}{\partial x_i} + \frac{\nabla \cdot \mathbf{u}|_{ij}}{H_k} \Gamma_{kk}^i + \frac{\nabla \cdot \mathbf{u}|_{ik}}{H_i} \Gamma_{ki}^j \right) \mathbf{e}_j, \\ \nabla \nabla \cdot \mathbf{u} &= \nabla_i \nabla_j u_j \mathbf{e}_i = \frac{1}{H_i} \frac{\partial}{\partial x_i} \left(\frac{1}{H_j} \frac{\partial u_j}{\partial x_j} + \frac{u_k}{H_j} \Gamma_{kj}^j \right) \mathbf{e}_i \end{aligned} \quad (24.21)$$

where $\nabla \mathbf{u}$ is defined by Eq. (24.9) and $\nabla \cdot \mathbf{u}$ by

$$\nabla \cdot \mathbf{u} = \nabla_i u_i = \frac{1}{H_i} \frac{\partial u_i}{\partial x_i} + \frac{u_k}{H_i} \Gamma_{ki}^i \quad (24.22)$$

For a correct formulation of the nonlocal problem of elasticity in addition to the equations of motion (2.19) it is necessary to assign boundary and initial conditions. Initial conditions consist in assigning specific values to the vector of displacements and its derivatives with respect to time in the initial moment of time $t = t_0$. Initial conditions are presented in the form

$$\mathbf{u}(\mathbf{x}, t_0) = \mathbf{u}^0(\mathbf{x}), \quad \partial_t \mathbf{u}(\mathbf{x}, t_0) = \mathbf{v}^0(\mathbf{x}), \quad \forall \mathbf{x} \in V \quad (24.23)$$

where $\mathbf{u}^0(\mathbf{x})$ and $\mathbf{v}^0(\mathbf{x})$ are initial values of the displacements vector and its derivatives with respect to time.

In case if plates and shells occupy an infinite region, conditions at infinity should also be satisfied. In general these conditions consist of restrictions of the displacement vector as well as the classical force stress tensor behavior at infinity i.e. for $r \rightarrow \infty$

$$\|\mathbf{u}(\mathbf{x}, t)\| \leq C_u r^{-1}, \quad \|\boldsymbol{\sigma}(\mathbf{x}, t)\| \leq C_\sigma r^{-2} \quad (24.24)$$

where $\|\cdot\|$ is the norm of the displacement vector in the corresponding functional space, $r = \sqrt{x_i x_i}$ is the length of a radius vector of a point with coordinates x_i , and C_u , and C_σ are arbitrary constants.

If the shell occupied a finite region V with the boundary ∂V , it is necessary to establish boundary conditions. The mixed boundary conditions can be presented in the form

$$\begin{aligned} \mathbf{u}(\mathbf{x}, t) &= \boldsymbol{\varphi}_u(\mathbf{x}, t), \quad \forall \mathbf{x} \in \partial V_u, \\ \mathbf{p}(\mathbf{x}, t) &= \boldsymbol{\sigma}(\mathbf{x}, t) \cdot \mathbf{n}(\mathbf{x}) = \mathbf{P}[\mathbf{u}(\mathbf{x}, t)] = \boldsymbol{\varphi}_p(\mathbf{x}, t), \quad \forall \mathbf{x} \in \partial V_p, \quad \forall t \in \mathfrak{I} \end{aligned} \quad (24.25)$$

where $\boldsymbol{\varphi}_u(\mathbf{x}, t)$ and $\boldsymbol{\varphi}_p(\mathbf{x}, t)$ are boundary values for displacements, and tractions, respectively.

The differential operators $\mathbf{P} = P_{ij} \mathbf{e}_i \otimes \mathbf{e}_j : \mathbf{u} \rightarrow \mathbf{p}$ are called stress operator. They transform the displacements into the tractions. For the homogeneous isotropic medium, they have the form

$$P_{ij} = \lambda \delta_{ni} n_k \nabla_k + \mu (n_i \nabla_j + n_j \nabla_i) \quad \text{and} \quad \nabla_{ni} = n_i \nabla_i \quad (24.26)$$

In a case where the thermodynamic parameters that describe the behavior of the plates and shells do not depend on time, the equations of nonlocal elasticity (24.19) are simplified and become of the form

$$\mu \nabla^2 \mathbf{u} + (\lambda + \mu) \nabla (\nabla \cdot \mathbf{u}) + \tilde{\mathbf{b}} = 0 \quad (24.27)$$

As was shown above, the problem of nonlocal elasticity consists in the solution of the equations of motion (24.19) with initial (24.23) and boundary conditions (24.25). They are formulated in an arbitrary orthogonal coordinates form. In order to solve a specific problem we have to introduce a specific system of coordinates and represent all parameters (24.1) as functions of those coordinates and all operators in a corresponding coordinate form. Taking into account that the 3-D equations of the nonlocal elasticity presented here are the basis for the development of the higher order theory of plates and shells, it is convenient to write them in the curvilinear orthogonal system of coordinates related to the middle surface of the shell. In analyzing the problem mathematical difficulties caused by the dimension of the problem are encountered. The problem can be partially simplified by considering plates and shells as thin-walled structure. In this case the dimension of the problem can be reduced.

24.3 Simplification of the 3-D Nonlocal Elasticity in Coordinates Related to the Middle Surface of a Shell

For the convenience and simplification of the higher order theory we introduce curvilinear coordinates related to the middle surface of the shell. In this case, coordinates $\mathbf{x}_\alpha(x_1, x_2)$ are associated with the main curvatures k_1 and k_2 of the middle surface of the shell and coordinate x_3 is perpendicular to it. The position vector $\mathbf{R}(\mathbf{x})$ of any point in domain V , occupied by material points of the shell may be presented as

$$\mathbf{R}(\mathbf{x}) = \mathbf{r}(\mathbf{x}_\alpha) + x_3 \mathbf{n}(\mathbf{x}_\alpha) \quad (24.28)$$

where $\mathbf{r}(\mathbf{x}_\alpha)$ is the position vector of the points located in the middle surface of the shell, and $\mathbf{n}(\mathbf{x}_\alpha)$ is a unit vector normal to the middle surface of the shell. In this case the 3-D equations of the nonlocal elasticity presented here can be simplified by taking into account that Lamé coefficients and their derivatives have the form

$$H_\alpha = A_\alpha(1 + k_\alpha x_3) \quad \text{for} \quad \alpha = 1, 2 \quad \text{and} \quad H_3 = 1$$

$$\frac{\partial H_\beta}{\partial x_\alpha} = \frac{\partial A_\beta}{\partial x_\alpha} (1 + k_\alpha x_3), \quad \frac{\partial H_\beta}{\partial x_3} = k_\beta A_\beta, \quad \frac{\partial H_3}{\partial x_i} = 0 \quad (24.29)$$

Here

$$A_\alpha(x_1, x_2) = \sqrt{\frac{\partial \mathbf{r}(x_1, x_2)}{\partial x_\alpha} \frac{\partial \mathbf{r}(x_1, x_2)}{\partial x_\alpha}}$$

are the coefficients of the first quadratic form of a surface.

By taking into account that we have considered relatively thin shells, the following assumptions can be made

$$1 + k_\alpha x_3 \approx 1 \rightarrow H_\alpha \approx A_\alpha, \quad \frac{\partial H_\beta}{\partial x_\alpha} = \frac{\partial A_\beta}{\partial x_\alpha}, \quad \frac{\partial H_\alpha}{\partial x_3} = k_\alpha A_\alpha, \quad \alpha, \beta = 1, 2 \quad (24.30)$$

Therefore Christoffel symbols (24.4) become

$$\Gamma_{\alpha\alpha}^\beta = \frac{1}{A_\alpha} \frac{\partial A_\beta}{\partial x_\alpha}, \quad \Gamma_{\alpha\alpha}^3 = -k_\alpha A_\alpha, \quad \Gamma_{3\alpha}^\alpha = k_\alpha A_\alpha, \quad \alpha, \beta = 1, 2 \quad (24.31)$$

The equations of motion after simplification have the same form as it presented in (24.19), but the divergence of classical force stress tensor $\sigma(\mathbf{x}, t)$ takes the form

$$\begin{aligned} \nabla \cdot \sigma|_\alpha &= \frac{1}{A_1 A_2} \frac{\partial (A_2 \sigma_{1\alpha})}{\partial x_1} + \frac{1}{A_1 A_2} \frac{\partial (A_1 \sigma_{2\alpha})}{\partial x_2} + \frac{\partial \sigma_{3\alpha}}{\partial x_3} + \frac{\sigma_{\alpha\beta}}{A_1 A_2} \frac{\partial A_\alpha}{\partial x_\beta} \\ &\quad - \frac{\sigma_{\beta\beta}}{A_1 A_2} \frac{\partial A_\beta}{\partial x_1} + (k_1 + k_2) \sigma_{3\alpha} + k_\alpha \sigma_{\alpha 3}, \\ \nabla \cdot \sigma|_3 &= \frac{1}{A_1 A_2} \frac{\partial (A_2 \sigma_{13})}{\partial x_1} + \frac{1}{A_1 A_2} \frac{\partial (A_1 \sigma_{23})}{\partial x_2} + \frac{\partial \sigma_{33}}{\partial x_3} \\ &\quad + \frac{A_2 k_1 + A_1 k_2}{A_1 A_2} \sigma_{33} - \frac{k_1}{A_1} \sigma_{11} - \frac{k_2}{A_2} \sigma_{22} \end{aligned} \quad (24.32)$$

After substituting Lamé coefficients (24.29) into relations (24.9) for gradient of the deformation tensor by taking into account (24.9) and (24.29) we have

$$\nabla \mathbf{u}|_{\alpha j} = \frac{1}{A_\alpha} \frac{\partial u_j}{\partial x_\alpha} - \frac{u_\alpha}{A_\alpha A_j} \frac{\partial A_\alpha}{\partial x_j} + \delta_{\alpha j} \sum_{\gamma=1}^2 \frac{u_\gamma}{A_\alpha A_\gamma} \frac{\partial A_\alpha}{\partial x_\gamma} + \delta_{\alpha j} k_\alpha u_3, \quad \nabla \mathbf{u}|_{3 j} = \frac{\partial u_j}{\partial x_3} \quad (24.33)$$

and result in kinematic Cauchy relations (24.8)

$$\varepsilon_{ij} = \begin{pmatrix} \frac{1}{A_1} \frac{\partial u_1}{\partial x_1} + \frac{u_2}{A_1 A_2} \frac{\partial A_1}{\partial x_2} + k_1 u_3 & \frac{1}{2} \left(\frac{1}{A_1} \frac{\partial u_2}{\partial x_1} - \frac{u_1}{A_1 A_2} \frac{\partial A_1}{\partial x_2} + \frac{1}{A_2} \frac{\partial u_1}{\partial x_2} - \frac{u_2}{A_1 A_2} \frac{\partial A_2}{\partial x_1} \right) & \frac{1}{2} \left(\frac{1}{A_1} \frac{\partial u_1}{\partial x_1} - k_1 u_1 + \frac{\partial u_1}{\partial x_3} \right) \\ \frac{1}{2} \left(\frac{1}{A_1} \frac{\partial u_2}{\partial x_1} - \frac{u_1}{A_1 A_2} \frac{\partial A_1}{\partial x_2} + \frac{1}{A_2} \frac{\partial u_1}{\partial x_2} - \frac{u_2}{A_1 A_2} \frac{\partial A_2}{\partial x_1} \right) & \frac{1}{A_2} \frac{\partial u_2}{\partial x_2} + \frac{\partial u_1}{A_1 A_2} \frac{\partial A_2}{\partial x_1} + k_2 u_3 & \frac{1}{2} \left(\frac{1}{A_2} \frac{\partial u_3}{\partial x_2} - k_2 u_2 + \frac{\partial u_3}{\partial x_2} \right) \\ \frac{1}{2} \left(\frac{1}{A_1} \frac{\partial u_1}{\partial x_1} - k_1 u_1 + \frac{\partial u_1}{\partial x_3} \right) & \frac{1}{2} \left(\frac{1}{A_2} \frac{\partial u_3}{\partial x_2} - k_2 u_2 + \frac{\partial u_3}{\partial x_2} \right) & \frac{\partial u_3}{\partial x_3} \end{pmatrix} \quad (24.34)$$

The Laplacian and gradient of the stress tensor in the curvilinear coordinates related to the middle surface of the shell become simple. Their explicit form can be obtained by substituting expressions for that Lamé coefficients (24.29), (24.30) and Christoffel symbols (24.31) in the Eqs. (24.16) and (24.17). The final equations become large and therefore are not presented here. Their explicit expressions in special systems of coordinates will be presented in the corresponding sections.

The differential equations of motion and equilibrium in the form of displacements have the form (24.19) and (24.27), respectively, but the Laplace and gradient of divergence operators of the displacements vector have the simpler form

$$\begin{aligned}
 \nabla^2 \mathbf{u}|_\beta &= \frac{1}{A_1 A_2} \left(\sum_{\alpha=1}^2 \left(\frac{\partial}{\partial x_\alpha} \left(\frac{A_1 A_2}{A_\alpha} \nabla_\alpha u_\alpha \right) + \frac{A_1 A_2}{H_\alpha H_\beta} \left(\nabla_\alpha u_\beta \frac{\partial A_\beta}{\partial x_\alpha} \right. \right. \right. \\
 &\quad \left. \left. \left. - \nabla_\alpha u_\alpha \frac{\partial H_\alpha}{\partial x_\beta} \right) \right) + (k_1 + k_2) \frac{\partial u_3}{\partial x_3} + \frac{\partial^2 u_3}{\partial x_3^2} \right) \mathbf{e}_\beta \\
 \nabla^2 \mathbf{u}|_3 &= \frac{1}{A_1 A_2} \left(\sum_{\alpha=1}^2 \left(\frac{\partial}{\partial x_\alpha} \left(\frac{A_1 A_2}{A_\alpha} \nabla_\alpha u_\alpha \right) - A_1 A_2 k_\alpha \nabla_\alpha u_\alpha \right) \right. \\
 &\quad \left. + (k_1 + k_2) \frac{\partial u_3}{\partial x_3} + \frac{\partial^2 u_3}{\partial x_3^2} \right) \mathbf{e}_3 \\
 \nabla(\nabla \cdot \mathbf{u})|_\alpha &= \frac{1}{A_\alpha} \frac{\partial}{\partial x_\alpha} \left(\frac{1}{A_1} \frac{\partial u_1}{\partial x_1} + \frac{u_1}{A_1 A_2} \frac{\partial A_2}{\partial x_1} + \frac{1}{A_2} \frac{\partial u_2}{\partial x_2} + \frac{u_2}{A_1 A_2} \frac{\partial A_1}{\partial x_2} \right. \\
 &\quad \left. + (k_1 + k_2) u_3 + \frac{\partial u_3}{\partial x_3} \right) \mathbf{e}_\alpha \\
 \nabla(\nabla \cdot \mathbf{u})|_3 &= \frac{\partial}{\partial x_3} \left(\frac{1}{A_1} \frac{\partial u_1}{\partial x_1} + \frac{u_1}{A_1 A_2} \frac{\partial A_2}{\partial x_1} + \frac{1}{A_2} \frac{\partial u_2}{\partial x_2} + \frac{u_2}{A_1 A_2} \frac{\partial A_1}{\partial x_2} \right. \\
 &\quad \left. + (k_1 + k_2) u_3 + \frac{\partial u_3}{\partial x_3} \right) \mathbf{e}_3
 \end{aligned} \tag{24.35}$$

In this section, the system of 3-D nonlocal theory of elasticity in a special system of coordinates related to the middle surface of the shell is considered in detail. These equations will be used in the next sections for the development of the approximate 2-D theories of plates and shells.

24.4 2-D Formulation of the Problem

In order to transform a 3-D problem into 2-D one let us expand all of the parameters that describe the stress-strain of the shell in the Legendre polynomials series along the coordinate x_3

$$\begin{aligned}
 \mathbf{u}(\mathbf{x}) &= \sum_{k=0}^{\infty} \mathbf{u}^k(\mathbf{x}_\alpha) P_k(\bar{w}), \quad \mathbf{p}(\mathbf{x}) = \sum_{k=0}^{\infty} \mathbf{p}^k(\mathbf{x}_\alpha) P_k(\bar{w}), \\
 \sigma(\mathbf{x}) &= \sum_{k=0}^{\infty} \sigma^k(\mathbf{x}_\alpha) P_k(\bar{w}), \quad \varepsilon(\mathbf{x}) = \sum_{k=0}^{\infty} \varepsilon^k(\mathbf{x}_\alpha) P_k(\bar{w}),
 \end{aligned}
 \tag{24.36}$$

where $\bar{w} = x_2/h \in [-1, 1]$ is a normalized variable and the coefficients of expansion have the form

$$\begin{aligned}
 \mathbf{u}^k(\mathbf{x}_\alpha) &= \frac{2k+1}{2h} \int_{-h}^h \mathbf{u}(\mathbf{x}_\alpha, x_3) P_k(\bar{w}) dx_3, \\
 \mathbf{p}^k(\mathbf{x}_\alpha) &= \frac{2k+1}{2h} \int_{-h}^h \mathbf{p}(\mathbf{x}_\alpha, x_3) P_k(\bar{w}) dx_3, \\
 \sigma^k(\mathbf{x}_\alpha) &= \frac{2k+1}{2h} \int_{-h}^h \sigma(\mathbf{x}_\alpha, x_3) P_k(\bar{w}) dx_3, \\
 \varepsilon^k(\mathbf{x}_\alpha) &= \frac{2k+1}{2h} \int_{-h}^h \varepsilon(\mathbf{x}_\alpha, x_3) P_k(\bar{w}) dx_3,
 \end{aligned}
 \tag{24.37}$$

Generally, all of the functions that are considered here also depend on time t , but to reduce typing the variable of time has been omitted.

For derivatives with respect to coordinates x_α and time, the following relations take place

$$\begin{aligned}
 \frac{2k+1}{2h} \int_{-h}^h \frac{\partial \mathbf{u}(\mathbf{x}_\alpha, x_3, t)}{\partial x_\alpha} P_k(\bar{w}) dx_3 &= \frac{\partial \mathbf{u}^k(\mathbf{x}_\alpha, t)}{\partial x_\alpha} \\
 \frac{2k+1}{2h} \int_{-h}^h \frac{\partial \sigma(\mathbf{x}_\alpha, x_3, t)}{\partial x_\alpha} P_k(\bar{w}) dx_3 &= \frac{\partial \sigma^k(\mathbf{x}_\alpha, t)}{\partial x_\alpha} \\
 \frac{2k+1}{2h} \int_{-h}^h \frac{\partial^2 \sigma(\mathbf{x}_\alpha, x_3, t)}{\partial x_\alpha^2} P_k(\bar{w}) dx_3 &= \frac{\partial_\alpha^2 \sigma^k(\mathbf{x}_\alpha, t)}{\partial x_\alpha^2} \\
 \frac{2k+1}{2h} \int_{-h}^h \frac{\partial^2 \mathbf{u}(\mathbf{x}_\alpha, x_3, t)}{\partial t^2} P_k(\bar{w}) dx_3 &= \frac{\partial^2 \mathbf{u}^k(\mathbf{x}_\alpha, t)}{\partial t^2}
 \end{aligned}
 \tag{24.38}$$

Derivatives of the displacements with respect to x_3 following Zozulya (1991b); Zozulya and Saez (2016) can be represented in the form

$$\frac{2k+1}{2h} \int_{-h}^h \frac{\partial \mathbf{u}(\mathbf{x}_\alpha, x_3)}{\partial x_3} P_k(\bar{w}) dx_3 = \underline{\mathbf{u}}^k(\mathbf{x}_\alpha).
 \tag{24.39}$$

where

$$\underline{\mathbf{u}}^k(\mathbf{x}_\alpha) = \frac{2k+1}{h}(\underline{\mathbf{u}}^{k+1}(\mathbf{x}_\alpha) + \underline{\mathbf{u}}^{k+3}(\mathbf{x}_\alpha) + \dots), \quad (24.40)$$

In the Eqs. (24.39) for the derivative of function $\mathbf{u}(\mathbf{x}_\alpha, x_3)$ the following representations have been used

$$\frac{\partial \mathbf{u}(\mathbf{x}_\alpha, x_3)}{\partial x_3} = \frac{1}{h} \sum_{k=0}^{\infty} \underline{\mathbf{u}}^k(\mathbf{x}_\alpha) \frac{\partial P_k(\varpi)}{\partial x_3}, \quad (24.41)$$

and the following relation between Legendre polynomials and their derivatives (Pelekh and Sukhorol'skii, 1980; Zozulya, 2017b)

$$\frac{\partial P_k(\varpi)}{\partial(\varpi)} = ((2k-1)P_{k-1}(\varpi) + (2k-5)P_{k-3}(\varpi) + \dots) \quad (24.42)$$

In the same way the second derivatives of the displacements with respect to x_2 can be presented in the form

$$\frac{2k+1}{2h} \int_{-h}^h \frac{\partial^2 \mathbf{u}(\mathbf{x}_\alpha, x_3)}{\partial x_3^2} P_k(\varpi) dx_3 = \underline{\underline{\mathbf{u}}}^k(\mathbf{x}_\alpha), \quad (24.43)$$

where

$$\underline{\underline{\mathbf{u}}}^k(\mathbf{x}_\alpha) = \frac{2k+1}{h}(\underline{\mathbf{u}}^{k+1}(\mathbf{x}_\alpha) + \underline{\mathbf{u}}^{k+3}(\mathbf{x}_\alpha) + \dots). \quad (24.44)$$

The derivatives of the stress tensor components with respect to x_3 can be represented in the form

$$\begin{aligned} \frac{\partial \boldsymbol{\sigma}(\mathbf{x}_\alpha, \mathbf{x}_3)}{\partial x_3} &= \sum_{k=0}^{\infty} \boldsymbol{\sigma}^k(\mathbf{x}_\alpha) \frac{\partial P_k(w)}{\partial x_3} = \sum_{k=0}^{\infty} \underline{\boldsymbol{\sigma}}^k(\mathbf{x}_\alpha) P_k(w) \\ \frac{\partial^2 \boldsymbol{\sigma}(\mathbf{x}_\alpha, \mathbf{x}_3)}{\partial x_3^2} &= \sum_{k=0}^{\infty} \underline{\underline{\boldsymbol{\sigma}}}^k(\mathbf{x}_\alpha) \frac{\partial P_k(w)}{\partial x_2} = \sum_{k=0}^{\infty} \underline{\underline{\boldsymbol{\sigma}}}^k(\mathbf{x}_\alpha) P_k(w) \end{aligned} \quad (24.45)$$

where

$$\begin{aligned} \underline{\boldsymbol{\sigma}}^k(\mathbf{x}_\alpha) &= \frac{2k+1}{h}(\boldsymbol{\sigma}^{k+1}(\mathbf{x}_\alpha) + \boldsymbol{\sigma}^{k+3}(\mathbf{x}_\alpha) + \dots), \\ \underline{\underline{\boldsymbol{\sigma}}}^k(\mathbf{x}_\alpha) &= \frac{2k+1}{h}(\underline{\boldsymbol{\sigma}}^{k+1}(\mathbf{x}_\alpha) + \underline{\boldsymbol{\sigma}}^{k+3}(\mathbf{x}_\alpha) + \dots), \end{aligned} \quad (24.46)$$

By substituting the Legendre's polynomial coefficients of the stress tensor into the equations of motion (24.6), and taking into account (24.38), we obtain 2-D equations of equilibrium in the form

$$\underline{\nabla} \cdot \boldsymbol{\sigma}^k + \tilde{\mathbf{b}}^k = \rho \ddot{\mathbf{u}}^k, \quad (24.47)$$

where divergences of the stress tensor have the form

$$\begin{aligned} \underline{\nabla} \cdot \sigma^k|_{\alpha} &= \frac{1}{A_1 A_2} \frac{\partial(A_2 \sigma_{1\alpha}^k)}{\partial x_1} + \frac{1}{A_1 A_2} \frac{\partial(A_1 \sigma_{2\alpha}^k)}{\partial x_2} + \frac{\sigma_{\alpha\beta}^k}{A_1 A_2} \frac{\partial A_{\alpha}}{\partial x_{\beta}} \\ &\quad - \frac{\sigma_{\beta\beta}^k}{A_1 A_2} \frac{\partial A_{\beta}}{\partial x_1} + \frac{A_2 k_1 + A_1 k_2}{A_1 A_2} \sigma_{3\alpha}^k + \frac{k_{\alpha}}{A_{\alpha}} \sigma_{\alpha 3}^k - \sigma_{3\alpha}^k \\ \underline{\nabla} \cdot \sigma^k|_3 &= \frac{1}{A_1 A_2} \frac{\partial(A_2 \sigma_{13}^k)}{\partial x_1} + \frac{1}{A_1 A_2} \frac{\partial(A_1 \sigma_{23}^k)}{\partial x_2} + \frac{A_2 k_1 + A_1 k_2}{A_1 A_2} \sigma_{33}^k \\ &\quad - \frac{k_2}{A_2} \sigma_{11}^k - \frac{k_1}{A_1} \sigma_{22}^k - \sigma_{33}^k \end{aligned} \quad (24.48)$$

and

$$\tilde{\mathbf{b}}^k(\mathbf{x}_{\alpha}) = \mathbf{b}^k(\mathbf{x}_{\alpha}) + \frac{2k+1}{h} (\sigma_{|3}^+(\mathbf{x}_{\alpha}) - (-1)^k \sigma_{|3}^-(\mathbf{x}_{\alpha})). \quad (24.49)$$

By substituting expansions in the Legendre polynomials series of the displacements vector, and strain tensor (24.36) and taking into account (24.38) and (24.39) in Eq. (24.34) the 2-D Cauchy kinematic relations can be presented in the form

$$\varepsilon_{ij}^k = \begin{pmatrix} \frac{1}{A_1} \frac{\partial u_1^k}{\partial x_1} + \frac{u_2^k}{A_1 A_2} \frac{\partial A_1}{\partial x_2} + k_1 u_3^k & \frac{1}{2} \left(\frac{1}{A_1} \frac{\partial u_2^k}{\partial x_1} - \frac{u_1^k}{A_1 A_2} \frac{\partial A_1}{\partial x_2} + \frac{1}{A_2} \frac{\partial u_1^k}{\partial x_2} - \frac{u_2^k}{A_1 A_2} \frac{\partial A_2}{\partial x_1} \right) & \frac{1}{2} \left(\frac{1}{A_1} \frac{\partial u_3^k}{\partial x_1} - k_1 u_1^k + \underline{u}_1^k \right) \\ \frac{1}{2} \left(\frac{1}{A_1} \frac{\partial u_2^k}{\partial x_1} - \frac{u_1^k}{A_1 A_2} \frac{\partial A_1}{\partial x_2} + \frac{1}{A_2} \frac{\partial u_1^k}{\partial x_2} - \frac{u_2^k}{A_1 A_2} \frac{\partial A_2}{\partial x_1} \right) & \frac{1}{A_2} \frac{\partial u_2^k}{\partial x_2} + \frac{u_1^k}{A_1 A_2} \frac{\partial A_2}{\partial x_1} + k_2 u_3^k & \frac{1}{2} \left(\frac{1}{A_2} \frac{\partial u_3^k}{\partial x_2} - k_2 u_2^k + \underline{u}_2^k \right) \\ \frac{1}{2} \left(\frac{1}{A_1} \frac{\partial u_3^k}{\partial x_1} - k_1 u_1^k + \underline{u}_1^k \right) & \frac{1}{2} \left(\frac{1}{A_1} \frac{\partial u_3^k}{\partial x_2} - k_2 u_2^k + \underline{u}_2^k \right) & \underline{u}_3^k \end{pmatrix} \quad (24.50)$$

In the same way, by substituting the Legendre's polynomial coefficients for stress tensors (24.36) and taking into account (24.38) and (24.45) in Eq. (24.16) its Legendre's polynomial coefficients for the 2-D Laplacian can be presented in the form

$$\begin{aligned} \nabla^2 \sigma^k|_{jl} &= \nabla_i \nabla_i \sigma_{jl}^k \left(\frac{1}{A_{\alpha}} \frac{\partial}{\partial x_{\alpha}} \nabla_{\alpha} \sigma_{jl}^k + \frac{\nabla_{\alpha} \sigma_{jl}^k}{A_{\beta}} \Gamma_{\beta\beta}^{\alpha} + \frac{\nabla_{\alpha} \sigma_{jl}^k}{A_{\alpha}} \Gamma_{\beta\alpha}^j \right. \\ &\quad \left. + \frac{\nabla_{\alpha} \sigma_{jl}^k}{A_{\alpha}} \Gamma_{\beta\alpha}^j + \frac{\sigma_{jl}^k}{A_{\beta}} \Gamma_{\beta\beta}^3 + \sigma_{jl}^k \right) \end{aligned} \quad (24.51)$$

where $\nabla_{\alpha} \sigma_{jl}^k$ is the 2-D gradient of the Legendre polynomials coefficients of the stress tensor. It has the form

$$\begin{aligned} \nabla \sigma^k|_{ijl} &= \nabla_i \sigma_{jl}^k = \left(\frac{1}{A_{\alpha}} \frac{\partial \sigma_{jl}^k}{\partial x_{\alpha}} + \frac{\sigma_{ml}^k}{A_{\alpha}} \Gamma_{m\alpha}^j + \frac{\sigma_{jm}^k}{A_{\alpha}} \Gamma_{m\alpha}^l + \sigma_{jl}^k \right), \\ \nabla \sigma^k|_{3jl} &= \nabla_3 \sigma_{jl}^k = \left(\frac{\partial \sigma_{jl}^k}{\partial x_3} + \sigma_{jl}^k \right) \end{aligned} \quad (24.52)$$

The nonlocal constitutive equations (24.18) for the Legendre’s polynomial coefficients (24.37) have the form

$$(1 - \tau^2 l_e^2 \nabla^2) \boldsymbol{\sigma}^k = \lambda(\text{tr} \boldsymbol{\varepsilon}^k) \mathbf{I} + 2\mu \boldsymbol{\varepsilon}^k \tag{24.53}$$

The differential equations of motion in form of displacements can be obtained by substituting (24.8) into the nonlocal constitutive relation (24.18).

Now, by substituting the kinematic relations for Legendre’s polynomial coefficients (24.51) in the nonlocal constitutive relations (24.53) and the obtained result into the equations of motion (24.47) we obtain 2-D equations of motion for the nonlocal theory of shells in the form

$$\mu \nabla^2 \mathbf{u}^k + (\lambda + \mu) \nabla \nabla \cdot \mathbf{u}^k + \mathbf{b}^k = \rho \ddot{\mathbf{u}}^k - \rho \tau^2 l_e^2 \nabla^2 \ddot{\mathbf{u}}^k \tag{24.54}$$

where $\nabla^2 \mathbf{u}^k$ is the 2-D Laplacian and $\nabla \nabla \cdot \mathbf{u}^k$ is the 2-D gradient of the divergences of the Legendre polynomial coefficients of the displacements vector of form

$$\begin{aligned} \nabla^2 \mathbf{u}^k|_i &= \frac{1}{A_\alpha} \frac{\partial \nabla_\alpha \cdot u_1^k}{\partial x_\alpha} + \frac{\nabla_\alpha \cdot u_1^k}{A_j} \Gamma_{\alpha j}^j + \frac{\nabla_\alpha \cdot u_j^k}{A_\alpha} \Gamma_{j\alpha}^j + \frac{u_i^k}{A_j} \Gamma_{3i}^3 + u_i^k, \\ \nabla \nabla \cdot \mathbf{u}^k|_\alpha &= \nabla_\alpha \nabla_j u_j \mathbf{e}_i = \frac{1}{A_\alpha} \frac{\partial}{\partial x_\alpha} \left(\frac{1}{H_j} \frac{\partial u_j}{\partial x_j} + \frac{u_k}{H_j} \Gamma_{kj}^j \right), \\ \nabla \nabla \cdot \mathbf{u}^k|_3 &= \nabla_3 \nabla_j u_j \mathbf{e}_i = u_3^k + \frac{u_\beta}{A_j} \Gamma_{kj}^j + \frac{1}{A_\beta} \frac{\partial u_\beta}{\partial x_\beta} + \frac{\partial}{\partial x_3} \frac{1}{A_\beta} \frac{\partial u_\beta}{\partial x_\beta} + u_k \frac{\partial}{\partial x_3} \frac{\Gamma_{kj}^j}{A_j} \end{aligned} \tag{24.55}$$

and

$$\mathbf{b}^k = (1 - \tau^2 l_e^2 \nabla^2) \mathbf{b}^k \tag{24.56}$$

As a result of the performed transformations, instead of the 3-D system of the differential equations in displacements (24.19) we have an infinite system of 2-D differential equations for coefficients of the Legendre’s polynomial series expansion (24.54). In order to simplify the problem an approximate theory has to be developed where only a finite number of members have to be taken into account in the expansion of (24.36) and in all of the relations above. For example, if we consider n -order approximate shell theory, only $n + 1$ members in the expansion (24.36) are taken into account

$$\begin{aligned} \mathbf{u}(\mathbf{x}) &= \sum_{k=0}^n \mathbf{u}^k(\mathbf{x}_\alpha) P_k(\varpi), \quad \mathbf{p}(\mathbf{x}) = \sum_{k=0}^n \mathbf{p}^k(\mathbf{x}_\alpha) P_k(\varpi), \\ \boldsymbol{\sigma}(\mathbf{x}) &= \sum_{k=0}^n \boldsymbol{\sigma}^k(\mathbf{x}_\alpha) P_k(\varpi), \quad \boldsymbol{\varepsilon}(\mathbf{x}) = \sum_{k=0}^n \boldsymbol{\varepsilon}^k(\mathbf{x}_\alpha) P_k(\varpi), \end{aligned} \tag{24.57}$$

In this case we consider that $\mathbf{u}^k = 0, \mathbf{p}^k = 0, \boldsymbol{\sigma}^k$, and $\boldsymbol{\varepsilon}^k = 0$ for $k < 0$ and for $k > n$.

Then the 2-D differential equations of nonlocal elasticity in displacements (24.54) can be presented in the matrix form

$$\mathbf{L}_u \cdot \mathbf{u} + \mathbf{b} = \rho \ddot{\mathbf{u}}^k - \rho \tau^2 l_e^2 \nabla^2 \ddot{\mathbf{u}}, \quad \forall \mathbf{x} \in V, \quad \forall t \in \mathfrak{S} = [t_0, t_1] \tag{24.58}$$

where \mathbf{L}_u is a block matrix \mathbf{u} and \mathbf{b} are block vectors of the form

$$\mathbf{L}_u = \begin{bmatrix} \mathbf{L}_u^{00} & \cdots & \mathbf{L}_u^{0n} \\ \vdots & \ddots & \vdots \\ \mathbf{L}_u^{n0} & \cdots & \mathbf{L}_u^{nn} \end{bmatrix}, \quad \mathbf{u} = \begin{bmatrix} \mathbf{u}^0 \\ \vdots \\ \mathbf{u}^n \end{bmatrix}, \quad \mathbf{b} = \begin{bmatrix} \tilde{\mathbf{b}}^0 \\ \vdots \\ \tilde{\mathbf{b}}^n \end{bmatrix} \quad (24.59)$$

The block matrices and block vectors in (24.59) can be represented in the form of 3-D matrix operators and 3-D vectors

$$\mathbf{L}_u^{rk} = \begin{bmatrix} \tilde{L}_{11}^{rk} & \tilde{L}_{12}^{rk} & \tilde{L}_{13}^{rk} \\ \tilde{L}_{21}^{rk} & \tilde{L}_{22}^{rk} & \tilde{L}_{23}^{rk} \\ \tilde{L}_{31}^{rk} & \tilde{L}_{32}^{rk} & \tilde{L}_{33}^{rk} \end{bmatrix}, \quad \mathbf{u}^k = \begin{bmatrix} u_1^k \\ u_2^k \\ u_3^k \end{bmatrix}, \quad \tilde{\mathbf{b}}^k = \begin{bmatrix} \tilde{b}_1^k \\ \tilde{b}_2^k \\ \tilde{b}_3^k \end{bmatrix} \quad (24.60)$$

The order of the system of differential equations depends on the assumption regarding thickness distribution of the stress-strain parameters of the shell. The higher the order of approximation, the better the accuracy of the result obtained using the proposed theory. The complete system of linear differential equations for the nonlocal theory of elasticity of any order can be obtained using the equations presented here. For the first order approximation theory block matrices and block vectors (24.59) have the form

$$\mathbf{L}_u = \begin{bmatrix} \mathbf{L}_u^{00} & \mathbf{L}_u^{01} \\ \mathbf{L}_u^{10} & \mathbf{L}_u^{11} \end{bmatrix}, \quad \mathbf{u} = \begin{bmatrix} \mathbf{u}^0 \\ \mathbf{u}^1 \end{bmatrix}, \quad \tilde{\mathbf{b}} = \begin{bmatrix} \tilde{\mathbf{b}}^0 \\ \tilde{\mathbf{b}}^1 \end{bmatrix} \quad (24.61)$$

In the next sections, we will consider the first order approximation theory for the plates in Cartesian and polar coordinates and for cylindrical and spherical shells in detail.

24.5 Higher Order Theory of Nonlocal Plates in Cartesian Coordinates

All of the above equations of the nonlocal theory of elasticity become much simpler for the case plates. Let us first consider the plate in the Cartesian coordinates. In order to simplify and present the corresponding equations in the traditional form we introduce the Cartesian coordinates $x_1 = x, x_2 = y$, and $x_3 = z$. In this case, coefficients of the first quadratic form of a surface and main curvatures are equal to $A_1 = 1, A_2 = 1, k_1 = k_2 = 0$. After the substitution of those parameters in all of the above equations, the equations that correspond to the higher order theory of nonlocal elasticity of the plates in Cartesian coordinates will be obtained.

The equations of motion for Legendre's polynomial coefficients in this case have the form (24.54) but the operator of divergence for the stress tensors become

$$\begin{aligned}
\tilde{\nabla} \cdot \boldsymbol{\sigma}^k|_x &= \frac{\partial \sigma_{xx}^k}{\partial x} + \frac{\partial \sigma_{yx}^k}{\partial y} - \underline{\sigma_{zx}^k}, \\
\tilde{\nabla} \cdot \boldsymbol{\sigma}^k|_y &= \frac{\partial \sigma_{xy}^k}{\partial x} + \frac{\partial \sigma_{yy}^k}{\partial y} - \underline{\sigma_{zy}^k}, \\
\tilde{\nabla} \cdot \boldsymbol{\sigma}^k|_z &= \frac{\partial \sigma_{xz}^k}{\partial x} + \frac{\partial \sigma_{yz}^k}{\partial y} - \underline{\sigma_{zz}^k},
\end{aligned} \tag{24.62}$$

where

$$\underline{\sigma_{zi}^k} = \frac{2k+1}{h} (\sigma_{zi}^{k-1} + \sigma_{zi}^{k-3} + \dots), \quad i = x, y, z \tag{24.63}$$

The Legendre's polynomial coefficients of the symmetric strain tensor have the form

$$\varepsilon_{ij}^k = \begin{vmatrix} \frac{\partial u_x^k}{\partial x} & \frac{1}{2} \left(\frac{\partial u_y^k}{\partial x} + \frac{\partial u_x^k}{\partial y} \right) & \frac{1}{2} \left(\frac{\partial u_z^k}{\partial x} + \underline{u_x^k} \right) \\ \frac{1}{2} \left(\frac{\partial u_y^k}{\partial x} + \frac{\partial u_x^k}{\partial y} \right) & \frac{\partial u_y^k}{\partial y} & \frac{1}{2} \left(\frac{\partial u_z^k}{\partial y} + \underline{u_y^k} \right) \\ \frac{1}{2} \left(\frac{\partial u_z^k}{\partial x} + \underline{u_x^k} \right) & \frac{1}{2} \left(\frac{\partial u_z^k}{\partial y} + \underline{u_y^k} \right) & \underline{u_z^k} \end{vmatrix}, \tag{24.64}$$

where

$$\underline{u_i^k}(\mathbf{x}_\alpha) = \frac{2k+1}{h} (u_i^{k+1}(\mathbf{x}_\alpha) + u_i^{k+3}(\mathbf{x}_\alpha) + \dots), \quad i = x, y, z \tag{24.65}$$

The 2-D Laplacian of the Legendre polynomial coefficients of the displacements vector presented by Eq. (4.20) significantly simplify and have the for

$$\underline{\underline{\nabla^2 u_i^k}} = \Delta_2 u_i^k + \underline{u_i^k}, \quad i = x, y, z \tag{24.66}$$

where $\Delta_2 = \frac{\partial^2}{\partial x_1^2} + \frac{\partial^2}{\partial x_2^2}$ is 2-D Laplacian of the scalar function in the Cartesian coordinates. By substituting the Eqs. (24.62)-(24.66) into the equations of motion (4.12) and taking into account that the divergence operator for the Legendre's polynomial coefficients of the stress tensors has form (24.62), we obtain the equations of motion in the form (24.58), where elements of the block matrices and block vectors (24.60) have the form

$$\mathbf{L}_u^{rk} = \begin{vmatrix} \tilde{L}_{xx}^{rk} & \tilde{L}_{xy}^{rk} & \tilde{L}_{xz}^{rk} \\ \tilde{L}_{yx}^{rk} & \tilde{L}_{yy}^{rk} & \tilde{L}_{yz}^{rk} \\ \tilde{L}_{zx}^{rk} & \tilde{L}_{zy}^{rk} & \tilde{L}_{zz}^{rk} \end{vmatrix}, \quad \mathbf{u}^k = \begin{vmatrix} u_x^k \\ u_y^k \\ u_z^k \end{vmatrix}, \quad \tilde{\mathbf{b}}^k = \begin{vmatrix} \tilde{b}_x^k \\ \tilde{b}_y^k \\ \tilde{b}_z^k \end{vmatrix} \tag{24.67}$$

Some elements of these matrices are differential operators, some are constants and some are equal to zero. Below, all elements of the matrices (24.67) for the case of the first order theory of nonlocal plates in Cartesian coordinates are presented in the form

$$\begin{aligned}
\tilde{L}_{xx}^{00} &= (\lambda + 2\mu) \frac{\partial^2}{\partial x^2} + \mu \frac{\partial^2}{\partial y^2}, \\
\tilde{L}_{xy}^{00} &= (\lambda + \mu) \frac{\partial^2}{\partial x \partial y}, \quad \tilde{L}_{xz}^{00} = 0, \quad \tilde{L}_{yx}^{00} = (\lambda + \mu) \frac{\partial^2}{\partial x \partial y}, \\
\tilde{L}_{yy}^{00} &= (\lambda + 2\mu) \frac{\partial^2}{\partial y^2} + \mu \frac{\partial^2}{\partial x^2}, \quad \tilde{L}_{yz}^{00} = 0, \quad \tilde{L}_{zx}^{00} = 0, \quad \tilde{L}_{xy}^{00} = 0, \\
\tilde{L}_{zz}^{00} &= \mu \left(\frac{\partial^2}{\partial x^2} + \frac{\partial^2}{\partial y^2} \right), \\
\tilde{L}_{xx}^{01} &= 0, \quad \tilde{L}_{xy}^{01} = 0, \quad \tilde{L}_{xz}^{01} = \frac{\lambda}{h} \frac{\partial}{\partial x}, \quad \tilde{L}_{yx}^{01} = 0, \quad \tilde{L}_{yy}^{01} = 0, \quad \tilde{L}_{yz}^{01} = \frac{\lambda}{h} \frac{\partial}{\partial y}, \\
\tilde{L}_{zx}^{01} &= \frac{\mu}{h} \frac{\partial}{\partial x}, \quad \tilde{L}_{zy}^{01} = \frac{\mu}{h} \frac{\partial}{\partial y}, \quad \tilde{L}_{zz}^{01} = 0, \\
\tilde{L}_{xx}^{10} &= 0, \quad \tilde{L}_{xy}^{10} = 0, \quad \tilde{L}_{xz}^{10} = \frac{3\lambda}{h} \frac{\partial}{\partial x}, \quad \tilde{L}_{yx}^{10} = 0, \quad \tilde{L}_{yy}^{10} = 0, \quad \tilde{L}_{yz}^{10} = \frac{3\lambda}{h} \frac{\partial}{\partial y}, \\
\tilde{L}_{zx}^{10} &= \frac{3\mu}{h} \frac{\partial}{\partial x}, \quad \tilde{L}_{zy}^{10} = \frac{3\mu}{h} \frac{\partial}{\partial y}, \quad \tilde{L}_{zz}^{10} = 0, \\
\tilde{L}_{xx}^{11} &= (\lambda + 2\mu) \frac{\partial^2}{\partial y^2} + \mu \frac{\partial^2}{\partial x^2} + \frac{3\mu}{h^2}, \quad \tilde{L}_{xy}^{11} = (\lambda + \mu) \frac{\partial^2}{\partial x \partial y}, \quad \tilde{L}_{xz}^{11} = 0, \\
\tilde{L}_{yx}^{11} &= (\lambda + \mu) \frac{\partial^2}{\partial x \partial y}, \\
\tilde{L}_{yy}^{11} &= (\lambda + 2\mu) \frac{\partial^2}{\partial y^2} + \mu \frac{\partial^2}{\partial x^2} + \frac{3\mu}{h^2}, \quad \tilde{L}_{yz}^{11} = 0, \quad \tilde{L}_{zx}^{11} = 0, \quad \tilde{L}_{xy}^{11} = 0, \\
\tilde{L}_{zz}^{11} &= \mu \left(\frac{\partial^2}{\partial x^2} + \frac{\partial^2}{\partial y^2} \right) + \frac{3\mu}{h^2}
\end{aligned} \tag{24.68}$$

A complete 2-D system of the differential equations for the higher order theory of nonlocal plates in the Cartesian system of coordinates is presented in this section. Explicit expressions for divergences of the Legendre's polynomial coefficients of the stress tensors (24.62), for the Legendre's polynomial coefficients of symmetric strain tensor (24.64), and for Laplacian of the Legendre's polynomial coefficients of the displacements vector (24.66) for higher order theory of plates are presented here. For the case of the first order approximation theory, elements of the matrix differential operators (24.67), that are included in the equations of motion (24.58) are also presented in the explicit form (24.68). They can be used for theoretical analysis, as well as analytical and numerical solutions of problems arising in science and engineering.

24.6 Higher Order Theory of Nonlocal Plates in Polar Coordinates

Sometimes polar and cylindrical coordinates are preferred for theoretical analysis as well as for analytical and numerical computations. Therefore, let us develop equations for the higher theory of the nonlocal plate in polar coordinates. In this case we have notations $x_1 = \rho, x_2 = \varphi$, and $x_3 = z$. Coefficients of the first quadratic form of a surface and main curvatures are equal to $A_1 = 1, A_2 = \rho$ and $k_1 = k_2 = 0$ respectively. By substituting those parameters in the Eqs. (24.47)-(24.54), the equations that correspond to the higher order theory of nonlocal elasticity of the plates in polar coordinates will be obtained.

The equations of motion for Legendre’s polynomial coefficients in this case have the form (24.54) but the operator of divergence for the nonlocal stress tensors become

$$\begin{aligned} \tilde{\nabla} \cdot \sigma^k|_\rho &= \frac{\partial \sigma_{\rho\rho}^k}{\partial \rho} + \frac{1}{\rho} \frac{\partial \sigma_{\varphi\rho}^k}{\partial \varphi} + \frac{\sigma_{\rho\rho}^k - \sigma_{\varphi\rho}^k}{\rho} - \underline{\sigma_{z\rho}^k}, \\ \tilde{\nabla} \cdot \sigma^k|_\varphi &= \frac{\partial \sigma_{\rho\varphi}^k}{\partial \rho} + \frac{\partial \sigma_{\varphi\varphi}^k}{\partial \varphi} \frac{1}{\rho} + \frac{\sigma_{\rho\varphi}^k - \sigma_{\varphi\rho}^k}{\rho} - \underline{\sigma_{z\varphi}^k}, \\ \tilde{\nabla} \cdot \sigma^k|_z &= \frac{\partial \sigma_{\rho z}^k}{\partial \rho} + \frac{1}{\rho} \frac{\partial \sigma_{\varphi z}^k}{\partial \varphi} + \frac{1}{\rho} \sigma_{\rho z}^k - \underline{\sigma_{zz}^k} \end{aligned} \tag{24.69}$$

where

$$\underline{\sigma_{zi}^k} = \frac{2k+1}{h} (\sigma_{zi}^{k-1} + \sigma_{zi}^{k-3} + \dots), \quad i = \rho, \varphi, z \tag{24.70}$$

The Legendre’s polynomial coefficients of the symmetric strain ϵ^k tensor have the form

$$\epsilon_{ij}^k = \begin{vmatrix} \frac{\partial u_\rho^k}{\partial \rho} & \frac{1}{2} \left(\frac{\partial u_\varphi^k}{\partial \rho} + \frac{1}{\rho} \frac{\partial u_\rho^k}{\partial \varphi} - \frac{u_\varphi^k}{\rho} \right) & \frac{1}{2} \left(\frac{\partial u_z^k}{\partial \rho} + \underline{u_\rho^k} \right) \\ \frac{1}{2} \left(\frac{\partial u_\varphi^k}{\partial \rho} + \frac{1}{\rho} \frac{\partial u_\rho^k}{\partial \varphi} - \frac{u_\varphi^k}{\rho} \right) & \frac{1}{\rho} \frac{\partial u_\varphi^k}{\partial \varphi} + \frac{u_\rho^k}{\rho} & \frac{1}{2} \left(\frac{1}{\rho} \frac{\partial u_z^k}{\partial \varphi} + \underline{u_\varphi^k} \right) \\ \frac{1}{2} \left(\frac{\partial u_z^k}{\partial \rho} + \underline{u_\rho^k} \right) & \frac{1}{2} \left(\frac{1}{\varphi} \frac{\partial u_z^k}{\partial \rho} + \underline{u_\varphi^k} \right) & \underline{u_z^k} \end{vmatrix}, \tag{24.71}$$

where

$$\underline{u_i^k}(\mathbf{x}_\alpha) = \frac{2k+1}{h} (u_i^{k+1}(\mathbf{x}_\alpha) + u_i^{k+3}(\mathbf{x}_\alpha) + \dots), \quad i = \rho, \varphi, z \tag{24.72}$$

The 2-D Laplacian of the Legendre polynomials coefficients of the displacements vector presented by Eq. (24.55) are significantly simplified and have the form

$$\begin{aligned}
\underline{\underline{\nabla}}^2 u_\rho^k &= \Delta_2 u_\rho^k - \frac{u_\rho^k}{\rho^2} - \frac{2}{\rho^2} \frac{\partial u_\rho^k}{\partial \varphi} + \underline{\underline{u}}_\rho^k, \\
\underline{\underline{\nabla}}^2 u_\varphi^k &= \Delta_2 u_\varphi^k - \frac{u_\varphi^k}{\rho^2} + \frac{2}{\rho^2} \frac{\partial u_\varphi^k}{\partial \varphi} + \underline{\underline{u}}_\varphi^k, \quad i = \rho, \varphi, z, \\
\underline{\underline{\nabla}}^2 u_z^k &= \Delta_2 u_z^k + \underline{\underline{u}}_z^k,
\end{aligned} \tag{24.73}$$

where $\Delta_2 = \frac{\partial^2}{\partial \rho^2} + \frac{1}{\rho} \frac{\partial}{\partial \rho} + \frac{1}{\rho^2} \frac{\partial^2}{\partial \varphi^2}$ is 2-D Laplacian of the scalar function in the polar coordinates.

By substituting the equations presented in this section into the equations of motion (24.54) and taking into account that the divergence operator for the Legendre's polynomial coefficients of the tensors has the form of (24.69) we obtain the equations of motion in the form (24.58), where elements of the block matrices and block vectors (24.60) have the form

$$\mathbf{L}^{rk} = \begin{bmatrix} \tilde{L}_{\rho\rho}^{rk} & \tilde{L}_{\rho\varphi}^{rk} & \tilde{L}_{\rho z}^{rk} \\ \tilde{L}_{\varphi\rho}^{rk} & \tilde{L}_{\varphi\varphi}^{rk} & \tilde{L}_{\varphi z}^{rk} \\ \tilde{L}_{z\rho}^{rk} & \tilde{L}_{z\varphi}^{rk} & \tilde{L}_{zz}^{rk} \end{bmatrix}, \quad \mathbf{u}^k = \begin{bmatrix} u_\rho^k \\ u_\varphi^k \\ fu_z^k \end{bmatrix}, \quad \tilde{\mathbf{b}}^k = \begin{bmatrix} \tilde{b}_\rho^k \\ \tilde{b}_\varphi^k \\ \tilde{b}_z^k \end{bmatrix} \tag{24.74}$$

Some elements of these matrices are differential operators, some are constants and some are equal to zero. Below, all elements of the matrices (24.74) for the case of the first order theory of nonlocal plates in polar coordinates are presented in the form

$$\begin{aligned}
\tilde{L}_{\rho\rho}^{00} &= (\lambda + 2\mu) \left(\frac{\partial^2}{\partial \rho^2} + \frac{1}{\rho} \frac{\partial}{\partial \rho} - \frac{1}{\rho^2} \right) + \frac{\mu}{\rho^2} \frac{\partial^2}{\partial \varphi^2}, \\
\tilde{L}_{\rho\varphi}^{00} &= (\lambda + \mu) \left(\frac{1}{\rho} \frac{\partial^2}{\partial \rho \partial \varphi} - \frac{1}{\rho^2} \frac{\partial}{\partial \varphi} \right) - \frac{2\mu}{\rho^2} \frac{\partial}{\partial \varphi}, \quad \tilde{L}_{\rho z}^{00} = 0, \\
\tilde{L}_{\varphi\rho}^{00} &= (\lambda + \mu) \left(\frac{1}{\rho} \frac{\partial^2}{\partial \rho \partial \varphi} - \frac{1}{\rho^2} \frac{\partial}{\partial \varphi} \right) - \frac{2\mu}{\rho^2} \frac{\partial}{\partial \varphi}, \\
\tilde{L}_{\varphi\varphi}^{00} u_y^0 &= (\lambda + 2\mu) \frac{1}{\rho^2} \frac{\partial^2}{\partial \varphi^2} + \mu \left(\frac{\partial^2}{\partial \rho^2} + \frac{1}{\rho} \frac{\partial}{\partial \rho} - \frac{1}{\rho^2} \right), \quad \tilde{L}_{\varphi z}^{00} = 0, \\
\tilde{L}_{z\rho}^{00} &= 0, \quad \tilde{L}_{z\varphi}^{00} = 0, \quad \tilde{L}_{zz}^{00} = \mu \left(\mu \frac{\partial^2}{\partial \rho^2} + \frac{1}{\rho} \frac{\partial}{\partial \rho} - \frac{1}{\rho^2} \frac{\partial}{\partial \varphi} \right), \\
\tilde{L}_{\rho\rho}^{01} &= 0, \quad \tilde{L}_{\rho\varphi}^{01} = 0, \quad \tilde{L}_{\rho z}^{01} = \frac{\lambda}{h} \frac{\partial}{\partial \rho}, \quad \tilde{L}_{\varphi\rho}^{01} = 0, \quad \tilde{L}_{\varphi\varphi}^{01} = 0, \quad \tilde{L}_{\varphi z}^{01} = \frac{\lambda}{h\rho} \frac{\partial}{\partial \varphi}, \\
\tilde{L}_{z\rho}^{01} &= \frac{\mu}{h} \left(\frac{\partial}{\partial \rho} + \frac{1}{\rho} \right), \quad \tilde{L}_{z\varphi}^{01} = \frac{\mu}{h\rho} \frac{\partial}{\partial \varphi}, \quad \tilde{L}_{zz}^{01} = 0, \\
\tilde{L}_{\rho\rho}^{11} &= (\lambda + 2\mu) \left(\frac{\partial^2}{\partial \rho^2} + \frac{1}{\rho} \frac{\partial}{\partial \rho} - \frac{1}{\rho^2} \right) + \frac{\mu}{\rho^2} \frac{\partial^2}{\partial \varphi^2} + \frac{3\mu}{h^2}, \\
\tilde{L}_{\rho\varphi}^{11} &= \frac{\lambda + \mu}{\rho} \left(\frac{\partial^2}{\partial \rho \partial \varphi} - \frac{1}{\rho^2} \frac{\partial}{\partial \varphi} \right) - \frac{2\mu}{\rho^2} \frac{\partial}{\partial \varphi}, \quad \tilde{L}_{\rho z}^{11} = 0,
\end{aligned}$$

$$\begin{aligned}
\tilde{L}_{\varphi\rho}^{11} &= \frac{\lambda + \mu}{\rho} \left(\frac{\partial^2}{\partial\rho\partial\varphi} - \frac{1}{\rho} \frac{\partial}{\partial\varphi} \right) - \frac{2\mu}{\rho^2} \frac{\partial}{\partial\varphi}, \\
\tilde{L}_{\varphi\rho}^{11} &= \frac{\lambda + 2\mu}{\rho^2} \frac{\partial^2}{\partial\varphi^2} + \mu \left(\frac{\partial^2}{\partial\rho^2} + \frac{1}{\rho} \frac{\partial}{\partial\rho} - \frac{1}{\rho^2} \right) + \frac{3\mu}{h^2}, \quad \tilde{L}_{\varphi z}^{11} = 0, \\
\tilde{L}_{z\rho}^{11} &= 0, \quad \tilde{L}_{z\varphi}^{11} = 0, \quad \tilde{L}_{zz}^{11} = \mu + \left(\frac{\partial^2}{\partial\rho^2} + \frac{1}{\rho} \frac{\partial}{\partial\rho} + \frac{1}{\rho^2} \frac{\partial^2}{\partial\varphi^2} \right) + \frac{3(\lambda + 2\mu)}{h^2} \quad (24.75)
\end{aligned}$$

A complete 2-D system of differential equations for the higher order theory of nonlocal plates in the polar system of coordinates is presented in this section. Explicit expressions for divergences of the Legendre's polynomial coefficients of the stress tensor (24.69), for the Legendre's polynomial coefficients of symmetric strain tensor (24.71) and for Laplacian of the Legendre's polynomial coefficients of the displacements vector (24.73) for higher order theory of plates are presented here. For the case of first order approximation theory, elements of matrix differential operators (24.74), that are included in the equations of motion (24.58) are also presented in explicit form (24.75). They can be used for theoretical analysis, as well as analytical and numerical solutions of the problems arising in science and engineering.

24.7 Higher Order Theory of Nonlocal Cylindrical Shell

Models of nonlocal shells of cylindrical geometry are very important and often used in theoretical analysis and applied in sciences and engineering. Therefore, we will develop equations for the higher order theory of nonlocal cylindrical shells here. Let us introduce cylindrical coordinates and such that $x_1 = x$, $x_2 = \varphi$ and $x_3 = r$, $r \in [R - h, R + h]$. Coefficients of the first quadratic form of a surface and main curvatures are equal to $A_1 = 1, A_2 = R$ and $k_1 = 0, k_2 = \frac{1}{R}$, respectively. By substituting these parameters in Eqs. (24.47)-(24.54), the equations that correspond to the higher order theory of nonlocal elasticity of the cylindrical shell will be obtained.

The equations of motion for Legendre's polynomial coefficients in this case have the form (24.54) but the operator of divergence for the stress tensor becomes

$$\begin{aligned}
\tilde{\nabla} \cdot \sigma^k|_x &= \frac{\partial \sigma_{xx}^k}{\partial x} + \frac{1}{R} \frac{\partial \sigma_{\varphi x}^k}{\partial \varphi} - \frac{\sigma_{rx}^k}{R}, \\
\tilde{\nabla} \cdot \sigma^k|_\varphi &= \frac{\partial \sigma_{x\varphi}^k}{\partial x} + \frac{1}{R} \frac{\partial \sigma_{\varphi\varphi}^k}{\partial \varphi} + \frac{\sigma_{\varphi r}^k}{R} - \frac{\sigma_{r\varphi}^k}{R}, \\
\tilde{\nabla} \cdot \sigma^k|_r &= \frac{\partial \sigma_{xr}^k}{\partial x} + \frac{\partial \sigma_{\varphi r}^k}{\partial \varphi} + \frac{\partial \sigma_{\varphi\varphi}^k}{R} - \frac{\sigma_{rr}^k}{R}
\end{aligned} \quad (24.76)$$

where

$$\underline{\sigma}_{ri}^k = \frac{2k+1}{h} (\sigma_{ri}^{k-1} + \sigma_{ri}^{k-3} + \dots), \quad i = x, \varphi, r \quad (24.77)$$

The Legendre’s polynomial coefficients of the asymmetric strain ε^k tensor have the form

$$\varepsilon_{ij}^k = \begin{pmatrix} \frac{\partial u_x^k}{\partial x} & \frac{1}{2} \left(\frac{\partial u_\varphi^k}{\partial x} + \frac{1}{R} \frac{\partial u_x^k}{\partial \varphi} \right) & \frac{1}{2} \left(\frac{\partial u_r^k}{\partial x} + \underline{u_x^k} \right) \\ \frac{1}{2} \left(\frac{\partial u_\varphi^k}{\partial x} + \frac{1}{R} \frac{\partial u_x^k}{\partial \varphi} \right) & \frac{1}{R} \left(\frac{\partial u_\varphi^k}{\partial \varphi} + u_r^k \right) & \frac{1}{2} \left(\frac{1}{R} \frac{\partial u_r^k}{\partial \varphi} - \frac{u_\varphi^k}{R} + \underline{u_\varphi^k} \right) \\ \frac{1}{2} \left(\frac{\partial u_r^k}{\partial x} + \underline{u_x^k} \right) & \frac{1}{2} \left(\frac{1}{R} \frac{\partial u_r^k}{\partial \varphi} - \frac{u_\varphi^k}{R} + \underline{u_\varphi^k} \right) & \underline{u_r^k} \end{pmatrix}, \quad (24.78)$$

where

$$u_i^k(\mathbf{x}_\alpha) = \frac{2k+1}{h} (u_i^{k+1}(\mathbf{x}_\alpha) + u_i^{k+3}(\mathbf{x}_\alpha) + \dots), \quad i = x, \varphi, r \quad (24.79)$$

The 2-D Laplacian of the Legendre polynomials coefficients of the displacements vector presented by Eq. (24.55) is significantly simplified and has the form

$$\begin{aligned} \underline{\underline{\nabla^2}} u_x^k &= \Delta_2 u_x^k + \underline{u_x^k}, \\ \underline{\underline{\nabla^2}} u_\varphi^k &= \Delta_2 u_\varphi^k - \frac{u_\varphi^k}{R^2} + \frac{2}{R^2} \frac{\partial u_z^k}{\partial \varphi} + \underline{u_\varphi^k}, \quad i = x, \varphi, r \\ \underline{\underline{\nabla^2}} u_z^k &= \Delta_2 u_z^k - \frac{u_z^k}{R^2} - \frac{2}{R^2} \frac{\partial u_\varphi^k}{\partial \varphi} + \underline{u_z^k} \end{aligned} \quad (24.80)$$

where $\Delta_2 = \frac{\partial^2}{\partial x^2} + \frac{1}{R^2} \frac{\partial^2}{\partial \varphi^2}$ is the 2-D Laplacian of the scalar function in the system of coordinates introduced here.

By substituting the equations presented in this section in the equations of motion (24.54) and taking into account that the divergence operator for the Legendre’s polynomial coefficients of the stress tensors has the form of (24.76) we obtain the equations of motion (24.58), where elements of the block matrices and block vectors (24.60) have the form

$$\tilde{\mathbf{L}}_u^{rk} = \begin{pmatrix} \tilde{L}_{xx}^{rk} & \tilde{L}_{x\varphi}^{rk} & \tilde{L}_{xr}^{rk} \\ \tilde{L}_{\varphi x}^{rk} & \tilde{L}_{\varphi\varphi}^{rk} & \tilde{L}_{\varphi r}^{rk} \\ \tilde{L}_{rx}^{rk} & \tilde{L}_{r\varphi}^{rk} & \tilde{L}_{rr}^{rk} \end{pmatrix}, \quad \mathbf{u}^k = \begin{pmatrix} u_x^k \\ u_\varphi^k \\ u_r^k \end{pmatrix}, \quad \tilde{\mathbf{b}}^k = \begin{pmatrix} \tilde{b}_x^k \\ \tilde{b}_\varphi^k \\ \tilde{b}_r^k \end{pmatrix} \quad (24.81)$$

Some elements of these matrices are differential operators, some are constants and some are equal to zero. Below, all elements of the matrices (24.74) for the case of the first order theory of nonlocal shells in the cylindrical coordinates related to the geometry of the shell are presented in the form

$$\tilde{L}_{xx}^{00} = (\lambda + 2\mu) \frac{\partial^2}{\partial x^2} + \frac{\mu}{R^2} \frac{\partial^2}{\partial \varphi^2}, \quad \tilde{L}_{x\varphi}^{00} = \frac{\lambda + \mu}{R} \frac{\partial^2}{\partial x \partial \varphi}, \quad \tilde{L}_{xr}^{00} = \frac{\lambda}{R} \frac{\partial}{\partial x},$$

$$\begin{aligned}
\tilde{L}_{\varphi x}^{00} &= \frac{\lambda + \mu}{R} \frac{\partial^2}{\partial x \partial \varphi}, \quad \tilde{L}_{\varphi \rho}^{00} = \frac{\lambda + 2\mu}{R^2} \frac{\partial R^2}{\partial \varphi^2} + \mu \left(\frac{\partial^2}{\partial x^2} - \frac{1}{R^2} \right), \quad \tilde{L}_{\varphi r}^{00} = \frac{\lambda + 3\mu}{R^2} \frac{\partial}{\partial \varphi}, \\
\tilde{L}_{rx}^{00} &= -\frac{\lambda}{R} \frac{\partial}{\partial x}, \quad \tilde{L}_{r\varphi}^{00} = \frac{\lambda + 3\mu}{R^2} \frac{\partial}{\partial \varphi}, \quad \tilde{L}_{rr}^{00} = \mu \left(\frac{\partial^2}{\partial x^2} + \frac{1}{R^2} \frac{\partial}{\partial \varphi} \right) - \frac{\lambda + 2\mu}{R^2}, \\
\tilde{L}_{xx}^{01} &= 0, \quad \tilde{L}_{x\varphi}^{01} = 0, \quad \tilde{L}_{xr}^{01} = \frac{\lambda}{h} \frac{\partial}{\partial x}, \quad \tilde{L}_{\varphi x}^{01} = 0, \quad \tilde{L}_{\rho\varphi}^{01} = 0, \quad \tilde{L}_{\varphi r}^{01} = \frac{\lambda}{hR} \frac{\partial}{\partial \varphi}, \\
\tilde{L}_{rx}^{01} &= \frac{\mu}{h} \frac{\partial}{\partial x}, \quad \tilde{L}_{r\varphi}^{01} = \frac{\mu}{hR} \frac{\partial}{\partial \varphi}, \quad \tilde{L}_{rr}^{01} = -\frac{\lambda}{hR}, \\
\tilde{L}_{xx}^{10} &= 0, \quad \tilde{L}_{x\varphi}^{10} = 0, \quad \tilde{L}_{xr}^{10} = \frac{3\mu}{h} \frac{\partial}{\partial x}, \quad \tilde{L}_{\varphi x}^{10} = 0, \quad \tilde{L}_{\varphi\varphi}^{10} = \frac{3\mu}{hR}, \quad L_{\varphi r}^{10} = \frac{3\mu}{hR} \frac{\partial}{\partial \varphi}, \\
\tilde{L}_{rx}^{10} &= \frac{3\lambda}{h} \frac{\partial}{\partial x}, \quad \tilde{L}_{r\varphi}^{10} = \frac{3\lambda}{hR} \frac{\partial}{\partial \varphi}, \quad \tilde{L}_{rr}^{10} = \frac{3\lambda}{hR}, \\
\tilde{L}_{xx}^{11} &= (\lambda + 2\mu) \frac{\partial^2}{\partial x^2} + \frac{\mu}{R^2} \frac{\partial^2}{\partial \varphi^2} + \frac{3\mu}{h^2}, \quad \tilde{L}_{x\varphi}^{11} = \frac{\lambda + \mu}{R} \frac{\partial^2}{\partial x \partial \varphi}, \quad \tilde{L}_{xr}^{00} = \frac{\lambda}{R} \frac{\partial}{\partial x}, \\
\tilde{L}_{\varphi x}^{11} &= \frac{\lambda + \mu}{R} \frac{\partial^2}{\partial x \partial \varphi}, \quad \tilde{L}_{\varphi\varphi}^{11} = \frac{\lambda + 2\mu}{R^2} \frac{\partial^2}{\partial \varphi^2} + \mu \left(\frac{\partial^2}{\partial x^2} + \frac{3R^2 - h^2}{R^2 h^2} \right) - \frac{3\mu}{Rh}, \\
\tilde{L}_{\varphi r}^{11} &= \frac{\lambda + 3\mu}{R^2} \frac{\partial}{\partial \varphi}, \quad \tilde{L}_{rx}^{11} = -\frac{\lambda}{R} \frac{\partial}{\partial x}, \\
\tilde{L}_{r\varphi}^{11} &= -\frac{\lambda + 3\mu}{R^2} \frac{\partial}{\partial \varphi}, \quad \tilde{L}_{rr}^{11} = \mu \left(\frac{\partial^2}{\partial x^2} + \frac{1}{R^2} \frac{\partial}{\partial \varphi} \right) - \frac{(\lambda + 2\mu)(3R^2 - h^2)}{R^2 h^2} \quad (24.82)
\end{aligned}$$

A complete 2-D system of the differential equations for the higher order theory of the nonlocal shells in the cylindrical system of coordinates related to the geometry of the shell is presented in this section. Explicit expressions for divergences of the Legendre's polynomial coefficients of the stress tensor (24.76), for the Legendre's polynomial coefficients of symmetric strain tensor (24.78) and for Laplacian of the Legendre's polynomial coefficients of the displacements vector (24.80) for higher order theory of plates are presented here. For the case of the first order approximation theory, elements of matrix differential operators (24.82), that are included in the equations of motion (24.58) are also presented in the explicit form (24.82). They can be used for theoretical analysis, as well as for analytical and numerical solutions of the problems arising in science and engineering.

24.8 Higher Order Theory of Nonlocal Spherical Shells

Let us consider the higher order model of the nonlocal elastic spherical shell, which is also important and often used in theoretical analysis as well as applied in sciences and engineering. Let us introduce spherical coordinates such as $x_1 = \varphi$, $x_2 = \Psi$, and $x_3 = r$, $r \in [R - h, R + h]$. The coefficients of the first quadratic form of a surface and main curvatures are equal to $A_1 = R$, $A_2 = R \sin(\Psi)$ and $k_1 = \frac{1}{R}$, $k_2 = \frac{1}{R}$, respectively. By substituting these parameters in the Eqs. (24.47)-(24.54), the equations that

correspond to the higher order theory of nonlocal elasticity for the spherical shell will be obtained. The equations of motion for Legendre’s polynomial coefficients in this case have the form (24.54) but the operator of divergence for the stress tensor becomes

$$\begin{aligned} \tilde{\nabla} \cdot \sigma^k|_{\varphi} &= \frac{1}{R} \frac{\partial \sigma_{\varphi}^k}{\partial \varphi} + \frac{\partial \sigma_{\psi\varphi}^k}{R \sin(\psi) \partial \psi} - \frac{\sigma_{r\varphi}^k}{R}, \\ \tilde{\nabla} \cdot \sigma^k|_{\psi} &= \frac{1}{R} \frac{\partial \sigma_{\varphi\psi}^k}{\partial \varphi} + \frac{1}{R \sin(\psi) \partial \psi} \frac{\partial \sigma_{\psi\psi}^k}{\partial \psi} + \frac{\sigma_{\psi r}^k}{R} - \frac{\sigma_{r\psi}^k}{R}, \\ \tilde{\nabla} \cdot \sigma^k|_r &= \frac{1}{R} \frac{\partial \sigma_{\varphi r}^k}{\partial \varphi} + \frac{\partial \sigma_{\psi r}^k}{\sin(\psi) \partial \psi} - \frac{\sigma_{\varphi\varphi}^k + \sigma_{\psi\psi}^k}{R} - \frac{\sigma_{rr}^k}{R}, \end{aligned} \tag{24.83}$$

where

$$\underline{\sigma}_{ri}^k = \frac{2k+1}{h} (\sigma_{ri}^{k-1} + \sigma_{ri}^{k-3} + \dots), \quad i = \varphi, \psi, r \tag{24.84}$$

The Legendre’s polynomial coefficients of the symmetric strain tensor have the form

$$\varepsilon_{ij}^k = \begin{vmatrix} \frac{1}{R} \left(\frac{\partial u_{\varphi}^k}{\partial \varphi} + u_r^k \right) & \frac{1}{2R} \left(\frac{\partial u_{\varphi}^k}{\sin(\psi) \partial \psi} + \frac{\partial u_{\psi}^k}{\partial \varphi} \right) & \frac{1}{2} \left(\frac{1}{R} \left(\frac{\partial u_r^k}{\sin(\psi) \partial \psi} - u_{\psi}^k \right) + u_{\psi}^k \right) \\ \frac{1}{2} \left(\frac{\partial u_{\varphi}^k}{\sin(\psi) \partial \psi} + \frac{\partial u_{\psi}^k}{\partial \varphi} \right) & \frac{1}{R} \left(\frac{\partial u_{\psi}^k}{\sin(\psi) \partial \psi} + u_r^k \right) & \frac{1}{2} \left(\frac{1}{R} \frac{\partial u_r^k}{\partial \varphi} - \frac{u_{\varphi}^k}{R} + u_{\varphi}^k \right) \\ \frac{1}{2} \left(\frac{\partial u_r^k}{\sin(\psi) \partial \psi} - u_{\psi}^k \right) + u_{\psi}^k & \frac{1}{2} \left(\frac{1}{R} \left(\frac{\partial u_r^k}{\partial \varphi} - u_{\varphi}^k \right) + u_{\varphi}^k \right) & u_r^k \end{vmatrix} \tag{24.85}$$

where

$$\underline{u}_i^k(\mathbf{x}_{\alpha}) = \frac{2k+1}{h} (u_i^{k+1}(\mathbf{x}_{\alpha}) + u_i^{k+3}(\mathbf{x}_{\alpha}) + \dots), \quad i = \varphi, \psi, r \tag{24.86}$$

The 2-D Laplacian of the Legendre polynomials coefficients of the displacements vector presented by Eq. (24.55) is significantly simplified and has the form

$$\begin{aligned} \underline{\underline{\nabla}}^2 u_{\varphi}^k &= \Delta_2 u_{\varphi}^k - \frac{u_{\varphi}^k}{R^2} + \frac{2}{R^2} \frac{\partial u_z^k}{\partial \varphi} + \underline{\underline{u}}_{\rho}^k, \\ \underline{\underline{\nabla}}^2 u_{\psi}^k &= \Delta_2 u_{\psi}^k - \frac{u_{\psi}^k}{R^2} + \frac{2(\psi)}{R^2} \frac{\partial u_z^k}{\partial \psi} + \underline{\underline{u}}_{\varphi}^k, \\ \underline{\underline{\nabla}}^2 u_z^k &= \Delta_2 u_z^k - \frac{2u_z^k}{R^2} - \frac{2}{R^2} \frac{\partial u_1^k}{\partial \varphi} - \frac{2(\psi)}{R^2} \frac{\partial u_2^k}{\partial \psi} + \underline{\underline{u}}_z^k, \end{aligned} \tag{24.87}$$

where $\Delta_2 = \frac{1}{R^2} \left(\frac{\partial^2}{\partial \varphi^2} - \cot(\psi)(\psi)^2 \frac{1}{R} \frac{\partial}{\partial \psi} + (\psi)^2 \frac{\partial^2}{\partial \psi^2} \right)$ is 2-D Laplacian of the scalar function in the system of coordinates introduced here. By substituting the equations of motion presented in this section in (24.54) and taking into account that the divergence operator for the Legendre’s polynomial coefficients of the stress tensors has the form of (24.83) we obtain the equations of motion (24.58), where elements of the block matrices and block vectors (24.60) have the form

$$\mathbf{L}_u^{rk} = \begin{bmatrix} \tilde{\mathbf{L}}_{\varphi\varphi}^{rk} & \tilde{\mathbf{L}}_{\varphi\psi}^{rk} & \tilde{\mathbf{L}}_{\varphi r}^{rk} \\ \tilde{\mathbf{L}}_{\psi\varphi}^{rk} & \tilde{\mathbf{L}}_{\psi\psi}^{rk} & \tilde{\mathbf{L}}_{\psi r}^{rk} \\ \tilde{\mathbf{L}}_{r\varphi}^{rk} & \tilde{\mathbf{L}}_{r\psi}^{rk} & \tilde{\mathbf{L}}_{rr}^{rk} \end{bmatrix}, \quad \mathbf{u}^k = \begin{bmatrix} \mathbf{u}_{\varphi}^k \\ \mathbf{u}_{\psi}^k \\ \mathbf{u}_r^k \end{bmatrix}, \quad \tilde{\mathbf{b}}^k = \begin{bmatrix} \tilde{\mathbf{b}}_{\varphi}^k \\ \tilde{\mathbf{b}}_{\psi}^k \\ \tilde{\mathbf{b}}_r^k \end{bmatrix} \quad (24.88)$$

Some elements of these matrices are differential operators, some are constants and some are equal to zero. Below, all elements of the matrices (24.81) for the case of the first order theory of nonlocal shells in the spherical coordinates related to the geometry of the shell are presented in the form

$$\begin{aligned} \tilde{\mathbf{L}}_{\varphi\varphi}^{00} &= \frac{\lambda + 2\mu}{R^2} \frac{\partial^2}{\partial\varphi^2} + \frac{\mu \operatorname{cosec}(\psi)^2}{R^2} \left(\frac{\partial^2}{\partial\psi^2} - \cot(\psi) \frac{\partial}{\partial\psi} \right) - \frac{\mu}{Rh}, \\ \tilde{\mathbf{L}}_{\varphi\psi}^{00} &= \frac{(\lambda + \mu) \operatorname{cosec}(\psi)}{R^2} \frac{\partial^2}{\partial\varphi\partial\psi}, \quad \tilde{\mathbf{L}}_{\varphi r}^{00} = \frac{2\lambda + 3\mu}{R^2} \frac{\partial}{\partial\varphi}, \quad \tilde{\mathbf{L}}_{\psi\varphi}^{00} = \frac{(\lambda + \mu) \operatorname{cosec}(\psi)}{R^2} \frac{\partial^2}{\partial\varphi\partial\psi}, \\ \tilde{\mathbf{L}}_{\psi\psi}^{00} &= \frac{(\lambda + 2\mu) \operatorname{cosec}(\psi)^2}{R^2} \left(\frac{\partial^2}{\partial\psi^2} - \cot(\psi) \frac{\partial}{\partial\psi} \right) + \frac{\mu}{R^2} \left(\frac{\partial^2}{\partial\varphi^2} - 1 \right), \\ \tilde{\mathbf{L}}_{\psi r}^{00} &= \frac{(2\lambda + 3\mu) \operatorname{cosec}(\psi)}{R^2} \frac{\partial}{\partial\psi}, \quad \tilde{\mathbf{L}}_{r\varphi}^{00} = \frac{(2\lambda + 3\mu) \operatorname{cosec}(\psi)}{R^2} \frac{\partial}{\partial\varphi}, \\ \tilde{\mathbf{L}}_{r\psi}^{00} &= \frac{(2\lambda + 3\mu) \operatorname{cosec}(\psi)}{R^2} \frac{\partial}{\partial\psi}, \\ \tilde{\mathbf{L}}_{rr}^{00} &= \frac{\mu}{r^2} \frac{\partial^2}{\partial\varphi^2} + \frac{\mu \operatorname{cosec}(\psi)^2}{R^2} \left(\frac{\partial^2}{\partial\psi^2} - \cot(\psi) \frac{\partial}{\partial\psi} \right) - \frac{4(\lambda + \mu)}{R^2}, \\ \tilde{\mathbf{L}}_{\varphi\varphi}^{01} &= \frac{\mu}{hR}, \quad \tilde{\mathbf{L}}_{\varphi\psi}^{01} = 0, \quad \tilde{\mathbf{L}}_{\varphi r}^{01} = \frac{\mu}{hR} \frac{\partial}{\partial\varphi}, \quad \tilde{\mathbf{L}}_{\psi\varphi}^{01} = 0, \quad \tilde{\mathbf{L}}_{\psi\psi}^{01} = \frac{\mu}{hR}, \quad \tilde{\mathbf{L}}_{\psi r}^{01} = \frac{\lambda \operatorname{cosec}(\psi)}{hR} \frac{\partial}{\partial\psi}, \\ \tilde{\mathbf{L}}_{r\varphi}^{01} &= \frac{\mu}{hR} \frac{\partial}{\partial\varphi}, \quad \tilde{\mathbf{L}}_{r\psi}^{01} = \frac{\mu \operatorname{cosec}(\psi)}{hR} \frac{\partial}{\partial\psi}, \quad \tilde{\mathbf{L}}_{rr}^{01} = -\frac{\lambda}{hR}, \quad \tilde{\mathbf{L}}_{\varphi\varphi}^{10} = -\frac{3\mu}{hR}, \\ \tilde{\mathbf{L}}_{\varphi\psi}^{10} &= 0, \quad \tilde{\mathbf{L}}_{\varphi r}^{10} = \frac{3\mu}{hR} \frac{\partial}{\partial\varphi}, \quad \tilde{\mathbf{L}}_{\psi\varphi}^{10} = 0, \quad \tilde{\mathbf{L}}_{\psi\psi}^{10} = -\frac{3\mu}{hR}, \quad \tilde{\mathbf{L}}_{\psi r}^{10} = \frac{3\mu \operatorname{cosec}(\psi)}{hR} \frac{\partial}{\partial\psi}, \\ \tilde{\mathbf{L}}_{r\varphi}^{10} &= \frac{3\lambda}{hR} \frac{\partial}{\partial\varphi}, \quad \tilde{\mathbf{L}}_{r\psi}^{10} = \frac{3\lambda \operatorname{cosec}(\psi)}{hR} \frac{\partial}{\partial\psi}, \quad \tilde{\mathbf{L}}_{rr}^{10} = \frac{6\lambda}{hR}, \\ \tilde{\mathbf{L}}_{\varphi\varphi}^{11} &= \frac{\lambda + 2\mu}{R^2} \frac{\partial^2}{\partial\varphi^2} + \frac{\mu \operatorname{cosec}(\psi)^2}{R^2} \left(\frac{\partial^2}{\partial\psi^2} - \cot(\psi) \frac{\partial}{\partial\psi} \right) - \frac{\mu(3R^2 - h^2)}{h^2 R^2}, \\ \tilde{\mathbf{L}}_{\varphi\psi}^{11} &= \frac{(\lambda + \mu) \operatorname{cosec}(\psi)}{R^2} \frac{\partial^2}{\partial\varphi\partial\psi}, \quad \tilde{\mathbf{L}}_{\varphi r}^{11} = \frac{2\lambda + 3\mu}{R^2} \frac{\partial}{\partial\varphi} + \frac{\mu \operatorname{cosec}(\psi)}{R} \frac{\partial}{\partial\psi}, \\ \tilde{\mathbf{L}}_{\varphi\varphi}^{11} &= \frac{(\lambda + \mu) \operatorname{cosec}(\psi)}{R^2} \frac{\partial^2}{\partial\varphi\partial\psi}, \\ \tilde{\mathbf{L}}_{\psi\psi}^{11} &= \frac{\mu}{R^2} \frac{\partial^2}{\partial\varphi^2} + \frac{(\lambda + 2\mu) \operatorname{cosec}(\psi)^2}{R^2} \left(\frac{\partial^2}{\partial\psi^2} - \cot(\psi) \frac{\partial}{\partial\psi} \right) + \frac{3\mu}{h^2} - \frac{\mu}{R^2}, \\ \tilde{\mathbf{L}}_{\psi r}^{11} &= \frac{(2\lambda + 3\mu) \operatorname{cosec}(\psi)}{R^2} \frac{\partial}{\partial\psi}, \quad \tilde{\mathbf{L}}_{r\varphi}^{11} = \frac{(2\lambda + 3\mu)}{R^2} \frac{\partial}{\partial\varphi}, \end{aligned}$$

$$\begin{aligned}\tilde{L}_{r\psi}^{11} &= \frac{(2\lambda + 3\mu)\operatorname{cosec}(\psi)}{R^2} \frac{\partial}{\partial\psi}, \\ \tilde{L}_{rr}^{11} &= \frac{\mu}{R^2} \frac{\partial^2}{\partial\varphi^2} + \frac{\mu\operatorname{cosec}(\psi)^2}{R^2} \left(\frac{\partial^2}{\partial\psi^2} - \cot(\psi) \frac{\partial}{\partial\psi} \right) + \frac{3(\lambda + 2\mu)}{h^2} - \frac{4(\lambda + \mu)}{R^2} \quad (24.89)\end{aligned}$$

A complete 2-D system of the differential equations for the higher order theory of nonlocal shell in the spherical system of coordinates related to the geometry of the shell is presented in this section. Explicit expressions for divergences of the Legendre's polynomial coefficients of the stress tensors (24.83), for the Legendre's polynomial coefficients of symmetric strain tensor (24.85) and for Laplacian of the Legendre's polynomial coefficients of the displacements vector (24.87) are presented here. For the case of the first order approximation theory, elements of matrix differential operators (24.88), that are included in the equations of motion (24.58) are also presented in explicit form (24.89). They can be used for theoretical analysis, as well as for analytical and numerical solutions for problems arising in science and engineering.

24.9 Conclusions

In this paper new higher order theories for nonlocal plates and shells have been developed. The 2-D theory is developed from general 3-D equations of nonlocal elasticity using the special curvilinear system of coordinates related to the middle surface of the shell and assuming that the shell is thin. The higher order theory is based on the expansion of the equations of the nonlocal theory of elasticity into Fourier series in terms of Legendre polynomials with respect to a thickness coordinate. All the functions that define the stress-strain state of the shell including stress, strain tensors, vectors of displacements and body forces have been expanded into Fourier series in terms of Legendre polynomials with respect to a thickness coordinate. Thereby, all equations of nonlocal elasticity including constitutive equations have been transformed to the corresponding equations for Fourier coefficients of the expansion. Then, for Fourier coefficients, the system of differential equations of motion in terms of displacements has been obtained in the same way as in the classical theory of elasticity. A complete 2-D system of the differential equations for the higher order theory of nonlocal plates in Cartesian and polar coordinates and of nonlocal cylindrical and spherical shells in cylindrical and spherical system of coordinates related to the geometry of the shell are presented here. Explicit expressions for divergences of the Legendre's polynomial coefficients of the stress tensor, for the Legendre's polynomial coefficients of symmetric strain tensor of the Legendre's polynomial coefficients of displacements vector and for Laplacian of the Legendre's polynomial coefficients of the displacements vector for higher order theory of plates are presented here. For the case of the first order approximation theory, elements of matrix differential operators that are included in the equations of motion are also presented in explicit form. The obtained equations can be used for

stress-strain calculation as well as for modeling thin walled structures in macro, micro and nano scales by taking into account nonlocal effects. Specially proposed models can be efficient in MEMS and NEMS modeling as well as computer simulation.

Acknowledgements The work presented in this paper was supported by the Committee of Science and Technology of Mexico (CONACYT) by the Research Grant (Ciencia Basica, Reference No 256458), which is gratefully acknowledged.

References

- Adali S (2011) Variational principles for vibrating carbon nanotubes modeled as cylindrical shells based on strain gradient nonlocal theory. *Journal of Computational and Theoretical Nanoscience* 8(10):1954–1962
- Altenbach H, Eremeyev V (2009) On the linear theory of micropolar plates. *ZAMM - Journal of Applied Mathematics and Mechanics / Zeitschrift für Angewandte Mathematik und Mechanik* 89(4):242–256
- Altenbach H, Eremeyev VA (2015) On the theories of plates and shells at the nanoscale. In: Altenbach H, Mikhasev GI (eds) *Shell and Membrane Theories in Mechanics and Biology, Advanced Structured Materials*, vol 45, Springer, Cham, pp 25–57
- Altenbach J, Altenbach H, Eremeyev VA (2010) On generalized Cosserat-type theories of plates and shells: a short review and bibliography. *Archive of Applied Mechanics* 80(1):73–92
- Ansari R, Rouhi H, Sahmani S (2014) Free vibration analysis of single- and double-walled carbon nanotubes based on nonlocal elastic shell models. *Journal of Vibration and Control* 20(5):670–678
- Arash B, Wang Q (2012) A review on the application of nonlocal elastic models in modeling of carbon nanotubes and graphenes. *Computational Materials Science* 51(1):303–313
- Arash B, Wang Q (2014) A review on the application of nonlocal elastic models in modeling of carbon nanotubes and graphenes. In: Tserpes KI, Silvestre N (eds) *Modeling of Carbon Nanotubes, Graphene and Their Composites*, Springer, New York, pp 57–82
- Arefi M, Rabczuk T (2019) A nonlocal higher order shear deformation theory for electro-elastic analysis of a piezoelectric doubly curved nano shell. *Composites Part B: Engineering* 168:496–510
- Askari H, Younesian D, Esmailzadeh E, Cveticanin L (2017) Nonlocal effect in carbon nanotube resonators: A comprehensive review. *Advances in Mechanical Engineering* 9(2):1–24
- Carrera E, Zozulya VV (2019) Carrera unified formulation (CUF) for the micropolar beams: Analytical solutions. *Mechanics of Advanced Materials and Structures* online first:1–25

- Carrera E, Brischetto S, Nali P (2011a) *Plates and Shells for Smart Structures. Classical and Advanced Theories for Modeling and Analysis*. John Wiley & Sons, Ltd., New Dehli
- Carrera E, Giunta G, Petrolo M (2011b) *Beam Structures. Classical and Advanced Theories*. John Wiley & Sons, Ltd., New Dehli
- Carrera E, Cinefra M, Petrolo M, Zappino E (2014) *Finite Element Analysis of Structures through Unified Formulation*. John Wiley & Sons, Ltd., New Dehli
- Chakraverty S, Behera L (2017) *Static and Dynamic Problems of Nanobeams and Nanoplates*. World Scientific Publishing Co., Singapore
- Czekanski A, Zozulya VV (2019) Vibration analysis of nonlocal beams using higher-order theory and comparison with classical models. *Mechanics of Advanced Materials and Structures* online first:1–17
- Elishakoff I, Dujat K, Muscolino G, Bucas S, Natsuki T, Wang CM, Pentaras D, Versaci C, Storch J, Challamel N, Zhang Y, Ghyselinck G (2012) *Carbon Nanotubes and Nanosensors: Vibration, Buckling and Ballistic Impact*. Wiley-ISTE
- Eremeyev VA, Altenbach H (2015) On the direct approach in the theory of second gradient plates. In: Altenbach H, Mikhasev GI (eds) *Shell and Membrane Theories in Mechanics and Biology, Advanced Structured Materials*, vol 45, Springer, Cham, pp 147–154
- Eringen AC (1972a) Linear theory of nonlocal elasticity and dispersion of plane waves. *International Journal of Engineering Science* 10(5):425–435
- Eringen AC (1972b) Nonlocal polar elastic continua. *International Journal of Engineering Science* 10(1):1–16
- Eringen AC (ed) (1976) *Continuum Physics*, vol IV. Polar and Nonlocal Field Theories. Academic Press, New York
- Eringen AC (1983) On differential equations of nonlocal elasticity and solutions of screw dislocation and surface waves. *Journal of Applied Physics* 54(9):4703–4710
- Eringen AC (2002) *Nonlocal Continuum Field Theories*. Springer, New York
- Ghavanloo E, Rafii-Tabar H, Fazelzadeh SA (2019) *Computational Continuum Mechanics of Nanoscopic Structures. Nonlocal Elasticity Approaches*. Springer Nature
- Gopalakrishnan S, Narendar S (2013) *Wave Propagation in Nanostructures. Nonlocal Continuum Mechanics Formulations*. Springer, New York
- Hoseinzadeh MS, Khadem SE (2011) Thermoelastic vibration and damping analysis of double-walled carbon nanotubes based on shell theory. *Physica E: Low-dimensional Systems and Nanostructures* 43(6):1146–1154
- Hoseinzadeh MS, Khadem SE (2014) A nonlocal shell theory model for evaluation of thermoelastic damping in the vibration of a double-walled carbon nanotube. *Physica E: Low-dimensional Systems and Nanostructures* 57:6–11
- Hu YG, Liew KM, Wang Q, He XQ, Yakobson BI (2008) Nonlocal shell model for elastic wave propagation in single- and double-walled carbon nanotubes. *Journal of the Mechanics and Physics of Solids* 56(12):3475–3485
- Jha AR (2007) *MEMS and Nanotechnology-Based Sensors and Devices for Communications, Medical and Aerospace Applications*. CRC Press

- Karlicic D, Murmu T, Adhikari S, McCarthy M (2016) *Non-local Structural Mechanics*. John Wiley and Son Inc., Hoboken
- Khoma IY (1987) *Generalized Theory of Anisotropic Shells (in Russ.)*. Naukova Dumka, Kiev
- Kil'chevskii NA (1965) *Fundamentals of the Analytical Mechanics of Shells*. NASA TT, F-292, Washington, D.C.
- Lurie S, Belov P, Altenbach H (2016) Classification of gradient adhesion theories across length scale. In: Altenbach H, Forest S (eds) *Generalized Continua as Models for Classical and Advanced Materials*, Springer, Cham, pp 261–277
- Lyshevski SE (2005) *Nano- and Micro-Electromechanical Systems. Fundamentals of Nano- and Microengineering*, 2nd edn. CRC Press
- Malikan M, Krashennnikov M, Eremeyev VA (2020) Torsional stability capacity of a nano-composite shell based on a nonlocal strain gradient shell model under a three-dimensional magnetic field. *International Journal of Engineering Science* 148:103,210
- Nemish YN, Khoma IY (1993) Stress-strain state of non-thin plates and shells. Generalized theory (survey). *International Applied Mechanics* 29:873–902
- Peddieson J, Buchanan GR, McNitt RP (2003) Application of nonlocal continuum models to nanotechnology. *International Journal of Engineering Science* 41(3):305–312
- Pelekh BL, Sukhorol'skii MA (1980) *Contact Problems of the Theory of Elastic Anisotropic Shells (in Russ.)*. Naukova Dumka, Kiev
- Polizzotto C (2001) Nonlocal elasticity and related variational principles. *International Journal of Solids and Structures* 38(42):7359–7380
- Rogula D (1983) *Nonlocal Theory of Material Media*. Springer, New York
- Vekua IN (1986) *Shell Theory. General Methods of Construction*. Pitman Advanced Pub. Program, Boston
- Voyiadjis GZ (ed) (2019) *Handbook of Nonlocal Continuum Mechanics for Materials and Structures*. Springer Nature
- Wang Q, Liew KM (2007) Application of nonlocal continuum mechanics to static analysis of micro- and nano-structures. *Physics Letters A* 363(3):236–242
- Wang Q, Varadan VK (2007) Application of nonlocal elastic shell theory in wave propagation analysis of carbon nanotubes. *Smart Materials and Structures* 16(1):178–190
- Wang YZ, LI FM (2012) Dynamical properties of nanotubes with nonlocal continuum theory: A review. *SCIENCE CHINA Physics, Mechanics & Astronomy* 55(7):1210–1224
- Zozulya VV (1989) The combined problem of thermoelastic contact between two plates through a heat conducting layer. *Journal of Applied Mathematics and Mechanics* 53(5):622–627
- Zozulya VV (1991a) Contact cylindrical shell with a rigid body through the heat-conducting layer in transitional temperature field. *Mechanics of Solids* (2):160–165
- Zozulya VV (1991b) Laminated shells with debonding between laminas in temperature field. *International Applied Mechanics* 42(7):842–848

- Zozulya VV (2007) Mathematical modeling of pencil-thin nuclear fuel rods. In: Gupta A (ed) *Structural Mechanics in Reactor Technology*, Toronto, vol C, pp C04–C12
- Zozulya VV (2013a) A high-order theory for functionally graded axially symmetric cylindrical shells. *Archive of Applied Mechanics* 83(3):331–343
- Zozulya VV (2013b) A high order theory for linear thermoelastic shells: comparison with classical theories. *Journal of Engineering* 2013(ID 590480):19
- Zozulya VV (2015) A higher order theory for shells, plates and rods. *International Journal of Mechanical Sciences* 103:40–54
- Zozulya VV (2017a) Couple stress theory of curved rods. 2-D, high order, Timoshenko's and Euler-Bernoulli models. *Curved and Layered Structures* 4(1):119–133
- Zozulya VV (2017b) Micropolar curved rods. 2-D, high order, Timoshenko's and Euler-Bernoulli models. *Curved and Layered Structures* 4(1):104–118
- Zozulya VV (2017c) Nonlocal theory of curved rods. 2-D, high order, Timoshenko's and Euler-Bernoulli models. *Curved and Layered Structures* 4(1):221–236
- Zozulya VV (2018a) Higher order couple stress theory of plates and shells. *ZAMM - Journal of Applied Mathematics and Mechanics / Zeitschrift für Angewandte Mathematik und Mechanik* 98(10):1834–1863
- Zozulya VV (2018b) Higher order theory of micropolar plates and shells. *ZAMM - Journal of Applied Mathematics and Mechanics / Zeitschrift für Angewandte Mathematik und Mechanik* 98(6):886–918
- Zozulya VV (2020) Nonlocal theory of a thermoelastic beams and its application to the MEMS/NEMS analysis and simulations. In: Altenbach H, Öchsner A (eds) *Encyclopedia of Continuum Mechanics*, Springer, Berlin, Heidelberg, pp 1892–1903
- Zozulya VV, Saez A (2014) High-order theory for arched structures and its application for the study of the electrostatically actuated MEMS devices. *Archive of Applied Mechanics* 84(7):1037–1055
- Zozulya VV, Saez A (2016) A high order theory of a thermo elastic beams and its application to the MEMS/NEMS analysis and simulations. *Archive of Applied Mechanics* 86(7):1255–1272
- Zozulya VV, Zhang C (2012) A high order theory for functionally graded axisymmetric cylindrical shells. *International Journal of Mechanical Sciences* 60(1):12–22